United States
Environmental Protection
Agency

Atmospheric Sciences Research
Laboratory
Research Triangle Park NC 27711

EPA/600/3-84/110
February 1985

Research and Development

EPA

EPA Complex Terrain Model Development

Fourth Milestone Report - 1984

EPA/600/3-84/110
February 1985

EPA COMPLEX TERRAIN MODEL DEVELOPMENT
Fourth Milestone Report - 1984

by

David G. Strimaitis
Thomas F. Lavery
Akula Venkatram
Donald C. DiCristofaro
Benjamin R. Greene
Bruce A. Egan

ENVIRONMENTAL RESEARCH & TECHNOLOGY, INC.
696 Virginia Road, Concord, Massachusetts 01742

Contract No. 68-02-3421

Project Officer

Francis A. Schiermeier
Meteorology and Assessment Division
Atmospheric Sciences Research Laboratory
Research Triangle Park, North Carolina 22771

ATMOSPHERIC SCIENCES RESEARCH LABORATORY
OFFICE OF RESEARCH AND DEVELOPMENT
U.S. ENVIRONMENTAL PROTECTION AGENCY
RESEARCH TRIANGLE PARK, NORTH CAROLINA 22771

NOTICE

The information in this document has been funded wholly by the United States Environmental Protection Agency under Contract No. 68-02-3421 to Environmental Research and Technology, Inc. It has been subject to the Agency's peer and administrative review, and it has been approved for publication as an EPA document.

Mention of trade names or commercial products does not constitute endorsement or recommendation for use.

FOREWORD

The Atmospheric Sciences Research Laboratory (ASRL) conducts intramural and extramural research programs in the physical sciences to detect, define, and quantify air pollution and its effects on urban, regional, and global atmospheres and the subsequent impact on water quality and land use. The Laboratory is responsible for planning, implementing, and managing research and development programs designed to quantify the relationships between emissions of pollutants for all types of sources with air quality and atmospheric effects, and to uncover and characterize hitherto unidentified air pollution problems. Information from ESRL programs and from the programs of other government agencies, private industry, and the academic community are integrated by the Laboratory to develop the technical basis for air pollution control strategies for various pollutants.

The Complex Terrain Model Development (CTMD) program is designed to develop reliable atmospheric dispersion models that are applicable to large pollutant sources located in complex terrain. The major field studies of this six-year program were conducted during 1980 at Cinder Cone Butte near Boise, Idaho, during 1982 at Hogback Ridge near Farmington, New Mexico, and during 1983-84 at the Tracy Power Plant near Reno, Nevada. Data from these field studies along with measurements of fluid modeling simulations performed in the EPA Fluid Modeling Facility are being used to quantify the effects of terrain obstacles on stable plume dispersion. A series of annual milestone reports has been issued to describe the development of the Complex Terrain Dispersion Model (CTDM) and to contrast the performance evaluation of the CTDM against existing complex terrain dispersion models. This Fourth Milestone Report describes the continuing development of the CTDM and evaluates the improved model's performance using measurement data from the field studies.

A. H. Ellison
Director
Atmospheric Sciences Research Laboratory

ABSTRACT

The Complex Terrain Model Development (CTMD) program is being sponsored by the U.S. Environmental Protection Agency to develop, evaluate and refine practical models for calculating ground-level air pollutant concentrations in mountainous terrain. The emphasis of the program is to develop models with known accuracy and limitations for simulating 1-hour concentrations in high terrain during stable conditions. At the time of preparation of this Fourth Milestone Report, two small hill impaction studies and a feasibility study at a full scale site, the Tracy Power Plant near Reno, Nevada have been conducted. This report describes the continuing modeling and analysis of the Cinder Cone Butte (CCB) and Hogback Ridge (HBR) data bases, results from the feasibility study, and plans for the Full Scale Plume Study (FSPS).

Substantial progress has been made in the development of the Complex Terrain Dispersion Model (CTDM) as a method for simulating tracer gas concentrations at CCB and as a practical regulatory model. CTDM includes explicit mathematical expressions that account for the important phenomena that control dispersion in mountainous terrain. The model also includes a method to use turbulence intensity measurements to estimate the vertical growth of a plume with downwind distance. The current version of CTDM was evaluated by comparing model calculations to (1) observed SF_6 concentrations, (2) concentration estimates based on a flat terrain model, and (3) concentration estimates based on the COMPLEX I/II plume path assumptions. The performance statistics show CTDM does better than the other two approaches in simulating concentrations observed at CCB.

To help understand the phenomena that control dispersion at the ridge site a simple empirical modeling approach was taken. A model was constructed by modifying the effective plume height as a function of H_c. Model simulations were performed using a subset of the SHIS #2 CF_3Br data base. These empirical model calculations were compared to observed CF_3Br concentrations and to calculations made with a flat terrain model and a model based on the half-height plume path assumption. The empirical model performed better than the other two models. Furthermore, for both CCB and HBR the flat terrain model underestimated concentrations while the COMPLEX (or half-height) model overestimated concentrations by roughly a factor of two.

The FSPS was conducted at the Tracy Power Plant (TPP) near Reno, Nevada in August 1984*. The Tracy station was selected based on a

*The FSPS will be discussed in the Fifth Milestone Report (June 1985).

feasibility study conducted at the site in November 1983. The feasibility experiment resulted in a data base that is useful for modeling and for showing the important differences between a full scale site and the two small hill sites. This Fourth Milestone Report presents a discussion of an initial analysis of the November Tracy data base and the plans for the FSPS.

This milestone report also includes two appendices prepared by scientists at the EPA Fluid Modeling Facility. Appendix A contains a report describing the results of a towing tank study designed to evaluate the validity of modeling a plume in the flow above H_c as if both the plume height and the terrain height were reduced by H_c. Appendix B contains a report describing a wind tunnel study designed to identify source-terrain relationships for which the effect of an idealized model of CCB on ground-level concentrations is greatest.

This report was submitted in partial fulfillment of contract 68-02-3421 by Environmental Research & Technology, Inc. under the sponsorship of the U.S. Environmental Protection Agency. This report covers the period June 2, 1983 to June 1, 1984.

CONTENTS

FIGURES

FIGURES (Continued)

FIGURES (Continued)

FIGURES (Continued)

FIGURES (Continued)

FIGURES (Continued)

FIGURES (Continued)

TABLES

TABLES (Continued)

SYMBOL	
a	Ratio of σ_w to u_*
a(z)	Radius of an ideal hill circular in horizontal cross section
α	Relaxation scale factor for decrease in terrain effect away from hill
ß	Boundary layer profile parameter
C	Concentration
C_m	Mean concentration from many "filament" plumes
C_o	Observed concentration
C_p	Modeled concentration
χ	Concentration
D	Diffusivity
D_m	Mean diffusivity over the interval s s_o
δ	Scale factor for LIFT-WRAP transition zone
Δh	Plume height change due to buoyancy of emission
ε	Error or residual
F	Buoyancy flux
Fr	Froude number based on hill height
Fr_L	Froude number based on hill length
F_u, F_v	Correction factors for non-cosine response of UVW propellers
g	Acceleration due to gravity
γ	Scale factor for the "stable" mixing length
Γ	Scale factor for the "neutral" mixing length
h	Terrain elevation above a reference elevation
h	Peak height (GC output signal)
H	Hill height (crest)
H_c	Critical dividing-streamline height
K_H	Eddy diffusivity for heat
K_z	Eddy diffusivity for momentum
θ_r	Direction from effective receptor position to source
θ	Wind direction

θ	Potential temperature
θ_s	Direction of the stagnation streamline
θ_m	Mean wind direction of approach flow
i_x, i_y, i_z	Turbulence intensities alongwind, crosswind, and vertical
k	Von Karman constant
L	Monin Obukhov length
ℓ	Mixing length
ℓ_n	Neutral mixing length
ℓ_s	Stable mixing length
λ	Wavelength of disturbances generated by the hill
m_a	Arithmetic mean
m_g	Geometric mean
N	Number
N	Brunt-Vaisala frequency
N_b	Bulk Brunt-Vaisala frequency for a layer
p	Power for wind speed profile power law
$P(\theta)$	Wind direction probability distribution function
$P(H_c')$	H_c probability distribution function
P	Pressure
ϕ_H	Nondimensional potential temperature gradient
Q	Source strength (mass flow rate)
Q_o	Kinematic heat flux
ρ	Density
r	Distance from source to hill center
R*	Universal gas constant
s	Distance from source to receptor along wind direction
(s,ℓ,h)	General point in a cartisian coordinate system with s-axis aligned with the mean flow, where s is the distance from the source
s_a	Arithmetic standard deviation
s_b	Distance from the source to the base of the hill
s_g	Geometric standard deviation
s_m	Mean of s and s_o

s_o	Distance along wind direction from source to terrain at the elevation of H_c for the LIFT domain; distance to terrain at the elevation of the receptor for the WRAP domain
s_r	Distance from source to receptor
σ	Standard deviation
σ_{Hc}	Standard deviation of H_c
σ_u	Standard deviation of alongwind velocity fluctuations about the mean wind
σ_v	Standard deviation of crosswind velocity fluctuations about the mean wind
$\sigma_{v\tau}$	σ_v value obtained for a sampling duration τ
$\sigma_{v\infty}$	σ_v value obtained for an infinite sampling duration
σ_w	Standard deviation of vertical velocity fluctuations
σ_y, σ_z	Crosswind horizontal and vertical standard deviation of tracer concentrations
σ_y^*, σ_z^*	σ_y and σ_z for a plume from point source element for the interval $s - s_o$
σ_{yo}, σ_{zo}	Value of σ_y and σ_z at $s = s_o$
σ_{ye}, σ_{ze}	Effective σ_y and σ_z after accounting for all terrain effects up to the location of the model receptor
σ_{ym}	Standard deviation of the horizontal meander component of the wind fluctuations
σ_{yT}	Total σ_y including terrain effects (σ_{ye}) on the "filament" plume and meander
σ_{zT}	Total σ_z including terrain effects (σ_{ze}) on the "filament" plume and H_c variations
σ_{zu}	Plume spread above plume centerline height
$\sigma_{z\ell}$	Plume spread below plume centerline height
T, T_o	Temperature
t	Time
T_h	Terrain factor for streamline distortion in the vertical direction
T_ℓ	Terrain factor for streamline distortion in the lateral direction

T_u	Terrain factor for plume transport speed
T_*	Scaling temperature
$T_{\sigma y}, T_{\sigma z}$	Terrain factors for diffusivity
T_y, T_z	Ratio of streamline distortion factor to diffusivity factor
T_E	Eulerian time scale
T_{iy}, T_{iz}	Terrain factors for turbulence intensity
T_L	Lagrangian time scale
T_{LT}	Lagrangian time scale of the transverse correlogram
T_m	Time scale of molecular mixing
T_P	Partial height factor (terrain factor)
t_ℓ	Time of travel below plume centerline height
t_u	Time of travel above plume centerline height
t	Sampling duration
u	Generic wind speed
u_*	Friction velocity
U_T	Wind tunnel transport wind speed
U_r	Wind speed at release height
(x,y,z)	General cartisian coordinates
x_{sep}	Distance of flow separation point from hill crest
x_r, y_r, z_r	Tracer release coordinates
x_R, y_R, z_R	Receptor coordinates
z_r	Plume release height
z_r^*	Plume centerline height after accounting for wind shear

ABBREVIATIONS

ARLFRD	Air Resources Laboratory Field Research Division
ASRL	Atmospheric Sciences Research Laboratory
ATDL	Atmospheric Turbulence and Diffusion Laboratory
cm	Centimeters
C	Centigrade
CF_3Br	Freon
CCB	Cinder Cone Butte
CSU	Colorado State University
CTDM	Complex Terrain Dispersion Model

CTMD	Complex Terrain Model Development
DEC	Digital Equipment Corporation
EPA	U.S. Environmental Protection Agency
EPRI	Electric Power Research Institute
ERT	Environmental Research & Technology, Inc.
FMF	Fluid Modeling Facility
ft	Feet
FSPS	Full Scale Plume Study
GC	Gas chromatograph
GLC	Ground level concentration
HBR	Hogback Ridge
Hz	Hertz
km	Kilometers
lb	Pounds
LASL	Los Alamos Scientific Laboratory
LMF	Linear mass flow meter
m	Meters
MCO	Maximum observed concentration
MCP	Maximum predicted concentration
MDA	Modelers' Data Archive
MDT	Mountain Daylight Time
MRI	Meteorology Research, Inc.
MSL	Mean Sea Level
MW	Megawatts
$\mu s/m^3$	Micro seconds per cubic meter
NAWC	North American Weather Consultants
NOAA	National Oceanic and Atmospheric Administration
ns/m^3	Nano-seconds per cubic meter
ppb	Parts per billion by volume
ppt	Parts per trillion by volume
PDF	Probability distribution function
PNM	Public Service Company of New Mexico
PPC	Plume path coefficient
PST	Pacific Standard Time
RTD	Resistance Thermometric Device

RTI	Research Triangle Institute
s	Seconds
SF_6	Sulfur hexafluoride
SHIS	Small Hill Impaction Study
TPP	Tracy Power Plant
TRC	TRC Environmental Consultants, Inc.
WPL	Wave Propagation Laboratory
WSSI	Western Scientific Services, Inc.

ACKNOWLEDGEMENTS

Many people have contributed their talents and energies to maintain continuing progress in the EPA CTMD program. In particular, we gratefully acknowledge the efforts of the following individuals:

- Bill Snyder and his colleagues at the EPA Fluid Modeling Facility who have performed many towing tank and wind tunnel simulations in support of the modeling;

- Wynn Eberhard and his colleagues at the Wave Propagation Laboratory who have supplied the lidar data and many meteorological measurements;

- Julian Hunt and Rex Britter of Cambridge University for their ideas and recommendations on modeling stable conditions in complex terrain and with whom we have had many useful discussions;

- Steve Andersen and Chris Johnson of ERT in Fort Collins who operated the 150-m meteorological tower and were responsible for all CTMD logistics at the Tracy Power Plant; and

- Ray Dickson and his staff at NOAA ARLFRD who were responsible for the flow visualization and tracer experiments.

We would like to acknowledge the Electric Power Research Institute (EPRI) who co-sponsored the November 1983 experiment at Tracy, and the EPRI contractors (Rockwell International, SRI International, TRC Environmental Consultants, and the Research Triangle Institute). Special thanks go to Mark Cher of Rockwell who provided the tracer gas data discussed in Section 5.

Finally, we give special thanks to Frank Schiermeier and George Holzworth, whose enthusiasm, support and encouragement have really helped us progress.

SECTION 1

INTRODUCTION

The U.S. Environmental Protection Agency (EPA) Complex Terrain Model Development (CTMD) project is a multi-year study to develop improved models for calculating ground level air pollutant concentrations that result from large emission sources located in mountainous terrain. At this time, the focus of the project is to develop models for simulating 1-hour average concentrations during stable atmospheric conditions.

These models are to be used in a wide variety of applications, such as the siting of new energy-development facilities and other sources of air pollution, regulatory decision making, and environmental planning. Therefore, the models should be easy to understand, easy to use, and of known accuracy and limitations. The CTMD project will recommend the types and extent of meteorological measurements needed to derive input to the models.

The objectives of the program were described by Holzworth (1980) and generally follow the recommendations of the participants of the EPA sponsored workshop to consider the issues and problems of simulating air pollutant dispersion in complex terrain (Hovind et al. 1979). The program was subsequently designed with a perspective toward modeling and includes model development efforts based on physical modeling, field experiments and theoretical work. The project started with field experiments and physical modeling for isolated simple terrain features and has progressed to the Full Scale Plume Study (FSPS), which was conducted at the Tracy Power Plant near Reno, Nevada in August 1984.

The program was begun in June 1980. The first major component was the Small Hill Impaction Study #1 (SHIS #1), a field experiment* conducted during the fall of 1980 at Cinder Cone Butte (CCB), Idaho.

* The prime contractor for the CTMD is Environmental Research & Technology, Inc. (ERT). The principal subcontractors for the CCB experiments were Western Scientific Services, Inc. (WSSI), responsible for fixed meteorological data (towers, instrumentation and data communication) and North American Weather Consultants (NAWC), responsible for the experimental field program (tracer and smoke releases, tracer data collection, photography, mobile meteorology, and field logistics). In allied activities, the EPA Fluid Modeling Facility (FMF) provided laboratory fluid modeling support; the NOAA Wave Propagation Laboratory (WPL) supported the field program with a manned lidar system; and TRC Environmental Consultants, Inc. provided independent data audits.

CCB is a roughly axisymmetric, isolated 100 meter tall hill located in the broad Snake River Basin near Boise, Idaho. The field program consisted of ten flow visualization (oil-fog) experiments and 18 multi hour tracer gas experiments with supporting meteorological, lidar and photographic measurements.

The second Small Hill Impaction Study (SHIS #2)** was conducted during October 1982 at the Hogback Ridge (HBR) near Farmington, New Mexico. SHIS #2 included tracer and flow visualization experiments with concurrent meteorological, lidar and photographic measurements. The experiment produced approximately 179 tracer hours and extended the modeling data base to include flow and dispersion around a two-dimensional ridge.

During the course of the CTMD project, three Milestone Reports (Lavery et al. 1982; Strimaitis et al. 1983; and Lavery et al. 1983) have been published. These reports, which are available from EPA, describe the progress in developing and evaluating complex terrain models using the CCB and HBR data bases. They also describe in detail the two Small Hill studies and a series of towing tank and wind tunnel studies performed at the EPA Fluid Modeling Facility (FMF) in support of the modeling.

This Fourth Milestone Report documents work accomplished from June 1983 through May 1984. It describes the further development of the Complex Terrain Dispersion Model (CTDM). In particular, it provides a detailed mathematical description of CTDM and shows how the important terrain effects on plume dispersion are specifically handled in the model. This latest version of CTDM has been tested using the CCB data base. An 80-hour subset of the data base has been partitioned into four classes: neutral, weakly stratified, impingement and very stable. CTDM calculations were compared to observed SF_6 concentrations and to concentrations calculated with (1) a flat terrain model and (2) a model that uses the COMPLEX I/II plume path assumptions. The results show that CTDM performs significantly better than the other models.

CTDM was also used to test the importance of using high resolution, onsite meteorological measurements as the basis for input to the model calculations. CTDM calculations were done with two sets of input data: (1) derived from the CCB Tower A 10-m and 150-m data and (2) derived from the 10-m data only. The results confirm the importance of using onsite turbulence data and measured vertical profiles of temperature and winds in the model simulations.

** During SHIS #2, ERT was responsible for field management, the 150 m and 60-m towers, site logistics, and quality assurance. Through an Interagency Agreement with EPA, NOAA Air Resources Laboratory Field Research Division (ARLFRD) conducted the flow visualization and tracer experiments, was responsible for the 10 m and 30-m towers, and operated a real-time data acquisition and analysis system. NOAA WPL provided lidar, acoustic sounders, a tethersonde, and optical and sonic anemometers. TRC provided independent performance audits.

This Fourth Milestone Report also presents the progress in refining the SHIS #2 tower meteorological data. It discusses new modeling of the HBR CF_3Br data base. To get an understanding of the phenomena that influence dispersion at a ridge setting, an empirical modeling approach was taken. The results again confirm the usefulness of the concept of a dividing-streamline (H_c) in discriminating between essentially horizontal flow and flows that go over HBR.

The Full Scale Plume Study (FSPS) was conducted at the Tracy Power Plant (TPP) near Reno, Nevada in August 1984. The Tracy station was selected based on a feasibility study conducted at the site in November 1983. The feasibility experiment resulted in a data base that is useful for modeling and for showing the important differences between a full scale site and the two Small Hill sites. This milestone report presents a discussion of an initial analysis of the November Tracy data base and the plans for the FSPS.

This report consists of a total of six sections and three appendices. Section 2 provides a detailed mathematical description of CTDM while Section 3 presents an evaluation of CTDM using the CCB data base. Section 4 presents the analysis and modeling of the Hogback data base. The results of the preliminary Tracy experiment and the plans for the FSPS are given in Section 5. Section 6 presents the summary, conclusion, and recommendations for future work.

Appendix A contains a report prepared by the EPA FMF describing the results of a towing tank study designed to evaluate the validity of modeling a plume in the flow above H_c as if both the plume height and the terrain height were reduced by H_c. Appendix B contains another report prepared by the EPA FMF describing a wind tunnel study designed to identify source-terrain relationships for which the effect of an idealized model of CCB on ground-level concentrations is greatest. Appendix C contains an overview of the ALPHA-1 airborne lidar observations of the oil-fog plume during the November 1983 preliminary experiment at the Tracy Power Plant near Reno, Nevada.

SECTION 2

THE COMPLEX TERRAIN DISPERSION MODEL

The Complex Terrain Dispersion Model (CTDM) is a point source plume model which incorporates several concepts about stratified flow and dispersion over an isolated hill. The emphasis to date has been on including those phenomena that are thought to be important in controlling the magnitude and distribution of plume concentrations across CCB and HBR. Although the formulation of modeling concepts contained in CTDM has general inherent applicability, certain details make explicit use of the geometry of CCB and HBR to simplify the code. Consequently, CTDM should be viewed as a research code at this time rather than a code suitable for regulatory applications.

We expect CTDM to evolve during the CTMD project. As more data are analyzed from SHIS #1 and SHIS #2, the specific formulations will change as will the range of phenomena contained in the model. In addition, analysis and modeling of the FSPS data that were obtained in August 1984 will undoubtedly require a more general treatment of terrain in the model, and certainly the inclusion of new phenomena. These changes will be treated as updates to CTDM rather than the basis for new model nomenclature.

A central feature of CTDM is its use of a critical dividing-streamline height (H_c) to separate the flow into two discrete layers. This basic concept was suggested by theoretical arguments of Drazin (1961) and Sheppard (1956) and was demonstrated through laboratory experiments by Riley et al. (1976), Brighton (1978), Hunt and Snyder (1980), Snyder et al. (1980) and Snyder and Hunt (1983). The flow below H_c is restricted to lie in a nearly horizontal plane, allowing little motion in the vertical. Consequently, plume material below H_c travels along and around the terrain, rather than up and over the terrain. The flow above H_c is allowed to rise up and over the terrain. Two separate components of CTDM compute ground-level concentrations resulting from material in each of these flows. LIFT handles the flow above the H_c, and WRAP handles the flow below H_c.

The following subsections contain descriptions of the LIFT and WRAP components, and also descriptions of the plume spread formulations contained in CTDM, and adjustments made to the plume height to account for buoyancy effects and wind speed shear effects.

2.1 The LIFT Component

The flow above H_c is considered to be weakly stratified. That is, the stratification is strong enough to influence the flow pattern (e.g., lee waves), but not strong enough to inhibit significant vertical motion. To simplify the modeling task, H_c is assumed to be a level surface, and the flow above H_c only "sees" that portion of the hill that lies above H_c.

A fluid modeling study has been performed by Snyder and Lawson at the EPA FMF to assess the utility of this approximation. The results of this study, presented in Appendix A, confirm that this approximation is reasonable with regard to estimating the locations and values of maximum ground-level concentrations and areas of coverage on the windward side of the hill. Poorer correspondence is found in the lee of the hill for plumes released well above H_c, and this is apparently due to lee wave effects.

The plume is allowed to develop as if the terrain were perfectly flat until it reaches the point where the H_c surface intersects the hill (at $x = x_r + s_o$, see Figure 1). If H_c is zero, then this zone extends from the source to the base of the hill, although it conceptually could extend to any point where the hill is thought to exert a significant influence on the flow. Beyond s_o, the plume material below H_c is disregarded by the LIFT component, and the evolution of the remaining material is modeled as if the terrain were flat, and the lower boundary were H_c (with full reflection). However, the wind speed, plume height above H_c, plume spread, and lateral position of the plume centerline relative to the receptor are all modified to reflect the net alteration of these properties between s_o and s (the distance from the source to the receptor) induced by the presence of the hill. The simplicity of the Gaussian plume solution is retained in this way, while the full dilution of the plume from the source to the hill (s_o) as well as the effects of the hill on both flow and dispersion beyond s_o are explicitly incorporated.

Aside from the obvious distinction of incorporating the primary influence of H_c on the plume-terrain interaction, this approach notably differs from the current regulatory modeling approach (at least as embodied in COMPLEX I and II) in that the terrain influence for a receptor on a hill only affects the diffusion of the plume once it is over the terrain. The mathematical formulation of the "partial plume height correction" approach of COMPLEX and similar models actually "lowers" the plume at the source. If this technique were engineered to produce the "correct" hill-influenced ground-level concentrations, the terrain correction factor for a particular receptor would need to be a function of downwind distance, terrain shape, and distance between source and terrain. As employed in regulatory modeling, however, the terrain correction factor depends only on the stability class, so that its use has led to problems of interpreting "surface reflection" from sloping terrain, as well as to problems in justifying values chosen for the terrain correction factor.

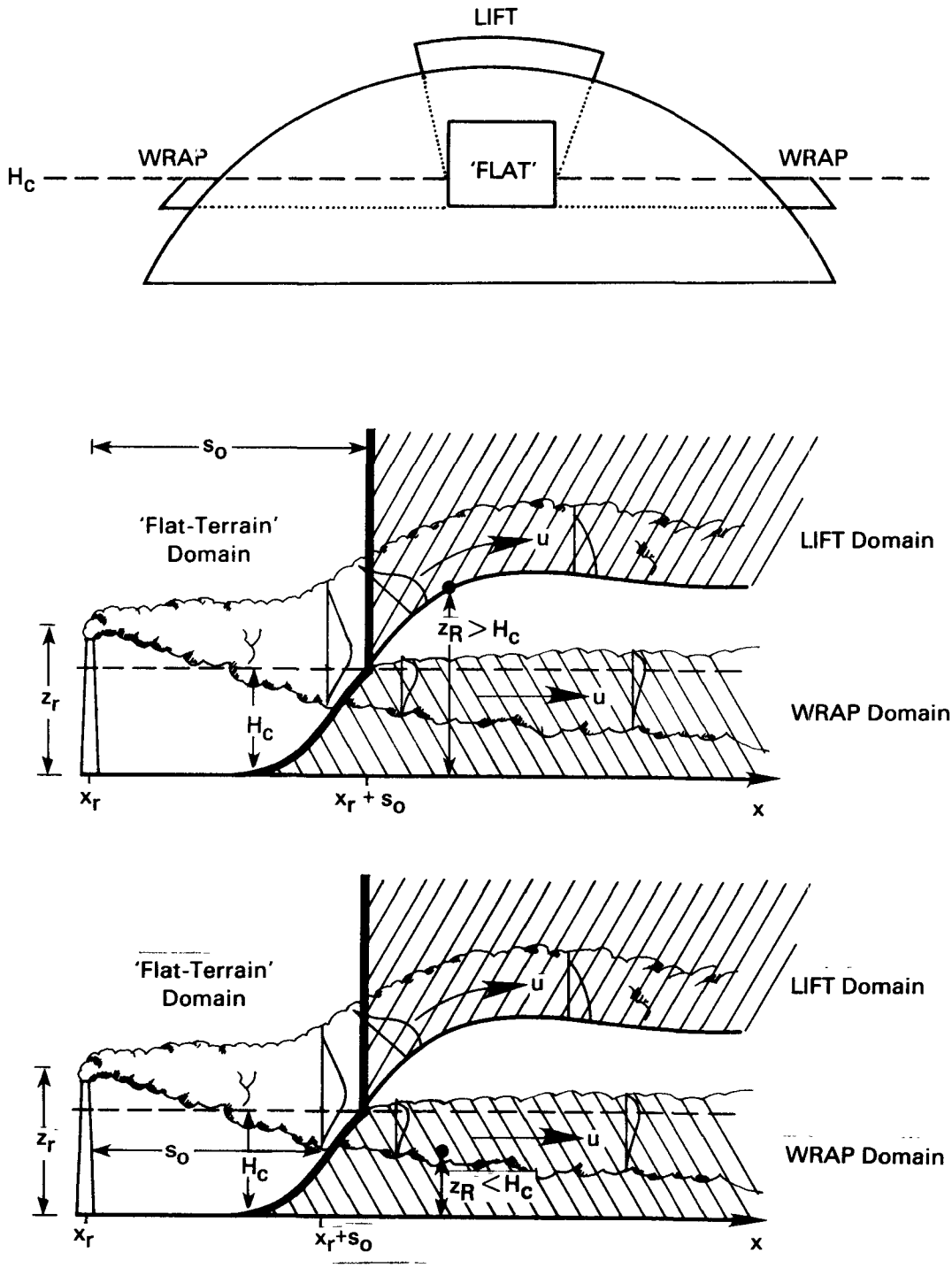

Figure 1. Idealized stratified flow about hills indicating domain of individual CTDM component algorithms. The distance s_o is the distance from the source to the intersection of H_c with the hill surface for receptors above H_c (the LIFT domain), and it is the distance from the source to the terrain-height contour equal in height to the receptor elevation for receptors below H_c (the WRAP domain). Note that in the upper figure the flow is into the page.

Terrain-induced modifications to the plume arise from the distortion of the flow over the hill. A streamline of the flow will be deflected to the side (unless it lies in a plane of symmetry) and its height above the surface will be reduced. Adjacent streamlines are deflected in much the same way, but are generally displaced by differing amounts, which in turn changes the spacing between streamlines and hence, causes changes in the local speed of the flow. As a result, the actual plume trajectory is curved, the time of travel does not vary linearly with distance, the plume distorts so that it is thinner in the vertical direction and wider in the lateral direction, the turbulence statistics vary, and as shown in Hunt and Mulhearn (1973), turbulent diffusion across streamlines is enhanced by the contraction in the distance between streamlines in the vertical direction, and retarded by the expansion in the distance between streamlines in the lateral direction.

Hunt and Mulhearn explicitly track these changes through the use of line integrals along the streamline that coincides with the plume centerline. LIFT has been designed to take average values of the changes in flow properties over the interval between s_o and s. These average values then guide the distortion applied to the concentration distribution at the distance s_o, and the flow speed used in the subsequent calculations. In essence, LIFT distorts the plume at s_o by an amount representative of the average distortion in the flow between s_o and s; it removes the hill and displaces the plume toward the surface by an amount representative of the average height of plume above the hill surface between s_o and s; and it then uses a flat terrain computation to estimate the effect of these distortions on the diffusion of material to the surface over the interval $s-s_o$. Hence, a continuous process is represented by a two-step process in which the distortion of the flow and the diffusion of the plume in the distorted flow are treated successively. This approach, while not as rigorous as the Hunt and Mulhearn approach, allows us to develop a modeling framework in which the terrain effects appear as simple factors within the flat terrain solution.

2.1.1 LIFT Structure

The terrain effect as modeled in LIFT includes re-initializing the flow at a distance s_o downwind of the release. This re-initialization can be illustrated first for flat terrain and uniform flow. The concentration at a receptor downwind of s_o is composed of contributions from the entire concentration distribution above H_c at s_o. Conceptually, the flux of plume material through the plane $x = x_r + s_o$ (note that the x-axis lies along the flow direction, and the plume is released at x_r, y_r, z_r) can be thought of as a distribution of point sources. If we track the plume material in terms of the distance downwind of the source, $s = x - x_r$, then the source strength of one of these point source elements is given by:

$$dQ(s_o,y,z) = C(s_o,y,z)u\ dy\ dz \qquad (1)$$

Because the flow beyond s_o is considered to be uniform, the influence of each of these sources follows the Gaussian plume solution to the advective diffusion equation:

$$dC(s,\ell,h;s_o) = \frac{dQ(s_o,y,z)}{2\pi\sigma_y^*\sigma_z^* u} \; e^{-0.5(\frac{y-\ell}{\sigma_y^*})^2} \; (e^{-0.5(\frac{z-h}{\sigma_z^*})^2} + e^{-0.5(\frac{z+h}{\sigma_z^*})^2}) \qquad (2)$$

where σ_y^*, σ_z^* denote the plume spread statistics for each point source element over the interval $s - s_o$ (see Figure 2a). The total concentration at a point (s,ℓ,h) is found by integrating Equation 2 over all point source elements, so that

$$C(s,\ell,h;s_o) = \int_0^{\infty} \int_{-\infty}^{+\infty} \frac{C(s_o,y,z)}{2\pi\sigma_y^*\sigma_z^* u} \; e^{-0.5(\frac{y-\ell}{\sigma_y^*})^2} (e^{-0.5(\frac{z-h}{\sigma_z^*})^2} + e^{-0.5(\frac{z+h}{\sigma_z^*})^2}) dy \; dz \qquad (3)$$

The plume spread statistics σ_y^* and σ_z^* for the interval $s-s_o$ are specified by the requirement that Equation 3 for flat terrain reduces to the expression obtained for the original point source located at $s = 0$. Equating the two expressions for C, where $h = 0$ for convenience,

$$\sigma_z^{*2} = \sigma_z^2(s) - \sigma_z^2(s_o) \equiv \sigma_z^2 - \sigma_{zo}^2 \qquad (4a)$$

$$\sigma_y^{*2} = \sigma_y^2(s) - \sigma_y^2(s_o) \equiv \sigma_y^2 - \sigma_{yo}^2 \qquad (4b)$$

Equations 3 and 4 illustrate the re-initialization technique for the limiting case of flat terrain and uniform flow. Overcamp (1983) has developed a similar technique for replacing a simple image source in a general treatment of the lower boundary condition for the case of non-Fickian diffusion.

Terrain influences are incorporated by <u>deforming</u> the source distribution at s_o (Equation 1), and by <u>altering</u> the flow in which the source elements diffuse. For a receptor located at (s,y_R) on the <u>surface</u> of a hill ($h = 0$), the concentration due to one elemental point source is obtained at $(s,y_R,0)$ through Equation 2 by replacing $y,z,\sigma_y^*,\sigma_z^*$, and u with y', z', $\sigma_y^{*'}$, $\sigma_z^{*'}$, and u' to simulate the average change in these properties over the interval $s-s_o$, caused by the influence of the terrain; and by introducing H_c' as the lower boundary--the effective hill surface. This treatment is illustrated in Figures 2b, 3a, and 3b.

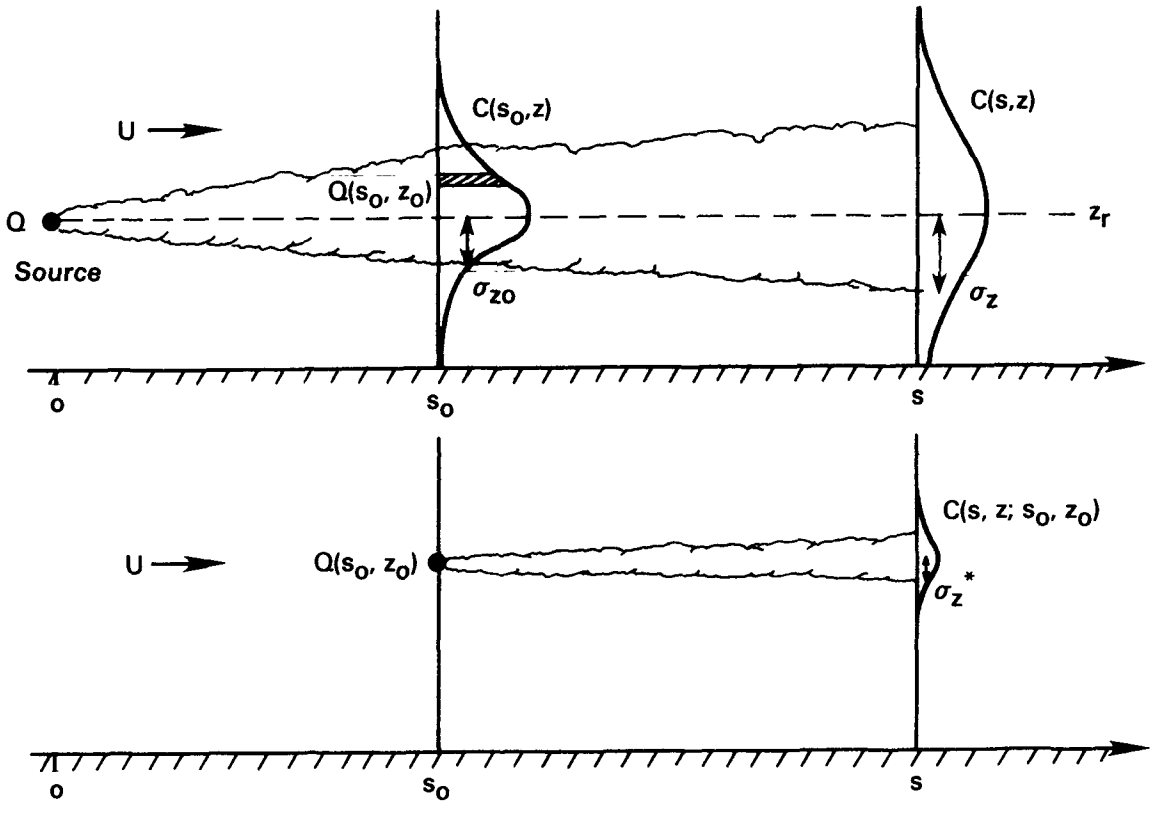

$$C(s, z) = \int_0^\infty C(s, z; s_o, z_o)dz_o$$

where $\sigma_z^{*2} = \sigma_z^2 - \sigma_{zo}^2$

Figure 2a. Illustration of the relationship between the crosswind-average concentration profiles at s_o and s, and the plume from one of many point-source elements representing the flux of material across the plane at s_o. The total concentration at a particular point C(s,z) is constructed by summing the contribution $C(s,z; s_o,z_o)$ from each point-source element $Q(s_o,z_o)$.

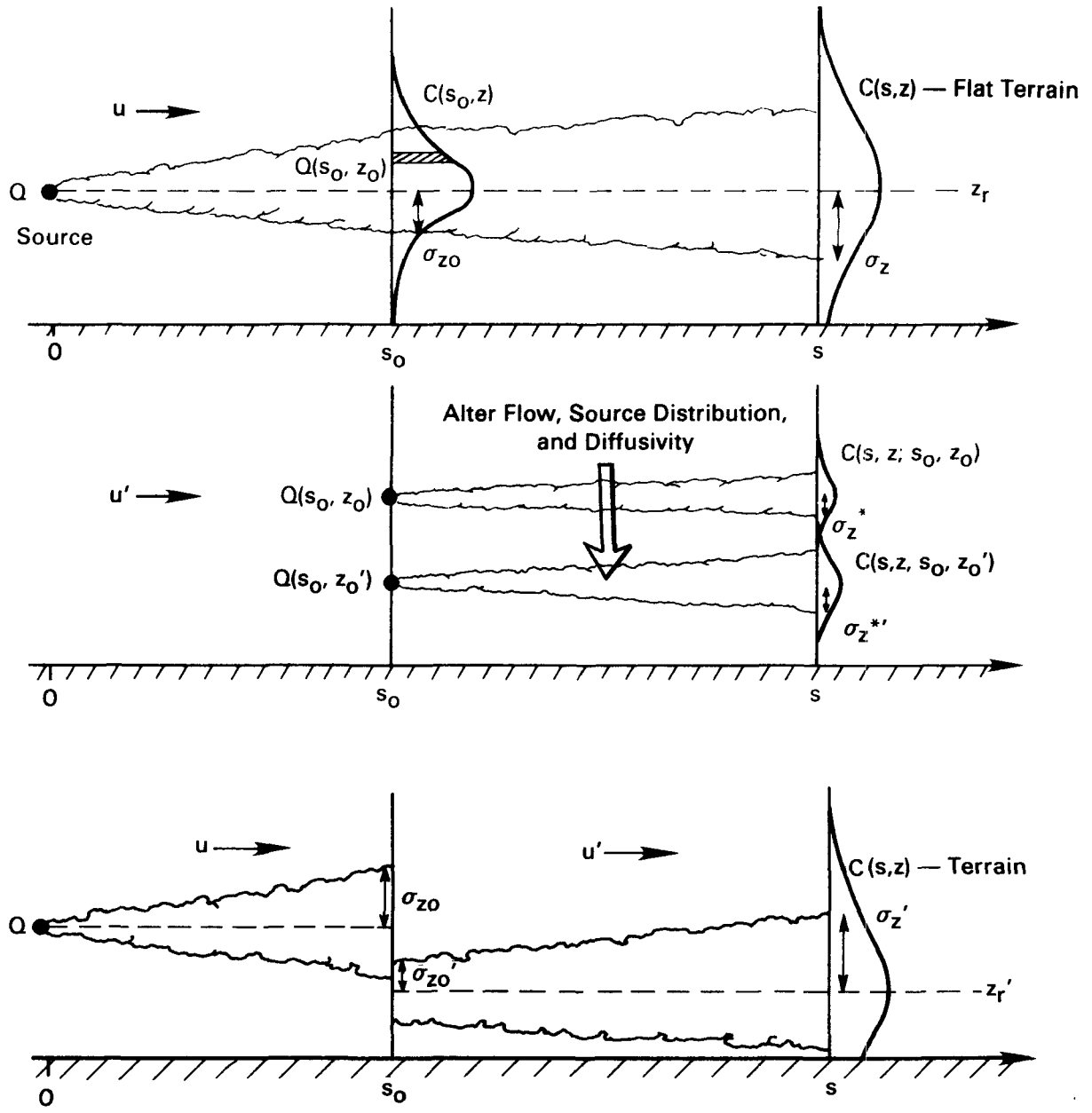

Figure 2b. Illustration of simulating terrain effects by shifting the point-source elements at s_o and altering the diffusivity and flow speed beyond s_o. All source elements are lowered by the factor $T_h = z_o'/z_o$, and the diffusivity in the altered flow is changed by the factor $T_{\sigma z} = \sigma_z^{*'}/\sigma_z^{*}$.

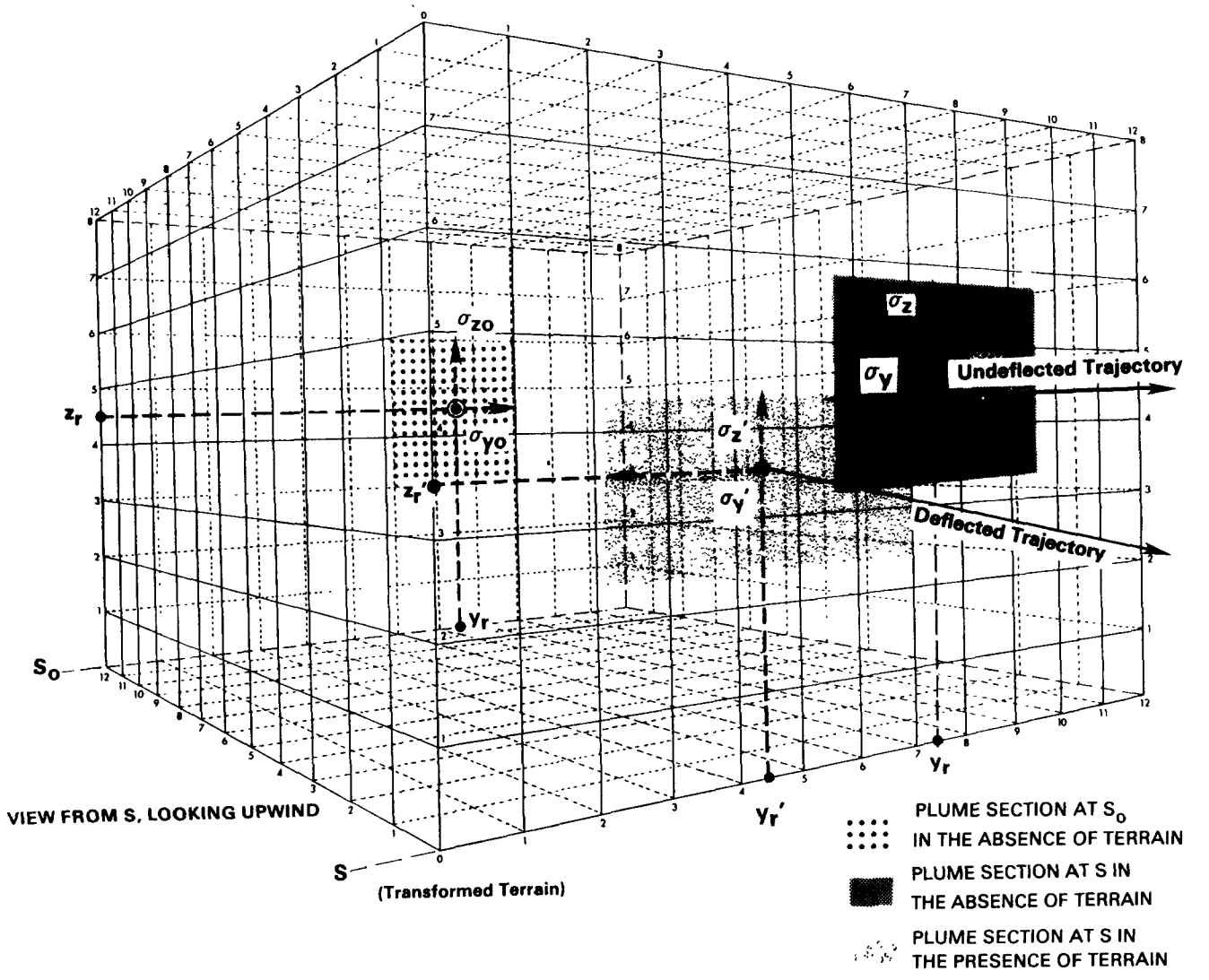

Figure 3a. Illustration of the displacement and distortion of the plume due to the influence of terrain as modeled in LIFT. In the absence of terrain, the plume at s remains centered at (y_r, z_r) as illustrated by the darkly shaded plume cross-section. In the presence of terrain, LIFT treats the terrain surface as flat, but lowers and deflects the centerline of the plume to one side. The deformed flow results in a decrease in the vertical size of the plume, and an increase in the horizontal size of the plume, as illustrated by the lightly-shaded plume cross-section at s. Note that the centroid height varies with the distance $s-s_o$, and in this depiction it follows a trajectory that carries the plume nearer the surface with increasing distance downwind.

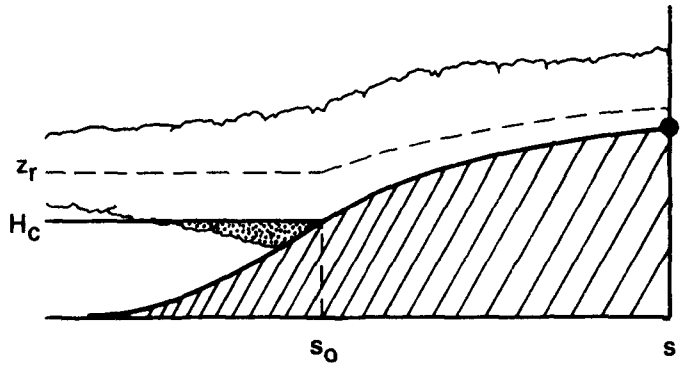

PHYSICAL PICTURE: material above H_c rides up and over hill in a distorted flow. Material below H_c passes round the side.

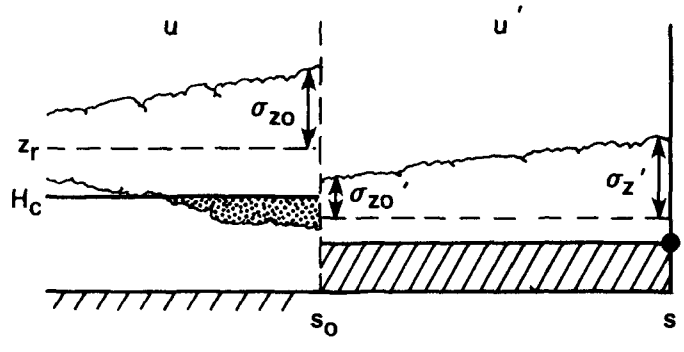

TERRAIN TREATMENT IN LIFE: terrain factors specify average terrain-induced flow modifcation from s_o to s.

$$z_r' - H_c' = T_h (z_r - H_c)$$
$$u' = T_u u$$
$$\sigma_{zo}' = T_h \sigma_{zo}$$
$$\sigma_z' = T_h \sigma_{ze}$$
$$\sigma_{ze}^2 = \sigma_{zo}^2 + (T_{\sigma z}^2 / T_h^2)(\sigma_z^2 - \sigma_{zo}^2)$$

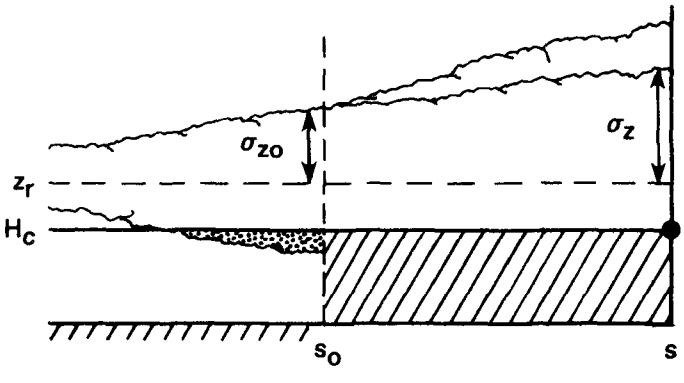

LIFT CALCULATION: net effect of flow distorition is to increase the effective rate of plume growth (σ_{ze}) over that in the absence of the hill (σ_z)

Figure 3b. Illustration of terrain effect on the vertical distribution of plume material above H_c as modeled in LIFT.

$$dC(s,y_R,0;s_o) = \frac{dQ(s_o,y',z')}{\pi\sigma^{*'}_y\sigma^{*'}_z u'} e^{-0.5(\frac{y'-y_R}{\sigma^{*'}_y})^2} \quad e^{-0.5(\frac{z'-H_c'}{\sigma^{*'}_z})^2} \tag{5}$$

where

$$\sigma^{*'2}_z = \sigma'^2_z(s) - \sigma'^2_z(s_o) \equiv \sigma'^2_z - \sigma'^2_{zo} \tag{6a}$$

$$\sigma^{*'2}_y = \sigma'^2_y(s) - \sigma'^2_y(s_o) \equiv \sigma'^2_y - \sigma'^2_{yo} \tag{6b}$$

Because the material from elemental point sources below H_c' at s_o are forced around the hill rather than over it, the total concentration contains contributions only from those source elements above H_c', so that Equation 3 becomes

$$C(s,y_R,0;s_o) = \int_{H_c'}^{\infty} \int_{-\infty}^{+\infty} \frac{C(s_o,y',z')}{\pi\sigma^{*'}_y\sigma^{*'}_z} e^{-0.5(\frac{y'-y_R}{\sigma^{*'}_y})^2} \cdot e^{-0.5(\frac{z'-H_c'}{\sigma^{*'}_z})^2} \, dy'dz' \tag{7}$$

where

$$C(s_o,y',z') = \frac{Q}{2\pi u'\sigma'_{yo}\sigma'_{zo}} e^{-0.5(\frac{y'-y'_r}{\sigma'_{yo}})^2} (e^{-0.5(\frac{z'-z'_r}{\sigma'_{zo}})^2} + e^{-0.5(\frac{z'+z'_r}{\sigma'_{zo}})^2}) \tag{8}$$

Note that the plume is originally released at the point (x_r,y_r,z_r). After the deformation at the distance s_o, the plume centerline passes through the point (s_o, y'_r, z_r).

Primed quantities in Equations 7 and 8 are related to the unprimed quantities of the undistorted flow by means of terrain factors (see Figure 3b). These factors are local in the sense that

they depend on the position of the receptor on the terrain, even though they represent the average terrain effect on the flow from s_o to s. T_h and T_ℓ are factors that specify the amount of streamline distortion in the vertical and lateral directions; T_u specifies the resultant change in the flow speed; and $T_{\sigma z}$ and $T_{\sigma y}$ specify changes in the diffusivity in the vertical and lateral directions.

The factor T_h should account for the effective contraction of the distance between streamlines in the vertical. A simple model for the change in streamline spacing applies a constant depression factor to all streamlines over a particular location on the terrain. This is particularly convenient for evaluating Equations 7 and 8. But note that the perturbation caused by a hill should decrease with height, so that this simple model must be viewed as an approximation which must be applied at plume centerline height. Similarly, T_ℓ is treated as a constant and is evaluated for a particular plume path. More details on the specifications of these flow deformation factors are given in subsection 2.1.2.

The speed factor, T_u, is obtained by conserving mass. The condition $T_u T_h T_\ell = 1$ must be maintained at every point in the flow.

The factor T_σ (denoting either $T_{\sigma z}$ or $T_{\sigma y}$) should account for the effective growth in the plume element in the altered flow between s and s_o and can be expressed in terms of the diffusivity. The diffusivity over the interval $s-s_o$ can be related to the growth of a plume element in the following way. For a uniform wind speed but a variable diffusivity (D) in a flow over level terrain,

$$\frac{d\sigma^2(s)}{ds} = \frac{2}{u} D(s) \tag{9}$$

If a mean diffusivity over the interval $s-s_o$ is denoted by D_m, then Equations 4 and 9 can be combined to give

$$\sigma^{*2} = \sigma^2 - \sigma_o^2 = (s-s_o)\frac{\Delta\sigma^2}{\Delta s} = \frac{2(s-s_o)}{u} D_m \tag{10a}$$

and

$$\sigma^{*\prime 2} = \sigma^{\prime 2} - \sigma_o^{\prime 2} = (s-s_o)\frac{\Delta\sigma^{\prime 2}}{\Delta s} = \frac{2(s-s_o)}{u'} D'_m \tag{10b}$$

Therefore T_σ, the factor that relates the growth of the terrain-influenced plume element $\sigma^{*\prime}$ to the uninfluenced growth σ^*, can be evaluated in terms of the diffusivity

$$T_\sigma^2 \equiv \sigma^{*\prime 2}/\sigma^{*2} = \left(\frac{D'_m}{u'}\right)/\left(\frac{D_m}{u}\right) \tag{10c}$$

and hence, can be evaluated with the aid of Equation 9 as discussed in subsection 2.1.2.

With these definitions, the explicit relationship between the initial plume and the distorted plume is given by the following equations:

$$z'_r = T_h z_r \quad ; \quad H'_c = T_h H_c \quad ; \quad y'_r = T_\ell y_r \quad ;$$

$$\sigma'_{zo} = T_h \sigma_{zo} \quad ; \quad \sigma'_{yo} = T_\ell \sigma_{yo} \quad ; \quad u' = T_u u \tag{11a}$$

Both the plume height in the approach flow and H_c are reduced by the factor T_h, as is the initial size of the plume in the vertical (σ_{zo}) because a constant compression in the vertical of the approach flow is applied at all elevations. When a constant distortion factor T_ℓ is applied to the horizontal spacing of streamlines as well, then the horizontal size of the plume at s_o is altered by the factor T_ℓ, as is the lateral position of the plume centerline.

Furthermore,

$$\sigma^{*\prime}_z = T_{\sigma z} \sigma^*_z \quad \text{and} \quad \sigma^{*\prime}_y = T_{\sigma y} \sigma^*_y$$

so that Equation 6(a,b) becomes

$$\sigma'^2_z = T_h^2 \sigma_{zo}^2 + T_{\sigma z}^2 \sigma_z^{*2} \equiv T_h^2 \sigma_{ze}^2 \tag{11b}$$

$$\sigma'^2_y = T_\ell^2 \sigma_{yo}^2 + T_{\sigma y}^2 \sigma_y^{*2} \equiv T_\ell^2 \sigma_{ye}^2$$

Equations 11b define what are later termed the effective sigmas:

$$\sigma_{ze}^2 = \sigma_{zo}^2 + \sigma_z^{*2}/T_z^2$$

$$\sigma_{ye}^2 = \sigma_{yo}^2 + \sigma_y^{*2}/T_y^2 \tag{11c}$$

where $T_z = T_h/T_{\sigma z}$ and $T_y = T_\ell/T_{\sigma y}$.

Upon solving the integrals in Equation 7 and substituting Equations 11 for the primed quantities, the resulting expression for the concentration is

$$C(s,y_R,0;s_o) = \frac{Qe^{-0.5\left(\frac{y_R/T_\ell - y_r}{\sigma_{ye}}\right)^2}}{2\pi\sigma_{ye}\sigma_{ze}u}\left[e^{-0.5\left(\frac{z_r-H_c}{\sigma_{ze}}\right)^2}\left(1-\mathrm{erf}\left(\frac{H_c-z_r}{\sqrt{2}\sigma_{ze}}\frac{\sigma_z^*/T_z}{\sigma_{zo}}\right)\right)\right. \tag{12}$$

$$\left. + e^{-0.5\left(\frac{z_r+H_c}{\sigma_{ze}}\right)^2}\left(1-\mathrm{erf}\left(\frac{H_c+z_r}{\sqrt{2}\sigma_{ze}}\frac{\sigma_z^*/T_z}{\sigma_{zo}}\right)\right)\right]$$

The terrain-induced modifications are easier to observe if H_c is set to zero:

$$C(s,y_R,0;s_o) = \frac{Qe^{-0.5\left(\frac{y_R/T_\ell - y_r}{\sigma_{ye}}\right)^2}}{\pi\sigma_{ye}\sigma_{ze}u}e^{-0.5\,(z_r/\sigma_{ze})^2} \tag{13}$$

Equation 13 differs from the simple flat terrain Gaussian plume equation only in the appearance of a distortion factor T_ℓ in the lateral distribution term, and in the appearance of <u>effective</u> plume spread parameters. If T_z and T_y are not equal to unity, the effective size of the plume differs from the unmodified plume and the effective lateral distance from the plume centerline to the receptor is altered. For illustration, let $y_r = 0$. Then if $T_\ell > 1$, which is generally the case because the streamlines spread out to some degree as the flow is deflected laterally, the apparent receptor location (y_R/T_ℓ) lies nearer the plume centerline. Aside from this lateral shift in the impact region on the terrain, the influence of the terrain is exhibited only through changes in the rate of <u>effective</u> plume growth. When T_z is less than unity (again, this is generally the case), σ_{ze} exceeds σ_z at s and so more plume material may lie "nearer" the surface. As a consequence, Equation 12 may estimate ground-level concentrations in excess of flat terrain estimates even when H_c is zero (see Figure 4).

If H_c is non-zero but less than z_r, Equation 12 will estimate even greater ground-level concentrations because the flow in the layer from the surface to H_c is "removed," allowing the less dilute portion of the plume to approach nearer the surface (see Figure 3). In particular, if $H_c = z_r$, then Equation 12 places the centerline concentration at ground level, producing a centerline "impingement" result.

In the development of Equation 12 and the terrain factors, the factors are considered local terrain effects factors for a specific receptor. The degree of flow deformation is dependent on whether the flow must go directly over the crest, or pass to one side in approaching the receptor. Once the local factors are obtained, they are applied to the entire plume. If there is a large amount of plume meander over the averaging period of the model computation, Equation 12 may not be appropriate.

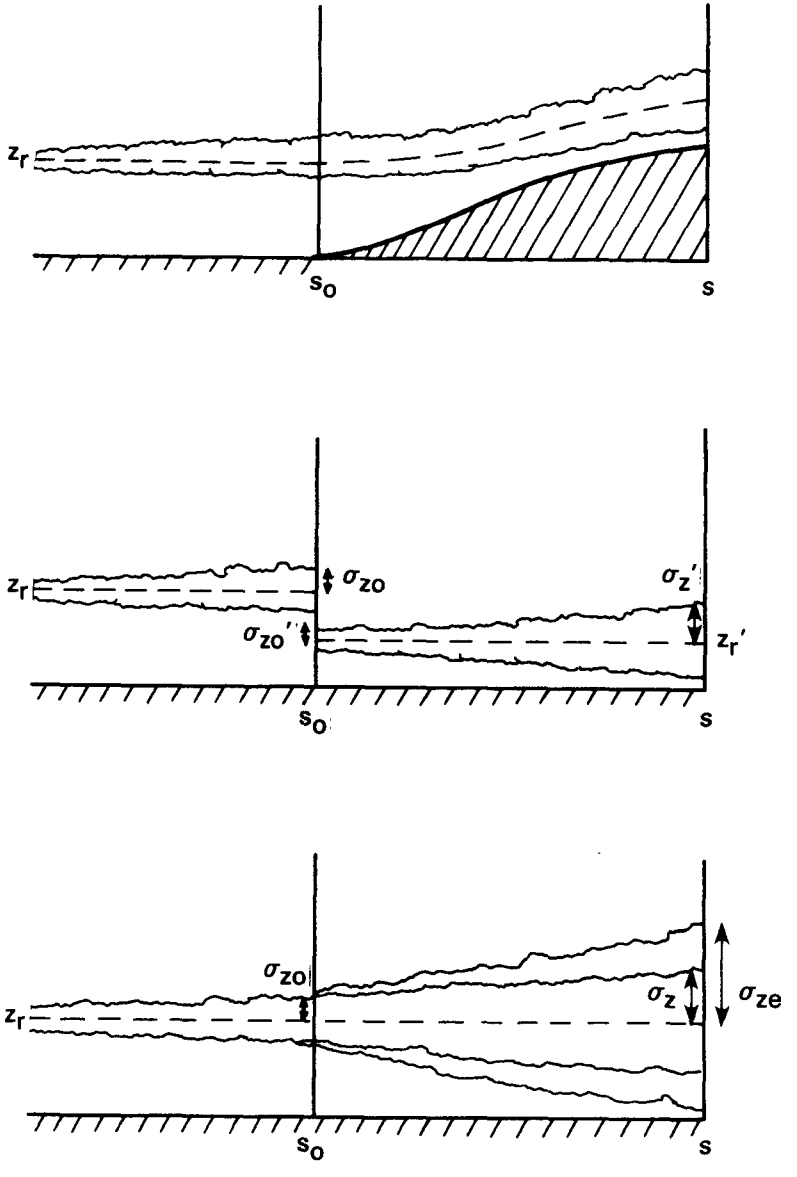

PHYSICAL PICTURE: all of the flow rides up and over the hill. The plume is distorted by the flow.

TERRAIN TREATMENT IN LIFT: plume is distorted at s_o, then allowed to diffuse in the modified flow.

LIFT CALCULATION: net effect of flow distortion is to increase the effective rate of plume growth (σ_{ze}) over that in the absence of the hill (σ_z). Ground-level concentrations are generally increased.

Figure 4. Schematic illustration of terrain effect on the vertical distribution of plume material when H_c=0.

Therefore, consider Equation 12 applicable to a "filament" plume. The "filament" plume is defined to be a plume described by the flow field statistics obtained for a sampling period commensurate with the time of travel from the source to the hill. The mean concentration at a receptor for an averaging period greater than the time of travel is a weighted average of many "filament" plumes:

$$C_m = \int_{-\infty}^{+\infty} C(s,\theta_r,0;s_o,\theta_i)\, P(\theta_i)\, d\theta_i \qquad (14)$$

$P(\theta)$ is the probability that the wind is from the θ direction during the averaging period, and $C(s,\theta_r,0;s_o,\theta)$ is the concentration resulting from a "filament" plume from direction θ, and θ_r is the direction from the apparent or effective receptor location to the source. Details explaining how θ_r is found are contained in subsection 2.1.3.

For a distribution of wind directions that has a single dominant mode at the mean wind direction θ_m, $P(\theta)$ may be approximated by a Gaussian distribution:

$$P(\theta) = \frac{e^{-0.5\left(\frac{(\theta-\theta_m)s}{\sigma_{ym}}\right)^2}}{\sqrt{2\pi}\,\sigma_{ym}/s} \qquad (15)$$

Using a similar arc length notation for lateral distance, $C(s,\theta_r,0;s_o,\theta)$ may be written as

$$C(s,\theta_r,0;s_o,\theta) = \frac{F_z(\theta)}{\sigma_{ye}}\, e^{-0.5\left(\frac{(\theta_r-\theta)s}{\sigma_{ye}}\right)^2} \qquad (16)$$

where $F_z(\theta)$ denotes the vertical distribution portion of Equation 12.

By assuming that the "filament" plume is narrow, set $F_z(\theta)$ to $F_z(\theta_r)$, and evaluate σ_{ye} for a plume from θ_r. This makes explicit the use of terrain factors that are local to the receptor. Equation 14 becomes:

$$C_m = \frac{F_z(\theta_r)s}{\sqrt{2\pi}\sigma_{ym}\sigma_{ye}} \int_{-\infty}^{+\infty} e^{-0.5\left(\frac{(\theta_i-\theta_r)s}{\sigma_{ye}}\right)^2} e^{-0.5\left(\frac{(\theta_i-\theta_m)s}{\sigma_{ym}}\right)^2} d\theta_i \qquad (17)$$

The solution of this integral is

$$C_m = \frac{F_z(\theta_r)}{\sigma_{yT}} e^{-0.5\left(\frac{(\theta_r-\theta_m)s}{\sigma_{yT}}\right)^2} \tag{18a}$$

where

$$\sigma_{yT}^2 = \sigma_{ym}^2 + \sigma_{ye}^2 \tag{18b}$$

Because σ_{ym} is viewed as the statistic for just the meander component of the wind fluctuations over the averaging period, and σ_{ye} is viewed as the measure (including the terrain modification) of the mean "filament" plume spread, $\sigma_{yT} = \sigma_{ye}$ in the absence of meander, and Equation 12 is obtained once again.

In applying LIFT to the CCB data base, the selection of wind statistics for the "filament" plume is limited to the 5-min sampling time, and the mean concentration is generally computed for a 1-hour interval. Also, when the average concentration is obtained from simulating each 5-min period separately, σ_{ym} is identically zero, and Equation 18 is used for both calculations.

Equation 18, in which $F_z(\theta_v)$ represents the portion of Equation 12 that contains the information on the vertical structure of the plume, provides the framework for estimating concentrations due to plume material that travels up and over a hill. As a framework, it shows how the influence of the terrain, expressed as terrain factors, affects the magnitude and distribution of plume material along the surface of the terrain. Consequently, the influence of particular hills on the flow-field must be prescribed in terms of these mean terrain factors before concentrations can be estimated by means of Equation 18. The following two subsections describe a method for obtaining mean terrain factors, and a method for estimating the effective position of a receptor after accounting for the lateral deflection of the plume.

2.1.2 Terrain Factors

Terrain-induced modifications to the flow over a hill are prescribed in terms of the undisturbed, rectilinear flow and the terrain factors $T_h(x,y,z)$, $T_\ell(x,y,z)$, and $T_u(x,y,z)$. The vertical coordinate (z) denotes the height of the plume in the approach flow, and the x-y plane is centered on the hill (presumably at the crest of the hill). The plane z = 0 is the flat surface away from the hill, generally taken to be the surface elevation beneath the plume near the source. The x-axis is assumed to be aligned with the flow direction that would take the plume centerline over the effective receptor location (see subsection 2.1.3 and Figure 11). If T(x,y,z) denotes any one of the three factors, then at the position (x,y_r) the distortion factor for the flow between streamlines originally

passing through (x_r,y_r,z_r) and $(x_r,y_r,0)$ is denoted by $T(x,y_r,z_r)$ (see Figure 5).

The factors actually applied in LIFT need to be expressed as average values for the interval $s-s_o$. Because the factors are expressed in the coordinates of the undistorted flow, an average along the trajectory of the flow is expressed as an integral along "x." Therefore the mean or effective terrain factor for the flow between streamlines passing through (x_r,y_r,z_r) and $(x_r,y_r,0)$ is given by:

$$T(s,y_r,z_r;s_o) = \int_{x_r+s_o}^{x_r+s} T(x,y_r,z_r)\, dx/(s-s_o) \qquad (19)$$

Note that only two of the three factors need be evaluated in this way because $T_u T_\ell T_h = 1$.

In principle, the factors could be computed from a flow model. However, the approach taken in LIFT involves <u>scaling</u> the magnitude of the flow modifications on the basis of flow computations rather than incorporating the results of those flow computations in detail. This scaling is accomplished by specifying the extreme values of T_h, T_ℓ and T_u. For neutral flow, these values occur at the crest of the hill. With a certain degree of stratification, these values shift to the leeward side of the hill. Away from the location of the extreme, the modification to the flow diminishes, and the terrain factors approach unity. This relaxation to unity is specified by a simple analytic function that includes length scales for the lateral and longitudinal "axes" of the hill. An example of a set of these extreme values for CCB can be found in subsection 3.3.1.

This method of incorporating the terrain-induced distortion allows the influence of the terrain to be incorporated by means of a limited number of parameters. The average terrain modifications required in the model can be specified analytically without the need for numerical integration. Consequently, several flow modeling assumptions can be readily investigated, and the parameters that specify the flow can also be treated as optimizing parameters so that the observed distribution of concentrations may be used to infer the flow modification.

For the case of an axisymmetric hill (an approximation for CCB) with a length scale equal to its radius at the elevation of the H_c surface, $a(H_c)$, the factor variation is given the form:

$$T(x,y,z_r) = 1 + (T_o(z_r)-1)e^{-\left(\frac{x-x_{sep}}{\alpha(a(H_c)+x_{sep})}\right)^2 - \left(\frac{y}{\alpha a(H_c)}\right)^2} \qquad (20)$$

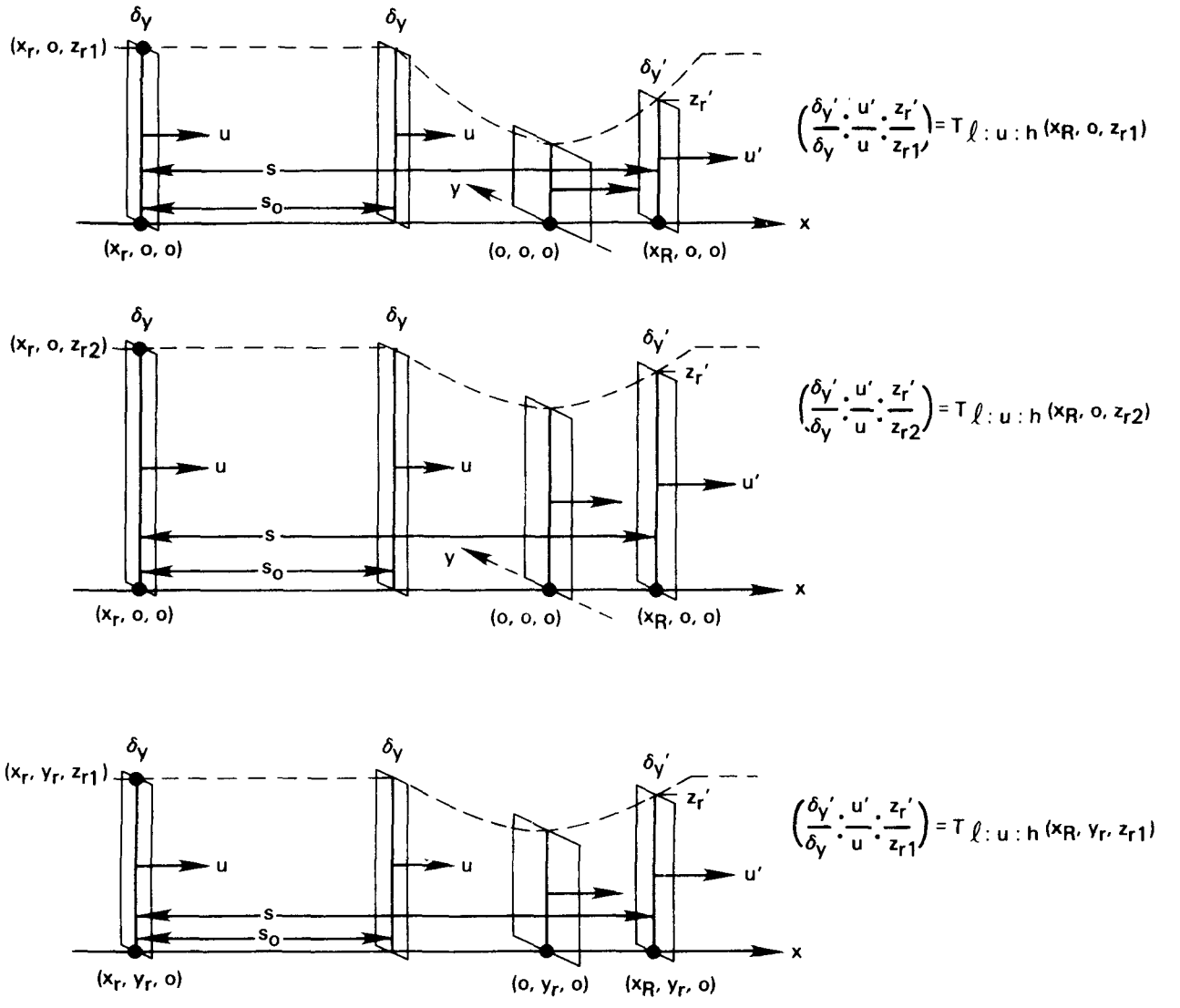

Figure 5. Depiction of how the terrain factors depend upon the height of the release (z_r) and the lateral offset of the trajectory from the crest of the hill. The flow is unaltered over the distance s_o in each of the three illustrations. Beyond s_o, the height of the plume above the surface (the plane z=o), the flow speed, and the lateral width of the bundle of streamlines selected for this illustration (δ_y) varies with distance from the hill crest depending upon the offset of the plume trajectory from the crest, and the height of the plume in the approach flow. These variations in turn define the terrain factors. Consequently, a particular terrain factor T(x, y, z) is specified by a location in the x-y plane, and by the plume height in the approach flow.

The quantity α is introduced to adjust the rate at which the factors relax to unity with distance from the location of the extrema. $T_o(z_r)$ denotes the extreme flow modification factor for the flow between streamlines passing through $(x_r,0,z_r)$ and $(x_r,0,0)$.

To simulate the effects of weak stratification, the variable x_{sep} is introduced to shift leeward the location of the nearest approach of streamlines to the surface. With weak stratification, the formation of the lee waves influences flow separation in the lee of a hill. On the basis of laboratory experiments and simple theory (e.g., Hunt and Snyder 1980), the separation point resides near the hill crest when one quarter of the wavelength of the lee wave exceeds the longitudinal half-length of the hill (measured at 1/2 the hill height) because the streamlines in the wave pattern exhibit a shallower slope than the terrain surface. When the wavelength is shorter than this, the separation is suppressed over the hill until the wave pattern causes the streamlines to rise again at three quarters of the wavelength of the wave. This point lies at one half wavelength from the crest of the hill (see Figure 6).

The wavelength of the lee wave is approximately equal to $2\pi u/N$. Because LIFT addresses the flow above H_c, u/N is taken to be representative of the flow above H_c as well. The criterion for where separation is likely to occur can be expressed in terms of the Froude number based on the horizontal length scale of the hill, Fr_L. With L defined as in Figure 6,

$$Fr_L = \frac{u}{NL} \tag{21}$$

Consequently, the separation point remains near the crest for $Fr_L > 2/\pi$. Therefore,

$$\begin{aligned} x_{sep} &= 0 \qquad Fr_L \geq 2/\pi \\ x_{sep} &= \pi u/N \qquad Fr_L < 2/\pi \end{aligned} \tag{22}$$

We shall assume that the streamlines above H_c come closest to the hill surface near x_{sep}.

Equations 19 through 22 allow the average factors T_h and T_ℓ to be specified for the flow through the source at height z_r toward a particular receptor. T_u is always obtained as the inverse of the product of T_ℓ and T_h. Consequently, T_h, T_ℓ and T_u depend on θ_r, the wind direction that brings the centerline of the plume over the receptor.

The fourth terrain effect factor, T_σ (denoting either $T_{\sigma y}$ or $T_{\sigma z}$), depends in part on T_h and T_u. T_σ is defined by Equation 10c, and requires the specification of the mean diffusivity.

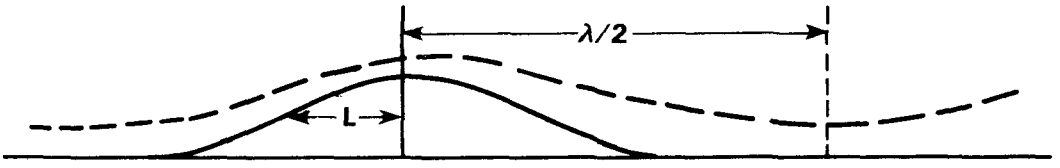

$\lambda > 4L$: Separation occurs near the crest

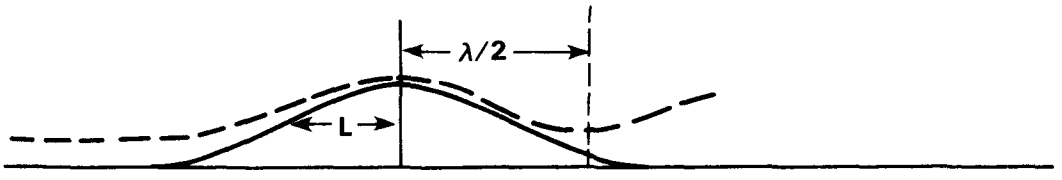

$\lambda < 4L$: Separation occurs near $\lambda/2$ beyond the crest

$$\lambda\ (= 2\pi u/N) = 4L \rightarrow Fr_L\ (= u/NL) = 2/\pi$$

Figure 6. Dependence of separation in the lee of a hill on stratification. The structure of the lee wave begins to influence the point of flow separation when the wavelength is less than 4L.

In the case of $T_{\sigma z}$, equations 9 and 60 indicate that

$D = u\, i_z^2\, s$ ("linear" growth range for σ_z)
$D = u\, i_z\, \ell$ ("square root" growth range for σ_z)

where

$$1/\ell = \frac{1}{\Gamma z_r} + \frac{N}{\gamma^2 u i_z} \quad . \tag{23}$$

These expressions are derived from the equation for σ_z presented in Section 2.4. An expression for D that approximates the transition between the two limits stated in Equation 23 is

$$D = \frac{u\, i_z^2\, s}{1 + s i_z/\ell} \tag{24}$$

Because D is linear with distance, or constant in Equation 23, D_m in the interval $s-s_o$ can be approximated by $D(s_m)$, where s_m is the mean of s and s_o. Then Equation 10c may be evaluated as

$$T_{\sigma z}^2 = \left(\frac{i'^2_z s_m}{1+s_m i'_z/\ell'}\right)\left(\frac{1+s_m i_z/\ell}{i_z^2 s_m}\right) \tag{25}$$

Substitute terrain factors to evaluate the primed quantities, and introduce T_{iz} to represent the factor for the change in turbulence intensity, and Equation 25 becomes

$$T_{\sigma z}^2 = T_{iz}^2 \frac{1+s_m\left(\frac{i_z}{\Gamma z_r} + \frac{N}{\gamma^2 u}\right)}{1+s_m\left(\frac{T_{iz} i_z}{T_h \Gamma z_r} + \frac{N}{T_u \sqrt{T_h}\gamma^2 u}\right)} \tag{26}$$

Parallel reasoning applies to $T_{\sigma y}^2$. For the equation developed in Section 2.5 for σ_y,

$$T_{\sigma y}^2 = T_{iy}^2\, T_u \frac{1+s_m/uT_{LT}}{T_u+s_m/uT_{LT}} \tag{27}$$

where T_{LT} is the Lagrangian time scale for the transverse correlogram.

2.1.3 Effective Receptor Location

The evaluation of Equation 18 and the development of subsection 2.1.2 require the specification of the effective, or apparent receptor location. In particular, the wind direction θ_r that transports the plume over the effective receptor must be obtained. In developing Equation 12, the plume centerline was shifted by a factor T_ℓ, which represents the average lateral shift along the trajectory. But a more accurate specification of the shift in the centerline position requires that the shift be evaluated at the receptor location without averaging along the path. The effective receptor location is then related to the actual receptor location by the terrain factor $T_\ell(x,y,z_r)$.

When the coordinate system, with origin at the hill center, is rotated to align the direction of the x-axis with the direction from the source to the effective receptor location, (i.e., the flow is due to wind from θ_r)

$$y_R = \int_0^{y_r} T_\ell(x_R,y,z_r)\, dy \quad . \tag{28}$$

That is, the cumulative deflection of the flow from the center of the hill out to the position (y_r) of the undistorted trajectory of the plume gives the lateral position (y_R) of the actual receptor over which the deflected plume trajectory travels at the downwind position x_R (see Figure 7). Upon substituting for $T_\ell(x_R,y,z_r)$,

$$y_R = y_r + \alpha a(H_c)\frac{\sqrt{\pi}}{2}\,\mathrm{erf}(y_r/\alpha a(H_c))(T_{\ell o}(z_r)-1)e^{-\left(\frac{x_R-x_{sep}}{\alpha(a(H_c)+x_{sep})}\right)^2} \tag{29}$$

Equation 29 must be solved numerically for y_r given y_R and x_R. But y_R and x_R are themselves only known once θ_r is known (due to rotating the coordinate system), which in turn requires that y_r and x_r be known. Thus, θ_r is obtained from this implicit set of relationships by iteration.

2.2 The WRAP Component

In CTDM, the flow below H_c is considered to be completely two-dimensional, allowing no motion in the vertical. Consequently, the flow must pass to one side or the other of the hill, and the one streamline that actually touches and passes round both sides of the hill separates the two flows, and is termed the stagnation streamline of the flow. The flow on either side of the stagnation streamline undergoes distortion in much the same way as that discussed in Section 2.1. A streamline in the flow will be deflected to the side, but will pass closer to the hill surface than its initial distance from the stagnation streamline. Adjacent streamlines are displaced by differing amounts, which in turn changes the horizontal spacing between streamlines and hence, causes changes in the local speed of

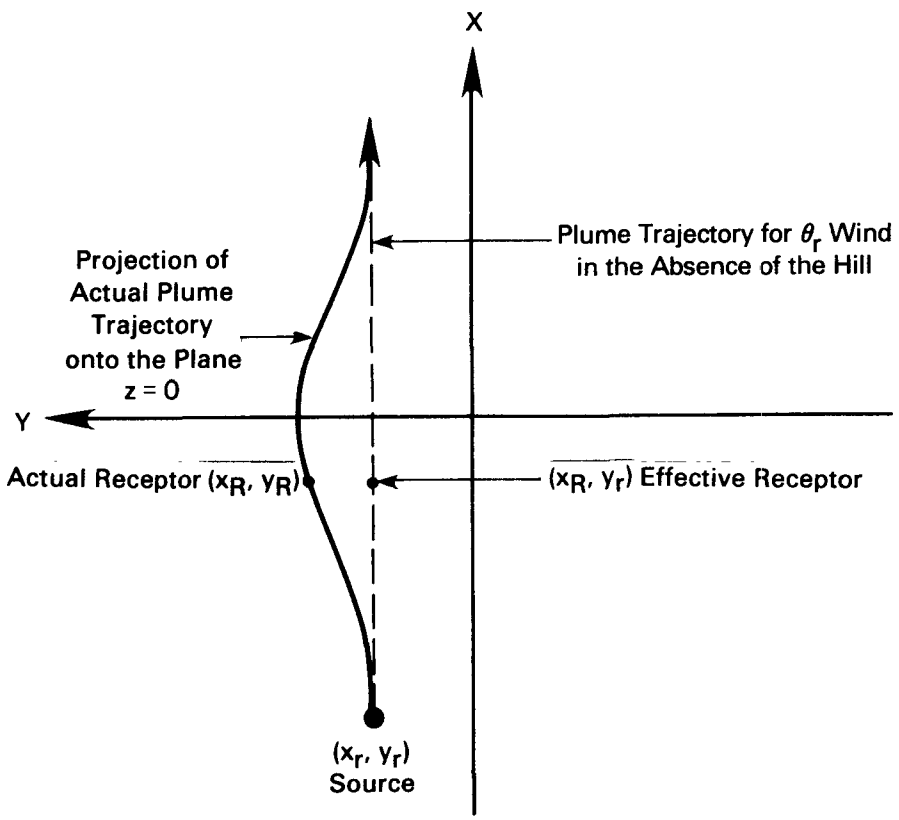

Figure 7. Definition sketch for deriving the effective receptor location. The x-axis is aligned with the flow due to a wind from direction θ_r.

the flow. The effect of these distortions on ground-level concentrations is similar to those formulated in LIFT for flow over a two-dimensional hill, except that the roles of T_ℓ and T_h are reversed.

The primary difference between WRAP and LIFT formulations arises from the location of solid boundaries and the relationship between the position of these boundaries and the wind direction fluctuations. The terrain effect is modeled in WRAP by re-initializing the flow at the distance s_o downwind of the source (see Figure 1). Note that receptors below H_c experience an s_o different from that experienced by receptors above H_c. Below H_c, s_o is the distance along the stagnation streamline from the source to the terrain contour equal in elevation to the receptor elevation. The concentration at a receptor downwind of s_o is composed of concentrations from that part of the concentration distribution at s_o that lies below H_c, and that also lies on the same side of the stagnation streamline as the receptor (see Figure 8). Reflection of plume material is allowed from the plane $z = 0$ over the entire distance s, and reflection is also allowed from the "stagnation streamline" beyond s_o. Note that the stagnation streamline forms the boundary of the hill surface in horizontal cross section.

The terrain influences are incorporated by deforming the source distribution at s_o (Equation 1), and by altering the flow in which the source elements diffuse. For a receptor located on the hillside at a distance s (see Figure 8) and a height z_R above the plane $z = 0$, the concentration due to one elemental point source located at (s_o,y',z') in the deformed plume is given by

$$dC(s,0,z_R;s_o) = \frac{dQ(s_o,y',z')}{2\pi u'\sigma^{*'}_y\sigma^{*'}_z} 2e^{-0.5(\frac{y'}{\sigma^{*'}_y})^2}(e^{-0.5(\frac{z'-z_R}{\sigma^{*'}_z})^2} + e^{-0.5(\frac{z'+z_R}{\sigma^{*'}_z})^2}) \quad (30)$$

Equation 30 assumes that the x-axis of the coordinate system points along the stagnation streamline, and that the source is located at (x_r,y_r,z_r). The total concentration at the receptor contains contributions from those elements below H_c (now represented as H_c'), and on the same side of the stagnation streamline as y_r (now represented as y_r'):

$$C(s,0,z_R;s_o) = \int_o^{H_c'}\int_{(o)}^{(\infty)} \frac{C(s_o,y'z')}{2\pi\sigma^{*'}_y\sigma^{*'}_z} 2e^{-0.5(\frac{y'}{\sigma^{*'}_y})^2}(e^{-0.5(\frac{z'-z_R}{\sigma^{*'}_z})^2} + e^{-0.5(\frac{z'+z_r}{\sigma^{*'}_z})^2})dy'dz' \quad (31)$$

where

$$C(s_o,y',z') = \frac{Q}{2\pi u'\sigma'_{yo}\sigma'_{zo}} e^{-0.5(\frac{y'-y'_r}{\sigma'_{yo}})^2}(e^{-0.5(\frac{z'-z'_r}{\sigma'_{zo}})^2} + e^{-0.5(\frac{z'+z'_r}{\sigma'_{zo}})^2}) \quad (32)$$

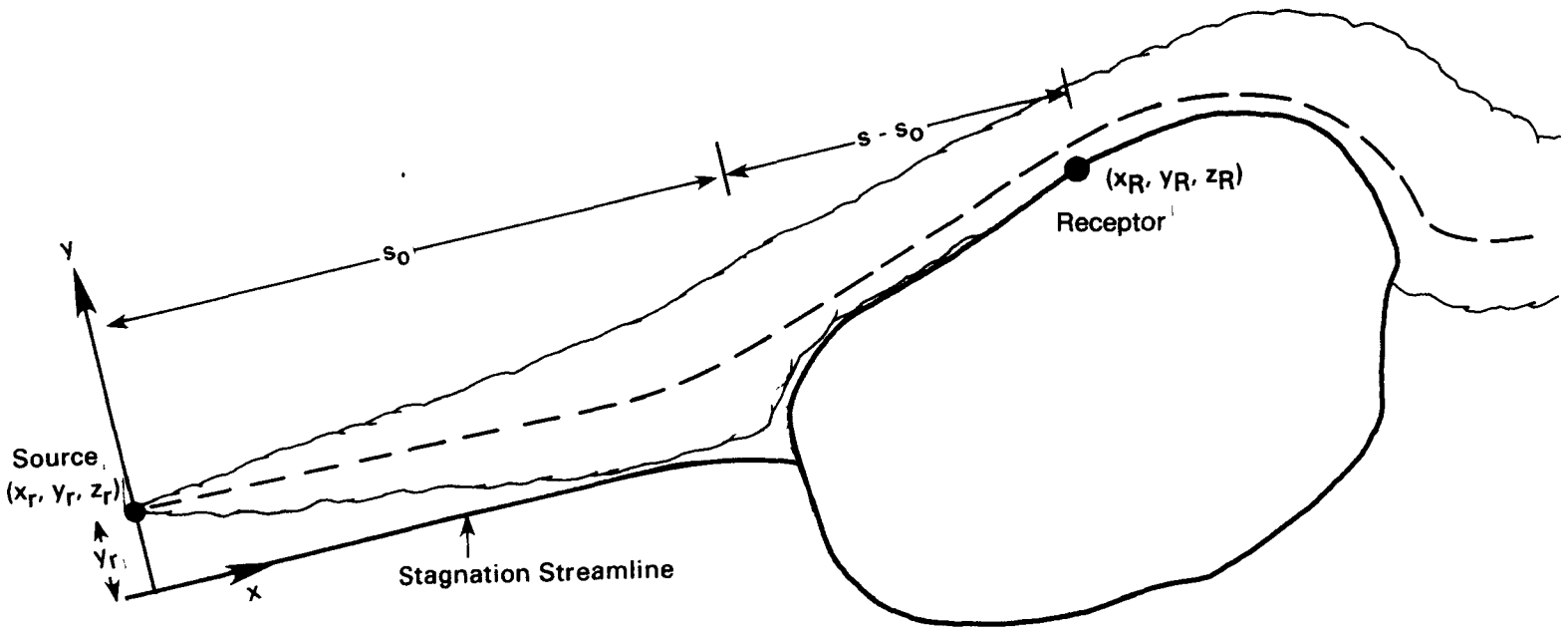

Figure 8. Top view of a plume in two-dimensional flow around a hill. The shape of the hill in crossection at the receptor height is assumed to be invariant with height so that the deformation of the entire plume round the hill is a function of the receptor location.

These expressions are analogous to Equations 5 through 8 of the LIFT component. The integral for dy' has the limits (o) and (∞). This is meant to denote integrating from 0 to + ∞ if the receptor lies on the "positive" side of the stagnation streamline, and integrate from -∞ to 0 if the receptor lies on the "negative" side.

Noting that $T_h = 1$ for this two-dimensional flow, the integrals in Equation 31 are evaluated and the primed quantities are replaced according to Equation 11 to obtain

$$C(s,0,z_R;s_o) = \frac{Q}{4\pi u \sigma_{ye}\sigma_{ze}} e^{-0.5(\frac{y_r}{\sigma_{ye}})^2}(1 + \text{sign}(y_R)\ \text{erf}(\frac{y_r\sigma_y^*/T_y}{\sqrt{2}\sigma_{yo}\sigma_{ye}}))$$

$$\cdot (B_1 e^{-0.5(\frac{z_r - z_R}{\sigma_{ze}})^2} + B_2 e^{-0.5(\frac{z_r + z_R}{\sigma_{ze}})^2}) \qquad (33)$$

Most of the notation here has already been encountered in Section 2.1. The factor $\text{sign}(y_R)$ denotes the sign of the receptor position in the coordinate system with x-axis aligned with the flow, and it results from the choice of integrating over the "positive" or "negative" portion of the flow in Equation 31. The factors B_1 and B_2 are given by

$$B_1 = \text{erf}(\frac{b_1 - b_2 - b_3}{b_o}) + \text{erf}(\frac{b_1 + b_2 + b_3}{b_o})$$

$$B_2 = \text{erf}(\frac{b_1 - b_2 + b_3}{b_o}) + \text{erf}(\frac{b_1 + b_2 - b_3}{b_o}) \qquad (34)$$

where

$$b_0 = \sqrt{2}\ \sigma_{ze}\ \sigma_{zo}\ \sigma_z^*$$
$$b_1 = T_z\ H_c\ \sigma_{ze}^2$$
$$b_2 = z_R\ \sigma_{zo}^2/T_{\sigma z}$$
$$b_3 = z_r\ \sigma_z^{*2}/T_z$$

The concentration estimate from Equation 33 is quite sensitive to the wind direction. The wind direction determines the stagnation streamline, and this in turn prescribes the relative position of both the source and the receptor in the undistorted flow through the quantities s, s_o, and y_r (see Figure 8). Because the terrain effects are characterized through factors that are local in the context discussed in Section 2.1, they also depend on y_r, s, and s_o. Therefore, the notion of a "filament" plume is implicit in the foregoing development, as it was in the development of the LIFT component. Consequently, an expression is needed for the mean concentration resulting from a meandering plume.

If the distribution of wind directions over the averaging time is highly non-Gaussian, then the mean concentration is probably best estimated by simulating a sequence of "filament" plumes. For the CCB data base, this would entail averaging the concentrations obtained from Equation 33 for a sequence of 5-minute average meteorology. However, for distributions closer in shape to the Gaussian distribution, an expression of the form of Equation 14 may be used with the Gaussian distribution specified in Equation 15.

Denote the concentration due to a "filament" plume for wind direction θ as

$$C(s,0,z_R;s_o) = \frac{F_z(\theta)}{\sigma_{ye}} e^{-0.5(\frac{y_r}{\sigma_{ye}})^2} \left(1 + \text{sign}(y_R)\ \text{erf}\ \left(\frac{y_r \sigma^*_y / T_y}{\sqrt{2}\sigma_{yo} s_{ye}}\right)\right) \quad (35)$$

where y_r, σ_{ye}, σ_{yo}, T_y and y_R are all functions of θ.
Let r denote the distance from the source to the hill center, s_r denote the distance from the source to the receptor, θ_r denote the direction from the receptor to the source, and let θ_s denote the direction from the center of the hill to the source. (The centerline of the plume impinges on the hill when the wind direction lies along the stagnation streamline through the source θ_s.) Then from the diagram in Figure 9,

$$\begin{aligned} s &= s_r \cos(\theta - \theta_r) \\ s_o &= r \cos|\theta - \theta_s| - a(z_R) \\ y_r &= r \sin(\theta - \theta_s) \end{aligned} \quad (36)$$

Integrating Equation 35 within Equation 14 to obtain the mean concentration C_m is simplified if we expect the "filament" plume to be narrow so that concentrations for wind directions much different from θ_s (and therefore θ_r as well) are insignificant. In that case, s and s_o may be treated as constants, and y_r can be represented by the small angle approximation so that

$$C_m = \frac{F_z(\theta_d)s}{\sqrt{2\pi}\sigma_{ye}\sigma_{ym}} \int_{-\infty}^{+\infty} e^{-0.5(\frac{(\theta-\theta_m)s}{\sigma_{ym}})^2} e^{-0.5(\frac{(\theta-\theta_s)r}{\sigma_{ye}})^2}$$

$$\cdot \left(1 + \text{sign}(y_R)\ \text{erf}\frac{(\theta-\theta_s)r\ \sigma^*_y / T_y}{\sqrt{2}\ \sigma_{yo}\sigma_{ye}}\right)d\theta \quad (37)$$

The solution of this integral is obtained by approximating the error function with a two-section piecewise-linear curve to obtain

$$C_m = \frac{Qe^{-\Lambda^2}}{4\pi u \sigma_{yT}\sigma_{ze}}\left(1 - \text{sign}(y_R)\left[\frac{\sigma_{ym} r}{\sigma_{yT} s}\right.\right. \frac{b_4}{\pi}\left.\left.(e^{-\zeta_+^2} - e^{-\zeta_-^2})\right.\right.$$

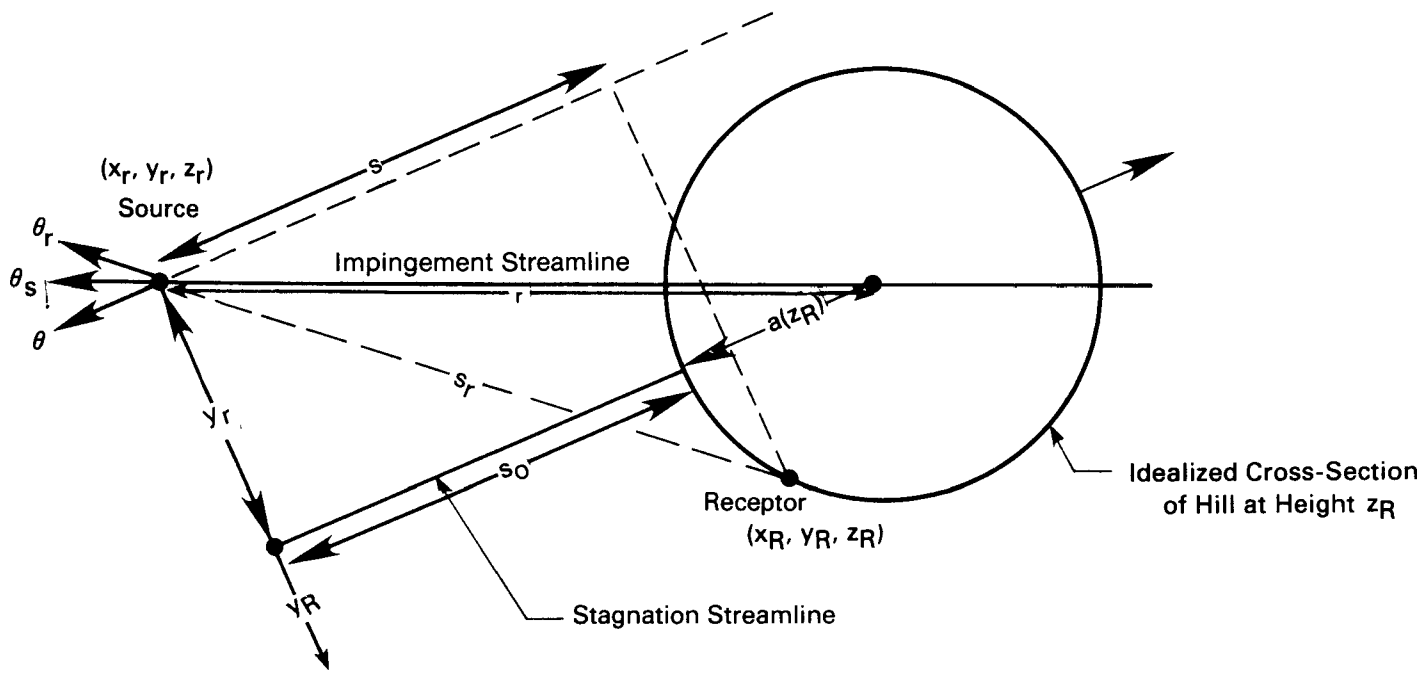

Figure 9. Diagram illustrating the geometry for specifying the dependence of WRAP modeling variables on the wind direction.

$$+ \left(\frac{1}{2} + \frac{b_4 \Lambda \sigma_{ye}}{\sqrt{\pi}\sigma_{yT}}\right)\text{erf}\ \zeta_+ + \left(\frac{1}{2} - \frac{b_4 \Lambda \sigma_{ye}}{\sqrt{\pi}\sigma_{yT}}\right)\text{erf}\ \zeta_-]$$

$$\cdot \left(B_1 e^{-0.5\left(\frac{z_r - z_R}{\sigma_{ze}}\right)^2} + B_2\ e^{-0.5\left(\frac{z_r - z_R}{\sigma_{ze}}\right)^2}\right) \tag{38a}$$

where

$$\Lambda = \frac{(\theta_s - \theta_m)r}{\sqrt{2}\sigma_{yt}} \tag{38b}$$

$$b_4 = \frac{\sigma^*_y / T_y}{\sigma_{yo}} \tag{38c}$$

$$\zeta_+ = \frac{\sigma_{yT}^s}{\sigma_{ym}^r}\left(\Lambda \frac{\sigma_{ye}}{\sigma_{yT}} + \frac{\sqrt{\pi}}{2b_4}\right) \tag{38d}$$

$$\zeta_- = \frac{\sigma_{yT}^s}{\sigma_{ym}^r}\left(\Lambda \frac{\sigma_{ye}}{\sigma_{yT}} - \frac{\sqrt{\pi}}{2b_4}\right) \tag{38e}$$

2.3 LIFT/WRAP Transition

The development of LIFT and WRAP has been facilitated by the notion that the flow can be split into two discrete layers at the height of the critical dividing-streamline height, H_c. However, a real flow is not expected to conform to such a simplification. Concentration distribution estimates from CTDM appear to suffer from this simplification in that a plume (or a plume segment) away from the stagnation streamline will be shifted laterally by differing amounts depending upon whether it lies above or below H_c. Consequently, a transition zone must be introduced to smooth the discontinuity in flow behavior near H_c.

A second simplification in CTDM has been the treatment of the H_c surface. Not only do we consider the surface to be entirely in a horizontal plane, we also treat it as a steady surface over the averaging period of the concentration estimate. But computations of H_c for the 5-minute averaging periods show that H_c can vary substantially over an hour, and variations may also be expected over the 5-minute periods themselves. Variability in the H_c presents us with the opportunity both to "soften" the estimated concentration distribution near H_c, and to reduce the sensitivity of model estimates to H_c which is itself an estimate subject to some uncertainty.

2.3.1 Lateral Deflection

LIFT and WRAP produce estimates of ground-level pollutant concentrations in distinctly different ways. Consider the idealized "filament" plume shown in cross section in Figure 10. The cross section is taken at the downwind distance s_o for the sake of illustration. In this example, the centerline of the plume lies neither along the stagnation streamline nor in the H_c plane; the relative positions of these quantities are identified in the figure. For this plume, concentrations at receptors below H_c are derived from the cut made by the stagnation streamline. Concentrations at receptors above H_c are derived from the cut made by the H_c surface.

Adjacent receptors located on either side of H_c illustrate the effect of these two cuts. Above H_c, the centerline of the plume may be deflected directly over the receptor (A). Below H_c, the lateral offset of the plume centerline from the receptor (B) is controlled entirely by the stagnation streamline. Consequently, distinctly different concentration estimates may be allocated to receptors adjacent to one another on either side of H_c.

A remedy for this situation may be constructed by altering the lateral deflection in LIFT in a zone near H_c. LIFT concentration estimates may be simply expressed as in Equation 18a

$$C_m = \frac{F_z(\theta_r)}{\sigma_{yT}} e^{-0.5\left(\frac{(\theta_r-\theta_m)s}{\sigma_{yT}}\right)^2} \qquad (39)$$

The vertical distribution factor F_z depends on the direction from the source to the effective receptor position--the position after lateral streamline deflection has been included. It is this position that determines the terrain effect magnitude. We shall leave this factor unchanged, and replace θ_r with θ_r' in the lateral distribution factor to simulate the transition region.

Close to H_c, θ_r' should nearly equal θ_s, the stagnation wind direction. Beyond the transition region, θ_r' should equal θ_r. The thickness of the transition region should depend on the scale of the hill and the stratification. H_c combines both of these quantities and is a convenient length scale for the region. Therefore, introduce the transition zone length scale as δH_c, and let θ_r' be defined as

$$\theta_r' = \theta_r + (\theta_s-\theta_r)\, e^{-(z_R-H_c)/\delta H_c} \qquad (40)$$

where z_r is the receptor elevation. Because it is unlikely that the transition zone could be as large as H_c, δ is probably of order 0.1.

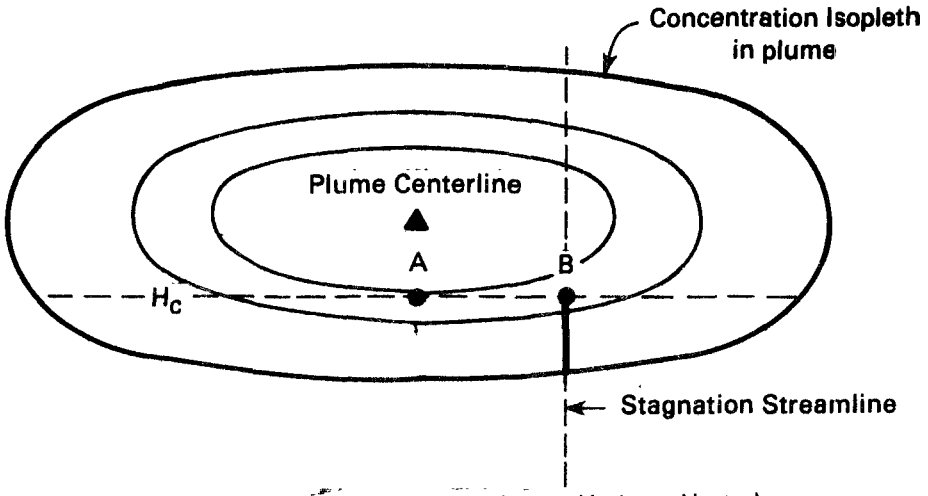

A: Concentration for Receptor Slightly Above H_c (x, y, $H_c + \varepsilon$)
B: Concentration for Receptor Slightly Below H_c (x, y, $H_c - \varepsilon$)

Figure 10. Cross-section of plume at s_o illustrationg how LIFT and WRAP concentration estimates differ at receptors on either side of H_c. Just downwind of s_o, LIFT concentration estimates are obtained from the cut made by the H_c surface through the plume, but WRAP concentration estimates are obtained from the cut made by the stagnation streamline through the plume (below H_c).

2.3.2 H_c Variability

Variability in the height H_c is specified in terms of a probability density function $P(H_c)$. If we assume a normal distribution about H_c, the mean value for the averaging period, then

$$C = \int_0^\infty C_m(H_c')P(H_c')dH_c' \tag{41}$$

where

$$P(H_c') = \frac{e^{-0.5\left(\frac{H_c'-H_c}{\sigma_{Hc}}\right)^2}}{\sqrt{\pi/2}\,\sigma_{Hc}(1+\mathrm{erf}\ H_c/\sqrt{2}\sigma_{Hc})} \tag{42}$$

C_m for the LIFT contribution is obtained from Equation 18, and C_m from the WRAP contribution is obtained from Equation 38. Note that the explicit dependence of Equation 18 on H_c is contained in F_z, as given by the vertical distribution factor in Equation 12, and the explicit dependence of Equation 38 on H_c is given by Equation 34.

The result of evaluating the integral in Equation 41 is too cumbersome to present here, but the leading factor of the result for LIFT is of some interest. With the H_c variation described above, the LIFT concentration estimate is proportional to

$$\frac{e^{-0.5\left(\frac{H_c-z_r}{\sigma_{zT}}\right)^2}}{\sigma_{zT}} \tag{43a}$$

where

$$\sigma_{zT}^2 = \sigma_{ze}^2 + \sigma_{Hc}^2 \tag{43b}$$

Therefore the effective size of the plume in the vertical is increased by the H_c variations. This arises from cutting off the flow below H_c. As H_c varies, the nearness of approach of the plume centerline to the surface varies, and this increases the apparent plume size in the mean.

A similar effect is not seen in the WRAP result. H_c variations have no effect well below H_c. Near H_c (within σ_{Hc} of H_c) the H_c variations modify the amount of plume material contained in the horizontal flow regime.

2.4 Formulation of σ_z (Venkatram, et al. 1984)

2.4.1 The Theoretical Framework

The σ_z formulation is based on the behavior described by

$$\sigma_z = \sigma_w t \quad ; \quad t << T_L \tag{44a}$$

$$\sigma_z = (2K_z t)^{0.5} \quad ; \quad t >> T_L \tag{44b}$$

In Equation 44a, σ_w is the standard deviation of vertical velocity fluctuations, t is the travel time from the source, T_L is the dispersion time scale, and K_z is the eddy diffusivity defined by

$$K_z \equiv \sigma_w \ell \quad , \text{ where } \ell = \sigma_w T_L \tag{45}$$

We suggest a plausible formulation for the "mixing length" ℓ by the following argument. In a stably stratified flow, a fluid element must overcome a stable potential temperature gradient in order to be displaced vertically. Simple energy arguments suggest that this gradient imposes a limit, which is defined by a length scale of the order of σ_w/N, to the vertical motion. Here N is the Brunt-Vaisala frequency. Consequently, we assume that the mixing length ℓ is proportional to this length scale so that

$$\ell = \gamma^2 \sigma_w/N \tag{46}$$

where γ is an undetermined constant. Hunt (1982) argues that γ should be a function of the molecular diffusivities of the fluid and the pollutant in the fluid. The vertical motion of a fluid element (a control volume larger than the turbulent microscale but much smaller than the macroscale) beyond σ_w/N depends on its ability to exchange its density with its surroundings. This exchange is governed by the molecular diffusivity of the fluid. The rate at which the pollutant escapes the fluid element is determined by the diffusivity of the pollutant in the fluid. Hunt suggests that the time scale of molecular mixing T_m can be long enough to inhibit the growth of σ_z beyond σ_w/N for long travel times. We will assume that T_m is always much smaller than the travel time t so that γ is independent of molecular diffusion processes. We will allow the comparison of our predictions with observations (presented later) to justify this assumption.

Surface-layer relationships (Businger 1973) are employed to estimate γ. When the nondimensional potential temperature gradient ϕ_H is independent of z, the kinematic heat flux Q_o can be written as

$$Q_o \equiv -T_* u_* = -\frac{k}{\beta} L u_* \frac{d\theta}{dz} \tag{47}$$

where L is the Monin-Obukhov length given by

$$L = -\frac{T_o}{g}\frac{u_*^3}{kQ_o} \tag{48}$$

Notice from Equation 47 that the eddy diffusivity for heat K_H is

$$K_H \equiv \frac{k}{\beta} u_* L \tag{49}$$

Substituting Equation 48 into Equation 47 we get

$$L = \frac{\sqrt{\beta}}{k}\frac{u_*}{N} \tag{50}$$

where N is given by

$$N = \frac{g}{T_o}\frac{d\theta}{dz}^{0.5} \tag{51}$$

If we now substitute Equation 50 into Equation 49, and recast K_H using the relationship $\sigma_w = au_*$

$$K_H = \sigma_w \frac{l}{\sqrt{\beta}a^2}\frac{\sigma_w}{N} \tag{52}$$

Assuming that $K_H = K_z$, we find that γ^2 is

$$\gamma^2 = \frac{1}{\sqrt{\beta}\ a^2} \tag{53}$$

With $\beta = 4.7$ and $a = 1.3$, γ equals 0.52. The expression for K_H was derived by Hunt (1982), but on the basis of arguments presented earlier, he maintains that K_H is not generally equal to K_z. He suggests that K_z/K_H ranges from 0.5 in the surface layer to 0.1 at higher elevations. Our observations of σ_z, to be described in later sections, do not support this contention. In our analysis we will take the stable mixing length ℓ_s to be given by

$$\ell_s = \gamma^2 \sigma_w/N \quad \text{where } \gamma = 0.52 \tag{54}$$

When N is small, ℓ_s can become very large, and it becomes necessary to consider the effect of the ground on limiting the length scale. In the absence of stratification, one expects the mixing length to scale with z,

$$\ell_n = \Gamma z \tag{55}$$

where the subscript n is used to distinguish the neutral length scale ℓ_n from the stable scale ℓ_s. To estimate Γ we notice that K_H can be written as

$$K_H = \sigma_w kz/(a\phi_H(0)) \tag{56}$$

Equation 56 indicates that

$$\Gamma = k/a\phi_H(0) \tag{57}$$

If we take the Kansas values (Businger 1973) $k = 0.35$ and $\phi_H(0) = 0.74$, Γ equals 0.36.

We have chosen to interpolate between ℓ_n and ℓ_s with the following formulation for ℓ:

$$1/\ell = 1/\ell_s + 1/\ell_n \tag{58}$$

Equation 58 has been used by other investigators (see Hunt et al., 1983 for example). Then the dispersion time scale is given by

$$T_L = \ell/\sigma_w \tag{59}$$

The σ_z formulation which interpolates between the linear and square-root growth rates is one used by other authors (Deardorff and Willis, 1975),

$$\sigma_z = \sigma_w t/(1 + t/2T_L)^{0.5} \tag{60}$$

Equation 60 was used to analyze the observations described in the next section.

2.4.2 Estimating σ_z from Observations

Data collected during SHIS #1 conducted in the fall of 1980 at CCB have been used to evaluate Equation 60. Estimates of σ_z are made from individual 5- or 10-minute long photographic time exposures, and from individual lidar scans of the oil-fog plume.

Four of the 18 CCB experiments have been analyzed for plume size in the vertical: Experiments 201, 206, 210 and 218. Lidar data have been reduced for two hours of Experiment 206, and two hours of 210. Consequently, the lidar data have been used to help determine a link between σ_z and the apparent vertical extent of the plume.

The lidar data were obtained and reduced by the NOAA Wave Propagation Laboratory (WPL). WPL furnished the laser backscatter intensities for each plume section, and also the second moments of the distribution of these data. We have computed the σ_z of the

backscatter intensities by integrating across the scan section along the lidar line-of-sight (nearly perpendicular to the transport direction), and fitting a reflected Gaussian envelope by the method of least squares. The location of the centerline is assumed to be equivalent to the centroid of the backscatter distribution, and the reflecting surface is set equal to the terrain elevation beneath the centroid. This fitting procedure provides both the centerline intensity and the best-fit σ_z for the cross-wind-integrated distribution of plume material. The estimates of σ_z from this procedure are nearly equal to the computed second moments of the distribution for most of the scans, and are used in preference to the calculated second moments only because the fitting procedure reduces the influence of "shadow zones" on σ_z.

Photographs of the oil-fog plume taken from positions off to the side of the plume trajectory have been analyzed for plume spread in the vertical at several distances along the plume trajectory. Daytime photographs were nearly instantaneous pictures of the plume, while nighttime photographs were time exposures over nominal 5-minute periods, although some photographs extended over 10-minute periods. Plume illumination at night was provided by moonlight or by a carbon arc lamp. When moonlight dominated, the edges of the plume in the photographs are generally diffuse owing to the blurring effect of passing puffs. When the arc lamp dominated, the plume image is made up of approximately ten distinct instantaneous plume images produced by the rotating lamp beam. These differences appear to have only a minor impact on estimates of σ_z.

Gifford's (1980) technique for deriving estimates of σ_z from photographs cannot, in general, be applied to the CCB photographs. This technique requires not only a reasonably uniform background and uniform illumination of the plume, but also that the plume be dispersed sufficiently within the field of view that the distance between the edges of the plume, defined as a particular light intensity value, can be seen to reach a maximum value. The latter two requirements are generally not satisfied in the CCB photographs. As a result, a comparison of plume thickness measurements with the lidar sections provides the best guidance in estimating σ_z from the plume photographs.

The lidar data and plume photographs from Experiment 210, hour 3 are the most detailed of the four experiments considered here. The plume image is well-defined in the 5-minute exposures, and one to two lidar scans upwind of the hill are available during nearly each 5-minute period of the hour. Pairing only those lidar and photo data from the same 5-minute time period, and within 50 m of each other in distance from the release point, we find that the six resulting data pairs produce an average ratio of plume depth to lidar-σ_z equal to 3.69 with a variance of 0.24. If we had assumed a top-hat distribution of plume material, this ratio would be expected to equal 3.46. If we had assumed a semi-circular distribution, it would be expected to equal 4.47. The average of 3.7 therefore appears consistent with the highly coherent nature of the plume during this

hour. Similar comparisons for the other three hours with lidar data are not as conclusive, but the result of each is not inconsistent with a ratio of about 3.7. Therefore, all estimates of the observed σ_z values used in the following analyses have assumed a factor of 3.7 in converting plume depths estimated from photographs to σ_z.

2.4.3 Comparison of Model Predictions with Observations

Figure 11 shows a plot of $\sigma_z/\sigma_w t$ versus t/T_L, where the dispersion time scale is

$$T_L = \frac{\ell}{\sigma_w} \quad ; \quad \frac{1}{\ell} = \frac{N}{\gamma^2 \sigma_w} + \frac{1}{\Gamma z_r} \tag{61}$$

where $\gamma = 0.52$, $\Gamma = 0.36$, and z_r is the height of release. Both σ_w and N are evaluated at z_r. The travel time t is taken to be x/u_r where u_r is the wind speed at z_r. Using z_r as the reference height implies that the scale of vertical variation of σ_w, N and u is larger than σ_z.

The solid line in the figure corresponds to Equation 60. We conclude that this theoretical curve explains the observations reasonably well. Note that the observations span the linear to the square root regions of σ_z growth. This supports the appropriateness of the T_L formulation. The circled points in the figure refer to a few 5-minute time periods in which the measured σ_w were small when the photographs clearly indicated large sigmas. We believe that the relatively large deviation of these points from the other data reflects the inevitable uncertainties associated with the measurement and interpolation of the micrometeorological variables. However, the overall agreement between theory and experiment is good. Note that over the range of t/T_L considered, the form of the interpolation contained in Equation 60 produces σ_z values that differ little from those produced by the σ_z expression based on an exponential correlogram for the vertical velocities.

The performance of Equation 60 is further illustrated in the scatterplot of Figure 12. The model for σ_z does seem to underpredict slightly at large σ_z. Note, however, that 95% of the 680 observations used in the analysis are within a factor of two of the σ_z predictions.

The importance of including ℓ_n (neutral length scale) in determining T_L is illustrated through Figure 13. Here σ_z is computed using only ℓ_s. Notice that most of the points are below the horizontal "perfect fit" line. For an adequate model, the points should be symmetrically distributed about unity if we make the assumption that the ratio σ_z (observed)/σ_z (predicted) is lognormally distributed. Note that ℓ_n becomes important when ℓ_s is comparable to ℓ_n. If ℓ_n is not accounted for, the overall length scale ℓ, and hence T_L is larger than it should be. This would lead to an overprediction of σ_z that is illustrated by the points near $\ell_s/\ell_n > 0.5$ (points for which $\ell_s > \ell_n$ are plotted at $\ell_s/\ell_n = 1$).

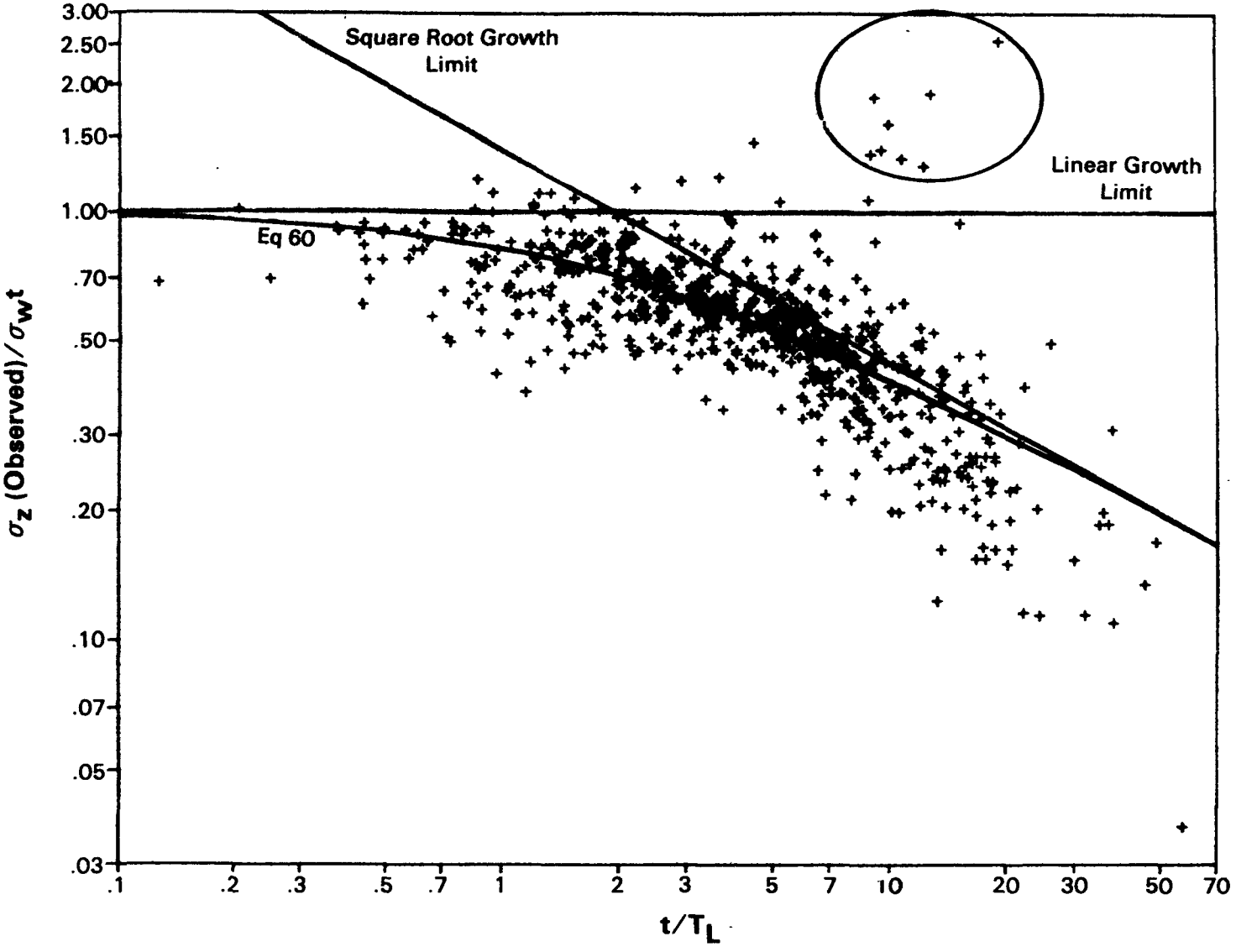

Figure 11. Variation of $\sigma_z/\sigma_w t$ with t/T_L.

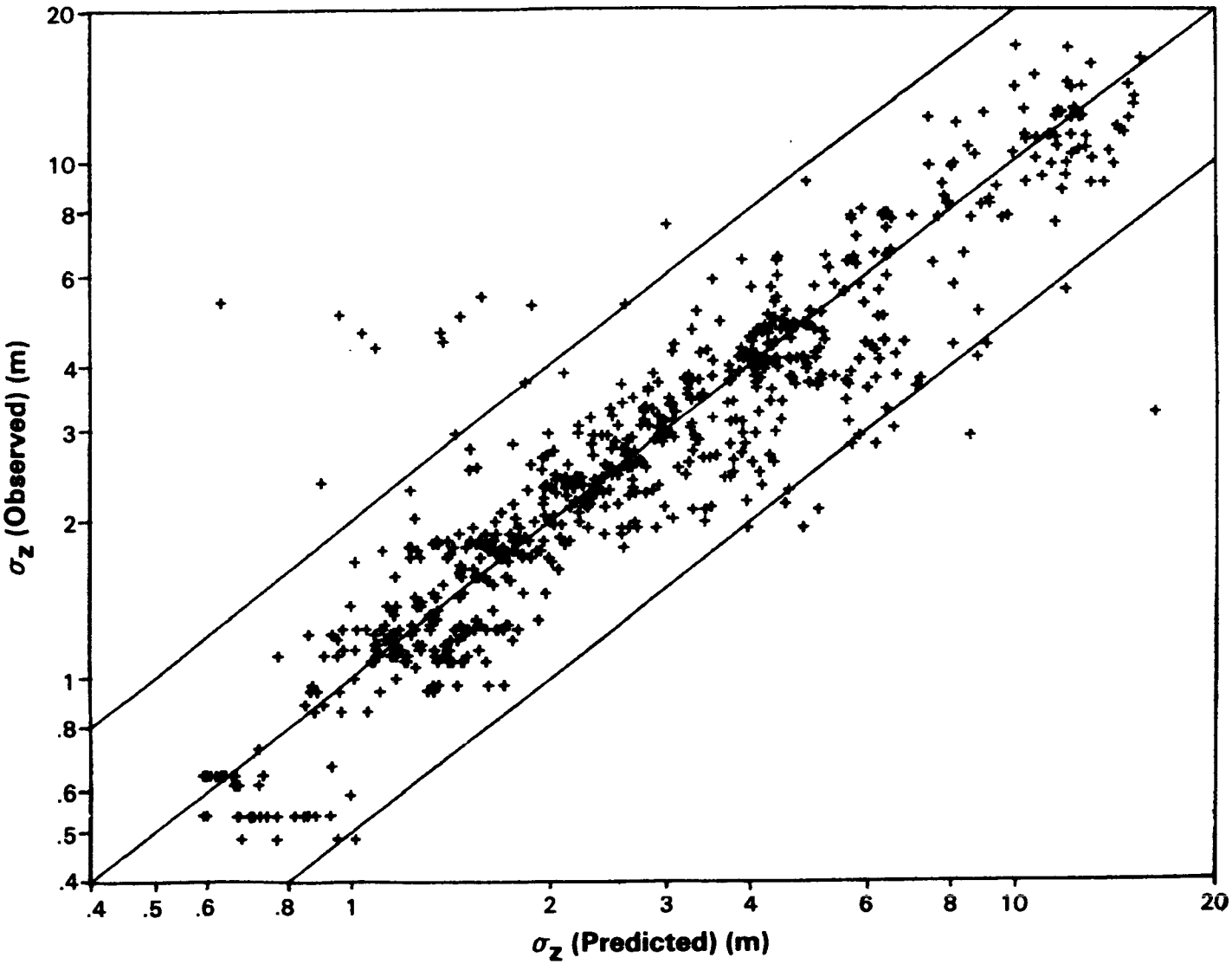

Figure 12. Scatterplot of σ_z (observed) against σ_z (predicted). Factor of 2 boundaries are marked in the figure.

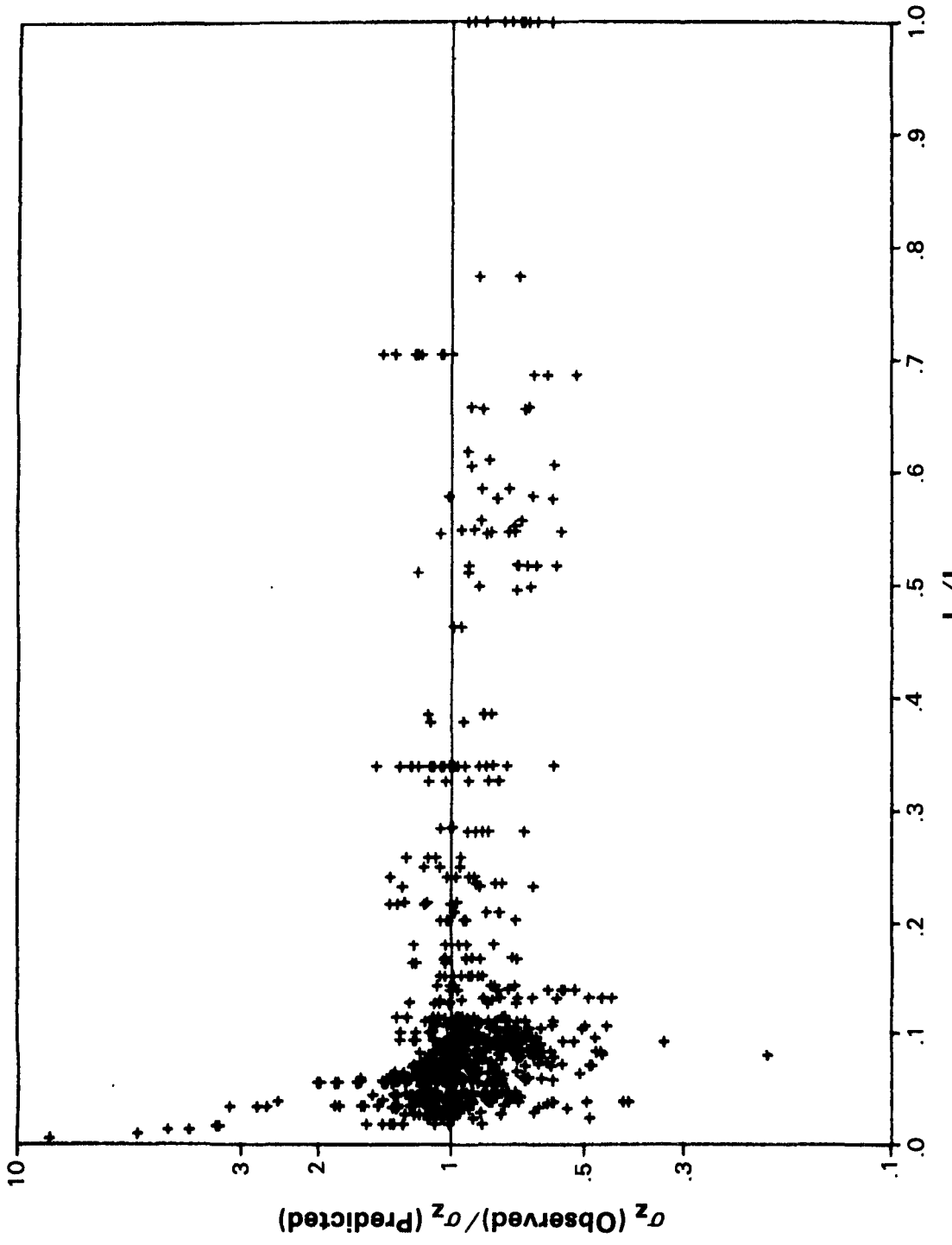

Figure 13. Variation of σ_z (observed)/σ_z(predicted) with ℓ_s/ℓ_n. Only ℓ_s is used in calculating σ_z.

Figure 14 shows the effect of including ℓ_n in the formulation for T_L. We see that there is an improvement in the distribution of points for $\ell_s/\ell_n > 0.5$.

2.5 Formulation of σ_y

Past versions of CTDM have estimated σ_y by assuming that the transverse spread of the plume grows linearly with time. This implies that the Lagrangian time scale for the transverse spectrum is long compared to the time of travel to the hill. While this may be the case for many of the CCB experiments, there are some experiment-hours in which the linear growth law appears to overestimate the dilution of the plume. This is deduced from comparisons of observed ground-level SF_6 concentrations with estimates of the plume "centerline" concentrations.

The Lagrangian time scale can be incorporated in the expression for σ_y by means of the interpolation contained in the σ_z formulation:

$$\sigma_y = i_y s/(1 + \frac{s}{2uT_{LT}})^{0.5} \tag{62}$$

The Lagrangian time scale for the transverse spectrum, T_{LT} cannot be estimated from the flow properties, but it may be estimated from the turbulence measurements. Pasquill and Smith (1983) point out that if the turbulence is assumed to be isotropic, and if the longitudinal correlogram is modeled by an exponential with an Eulerian time scale of T_E, then

$$(\frac{\sigma_{v\tau}}{\sigma_{v\infty}})^2 = 1 - \frac{T_E}{\tau}\ (1 - e^{-\tau/T_E}) \tag{63}$$

gives the relationship between the crosswind turbulence measured over a time τ, to that measured for an infinite sampling time. Because we have measured i_y (5-min) and i_y (60-min), we can solve for T_E. Then the Lagrangian time scale for the transverse spectrum (Pasquill and Smith 1983) is approximately equal to

$$T_{LT} = 0.5\ T_L = 0.5\ T_E\ (0.68/i_{y\infty}) \tag{64}$$

where

$$i^2_{y\infty} = \frac{i^2_y\ (5\text{-min})}{1-\frac{T_E}{300}(1-e^{-300/T_E})} \tag{65}$$

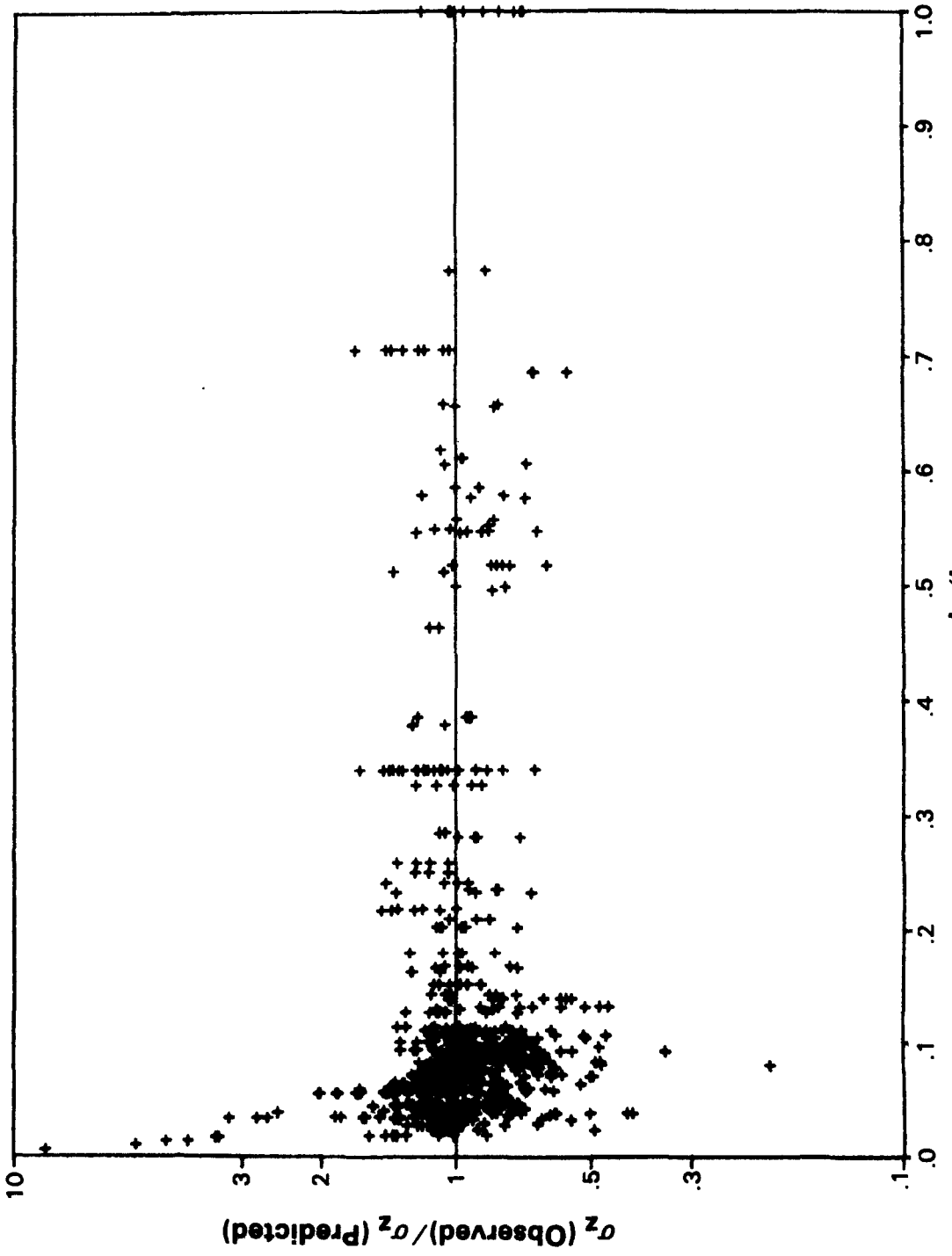

Figure 14. Same as Figure 13, except ℓ_n is included in the formulation of σ_z.

2.6 Other Revisions

2.6.1 Density of the Tracer Gas

SF_6 has a molecular weight of 146, and CF_3Br has a molecular weight of 149. Dry air has a molecular weight of only 29, so that both tracers are approximately five times as dense as air. Because the tracers were not mixed into the fogger jet at CCB, they undoubtedly experienced some fall in height beyond the release point. The same is true for the CF_3Br released at HBR because it was released at a height different from the oil-fog generator. The SF_6 was completely mixed into the jet fogger at HBR.

This fall is estimated by means of the Briggs (1975) stable and neutral plume rise formulas:

$$\Delta h_n = 1.6\ (F\ s^2)^{0.33}/u \qquad \text{(neutral)}$$
$$\Delta h_s = 2.03\ (F/uN'^2)^{0.33}\ (1-\cos(N's/u)^{0.33} \qquad \text{(stable)} \tag{66}$$

where $N'^2 = N^2M_{eff}/M = N^2/2.25$

Note that M is the flux of vertical momentum within a bent-over plume, and M_{eff} if the effective flux. For the stable rise formula, Δh_s is constant beyond $s=1.5\pi u/N'$. In practice, the minimum of the two height change formulas is taken.

The buoyancy flux F is the product of the buoyancy and the volume flux of the tracer gas. For SF_6,

$$F = ((\rho_{SF6} - \rho_{air})g/\rho_{air}) \cdot (Q/\rho_{SF6}) \tag{67}$$

The densities of air and, in this example, SF_6 are given by

$$\rho_{air} = \frac{P}{R^*T}\ 28.966$$
$$\rho_{SF6} = \frac{P}{R^*T}\ 146.05 \tag{68}$$

where $R^* = 8.3144$ J/mole/°K. For T = 0°C and P = 840mb, the buoyancy flux of SF_6 is related to the emission rate (g/sec) by

$$F = 0.00733\ Q\ (m^4/gs^2) \tag{69}$$

Equation 66 will probably overestimate the height change resulting from the weight of the tracer. These relationships do not account for the turbulent mixing caused by the eddies in the wake of the release crane. Also, when the tracer was released near the oil-fog generator, it may at times have been mixed by the turbulent eddies induced by the fogger jet.

2.6.2 Wind Speed Shear

The increase in wind speed with height is significant in many of the CCB experiments. When K_z is considered constant with height, the effect of this shear on the vertical distribution of plume material can be estimated.

Hunt (1981) quotes a result obtained by Lauwerier (1954) for the plume concentration profile in the vertical for K_z constant. This result is approximate, and is valid near the centerline of the plume (say, within $\sigma_z/2$ of the plume centerline). When a new Gaussian distribution is fit to this vertical distribution, the effective plume height is found to be lower than the original height, and it is nearly equal to the height of maximum concentration in Lauwerier's solution:

$$z_r^* = z_r - \frac{u}{du/dz}\left[1 - \left(1 - \left(\frac{\sigma_z\, du/dz}{u}\right)^2\right)^{0.5}\right] \qquad (70)$$

Consequently, the shear-altered vertical distribution of plume material is approximated in CTDM by a reduction of the plume height as estimated above. The point chosen for evaluation in the LIFT module is "s_o."

SECTION 3

MODELING CCB

3.1 Data Analysis and Interpretation--the Modelers' Data Archive (MDA)

Meteorological data obtained at the 150-m tower (Tower A) and inferred from lidar data and the available photographs of the oil-fog plume have been compared for all CCB experiments. The comparisons include estimates of the wind direction and the vertical intensity of turbulence at the height of the oil-fog plume.

3.1.1 Wind Direction

Photographs taken from behind the release crane looking along the plume trajectory and those taken from atop CCB looking back toward the release crane are the key views of the oil-fog plume that are most important in estimating wind directions. For those views from behind the crane, wind directions are most easily estimated when the plume passes over some recognizable portion of the hill. Any horizontal displacement of streamlines that may occur when the plume is close to the hill is subjectively taken into account. For views from the hilltop, wind directions are most easily estimated when the plume passes over one of the camera positions on either peak, or when the plume obscures a known landmark on the ground away from the hill (such as a turn in a road). The wind direction estimates from the photographs are least accurate when the plume misses the hill to one side or the other. The most useful information that can be obtained during such periods when the plume is off to the side of the hill is that the plume is not currently contributing to one-hour-average tracer concentrations measured in the sampler array.

The comparisons between the photo estimates of wind direction and those interpolated to the release height from the Tower A wind data are shown in Figure 15 (a-e). In these figures, the direction from the origin of the polar grid coordinate system (at the "center" of CCB) to the source is indicated by the solid horizontal line. The MDA wind directions at plume height are indicated by a dashed line. Estimates of wind directions taken directly from the photographs are indicated by a solid line labeled with a "p." When the photographs were ambiguous, the photos in combination with other sources of information were used to estimate the wind directions. For these periods the solid line is labeled with a "x."

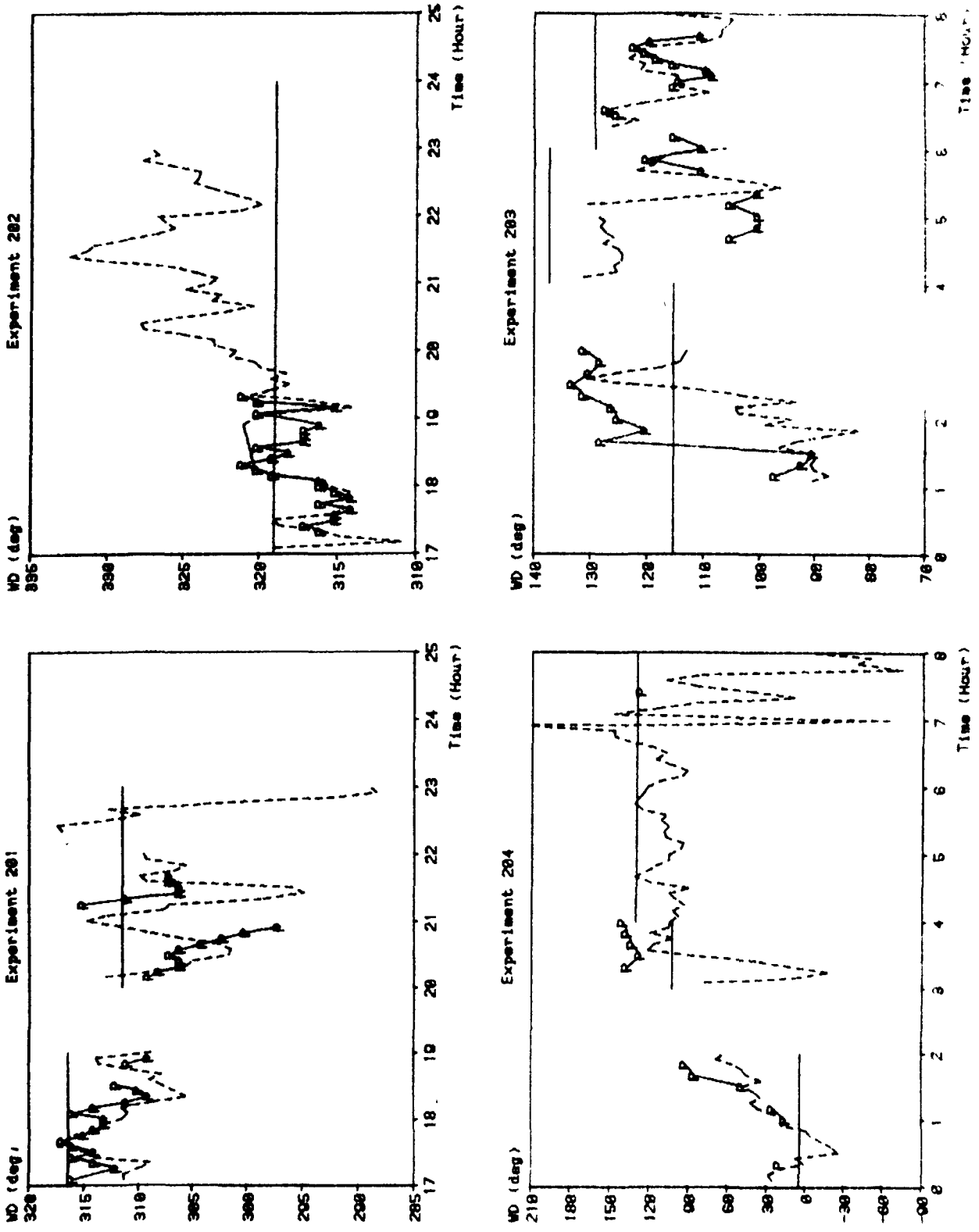

Figure 15a. Time series of MDA wind directions at oil-fog height (---) and estimates made from photographs (-p-). Estimates derived from the photos and other sources of information are denoted by (-x-).

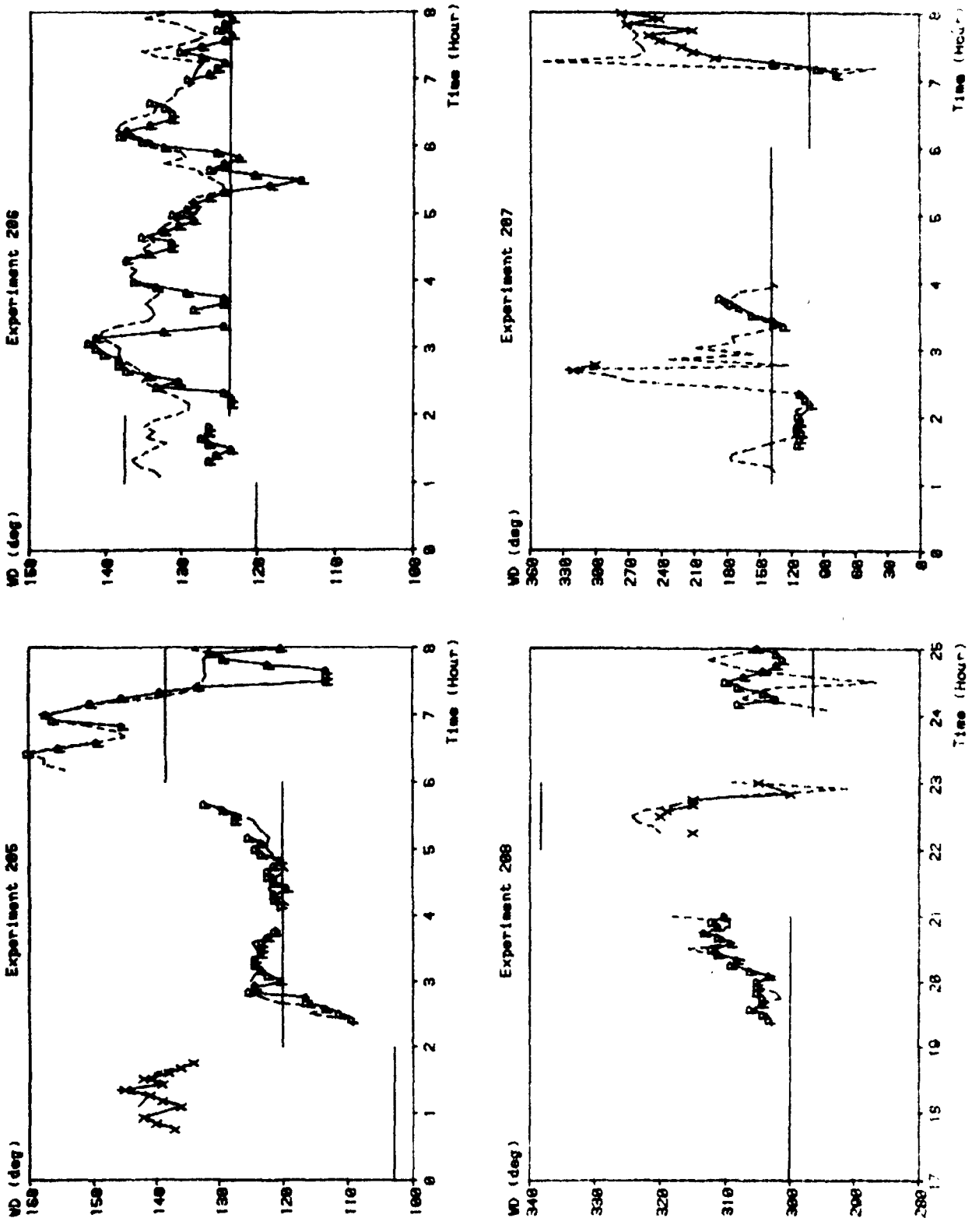

Figure 15b. Time series of MDA wind directions at oil-fog height (- - -) and estimates made from photographs (-p-). Estimates derived from the photos, and other sources of information are denoted by (-x-).

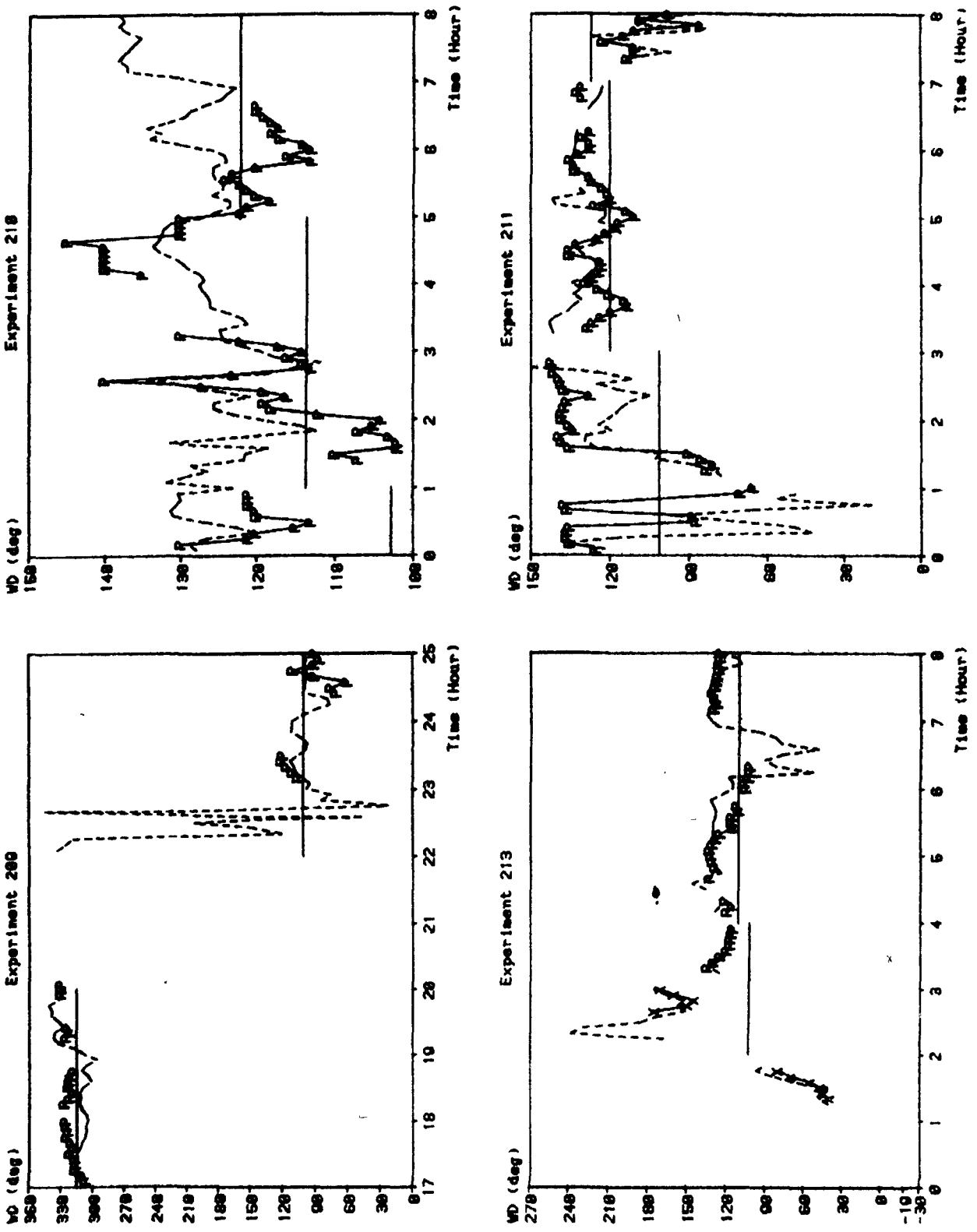

Figure 15c. Time series of MDA wind directions at oil-fog height (---) and estimates made from photographs (-p-). Estimates derived from the photos and other sources of information are denoted by (-x-).

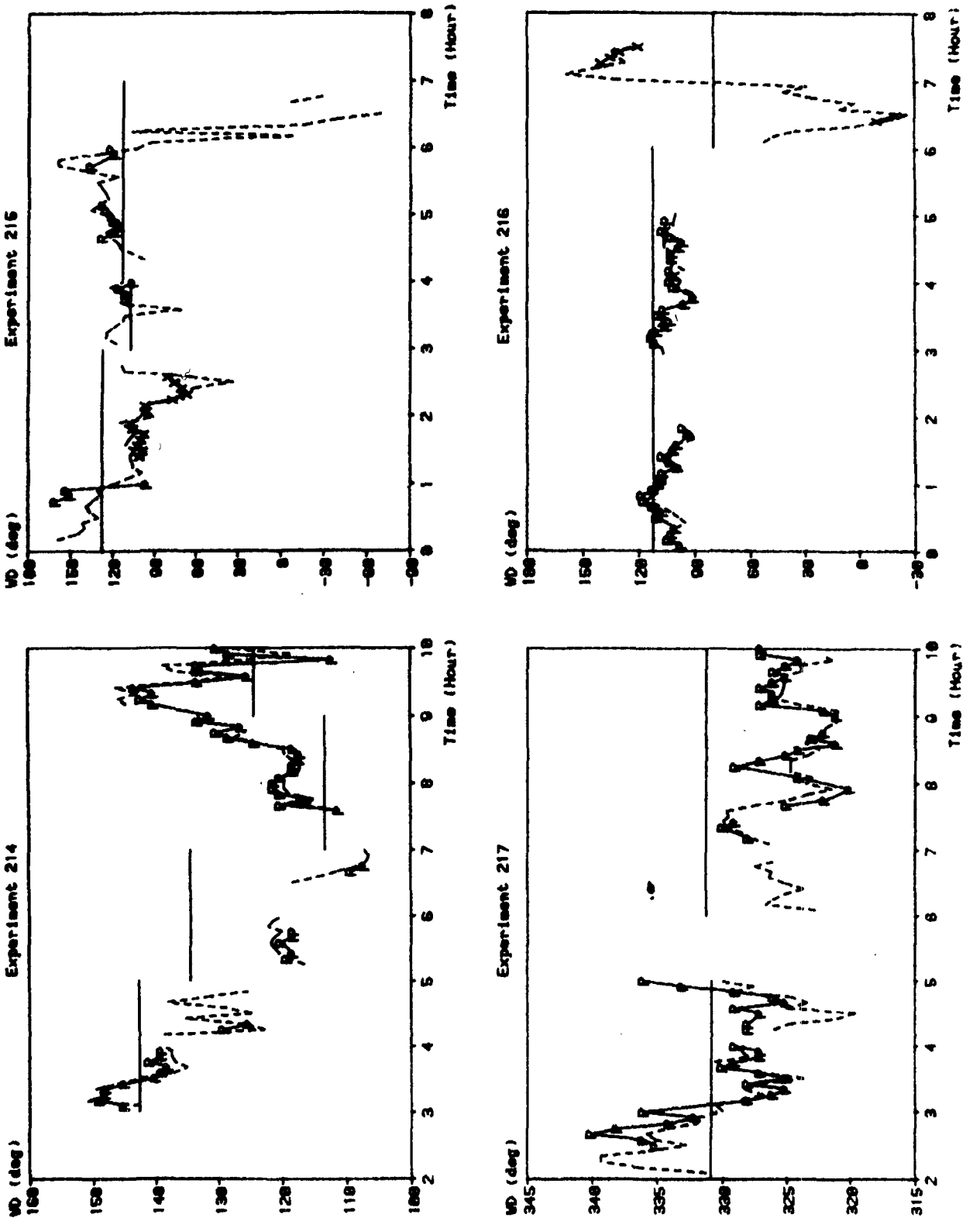

Figure 15d. Time series of MDA wind directions at oil-fog height (---) and estimates made from photographs (-p-). Estimates derived from the photos and other sources of information are denoted by (-x-).

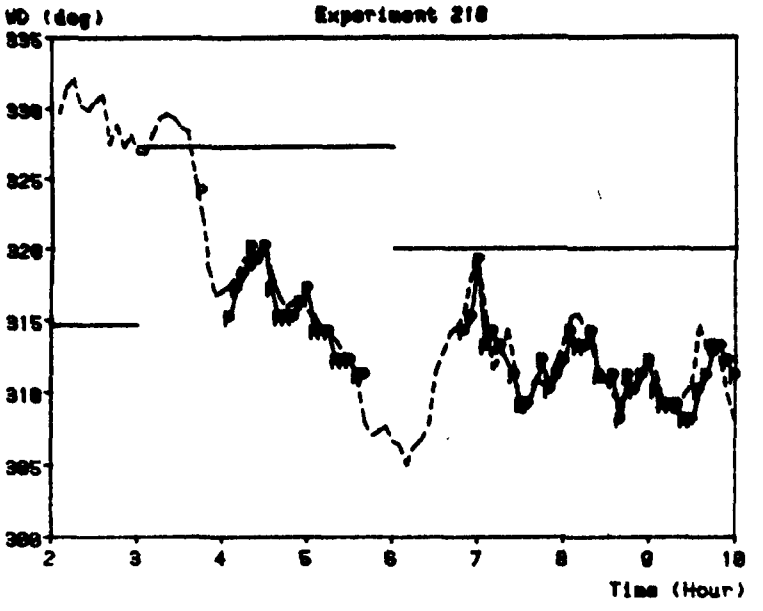

Figure 15e. Time series of MDA wind directions at oil-fog height (---) and estimates made from photographs (-p-). Estimates derived from the photos and other sources of information are denoted by (-x-).

In general, the oil-fog plume trajectory agrees with the wind direction data from Tower A interpolated to release height. Significant deviations from the photographic evidence do occur and these are summarized in Table 1. Many of the discrepancies may be readily attributed to errors in estimating trajectory directions for plumes traveling to the side of the hill. In other cases, the discrepancies appear to arise from insufficient vertical resolution in measuring the wind field. The 40-m level wind directions are not available for four experiments.

3.1.2 Vertical Intensity of Turbulence

Estimates of σ_z are made from individual instantaneous photographs, individual 5- or 10-minute-long photographic time exposures, and from individual lidar scans of the oil-fog plume. Photographs suitable for inferring values of σ_z are available from all CCB experiments except Experiment 216, and lidar data are available from 11 experiments. The method used to calculate σ_z from the lidar data and the photographs is described in Section 2.4. The estimates of σ_z obtained from the lidar data and the photographs, the inferred distance from the source to the observation (s), and the MDA values of the wind speed (u) and the Brunt-Vaisala frequency (N) for each 5- or 10-minute period are used to find an optimum value of i_z. The following formulation for σ_z is used

$$\sigma_z = \frac{i_z s}{\left(1 + \frac{i_z s}{2}\left(\frac{N}{\gamma^2 i_z u} + \frac{1}{\Gamma z_r}\right)\right)^{0.5}} \qquad (71)$$

where $\gamma^2 = 0.27$, $\Gamma = 0.36$ and z_r is the release height.

As shown in Figure 16 (a-e), the lidar and photo estimates of i_z are in general agreement with the MDA values of i_z. Significant deviations (differing by more than a factor of two) from the photographic and lidar values do occur and these are summarized in Table 2. The values of i_z interpolated to the release height from Tower A data are generally appropriate, although the lower values of i_z which approach 0% appear consistently too small. Whether or not the response of the instruments can detect values that approach 0% is not known. The lowest photo-inferred value of i_z is 1%.

Wider variability in the lidar estimates are to be expected because the lidar estimates for each 5-minute period are obtained from one to two instantaneous scans of the plume. The lidar estimates tend to be biased toward under-representing the magnitude of the 5-minute i_z data. The lidar estimates corroborate the large photo-inferred values of i_z (>10%) for Experiments 204 and 209. The estimates of i_z differ by less than a factor of two. Conversely, the lidar estimates contradict the large photo-inferred values of i_z observed during Experiment 213. The photo observations are more than a factor of three times the lidar estimates of i_z.

TABLE 1. PERIODS OF SIGNIFICANT DISCREPANCY BETWEEN WIND DIRECTION ESTIMATES MADE ON THE BASIS OF TOWER A DATA AND PLUME TRAJECTORIES INFERRED FROM PHOTOGRAPHS

Exp.	Time	Release Ht (m)	Release	Splined Profile WS	Splined Profile Δ θ (± 10m)**	Probable Cause of Discrepancy
201	2100–2300	30	NW	4	25°	Apparent time shift unexplained
202	1800–1900	50	NW	10	1°	Missing tower data interpolated in time
203	0130–0230	30	SE	3	30°	Directional wind shear
	0430–0500	59	SE	4	1°	Unknown
204	0130–0200	30	N	1	1°	Very large (30°–60°) trajectory angle to hill
	0300–0400	30	SE	1	30°	Light, variable winds; directional wind shear
205*	0720–0740	30	SE	3	2°	Faint, instantaneous plume image
206	0100–0200	46	SE	7	1°	Missing 40-m data
	0300–0400	35	SE	5	2°	Missing 40-m data
	0520–0540	35	SE	2	60°	Missing 40-m data
208	0000–0100	30	NW	4	20°	Directional wind shear
210*	0030–0100	40	SE	3	15°	Large (25°) trajectory angle to hill
	0100–0230	57	SE	5	5°	Missing 40-m data
	0400–0430	58	SE	–	–	Large (15°) trajectory angle to hill
	0540–0640	58	SE	8	1°	Missing 40-m data
211*	0000–0100	30	SE	2	110°	Missing 40-m data
	0200–0300	30	SE	4	35°	Large trajectory angle to photographer
	0300–0400	58	SE	6	2°	Missing 40-m data
	0500–0525	20	SE	4	15°	Missing 40-m data
	0630–0700	58	SE	6	1°	Missing 40-m data
213	0500–0600	58	SE	3	4°	Unknown
215	0040–0100	57	SE	5	2°	Unknown

*40-m level wind direction is not available.
**Wind direction shear estimated within 10 m of the release height.

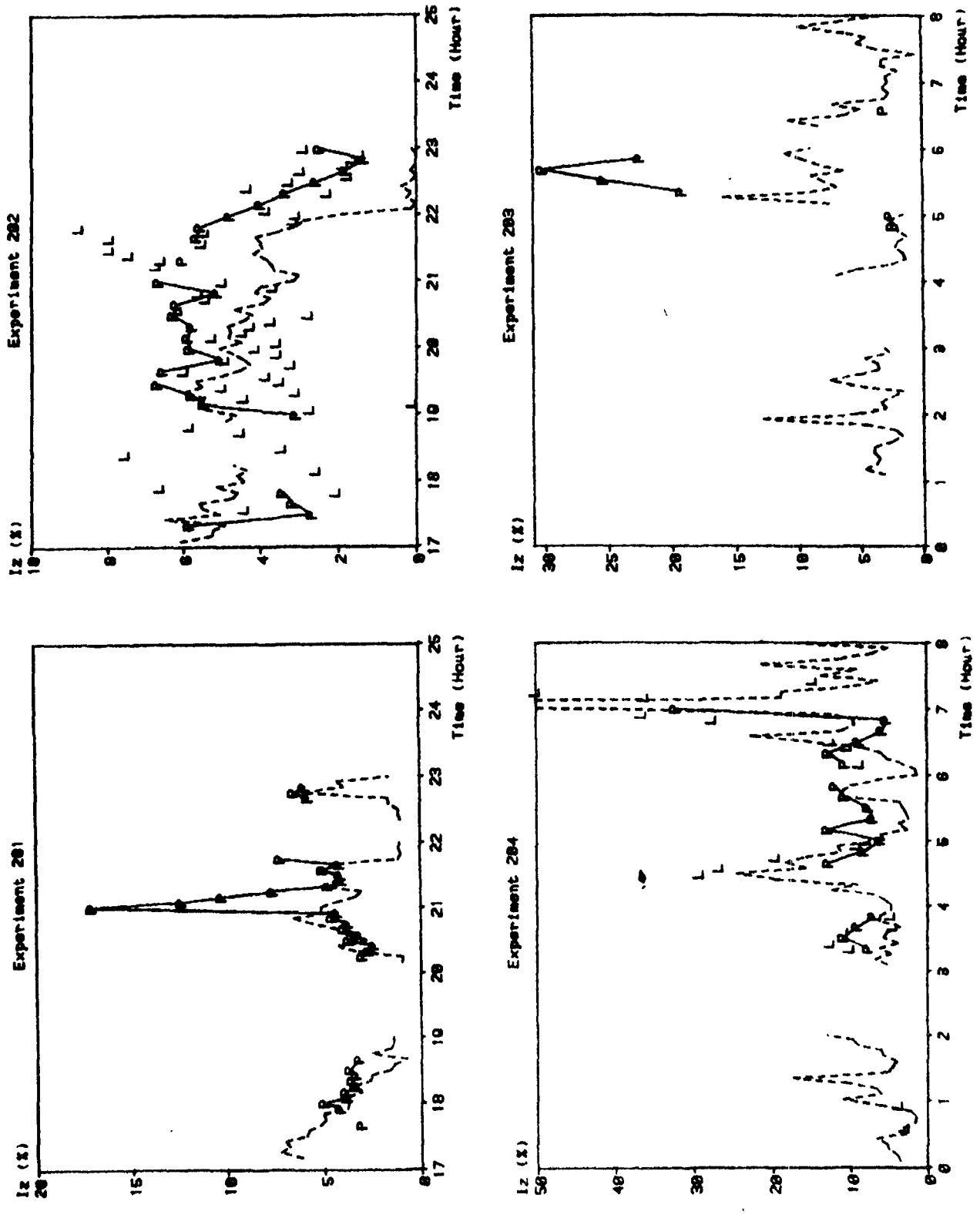

Figure 16a. Time series of MDA vertical turbulent intensities at oil-fog height (---), photo estimates (-p-), and lidar estimates (L).

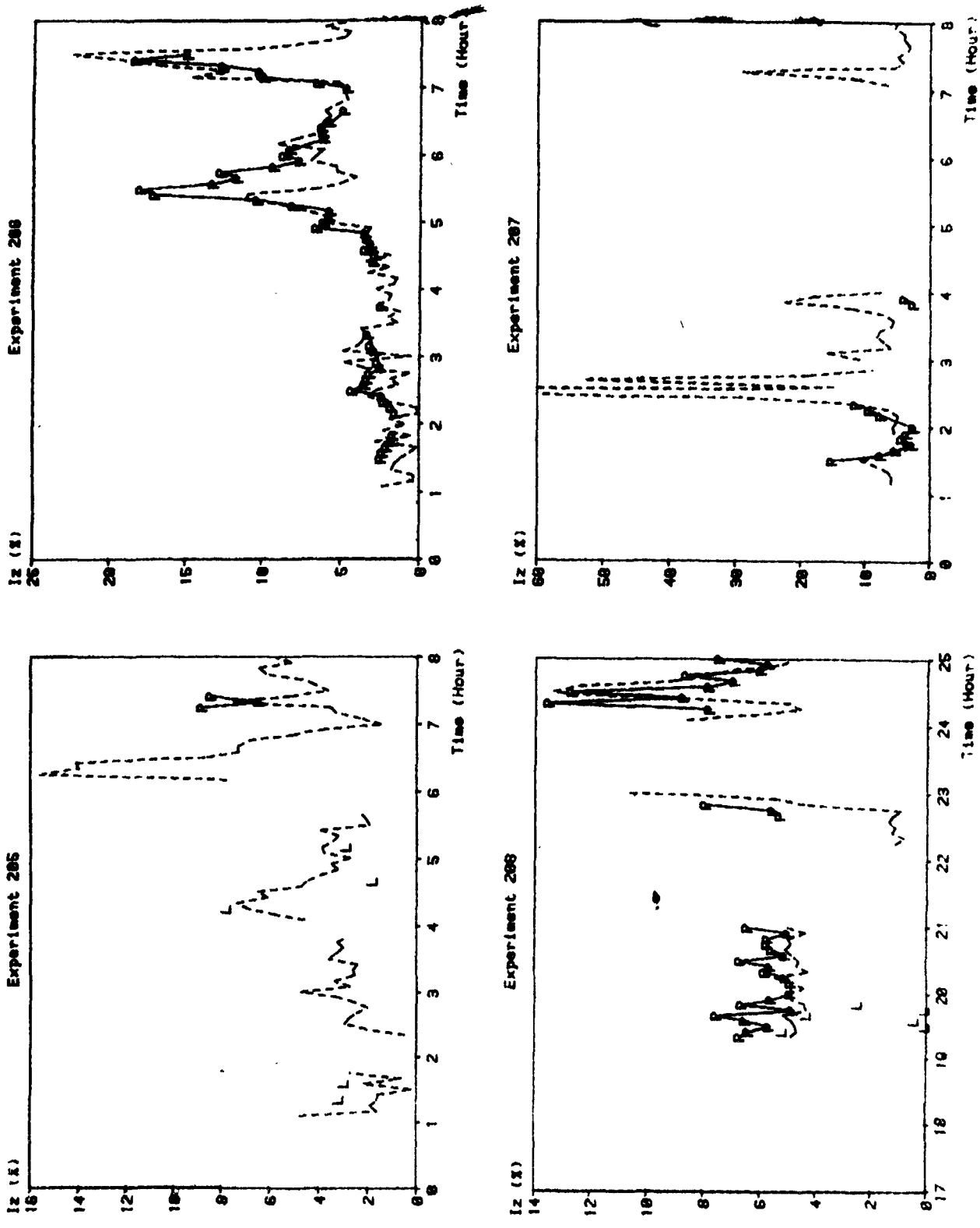

Figure 16b. Time series of MDA vertical turbulent intensities at oil-fog height (---), photo estimates (-p-), and lidar estimates (L).

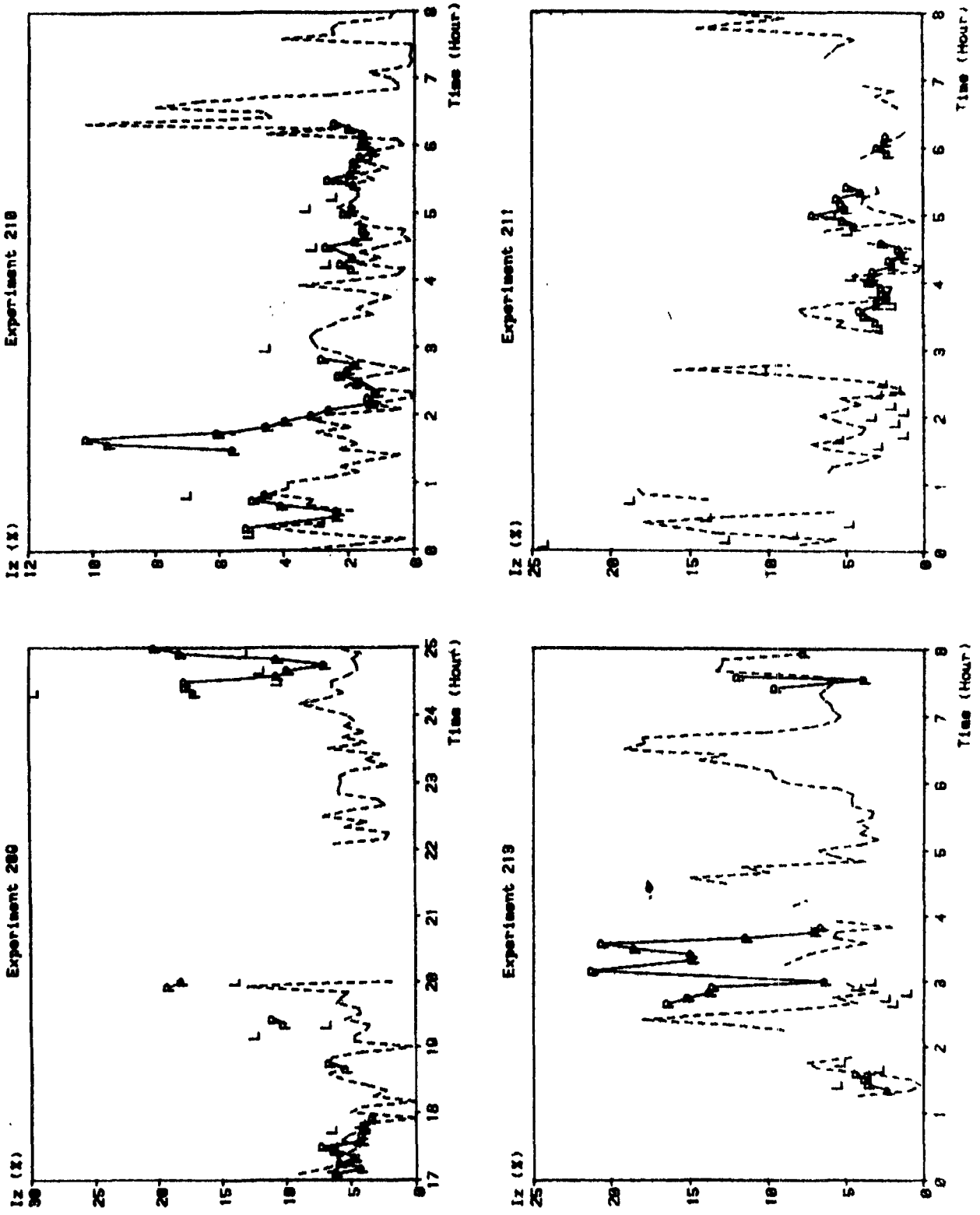

Figure 16c. Time series of MDA vertical turbulent intensities at oil-fog height (---), photo estimates (-p-), and lidar estimates (L).

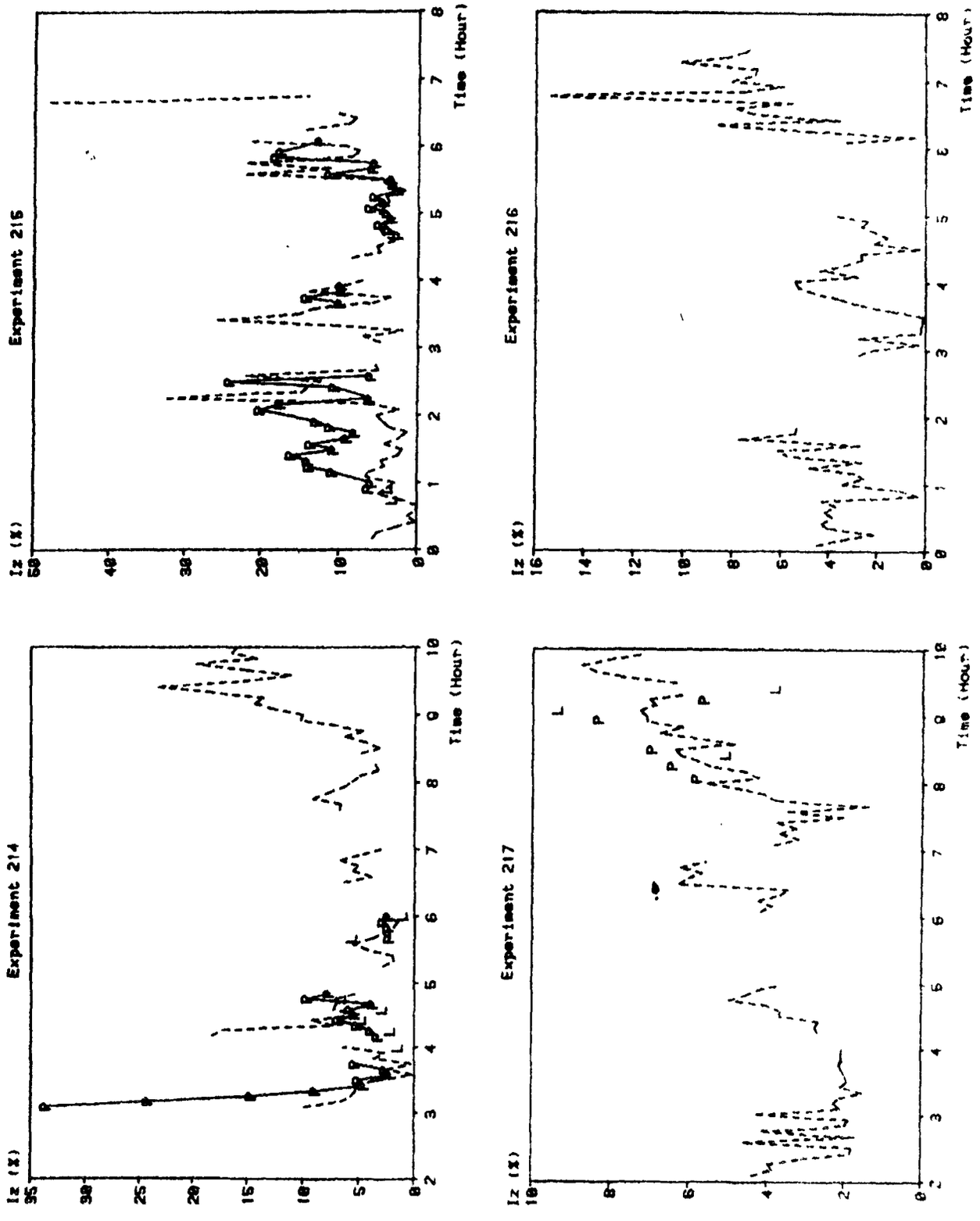

Figure 16d. Time series of MDA vertical turbulent intensities at oil-fog height (---), photo estimates (-p-), and lidar estimates (L).

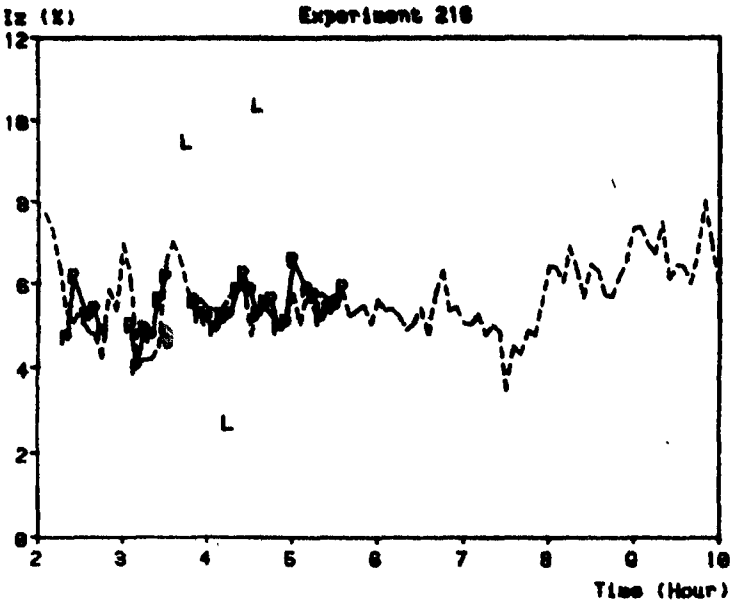

Figure 16e. Time series of MDA vertical turbulent intensities at oil-fog height (---), photo estimates (-p-), and lidar estimates (L).

TABLE 2. PERIODS OF SIGNIFICANT DISCREPANCY BETWEEN i_z ESTIMATES MADE ON THE BASIS OF TOWER A DATA AND i_z VALUES INFERRED FROM PHOTOGRAPHS

Exp.	Time	Release Ht (m)	Release	Probable Cause of Discrepancy
201	2100-2200	30	NW	Time Shift/interpolation
202	1700-1800	50	NW	Instantaneous photos
	2200-2300	40	NW	MDA i_z approaches 0% (Photo i_z agrees with 10-m Tower A i_z with a time shift)
203	500-600	30	SE	Horizontal plume meander/faint plume image
206*	500-600	35	SE	Missing 40-m data
207	350-400	30	SE	Unknown
209	1755,1810,1900	40	NW	MDA i_z approaches 0%
	1905-2000	40	NW	Unknown
	2400-2500	30	SE	Interpolation (i_z at 10m is 2 to 5 times larger than i_z at 40m)
210*	100-200	57	SE	Missing 40-m data
211*	410-415	58	SE	MDA i_z approaches 0% (Photo i_z agrees with 2-m and 30-m Tower B i_z and 10-m Tower C i_z)
	455	20	SE	MDA i_z approaches 0% (Photo i_z agrees with 2-m Tower D i_z)
213	125	40	NW	MDA i_z approaches 0%
	300-400	50/30/40	SE	Interpolation
214	305-320	47	SE	Tower A not representative (Photo i_z agrees with 10-m Tower C, D, and F values of i_z)
	335, 345	47	SE	MDA i_z approaches 0% (Photo i_z agrees with 10m Tower C i_z)
215	100-200	57	SE	Tower A not representative (Photo i_z agrees with 2-m and 10-m Tower C i_z)

*40-m wind speed not available.

Other possible sources of discrepancy are listed below. The larger values of i_z estimated from the photographs often occur during periods of significant horizontal plume meander and this horizontal "smearing" could appear as an increase in the vertical dimension of the plume in the photographs. The larger photo-inferred values of i_z do not agree with the MDA values but are often corroborated by values of i_z measured at the 10-m and 30-m towers on CCB. Some of the photo-inferred values of i_z were obtained from instantaneous photographs and 10-minute long photographic time exposures; whereas the MDA values were obtained from 5-minute averaged Tower A data.

3.2 Classification of CCB Experiment Hours

The CCB MDA for SF_6 has been partitioned according to the relationship between the tracer release height above ground and the one-hour average value of H_c. A "neutral" class contains all hours in which H_c is less than or equal to 2 m (the lowest instrumented level at the 150-m tower). A "very stable" class contains all hours in which H_c is considerably greater than the release height. For this classification, H_c values nearly equal to or greater than z_r + 10 m are included. The 10-m value is chosen so that the bulk of a typical stable plume would be below H_c. A third class contains all hours in which H_c is nearly equal to z_r, i.e., H_c approximately equals $z_r \pm 10$ m. This class includes the hour in which the greatest scaled concentration (χ/Q) was observed. The fourth class contains all remaining hours.

Of the 111 hours in the SF_6 MDA, 22 are in the class $H_c \leq 2$ m; 29 are in the class $H_c \geq z_r + 10$ m; 26 are in the class $H_c = z_r \pm 10$ m; and 34 are in the remaining class. In the modeling presented in the following sections, we are primarily interested in evaluating model performance for those hours in which a reasonably good concentration pattern was observed. Hours with near zero concentrations at all but a few samplers near the base of the hill (to one side or other with respect to the release position) may be "modelable," but are not as important from the point of view of developing and testing a model for stable plume impingement conditions. When these hours are removed, 21 hours remain in the class $H_c \leq 2$ m; 20 remain in the class $H_c \geq z_r + 10$ m; 20 remain in the class $H_c = z_r \pm 10$; and 26 remain in the fourth class.

Each of these hours has been reviewed to see to what extent the MDA data reflect the wind directions (WD) and intensities of vertical turbulence (i_z) inferred from smoke photographs and lidar data, as well as the temporal and spatial concentration patterns revealed by the 10-minute average concentration data. The MDA was changed whenever possible when significant discrepancies were found. In some cases, an hour had to be removed because the directional wind shear was too great between measurement heights on the tower to adequately reconcile the MDA and the smoke plume appearance. Furthermore, a few additional hours were removed because the Tower A data were thought to

be unrepresentative of the release location, or because the observed concentrations appeared to make no "sense." Tables 3 through 6 summarize several meteorological variables of each hour remaining, and indicate which hours were modeled with the modified MDA.

The class boundaries prescribed above were obtained somewhat arbitrarily. In particular, the choice of a 10-m zone above and below the release height in defining what is meant by "z_r approximately equal to H_c" was guided mainly by the vertical size of a representative stable plume. However, for the range of release heights in the CCB data base, this choice of class boundaries is nearly equivalent to the statements:

"Very Stable": $H_c/z_r \geq 1.25$
"z_r nearly equals H_c": $1.25 > H_c/z_r > 1/1.25$
"Moderately Stable": $1/1.25 > H_c/z_r > 0$
"Weakly Stratified": $H_c = 0$

where $H_c = 2$ m is considered to be equivalent to $H_c = 0$. This form of classification could provide a better indication of what streamline patterns may be expected in each class.

3.3 Model Performance

The performance of CTDM is prescribed in an absolute sense by presenting the statistics of the residuals of the observed and modeled concentrations. These statistics are compiled for the concentration fields grouped by experiment hour, grouped by the four classes discussed above, and grouped together for the entire 80-hour SF_6 data base selected for this evaluation. The specific statistical measures are discussed in subsequent subsections.

The performance of CTDM is prescribed in a relative sense by comparing its residual statistics with those from a "flat terrain" version of the model, and a version that incorporates the plume path assumptions of COMPLEX I/II. This type of comparison places the performance of CTDM in perspective by contrasting it with that of two well-known modeling approaches. The relative performance of these three models in each of the four classes will indicate when terrain effects are most important, and when the simpler modeling algorithms are just as good or better than the more complex algorithms of CTDM.

The performance of CTDM is also evaluated for three alternative sets of meteorological data which reflect varying quantities of on-site meteorological information.

3.3.1 Absolute and Relative Performance

CTDM

Several parameters need to be specified before CTDM can produce concentration estimates. These are

TABLE 3. SF_6 TRACER HOURS AT CCB WITH $H_c \leq 2$ m

Exp-hr	Time Ending	u (m/s)	z_r (m)	H_c (m)	MDA Modifications
201-1	18	6.8	30	0	-
202-1	18	10.3	50	0	-
202-3	20	7.7	20	0	-
202-4	21	7.0	20	1	i_z
208-3	20	9.1	30	0	-
208-4	21	8.4	30	0	-
214-8*	10	2.4	24	0	WD
217-1	3	4.8	30	2	-
217-3	5	5.4	25	2	WD
217-5*	7	7.2	40	0	-
217-6*	8	7.2	40	0	-
217-7*	9	6.7	40	0	-
217-8*	10	5.8	40	0	-
218-2	4	6.7	30	0	-
218-3	5	8.7	30	0	-
218-4	6	8.1	30	0	-
218-5*	7	7.2	30	0	-
218-6*	8	7.9	30	0	-
218-7*	9	6.9	15	0	-
218-8*	10	8.5	15	0	-

Total Number of Hours: 20

*Oil-fog and SF_6 were not released at the same height for all or part of the hour.

TABLE 4. SF_6 TRACER HOURS AT CCB WITH $H_c \geq z_r$ +10 m

Exp-hr	Time Ending	u (m/s)	z_r (m)	H_c (m)	MDA Modifications
204-1	1	2.2	30	61	-
204-2	2	1.1	30	81	-
204-5	5	1.2	30	44	-
204-6	6	1.7	30	39**	i_z
204-7	7	1.0	30	45	i_z
204-8	8	0.5	30	52	-
205-7	7	1.7	30	41	-
213-5*	5	1.2	30	42	-
213-6*	6	0.7	30	49	-
213-7*	7	1.1	30	44	-
213-8*	8	1.0	30	40	WD
214-2*	4	1.2	17	31	-
214-3*	5	1.6	24	43	-
215-4	4	2.3	30	37**	-
215-6*	6	1.4	30	42	i_z

Total Number of Hours: 15

*Oil-fog and SF_6 were not released at the same height for all or part of the hour.

**Two hours are included in this class even though they do not meet the criterion $H_c \geq z_r$ + 10 m.
These are included because: (1) This class has the fewest members.
(2) H_c lies substantially above the plume elevation.

TABLE 5. SF_6 TRACER HOURS AT CCB WITH $H_c = z_r \pm 10$ m

Exp-hr	Time Ending	u (m/s)	z_r (m)	H_c (m)	MDA Modifications
201-4	21	3.8	30	23	WD, i_z
201-5	22	3.7	30	26	WD, i_z
201-6	23	3.2	30	31	-
203-2	2	3.0	30	33	WD
203-3	3	2.5	30	31	WD
203-8	8	3.4	50	40	-
205-8	8	2.8	30	30	WD
206-6	6	1.8	35	37	WD, i_z
206-7	7	2.4	35	31	-
206-8	8	1.8	35	37	WD
209-3	20	2.2	40	37	-
209-8*	25	2.3	40	45	-
211-2	2	3.0	30	27	-
211-3	3	2.5	30	33	-
211-5*	5	2.3	20	25	-
211-6*	6	3.4	20	20	WD
211-7*	7	2.8	20	21	-
214-4*	6	3.2	24	23	-
215-1*	1	2.8	30	23	-
215-5*	5	3.5	30	26	-

Total Number of Hours: 20

*Oil-fog and SF_6 were not released at the same height for all or part of the hour.

TABLE 6. SF_6 TRACER HOURS AT CCB WITH 2 m < H_c < z_r-10 m

Exp-hr	Time Ending	u (m/s)	z_r (m)	H_c (m)	MDA Modifications
201-2	19	5.4	30	8	WD, i_z
202-5	22	7.6	30	7	i_z
202-6	23	9.3	40	7	i_z
205-3	3	7.0	40	8	-
205-4	4	6.2	40	15	-
205-6	6	6.2	30	12	-
206-3	3	6.7	46	16	WD, i_z
206-4	4	4.5	35	20	WD
206-5	5	4.1	35	21	-
207-2	2	3.6	30	13	-
207-4	4	3.0	30	13	-
209-1	18	4.4	40	3	WD, i_z
209-2	19	3.1	40	17	WD
210-2	2	4.8	57	35	WD, i_z
210-3	3	6.4	57	26	WD, i_z
210-4	4	6.8	57	22	-
210-6	6	7.2	58	9	WD
210-7	7	7.4	58	15	WD
214-5*	7	4.1	24	12	-
214-7*	9	2.7	24	11	-
216-1*	1	3.9	30	5	-
216-2	2	2.7	30	11	-
216-3*	3	3.1	30	15	-
216-4*	4	4.0	30	8	-
217-2	4	5.1	30	4	-

Total Number of Hours: 25

*Oil-fog and SF_6 were not released at the same height for all or part of the hour.

1. turbulence modification factors: T_{iz}, T_{iy}
2. extreme flow modification factors: $T_{ho}(z_r)$, $T_{\ell o}(z_r)$, $T_{uo}(z_r)$
3. flow relaxation length scale factor: α
4. LIFT-WRAP transition length scale factor: δ

Guidance for specifying each of these may come from both laboratory and theoretical studies. They may also be inferred from field studies such as SHIS #1 and #2 and the FSPS. In this evaluation of CTDM, only the flow modification factors are taken from theory. The turbulence modification factors are assumed to be unity because the data obtained at the 10-m and 30-m towers on CCB do not show substantial variations in the turbulence intensity compared to that measured on Tower A. An increase in σ_w is observed, but this is generally accompanied by an increase in the flow speed as well, so that i_z remains about the same. Note that these measurements were made on towers at terrain elevations greater than 70 m, so that the structure of turbulence closer to the base of the hill is not documented.

The flow relaxation length scale factor, α, is assumed to be 1/1.5. This factor assures that the flow modification at the base of the hill is about one tenth of its extreme value at the crest. The LIFT-WRAP transition length scale factor, δ, is assumed to be 0.1, so that the e-folding scale of the transition region is 0.1 H_c.

Flow modification factors are obtained from flow deformations estimated from potential flow theory. In the case of the LIFT component, CCB is assumed to be an ellipsoid of revolution about the vertical axis, with a half-length equal to 2.7 times its height. The streamline height modification factor T_{ho} evaluated at the crest for plume heights equal to .2H, .4H, and .6H equal .47, .51, and .54, respectively. The corresponding factors $T_{\ell o}$ and T_{uo} are 1.73, 1.61, 1.54 and 1.23, 1.22, 1.20, respectively. Because the majority of the plume heights at CCB are between .3H and .6H, representative values are used for all LIFT calculations; $T_{ho} \doteq .5$, $T_{\ell o} = 1.6$, $T_{uo} = 1.25$. In the case of the WRAP component, T_{ho} is unity. Because the flow is considered to be two-dimensional in the x-y plane, $T_{\ell o} = .5$, and $T_{uo} = 2.0$. These values are consistent with flow about a two-dimensional circular cylinder.

FLAT

Flat-terrain concentration estimates are obtained by replacing the terrain-modified portions of the CTDM code with the straightforward Gaussian plume solution. Therefore, calculations of σ_y and σ_z are done the same way as in LIFT and WRAP, as are calculations of all other quantities that are not influenced by the terrain. Ground-level concentrations are then estimated by

$$C_m = \frac{Q}{\pi u \sigma_{yT} \sigma_z} e^{-0.5 \left(\frac{z_r}{\sigma_z}\right)^2} e^{-0.5 \left(\frac{y_r - y_R}{\sigma_{yT}}\right)^2} \qquad (72)$$

where σ_{yT} is the horizontal spread of the plume due to both the 'filament' and 'meander' portions of the crosswind turbulence statistics, as done in CTDM. z_r is the plume centerline height, and y_r is the lateral position of the release point in a coordinate system with origin at the hill center, and x-axis aligned in the direction of the mean flow. The quantity y_R is the lateral position of the receptor in the same coordinate system.

CMPLX

Plume path modifications contained in the COMPLEX I/II codes are tested within the context of CTDM by introducing the partial height factor T_p into the vertical distribution factor of Equation 72 so that

$$e^{-0.5\left(\frac{z_r}{\sigma_z}\right)^2} \rightarrow e^{-0.5\left(\frac{T_p z_r}{\sigma_z}\right)^2} \tag{73}$$

The factor T_p is specified by a plume path coefficient (PPC), and the relative heights of the plume centerline (z_r) and the receptor (z_R)

$$\begin{aligned} T_p &= PPC && z_R \geq z_r \\ T_p &= 1 - (1 - PPC)\, z_R/z_r && z_R < z_r \end{aligned} \tag{74}$$

In COMPLEX I/II, the recommended value of PPC varies by stability class. PPC equals 0.5 ("half-height") for stability classes A, B, C, and D; and PPC equals 0.0 for classes E and F. However, the product $T_p z_r$ is allowed to be no smaller than 10 m , the minimum "stand off" distance.

Performance Results

The performance of each model is summarized in Table 7. Geometric means and standard deviations are computed so that the degree of model over- or underestimation is readily apparent. Specifically, the geometric means and standard deviations are computed using N-weighting as

$$\begin{aligned} m_g &= \exp\left(\overline{\ln C_o/C_p}\right) \\ s_g &= \exp\left(\left(\overline{\ln C_o/C_p)^2} - \overline{\ln C_o/C_p}^{\,2}\right)^{0.5}\right) \end{aligned} \tag{75}$$

A problem with statistics generated from the ratio C_o/C_p is that zero values of C_o or C_p must be excluded. This problem is approached in two ways. First, the statistics are computed only for

TABLE 7. MODEL PERFORMANCE STATISTICS FOR 80 HOURS OF SF_6 DATA AT CCB

Top 5 (Time-and-space-paired)		CTDM			FLAT			CMPLX		
		m_g	s_g	#	m_g	s_g	#	m_g	s_g	#
Neut:	avg.	1.46	2.0	0	2.31	2.8	0	0.73	2.2	0
	all	1.47	4.5	0	2.48	8.3	0	0.75	8.2	0
Weak:	avg.	1.38	3.5	6	3.62	4.1	15	0.92	7.0	0
	all	1.32	10.0	6	3.22	23.6	15	0.85	55.8	0
Impg:	avg.	0.53	2.8	1	9.61	10.7	11	2.40	34.5	0
	all	0.52	7.6	1	9.99	69.5	11	2.10	26271	0
Stab:	avg.	0.40	1.9	0	3.06	11.7	3	0.42	5.1	0
	all	0.40	9.1	0	2.71	607	3	0.35	61.1	0
Comb:	avg.	0.85	3.0	7	3.47	6.4	29	0.95	10.1	0
	all	0.84	8.2	7	3.53	63.5	29	0.90	426	0
Top 5 (Time-paired)										
Neut:	peak	1.57	2.0	0	2.06	2.2	0	0.71	1.7	0
	avg.	1.45	1.9	0	1.80	2.3	0	0.63	1.8	0
	all	1.45	2.0	0	1.80	2.3	0	0.63	1.9	0
Weak:	peak	1.37	2.5	5	3.21	2.1	14	0.48	2.6	0
	avg.	1.20	3.1	5	2.56	2.7	14	0.40	3.0	0
	all	1.20	3.2	5	2.56	2.8	14	0.40	3.1	0
Impg:	peak	0.63	2.5	0	5.91	1.7	10	0.55	2.6	0
	avg.	0.53	2.4	0	5.18	2.0	10	0.43	2.6	0
	all	0.53	2.5	0	5.18	2.1	10	0.43	2.6	0
Stab:	peak	0.67	1.8	0	1.71	2.4	3	0.31	2.3	0
	avg.	0.46	1.8	0	1.25	2.2	3	0.24	2.5	0
	all	0.46	1.9	0	1.25	2.4	3	0.24	2.7	0
Comb:	peak	1.00	2.5	5	2.64	2.4	27	0.51	2.4	0
	avg.	0.84	2.7	5	2.18	2.6	27	0.42	2.7	0
	all	0.84	2.8	5	2.18	2.7	27	0.42	2.8	0

Notes: # denotes number of hours excluded because the mean of the five largest modeled concentrations was less than $1 \mu s/m^3$.

the top "N" observed or modeled concentrations to quantify model performance for the region(s) of greatest observed or modeled impact. And second, hours in which the mean of the top "N" modeled concentrations is less than 1 $\mu sec/m^3$ are removed. The 1 $\mu sec/m^3$ threshold is chosen because it provides a convenient flag for cases in which the modeled plume impact is virtually insignificant. In Table 7, the number of hours that fall into this category is indicated in the data column headed by the # symbol.

Statistics are computed for the following classes:

Neut:	$H_c \leq 2$ m	("neutral")
Weak:	$2 \text{ m} \leq H_c < z_r - 10$ m	("weakly stratified")
Impg:	$z_r - 10 \text{ m} \leq H_c < z_r + 10$ m	("impingement")
Stab:	$z_r + 10 \text{ m} < H_c$	("very stable")

They are also computed for two pairing possibilities. The top "N" time-paired statistics are computed from N pairs which represent the N largest C_o values, and the N largest C_p values. For example, the largest C_o value for the hour is paired with the largest C_p value for the hour; second largest C_o with second largest C_p; etc., to the N^{th} largest values. These pairs are not required to be paired in space, but are paired in time. The top "N" time-and-space-paired statistics are computed from as many as 2N pairs which represent the N largest C_o values and their corresponding C_p values, plus the N largest C_p values and their corresponding C_o values. Each pair is included only once. Thus the total number of pairs may be less than 2N, but not less than N. If the observed and modeled concentration patterns overlap well, then the number of pairs should be nearer N than 2N. Consequently, the time-paired statistics characterize how well the larger observed and modeled concentrations agree without regard for where these values occur, while the time-and-space-paired statistics characterize how well the region of greatest impact is modeled.

Within the time-and-space-paired subset, residual statistics are based on all of those individual concentration pairs, and statistics are also based on the mean C_o and C_p from these pairs for each of the 80 experiment-hours. The "avg." label denotes those statistics for the 80 (less the number of hours in the # column) hourly geometric mean residuals, and the "all" label denotes those statistics for all individual pairs in this subset. Within the time-paired subset, the "avg." and "all" labels have the same meaning, and a third label (peak) is added to denote the statistics of the residuals of the hourly peak observed and modeled concentrations.

The number "N" chosen to evaluate model performance for these 80 hours is 5. Although arbitrary, this selection was guided by the need to avoid averaging over a region large compared to the peak impact region, as well as the need to avoid limiting the pairs to the extreme values. With a total sampler number of about 100, the paired statistics cover as many as 10% of the total sampler positions.

Because the plume impact could at times be limited to roughly 20 to 25 of the samplers, the value of 5 is thought to be a reasonable choice for "N." The sensitivity of the comparison statistics to "N" has not been tested.

CTDM generally performs better than the other two "models." In the case of the time-paired statistics, FLAT underestimates observed concentrations in the mean, while CTDM and CMPLX tend to overestimate these concentrations. The noise (s_g) is similar for each model, but note that 5 hours were "missed" by CTDM, and 27 hours were "missed" by FLAT. These hours are not included in the statistics. When broken out by meteorology, CTDM tends to overestimate concentrations for the "impingement" and "very stable" classes ($H_c \geq z_r - 10$ m). On the other hand, FLAT tends to underestimate in all classes, and CMPLX overestimates in all classes.

The time-and-space paired statistics generally indicate a greater degree of noise for each of the models. The increase in the noise is indicative of differences in the spatial distribution of the concentrations. It is evident that CTDM fares far better in the s_g statistics for the concentrations paired in time and space than does either FLAT of CMPLX. Hence, we would expect the CTDM estimate of the distribution of concentrations to be a better representation of the observed distribution then either the FLAT or CMPLX distributions.

Both the time-and-space-paired and time-paired statistics indicate that CTDM performs the worst when $2 \text{ m} < H_c \leq z_r - 10$ m, what is termed the weakly stratified class. The number of "misses" in this class indicates that too little plume material reaches the surface in several of the hours in this class. Unlike the more neutral class, plumes for many of these hours may be quite narrow in the vertical. Hence, the concentrations may be particularly sensitive to estimates of H_c, i_z, and possibly the specification of the influence of the hill on the turbulence in the vicinity of the hill. The CMPLX results for this class include no "misses", while the FLAT results show many more. It may be possible to model this class better with alternate choices of several of the "free" parameters in CTDM.

The FLAT results are of interest in themselves. In answer to the query: when is a flat-terrain calculation at CCB as good as CTDM?, we can answer: never. However, among the FLAT simulations the "neutral" class is clearly modeled best. This is reasonable in that one would expect the hill effect to be weakest when H_c is virtually zero, and (presumably) when the wind speed is greatest so that the boundary layer shear zone encompasses both the hill height and the plume. FLAT tends to underestimate concentrations to a greater extent as the flow becomes more stably stratified. But when the most stable class is reached, FLAT tends to do better again in estimating the magnitude of the impact, although the spatial distribution is not reproduced well. The success of FLAT in the time-paired results for the "stable" class would appear to result from deflecting the plume too much in the vertical, but not enough in the horizontal. That is, FLAT seems to benefit from compensating errors.

With a 10-m minimum "standoff distance" for the most stable flows, CMPLX does not deflect the plume "too much" in the vertical, and it does not deflect it at all in the horizontal. As a result, the larger concentrations are overestimated to the greatest degree in the "stable" class.

Taken together, these results indicate that the structure of CTDM is necessary to overcome deficiencies in both the flat-terrain algorithm and the terrain algorithm contained in COMPLEX I/II. The importance of both the critical dividing-streamline height and the stagnation streamline can be seen in the modeling results. Furthermore, the present choices of the "free" parameters in CTDM appear to be reasonable, but more work is needed to understand the reasons for the poorer model performance in the "weakly stratified" class. Also, the trend towards underestimating the "neutral" class hours by about 50%, while overestimating the "impingement" and "stable" class hours by a factor of two should be explored. Changes to the turbulence over the hill and possibly just upwind of the hill may account for some of the discrepancy. Also, the variation of wind speed, direction, and turbulence with height may be an important factor during some of these hours.

3.3.2 Model Performance for Alternate Meteorological Data

The sensitivity of CTDM performance measures to the input meteorological data has been tested by forming 1-hour concentration fields from simulations with the 5-minute sequence of meteorological data in the MDA, by constructing the 1-hour wind and temperature structure from data at 10 m and 150 m, and by constructing the data from 10-m measurements alone. In each case, however, the wind direction is taken from the MDA--we already know how sensitive the concentration pattern is to the wind direction.

The 10 m - 150 m construction is analogous to assuming that a site has a tower with wind and temperature measurements at two elevations. No turbulence data is presumed to be measured. A stability class is prescribed on the basis of the 5-minute sequence of 10-m wind speeds, and net radiation data (the stability class is already contained in the MDA, and its computation is described in the CTDM Third Milestone Report). The Froude number between 2 m and 150 m is contained in the MDA, and this is used to obtain H_c by the relation:

$$H_c = (1 - Fr)\, H \qquad (Fr \leq 1.0) \qquad (76)$$

$$H_c = 0 \qquad (Fr > 1.0)$$

where H is the height of the hill. For this evaluation, we have also assumed the MDA wind speed at release height is similar to what would have been interpolated between 10 m and 150 m, so that N is obtained from the relation:

$$N = \frac{u}{Fr\ H} \qquad (77)$$

The bulk Froude number for the layer above H_c is taken to be the greater of 1.0 or Fr.

Turbulence intensities are inferred on the basis of the stability class for each five minutes. The σ_y and σ_z relations proposed by Briggs (1973) contain turbulence intensities i_y and i_z that are consistent with the PG sigma curves:

$i_y = .22$	$i_z = .20$	(Class A)
$i_y = .16$	$i_z = .12$	(Class B)
$i_y = .11$	$i_z = .08$	(Class C)
$i_y = .08$	$i_z = .06$	(Class D)
$i_y = .06$	$i_z = .03$	(Class E)
$i_y = .04$	$i_z = .016$	(Class F)

These intensities are used in place of the intensities contained in the MDA.

The data set based on measurements at 10 m contains "default" wind and temperature profiles. As is the practice in many regulatory models, the temperature lapse rate values depend on the stability class, and the change in wind speed with height follows a power law profile, with the power exponent tied to the stability class.

The wind speed at release height is estimated as

$$u = u_{10} \, (z_r/10)^p \tag{78}$$

where the exponent depends on the stability class in the following way:

$p = .10$	(Class A)
$p = .15$	(Class B)
$p = .20$	(Class C)
$p = .25$	(Class D)
$p = .30$	(Class E)
$p = .30$	(Class F)

The wind direction is taken directly from the MDA. The potential temperature gradient also varies by stability class:

$d\theta/dz = 0$ °K/m	(Classes A-D)
$d\theta/dz = 0.02$ °K/m	(Class E)
$d\theta/dz = 0.035$ °K/m	(Class F)

With these values of the potential temperature gradient, the Brunt-Vaisala frequency is computed from

$$N = ((g/T) \, d\theta/dz)^{0.5} \tag{79}$$

where g is the acceleration due to gravity, and T is the temperature interpolated to release height in the MDA (°K). For consistency, T should have been the temperature at 10 m, but this value is not contained in the MDA.

The bulk Froude number is obtained from this estimate of N, the hill height H, and the wind speed at one half the hill height (~ 50 m) u_{50}:

$$Fr = u_{50}/(N\ H) \tag{80}$$

where u_{50} is obtained from the power law profile. Now the critical dividing-streamline height is again given by Equation 76, and the bulk Froude number above H_c is the greater of 1.0 and Fr. The turbulence intensities are obtained from the Briggs σ_y and σ_z relations, as described above.

Table 8 contains the performance statistics for CTDM as driven by each of the three meteorological data sets just described.

Modeling performed with the sequence of 5-minute meteorological data has led to an improvement in model performance in none of the classes. The number of "misses" in the "weakly stratified" class drops, but additional hours are now "missed" in the "stable" class. Furthermore, although the overall bias lies closer to unity, the noise has increased slightly. Therefore, although the 5-minute modeling has helped a few hours, it tends to degrade model performance in general.

Modeling performed with the 10 m - 150 m "tower" data is substantially inferior. A total of 39 out of 80 hours is "missed." For the hours remaining, the modeled spatial distribution of concentrations is generally quite poor. The best performance is seen in the "neutral" class, and the worst is seen in the "weakly stratified" class on the basis of the time-paired statistics. Apparently, the use of the bulk Froude number between 2 m and 150 m underestimates the stability of the flow, and therefore H_c as well.

Modeling performed with the 10-m data alone is better in that far fewer (24) hours are "missed." But the statistics for the remaining hours are still quite poor. The time-and-space-paired statistics indicate that modeled and observed concentration patterns are generally dissimilar. Once again, however, model performance is best for the "neutral" class.

These results show that the resolution of the meteorological data in the vertical is a key factor in modeling CCB successfully. This is probably due to the relatively narrow plumes at CCB in combination with the complex vertical structure of the lower atmosphere. The model must know what is going on at plume height.

TABLE 8. EFFECT OF METEOROLOGICAL DATA RESOLUTION ON CTDM MODEL PERFORMANCE FOR 80 HOURS OF SF_6 DATA AT CCB

Top 5 (Time-and-space-paired)		5-minute Met.			10 m - 150 m Met.			10 m Met.		
		m_g	s_g	#	m_g	s_g	#	m_g	s_g	#
Neut:	avg.	1.62	2.0	0	1.70	2.2	0	1.54	1.9	2
	all	1.71	5.0	0	1.67	4.4	0	1.57	4.3	2
Weak:	avg.	2.39	7.4	4	4.82	2.4	19	374	36621	8
	all	2.09	31.1	4	5.19	20.1	19	777	*.*	8
Impg:	avg.	0.54	2.5	1	89.2	834	12	312	336	5
	all	0.56	8.5	1	85.1	874011	12	353	*.*	5
Stab:	avg.	0.51	1.9	3	16274	4.5	10	99542	7.0	11
	all	0.50	6.1	3	17341	*.*	10	108302	*.*	11
Comb:	avg.	1.12	4.2	8	9.97	67.0	41	75.5	1640	26
	all	1.08	12.4	8	11.70	8270	41	110.2	786052	26
Top 5 (Time-paired)										
Neut:	peak	1.69	1.9	0	1.74	2.3	0	1.44	2.0	2
	avg.	1.54	2.0	0	1.68	2.2	0	1.46	1.9	2
	all	1.54	2.1	0	1.68	2.3	0	1.46	2.0	2
Weak:	peak	1.58	2.8	4	2.98	4.4	17	1.21	3.8	6
	avg.	1.48	3.5	4	3.49	6.5	17	4.01	36.9	6
	all	1.48	3.7	4	3.49	7.1	17	4.01	87.7	6
Impg:	peak	0.62	2.3	0	0.32	1.6	12	0.29	2.7	5
	avg.	0.49	2.1	0	0.38	1.9	12	0.96	15.3	5
	all	0.49	2.2	0	0.38	2.2	12	0.96	21.2	5
Stab:	peak	1.01	2.8	2	0.39	2.4	10	0.50	1.5	11
	avg.	0.87	3.8	2	0.78	4.7	10	0.89	2.7	11
	all	0.87	3.9	2	0.78	5.2	10	0.89	4.5	11
Comb:	peak	1.16	2.7	6	1.22	3.5	39	0.83	3.4	24
	avg.	1.01	3.1	6	1.35	3.9	39	1.80	14.3	24
	all	1.01	3.2	6	1.35	4.2	39	1.80	24.1	24

Notes: # denotes number of hours excluded because the mean of the five largest modele concentrations was less than 1 $\mu s/m^3$.
. denotes a number greater than 999,999.

SECTION 4

MODELING HOGBACK RIDGE

4.1 Refinement of Tower Data

Four meteorological towers were instrumented for SHIS #2 at the Hogback Ridge site. The 150-m tower (Tower A) was erected about 800 m east of the crest of the ridge and instrumented at 10 levels; the 30-m tower (Tower B) was among the hillocks at the base of the ridge on the east and was instrumented at five levels; a 10-m tower (Tower C) was located on the crest of the ridge and was instrumented at three levels; and an existing 60-m tower (Tower P) approximately 4 km east of the ridge was instrumented at two levels. The signal conditioning electronics for the 150-m and 60-m towers were enclosed in aluminum-clad, environmentally controlled, insulated shelters; those for the 10- and 30-m towers were in naturally ventilated steel enclosures.

The instruments on all the towers were scanned once per second by the data acquisition system. Data from the 150-m tower's shelter were communicated over shielded signal cables to the bus containing the data acquisition computer, a distance of about 50 m. Radio communications links telemetered the data from the other three towers. Further details regarding this data system are reported in the Third Milestone Report.

At least three different sorts of noise were observed in the 1-sec data during the SHIS #2 experiments--large "hits," which drove the instrument output voltages outside their 0-to-5 VDC range; "channel-skipping," in which the data from one input channel was skipped and replaced by the data from the next sequentially polled channel, with the shift of data continuing to the end of the 16-channel multiplexor; and "high-frequency" noise bursts that caused a few seconds of data to oscillate unrealistically at consistent periods within each 5-minute averaging period. These types of noise are described more fully in the Third Milestone Report.

The large hits are generally easy to identify and remove from the data; the other two types of noise are less so. ARLFRD developed a "filtering" routine that examined the second-to-second changes in instrument output and replaced values that exceeded what they regarded as reasonable limits for such changes; these limits are shown in Table 9. Data removed from the time series by this filtering procedure are replaced by linear interpolation in time between the last good value and the next good value.

An interim tower data base was produced by ARLFRD in September 1983 in order that the modelers could begin analyzing the Hogback

data. The 5-min and 1-hr values were produced from 1-sec data edited by the filtering and "filling" routine described above. The anemometer data were also treated by calibrations specific to each instrument that had been made by ARLFRD in their wind tunnel prior to installation at the Hogback. The UVW propeller anemometer data were modified at the 1-sec level by cosine-response corrections developed by John Clarke of EPA from wind tunnel experiments on propeller systems manufactured by R.M. Young Co.

Examination of the data in the interim data base suggests there are consistent errors remaining that might be removed by further or different processing. Examples are shown in Figures 17 to 22 for data from the 40-m level of Tower A.

Figure 17 shows the difference between the scalar mean wind direction from the F460 vane (DX) and that from the UVW propeller anemometers (D) as a function of vane direction for all 5-min average data from SHIS #2. Although the data are somewhat scattered, particularly for light winds, clear trends are evident, and the differences are often larger than those observed in the SHIS #1 data before they were corrected, exceeding 25° with winds from the south.

Figure 18 is a plot of the differences between cup-derived wind speeds (SX) and prop-derived wind speeds (S) expressed as a fraction of the cup speed and plotted as a function of vane direction. Again, some trends can be seen through the scatter, and the magnitude of the differences is like that of the uncorrected SHIS #1 data.

The 5-min σ_w's from the sonic and propeller anemometers during Experiment 4 are plotted as time series in Figure 19. The problem of noise in the data acquisition had not been addressed by changes in the wiring to improve the grounding at this stage of SHIS #2. The propeller σ_w's are about twice as large as the sonic values and show no obvious correlation with them. Figure 20 is a similar plot for the 5-m Tower A data. At this level the propeller should have been incapable of responding to a large fraction of the turbulence in stable conditions because of its high frequency but still it yielded values two to three times as large as the sonic system at 5 m. Comparison of the propeller data in Figures 19 and 20 reveals a high correlation between the two levels. The 5-m and 40-m W-propeller signals passed through the same multiplexor and were subject to many of the same noise bursts and channel-skipping.

Figures 21 and 22 are the corresponding plots for Experiment 14 after the noise problems had been reduced by improved grounding of the DAS and the reconfiguration of the data channels so that each analog-to-digital converter and multiplexor served only one tower. Here the sonic and propeller σ_w's are much better correlated; the 5-m propeller values are generally lower than the 40-m, as expected and as verified by the sonic data; and the prop values seldom exceed the sonic values, as they should not.

It would appear then that a significant amount of noise remains in the interim data from the early experiments of SHIS #2. Although

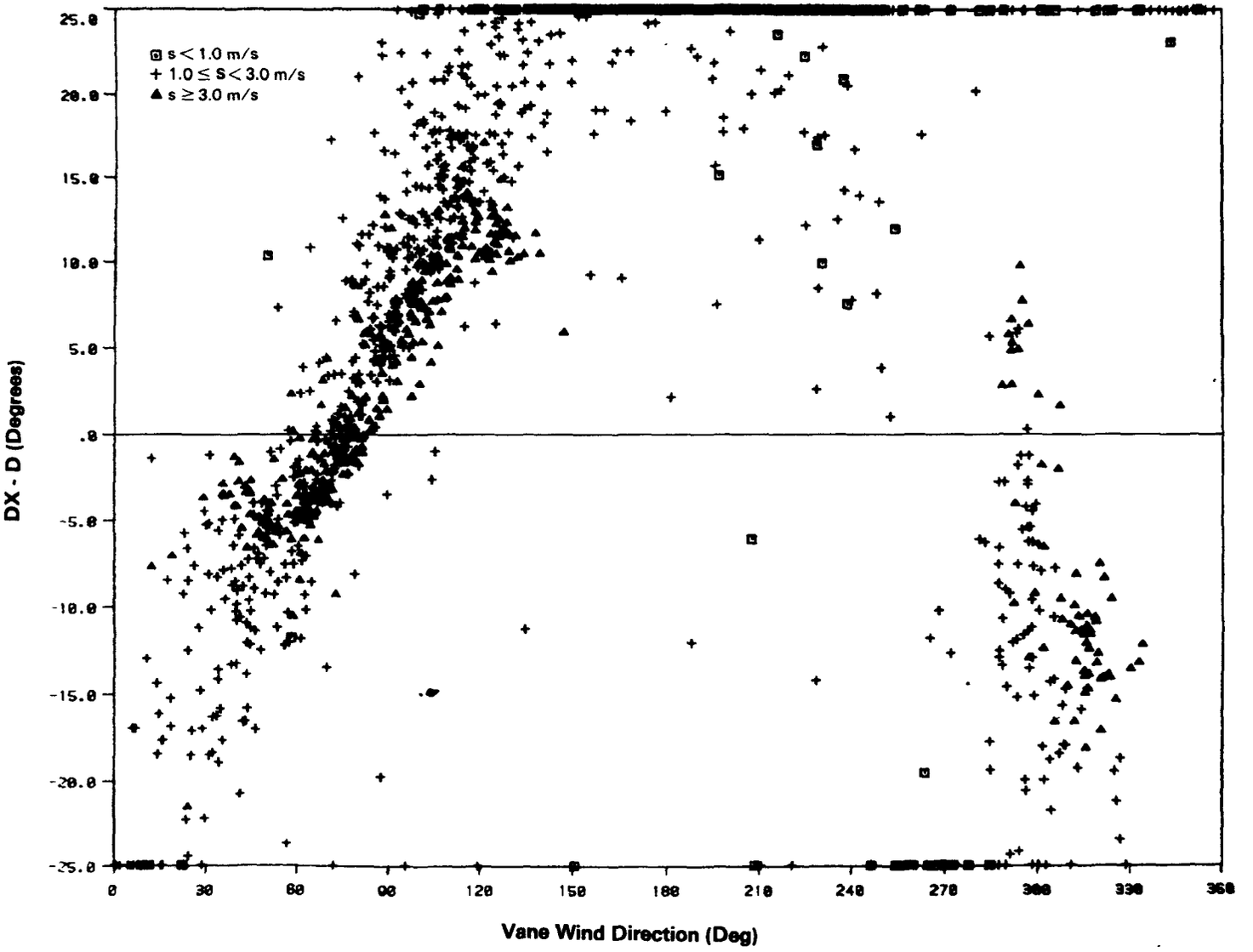

Figure 17. Difference between the scalar mean wind direction from the F460 vane and that from the UVW propeller anemometers as a function of vane direction for all 5-min average data from SHIS #2.

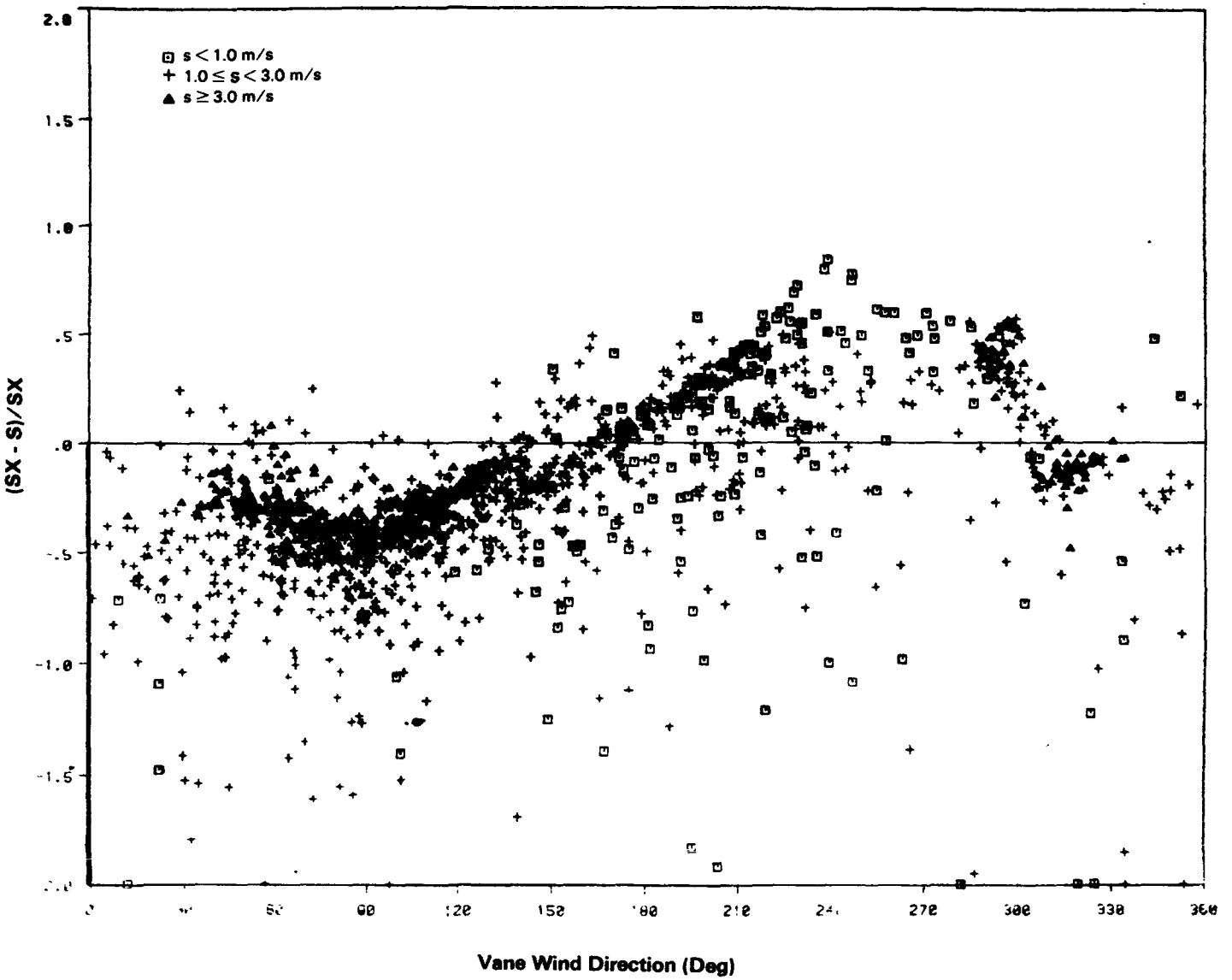

Figure 18. Plot of the difference between cup-derived wind speeds and prop-derived wind speeds.

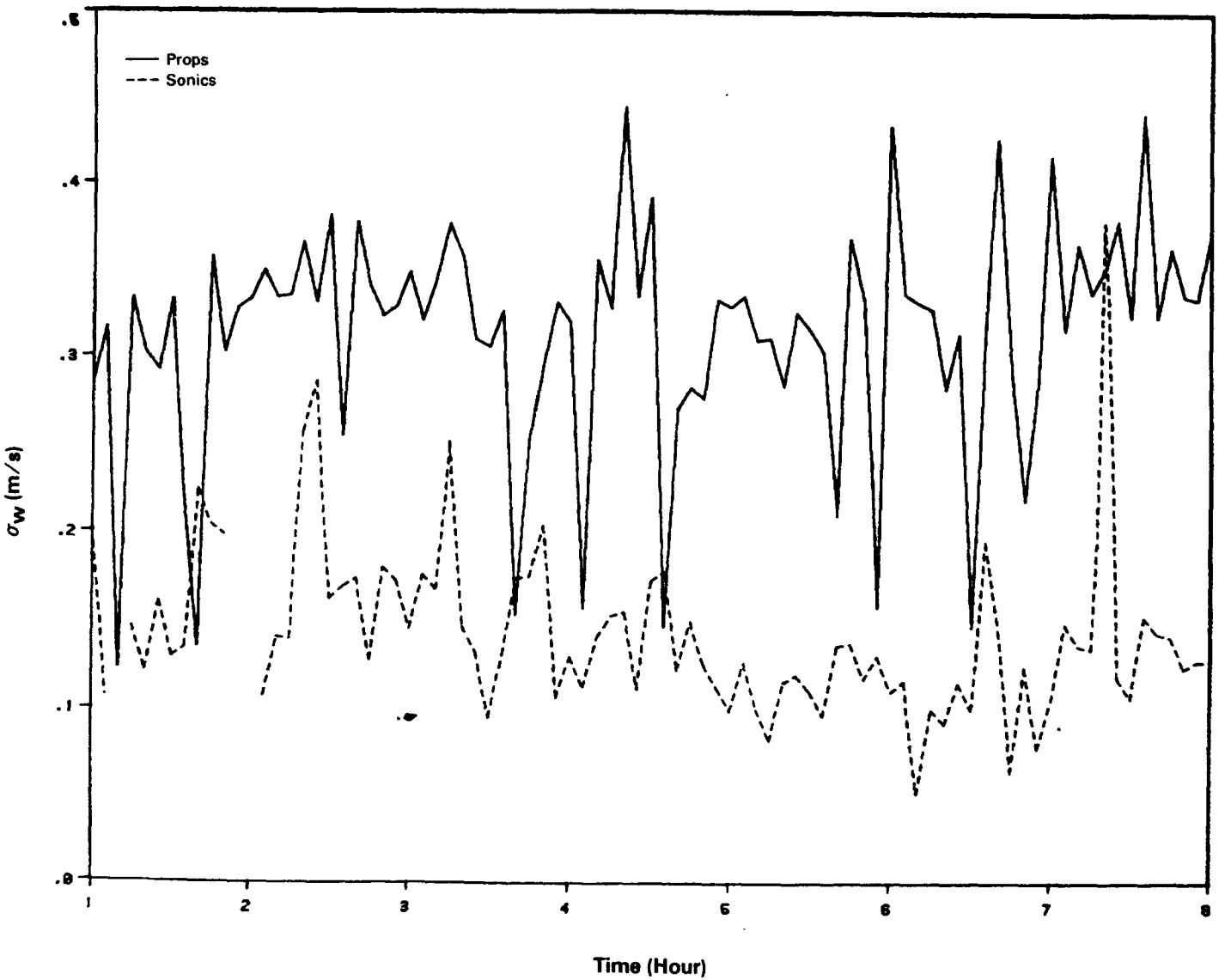

Figure 19. Five-minute σ_w's from the sonic and propeller anemometers (40-m) during Experiment 4.

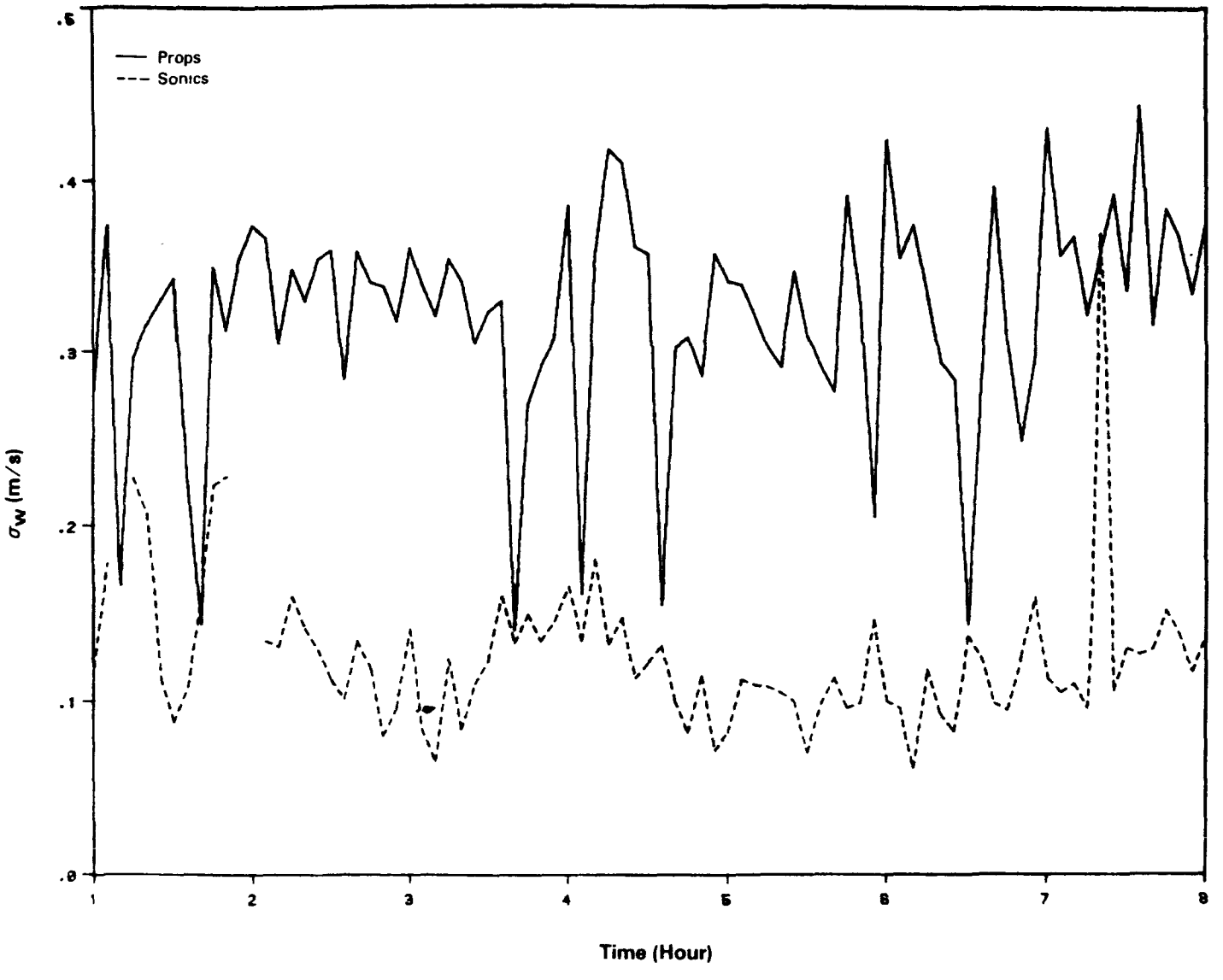

Figure 20. Five-minute σ_w's from the sonic and propeller anemometers (5-m) during Experiment 4.

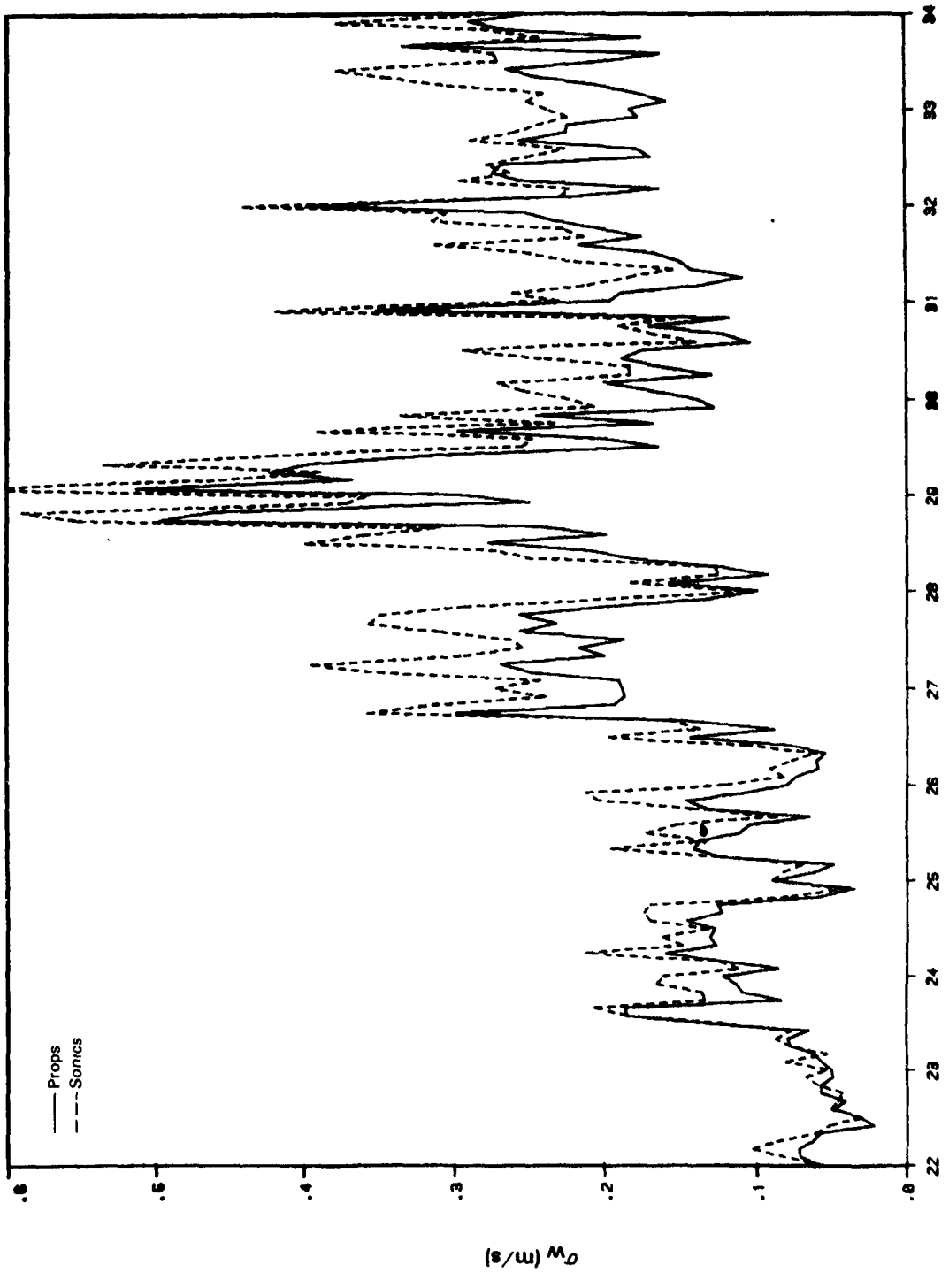

Figure 21. Five-minute σ_w's from the sonic and propeller anemometers (40-m) during Experiment 14.

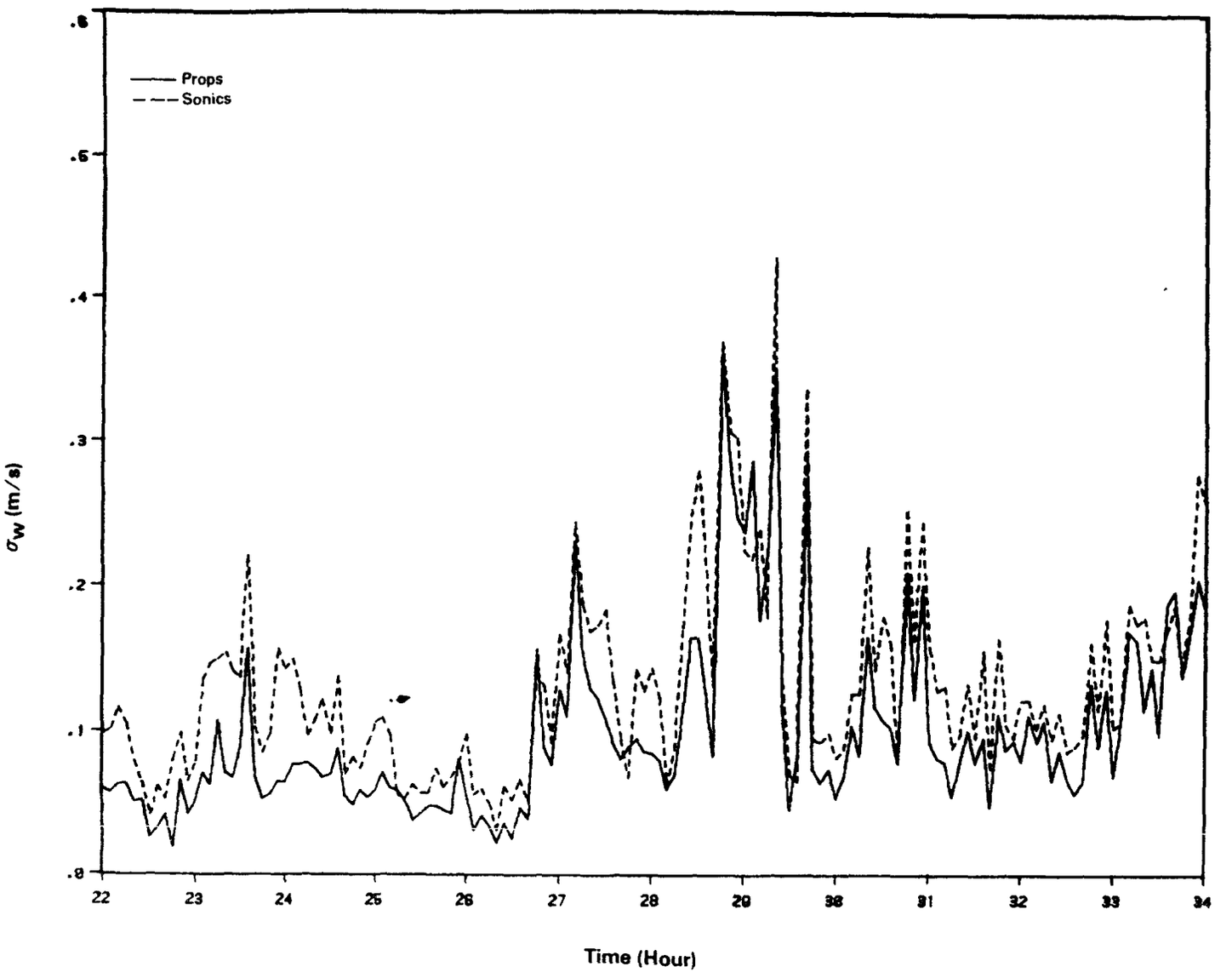

Figure 22. Five-minute σ_w's from sonic and propeller anemometers (5-m) during Experiment 14.

some of it may not be recognizable, further attempts will be made at signal-processing to improve data quality. A first step might be to reduce the allowable second-to-second changes (See Table 9, p. 94) to capture more noisy values and cases of channel-skipping. The noise remaining in the present interim data probably affects variances and covariances more than the means, but removing some of it will also reduce the scatter in Figures 17 and 18.

4.1.1 Wind Tunnel Studies

The Third Milestone Report recommended that further wind tunnel studies be performed at the EPA Fluid Modeling Facility (FMF) to characterize the response of the Climatronics UVW propeller anemometers more completely than had earlier experiments done by ERT in the wind tunnel at Colorado State University (CSU) in 1981, from which the corrections for the SHIS #1 data were largely derived. The experiments were performed by ERT with the cooperation of FMF staff in June 1983. Primary objectives of the experiments were to determine not only the non-cosine response corrections but also the calibration lines for 0° angle of attack.

Calibrations of UVW Propeller Anemometers

The calibrations of the propeller anemometers done by ARLFRD in summer 1982 showed a nonlinearity of response at low wind speeds when plotted against the estimated tunnel speed but not when plotted against the "counts" data from the output of their standard cup anemometer. ERT's calibrations of the propeller sets in the CSU tunnel did not have this characteristic, but they had not been well defined at light winds. Since the SHIS #2 data have been processed with ARLFRD's calibrations, and since most of the SHIS #2 data indicate light winds, it was important to try to verify the nonlinearity in another facility.

The six component arms of two UVW sets were calibrated in the large wind tunnel at the FMF, the test section of which is 2.1 m high and 3.7 m wide. Air speed during the calibrations was varied from approximately 0.5 to 8.0 m/s, the maximum speed possible in the tunnel. Fan tachometer settings were used to determine air speed after linear regression relationships were derived between tachometer settings and pitot tube readings for speeds over about 1.7 m/s and from smoke puff tracking experiments for lower speeds. The calibration of tunnel air speed vs. fan speed is based on the following premises:

- Air speed for a given fan speed is independent of air density.
- Pitot tube readings, when corrected for pressure and temperature (i.e., density), give adequate air speeds above about 2 m/s.
- Timing the passage of smoke puffs yields adequate air speeds at low fan speeds.

Separate calibration lines were derived for fan tachometer settings between 59 and 190 and for settings in excess of 190. The lower speed calibration was derived from data on passage of smoke puffs and the higher speed calibration from pitot tube pressure differences corrected for ambient temperature and pressure. Although the smoke puff experiments included data from tachometer settings of 20 to 40, these data were not used because no evaluations of the propeller anemometers were done at such low tunnel settings. The results of the linear regressions of air speed on tachometer settings are as follows:

U_T (smoke) = .009577 * tach - .13129 for tach $\leq$ 190
Coefficient of determination R^2 = 0.99963, N=5
(Each of 5 data points is the average from 5 or 6 smoke puffs)

U_T (ΔP) = .009854 * tach - .12607 for tach > 190
Coefficient of determination R^2 = 0.99990, N=73.

At tach = 190, the smoke derived calibration gives U_T = 1.688 m/s and the ΔP derived calibration gives U_T = 1.746 m/s. The difference is consistent with the general observation that FMF tunnel speeds determined from pitot tube measurements are consistently higher (by about 4%) than those derived from smoke puffs. The precision of the smoke puff measurements at 1 m/s is about 1.2 percent, so it would appear that the pitot tube may overestimate the velocity at the center of the tunnel. This possibility is consistent with the fact that lower fractions of estimated tunnel speed were indicated by the propellers when facing directly into the wind in the FMF tunnel than in the CSU tunnel, but this evidence is only suggestive.

An analysis was made of the "group" performance of the six propeller anemometers calibrated in the EPA/FMF. Linear regressions of best estimates of tunnel speed vs. instrument output voltage were very similar for the six transmitters, as shown in Table 10 (p. 95). When the slopes of the "W"-props' regression lines are multiplied by 2.5 to make them equivalent in voltage vs. speed to the "U" and "V" props, the range of the slopes is only 10.337 to 10.524 or 1.8%. Inclusion of the zero-speed points, which were available for the first three sensors, didn't cause the slopes to change appreciably and in fact slightly improved the coefficients of determination R^2, all of which lie between 0.99996 and 0.99998. This result implies that there is very little fall-off from linear response as the ambient speed goes to zero. There are some minor departures of response from linearity at low speeds (<1.5 m/s), but some part of this uncertainly is probably due as much to errors in estimating tunnel speed as to imprecise instrument response. In any event, the nonlinearities observed in the ARLFRD tunnel are not apparent in the FMF tunnel.

Refinement of the SHIS #2 propeller data would be much simplified if the same calibration curve could be used for all the sensors. The apparent group precision of these six transmitters (and the similar results for the experiments with propeller systems at Colorado State) suggests that this should be possible without substantial increase in uncertainty.

Non-Cosine Response Corrections for Propeller Systems

Analysis of the cosine response data obtained in the FMF wind tunnel with the project's Climatronics UVW propeller anemometers indicates the data are generally consistent with both the results of the experiments done for the CTMD program in the Colorado State University wind tunnel and the results of the tests of R.M. Young UVW systems done by EPA's John Clarke. The experiments in the FMF were somewhat more detailed than the CSU experiments in an attempt to define the local maximum of response at 60° angles of attack and the response near the stall regions around 90° angle of attack.

Two sets of instruments were studied, but time allowed for experimentation with the response of only one W-propeller. Responses were recorded at three tunnel speeds--approximately 0.5, 1.9, and 4.9 m/s. Low speeds were emphasized because most of the CTMD experiments have been done in fairly light winds.

The results of the FMF experiments are plotted in Figures 23, 24, and 25, with each plot displaying data for both sets of horizontal propellers at one wind speed. The "angle of wind" θ in the plots is oriented for the way the U-props are mounted in the field so that 90° is a wind blowing directly into the outward face of the propeller. The V-prop output is plotted vs. 90°-θ to show the general (and expected) symmetry of the UVW system about the 225°-45° line. The principal departure from symmetry is at wind angle 270° (V-prop angle 180°), where the V-prop response is reduced below that of the U-prop because of the wake of the signal cable connector, which extends to the west (270°) from the connector block to which all three component arms join.

The fractions of cosine response shown in the analysis are determined with the instruments' output when facing "upwind" (wind angle 90°) taken as the normalizing factor so that the fraction of response is 1.00 for all component arms when in this orientation.

The results shown in the accompanying figures support the following generalizations:

- The local increase in response at 60° angles of attack is consistent from prop to prop.
- The responsiveness of the instruments is nearly independent of wind speed outside the stall regions.
- The angular width of the stall region is inversely related to wind speed, as expected.
- The U-prop of the second set of instruments is not like the other three horizontal props, displaying large over-responses on either side of the broad stall region. This characteristic was not recognized during the

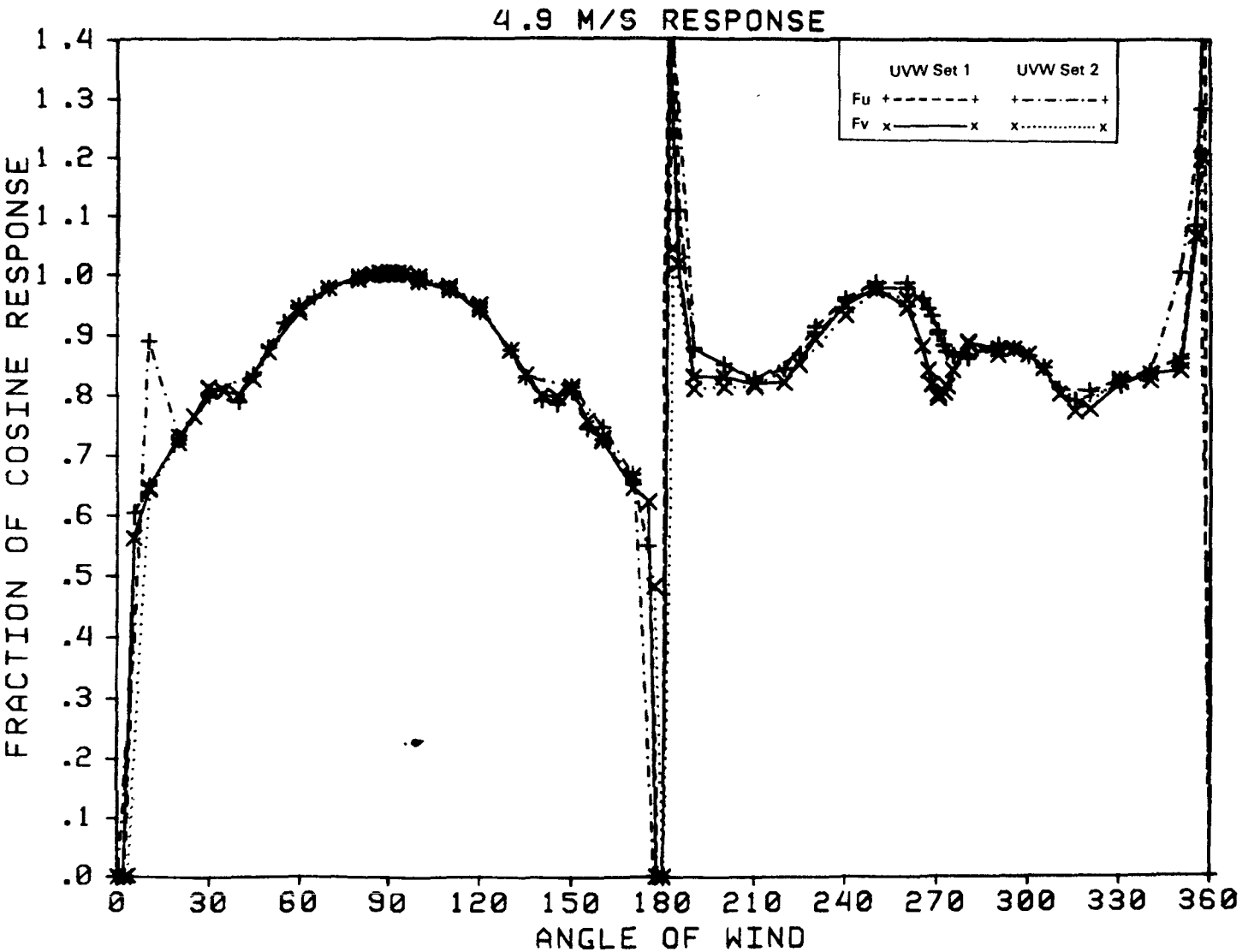

Figure 23. Fractions of cosine response shown by Climatronics UVW propeller anemometer in EPA/FMF wind tunnel at 4.9 m/s. Angle of wind θ is for U-prop (facing outwards to the east). V-prop response data plotted vs. 90°-θ to show symmetry.

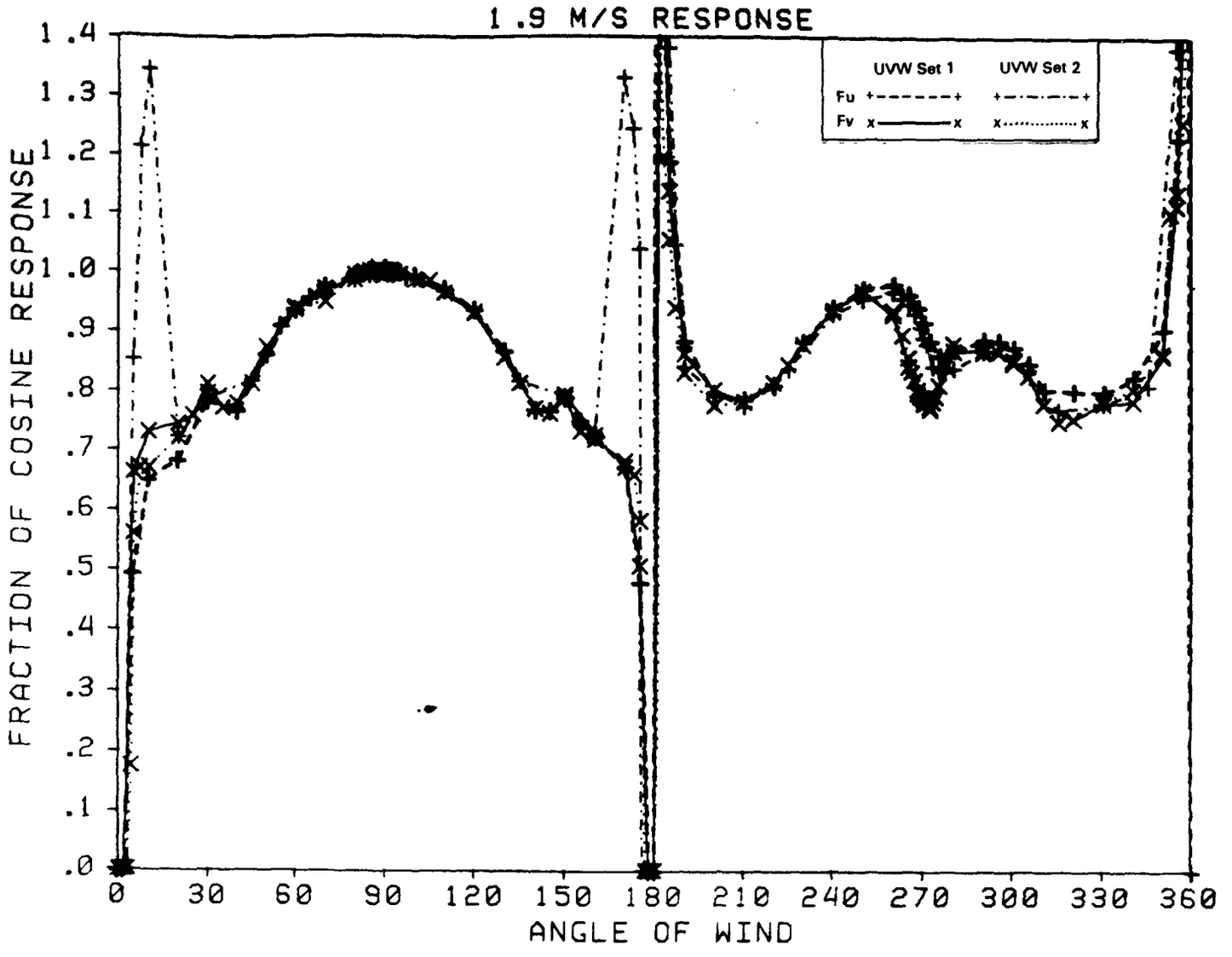

Figure 24. Fractions of cosine response shown by Climatronics UVW propeller anemometer in EPA/FMF wind tunnel at 1.9 m/s. Angle of wind θ is for U-prop (facing outwards to the east). V-prop response data plotted vs. 90°−θ to show symmetry.

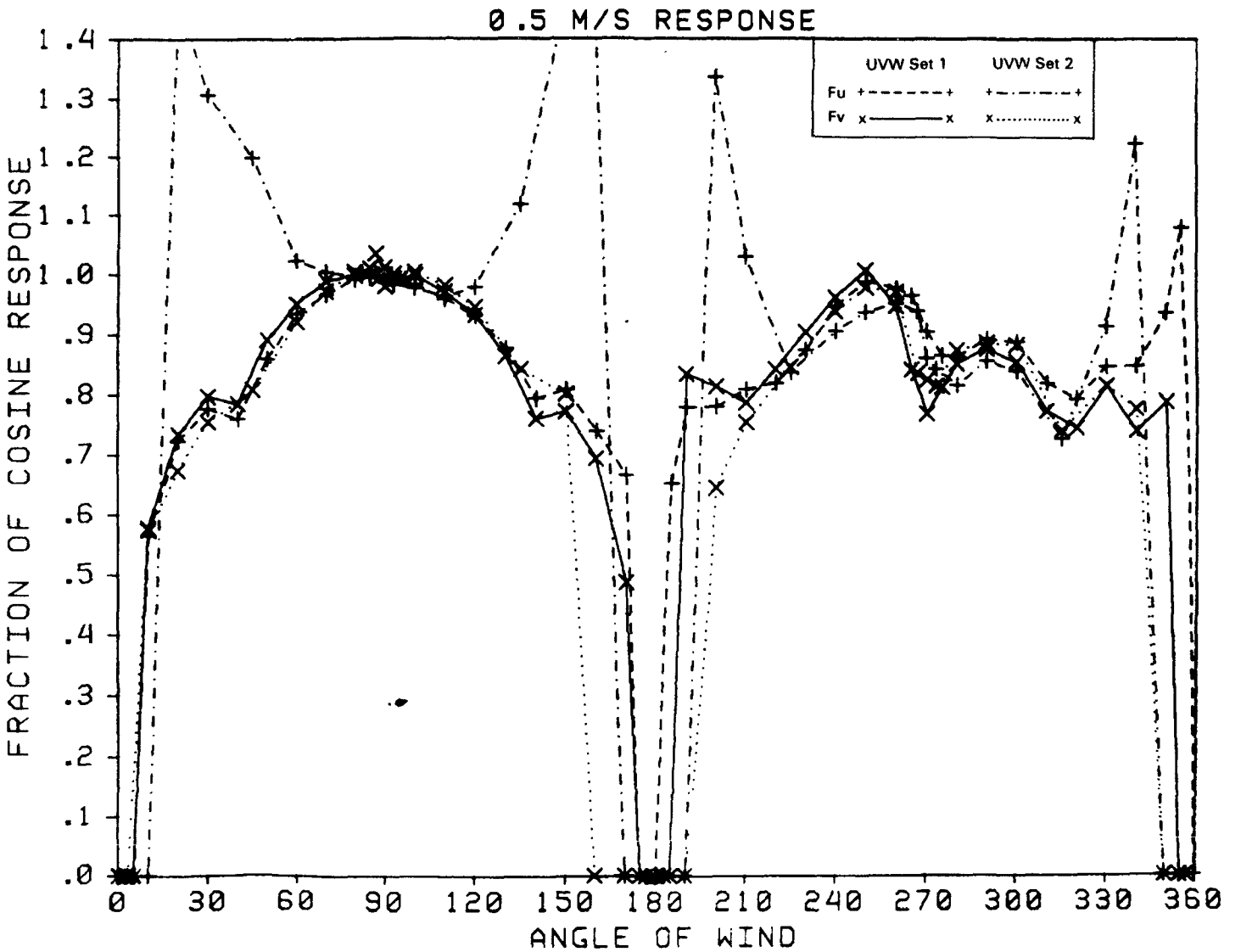

Figure 25. Fractions of cosine response shown by Climatronics UVW propeller anemometer in EPA/FMF wind tunnel at 0.5 m/s. Angle of wind θ is for U-prop (facing outwards to the east). V-prop response data plotted vs. 90°-θ to show symmetry

experiments, and consequently neither the propeller nor the precision of its mounting on the transmitter shaft was examined for causes of anomalous behavior.

The responses of the Climatronics instruments are generally a few percent lower than those derived by Clarke for the R.M. Young anemometers. The stall regions of the Climatronics instruments may also be wider; and the over-response for non-stalled props between 92° and 95° and between 265° and 268° for the V-prop (similar regions for the U-prop) seems not to have occurred with the R.M. Young devices.

The reason for this latter effect may be the propeller shaft extensions on the Young instruments. Another possible contributor, however, is a general divergence of flow around the Climatronics UVW system. A smoke streak in the FMF tunnel aimed into the center of the vertical W-arm rose quite noticeably as it approached the equipment; this accounts for the fact that the W-props frequently turned in the positive (upward) sense when the horizontal arms were being tested for response. It may also account for the small positive mean vertical wind speeds often measured by the props on the 150-m tower at Cinder Cone Butte.

Listed in Table 11 (p. 96) are the correction factors ERT recommends for the Climatronics UVW data from SHIS #2. Because of the variability and rapid changes in response shown by the instruments near the stall regions, the corrections in these areas are ill-defined. It is not clear how best to refine the data from times when one propeller is near or in its stall region. The wind component speed will generally be quite low when this occurs, so that the effect on resultant wind speed may be quite small, but the effect on resultant direction may be several degrees. Over a five-minute averaging period, unless the winds are very steady, however, even the error on average direction may be less than three to five degrees. Measures of lateral wind variability may be the most adversely affected.

The response of the W-prop shows it to be similar to the horizontal props but with a narrower stall region at low speeds, as might be expected because of the reduced inertia due to gravitational forces on any propeller imbalance. Otherwise it seems to fall into the general range of response exhibited by the U and V props. The differences between responses with effective wind direction at 90° or 270° are also not great. In short, the tests in the FMF wind tunnel do not provide evidence that the W-prop's response is substantially different from the U and V. We are aware of no other studies that corroborate or contradict this premise.

The non-cosine response corrections that were applied to the SHIS #1 data were combinations of the results of the CSU experiments and factors determined from comparison of data from nearly collocated propeller and cup-and-vane systems at Cinder Cone Butte. The values in the COSCO (COSine COrrection) algorithm used by ARLFRD for the interim SHIS #2 data are derived from experiments with modified R.M. Young instruments by EPA's John Clarke.

The principal differences among the three sets of results are:

- Clarke's (and COSCO's) corrections are the same for the U-, V-, and W-props, and the corrections in the first 180° of wind direction are assumed to be mirrored exactly in the second 180°. This assumption is probably more accurate with Clarke's R.M. Young instruments, which had the U- and V-arms offset vertically to reduce the effects of one arm's wake on the other. In the Climatronics results, the effects of these wakes can be seen in the reduced response between 280° and 340° in comparison to that between 200° and 260°.

- Clarke's propellers were 23-cm polypropylene and the CTMD's are 19-cm polystyrene. The smaller, lighter props were selected for CTMD because of their increased responsiveness, but the polypropylene props are smoother and harder. Clarke's instruments also had extensions of the propeller shafts outwards from the hub. Both of these differences may improve the response of propeller anemometers near the stall regions around 90° angles of attack. The roughness of the polystyrene props is not uniform over their surfaces, which may contribute to the large variability of response among units at low component wind speeds. The softness of the material and the fact that they have been put on and taken off the shafts several times makes their hub holes vulnerable to enlargement and distortion, and consequently their mounting may be imbalanced or skewed. The effect of imbalance was evident during the experiments; on several occasions a prop would oscillate several degrees but not turn. This behavior results in apparently unpredictable results that depend on whether the motion causes light signals in the three-hole chopper wheel. The instrument responses in the present analysis have been set to zero speed when visual observations indicated the prop was not turning.

- ERT's experiments in the CSU wind tunnel differed from the FMF experiments in several ways. First, the FMF tunnel maintained steady low speeds better than CSU's so that we now have valid responses for a speed of approximately 0.5 m/s. Second, the instrument response from the CSU tunnel was mechanically determined by counting the number of pulses from each transmitter in a 30-second sample, whereas the instrument response during the FMF experiments was the voltage produced by the translator card. This output was measured both by the FMF's data acquisition system (DAS) sampling at 10Hz for 20 seconds and by ERT's digital volt meter (DVM). Also, the tunnel speeds at CSU were estimated from the output of ERT's "transfer standard" cup anemometer, which had been calibrated in the National Bureau of Standards wind tunnel in Gaithersburg, MD. The tunnel speeds at the FMF were estimated from the fan tachometer settings as described above.

In summary, the interim HBR data base still contains noise, especially in the data from the early SHIS #2 experiments. We plan a reanalysis of this data base to remove some of the residual noise. The first step will be additional signal processing to reduce the allowable second-to-second variations listed in Table 9. The second step will be an analysis and subsequent removal of the high frequency noise apparent in the data. For the propeller anemometer data we will apply the calibration factors listed in Table 10 and the correction factors for non-cosine response given in Table 11 after filtering the noise. The fourth step will involve correction for physical misalignments of instruments to true north. Finally, the 5-minute and 1-hour averages of the measurements and derived measures will be recalculated.

4.2 SHIS #2 Preliminary Modeler's Data Archive

The preliminary MDA developed from the SHIS #2 data archive contains 1-hour average tracer gas concentration data for each of the hours during SHIS #2 in which either SF_6 or CF_3Br tracer gas was released. The MDA excludes the 19 hours which were withheld by the EPA Project Officer for independent model validation purposes (p. 184 Third Milestone Report). The tracer release and meteorological data portion of the MDA has been compiled only for those hours in which CF_3Br tracer gas was released because the analysis of plume rise for the coincidental oil-fog and SF_6 tracer gas plume is not yet complete.

The SF_6 data base, along with a revised meteorological--CF_3Br data base, will be compiled once final refinements have been made to the tower meteorological data. Refined estimates of wind directions and σ_z values as derived from photographs and lidar will be included in the MDA in the future.

4.2.1 Tracer Concentration Data

Tracer gas data that were selected for the MDA are included as 1-hour average values of the concentrations scaled by the emission rate. These averages include concentrations from all 1-hour sampling bags, the largest of the two samples collected at collocated sampler sites, and the average of 10-minute concentrations at standard 10-minute sampler sites. For the 10-minute samples, 1-hour averages are included only if no more than one 10-minute period is missing. All concentrations are given in units of nanoseconds/m^3.

The tracer gas archive also includes the position of each sampler. A Cartesian coordinate system is used with the origin at Tower A. The x-axis is oriented toward true east and the y-axis is oriented toward true north. The sampler elevation is reported as the height in meters above 1600 m MSL. The sampler position identification code and a data quality flag are also included for each concentration. The intake port for the sampler is approximately 0.5m above the ground.

A map of HBR with each sampler and release position is presented in Figure 26. The solid lines are terrain contours and the dashed

TABLE 9. ALLOWABLE SECOND-TO-SECOND SENSOR CHANGES USED TO FILTER RAW DATA IN PROCESSING OF PRELIMINARY DATA BASE

Sensor	Max voltage Increment	Approx. change in units
u, v prop	0.200	2.0 m/sec
w prop	0.200	0.8 m/sec
cup anemometer	0.200	2.0 m/sec
wind vane	0.150	16.0 degrees
temperature	0.100	1.6 degrees C
delta temperature	0.100	0.4 degrees C
fast temperature	0.100	1.6 degrees C

TABLE 10. SUMMARY OF FMF UVW PROPELLER CALIBRATIONS

Serial No.	Component	Regression Line	No. Pts.	R^2	Equivalent m/s** 2.550v	2.600v	2.800v
21	V	u = 10.483 (volts - 2.500)*	15	.99997	.524 m/s	1.048 m/s	3.145 m/s
55	U	u = 10.524 (volts - 2.500)*	15	.99997	.526	1.052	3.157
19	W	u = 4.1724 (volts - 2.508)	16	.99998	.438	0.960	3.046
14	V	u = 10.494 (volts - 2.503)	13	.99998	.493	1.018	3.117
53	U	u = 10.337 (volts - 2.503)	13	.99997	.486	1.003	3.070
54	W	u = 4.1856 (volts - 2.504)	13	.99996	.481	1.005	3.097
Manufacturer's Calibration		u = 10.000 (volts - 2.500)			0.500	1.000	3.000
		Average error (bias)			-.009	+.014	+.105
		Std. deviation of error (precision)			.032	.034	.043
		Std. deviation of error (as percent)			6.4	3.4	1.4

*Output voltages corrected for electronic alignment errors.
**Response implied by regression line; it has been multiplied by 2.5 for the "W"-props for comparison with "U"- and "V"- props.

TABLE 11. RECOMMENDED CORRECTION FACTORS FOR NON-COSINE RESPONSE OF CLIMATRONICS UVW PROPELLERS

Angle	F_u	F_v	Angle	F_u	F_v	Angle	F_u	F_v
0°	(0.50)	1.00	120	.94	.81	225	.86	.85
1	(0.30)	1.00	125	.91	.79	230	.88	.83
2	(0.35)	1.00	130	.88	.77	235	.91	.81
3	(0.38)	1.00	135	.83	.77	240	.94	.80
4	.40	1.00	140	.78	.78	245	.96	.80
5	.48	1.00	145	.78	.83	250	.97	.81
7	.58	1.00	150	.80	.86	255	.98	.83
10	.62	.995	155	.75	.87	260	.97	.83
15	.68	.99	160	.73	.87	265	.95	1.05
20	.72	.97	165	.70	.88	270	.90	(0.50)
25	.75	.96	170	.66	.88	273	.86	(0.40)
30	.79	.94	173	.60	.85	275	.86	.57
35	.77	.91	175	.48	.82	280	.85	.65
40	.78	.87	176	.35	.81	285	.87	.68
45	.82	.83	177	(.35)	.80	290	.88	.72
50	.86	.79	178	(.35)	.78	295	.88	.75
55	.91	.78	179	(.30)	.78	300	.87	.80
60	.94	.80	180	(.50)	.79	305	.85	.78
65	.96	.76	181	(1.80)	.79	310	.81	.78
70	.97	.73	182	(1.60)	.81	315	.78	.83
75	.98	.69	183	(1.40)	.83	320	.79	.87
80	.99	.64	184	(1.20)	.84	325	.80	.91
85	1.00	.57	185	.90	.86	330	.81	.94
88	1.00	(0.35)	190	.87	.94	335	.81	.96
90	1.00	(.50)	195	.84	.97	340	.83	.97
92	1.00	(1.60)	200	.82	.97	345	.84	.98
95	.995	1.10	205	.80	.96	350	.89	.99
100	.99	.84	210	.80	.94	355	(1.10)	.995
105	.98	.81	215	.81	.92	357	(1.40)	1.00
110	.97	.80	220	.84	.89	359	(1.80)	1.00
115	.96	.81				360	(0.50)	1.00

F_u and F_v are the fractions of correct cosine response shown by the Climatronics U and V props in the tunnel with the wind from direction "angle." F_u^{-1} and F_v^{-1} are the corresponding correction factors.

Values in ( ) are not firmly founded from experiments but are estimates to be used for completeness and program coding.

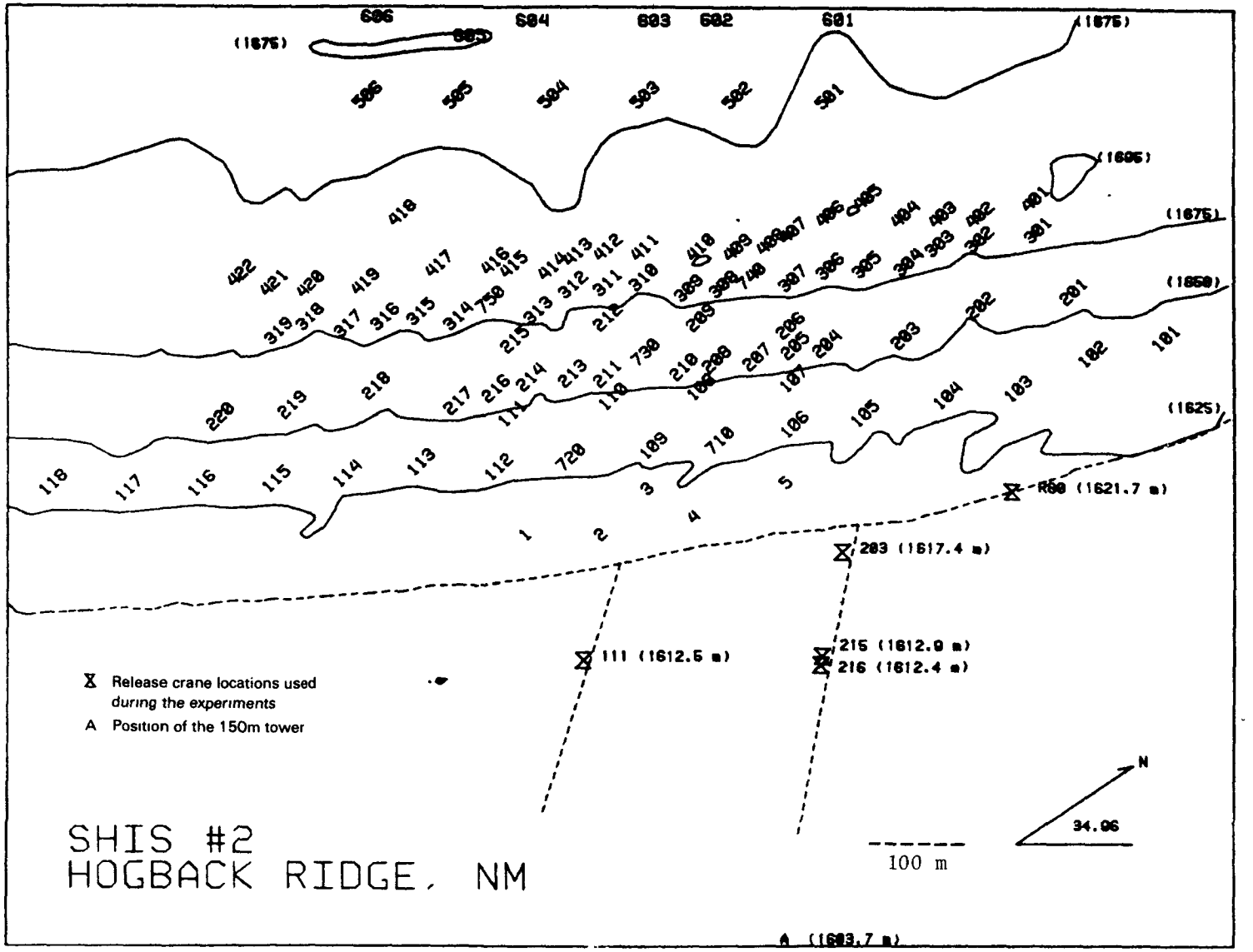

Figure 26. SHIS #2 tracer release and sampler locations.

lines are roads. Elevations (MSL) for each contour and release location are presented in meters. The towers and collocated sampling positions are not shown.

4.2.2 Tracer Release Information

The MDA contains the average emission rate of the tracer gas, the polar coordinates of the position of the source, the elevation of the ground beneath the source, the height of the source above the ground, and the times at which the tracer gas was turned on and turned off.

The emission rate (g/s) is an average mass release rate from the time at which the release valve was opened to the time at which it was closed. In some cases, this period was less than 1 hour, but in most cases it was several hours. The start and stop times for the release are referenced to the beginning and ending times of each experiment hour, respectively. A start time of -10 (minutes) indicates that the tracer was released ten minutes before the start of the sampling hour. An end time of -5 (minutes) indicates that the release ended 5 minutes before the end of the hour.

Coordinates of the source position are expressed in the hill coordinate system, a polar grid centered on Tower A. The zero height contour in this system corresponds to the 1600-m elevation MSL. Release elevations are presented in meters above the ground, and the elevation of the ground at the release position is given as the difference in meters from 1600 m MSL. A topographic map of HBR can be found in the Third Milestone Report.

4.2.3 Meteorological Data

Meteorological data contained in the MDA differ from those contained in the SHIS #2 data base in that: all quantities apply to the release height of the tracer gas rather than to the height of the fixed instrument levels; derived parameters computed from the MDA are included; and 1-hour averages are ultimately utilized in the modeling.

First, the sequence of 5-minute data in the MDA was constructed as follows:

- The NOAA/WPL sonic anemometers on Tower A at 5 m and 40 m acquire mean vertical wind speed and direction and vector mean horizontal wind speed and direction, and the turbulence velocity scales (σ_u, σ_v, σ_w). These sonic data are linearly interpolated to the plume height. All the CF_3Br tracer release heights are between 5 m and 40 m, except one hour when CF_3Br was released at 50 m.

- The dividing-streamline height, H_c, is obtained from splined (splined under tension) profiles of temperature and wind speed by means of the integral formula presented in the First Milestone Report. The 5-minute temperature and propeller wind speed profiles (as received from ARLFRD in October 1983) from Tower A are used. The effective height of HBR is taken to be 85 m.

- A bulk hill Froude Number (Fr) is calculated for the layer between H_c and the top of the tower (150 m) and also for the layer between 2 m and 150 m. The hill height in both calculations is the difference between 85 m and the height of the bottom of the layer (either H_c or 2 m).

- The local Brunt-Vaisala frequency (N) is estimated at source height by evaluating the temperature change along the splined Tower A temperature profile in the immediate vicinity (release height $\pm$ 0.1 m) of the source height to obtain the local temperature gradient. The bulk Brunt-Vaisala frequency (N_b) is estimated at source height by evaluating the temperature change between 2 m and the release height.

Then, the 1-hour average data in the MDA are constructed as follows:

- The 1-hour averages of speed and direction reported by the NOAA/WPL system are vector averages. These speeds and directions as well as σ_u, σ_v, and σ_w are linearly interpolated to release height. The 1-hour "scalar" wind speed and wind direction averages are computed from the 5-minute vector average data interpolated to release height. The 5-minute average wind data interpolated to release height are also used to compute a vector average of unit vectors along each 5-minute wind direction.

- The parameters calculated from the splined profiles of the 5-minute temperature and wind data from Tower A (H_c, F_r, N, N_b) are averaged to provide 1-hour average values.

The tracer release and meteorological data portion of the MDA have been compiled only for the CF_3Br tracer release hours. There were 90 hours of CF_3Br tracer releases, data from 11 of which were withheld by the EPA Project Officer for independent model validation purposes, leaving a total of 79 CF_3Br MDA hours (Table 12). Sonic anemometer data are not available for 12 hours. Of the remaining 67 hours, nine hours were judged inadequate for modeling because there were few non-zero concentrations observed, or the plume missed the sampler array, or the release was from Tower C on top of HBR. Thus, a total of 58 hours are available for modeling.

4.3 Modeling HBR

The development of CTDM has been largely guided by a theoretical understanding of dispersion and flow about simple, three-dimensional hills. A different approach has been taken in the initial stages of developing a model for HBR. Although many of the theoretical concepts contained in CTDM are applicable at HBR, the nature of the flow below a "critical dividing-streamline" at HBR appears to differ from that at CCB. The flow below H_c at HBR was frequently more unsteady than the flow above H_c. The plume tended to travel along the ridge, either toward the south or the north, before reaching the surface.

TABLE 12. CF_3Br DATA BASE SUMMARY STATISTICS
(EXCLUDING WITHHELD HOURS)

I. Number by release location

216/215	203	111	A	C
15	27	3	32	2

II. Number by height of source above the ground

<10m	11-20m	21-30m	31-40m	>40m
12	30	21	15	1

III. Number by wind direction*

N (316°-45°)	E (46°-120°)	S (121°-225°)	W (226°-315°)
19	26	18	4

*Sonic anemometer data not available for 12 hours.

IV. Number by release height (z_r) vs. H_c

$z_r \geq H_c$	$z_r \simeq H_c$	$z_r < H_c$
21	10	48

Fluctuations in this "blocked" flow and the two dimensionality of the ridge make the use of a single stagnation streamline concept inappropriate. A dispersion model for HBR must include a description of the nature of this blocked flow and its effects on dispersion. Because the analyses involved in specifying H_c for the unsteady flow in this blocked region have just begun, we have developed an empirical model for HBR as the first step towards structuring a theoretically based model. Once we have an adequate empirical understanding of the relationship between concentrations and observed meteorological conditions, we can attempt to develop a better theoretical understanding of the processes.

4.3.1 Importance of H_c at HBR

Analysis of data collected during the Cinder Cone Butte (CCB) experiment shows that the concept of the dividing-streamline height (H_c) plays a critical role in the description of dispersion in complex terrain. A plume below H_c tends to remain horizontal as it flows around CCB, while one above H_c has enough energy to climb over the hill.

A plume released near H_c can, under certain circumstances, "impinge" on the hill and cause concentrations that can be as large as the centerline concentration. This was the case at CCB, where the highest concentrations occurred when z_r was approximately equal to H_c. At HBR, the highest CF_3Br concentrations were observed when z_r was less than H_c, i.e., in the blocked flow upwind of the ridge. This is one of the major differences in dispersion between the two sites. Figure 27 shows that the averages of the top five concentrations observed during each hour at HBR take on their largest values when the release height z_r is below H_c. Because a plume released below H_c has a tendency to remain horizontal, one would expect the position of the maximum concentration to be lower on the hill than it would have been had the plume been lifted as it traveled toward the ridge. This hypothesis can be examined by comparing the locations of the observed maximum concentrations to those estimated by a flat terrain model formulated in terms of a terrain-following coordinate system (the height of the plume centerline above the terrain remains constant).

The flat terrain model used for this analysis includes a method to account for the large wind shear observed during stable conditions. This method is based on a model to simulate the dispersion of plumes released into a sheared boundary layer (Venkatram and Paine, 1984). The performance of this flat terrain model was improved significantly by incorporating the variation of wind and turbulent velocities into the sigma-z formulation. Figure 28 shows a schematic of plume behavior and the assumed speed profile. The upper and lower parts of the plume grow at different rates because of the speed change with height. It is assumed that σ_{zu} and $\sigma_{z\ell}$ can be written as:

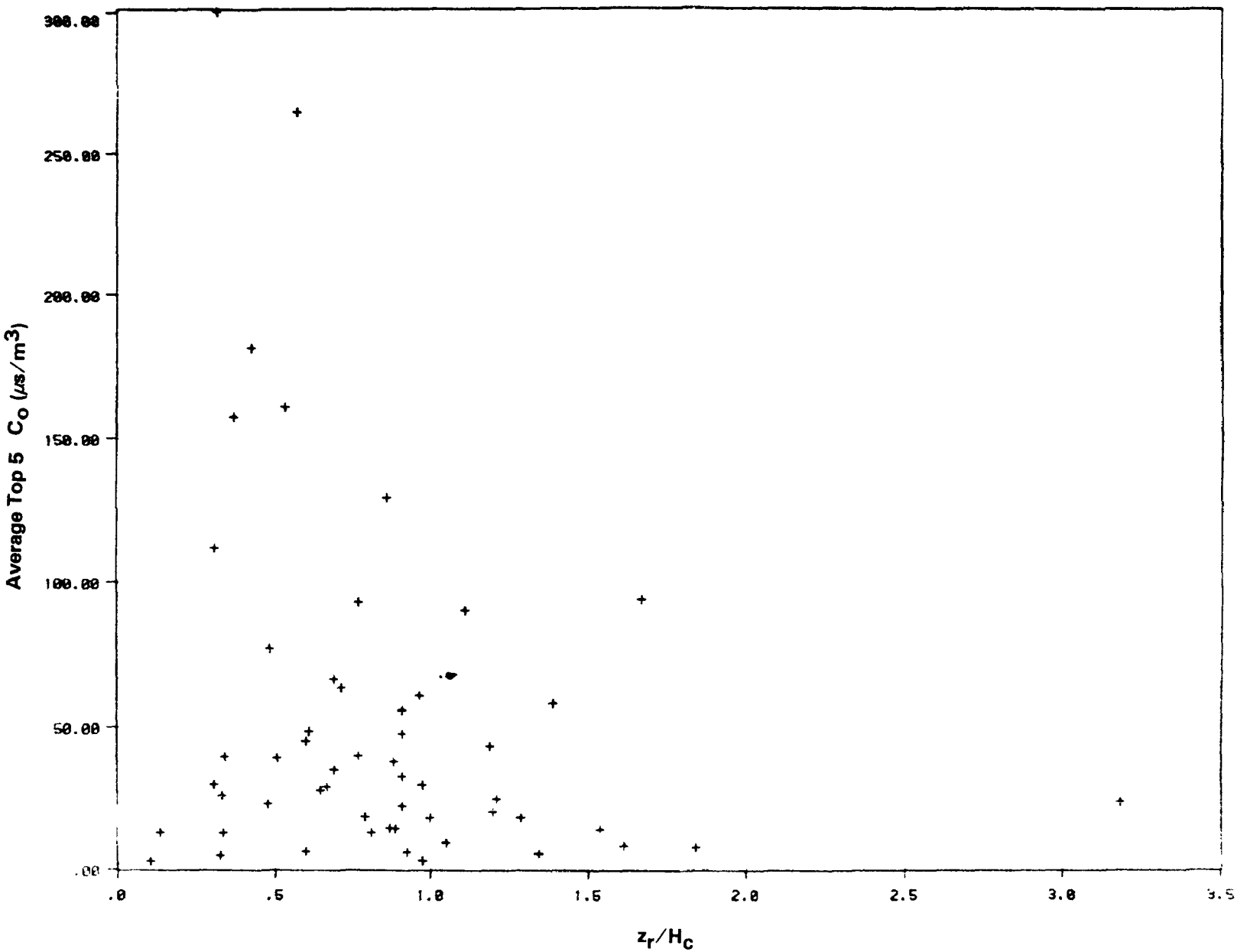

Figure 27. Variation of average five highest concentrations in each hour with the ratio of the release height to the critical dividing-streamline height at HBR.

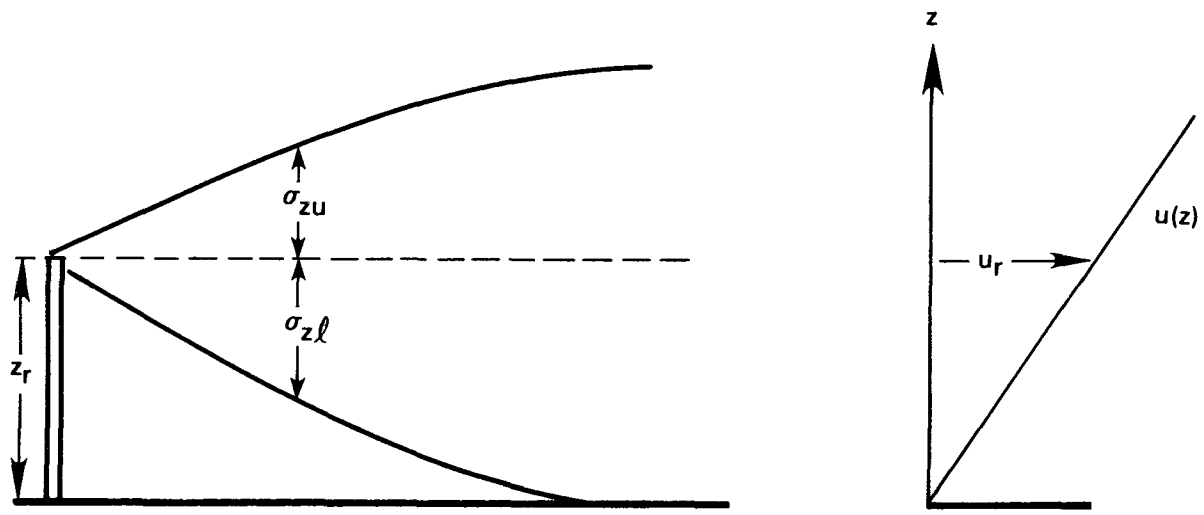

Figure 28. Schematic illustrating a Gaussian model that accounts for wind speed shear.

$$\sigma_{zu} = \frac{\sigma_w t_u}{(1 + t_u/2T_L)}^{0.5} \tag{81}$$

$$\sigma_{z\ell} = \frac{\sigma_w t_\ell}{(1 + t_\ell/2T_L)}^{0.5} \tag{82}$$

where the times of travel t_ℓ and t_u are implicitly given by

$$s = \int_0^{t_\ell} u_{e\ell} dt \tag{83a}$$

and

$$s = \int_0^{t_u} u_{eu} dt \tag{83b}$$

where s is the along-wind distance to the receptor, and

$$u_{e\ell} = \frac{u_r}{z_r} (z_r - \sigma_{z\ell}/2); \; \sigma_{z\ell} \leq z_r \tag{84a}$$

$$= \frac{u_r}{2z_r} \sigma_{z\ell} \; ; \; \sigma_{z\ell} > z_r \tag{84b}$$

and

$$u_{eu} = \frac{u_r}{z_r} (z_r + \sigma_{zu}/2) \tag{85}$$

The effective transport velocities u_{eu} and $u_{e\ell}$ correspond to the "midpoints" of the upper and lower plumes. The sonic observations of $\sigma_w(z)$ show that σ_w is approximately constant with height. The Lagrangian time scale $T_L(z)$ corresponds to the meteorological variables at source height z_r (see Section 2.4). Equations 81 and 85 are combined to yield implicit equations for t_ℓ and t_u which are then solved iteratively.

Figure 29 shows the variation of $\sigma_{z\ell}$ and σ_{zu} for a typical case. As expected $\sigma_{z\ell}$ is larger than σ_{zu} because of the lower wind speeds encountered by $\sigma_{z\ell}$. Notice that $\sigma_{z\ell}$ grows more rapidly than σ_{zu} as the lower part of the plume descends towards the ground. Once $\sigma_{z\ell} > z_r$, the effective wind speed associated with the travel time of $\sigma_{z\ell}$ starts increasing and the growth rate of $\sigma_{z\ell}$ becomes comparable to that associated with σ_{zu}. The figure shows that $(\sigma_{zu} + \sigma_{z\ell})/2$ does not differ very much from σ_z obtained by setting $t = s/u_r$.

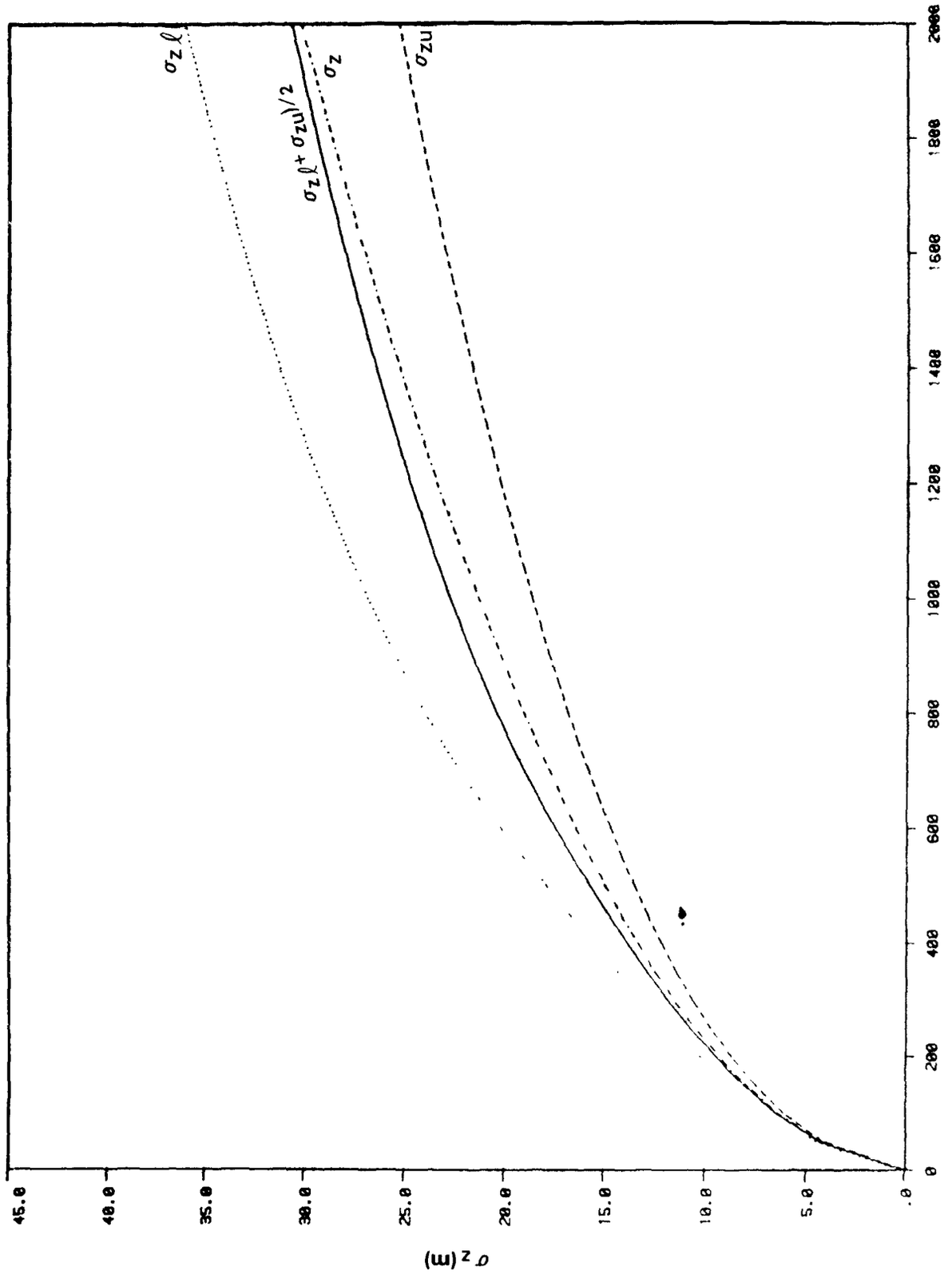

Figure 29. Variation of σ_z with distance for a typical case.

Therefore, the new σ_z formulation does not alter the centerline concentration. Its main effect is to decrease the distance at which the maximum ground-level concentration occurs.

Ground-level concentrations are expressed in terms of the two sigma-z values by

$$C(s,y_R,0) = \frac{2Q}{\pi u_r(\sigma_{z\ell}+\sigma_{zu})\sigma_y} \exp\left[\frac{-z_r^2}{2\sigma_{z\ell}^2}\right] \exp\left[\frac{(y_R-y_r)^2}{2\sigma_y^2}\right] \qquad (86)$$

where y_R is the crosswind coordinate of the receptor (see Figure 30). The crosswind spread σ_y is taken to be $i_y s$, where s is measured along the profile of the hill.

Equation 86 was used to calculate concentrations at the receptors on HBR. Figure 31 shows the ratio of the height of the receptor at which the predicted maximum occurred to that at which the observed maximum occurred as a function of z_r/H_c. As the release height moves below H_c, the positions of the largest concentrations produced by the flat terrain model become higher on the hill than were observed. This analysis suggests the importance of including H_c in the modeling of HBR.

4.3.2 Performance of the Flat Terrain Model

Figure 30 shows the idealized geometry used to model Hogback ridge. We assume that the ridge is two-dimensional and the stagnation streamline can be defined by a line through the source perpendicular to the ridge. The travel time to the receptor is calculated using the distance $(s^2 + (y_R-y_r)^2)^{1/2}$. The model was applied to 58 case hours listed in Table 13. Because the model assumes steady state conditions, and does not account for "sloshing" along the ridge, we chose to concentrate on a subset of hours for which $u_r > 0.5$ m/s and for which the wind direction falls in the range $55° \leq \theta_m \leq 180°$. With $\theta_s = 117°$, this choice of wind directions selects those cases in which the mean wind was directed towards the hill. This subset consists of 35 case hours which are indicated by asterisks in Table 13. All models discussed in this section are evaluated with this subset of 35 hours.

In this preliminary analysis we have chosen to quantify the performance of the models with the ratio of the average of the top two observations with that of the model predictions (see also Section 4.3.5). Figure 32 shows the variation of this ratio for the flat terrain model as a function of $(z_r-H_c)/H_c$. Note that the performance of the model deteriorates as the release height becomes less than H_c. This behavior is expected in a model that does not account for hill effects on dispersion.

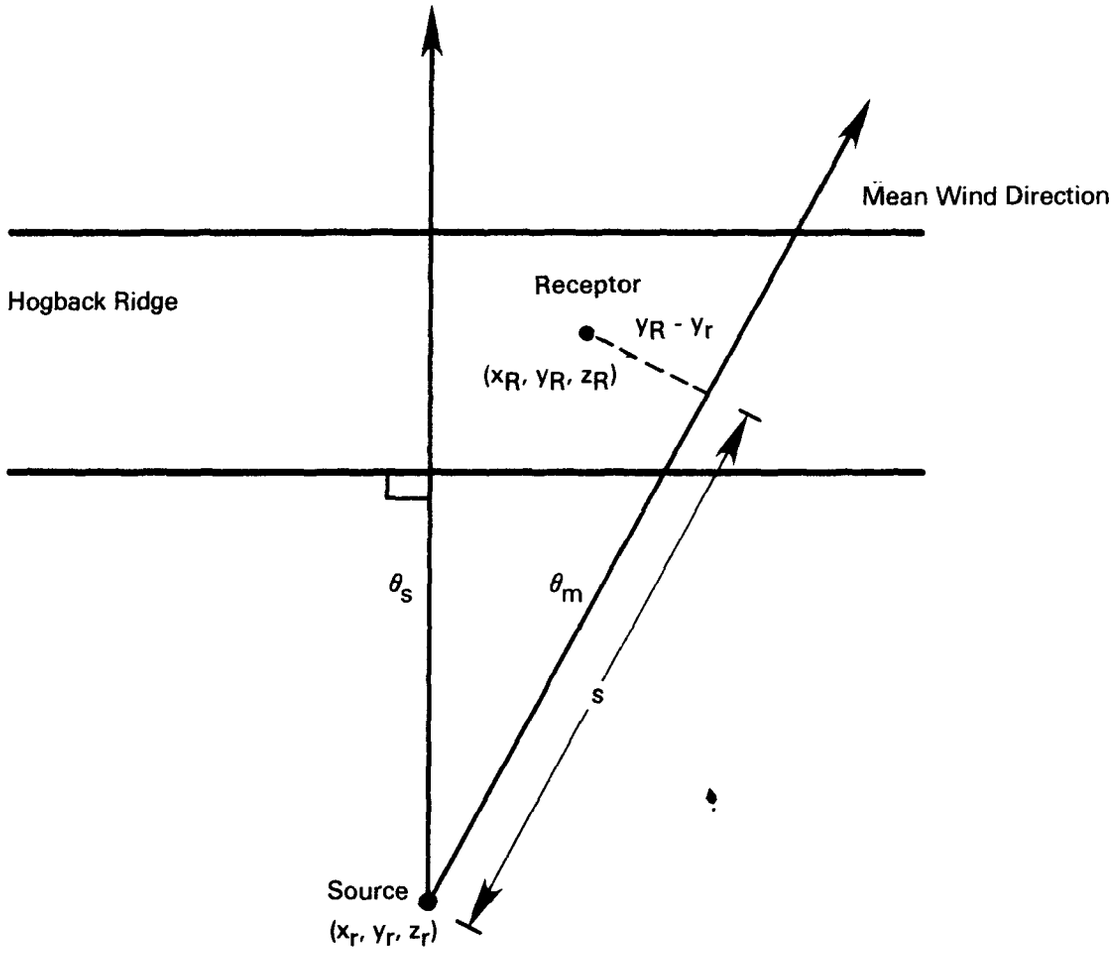

Figure 30. Geometry for modeling Hogback Ridge.

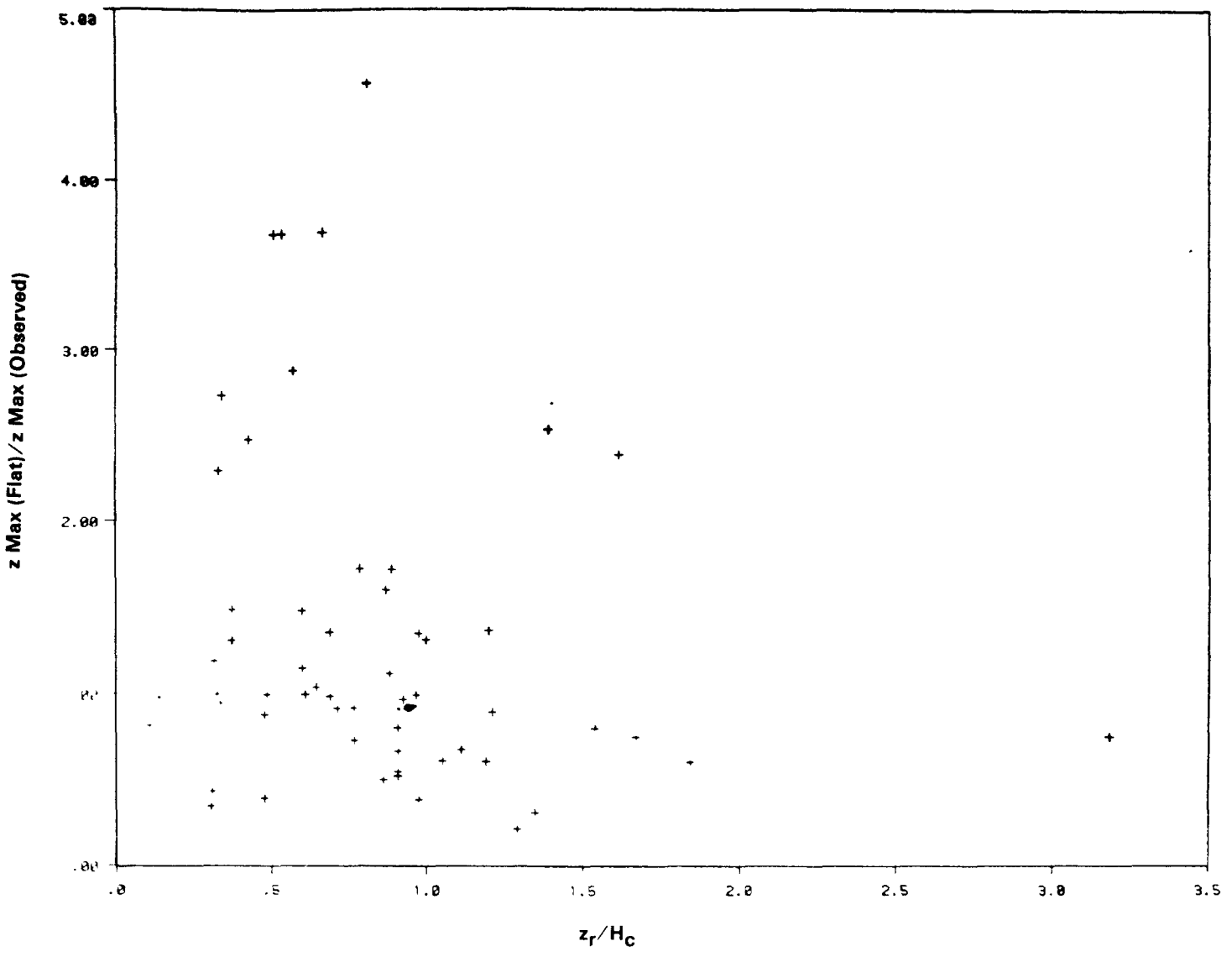

Figure 31. Variation of the height of the maximum observed concentration relative to that estimated by the flat terrain model with the ratio of the release height over the dividing-streamline height.

TABLE 13. HOGBACK RIDGE MODELING DATA

Exp	Exp-Hour	zr (m)	Hc (m)	u (m/s)	thta (deg)	sigma-v (m/s)	sigma-w (m/s)	N (1/s)
4	2	10.0	30.0	.9	10.5	.484	.136	.0326
4	3	20.0	26.0	.7	30.9	.512	.157	.0185
4	5	10.0	31.0	.2	187.4	.547	.115	.0540
4	6	20.0	47.0	.3	261.7	.611	.122	.0321
*4	7	20.0	29.0	.5	119.7	.449	.165	.0501
*5	1	25.0	18.0	2.4	55.7	.464	.139	.0519
5	2	15.0	31.0	.8	26.9	.547	.151	.0246
5	3	20.0	29.0	1.1	28.3	.386	.136	.0274
*5	4	20.0	30.0	.4	170.7	.376	.083	.0306
5	5	15.0	49.0	.5	186.4	.585	.112	.0401
*5	6	15.0	48.0	.7	178.2	.770	.095	.0415
*6	1	30.0	25.0	1.3	131.3	.366	.118	.0215
6	3	20.0	22.0	2.0	33.7	.491	.163	.0427
*6	6	30.0	31.0	1.5	64.0	.792	.201	.0292
6	8	25.0	29.0	1.3	45.3	.534	.167	.0226
*6	9	20.0	35.0	1.0	67.1	.495	.098	.0225
*8	1	20.0	61.0	.7	99.3	.629	.096	.0243
8	2	10.0	33.0	.6	322.3	1.117	.118	.0663
8	3	5.0	48.0	1.7	17.6	.262	.143	.1031
8	4	5.0	37.0	1.5	15.9	.338	.128	.0659
8	5	30.0	56.0	.8	276.0	.146	.088	.0340
8	6	25.0	41.0	.9	53.0	.436	.092	.0356
*8	7	25.0	35.0	1.2	83.7	.697	.207	.0363
*8	8	30.0	39.0	1.1	141.8	.788	.198	.0276
*8	9	15.0	25.0	.8	81.8	.614	.150	.0365
9	1	20.0	20.0	1.2	38.7	.379	.125	.0233
9	2	20.0	13.0	2.1	24.1	.521	.217	.0243
9	3	20.0	19.0	2.6	29.8	.694	.265	.0393
*9	4	20.0	22.0	1.5	65.2	.539	.283	.0254
*10	3	30.0	37.0	.9	120.7	.295	.116	.0181
*10	4	30.0	50.0	.5	139.6	.328	.136	.0198
10	5	30.0	59.0	.4	247.0	.396	.138	.0316
*10	6	30.0	33.0	1.3	75.6	.362	.137	.0337
*10	7	30.0	34.0	1.0	65.4	.484	.196	.0281
*10	8	30.0	38.0	.9	58.8	.522	.235	.0355
*11	1	20.0	59.0	.8	59.3	.475	.111	.0302
*11	3	20.0	42.0	.8	109.8	.506	.233	.0451
11	4	20.0	54.0	.9	298.2	.245	.107	.0433
11	7	25.0	27.0	1.5	51.3	.543	.241	.0258
*11	8	25.0	21.0	1.6	93.9	.491	.236	.0237
11	9	10.0	27.0	.6	25.7	.451	.188	.0391
*11	10	10.0	21.0	.8	67.3	1.025	.223	.0287
*12	2	40.0	46.0	1.5	167.1	.875	.115	.0436
*12	3	50.0	31.0	2.4	136.4	.793	.385	.0376
*14	5	20.0	31.0	.7	55.9	.690	.142	.0275
*14	6	20.0	18.0	1.2	59.3	.787	.218	.0204
14	7	20.0	12.0	1.6	41.0	.682	.298	.0115
*14	8	20.0	22.0	.9	137.2	.743	.293	.0133
*14	10	35.0	26.0	.8	132.2	.872	.253	.0073
14	11	35.0	19.0	.6	48.9	.484	.242	.0037
*14	12	35.0	11.0	1.2	102.8	.744	.294	.0041
*15	2	40.0	41.0	.9	63.0	.461	.159	.0276
*15	4	40.0	45.0	1.4	151.3	.388	.151	.0405
*15	5	40.0	44.0	1.0	146.1	.324	.175	.0293
*15	7	40.0	31.0	1.5	97.5	.597	.298	.0308
*15	8	40.0	33.0	1.4	106.9	.508	.206	.0296
*15	9	40.0	41.0	.9	144.6	.501	.212	.0356
*15	11	40.0	1.0	4.6	114.4	.867	.536	.0056

*Mean wind was directed toward the ridge.

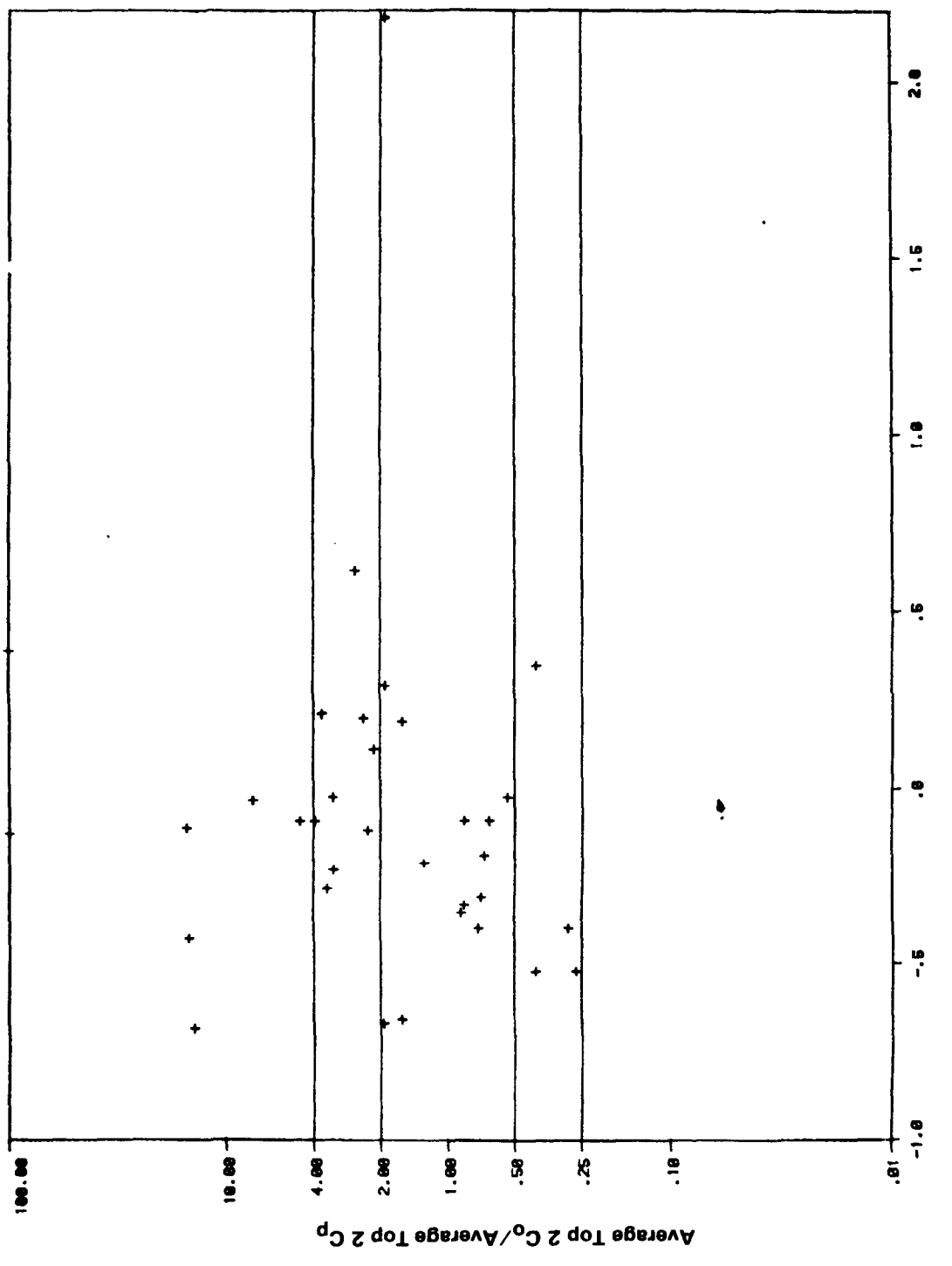

Figure 32. Variation of residual with release height relative to H_c for the flat terrain model over the subset of 35 hours.

It is informative to examine the performance of the model when the traditional "half-height" plume path modification is incorporated into it. The version of the modification that was used is given by

$$T_p = 1 - \frac{1}{2}\frac{z_R}{z_r} \quad ; \; z_R \leq z_r \tag{87a}$$

$$= \frac{1}{2} \quad ; \; z_R > z_r \tag{87b}$$

and is equivalent to that defined in Equation 74. Here z_R is the receptor height. It should be noted that the "half-height" modification has been widely used to simulate non-stable or slightly stable conditions in complex terrain. It has only been occasionally used to simulate very stable conditions. Nevertheless, the half-height modification has been applied to all 35 HBR hours. Figure 33 shows a plot of the residuals with release height. It is seen that the half-height modification moves most of the points down into the "overprediction" region for releases below H_c. Performance statistics for both tests are compared in subsection 4.3.5.

4.3.3 Development of the Empirical Complex Terrain Model for HBR

In developing the empirical HBR model, we assume that the effects of complex terrain on dispersion occur largely as a result of the influence of H_c and can be accounted for empirically by reducing the effective height of the plume centerline over the terrain. Future efforts will attempt to develop a theoretical description of actual plume behavior.

Before introducing the height correction, it is useful to re-examine the residual plots presented earlier. In Figures 34 and 35 the residuals have been replotted as a function of the predicted concentration. For an "adequate" model, we know that the residuals should not exhibit any trend with C_p (see First Milestone Report). It is seen from the figures that residuals from both the flat-terrain and the half-height model do not follow this behavior; C_o/C_p decreases with C_p. The flat-terrain model tends to underestimate as C_p decreases while the half-height model tends to overestimate as C_p increases. While the flat terrain model produces underestimates on an average, the half-height model provides estimates that are larger on an average than the observed concentrations.

The results from towing tank experiments (Appendix A) show that, at least for a three-dimensional hill, the H_c surface can be approximated by a ground plane in simulating the flow above H_c. This would suggest the following form for T_p:

$$T_p = (z_r - H_c)/z_r \qquad j \; z_r \geq H_c \tag{88}$$

$$T_p = 0 \qquad i \; z_r < H_c$$

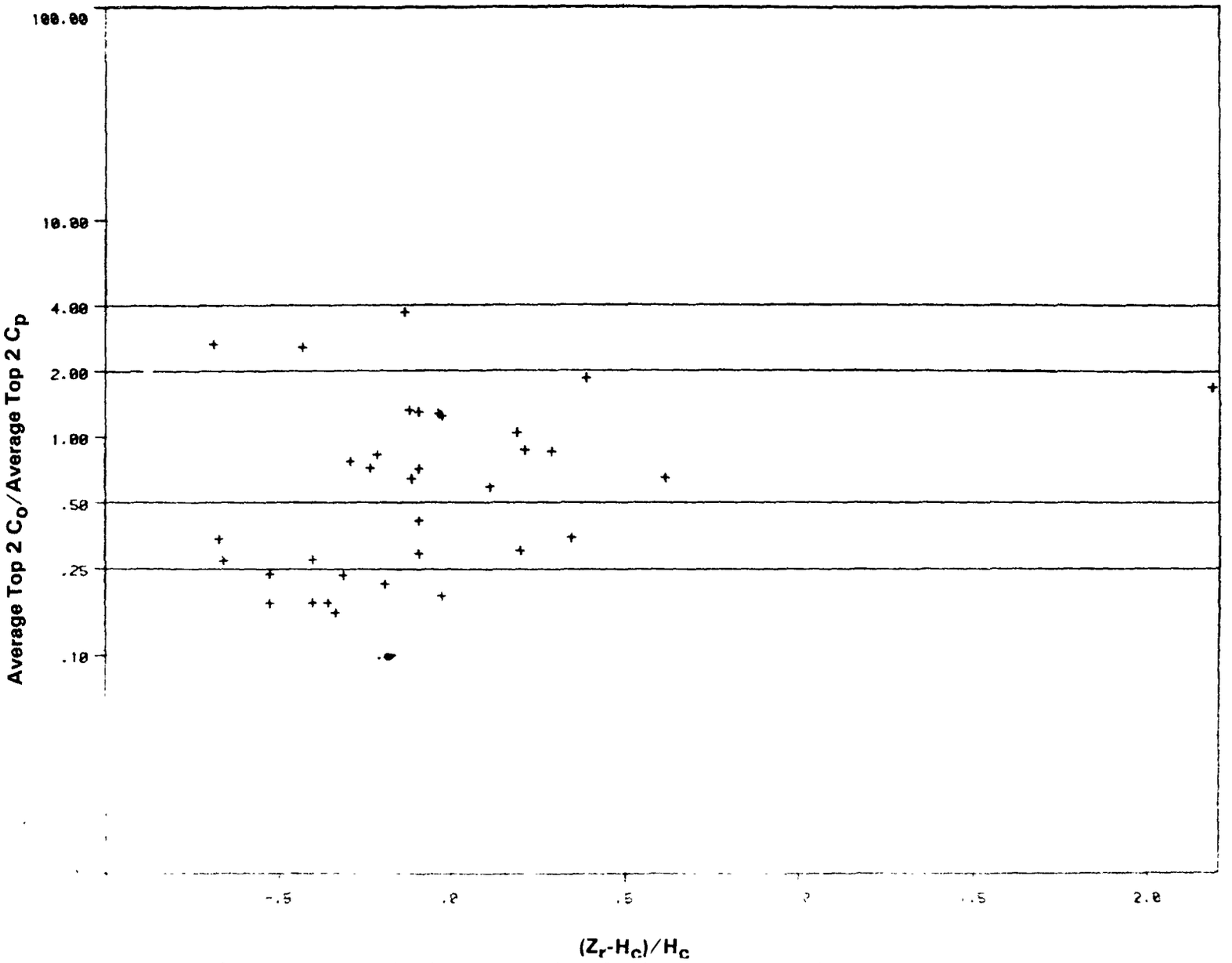

Figure 33. Variation of residual with release height relative to H_c for model with half-height correction (subset of 35 hours).

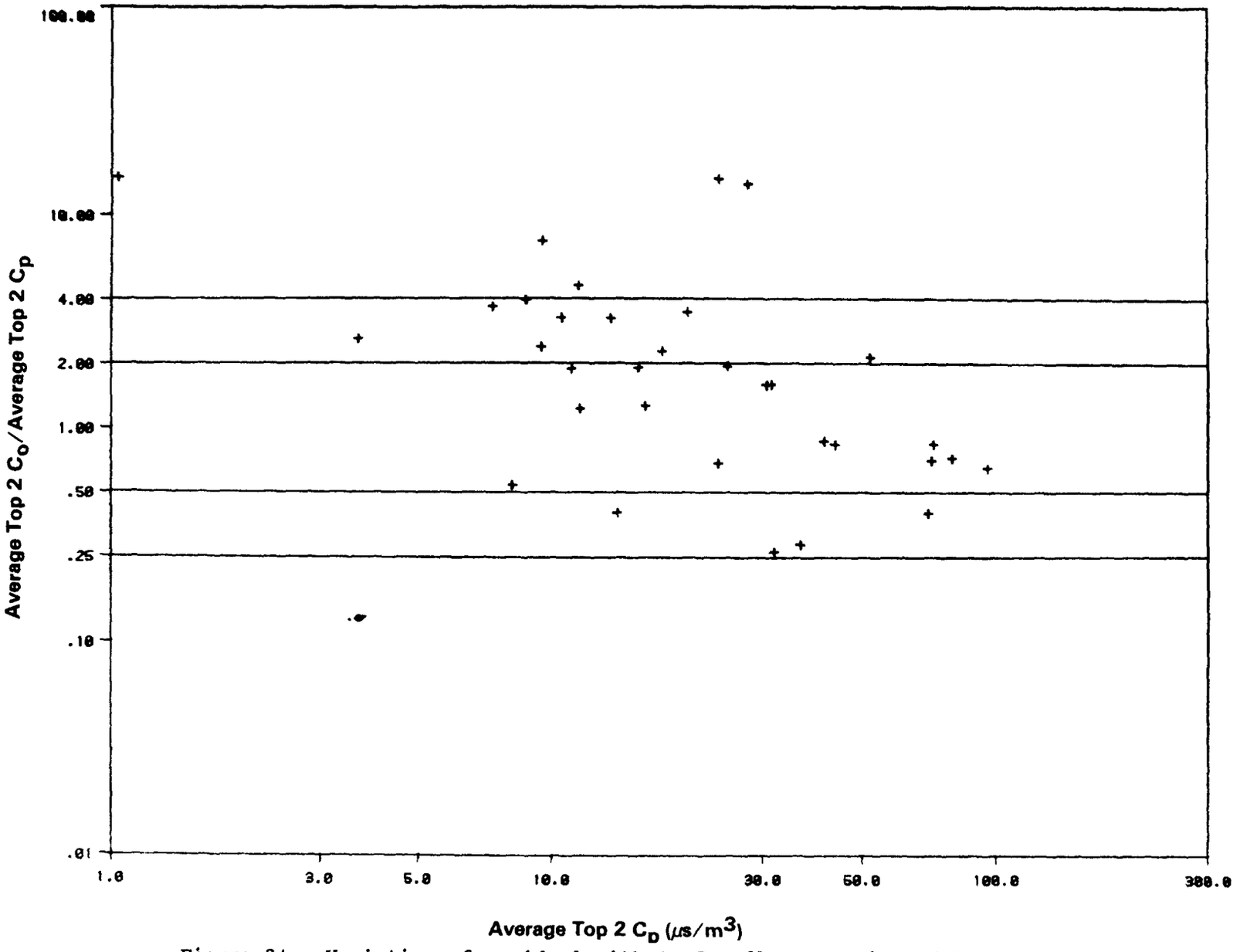

Figure 34. Variation of residual with C_p for flat terrain model (subset of 35 hours).

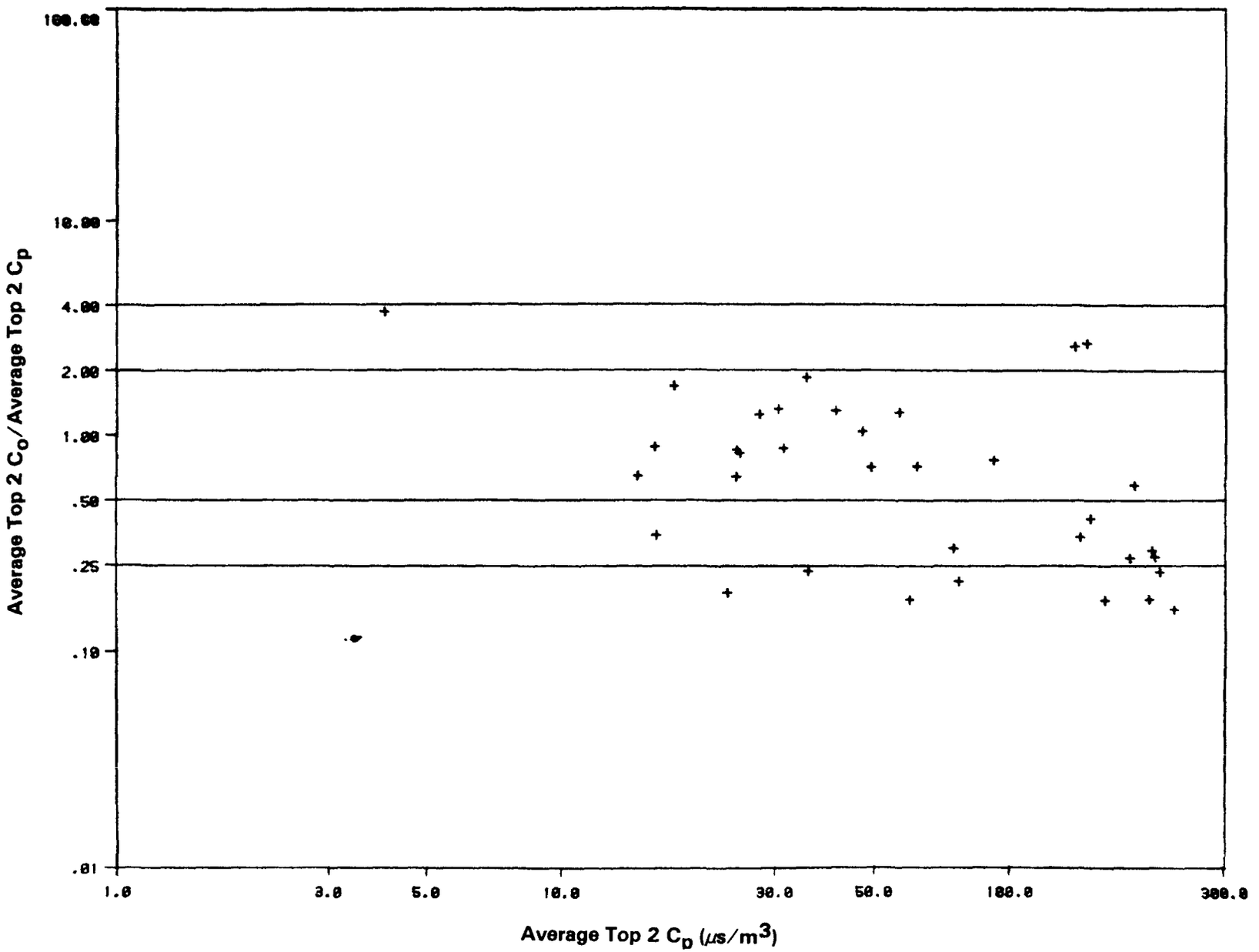

Figure 35. Variation of residual with C_p for flat terrain with "half-height" correction (subset of 35 hours).

The main problem with this formulation is that it is equivalent to assuming that the plume height is a constant ($z_r - H_c$) from the source to the receptor. This in turn leads to problems in properly accounting for the dispersion of plume material over terrain well upwind of the hill. To get around this problem we assume that T_p varies linearly from unity at the source to its minimum value given by Equation 88 at s_o where H_c intersects the hill surface. Beyond s_o it remains at this minimum value (T_{pm}). Then the variation of T_p is given by

$$T_p = 1 - \left(\frac{1-T_{pm}}{s_o}\right) s_a \quad ; \quad s_a \leq s_o \tag{89a}$$

$$= T_{pm} \quad ; \quad s_a > s_o \tag{89b}$$

where the along-wind distance s_a is measured along the profile of the hill so that

$$s_a = s_o + ((s-s_o)^2 + (z_R-z_r)^2)^{0.5} \quad \text{for } s > s_o \tag{90}$$

$$s_a = (s^2 + (z_R - z_r)^2)^{0.5} \quad \text{for } s \leq s_o$$

and T_{pm} is the minimum value given by Equation 88. The terrain correction factor T_p used in the Gaussian dispersion equation is then the average of T_p over the distance s_a,

$$\bar{T}_p = \frac{1}{2}\frac{s_o}{s_a} + T_{pm}\left[1 - \frac{1}{2}\frac{s_o}{s_a}\right] \quad ; \quad s_a \geq s_o \tag{91a}$$

and

$$\bar{T}_p = 1 - \frac{(1-T_{pm})}{2}\frac{s_a}{s_o} \quad ; \quad s_a < s_o. \tag{91b}$$

For completeness we rewrite Equation 88

$$T_{pm} = (z_r - H_c)/z_r \quad ; \quad z_r \geq H_c \tag{92a}$$

$$= 0 \quad ; \quad z_r < H_c \tag{92b}$$

4.3.5 Summary of Model Performance

This section compares the performance of the empirical HBR model, the half-height model, and the flat terrain model. We have chosen to quantify the performance of the models with the residual ε defined by

$$\epsilon = \frac{\text{Average of top N observed}}{\text{Average of top N predicted}}$$

where N is taken to be 1, 2 or 5 and the concentrations are paired in time but not in space. If we assume that ϵ is lognormally distributed, an adequate model (see Section 5.3 of the First Milestone Report) should yield an ϵ that is randomly distributed about unity when it is plotted on a logarithmic scale. For an ideal model, $m_g \equiv \ln \epsilon$ should be unity and the logarithmic standard deviation should be small. Figures 32 and 33, presented earlier, and Figure 36 show the variation of $\epsilon(N=2)$ for the flat terrain model, half-height model and the empirical HBR model as a function of $(z_r-H_c)/H_c$. As discussed earlier, the flat terrain model performs poorly and underpredicts the concentrations by large margins. There is some indication that the performance is better when z_r becomes much greater than H_c.

The half-height model overestimates the observed concentrations with the tendency to overpredict increasing as z_r becomes less than H_c. The residual pattern for the empirical HBR model is similar to that for the half-height model except that the tendency toward overestimation for z_r less than H_c has been reduced. This reduction in the tendency to overestimate peak observed concentrations for z_r less than H_c also reduces the degree of overestimation as C_p increases. A plot of the residual versus C_p presented in Figure 37 shows that the empirical HBR model has improved upon the performance of the half-height model (Figure 35) in this aspect of model performance.

The relative performance of the models is better illustrated through the statistics presented in Table 14. Because the sample size was relatively small (=35) it was necessary to calculate m_g and s_g using a method that weighted the outliers less than the residuals near the middle of the distribution. We assumed that an appropriate estimate of m_g was the median of the 35 ratios of the observed to the predicted concentrations. To estimate s_g we assumed that ϵ was lognormally distributed. Then $\ln s_g$ corresponded to the standard deviation of a normal distribution with the observed fraction of residuals within a factor of two of unity.

We see from Table 14 that the flat terrain model underestimates the concentrations by almost a factor of two. (An m_g greater than one indicates an underestimation). The standard deviation s_g is relatively large. The model with the half-height terrain correction factor overestimates the observed concentration by a factor of 1.5 for all the chosen values of N. The s_g, while smaller than that of the flat terrain model, is still large.

The empirical HBR has an m_g which is close to the ideal value of unity. Notice that the best combination of the m_g and s_g statistics correspond to the largest observed concentrations (N = 1). The empirical HBR model outperforms the other two models for all three values of N.

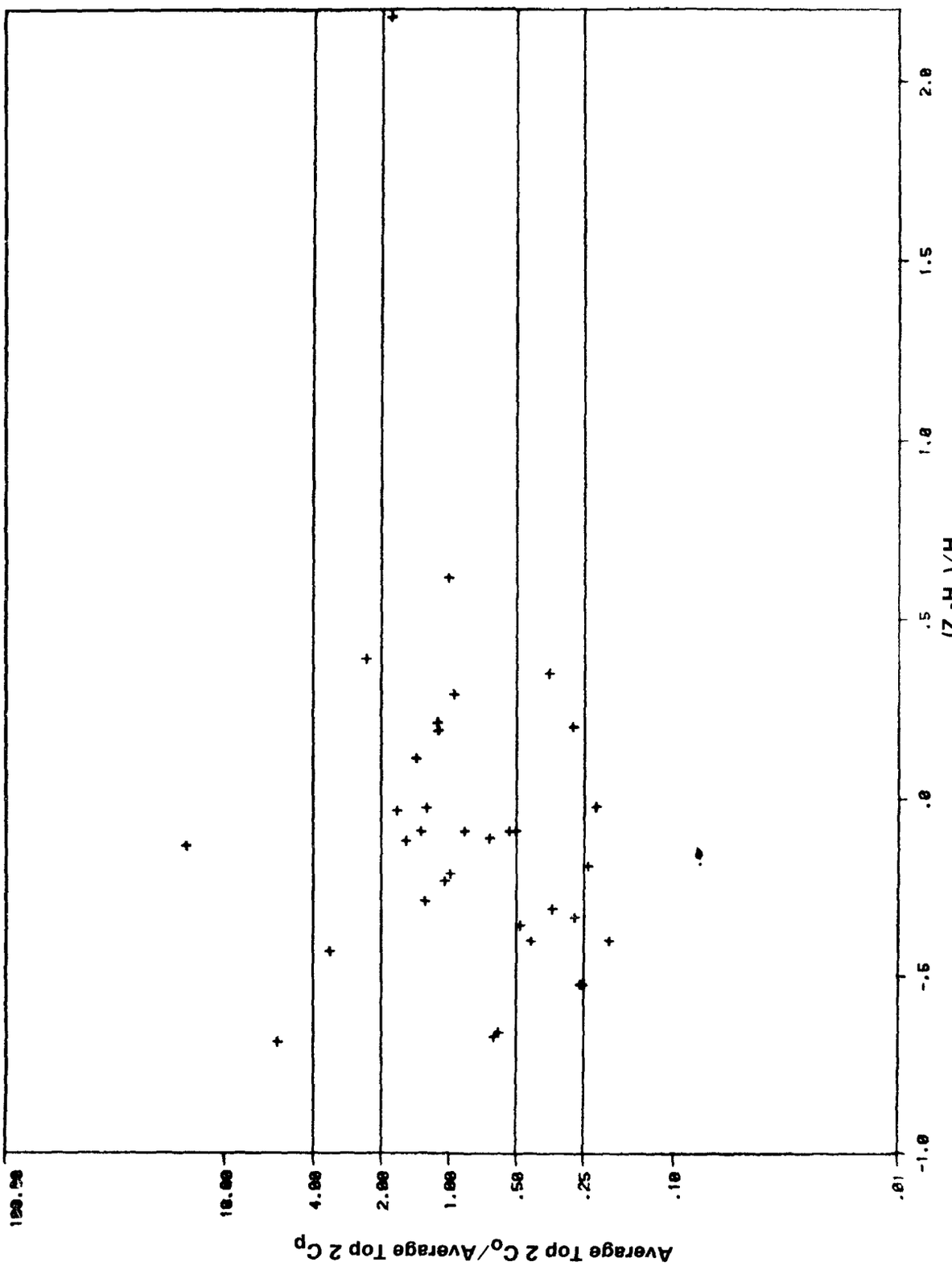

Figure 36. Variation of residual with release height relative to H_c for the empircal HBR model (subset of 35 hours).

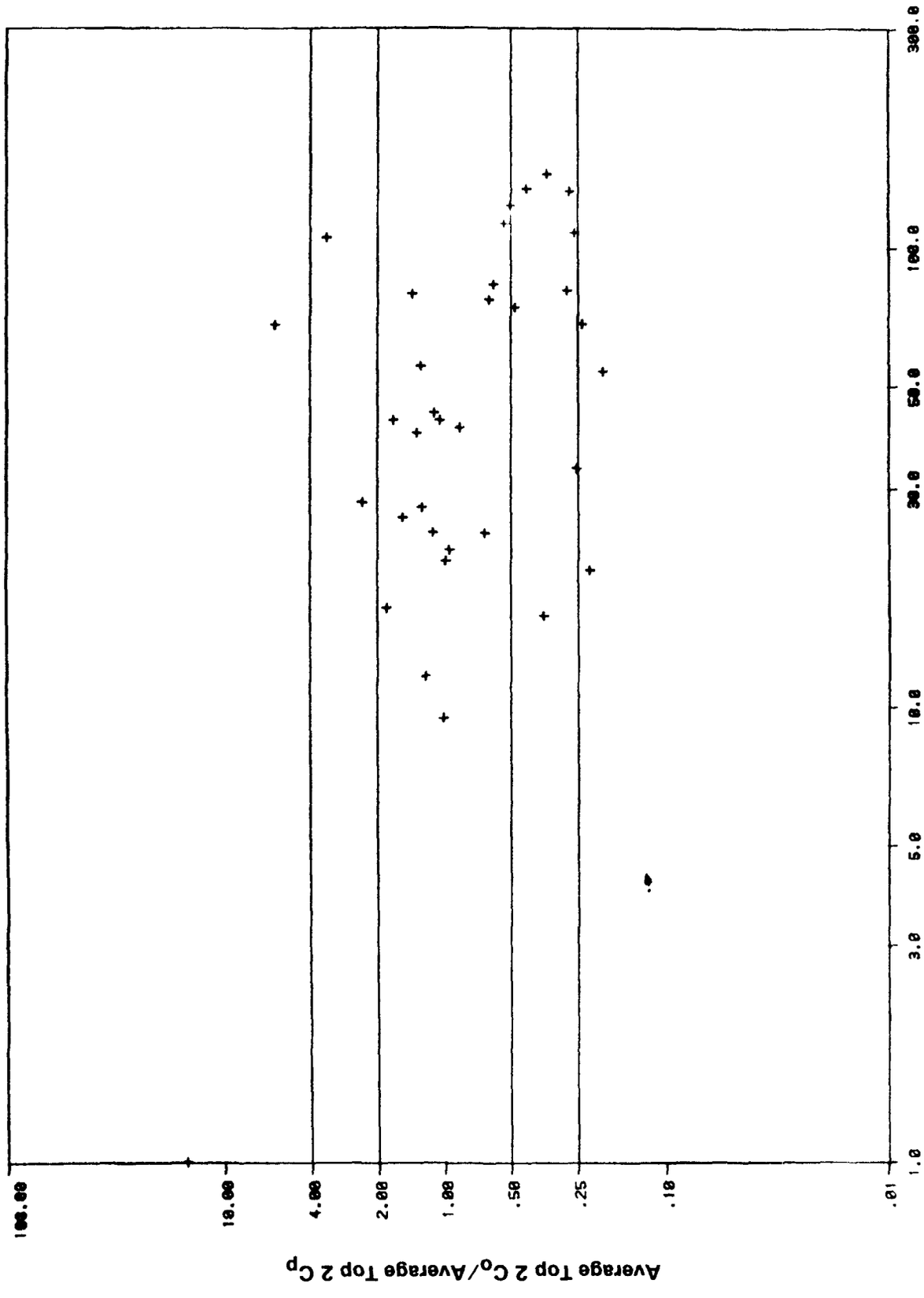

Figure 37. Variation of residual with C_p for the empirical HBR model (subset of 35 hours).

TABLE 14. RELATIVE PERFORMANCE OF MODELS

35 Hours

Model	N=1		N=2		N=5	
	m_g	S_g	m_g	S_g	m_g	S_g
Flat	1.98	3.70	1.91	3.37	1.62	3.37
Half-Height	0.67	2.90	0.66	2.90	0.64	2.55
HBR Model	0.99	2.28	0.95	2.40	0.87	2.70

$z_r > H_c$ (10 Hours)

Model	N=1		N=2		N=5	
	m_g	S_g	m_g	S_g	m_g	S_g
Flat	2.11	3.74	2.02	3.74	1.75	2.79
Half-Height	0.84	1.72	0.87	1.72	0.81	1.72
HBR	1.12	1.95	1.12	1.95	1.06	1.95

$z_r < H_c$ (25 Hours)

Model	N=1		N=2		N=5	
	m_g	S_g	m_g	S_g	m_g	S_g
Flat	1.66	3.74	1.60	3.27	1.21	3.14
Half-Height	0.42	4.37	0.42	4.37	0.46	3.74
HBR	0.64	2.45	0.63	2.67	0.58	3.28

Table 14 also includes the statistics for the three models when the hours are separated into two classes: (1) z_r greater than H_c and (2) z_r less than H_c. Although the number of hours in each class is considerably smaller than the total number of hours, the statistics are still instructive. For z_r greater than H_c the half-height model and the empirical HBR model have virtually the same s_g, and the half-height model overestimates by approximately the same amount that the empirical HBR model underestimates. For z_r less than H_c, the empirical HBR model exhibits a smaller tendency toward overestimating the observed peak concentrations than the half-height model. The HBR model also performs a little better in reproducing the peak concentrations (N = 1 and 2) for releases below H_c than the two other models. However, for N = 5 the flat terrain model performs as well as the empirical model.

4.4 Selected Case-Study Results

A total of 58 hours have been used in the modeling analysis. Of these 58 hours, 36 hours are classified as $z_r < H_c$, 12 as $z_r > H_c$, and 10 as $z_r \simeq H_c$.

To illustrate plume behavior at HBR, detailed analyses of four of the hours modeled are presented in this section. These hours include:

- Experiment 11, 0600-0700 MDT, $z_r > H_c$
- Experiment 14, 0300-0400 MDT, $z_r \simeq H_c$
- Experiment 6, 0700-0800 MDT, $z_r < H_c$
- Experiment 8, 0500-0600 MDT, $z_r < H_c$

These four case-studies include those hours in which the highest concentrations were observed for release heights greater than, equal to, and less than H_c. Also, these hours were selected because the MDA wind directions are consistent with the observed concentration patterns. Each case-study analysis includes a description of the release information, meteorological data, and observed CF_3Br concentrations. Also, the performance of the flat-terrain model and the empirical HBR model discussed in subsection 4.3.3 are contrasted for each case-study hour. These two models are referred to as HBR (Flat) and HBR (Terrain), respectively.

4.4.1 Experiment 11, Experiment-Hour 8 (0600-0700 MDT)

Release Description

The CF_3Br tracer gas was released 25 m above the ground from Tower A for the entire hour. The release was continuous from the previous two hours; therefore, the tracer plume was well established by the beginning of experiment-hour 8.

Local terrain elevations near the release point are estimated to be 3.7 m above the base elevation of the hill coordinate system, so the net release height corresponds to the 28.7 m height level on the ridge. The CF_3Br release rate is calculated to be 1.31 g/s.

Meteorological Information

The 5-minute temperature and propeller wind data measured during the hour at the 10 instrument levels of Tower A (2, 5, 10, 20, 30, 40, 60, 80, 100, 150 m) are used to characterize the flow in terms of the dividing-streamline height (H_c) and the bulk hill Froude number above H_c (Fr). Time series plots of the calculated 5-minute H_c and Fr values for this hour are presented in Figure 38. The dashed line shown in the H_c time series plot represents the tracer gas release height. H_c drops from a high of 30 m at the beginning of the hour to a low of 14 m, then rises to approximately 22 m for the last 25 minutes of the hour. The average of the 5-minute values over the hour is 21 m. Because H_c is greater than the release height for only one 5-minute period, this hour is representative of flow above the dividing-streamline height. Fr varies from a low of 0.7 during the first half of the hour to a high of 1.3 during the last half of the hour. The one-hour average value of Fr above 21 m is 1.0, which indicates that stratification has a significant influence on the flow over the top of the ridge.

Time series plots of the 5-minute sonic anemometer data from Tower A are presented in Figure 39. The dashed line represents data from the 5-m level of Tower A and the dotted line represents data from the 40-m level. The 5-m and 40-m data are linearly interpolated to the tracer gas release height and these release height values are represented by the solid line.

The 5-m winds are light and variable during the hour with speeds ranging from 0.3 to 1.2 m/s and wind directions ranging from 350 to 140°. The 40-m winds are steadier with speeds ranging from 2.2 to 3.0 m/s and wind directions ranging from 90 to 115° during the hour. The hourly averaged vector wind direction and wind speed at the tracer release height are estimated to be 93.9° and 1.6 m/s, respectively.

The vertical turbulence intensity (i_z) values at the tracer release height vary from 8 to 17% and the σ_w values at the release height vary from 0.15 to 0.32 m/s. The 1-hour value for σ_w estimated at the tracer release height is 0.24 m/s (i_z = 15%).

An hourly average of the 5-minute temperature and propeller wind data measured during this hour at the 10-instrument levels of Tower A are used to construct vertical profiles. A "spline under tension" method is used to interpolate the meteorological variables for every 5 m between instrument levels on Tower A. Figure 40 shows the vertical profiles of hourly averaged wind direction, wind speed, and temperature. The wind data from the propeller anemometer at 5 m and 40 m compare favorably with the sonic anemometer wind data at the same levels. Also, the vertical profiles between 5 m and 40 m are approximately linear, so the linear interpolation used to estimate MDA values for wind speed and direction at the release height should be acceptable. The interpolated profile values for the wind direction and speed at the tracer gas release height are 98° and 2.0 m/s, respectively. These values do indeed indicate that the linear

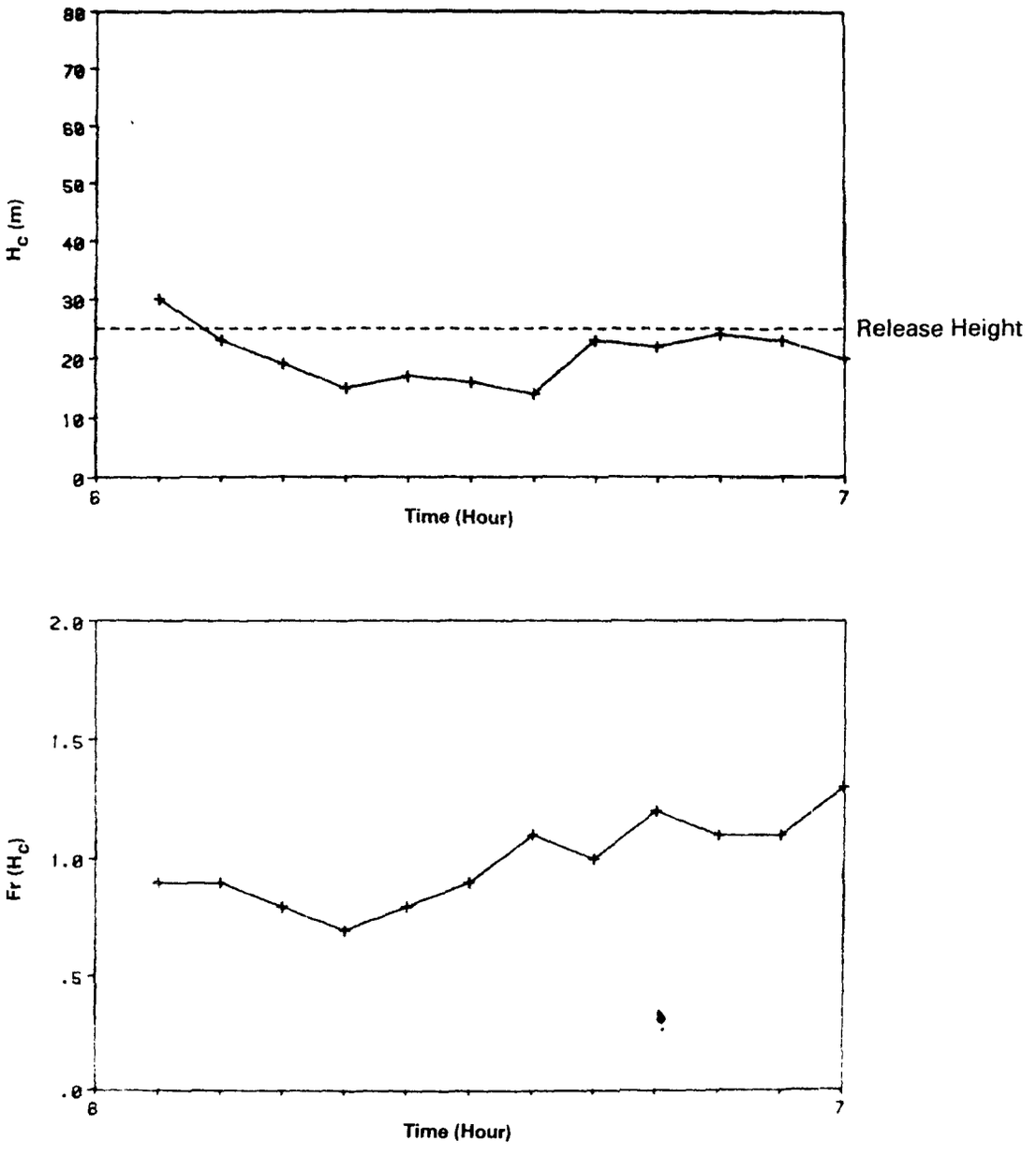

Figure 38. Time series of 5-minute calculated dividing-streamline heights (H_c) and bulk hill Froude numbers above H_c ($F_r(H_c)$) (Experiment 11, 10/23/82, 0600-0700 MDT).

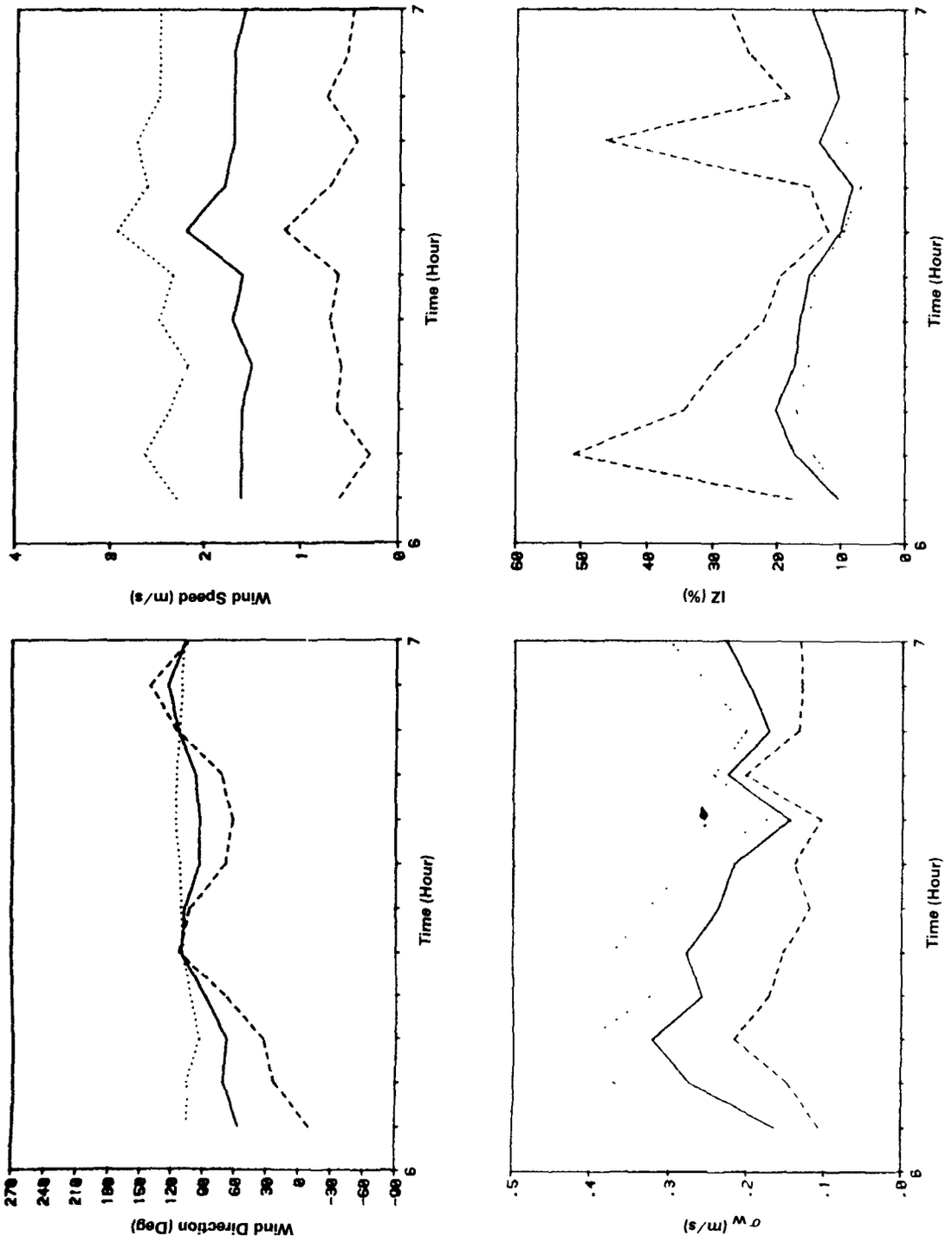

Figure 39. Time series of 5-minute sonic data from Tower A (Experiment 11, 10/23/82, 0600-0700 MDT). Values at CF_3Br release height (____) are interpolated from measurements at 5 (_ _ _) and 40 (. . .) m.

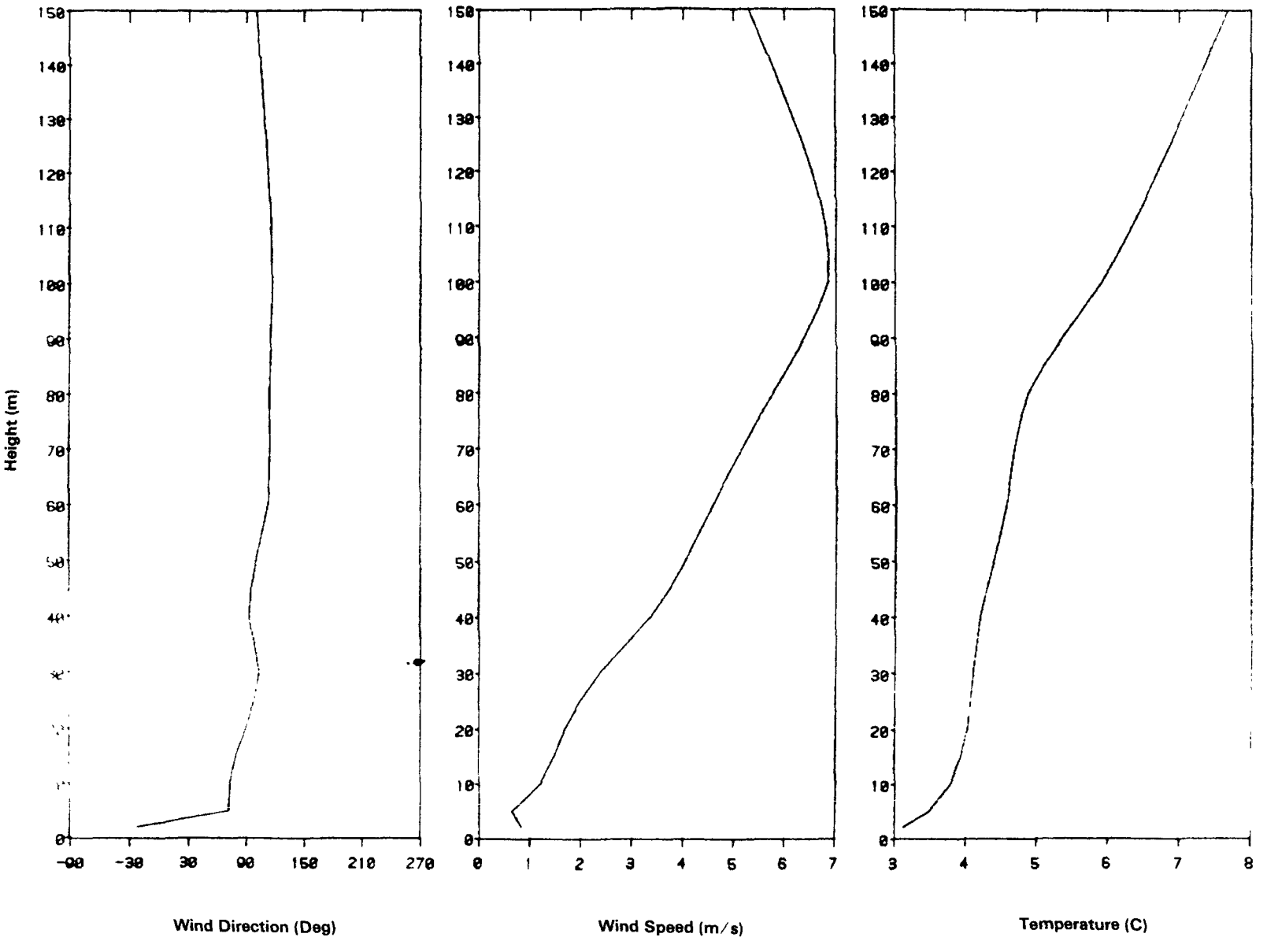

Figure 40. Vertical profiles of hourly meteorological data from Tower A (Experiment 11, 10/23/82, 0600-0700 MDT).

interpolation used to construct the MDA apparently provides a reasonable estimate of the meteorology at release height.

In summary, the plume was released above H_c into a flow characterized by some plume meander, 1.6 to 2.2 m/s wind speeds, and a hill Froude number equal to unity. The largest observed concentrations are expected to be found near or above H_c.

CF_3Br Concentrations

The distribution of the observed hourly averaged CF_3Br concentrations scaled by the emission rate ($\mu s/m^3$) is shown in Figure 41. The concentrations from samplers suspended from Towers B (sampler id: 702 and 703) and C (701) are listed above the release information. In this figure, the 5-minute average wind flow vectors estimated at the tracer gas release height are drawn at the release position. The length of each flow vector is proportional to the 5-minute vector wind speed. The 1-hour average flow vector, derived from a vector average of the 12 5-minute vector wind directions, is depicted by the long dotted line emanating from the release position.

The largest concentrations are found towards the middle of the sampler array near or above the hourly average H_c value (21 m above the release base). The maximum observed concentration (52 $\mu s/m^3$) is found near the estimated hourly-averaged plume centerline at sampler 112.

Model Performance

The hourly-averaged scaled concentrations estimated from the HBR (Flat) model are presented in Figure 42. The summary table, shown in the lower right-hand corner of the figure, includes statistics for all one-hour average concentrations except those from samplers suspended from Towers B and C. MCO/MCP is the ratio of the maximum observed to the maximum predicted concentrations, unpaired in space. The estimated concentration pattern compares favorably with the observed (r^2 = 0.61), but peak concentrations are underestimated (MCO/MCP = 1.62).

The hourly-averaged scaled concentrations estimated from the HBR (Terrain) model (see subsection 4.3.3) are presented in Figure 43. The maximum predicted concentration has increased from 32 $\mu s/m^3$ from the flat-terrain version to 47 $\mu s/m^3$. This still underestimates the maximum observed concentration of 52 $\mu s/m^3$. Overall, the estimated concentration pattern compares well with the observed (r^2 = 0.61) with the ratio of the mean observed to the mean predicted equal to 0.89.

4.4.2 Experiment 14, Experiment-Hour 6 (0300-0400)

Release Description

The CF_3Br tracer gas was released from position 203 at 20 m above the ground for the entire hour. The release was continuous from the previous hour at a rate of 0.93 g/s.

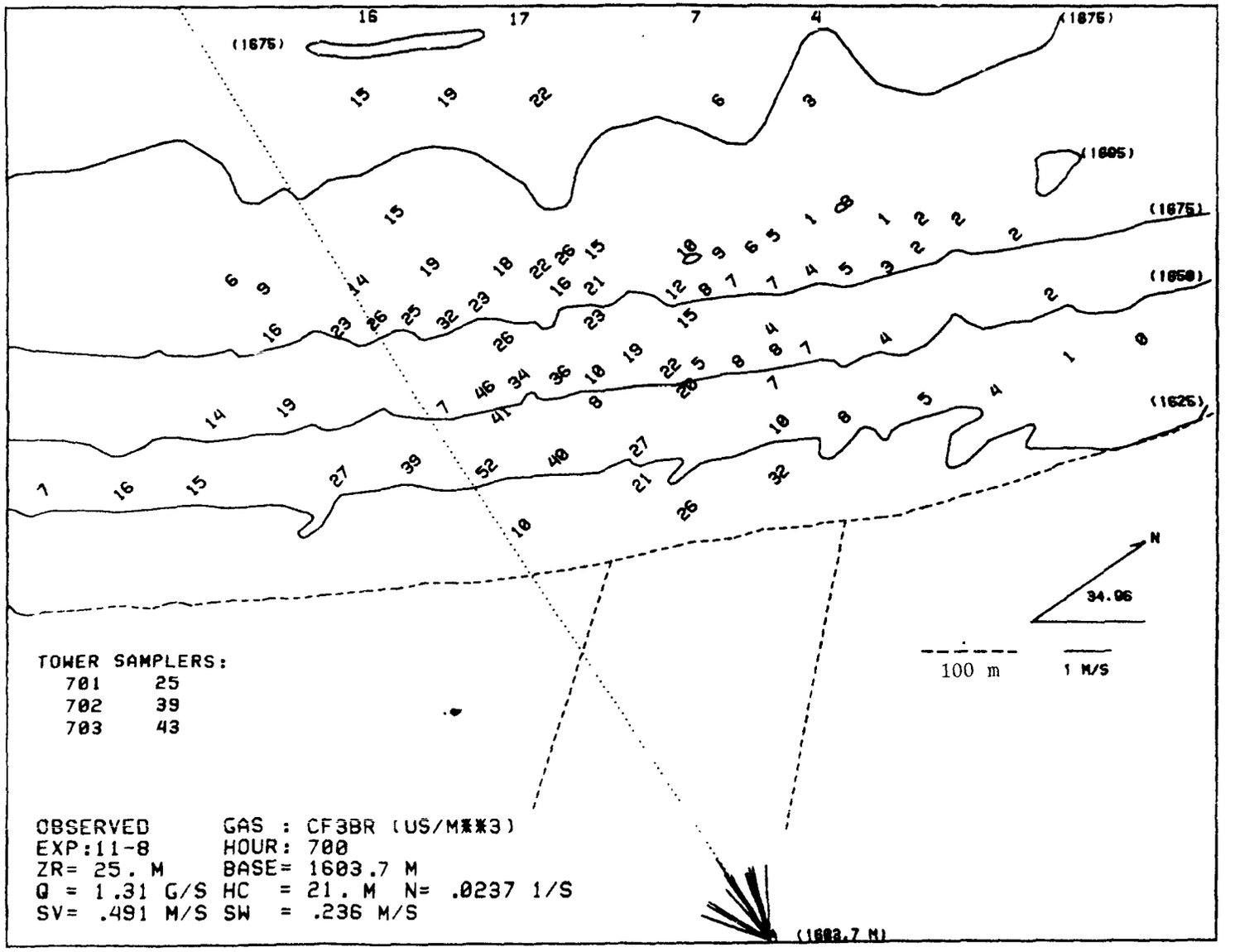

Figure 41. One-hour average observed CF_3Br concentrations scaled by emission rate ($\mu s/m^3$) (Experiment 11, 10/23/82, 0600-0700 MDT).

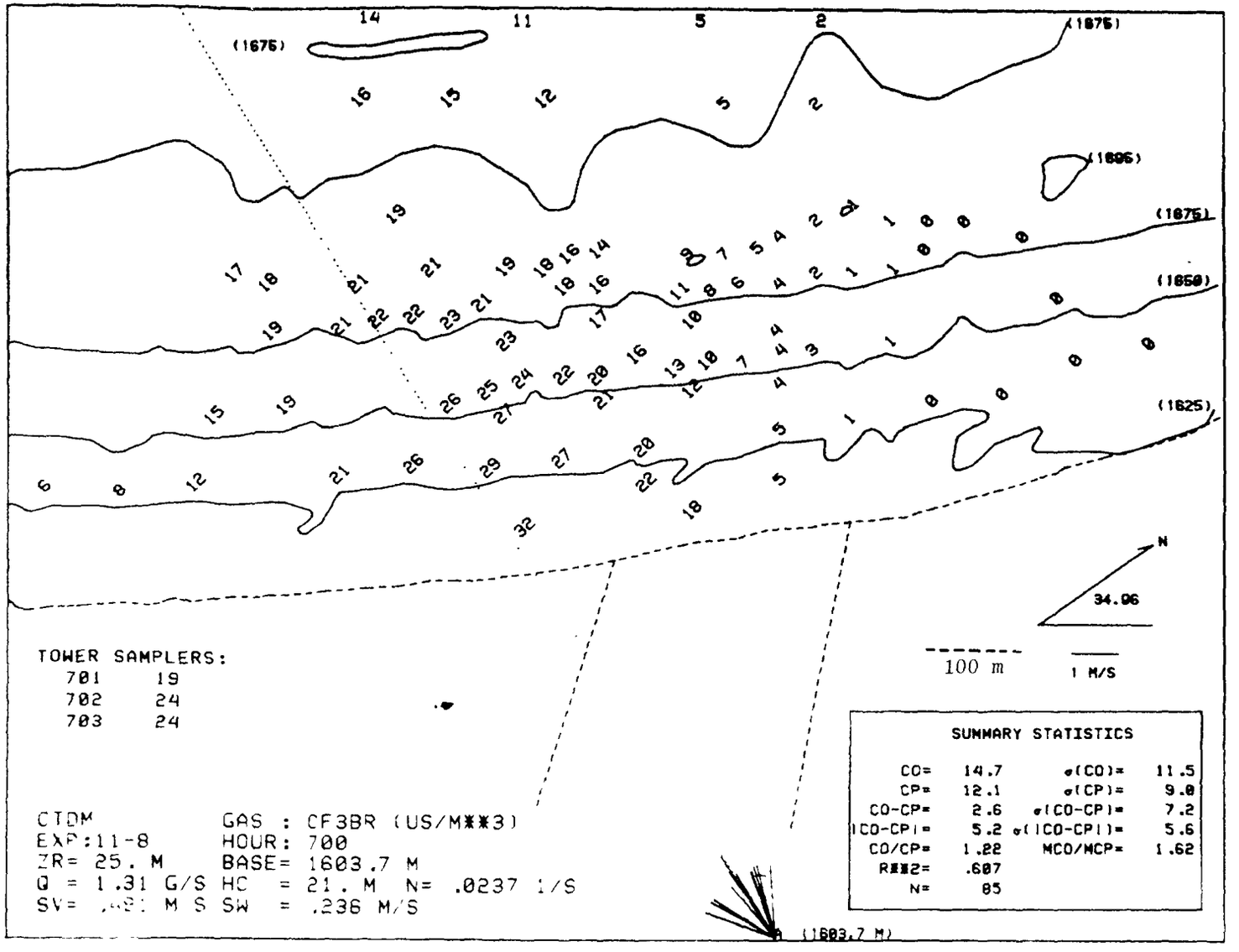

Figure 42. One-hour average predicted scaled concentrations ($\mu s/m^3$) from the HBR (Flat) model (Experiment 11, 10/23/82, 0600-0700 MDT).

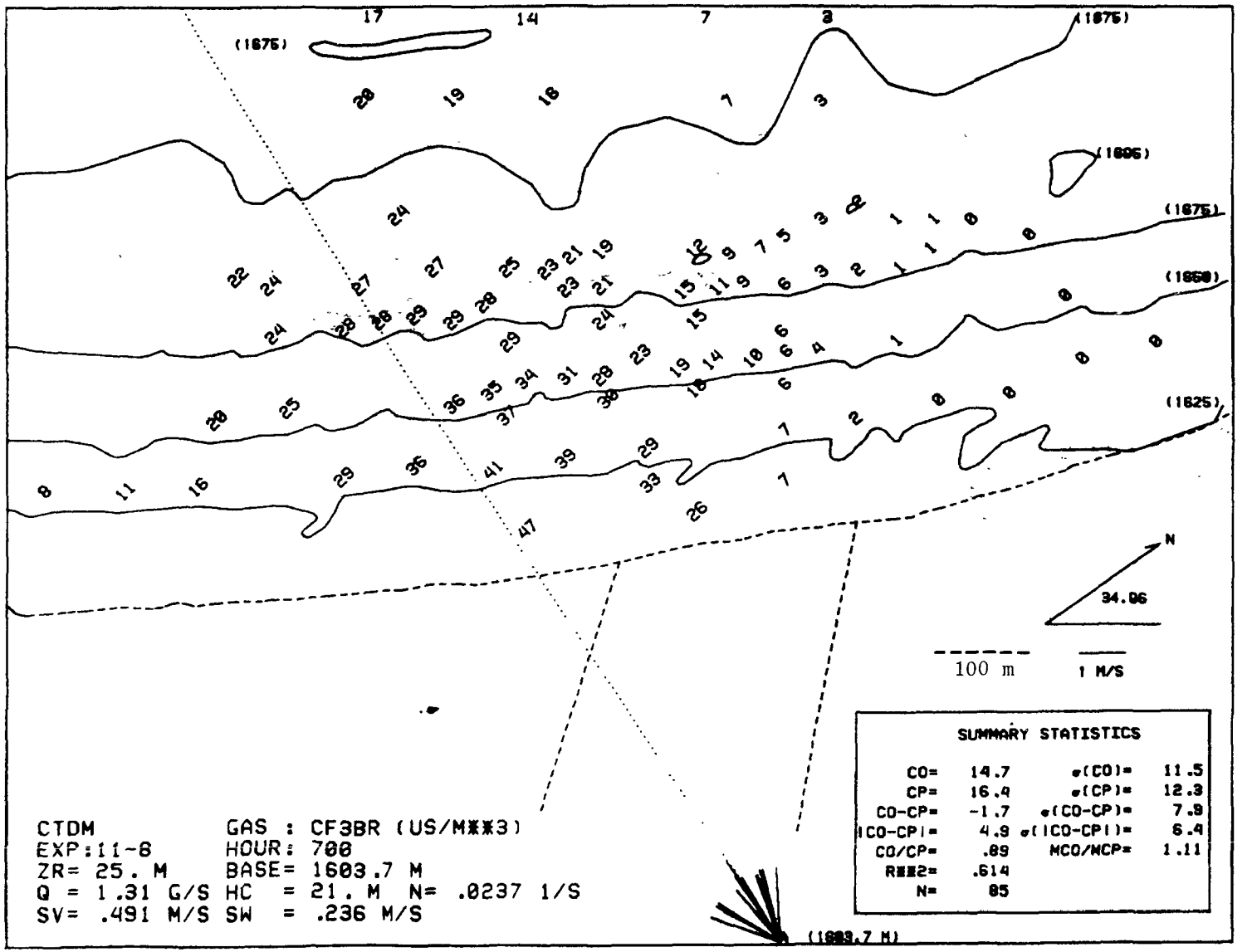

Figure 43. One-hour average predicted scaled concentrations ($\mu s/m^3$) from the HBR (terrain) model (Experiment 11, 10/23/82, 0600-0700 MDT).

Local terrain elevations near the release point are estimated to be 17.4 m above the base elevation of the hill coordinate system, so the net release height corresponds to the 37.4 m height level on the ridge.

Meteorological Information

Figure 44 contains plots of the 5-minute H_c and Fr values for this hour. H_c decreases from 23 m in the beginning of the hour to 5 m half-way through the hour, then rises to 34 m during the latter part of the hour before decreasing to 10 m at the end of the hour. The average of the 5-minute values over the hour is 18 m. Fr gradually rises from 1.3 to 1.8 during the hour. The one-hour average value of Fr above H_c is 1.5, which is an indication that stratification has only a weak effect on the flow over the top of the hill.

The hourly averaged vector wind direction and wind speed at the tracer release height are estimated to be 59.3° and 1.2 m/s, respectively. Figure 45 shows the trend in wind speeds and directions between 5 m and 40 m during the hour. There is little directional wind shear for approximately two-thirds of the hour, but there is up to 100° of directional wind shear during the remaining third of the hour. Large directional wind shear between 5m and 40 m occurs in combination with increasing H_c above 5 m. The flow direction is more variable well below H_c than above and this is apparently due to the blocking effect of the nearly two-dimensional ridge. The wind speed time series varies inversely with the H_c time series. As the wind speed increases during the first half of the hour, H_c decreases; conversely, as the wind speed decreases during the second half of the hour, H_c increases.

The vertical turbulent intensity values estimated at the tracer release height vary from 8 to 27% and the σ_w values estimated at the tracer release height vary from 0.18 to 0.29 m/s during the hour. The one-hour value for σ_w estimated at the release height is 0.22 m/s (i_z = 18%).

The vertical profiles of the hourly averaged wind direction, wind speed, and temperature are shown in Figure 46. For the layer 10 m above and below the release height, the wind speed shear is 0.5 m/s and the directional shear is 32°. The wind data from the propeller anemometers at 5 m and 40 m compare favorably with the sonic anemometer wind data at the same levels. The wind direction profile between 5 m and 40 m is approximately linear, so the MDA value for the wind direction should be reasonable. The hourly average of the 5-minute propeller wind direction and wind speed values measured at the tracer gas release height are 50° and 1.7 m/s which corroborate the one-hour average MDA values.

In summary, the plume was released above H_c during the first half of the hour and below H_c during the second half of the hour. The hourly average value for H_c is 18 m which is close to the release height. The flow is characterized by substantial wind

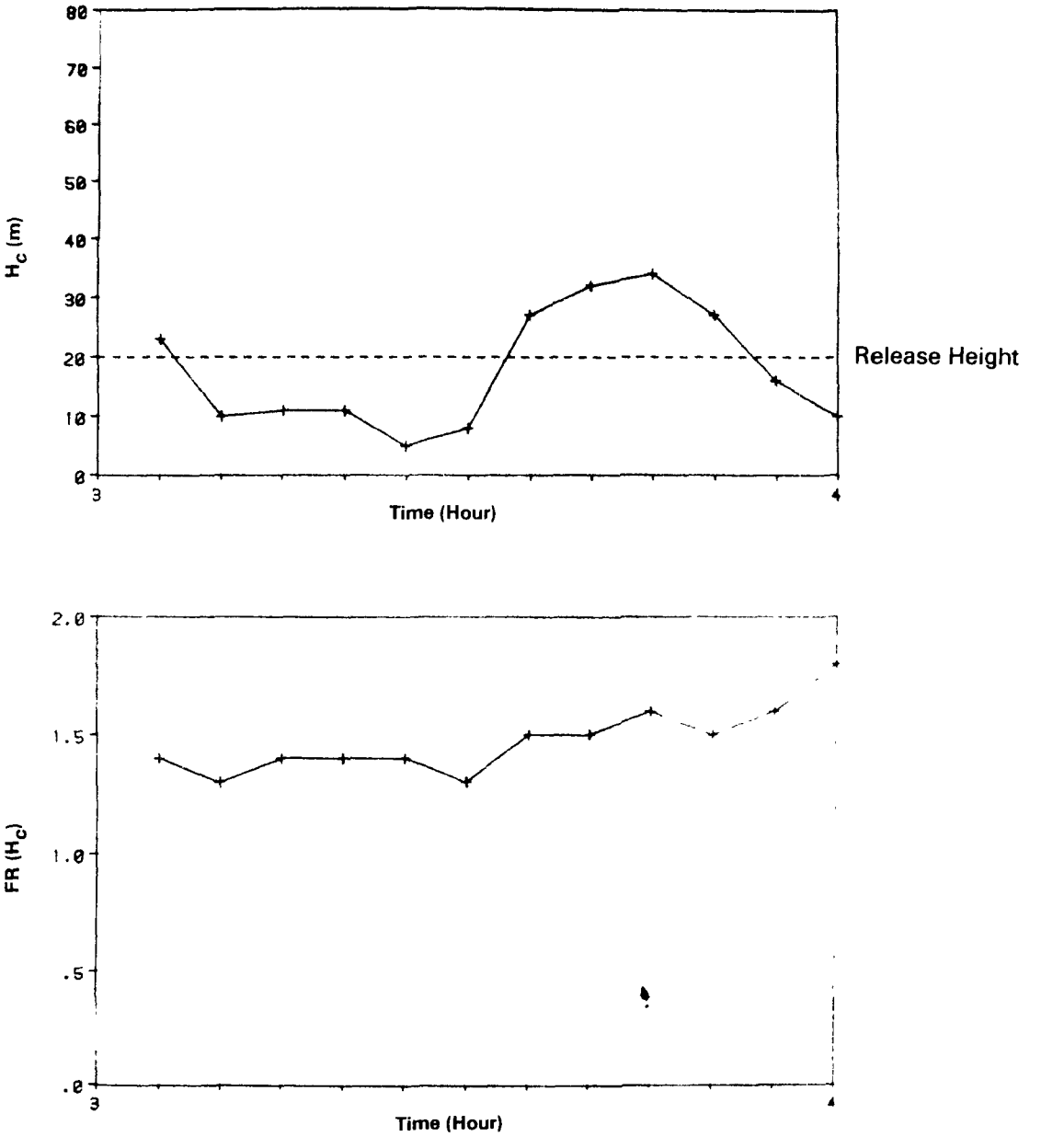

Figure 44. Time series of 5-minute calculated dividing streamline heights (H_c) and bulk hill Froude numbers above H_c ($F_r(H_c)$ (Experiment 14, 10/26/82, 0300-0400 MDT).

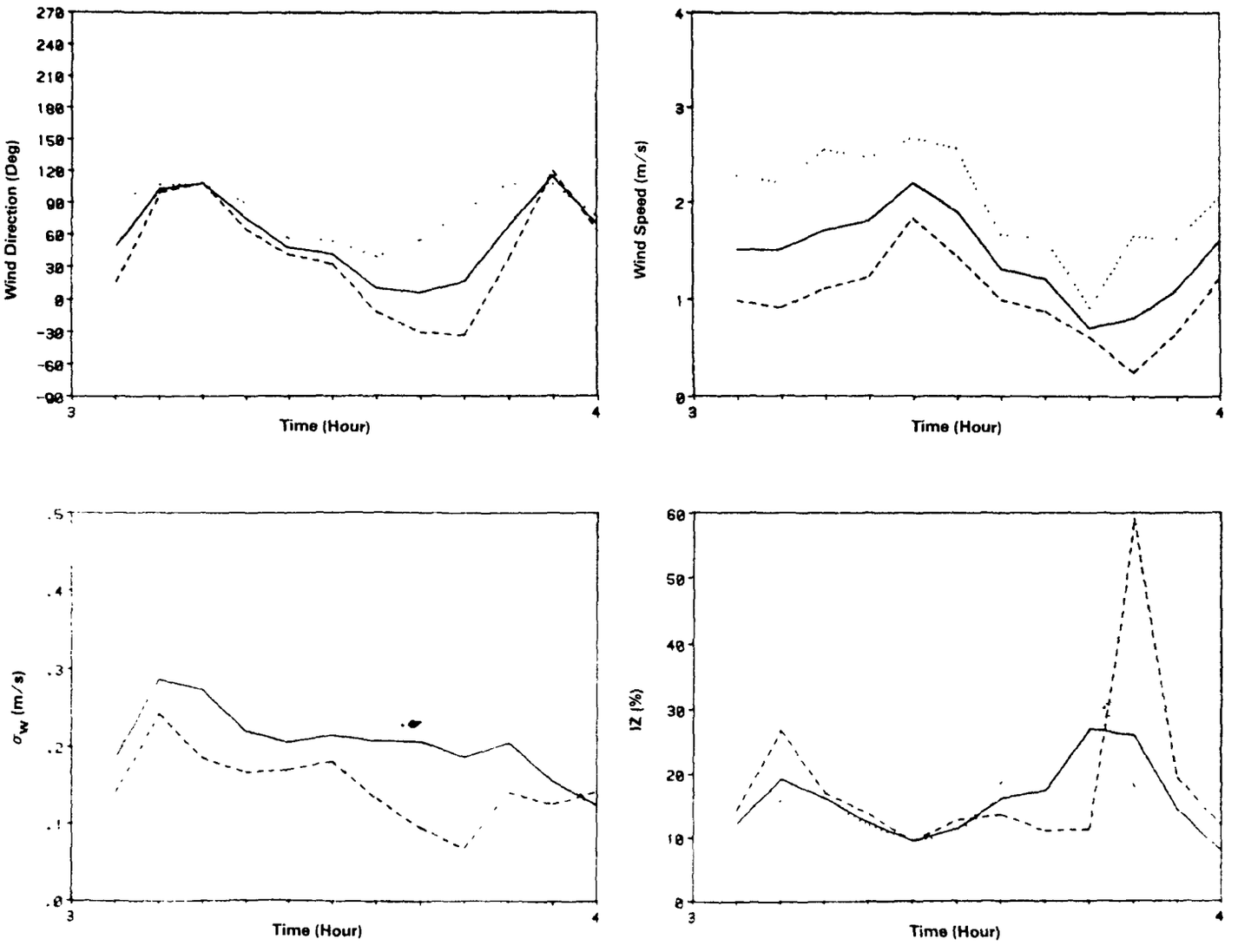

Figure 45. Time series of 5-minute sonic data from Tower A (Experiment 14, 10/26/82, 0300-0400 MDT). Values at CF_3Br release height (___) are interpolated from measurements at 5 (_ _ _) and 40 (...) m.

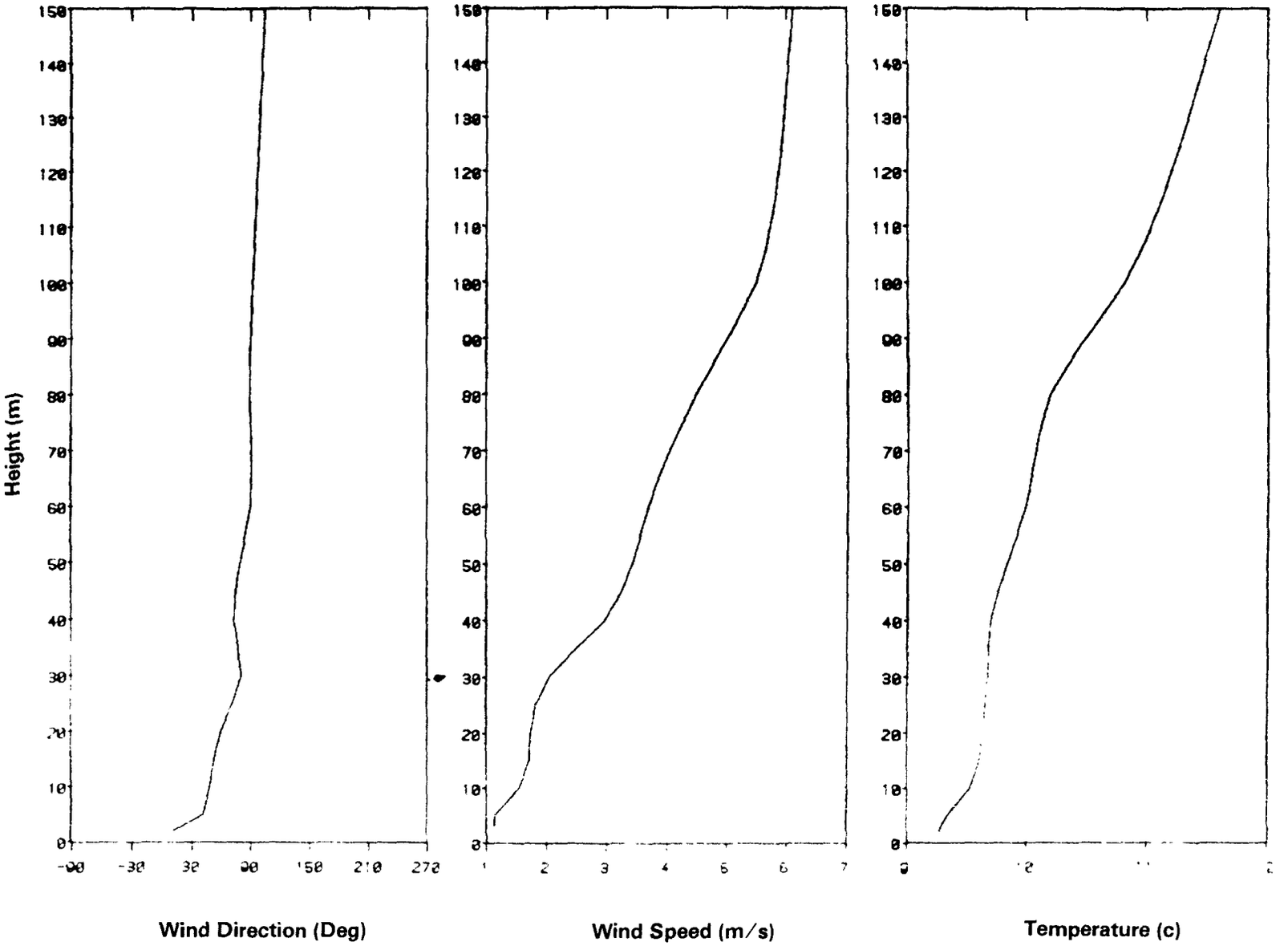

Figure 46. Vertical profiles of hourly meteorological data from Tower A (Experiment 14, 10/26/82, 0300-0400 MDT).

meander, wind speeds varying from 0.7 to 2.2 m/s, and a hill Froude number of 1.5.

CF_3Br Concentrations

The distribution of the observed hourly averaged CF_3Br concentrations over the surface of the ridge is shown in Figure 47. The concentration pattern is consistent with the variable wind directions observed during the hour. The largest concentrations are found near the bottom-half of the sampler array at an elevation that is less than H_c. The maximum observed concentration (117 $\mu s/m^3$) is found near the estimated hourly-averaged plume centerline. There is a sharp decrease of observed tracer concentrations above the H_c surface (1635 m).

Model Performance

Results from the HBR (Flat) model are displayed in Figure 48. Overall, the mean of the concentration estimates is in close agreement with the mean of the observed concentrations ($\overline{C}_o/\overline{C}_p$ = 1.04,) but the spatial correlation is poor (r^2 = 0.31). The maximum observed concentration (117 $\mu s/m^3$) is more than a factor of two greater than the maximum modeled concentration (52 $\mu s/m^3$).

Estimates from the HBR (Terrain) model, shown in Figure 49, are somewhat larger than the flat-terrain estimates. The maximum modeled concentration (79 $\mu s/m^3$) is less than the maximum observed concentration (117 $\mu s/m^3$), although on average, the model is over estimating ($\overline{C}_o/\overline{C}_p$ = 0.74). Because the distribution of the peak observed concentrations in space is so unlike that estimated by the model using one-hour average data, the temporal variations in the meteorology (particularly i_z) may be responsible for the poor model performance in estimating the peak concentrations.

4.4.3 Experiment 6, Experiment-Hour 9 (0700-0800)

Release Description

The CF_3Br tracer gas was released from position 203 for the entire hour at a release height 20 m above the ground. The release was continuous from the previous three hours. The CF_3Br release rate is calculated to be 1.30 g/s.

Local terrain elevations near the release point are estimated to be 17.4 m above the base elevation of the hill coordinate system, so the net release height corresponds to the 37.4 m height level on the ridge.

Meteorological Information

The plots of the 5-minute H_c and Fr values for this hour are displayed in Figure 50. The 5-minute values of H_c are all greater than the release height, except for the second 5-minute period when H_c drops to 14 m. This sudden drop in H_c corresponds to a 1.0 m/s

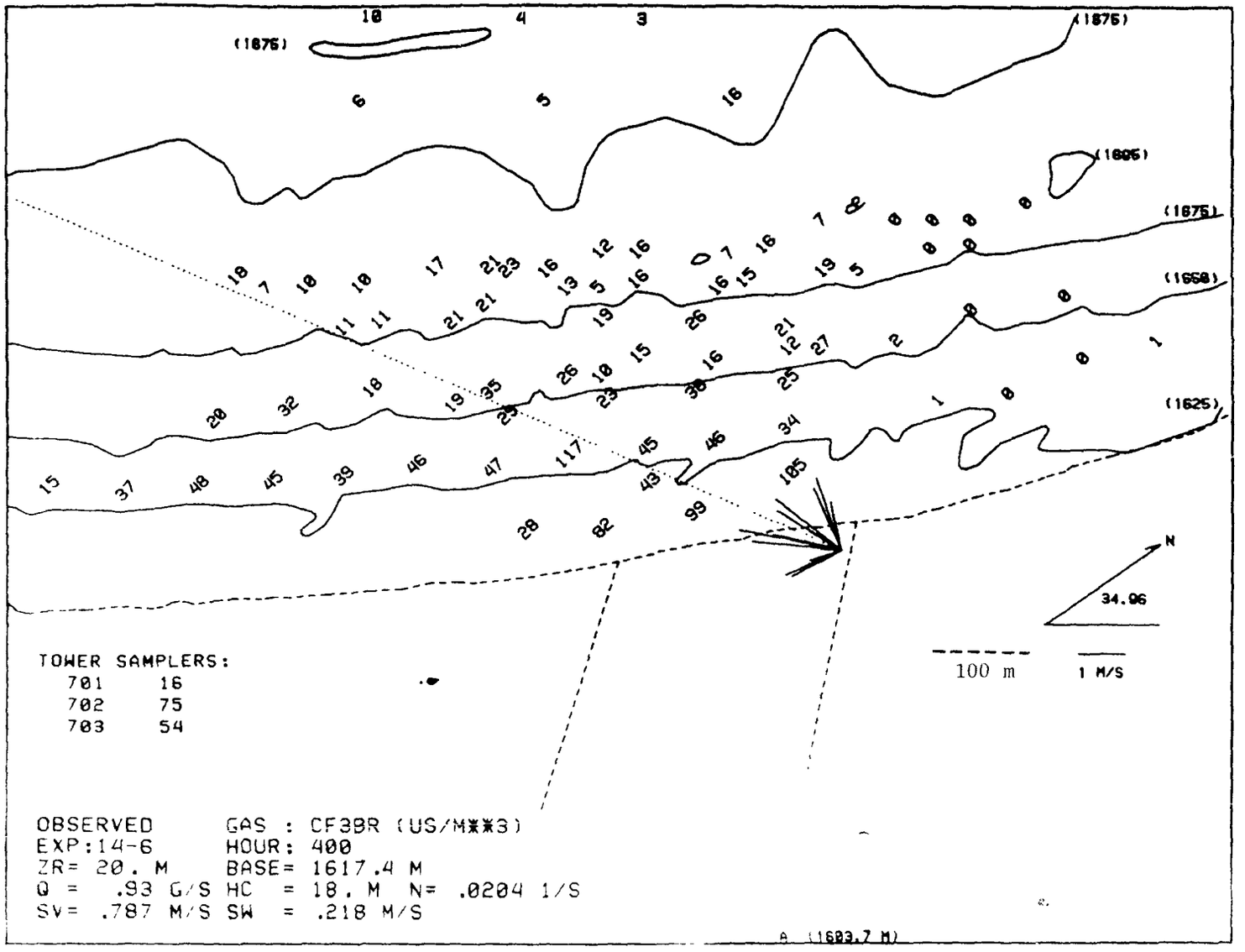

Figure 47. One-hour average observed CF_3Br concentrations scaled by emission rate ($\mu s/m^3$) (Experiment 14, 10/26/82, 0300-0400 MDT).

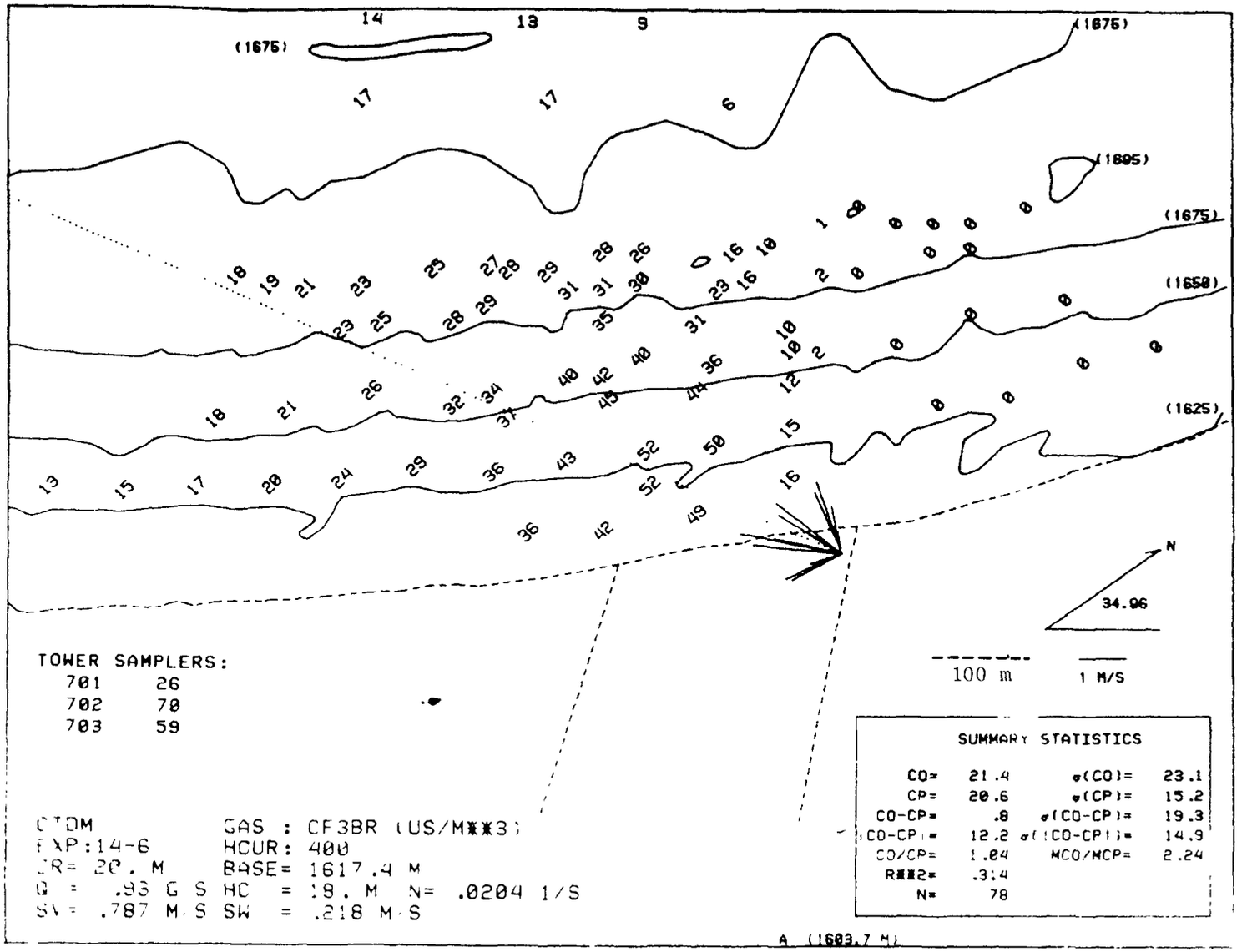

Figure 48. One-hour average predicted scaled concentrations ($\mu s/m^3$) from the HBR (Flat) model (Experiment 14, 10/26/82, 0300-0400 MDT).

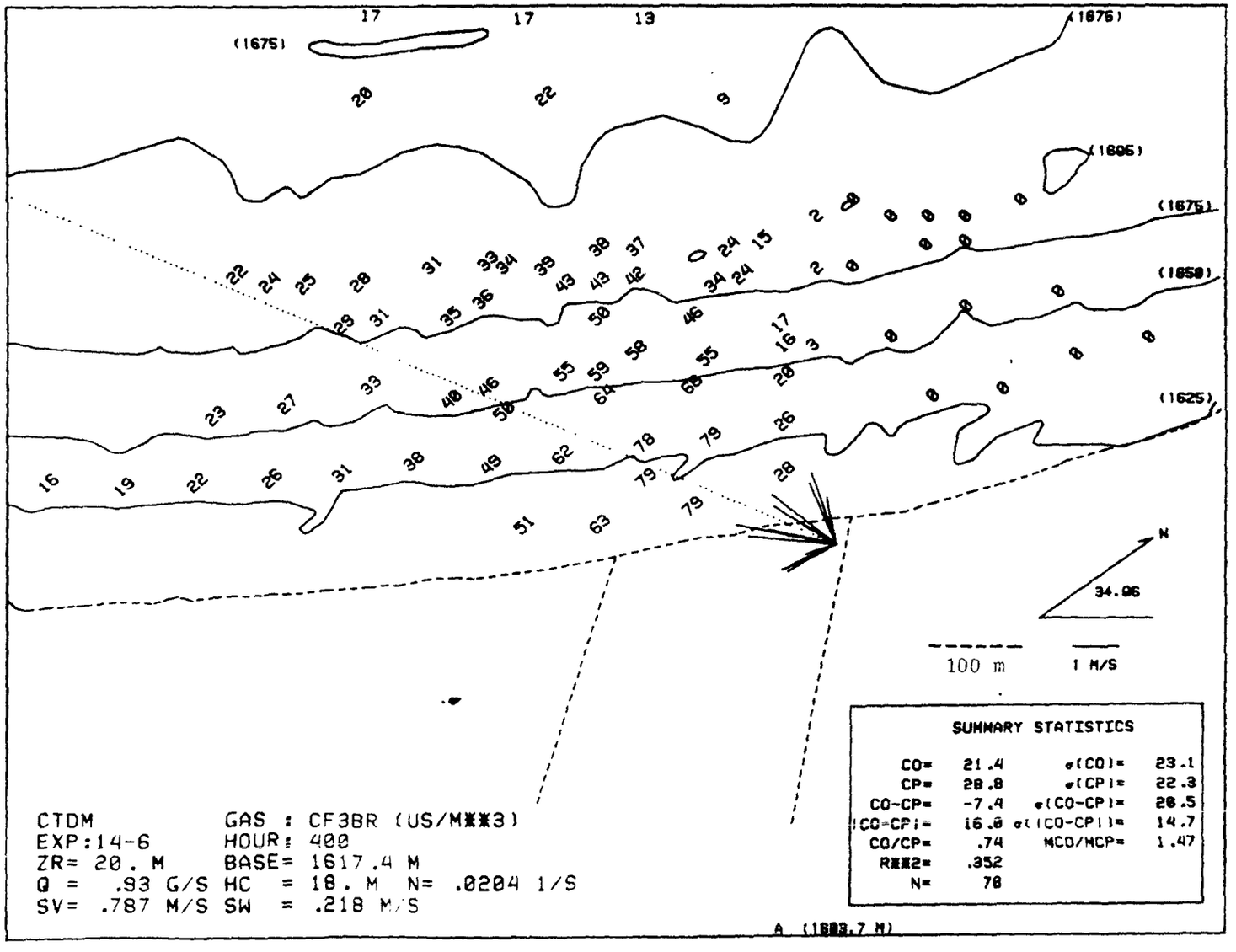

Figure 49. One-hour average predicted scaled concentrations ($\mu s/m^3$) from the HBR (terrain) model (Experiment 14, 10/26/82, 0300-0400 MDT).

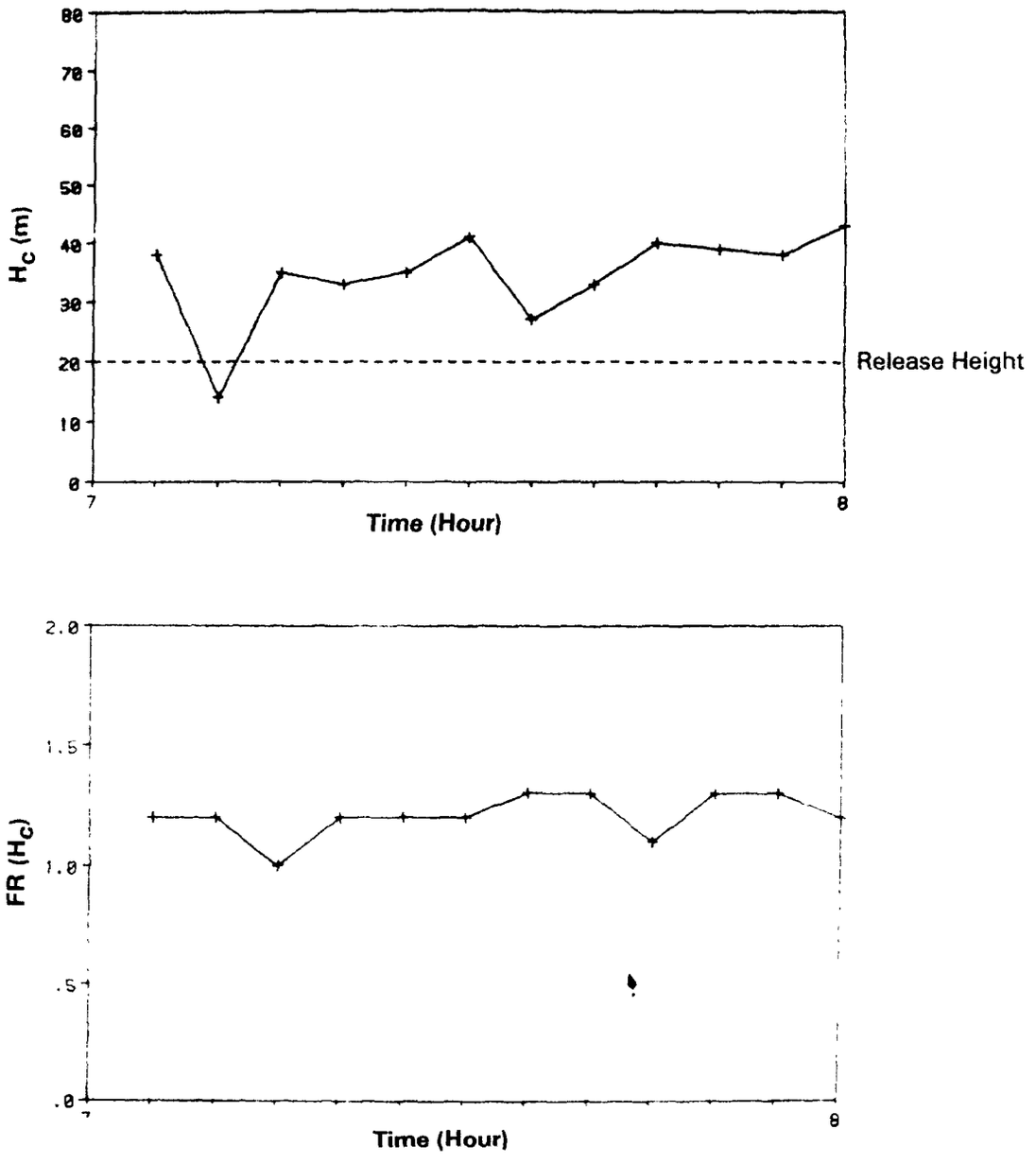

Figure 50. Time series of 5-minute calculated dividing-streamline heights (H_c) and bulk hill Froude numbers above H_c ($F_r(H_c)$) (Experiment 6, 10/31/82, 0700-0800 MDT).

increase in Tower-A propeller wind speeds. This increase in speed is not corroborated by the sonic anemometer wind data. The average of the 5-minute H_c values over the hour is 35 m. Because H_c is less than the release height for only one 5-minute period and this value is suspect, this hour is considered representative of flow below H_c. Fr remains steady during the hour varying from 1.0 to 1.3, with the one-hour value of Fr above H_c being 1.2.

The hourly averaged wind speed and direction estimated at the tracer release height are 1.0 m/s and 67.1°, respectively. Figure 51 shows the trend in wind speeds and directions between 5 m and 40 m during the hour. The linearly interpolated values estimated at the tracer release height are also shown. The 5-m wind directions vary from 1 to 51° during the hour and the 40-m wind directions vary from 72 to 164°. The wind speed measured at 5 m oscillates from a high of 1.5 m/s during the beginning of the hour to a low of 0.6 m/s in the middle of the hour, then increases to 1.2 m/s towards the end of the hour. The wind speed measured at 40 m steadily decreases from 1.6 to 0.6 m/s during the hour, with the exception of a 1.7 m/s peak measured during the seventh 5-minute period.

The trend in i_z and σ_w values during the hour are shown in Figure 51. The values of i_z and σ_w estimated at the tracer release height vary from 7 to 10% and 0.06 to 0.13 m/s, respectively. The one-hour value for σ_w estimated at the tracer release height is 0.10 m/s (i_z = 10%).

The vertical profiles of the hourly averaged wind direction, wind speed, and temperature are shown in Figure 52. A large amount of directional wind shear is found near the vicinity of the tracer release height. This is corroborated by the wind directions obtained from the sonic anemometers on Tower A. The 5 m and 40 m propeller wind data are consistent with the sonic wind data, although the profiles of the propeller anemometer data are not linear between 5 and 40 m. The hourly average of the 5-minute wind directions and wind speeds from the propeller anemometer measured at the tracer gas release height are 65° and 1.3 m/s. These values are in close agreement with the hourly averaged MDA values. Therefore, even though the speed and direction profiles are nonlinear, the error introduced by assuming linearity is apparently small at the release height.

In summary, the plume was released below H_c into a flow characterized by significant directional wind shear, 0.8 to 1.5 m/s wind speeds, and a hill Froude number above H_c equal to 1.2. The largest observed concentrations are expected to be found below H_c.

CF_3Br Concentrations

The distribution of the observed hourly averaged CF_3Br concentrations over the surface of the ridge is shown in Figure 53. The largest concentrations are found near the bottom half of the sampler array at an elevation that is less than H_c. The maximum observed concentration (445 $\mu s/m^3$) is found at sampler 109 near the estimated hourly-averaged plume centerline at 10 m above the

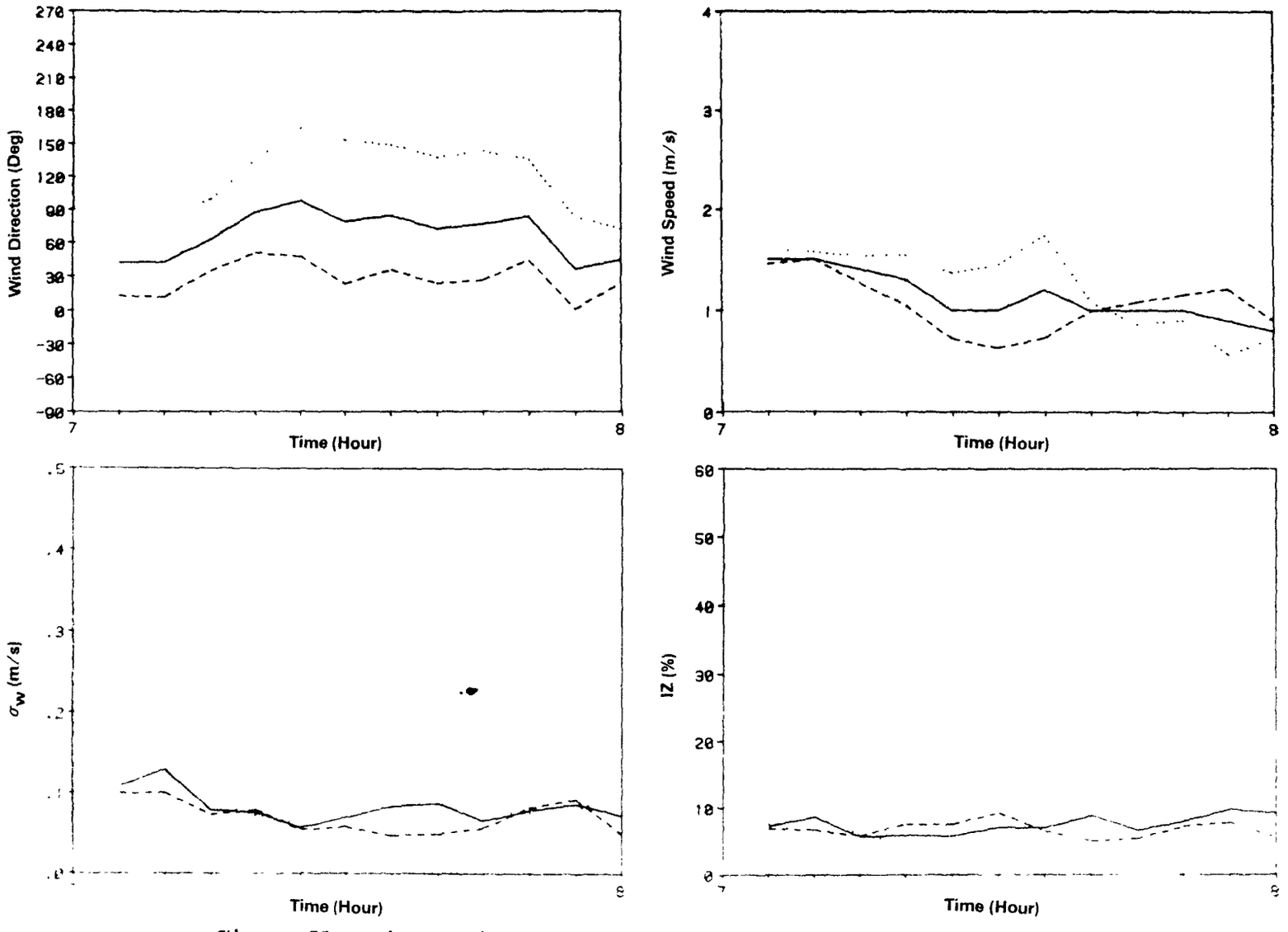

Figure 51. Time series of 5-minute sonic data from Tower A (Experiment 6, 10/13/82, 0700-0800 MDT). Values at CF_3Br release height (___) are interpolated from measurements at 5 (_ _ _) and 40 (...) m.

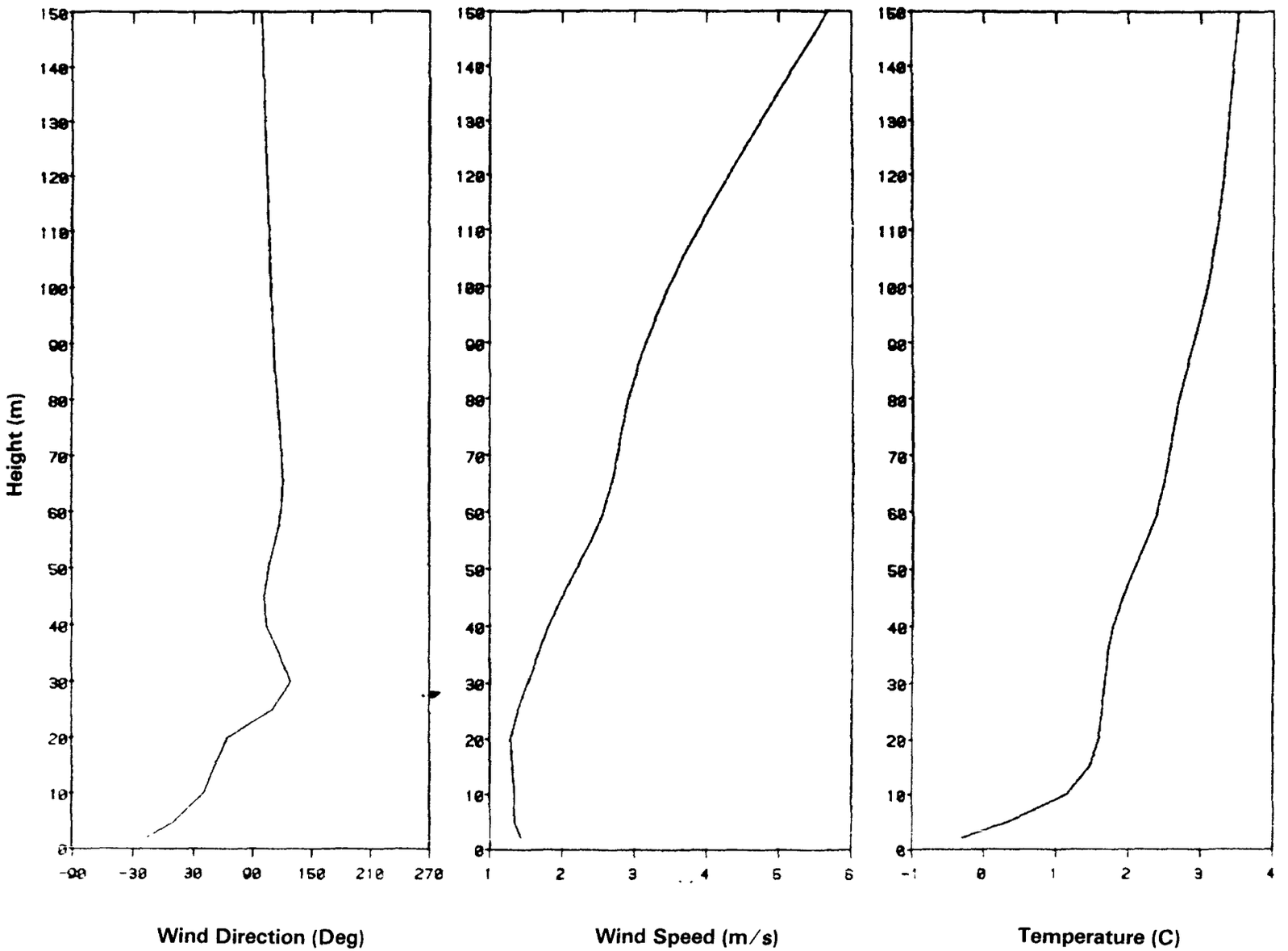

Figure 52. Vertical profiles of hourly meteorological data from Tower A (Experiment 6, 10/13/82, 0700-0800 MDT).

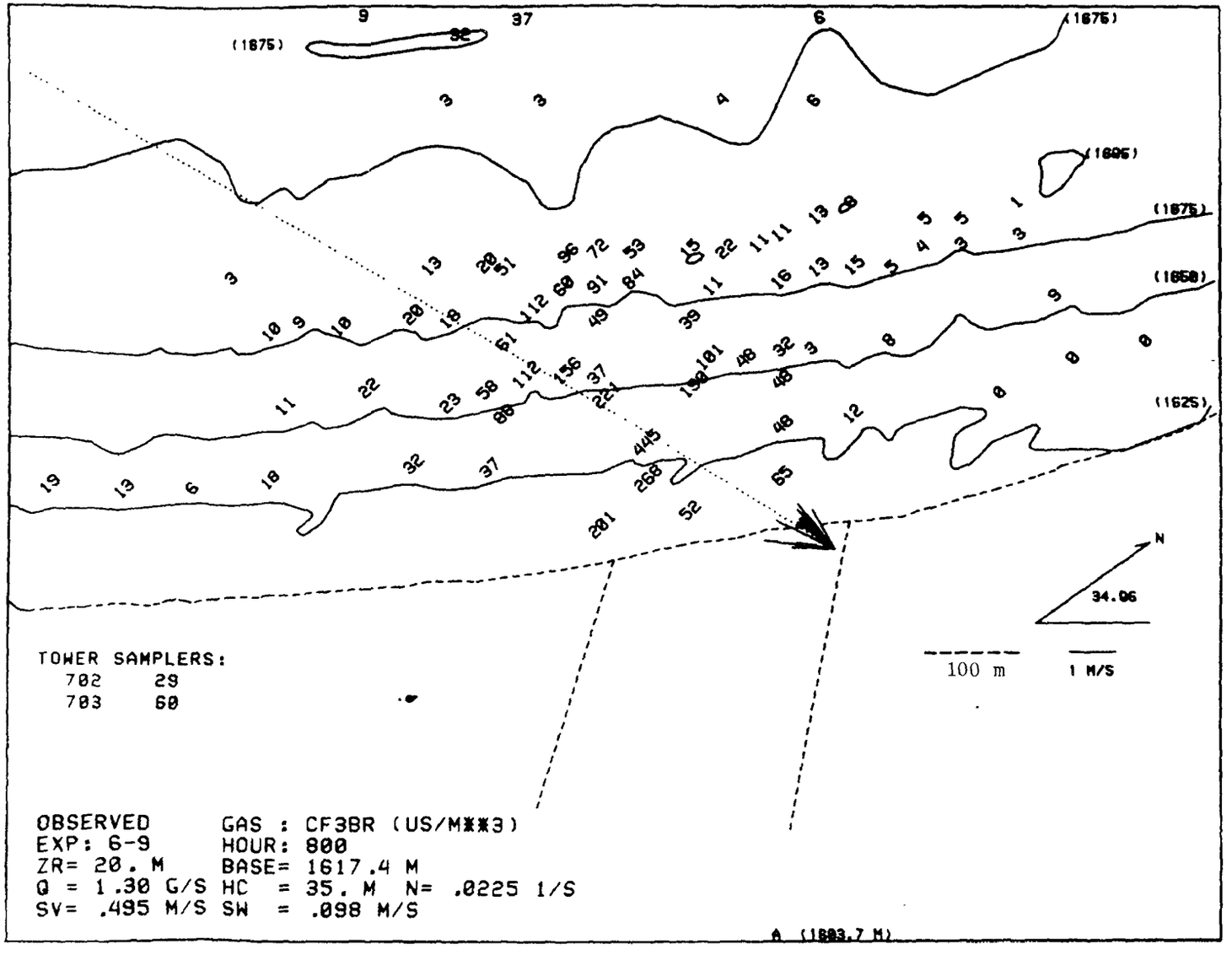

Figure 53. One-hour average observed CF_3Br concentrations scaled by emission rate ($\mu s/m^3$) (Experiment 6, 10/13/82, 0700-0800 MDT).

release height. This is the largest observed concentration found in the CF_3Br modeling data set. Also, this sampler is collocated with sampler 809 where the observed concentration is 425 $\mu s/m^3$. A sharp decrease of observed tracer concentrations is found above the mean H_c surface (1652 m).

Model Performance

The hourly averaged scaled concentrations estimated from the HBR (Flat) model are shown in Figure 54. The model grossly underestimates the mean of the observed concentrations by more than a factor of 4 with $\overline{C_o}/\overline{C_p}$ = 4.71 and r^2 = .004. The maximum observed concentration (445 $\mu s/m^3$) is found towards the bottom-half of the ridge at an elevation of 26 m; whereas, the maximum estimated concentration (24 $\mu s/m^3$) is found towards the top of the ridge at 75 m.

Estimates from the HBR (Terrain) model, shown in Figure 55, are considerably larger than the flat-terrain estimates with $\overline{C_o}/\overline{C_p}$ = 1.02. However, the maximum estimated concentration (105 $\mu s/m^3$) found towards the center of the sampler array at 56 m is still much less than the observed maximum concentration, and occurs at a location too far up on the hill. The model performance apparently suffers during this hour because the plume seems to have "dropped" in height over a short distance from the release and HBR (Terrain) does not account for this.

4.4.4 Experiment 8, Experiment-Hour 7 (0500 - 0600 MDT)

Release Description

The CF_3Br tracer gas was released from position 215 at 25 m above the ground for the entire hour. The CF_3Br release rate is computed to be 0.97 g/s.

Local terrain elevations near the release point are estimated to be 12.9 m above the base elevation of the hill coordinate system, so the net release height corresponds to the 37.9 m height level on the ridge.

Meteorological Information

Figure 56 contains plots of the 5-minute H_c and Fr values for this hour. The tracer gas release height is less than H_c for the first eight 5-minute periods of the hour. The average of the 5-minute values over the hour is 35 m. Fr is steady during the first eight 5-minute periods of the hour ranging from 0.8 to 1.0. For the last third of the hour, Fr rises to 1.5. The one-hour average value of Fr above H_c is 1.0.

Time series plots of the sonic anemometer data from Tower A for this experiment-hour are presented in Figure 57. Large directional wind shear is found between 5 m and 40 m until the tenth 5-minute period when the 5-m wind direction shifts from 56 to 152°. There is

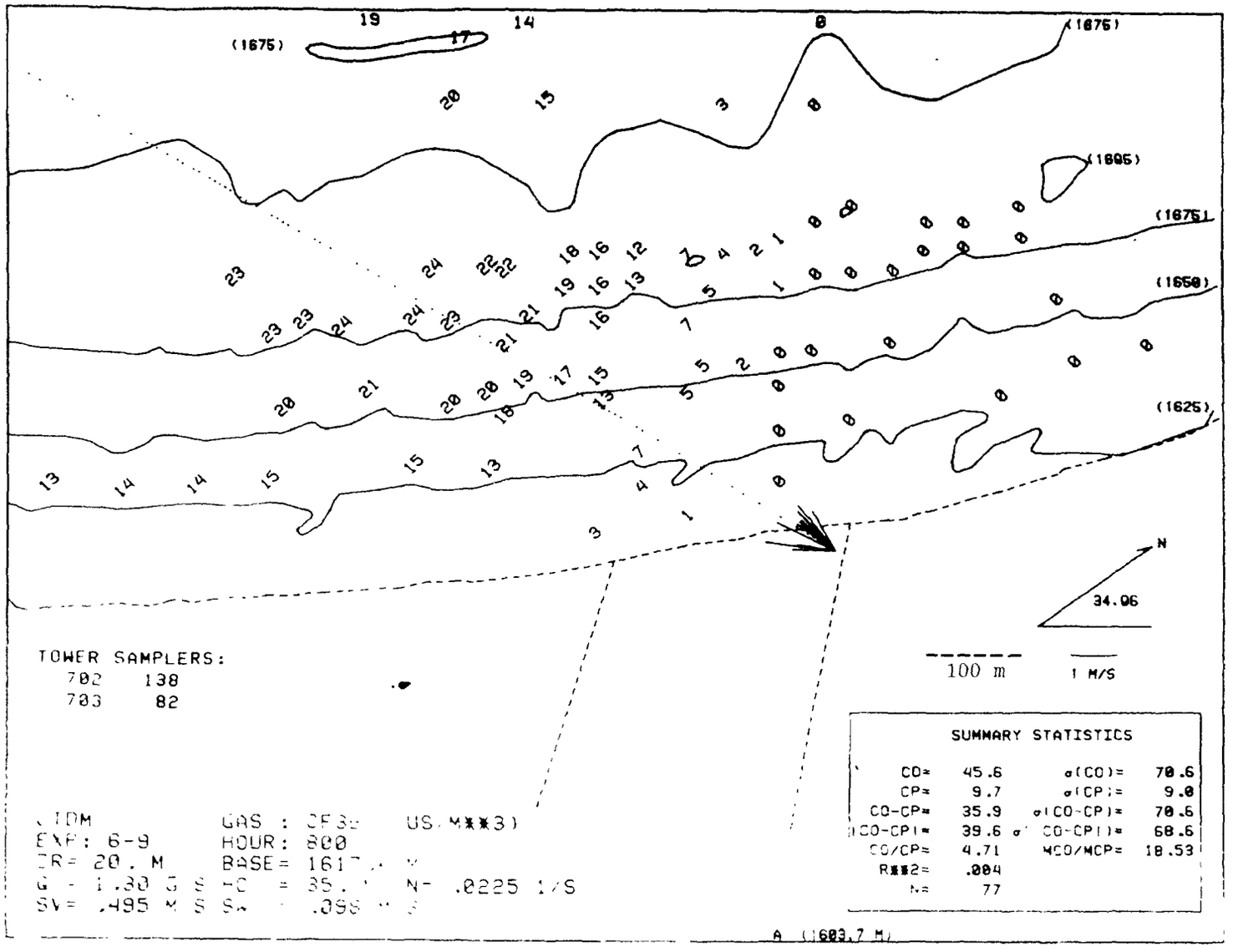

Figure 54. One-hour average predicted scaled concentrations ($\mu s/m^3$) from the HBR (Flat) model (Experiment 6, 10/13/82, 0700-0800 MDT).

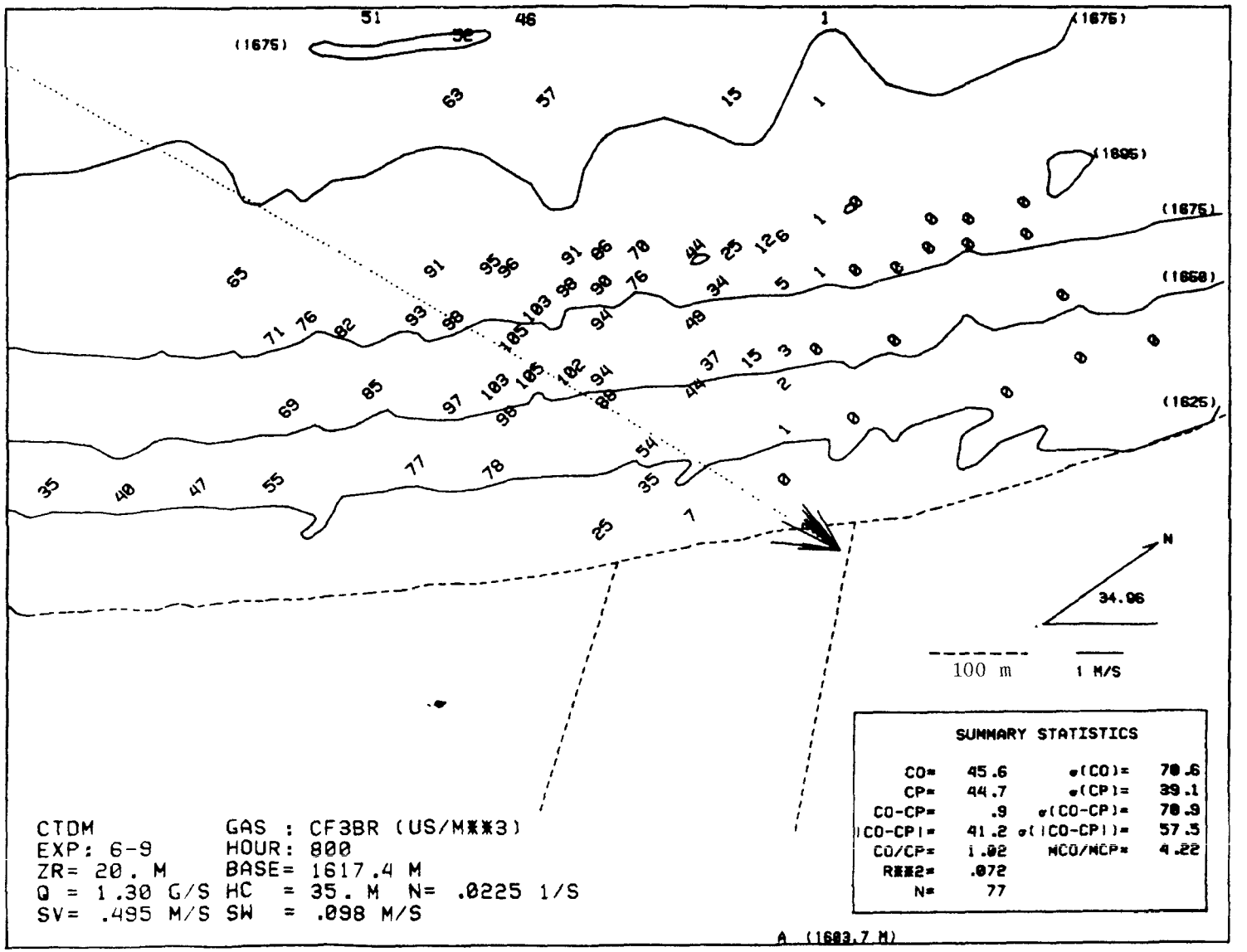

Figure 55. One-hour average predicted scaled concentrations ($\mu s/m^3$) from the HBR (terrain) model (Experiment 6, 10/13/82, 0700-0800 MDT).

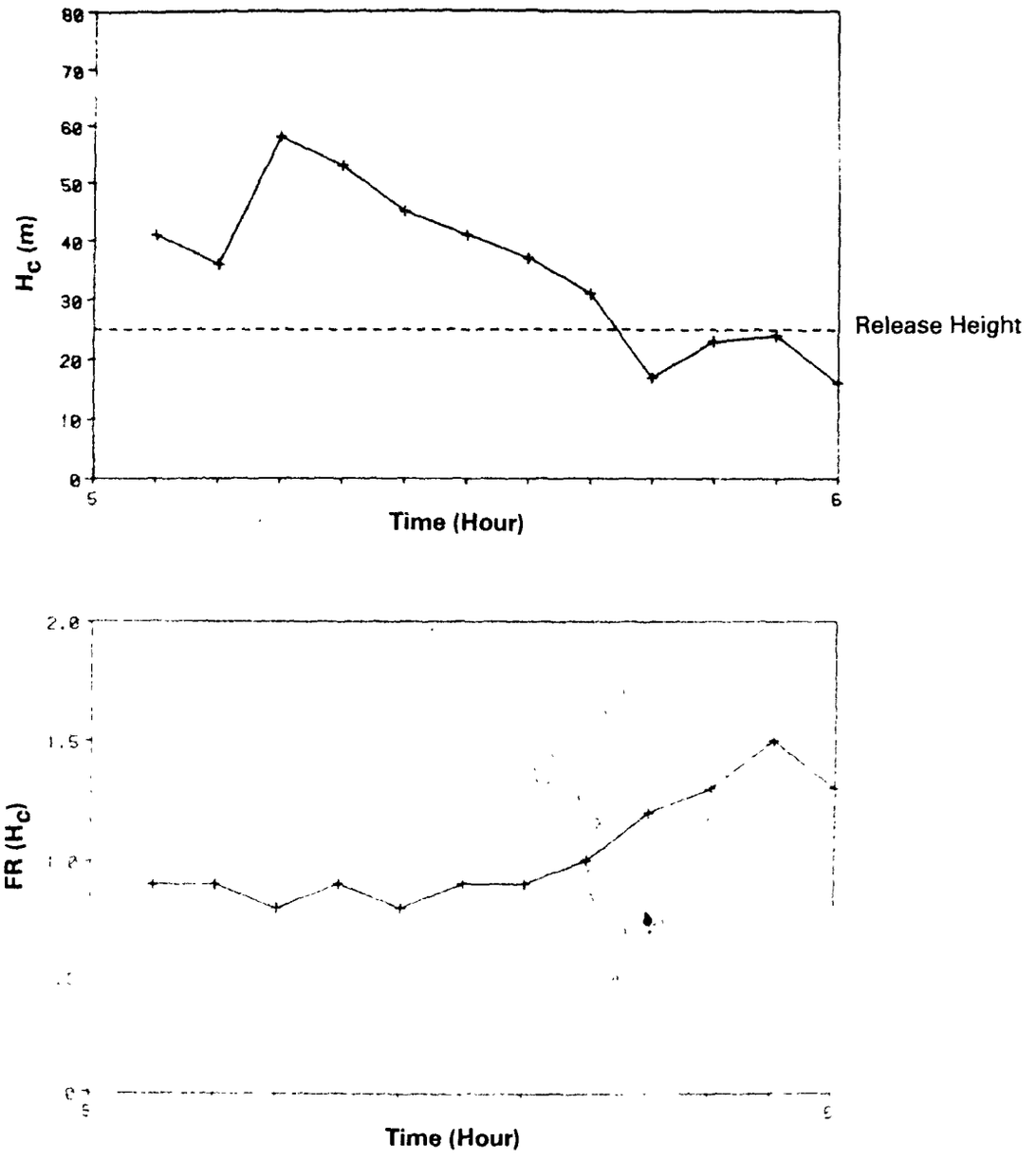

Figure 56. Time series of 5-minute calculated dividing-streamline heights (H_c) and bulk hill Froude numbers above H_c ($F_r(H)$) (Experiment 8, 10/15/82, 0500-0600 MDT).

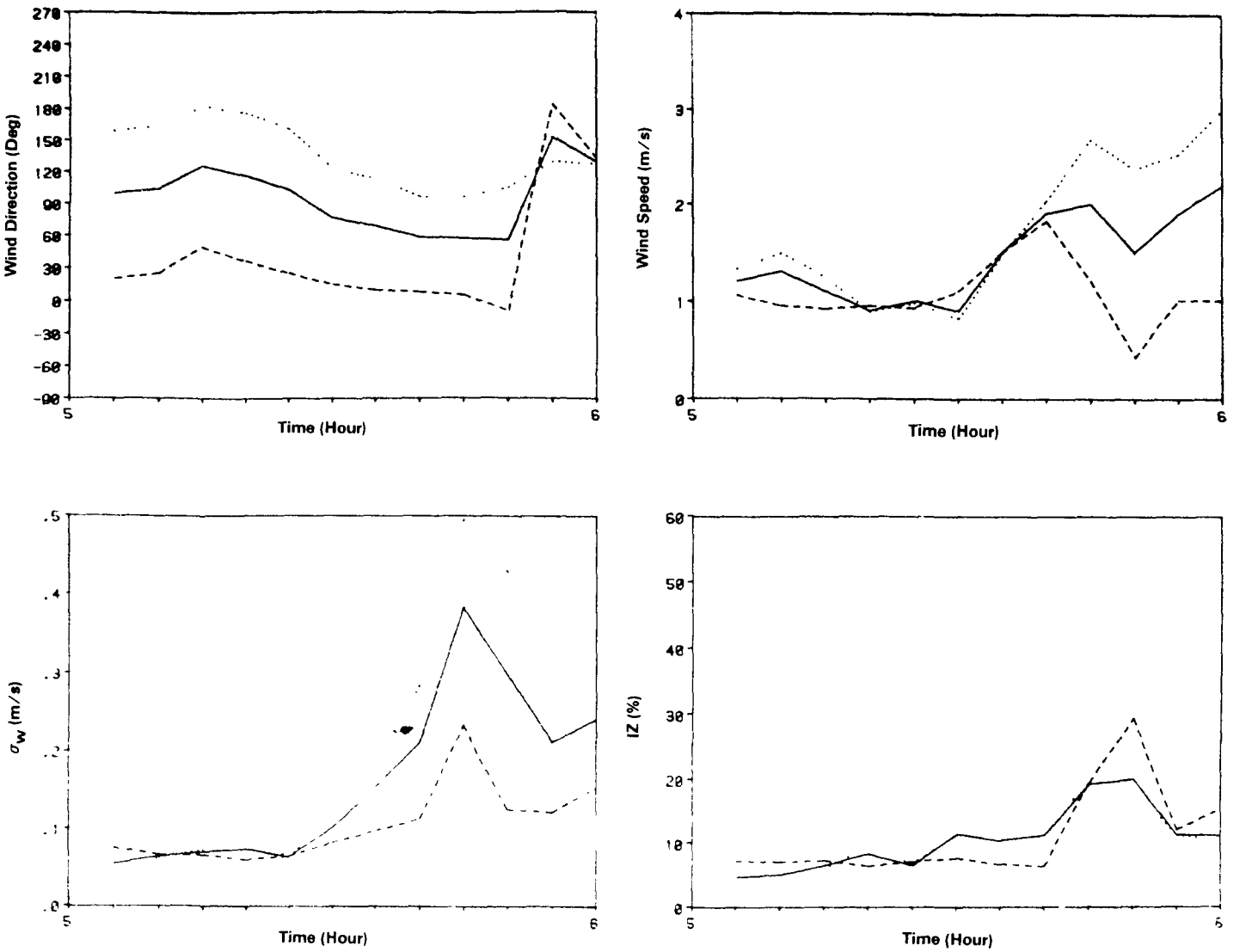

Figure 57. Time series of 5-minute sonic data from Tower A (Experiment 8, 10/15/82, 0500-0600 MDT). Values at CF_3Br release height (___) are interpolated from measurements at 5 (_ _ _) and 40 (...) m.

little wind speed shear for the first eight 5-minute periods of the hour. During the final third of the hour, the wind speeds between 5 m and 40 m differ by as much as 2.0 m/s. The hourly averaged vector wind direction and wind speed estimated at the tracer release height are 83.7° and 1.2 m/s, respectively.

The i_z and σ_w values are fairly steady and low for the first half of the hour with i_z values less than 10% and σ_w values less than 0.1 m/s. During the second half of the hour, there is a sharp increase in measured turbulence. The estimated value of σ_w at the release height peaks at 0.4 m/s and i_z peaks at 30%. The one hour value of σ_w estimated at the tracer release height is 0.21 m/s (i_z = 17.5%).

The vertical profiles of the hourly averaged wind direction, wind speed, and temperature are shown in Figure 58. There is approximately 60° of directional shear in the vicinity ($\pm$10 m) of the tracer release height. The wind speed decreases for the 10-m layer below the release height. The wind data from the propeller anemometers at 5 m and 40 m are in fair agreement with the sonic anemometer data at the same levels. However, the vertical profiles of the propeller wind data between 5 m and 40 m are not linear. The hourly average of the 5-minute propeller wind direction and wind speed values interpolated to the tracer gas release height are 130° and 1.3 m/s, respectively. The wind speed value is in close agreement with the hourly averaged MDA value. However, the wind directions differ by 46° which indicates that the linear interpolation is questionable. In this case, the 40 m sonic wind direction (128°) is better than the interpolated value.

In summary, the plume was released on average below H_c into a flow characterized by significant directional wind shear, 0.9 to 2.2 m/s wind speeds, and a hill Froude number above H_c equal to unity.

CF_3Br Concentrations

The distribution of the observed hourly averaged CF_3Br concentrations over the surface of the ridge is shown in Figure 59. The largest concentrations are found towards the middle of the sampler array at an elevation that is near or less than the hourly averaged value for H_c. The maximum observed concentration (72 $\mu s/m^3$) is found away from the estimated hourly-averaged plume centerline at sampler 205. This large concentration may be associated with the last third of the hour when H_c was near the tracer release height and the wind direction was towards this sampler. The second highest observed concentration (69 $\mu s/m^3$) is located near the estimated hourly averaged plume centerline at an elevation that is less than H_c. It is most likely that the estimated hourly-averaged plume centerline is incorrect. The concentration pattern is more representative of flow from 130°, as indicated by the propeller anemometer data.

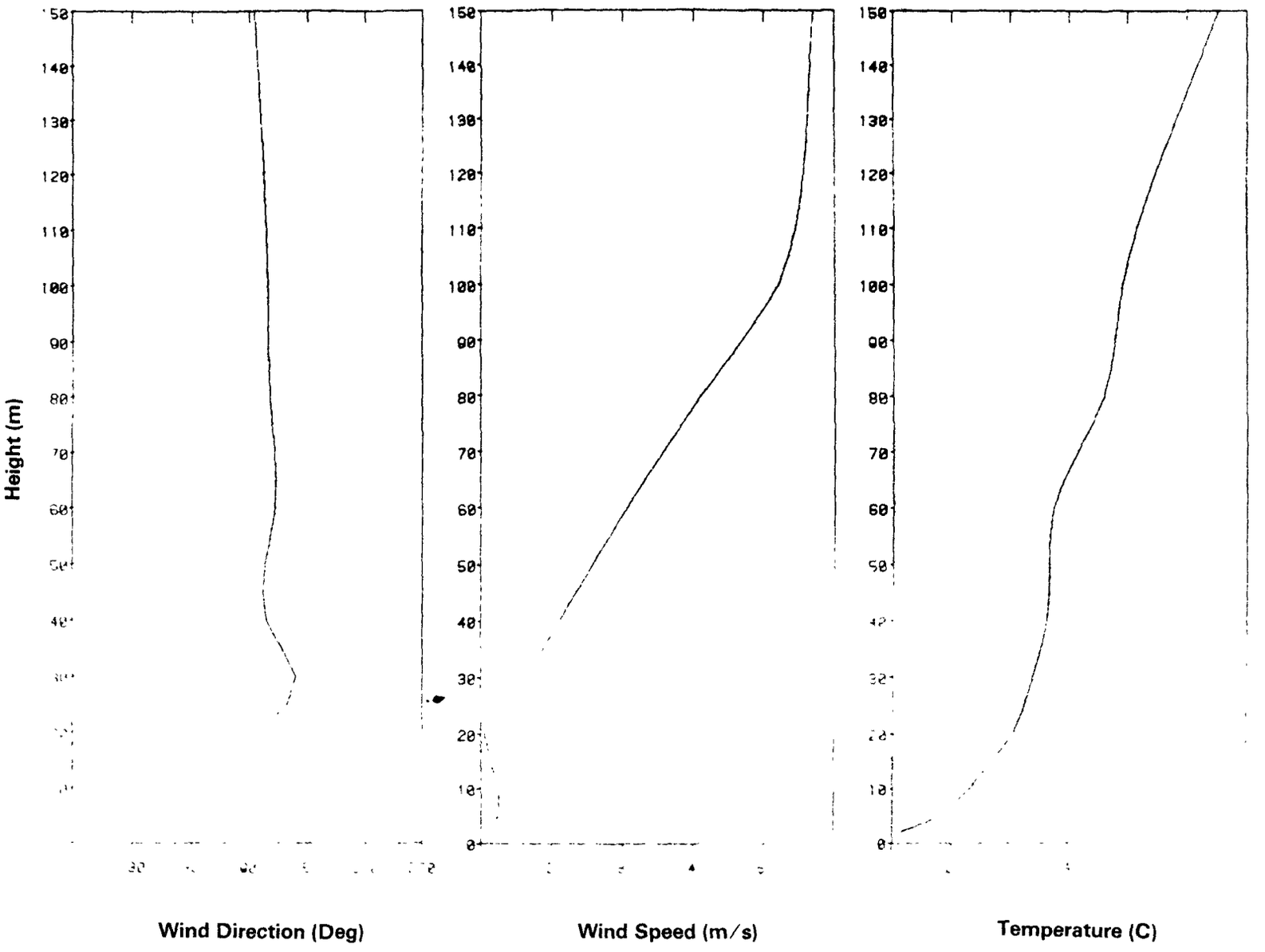

Figure 58. Vertical profiles of hourly meteorological data from Tower A (Experiment 8, 10/15/82, 0500-0600 MDT).

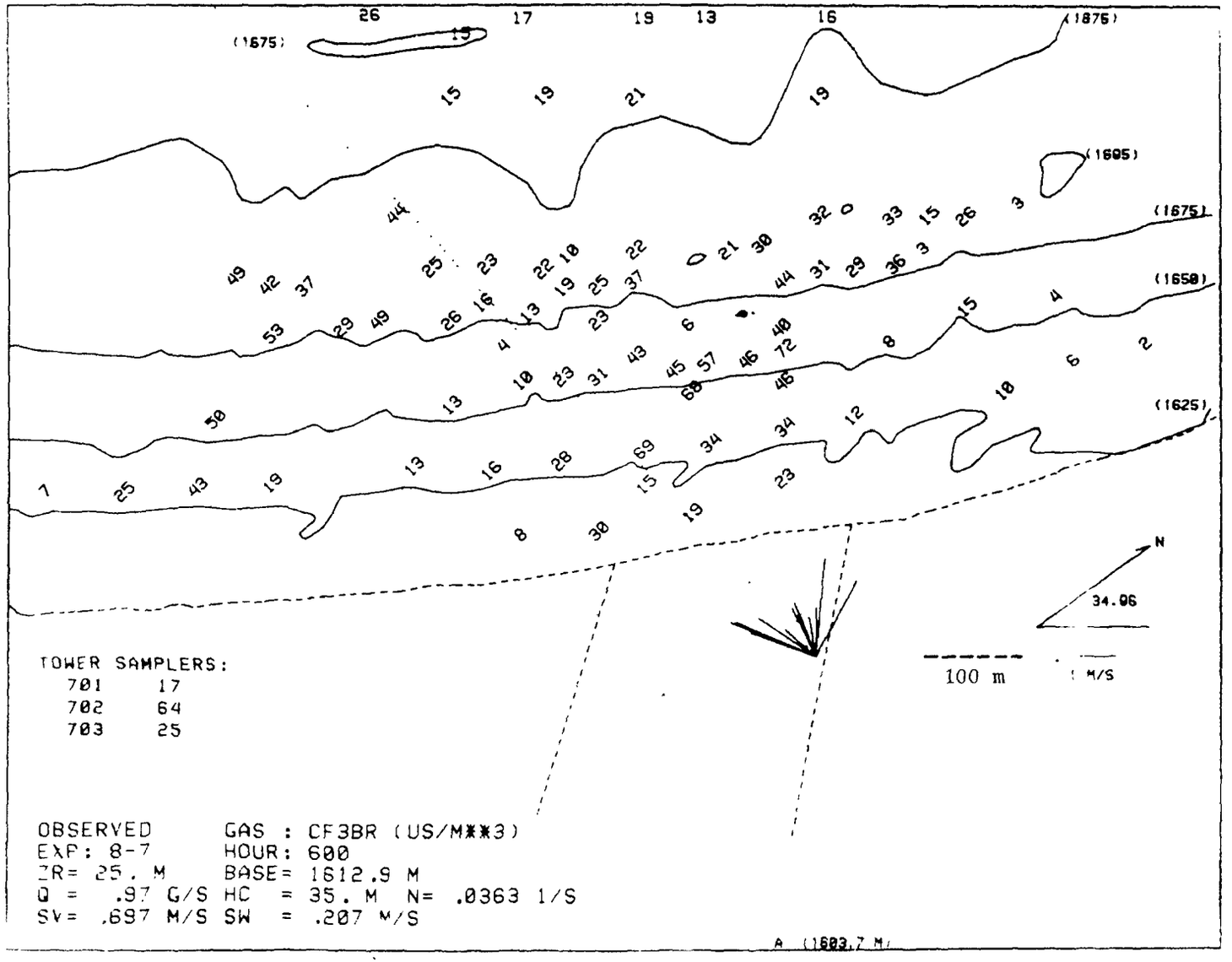

Figure 59. One-hour average observed CF_3Br concentrations scaled by the emission rate ($\mu s/m^3$) (Experiment 8, 10/15/82, 0500-0600 MDT).

Model Performance

Scaled concentrations from the HBR (Flat) model, shown in Figure 60, are much less than the observed concentrations with C_o/C_p = 2.17 and r^2 = 0.05. The largest estimated concentrations (20 $\mu s/m^3$) are found near the crest of the ridge at a total of nine sampler locations.

Scaled concentrations estimated from the HBR (Terrain) model are shown in Figure 61. On average, the model does well with $\overline{C_o}/\overline{C_p}$ = 0.88 and MCO/MCP = 1.29, although the correlation is low (r^2 = .08). The observed concentration pattern exhibits a bi-modal tendency which mirrors the wind direction pattern. This appears to contribute to the low correlation with the concentration pattern estimated with a Gaussian distribution about the mean wind direction.

4.4.5 Summary

The flat terrain model and the empirical HBR model have been tested against CF_3Br observations for four case-study hours. These case study hours represent three classes of meteorology ($z_r < H_c$, $z_r \simeq H_c$, $z_r > H_c$) and include the highest concentrations observed within the three classes. Also, the MDA wind directions are, in general, consistent with the observed concentration patterns during these hours.

Comparisons were made between the sonic and propeller anemometer data to evaluate the method used to construct the preliminary MDA for the release height. In general, data from the sonic anemometers compare favorably with data from the propeller anemometer for these case study hours. However, there are many hours in the preliminary CF_3Br MDA that contain uncertain meteorological data, probably because the linear interpolation between 5 m and 40 m is inappropriate. The greater vertical resolution provided by the Tower A propeller anemometer data will most likely provide more representative meteorological data which should improve the modeling results.

For each case-study hour, the ratio of the maximum observed to the maximum predicted concentration (unpaired in space) is closer to unity for the empirical HBR model than the flat-terrain model. Significant discrepancies between observed and modeled concentrations (from the empirical HBR model) appear to result in part from variations in the meteorology during the hour that are not adequately represented in the "hourly" Gaussian plume formulation.

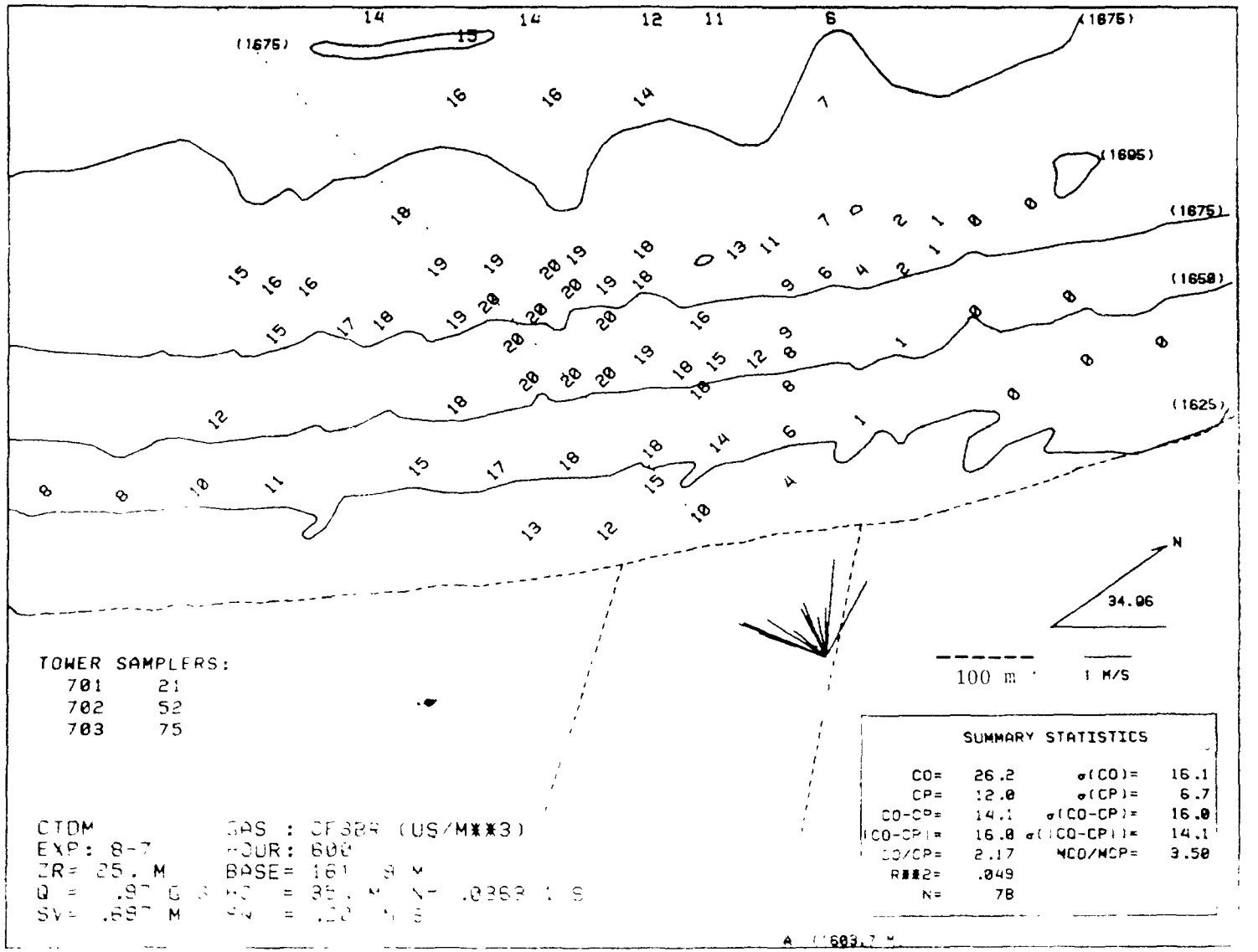

Figure 60. One-hour average predicted scaled concentrations ($\mu s/m^3$) from the HBR (Flat) model (Experiment 8, 10/15/82, 0500-0600 MDT).

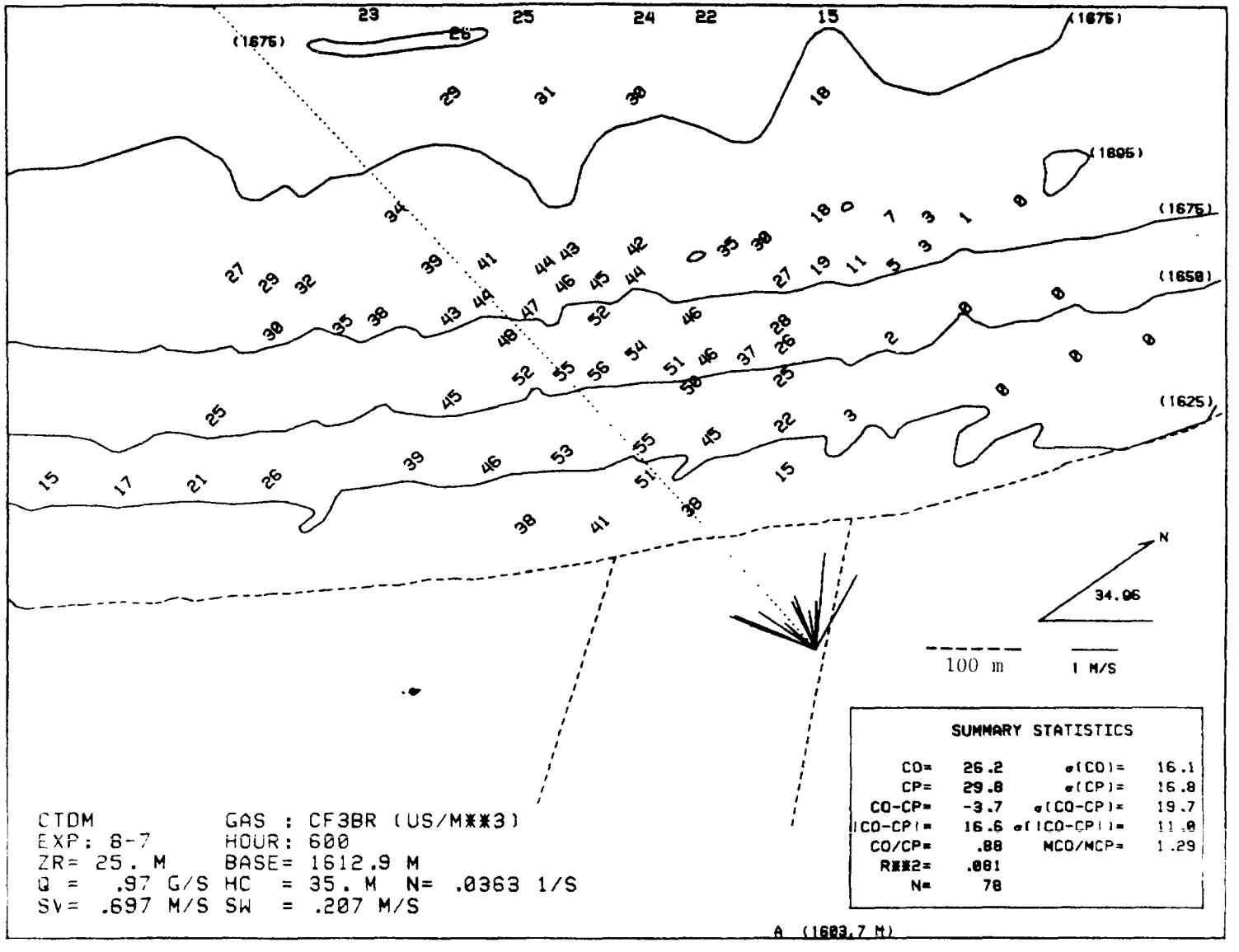

Figure 61. One-hour average predicted scaled concentrations ($\mu s/m^3$) from the HBR (terrain) model (Experiment 8, 10/15/82, 0500-0600 MDT).

SECTION 5

THE PRELIMINARY TRACY EXPERIMENT

5.1 Geographic and Meteorological Setting

The Tracy Power Plant (TPP) near Reno, Nevada has been selected as the site for the Full Scale Plume Study (FSPS), the third field experiment in the CTMD project. The Tracy plant was tentatively selected in May 1983 after (1) a review of operating power plants in the western United States and of available topographic, meteorological and air quality data, and (2) site visits to three power plants. The final selection was made after a preliminary experiment that was conducted at Tracy in November 1983. This section summarizes the results from the preliminary experiment and discusses the plans for the FSPS.

The Tracy station is operated by Sierra Pacific Power Company. The Sierra Pacific personnel had agreed to participate in the program and were very cooperative in the design of the FSPS. The power plant is located about 27 km (17 mi) east of Reno, Nevada in the Truckee River Valley. It has three units--53 MW, 80 MW and 120 MW, although only the latter has been used recently. The 120-MW unit is serviced by a 91.4-m (300-ft) stack. This stack was used to release the oil-fog and SF_6 during the preliminary experiment.

Figure 62 shows the location of the Tracy station on a 1:250,000 scale topographic map. The plant is located east of the Reno-Sparks metropolitan area and about 40 km (25 mi) east of the Sierra Nevada Mountains, the source of the Truckee River. The river runs eastward near the plant and eventually drains into Pyramid Lake.

The 91.4-m stack is located near the southwest corner of the plant (Figure 63) south of the Truckee River. The plant site is in a relatively narrow valley with mountains surrounding the plant on all sides. Figure 64 shows the location of the plant on a 1:62,500 scale map. Mountain peaks rise to elevations of 900 m above the stack base elevation within 6.5 km of the plant. The area is characterized by a sparse vegetative cover of shrubs and grasses. Much of the uncultivated area in the immediate plant environs is covered by small boulders.

The Truckee River enters the valley through a narrow opening near Patrick. It flows eastward just north of the plant and then takes an abrupt turn to the north about 4 km east of the plant. The river flows between two mountains at its northward bend. These two mountains are the primary "target" areas for the dispersion experiments.

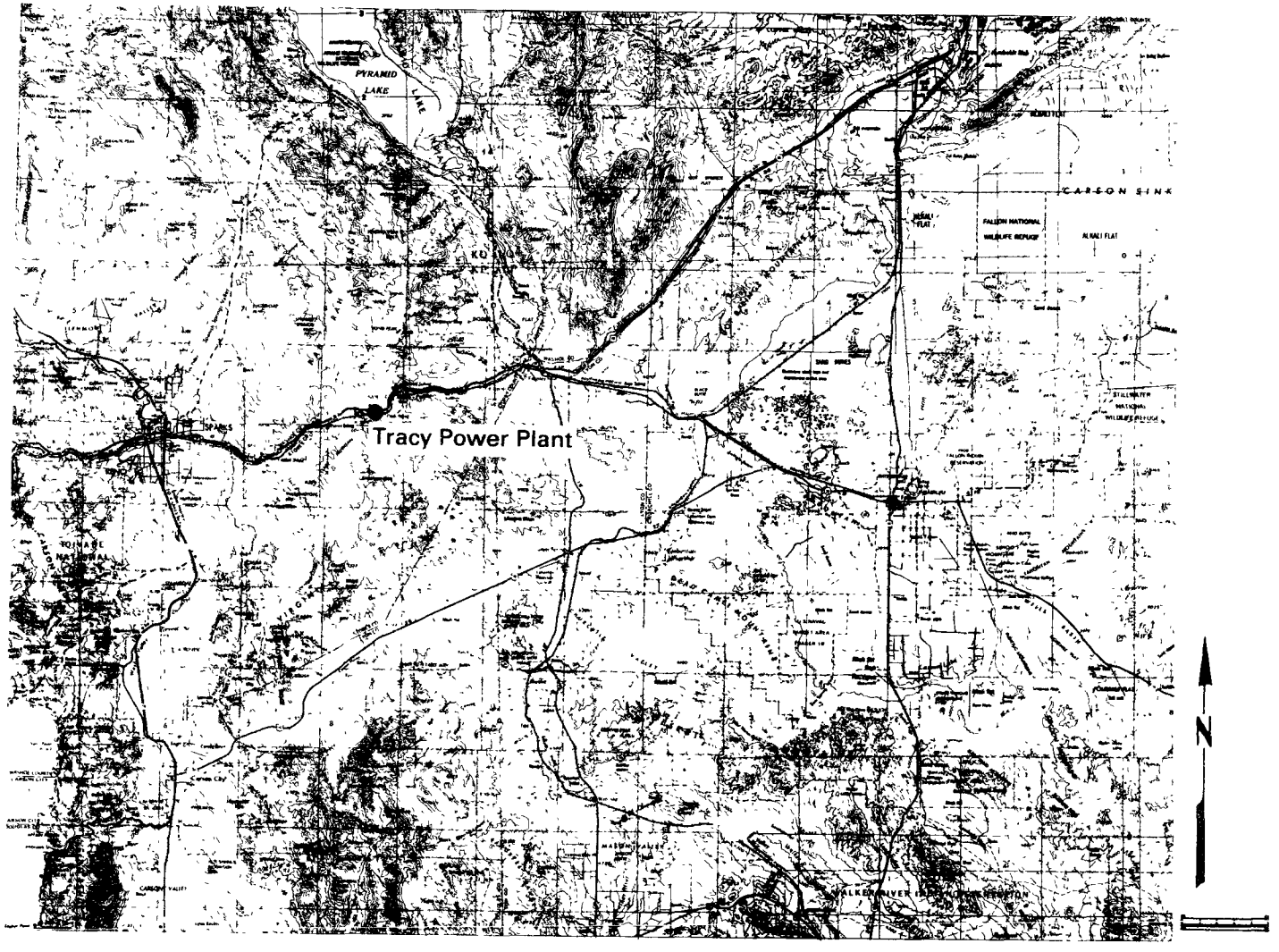

Figure 62. The region around the Tracy Power Plant.

Figure 63. 91.4-m (300-ft) stack, located near the southwest corner of the Tracy Power Plant site.

Figure 64. Location of the Tracy Power Plant.

In addition to the Tracy station, there is a diatomaceous earth plant run by Eagle Picher Industries Inc. in the valley near Clark. There are also a few ranches in the valley. Interstate-80 runs north of the plant along the river.

No historical meteorological record is available from anywhere in the valley. However, a previous field program (Kapsha et al. 1976), which included aircraft and mobile van measurements of SO_2 as well as pilot balloon data, suggested plume transport from the Tracy stack to locations that would produce ground-level concentrations on mountains 5229 (called beacon hill) and 5764 (called target mountain) east of the plant and around the mountain 5610 complex northwest of the plant. This field program was conducted in December 1975 and experienced easterly wind flows* associated with transistory anticyclones, as well as the more usual stable drainage winds. In July 1983, as part of their initial feasibility testing, ARLFRD released oil-fog from the Tracy stack, and the smoke plume was transported to and interacted with target mountain and beacon hill. Although there is currently no corroborative data base, it is expected that during the late summer, nighttime winds in the valley will be dominated by terrain effects--probably producing a prevailing westerly wind down the Truckee River with superimposed local katabatic effects.

5.2 Experimental Design

The preliminary flow visualization and tracer experiment that was conducted during the period November 7-20, 1983 was co-sponsored by EPA and the Electric Power Research Institute (EPRI). The EPRI participation was in anticipation of a complex terrain field experiment as part of their Plume Model Validation and Development project. The results of the preliminary Tracy experiment will be used to guide the design of the next PMV&D field experiment and to provide the PMV&D modelers preliminary information on the relationship among emissions, meteorological conditions, and observed concentrations in a complex terrain setting.

The EPA objectives of the November experiment were (1) to assess the feasibility of the Tracy site for the FSPS and (2) to obtain sufficient information to design and plan the full scale experiment. These objectives were satisfied and the site was selected for the FSPS.**

The experimental methods were similar to those used and tested at CCB and HBR and at the two previous EPRI field sites. The experiment included:

- Releases of SF_6 and oil-fog from the 91.4-m stack;†

---

*Easterly winds were also experienced during the 1983 Tracy experiment. See Section 5.5

**A detailed work plan for the FSPS was prepared. See also Section 5.6.

† In the two small hill experiments, releases were made from mobile cranes.

- Ground-level SF_6 concentration measurements at up to 53 sites;
- Fixed meteorological measurements:
  - a 150-m tower instrumented at four levels (5, 10, 100 and 150 m),
  - two 10-m towers instrumented at one level,
  - two monostatic acoustic sounders,
  - a doppler acoustic sounder, and
  - two optical crosswind anemometers;
- Two tethersondes;
- T-sonde releases with double theodolite tracking at two locations;
- Two solar-powered electronic weather stations;
- Airborne lidar; and
- Photographs and videotapes.

The participants and their principal responsibilities were:

- ERT (EPA prime contractor)
  (1) directed experiment operations in consultation with other participants;
  (2) operated the command post (Sierra Pacific Power provided office space at the Tracy station);
  (3) provided smoke candles, two carbon arc lamps, cameras and personnel for flow visualization experiments and scientific observations;
  (4) provided, installed and operated two electronic weather stations to measure winds and temperature at two locations;
  (5) provided, installed, and operated a 150-m tower instrumented at four levels to measure winds, turbulence, and temperature;
  (6) provided for other site logistics as needed; and
  (7) produced the master data archive and disseminated it to participants.

- NOAA ARLFRD (via an interagency agreement with EPA)
  (1) provided, installed, and operated two 10-m towers with wind and temperature instruments telemetering to command post for display and storage;
  (2) provided data logging equipment; archived, reduced and disseminated the meteorological data;
  (3) adapted fogger to Tracy flue, provided oil and operated fogger; provided SF_6 and injected into flue (with oil fog);
  (4) provided one tethersonde and operator;
  (5) provided radios and repeater station;
  (6) provided for photography contract (two photographers, about four time-exposures/hr and one video during daylight).

- NOAA WPL (via an interagency agreement with EPA)
  (1) provided one tethersonde and operator,
  (2) provided Doppler acoustic sounder and operator,

(3) provided two monostatic acoustic sounders,
(4) provided two optical crosswind anemometers.

- SRI International (EPRI contractor)
  (1) provided and operated airborne lidar (approximately two 3-hour missions per experiment).

- Rockwell International (EPRI contractor)
  (1) provided 1-hour sequential (9 hrs) syringe samplers (including spares) to operate on consecutive nights at 53 locations, and provided necessary deployment crews and vehicles (including helicopter);
  (2) determined SF_6 concentrations (by GC) in all syringes and bags with a turnaround time of about 24 hours;
  (3) provided equipment and took T-sondes to 2.5-3 km above ground at 1-hr intervals at two locations during tracer releases; and
  (4) provided survey/identification of all SF_6 samplers, meteorological instruments, and fixed photography locations.

- Research Triangle Institute (EPRI "External Audits" contractor)
  (1) provided an independent review of QC plans of other EPRI contractors; conducted onsite systems audits of the field measurements and the data handling activities;
  (2) provided independent checks of the precision and accuracy of the field measurements and data handling results. Onsite performance audits were performed at the Tracy Power Plant for the following measurements systems: tracer, T-sonde, tethersonde, and two 10-m towers with wind speed, direction, turbulence, and temperature measurement systems; and
  (3) provided reports to EPRI, through TRC, on the results of systems and performance audit results.

- TRC Environmental Consultants (EPRI technical management contractor)
  (1) represented EPRI in the field and coordinated EPRI contractors, and
  (2) undertook scientific observations and analyses as appropriate.

5.2.1 Oil-fog and Tracer Gas Release System

ARLFRD provided an oil-fog generator and a SF_6 release system to inject oil-fog and SF_6 directly into the 91.4-m stack flue at the Tracy station. The injections were made through a "door" into the ducting leading to the 91.4-m stack (Figure 65). The SF_6 tracer gas was stored in two compressed gas cylinders at ground level. Piping carried the gas through a linear mass flow meter (LFM) system to the point of discharge into the stack. The LFM measured and displayed the rate of gaseous tracer discharge via real-time digital

Figure 65. Oil-fog and SF_6 injections were made through a "door" into the ducting leading to the 91.4-m (300-ft) stack.

display, the total amount of gas discharged via a digital counter, and the analog output voltage directly proportional to the flow rate. The voltage was logged and monitored on a strip chart recorder. Pre and post-test release weights of gas tracer cylinders were measured by certified scales. Similarly, the oil consumption rate was logged to document the quantity of oil-fog injected through the 91.4-m stack.

A nominal SF_6 release rate of 1.26 g/s (10 lb/hour) was used for the Tracy experiment. The SF_6 and oil-fog releases commenced approximately 30 minutes prior to the start of the sampling to ensure that the tracer gas had actually reached the sampling grid when the samplers were turned on. During the course of the experiment, the 91.4-m stack was vented through the use of a fan located at the bottom of the stack. Only occasionally during the experiment was the unit used to generate electricity. During these times the generation rate was typically 20 MW.

5.2.2 Tracer Sampling and Analysis

Fifty-three syringe samplers were deployed by Rockwell International (Cher 1984) to sample hourly concentrations. Sampling sites were selected from 63 sampler locations (Figure 66). Forty-three locations were specified to sample concentrations during westerly winds and were used during the first few experiments. During the course of the experiment, easterly winds were experienced frequently so it was decided to select additional sites west of the plant.

The samplers used in the program were sequential syringe samplers manufactured by D&S Instruments. Nine 30 cm^3 syringes were housed in each sampler. The syringe samplers functioned over a 9-hour period with syringes sampling for consecutive 1-hour periods. Because of the rough terrain, deployment of samplers required the use of either a helicopter or a 4-wheel drive vehicle.

In order to identify each sample by date, location, and time, a numbering system was devised whereby each sampler, stake, and syringe was given a unique number code. The numbers were printed on special, double-sided labels using a computer generated bar code system. Labels were attached to the samplers, stakes, and syringes. Upon deployment of each sampler, stake labels and sampler labels were affixed to a data sheet, which also contained information on the syringe codes associated with the sampler. During analysis, a section of the double-sided label from the stake, sampler, and each syringe was transferred to the strip chart record containing the corresponding trace. In this way, the strip chart record and the deployment data sheet contained complete, redundant records of the deployment history of each sample. When the strip chart records were read, all labels were scanned with a bar code reader, and therefore all identifying information was automatically transferred to the computer with essentially no transcription errors.

A typical experiment ran from midnight to 9 A.M. Samplers were loaded with syringes two days before the scheduled test. Loading consisted of labelling the new plastic syringes, attaching the

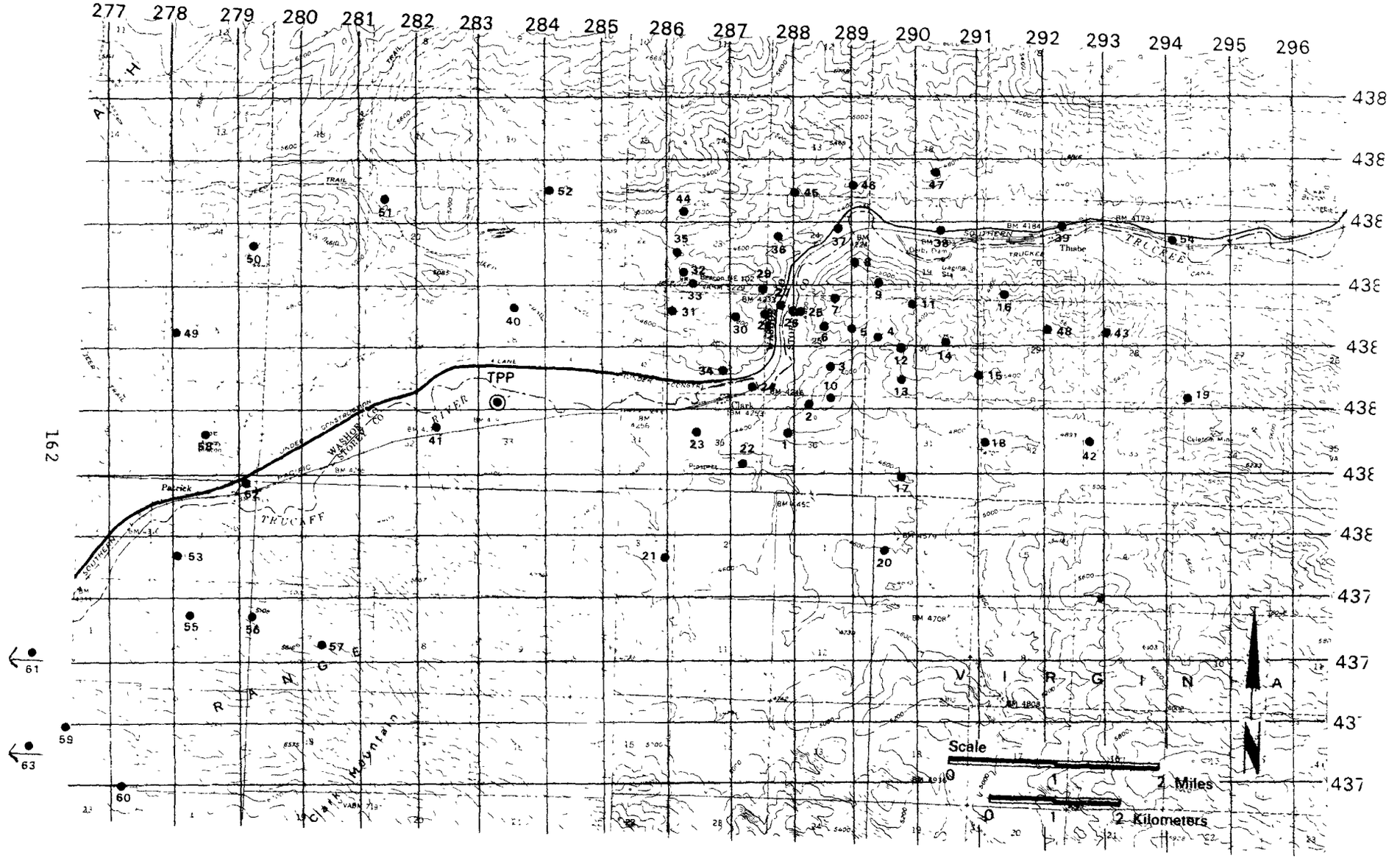

Figure 66. Sampler locations.

needles, installing the units in the sampler, replacing any missing septa, and setting the timers for the desired timing sequence and starting time.

Deployment of the samplers occurred the day before the test and exposed samplers were retrieved at the end of the test. For this program a sufficient number of samplers were available so that deployment and retrieval of samplers from the previous test could be done simultaneously. Deployment and retrieval times were entered in the data sheets for the two tests, and the stake identifying label was also transferred to the deployment sheet at this time. To avoid mixing samplers from different tests, the exposed samplers were marked upon retrieval with an identifying tag. Analysis of the air samples was usually performed on the same day as the test.

In addition to the syringe samplers, ARLFRD provided five sequential bag samplers. These were collocated with five syringe samplers for quality assurance purposes.

The analyses of the air samples were performed by gas chromatography using an electron capture detector. Three Varian 3700 gas chromatographs were used, of which two were fitted with dual columns to speed up the analyses. The columns were 3.175 mm x 1.829 m stainless steel packed with molecular sieve 5A. The oven temperature was 50°C, the detector temperature was 150°C, and the carrier gas was nitrogen flowing at the rate of 50 cm^3/min. Under these conditions, the elution time of SF_6 and O_2 were approximately 25 and 40 seconds, respectively. The entire analysis time (with backflushing starting as soon as the oxygen peak began to elute) was approximately 2.5 min.

Each column-detector combination was calibrated using standards obtained from compressed gas cylinders (Scott Specialty Gases) containing manufacturer-certified SF_6 concentrations of 17, 83, 505, and 1145 ppt SF_6. Calibrations were repeated every two hours. The response of the gas chromatographs remained constant within 10%. Because the response of one of the gas chromatographs was slightly non-linear, the response curves for all calibrations were determined by fitting calibration data to a quadratic equation of the form:

$$\text{concentration} = ah(1+bh)$$

where a and b are calibration constants, and h is the peak height. For the highest concentration used (1145 ppt) and the most non-linear response gas chromatograph, the ratio of the quadratic term to the linear term bh was approximately 0.15-0.20 or 15-20%. All calibration constants were stored on disk using a DEC Professional 350 Computer. The SF_6 peak heights were digitized electronically using a Science Accessories Corporation sonic digitizer Model GP6-40 connected directly to the computer. Peak heights were converted to concentrations by applying the appropriate calibration constants.

5.2.3 Plume Photographs

Two dedicated photographers took 5-minute exposures of the oil-fog plume approximately every 15-minutes during the course of the experiment. Their locations are depicted in Figure 67. The plume was illuminated by two carbon arc lamps--one located south and one north of the river. In addition, the ERT scientific observers took plume photographs of interest from a number of locations.

5.2.4 Airborne Lidar Sampling

SRI International provided the ALPHA-1 airborne lidar to document the three-dimensional interaction of the oil-fog plume with the terrain. The aircraft flew a "creeping-ladder" pattern from the stack to approximately five to ten kilometers downwind. The flight pattern legs were approximately at right angles to the mean plume direction. The aircraft typically flew two three-hour missions during each experiment. Facsimile lidar cross sections of the plume were available at the end of each experiment for analysis by the project scientists.

A separate report on the Alpha-1 observations was prepared by Uthe and Morley (1984). Some of their material is presented in Appendix C.

5.2.5 Meteorological Measurements

Table 15 lists the meteorological instruments used during the November experiment. Their approximate locations are depicted in Figure 67. The minisondes were released and tracked hourly on the hour. The tethersondes were used to obtain vertical profiles of winds and temperature up to 600 m. The tethersonde ascents occurred during the first half-hour of each hour and the descents during the second half. The tethersonde data were processed continuously so that the data were available for near real-time analysis and operational planning.

All data (including SF_6) were achived and identified by the end time (PST) of the averaging period, e.g., an hourly average wind direction for the period 0200-0300 is identified as a 1-hour average ending at 0300. Shorter-term measurements were also identified by the end time of the measurement, e.g., Doppler wind data at 0200, 0220, 0240.

5.3 Preliminary Field Study Results

5.3.1 Summary of Data Base

Ten experiments were conducted for 73 hours during the period 7-20 November 1983. The use of 43 sampling sites was planned for the first four days and 53 for the last six. Because of high winds and snow, only 37 and 30 samplers were deployed for two experiments. During the first four days, unfavorable weather conditions resulted in

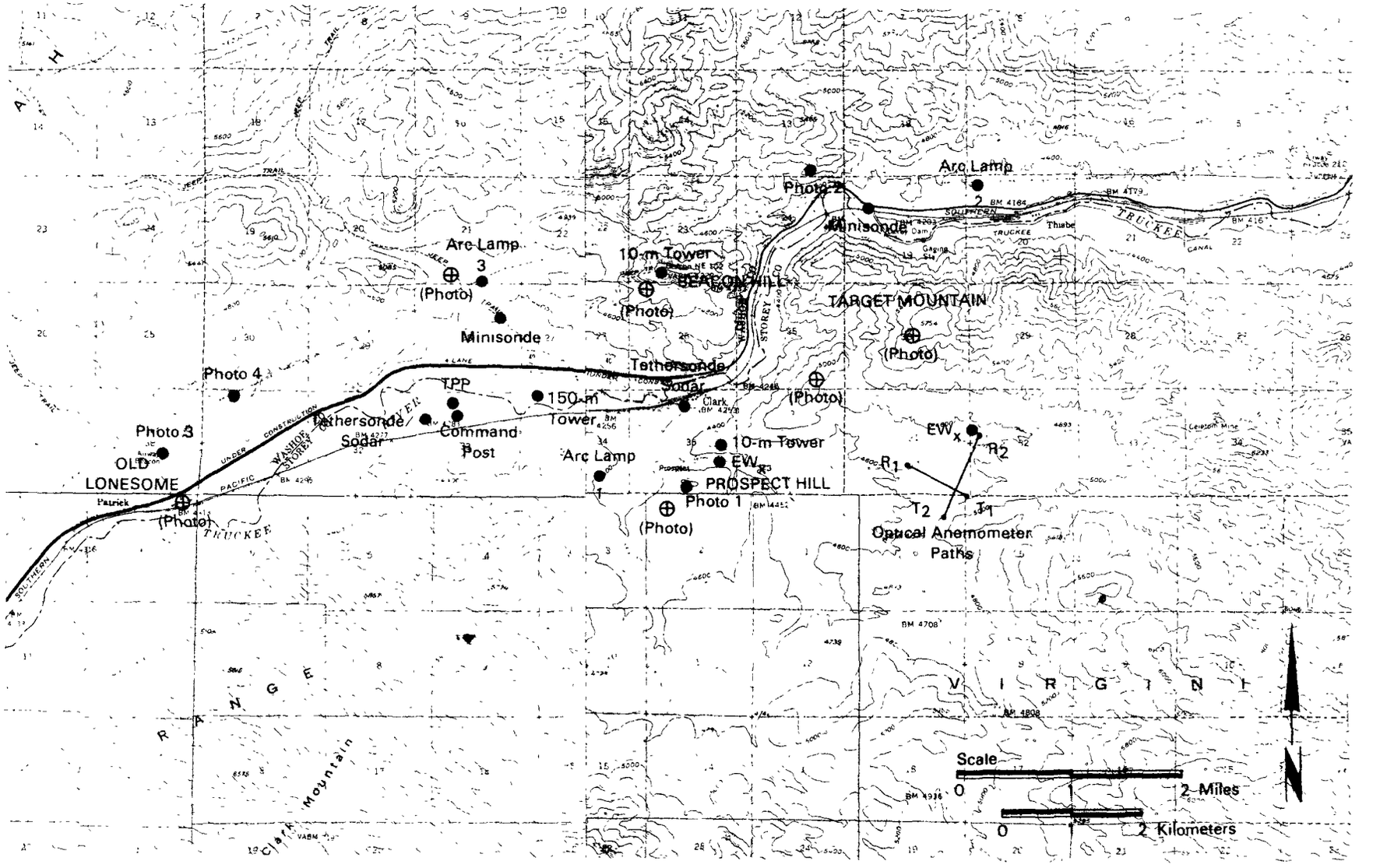

Figure 67. Preliminary Tracy Experiment layout.

TABLE 15. METEOROLOGICAL INSTRUMENTS AT THE PRELIMINARY TRACY EXPERIMENT

Instrument	Purpose
T-sonde (two)	To provide wind and temperature data throughout the boundary layer (up to 3000 m) near the west and east boundaries of the experiment-region.
Tethersonde (two)	To provide wind and temperature data up to 600 m in (1) the flow upwind of the stack and at (2) the flow upwind of the bend to the north of the Truckee River.
Doppler acoustic sounder	To provide real-time information on the vertical profile of winds near the source location; data are archived every 10 minutes.
Fixed meteorological sensors - two 10-m towers (winds and temperature) - two electronic weather stations (winds and temperature) - one 150-m tower east of the stack (winds, turbulence and temperature at four levels - 5 m, 10 m, 100 m, 150 m)	To provide (1) real-time information on meteorological conditions in the high terrain, (2) data on the drainage flow, and (3) data (historical only) representative of plume conditions.
Monostatic acoustic sounders (two)	To provide information on the structure of the boundary layer (1) upwind of the source, and (2) upwind of the bend in the river.
Optical anemometers (two)	To provide information on the drainage flow on the south side of target mountain.

few ground-level SF_6 concentrations. Table 16 summarizes the available concentration data from the entire Tracy experiment. A total of 3167 SF_6 concentrations are in the data base. All the remaining measurements have also been delivered to ERT and are now part of the Tracy Preliminary data base, which is summarized in Table 17.

The complete data base was delivered to EPA accompanied by a descriptive data report. The data base will be available from the EPA Project Officer.

Maps of the SF_6 concentrations and the various meteorological data were examined to assess which hours are sufficient for modeling. From the 68-hour tracer data base, it was judged that approximately 34 "good" hours and 13 "marginal" hours* are available for modeling purposes. Table 18 summarizes the modeling data base.

5.3.2 Overview of Results

The November experiment did achieve the program objectives: (1) the Tracy site is feasible for the FSPS; and (2) the tracer gas, meteorological and photographic data base are sufficient to design the FSPS (see Section 5.6). Although the data base from the November experiment is small compared to the CCB and HBR data bases, the experiment did capture a wide variety of dispersion conditions. Tracer gas concentrations were observed in the primary target areas during stable conditions and also during windy, neutral conditions. The data can be used to evaluate the CTMD modeling approaches and to extend the hill and ridge data bases.

5.4 Example Results from Specific Experiments

To illustrate some of the experimental results, a few hours from three experiment days are described qualitatively in terms of the relationship among emissions, observed meteorological conditions and subsequent ground-level tracer gas concentrations. Predominantly stable atmospheric conditions occurred during the first two days and windy, neutral conditions on the third day.

Experiment 5 (November 12, 1983) 0000-0500 PST

SF_6 concentrations were observed in the high terrain of the primary target areas during the course of Experiment 5. Figure 68 shows the geographical distribution of hourly concentrations observed during the first five hours. In this figure, the dotted lines indicate the position of Interstate-80 and the Eagle Picher haul road. The river flows from the lower left to the upper right and it parallels Interstate-80. The X in the middle of the diagram represents the location of the stack. The concentration range of SF_6 is indicated by the numerical symbols, defined as follows:

*The criteria for good hours are qualitative and subjective.

TABLE 16. SUMMARY OF ACQUISITION OF SF_6 CONCENTRATION DATA

Experiment	Date	Number of Sampling Sites	Sampling Hours	Samplers Analyzed	Hours Analyzed	Total Number of Samples Analyzed
1 (A)	Nov 7	43	9	43	6	258
2 (B)	Nov 8	37	9	37	4	148
3 (C)	Nov 9	43	9	43	2	86
4 (D)	Nov 10	43	9	10	2	20
5 (E)	Nov 12	53	9	53	9	477
6 (G)	Nov 14	30	9	30	9	270
7 (H)	Nov 15	53	9	53	9	477
8 (I)	Nov 16	53	9	53	9	477
9 (J)	Nov 18	53	9	53	9	477
10 (K)	Nov 19	53	9	53	9	477
				Total	68	3167

TABLE 17. DATA BASE, PRELIMINARY TRACY EXPERIMENT

Information	Averaging Time	Comments
SF_6 Concentration	1-hour	Available for 68 hours
SF_6 emission rate	15-min	-
150-m tower met data: WS, WD, σ_θ, w, σ_w, T, ΔT from 5, 10, 100, 150-m, levels	5-min & 1-hour	-
10-m tower met data: WS, WD, T	5-min	Two towers
Doppler sounder data: WS, WD	10-min	-
electronic weather station data: WS, WD	1-hour	T available from one of the two stations
monostatic sounder	continuous	Facsimile record from two locations
optical anemometers	5-min	Path average wind speed for two paths
tethersonde data: WS, WD, T	instantaneous	Two profiles per hour to 600 m at two sites. RH available from Clark site, pressure from site west of plant.
T-sonde data: WS, WD, T	instantaneous	One profile per hour to 3,000 m at two sites
Lidar data	continuous during each mission	Facsimile records and aircraft position (See Uthe & Morley 1984)
Photographs	5-min	Five-minute exposures every 15 minutes
Base Log	-	Available from
Observer notes	-	Project Officer

Definitions
WS wind speed
WD wind direction
σ_θ standard deviation of horizontal wind
w vertical wind speed
σ_w standard deviation of vertical wind
T temperature
ΔT temperature difference (5-10, 5-100, 5-150 m)
RH relative humidity

TABLE 18. CHARACTERIZATION OF THE PRELIMINARY TRACY EXPERIMENTS

Experiment	Date	Hours*	Valid Hours for Modeling**	Comments
1 (A)	11/7/83	00-06	0G,3M	Strong westerly winds, neutral conditions
2 (B)	11/8/83	00-03	0G,0M	Very light and variable winds; considerable plume rise
3 (C)	11/9/83	02-07	0G,0M	Very light easterly winds; no impact on samplers
4 (D)	11/10/83	00-05	0G,0M	Light easterly and southerly winds throughout experiment
5 (E)	11/12/83	00-09	7G, 2M	Measured GLC+ on primary target area as well as new samplers to the west
6 (G)	11/14/83	00-09	8G, 1M	Good SF_6 all night
7 (H)	11/15/83	00-09	6G, 1M	SF_6 almost everywhere after 0200
8 (I)	11/15-16/83	21-06	4G, 3M	Cloudy and windy
9 (J)	11/17-18/83	22-07	3G, 2M	Persistent WNW winds until 0200
10 (K)	11/19/83	00-09	6G, 1M	Winds varying between ENE & WSW; SF_6 everywhere 0300-0900

*PST

**G ≡ good; M ≡ marginal

+GLC is ground-level concentration

Data for Hour Ending 0100 on 12-November-1983

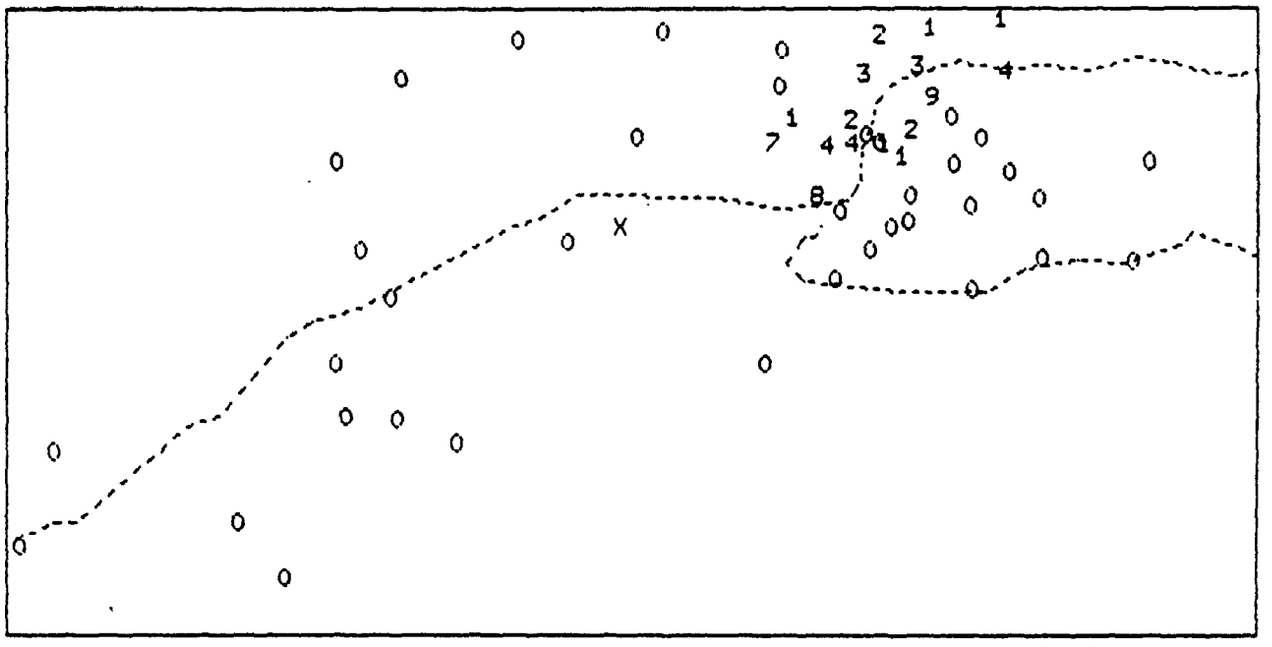

Data for Hour Ending 0200 on 12-November-1983

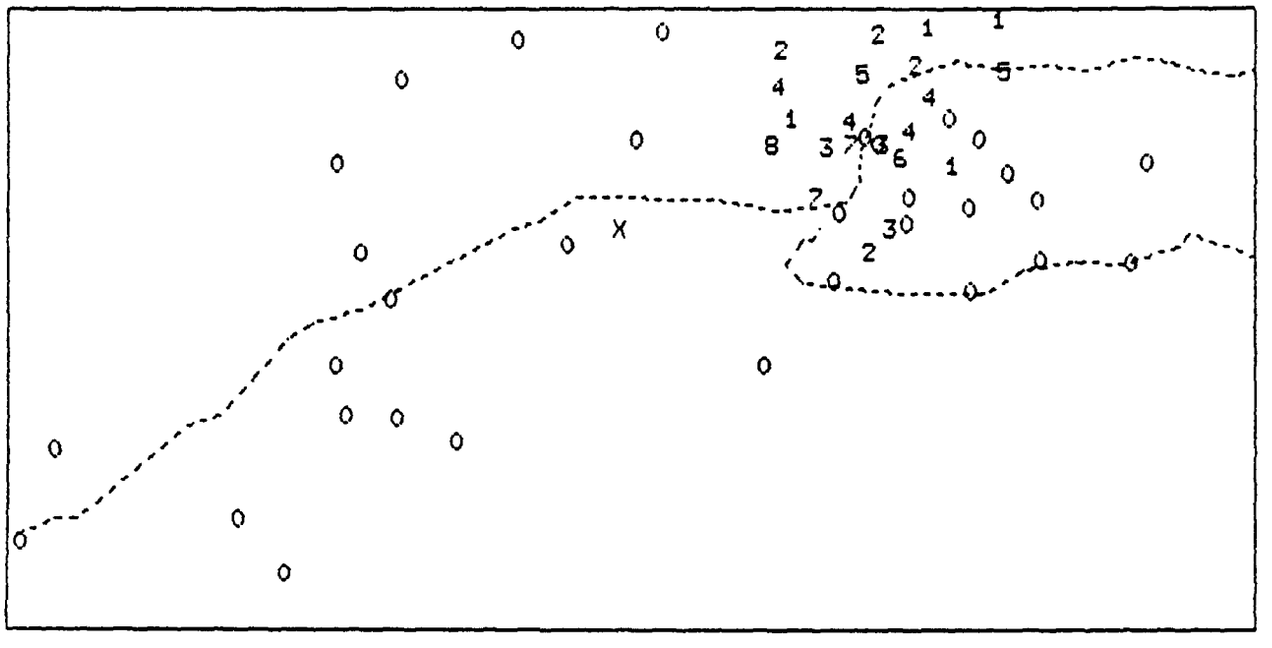

Figure 68. Hourly SF_6 concentrations November 12, 1983 0000-0500.

Data for Hour Ending 0300 on 12-November-1983

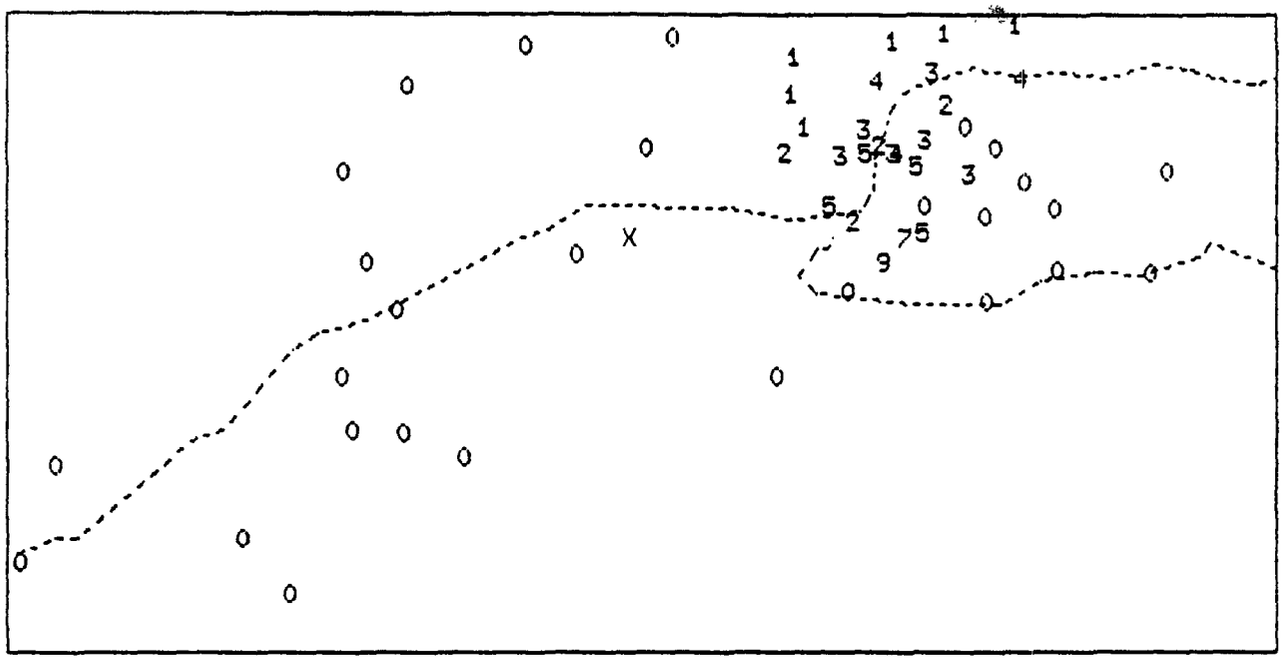

Data for Hour Ending 0400 on 12-November-1983

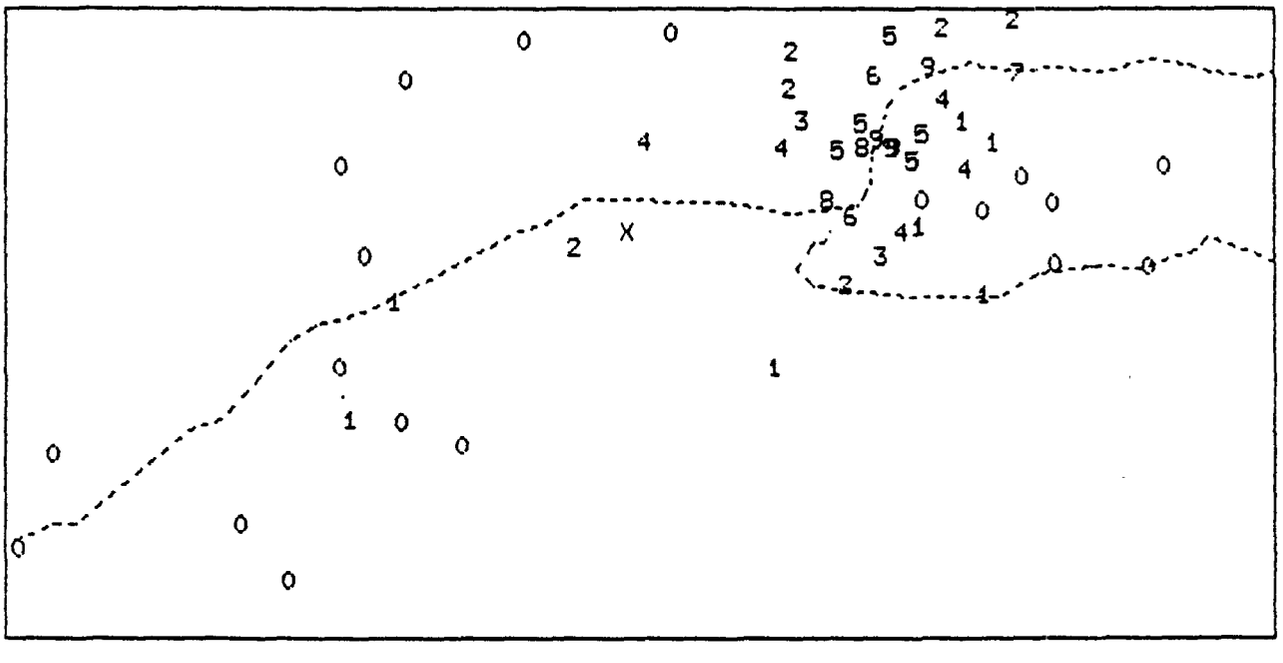

Figure 68 (Continued). Hourly SF_6 concentrations November 12, 1983 0000-0500.

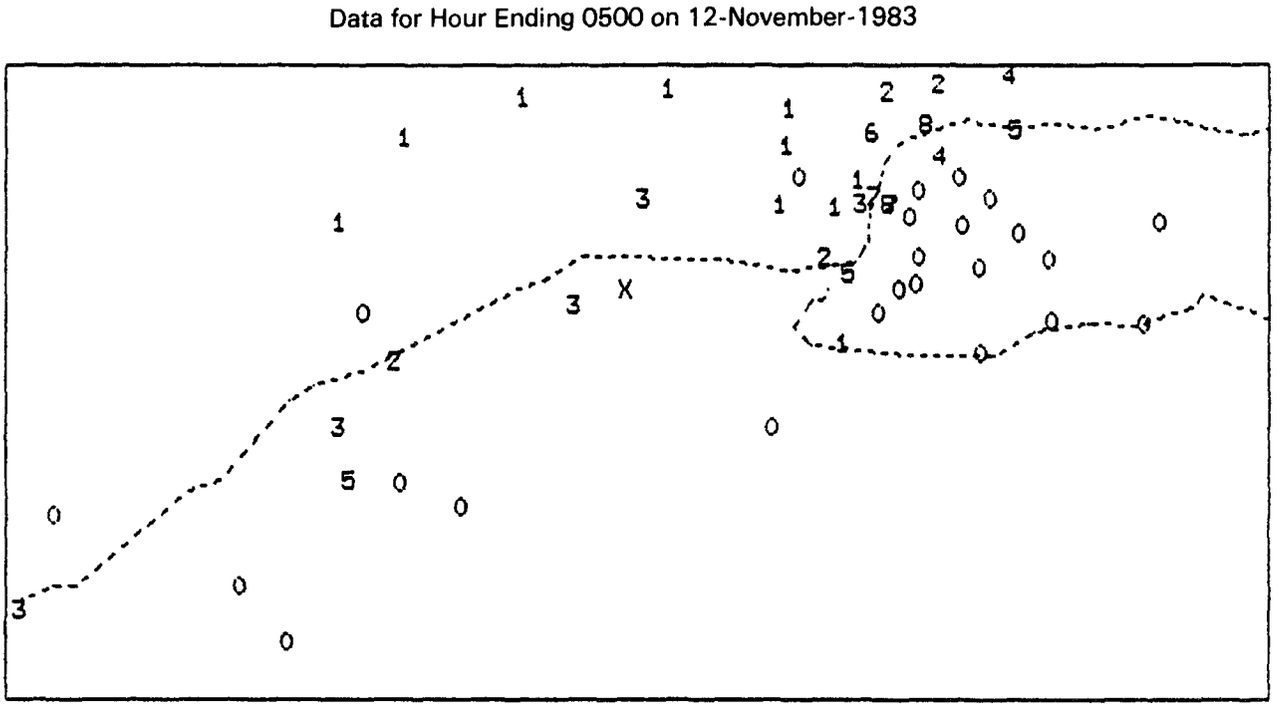

Figure 68 (Continued). Hourly SF_6 concentrations November 12, 1983 0000-0500.

Symbol	Concentration Range (ppt) Min	Max
0	0	19
1	20	39
2	40	59
3	60	79
4	80	99
5	100	124
6	125	149
7	150	174
8	175	199
9	>200	

During the first three hours, the highest concentrations were measured at elevations typically 60-80 m above the top of the Tracy stack. During the period 0300-0500, the highest concentrations were observed along the valley floor in the gorge where the Truckee River bends to the north. The highest concentrations, their location and elevation above the stack base are (Cher 1984):

Time (Ending Hour)	Sampler Site	Conc. ppt	R km	θ deg	ΔZ m*
0100	8	211	6.2	68	169
	34	178	3.6	82	108
	31	159	3.2	62	170
0200	31	176	3.2	62	170
	28	154	4.5	71	113
	34	149	3.6	82	108
	6	146	5.3	77	159
0300	1	310	4.6	95	158
	2	169	5.0	90	170
	6	119	5.3	77	159
0400	25	241	5.1	73	20
	26	216	5.0	73	-15
	37	207	6.2	63	-13
	27	206	4.8	71	-8

0500	26	190	5.0	73	-15
	37	188	6.2	63	-13
	25	171	5.1	73	20

*ΔZ measured from the base of stack. Stack height is about 91 m.

Figure 69 gives a 5-minute exposure of the oil-fog plume as taken from Prospect hill (photography position #1, see Figure 67) at 0000 PST. Notice the dispersion of a stable plume from the Tracy stack toward the east at an elevation near the top of the 150-m tower. Figures 70 and 71 show 5-minute exposures, again taken from Prospect hill, at 0015 and 0030, respectively. The plume is apparently producing ground-level concentrations on beacon hill. A 5-minute exposure taken from Old Lonesome at the west end of the valley (photography position #3) is shown in Figure 72. It illustrates the extensive crosswind growth of the plume and shows some plume material reaching the northwest sections of target mountain.

Hourly average wind directions and speeds taken at the 150-m tower during the five hours are given in Figures 73 and 74. Winds near plume height during the first three hours have a westerly component, consistent with the observed concentrations, photographs and observer comments. During the last two hours the winds have an easterly component. Figure 75 gives 5-minute values of wind direction and speed and σ_w from the 150-m level of the tower. Again, the winds are primarily westerly until about 0300, and then primarily easterly. Notice the increase in turbulence after 0300. Figure 76 gives doppler profiles of wind direction and speed taken at 0020, 0130 and 0400.

A five-minute exposure of the oil-fog plume taken at 0130 from Prospect Hill is shown in Figure 77. The plume is still being transported toward the east, but notice that the top of the smoke plume is below the top of the 150-m tower. Figure 78 shows the geographic distribution of winds at the approximate elevation of the plume above the base elevation of the 150-m tower for each of the five hours. This figure and the doppler wind data illustrate the complexity of the wind fields in the valley.

In any event, it is clear that the SF_6 plume was transported directly to the samplers during the first three hours. Values of H_c were calculated based on the elevation of beacon hill and using the 150-m tower data. A time series of 5-minute values of H_c are listed along with other meteorological data in Table 19. The three hourly H_c averages are 218,222 and 219 m. The elevations of the higher concentrations are always less than H_c during these three hours. Plume material was not transported to the samplers at the highest elevations.

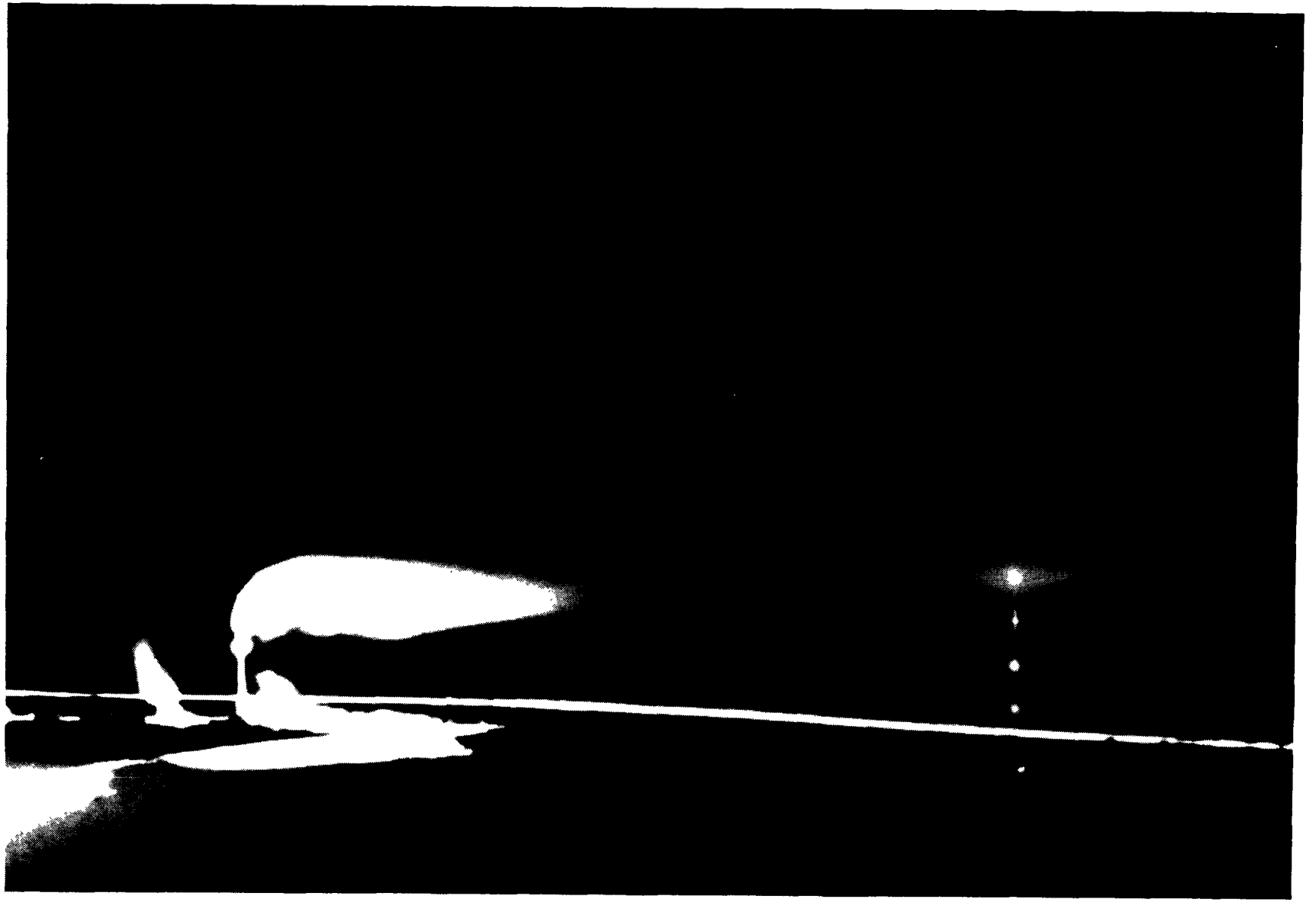

Figure 69. Five-minute exposure (Camera 1) November 12, 1983 at 0000.

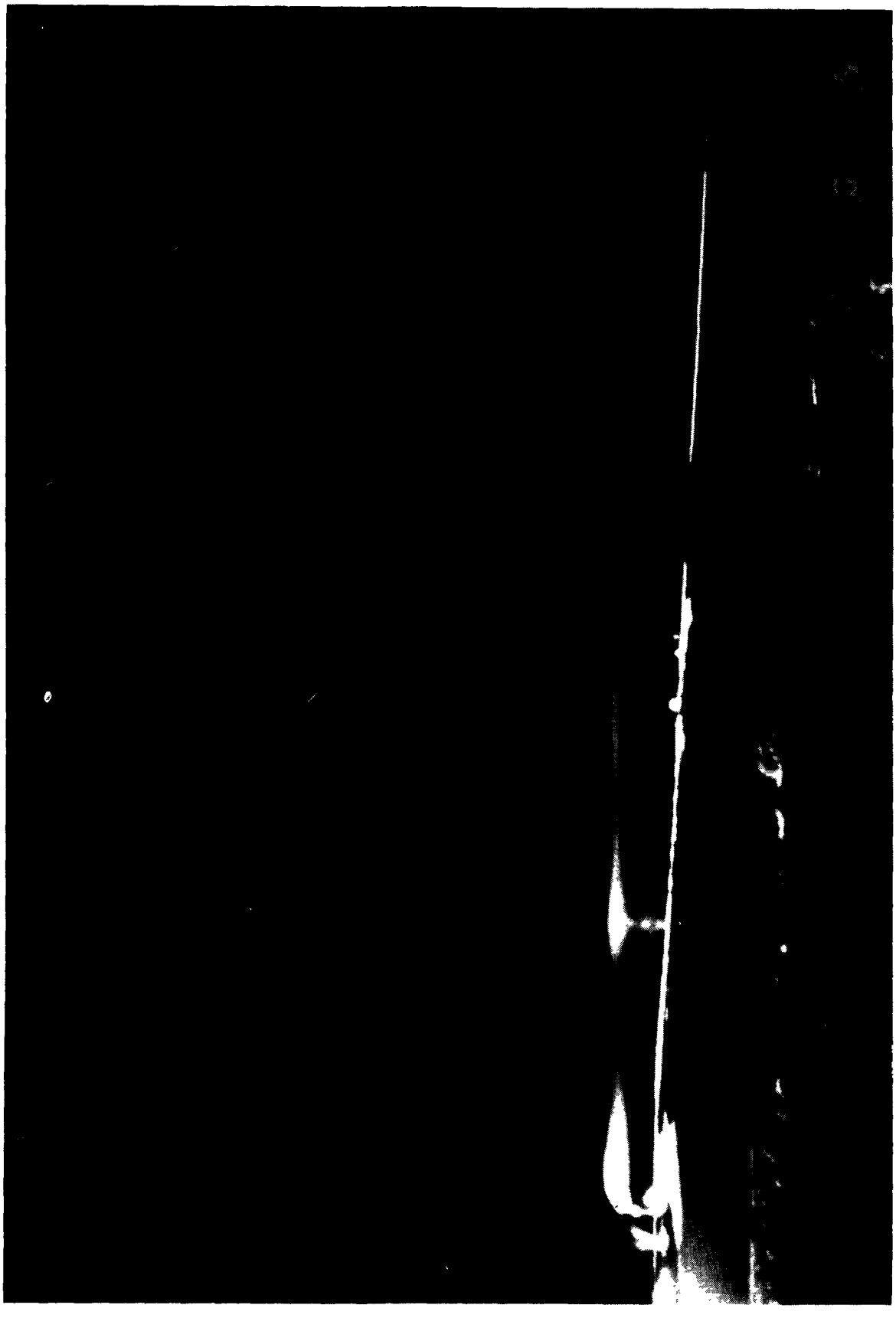

Figure 70. Five-minute exposure (Camera 1) November 12, 1983 at 0015.

Figure 71. Five-minute exposure (Camera 1) November 12, 1983 at 0030.

Figure 72. Five-minute exposure (Camera 3) November 12, 1983 at 0030.

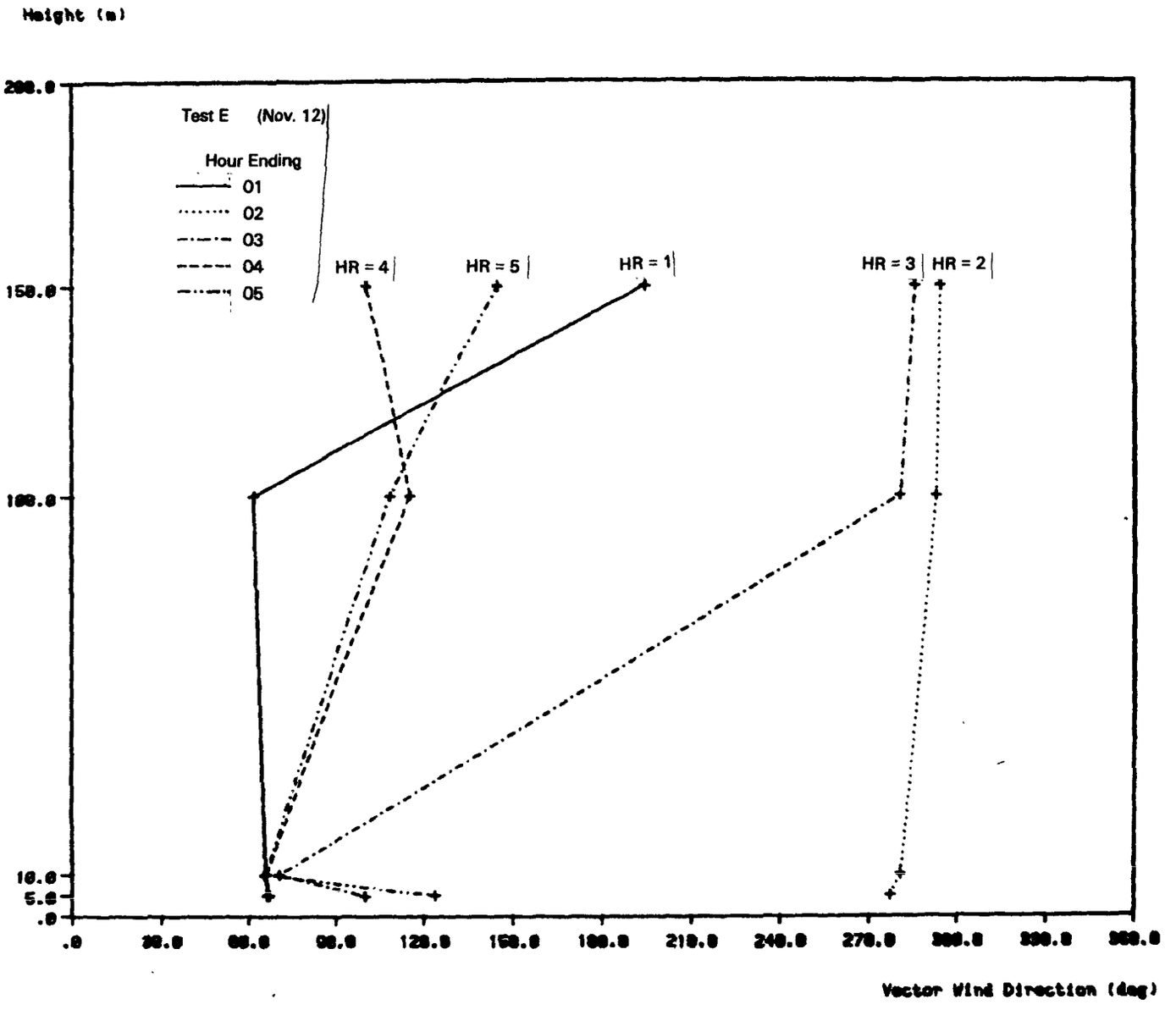

Figure 73. Wind directions measured on 150-m tower.

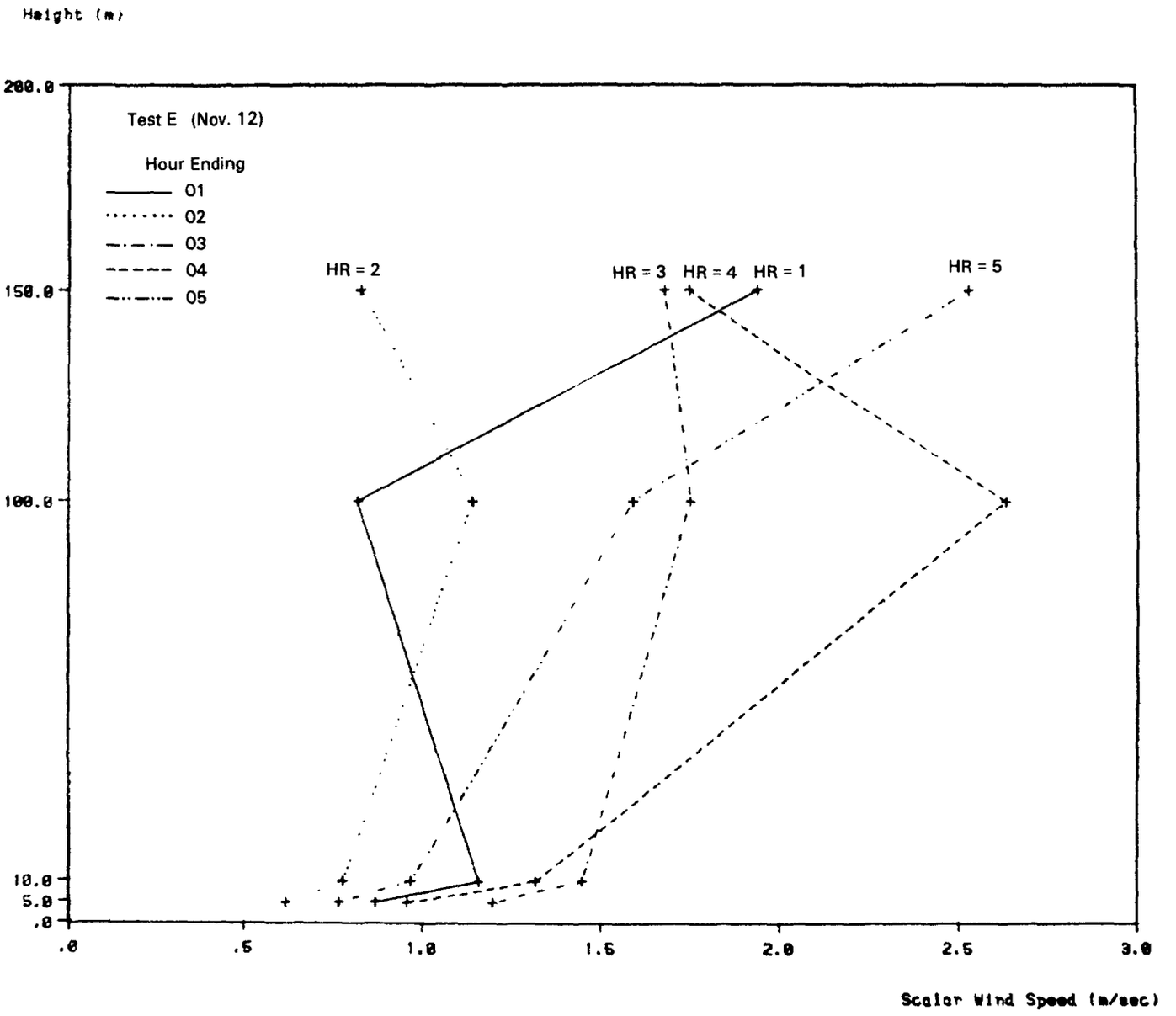

Figure 74. Wind speeds measured on 150-m tower.

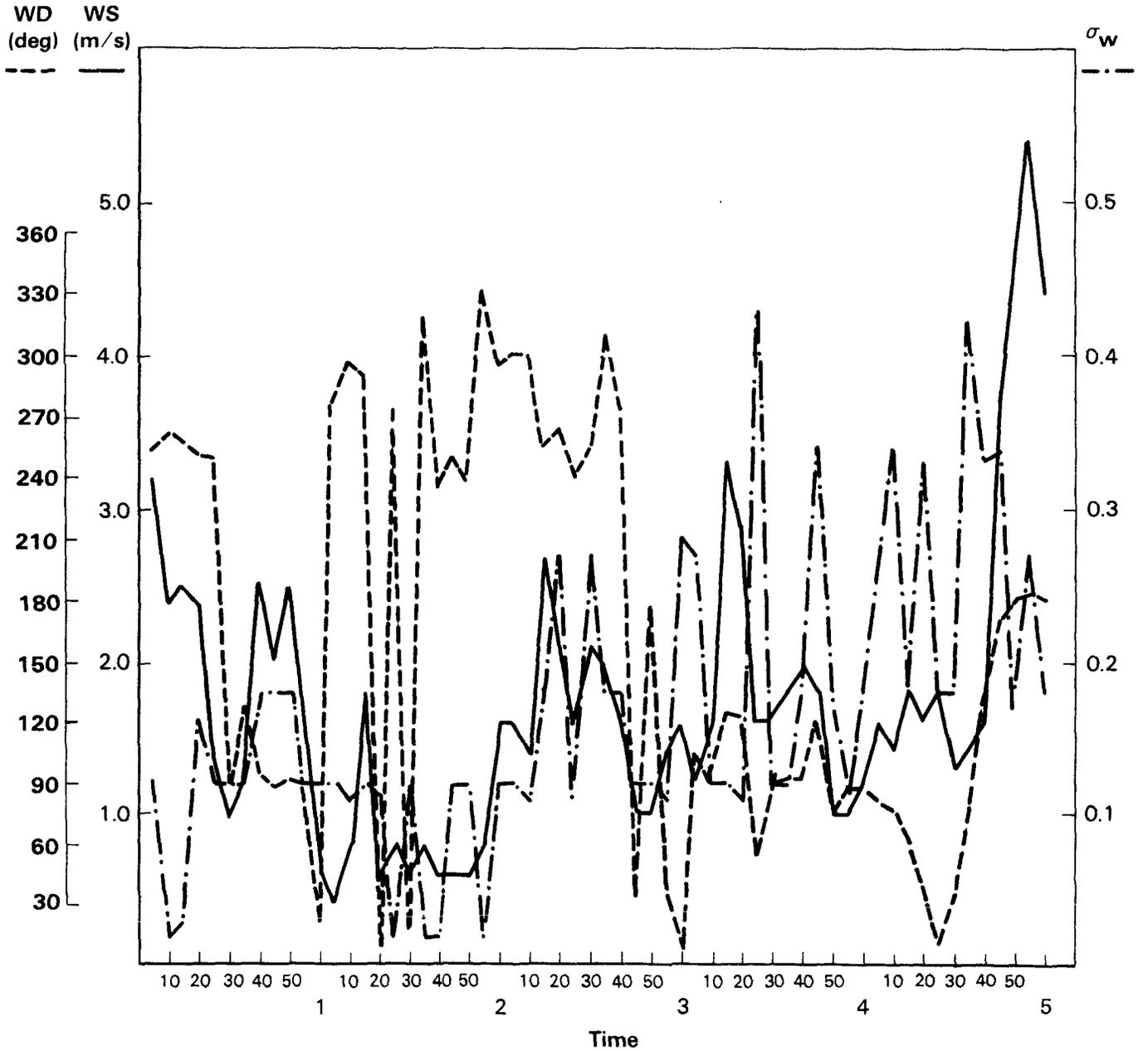

Figure 75. Meteorological data 150-M level November 12, hour 0000-0500.

400	-9.9	999
375	1.8	265
350	1.1	247
325	1.3	249
300	-9.9	999
275	1.8	203
250	1.4	222
225	1.7	208
200	1.9	213
175	2.1	229
150	2.0	235
125	2.1	236
100	1.4	214
75	0.6	157
50	1.0	82

1 1 / 1 2 0 : 2 0

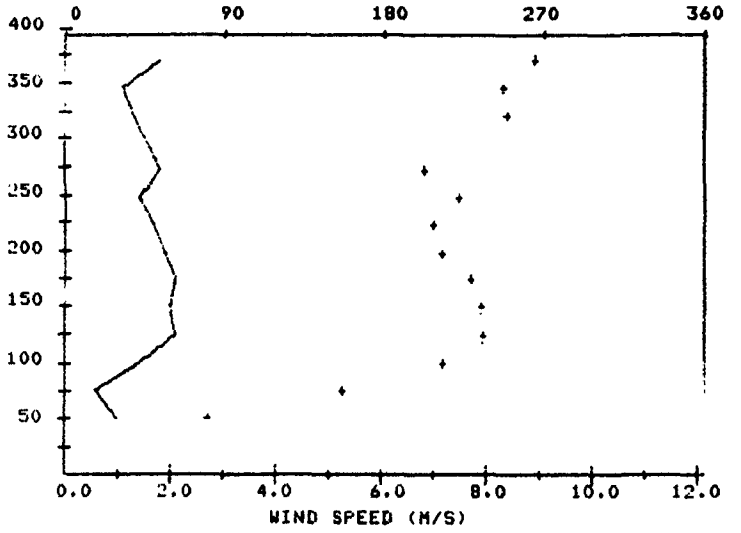

HEIGHT (M)	SPEED (M/S)	DIRECTION (DEG FM N)
400	-9.9	999
375	-9.9	999
350	-9.9	999
325	1.6	169
300	0.0	189
275	1.6	168
250	1.4	163
225	1.4	150
200	1.7	147
175	1.3	153
150	0.9	171
125	0.6	178
100	0.5	220
75	1.0	240
50	1.2	221

1 1 / 1 2 1 : 3 0

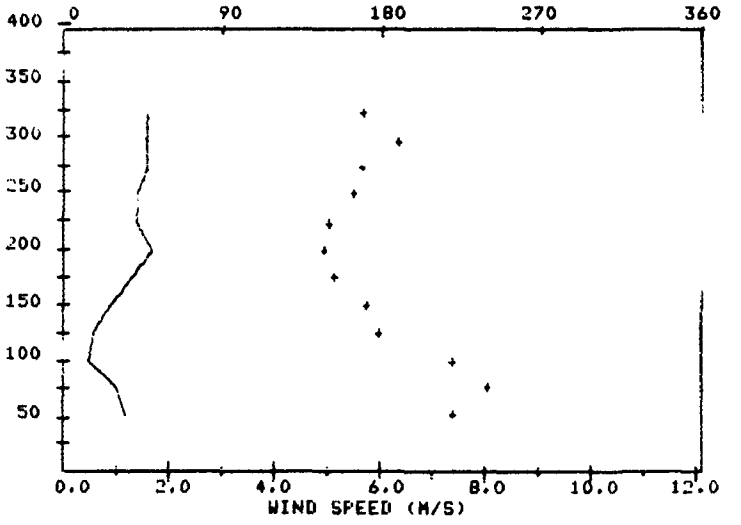

400	-9.9	999
375	-9.9	999
350	4.3	183
325	4.2	179
300	4.5	182
275	4.0	172
250	2.9	151
225	3.0	126
200	2.5	109
175	2.2	82
150	2.1	88
125	2.4	89
100	2.4	88
75	1.6	72
50	1.5	67

1 1 / 1 2 4 : 0

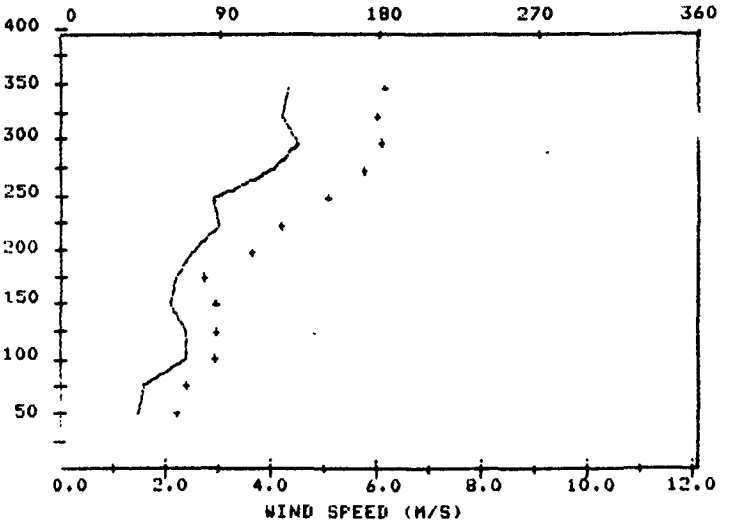

Figure 76. Doppler sounder wind profiles.

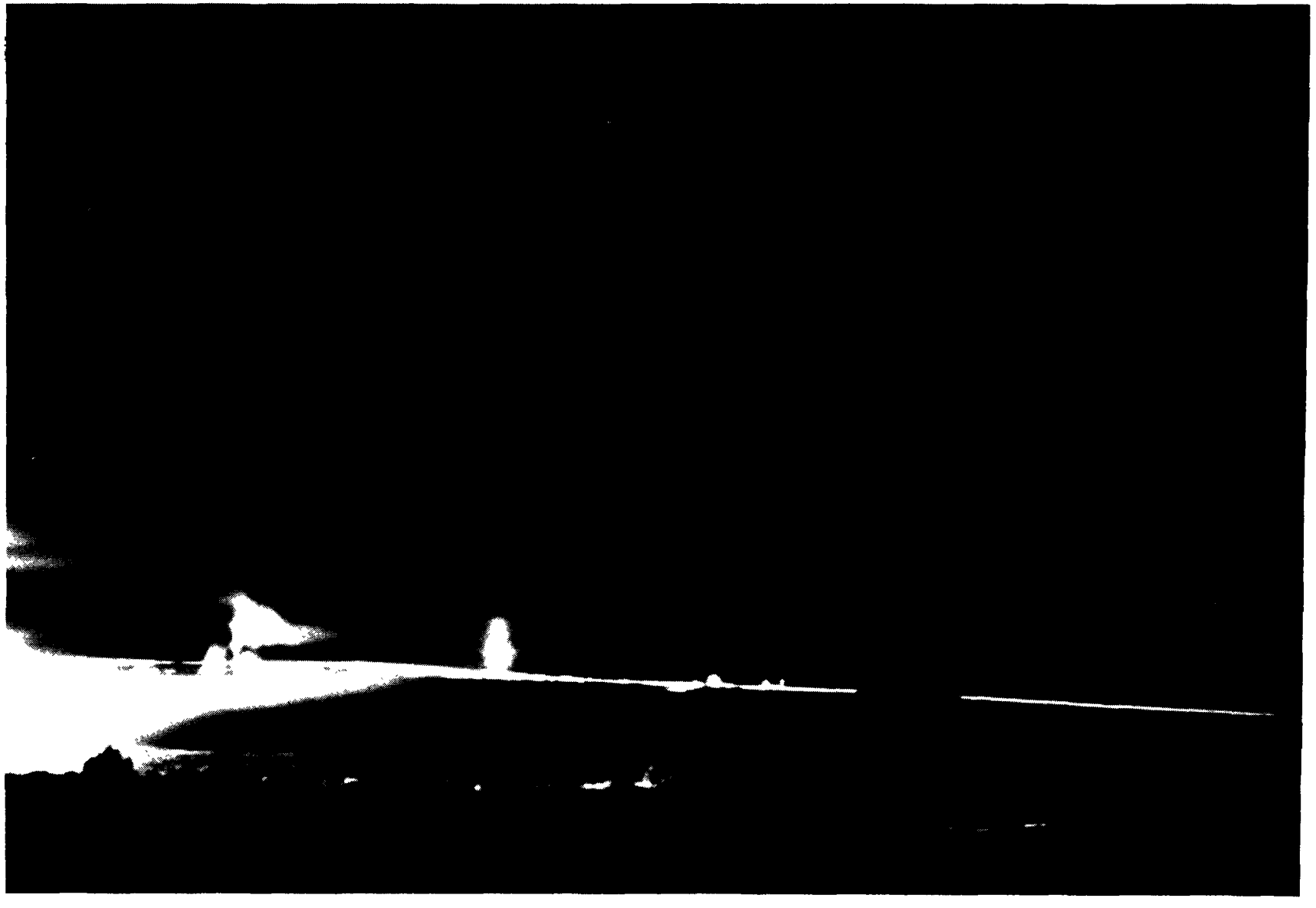

Figure 77. Five-minute exposure (Camera 1) November 12, 1983 at 0130.

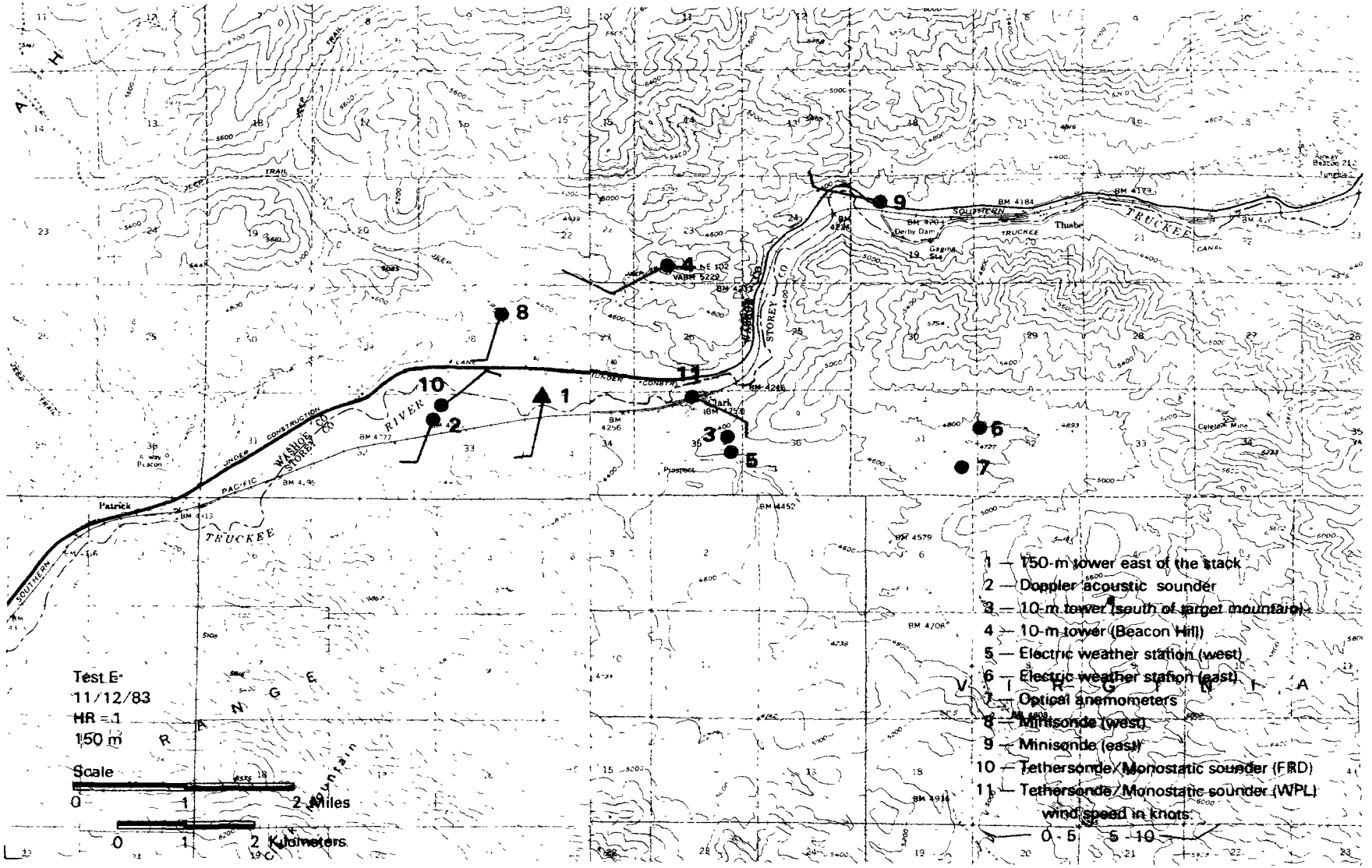

Figure 78. Geographic distribution of winds at approximate plume height.

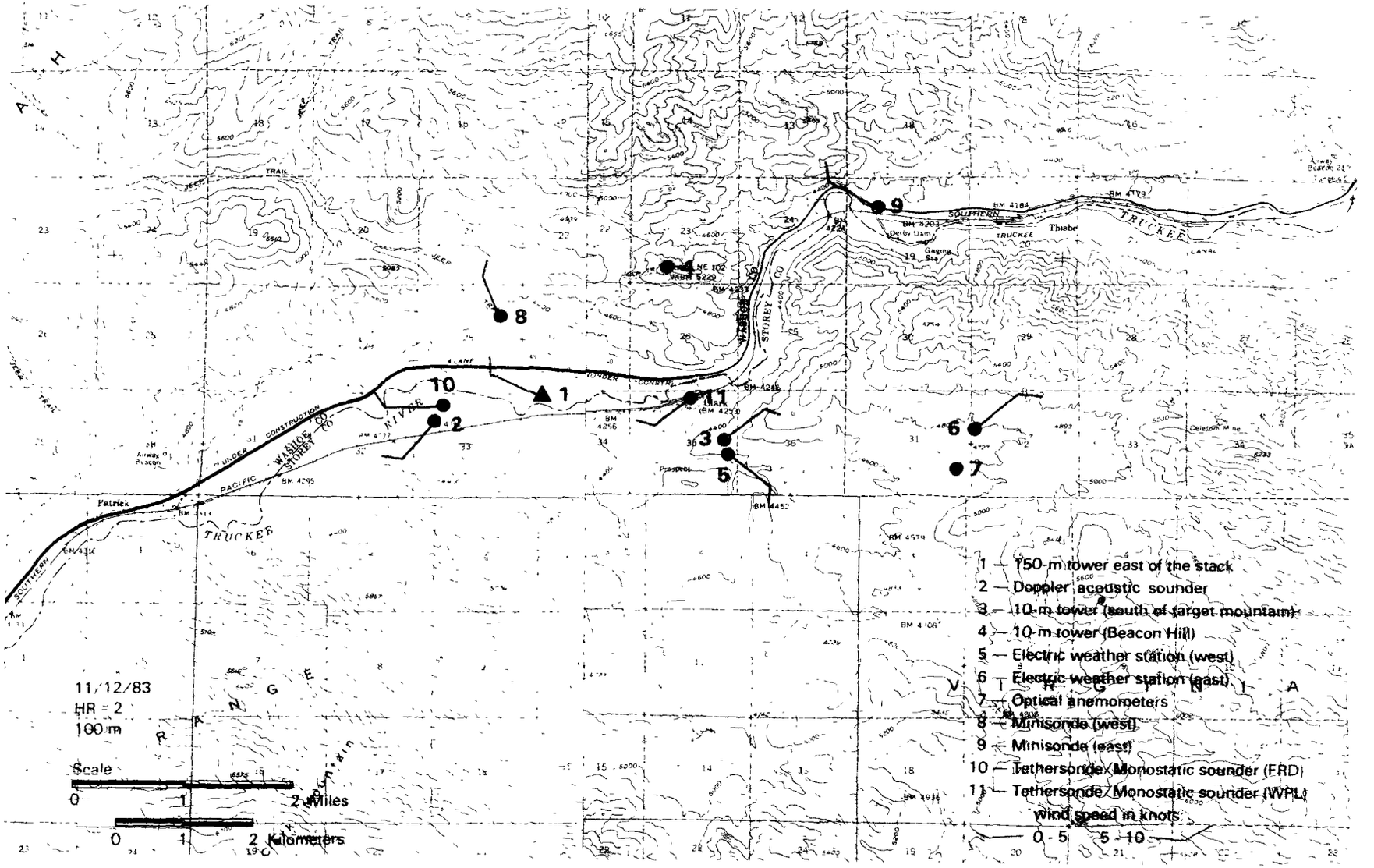

Figure 78 (Continued). Geographic distribution of winds at approximate plume height.

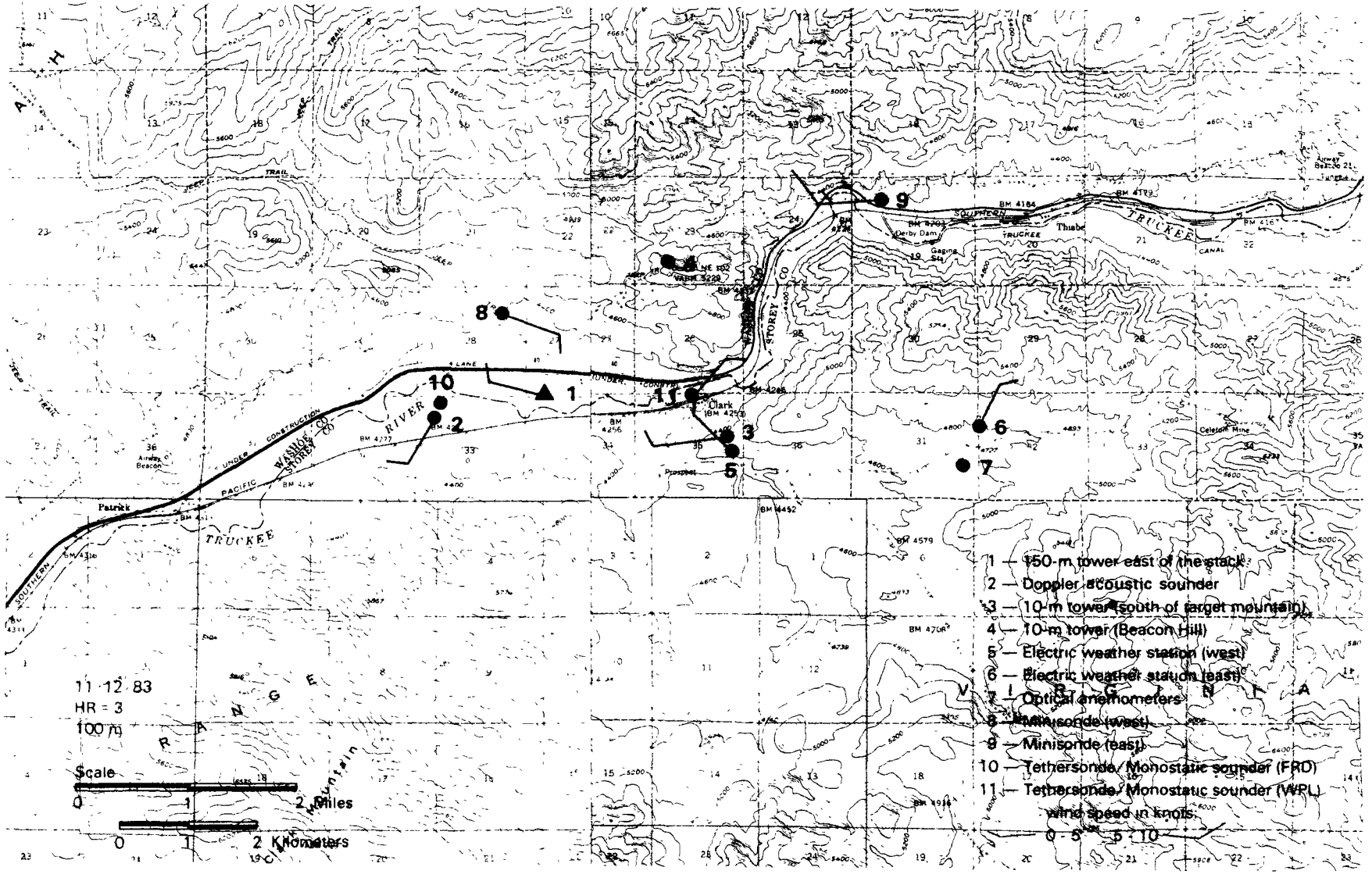

Figure 78 (Continued). Geographic distribution of winds at approximate plume height.

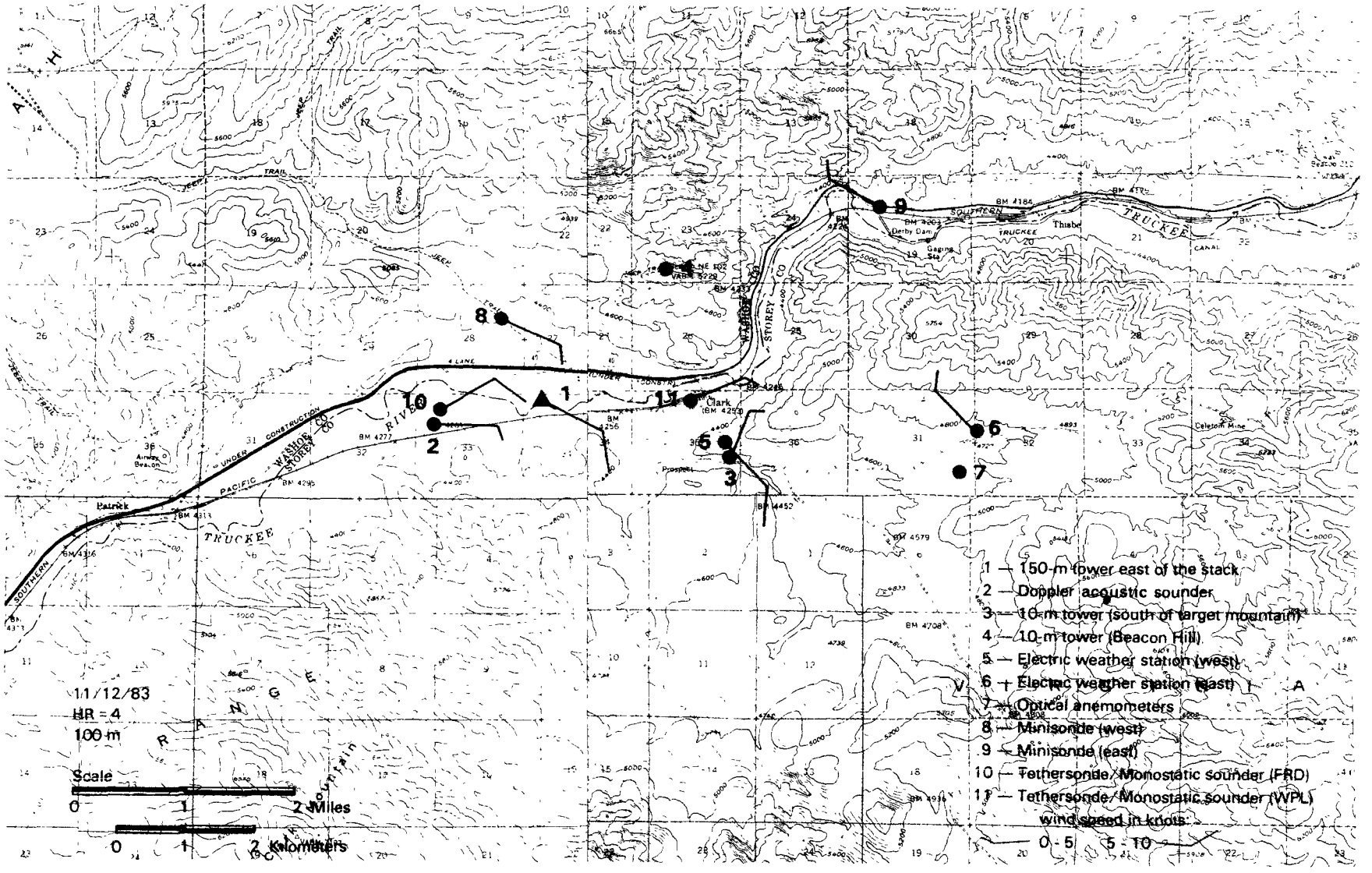

Figure 78 (Continued). Geographic distribution of winds at approximate plume height.

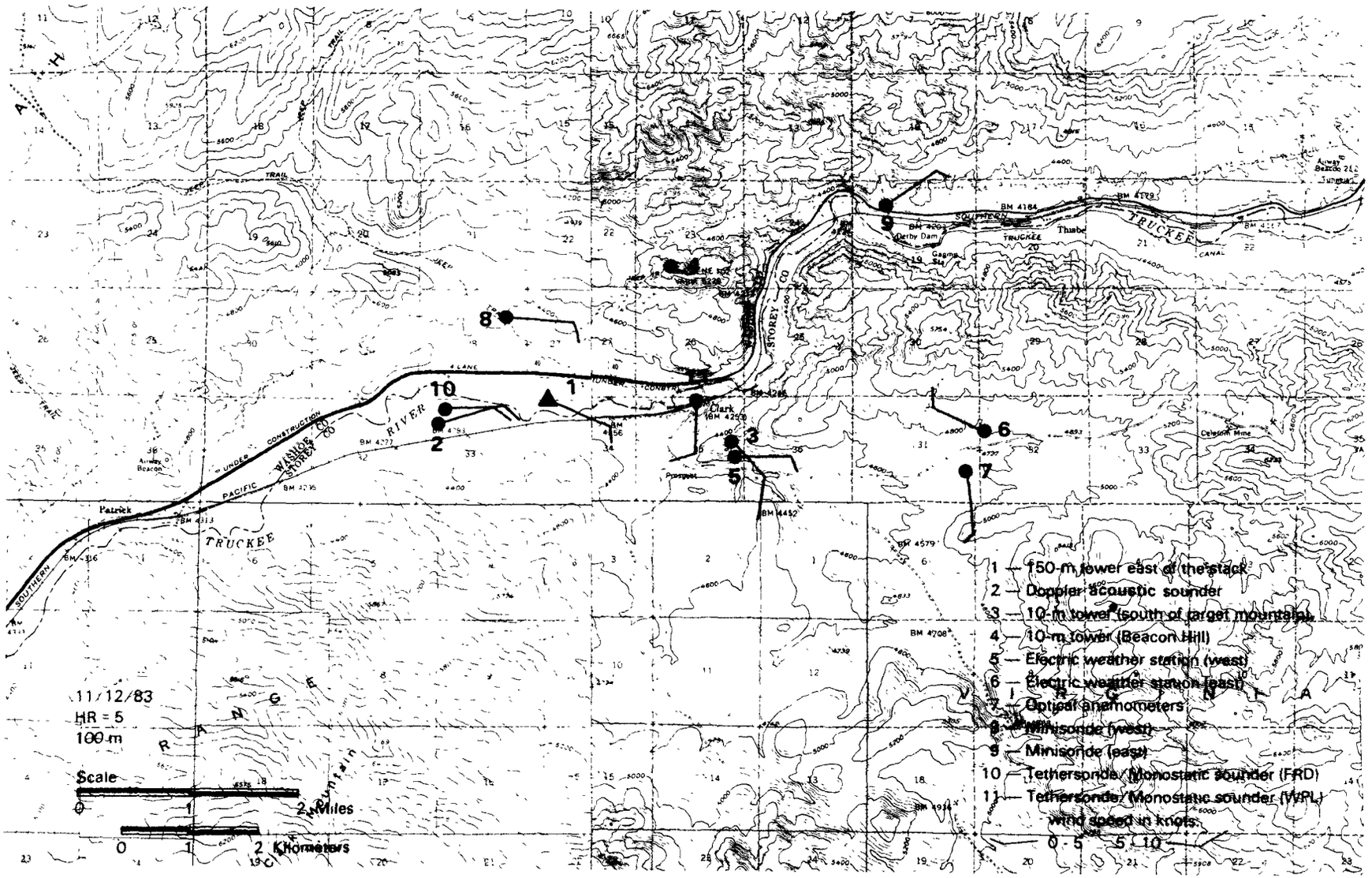

Figure 78 (Continued). Geographic distribution of winds at approximate plume height.

TABLE 19. FIVE-MINUTE METEOROLOGICAL DATA*

NOVEMBER 12, 1983, 0000-0300 PST

Hr	Sec	WS	WD	W	Sigma-v	Sigma-w	H_c	$Fr(H_c)$	Fr	N	Bulk N
0	300	1.1	237.0	-.1	.253	.200	178.0	1.1	.2	.0328	.0376
0	600	.9	249.0	.1	.291	.120	198.0	1.2	.2	.0297	.0381
0	900	.5	253.0	.1	.093	.130	143.0	.5	.1	.0318	.0381
0	1200	.3	253.0	.1	.046	.140	166.0	.6	.1	.0363	.0333
0	1500	.3	10.0	.1	.202	.130	187.0	.8	.1	.0260	.0360
0	1800	.9	70.0	.1	.330	.130	246.0	1.2	.1	.0256	.0371
0	2100	1.1	112.0	-.1	.215	.200	254.0	1.3	.1	.0253	.0349
0	2400	1.3	70.0	-.1	1.021	.200	240.0	1.3	.2	.0345	.0381
0	2700	1.1	87.0	.1	.167	.130	242.0	1.4	.2	.0333	.0386
0	3000	1.1	54.0	-.1	.129	.200	259.0	1.8	.2	.0325	.0409
0	3300	.5	7.0	-.1	.286	.130	253.0	1.4	.1	.0303	.0423
1	0	.7	310.0	-.1	.247	.200	267.0	1.2	.1	.0317	.0385
1	300	1.6	291.0	-.1	.360	.130	247.0	.9	.1	.0325	.0365
1	600	1.7	296.0	.1	.258	.130	238.0	1.0	.1	.0327	.0370
1	900	1.9	288.0	.1	.345	.120	229.0	1.3	.1	.0288	.0360
1	1200	.7	347.0	.1	.445	.120	211.0	.3	.1	.0320	.0376
1	1500	.7	237.0	.1	.097	.120	230.0	.9	.1	.0339	.0360
1	1800	.1	305.0	-.2	.081	.130	253.0	1.0	.0	.0315	.0400
1	2100	.9	270.0	.1	.245	.120	220.0	.4	.1	.0350	.0365
1	2400	1.1	249.0	.1	.394	.120	188.0	.1	.1	.0349	.0309
1	2700	.7	277.0	-.1	.349	.130	230.0	.7	.1	.0358	.0355
1	3000	.7	281.0	.1	.127	.280	159.0	.1	.0	.0402	.0309
1	3300	2.1	319.0	-.1	.451	.200	226.0	.8	.1	.0311	.0349
2	0	1.5	317.0	.1	.217	.130	233.0	1.2	.1	.0312	.0355
2	300	1.3	314.0	.1	.145	.200	227.0	1.1	.1	.0308	.0349
2	600	1.5	282.0	.1	.749	.200	238.0	1.2	.1	.0297	.0338
2	900	3.2	249.0	.1	.743	.200	206.0	1.7	.2	.0220	.0327
2	1200	2.5	253.0	-.1	.489	.280	227.0	1.5	.1	.0250	.0390
2	1500	1.7	218.0	.1	.383	.120	216.0	1.1	.1	.0319	.0395
2	1800	2.3	256.0	-.1	.711	.280	219.0	1.3	.1	.0303	.0400
2	2100	1.7	323.0	.1	1.397	.280	224.0	1.0	.2	.0353	.0360
2	2400	1.6	298.0	-.1	.360	.360	182.0	.5	.2	.0333	.0321
2	2700	1.1	29.0	.1	1.092	.510	222.0	1.0	.2	.0297	.0338
2	3000	.7	128.0	-.1	.651	.200	179.0	.3	.1	.0374	.0326
2	3300	1.7	77.00	.3	.730	.200	260.0	1.2	.1	.0323	.0284
3	0	1.7	38.0	-.1	1.311	.200	213.0	.6	.2	.0339	.0327

*Collected at the upper level of the 150-m tower.

During the last two hours, 0300-0500, the highest SF_6 concentrations were measured in the gorge at the valley floor level, yet the meteorological data suggest the plume was transported toward the west. Figure 79, a 5-minute exposure taken from the west end of the valley at 0315, shows the plume near the stack being transported toward the west with considerable plume material remaining in the target area. The Alpha-1 lidar observations* (Figure 80) also show plume material at valley level in the gorge.

How did elevated plume material enter the gorge and produce high concentrations on the valley floor? ERT observer comments suggest the turbulent transport by drainage winds off beacon hill and target mountain. The monostatic sounder at Clark also showed an increase in turbulence after 0300. See also the 150-m tower σ_w data in Figure 75. Figure 81 depicts a photograph of the monostatic sounder facsimile record for 12 November. During 0000-0300 the sounder data show decoupled layers with waves in the lower atmospheric boundary layer. At 0300 the record shows the interaction of layers--implying transport of elevated plume material from aloft--and complete mixing by about 0440.

In summary, the first three hours of Experiment 5 illustrate stable plume impingement conditions. The SF_6 plume evidently produced ground-level concentrations at samplers whose elevations were below the calculated H_c. The hours 0300-0500 illustrate the occurrence of high concentrations on the valley floor. The concentrations evidently resulted from the turbulent transport by drainage winds of elevated plume material.

Experiment 7 (November 15, 1983) 0300-0800

SF_6 was observed by samplers located east and west of the TPP stack during the morning of the 15th. Figure 82 shows maps of hourly concentrations over the five hours from 0300-0800. Plan view maps of the winds representative of 100 m and 150 m are given in Figures 83 and 84. Evidently, the winds in the valley switched back and forth from westerly to easterly and then back to westerly during the five hours. Figure 85 gives time series of wind direction and speed and σ_w measured at the 150-m level of the tower. Notice the very low values of σ_w. The highest concentrations, their locations and elevations are (Cher 1984):

*See Appendix C for an explanation of the Alpha-1 observations.

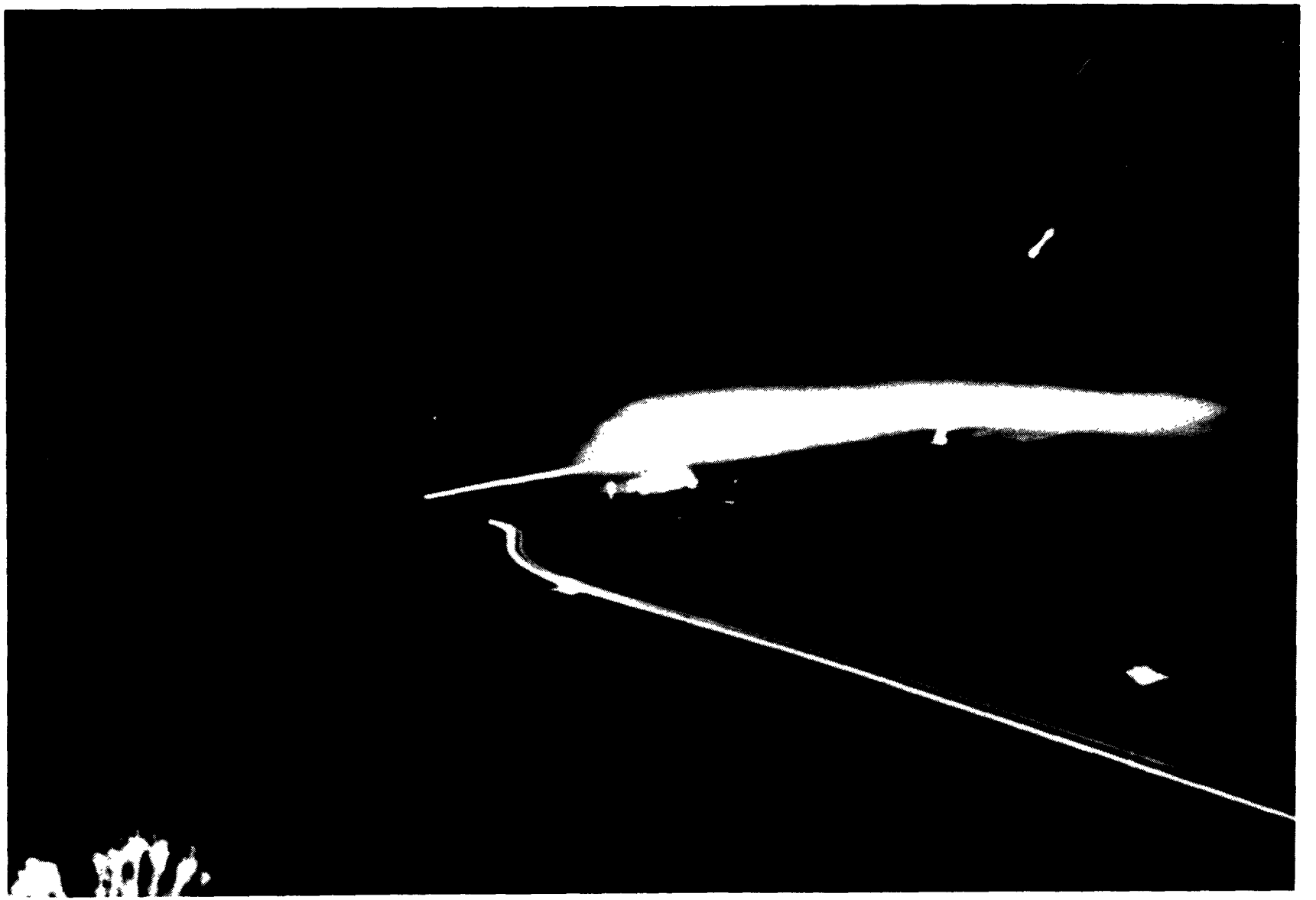

Figure 79. Five-minute exposure (Camera 3) November 12, 1983 at 0315.

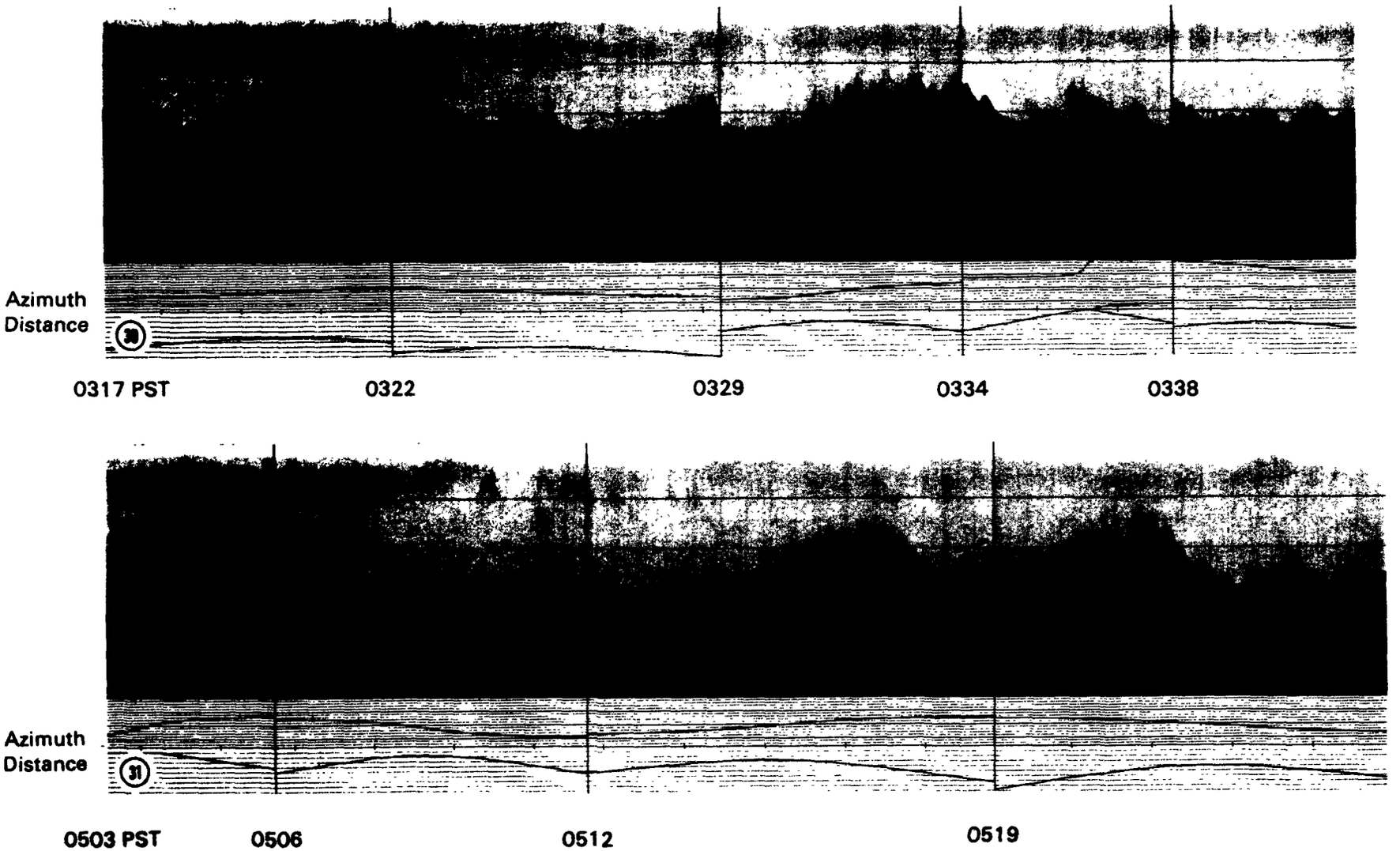

Figure 80. ALPHA-1 observations of Tracy Plume, November 12, 1983. See Appendix C for key.

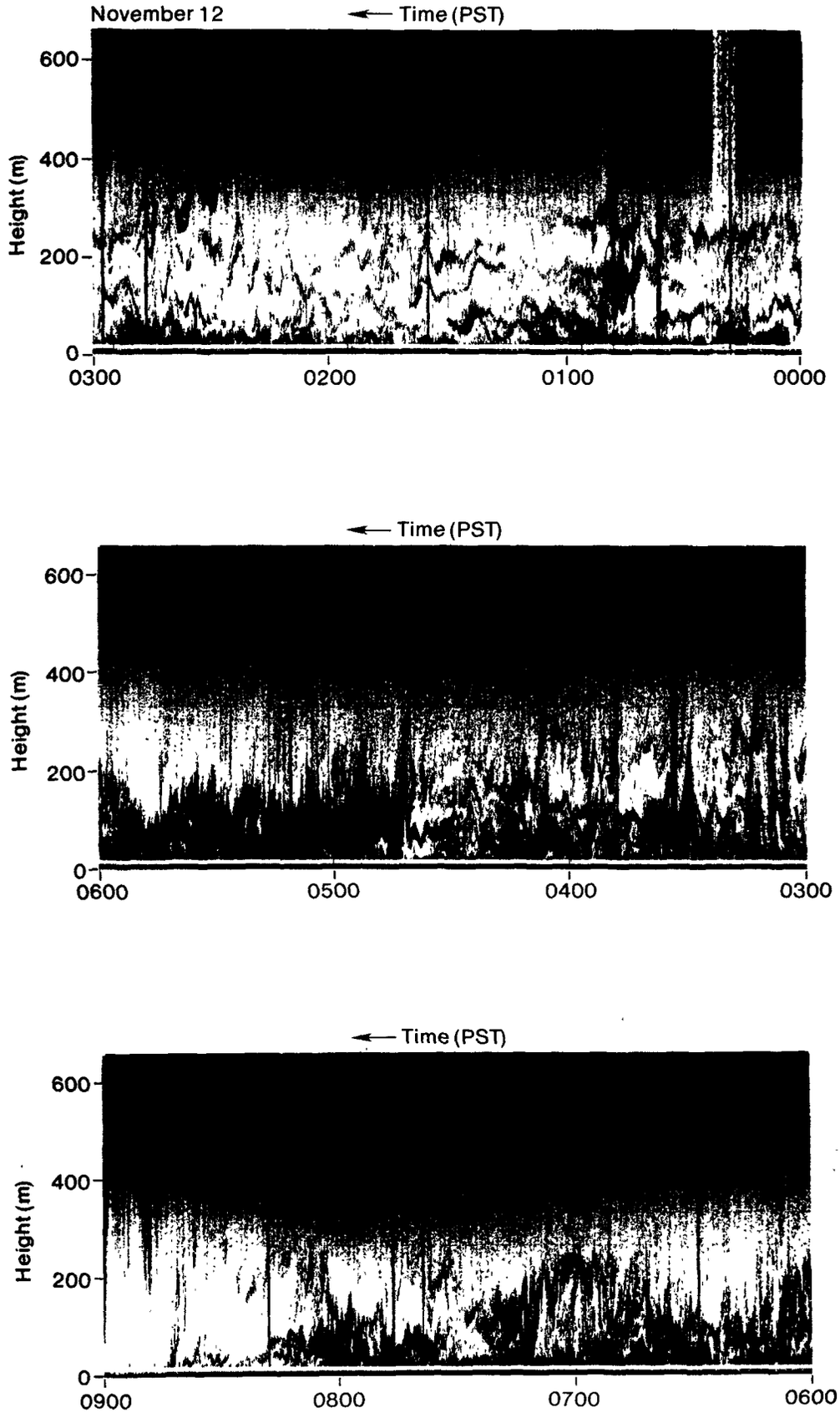

Figure 81. Eagle Picher acoustic sounder records.

Data for Hour Ending 0400 on 15-November-1983

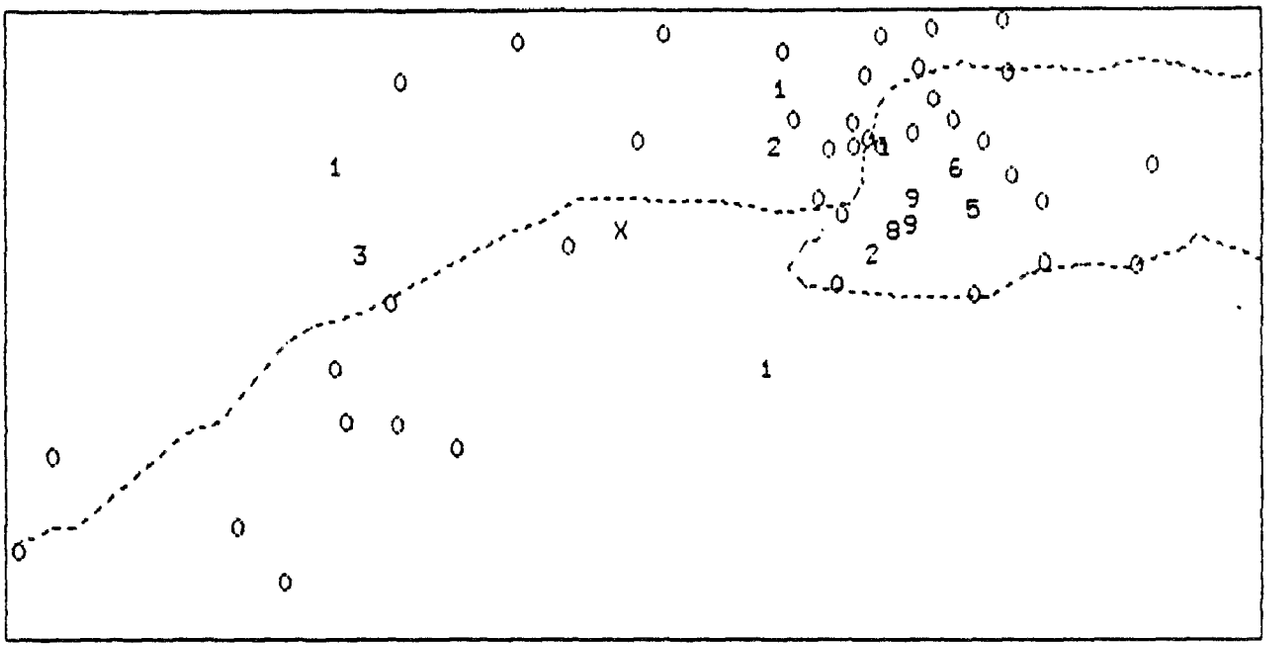

Data for Hour Ending 0500 on 15-November-1983

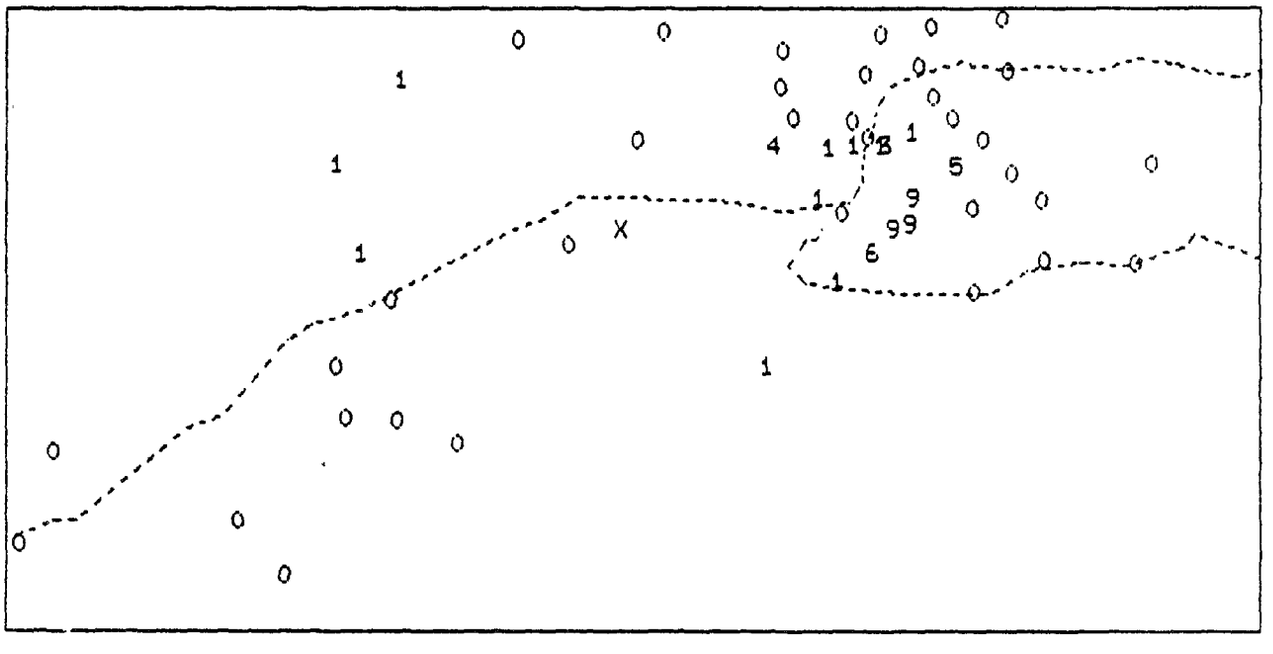

Figure 82. Hourly SF_6 concentrations November 15, 1983 0300 0800.

Data for Hour Ending 0600 on 15-November-1983

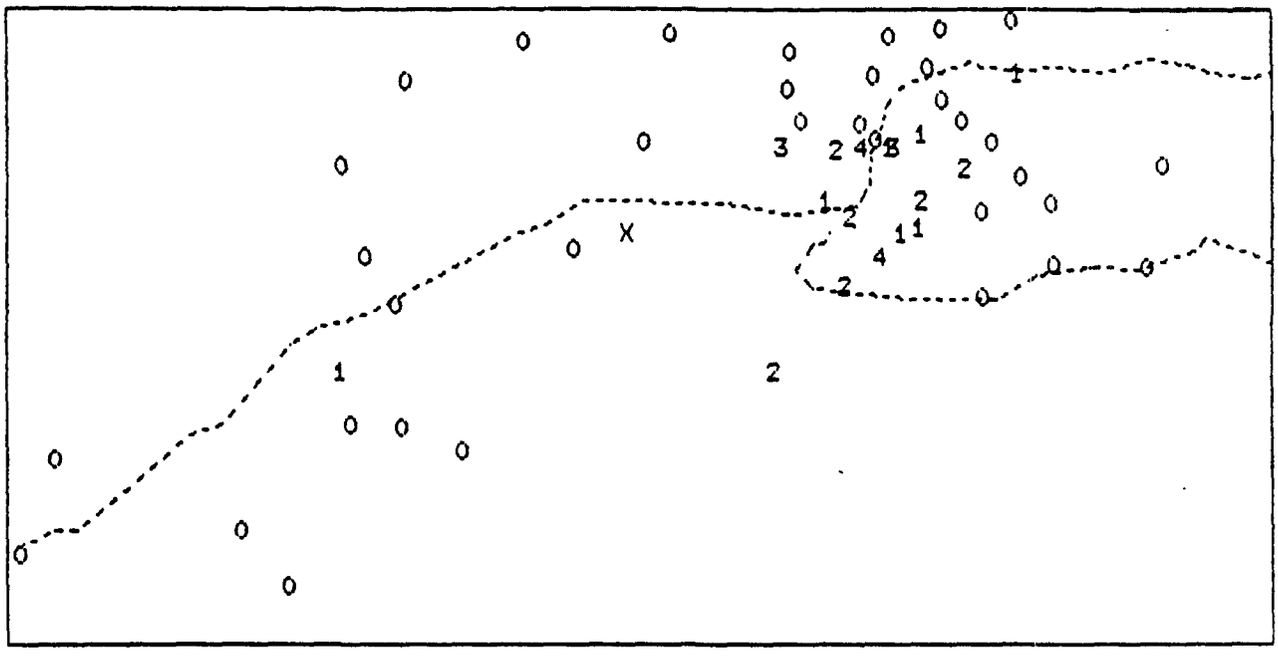

Data for Hour Ending 0700 on 15-November-1983

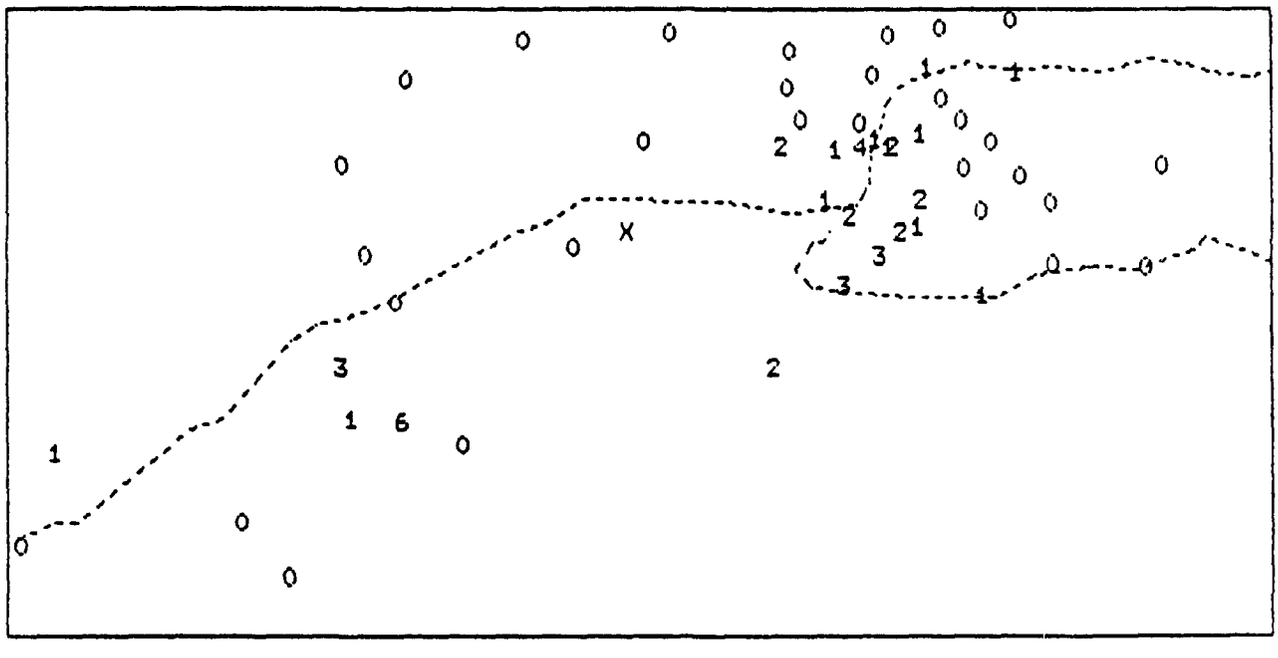

Figure 82 (Continued). Hourly SF_6 concentrations November 15, 1983 0300-0800.

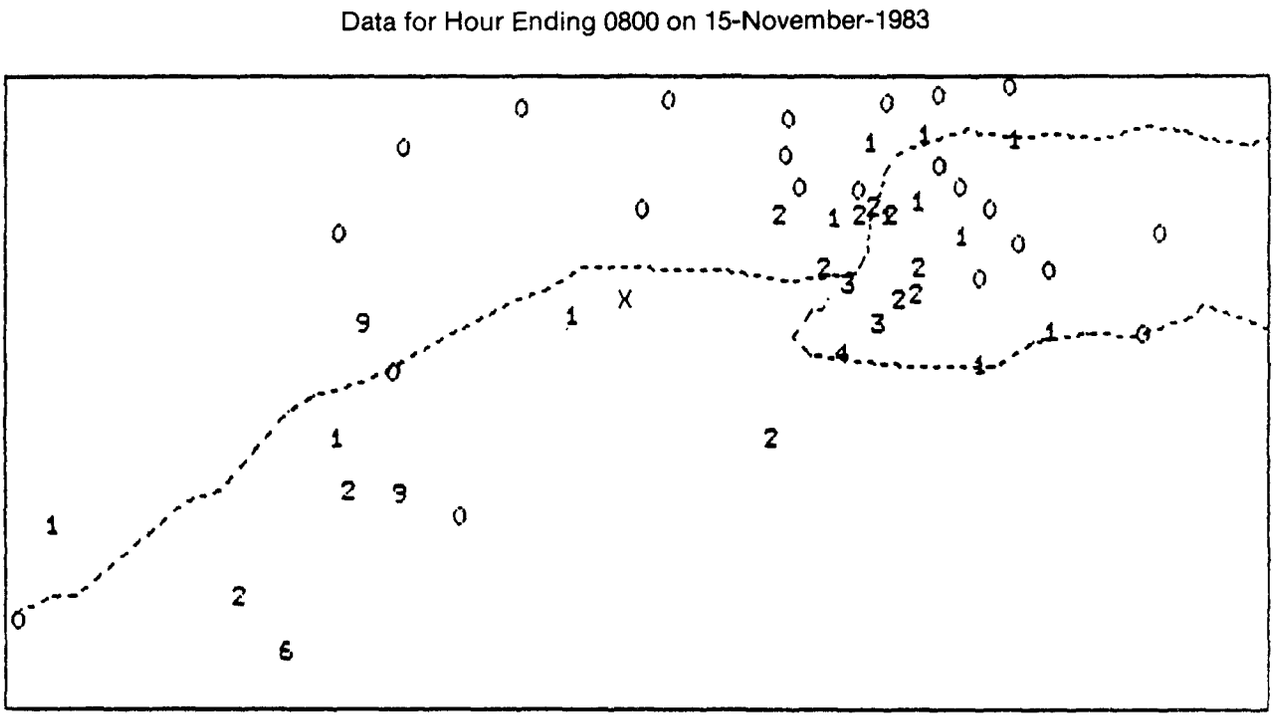

Figure 82 (Continued). Hourly SF_6 concentrations November 15, 1983 0300-0800.

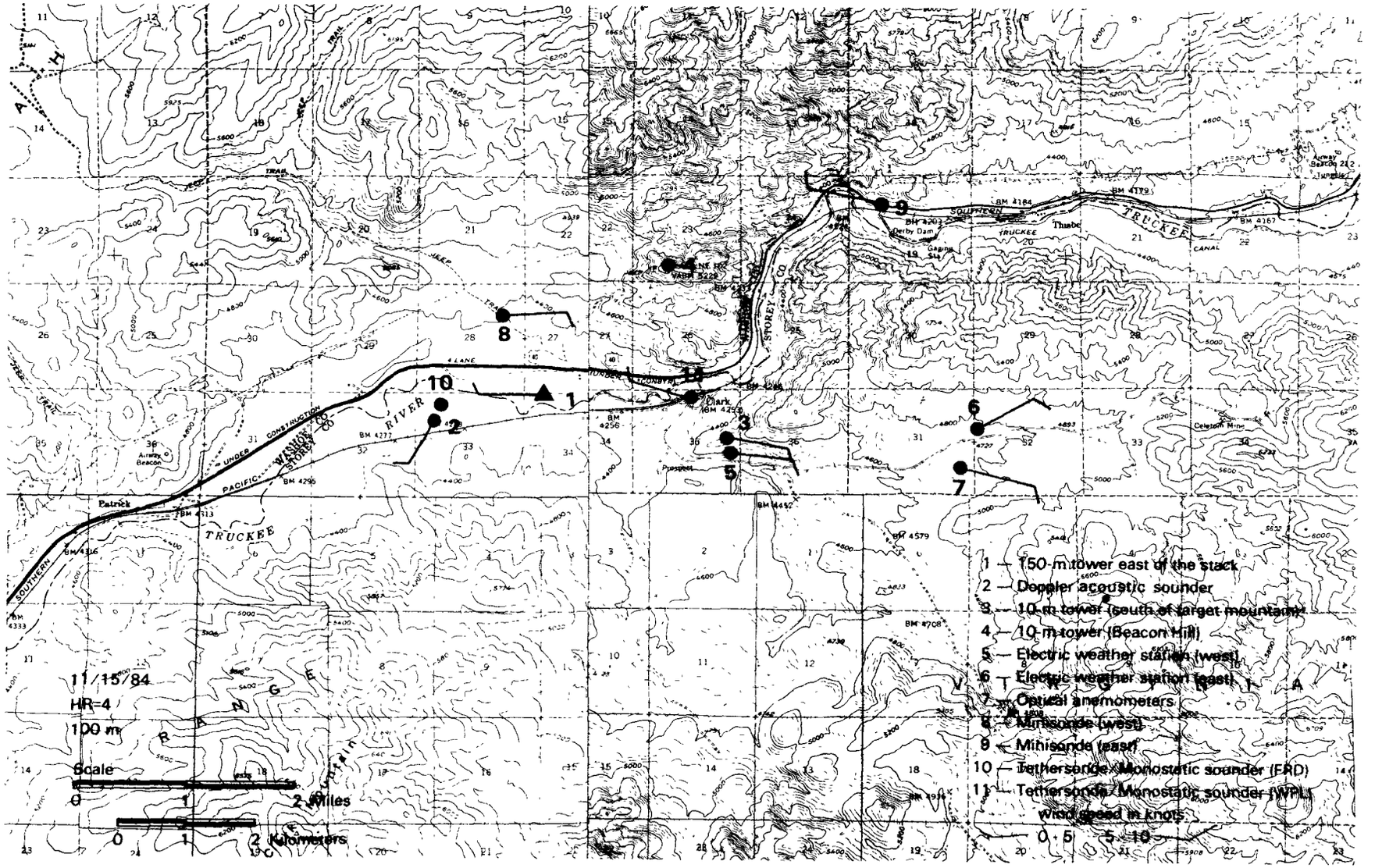

Figure 83. Geographic distribution of 100-m winds, November 15, 1983, 0300-0800.

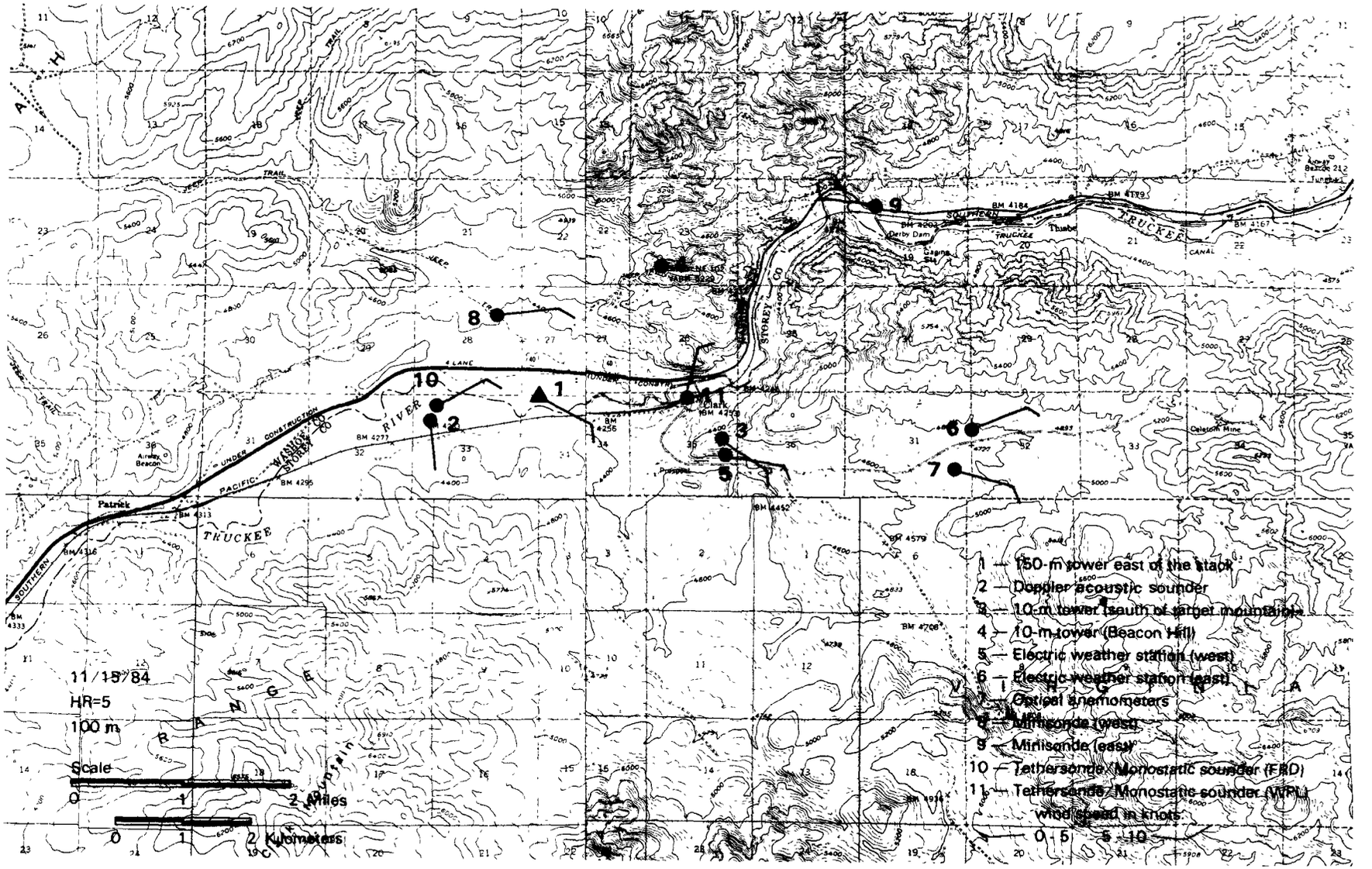

Figure 83 (Continued). Geographic distribution of 100-m winds, November 15, 1983.

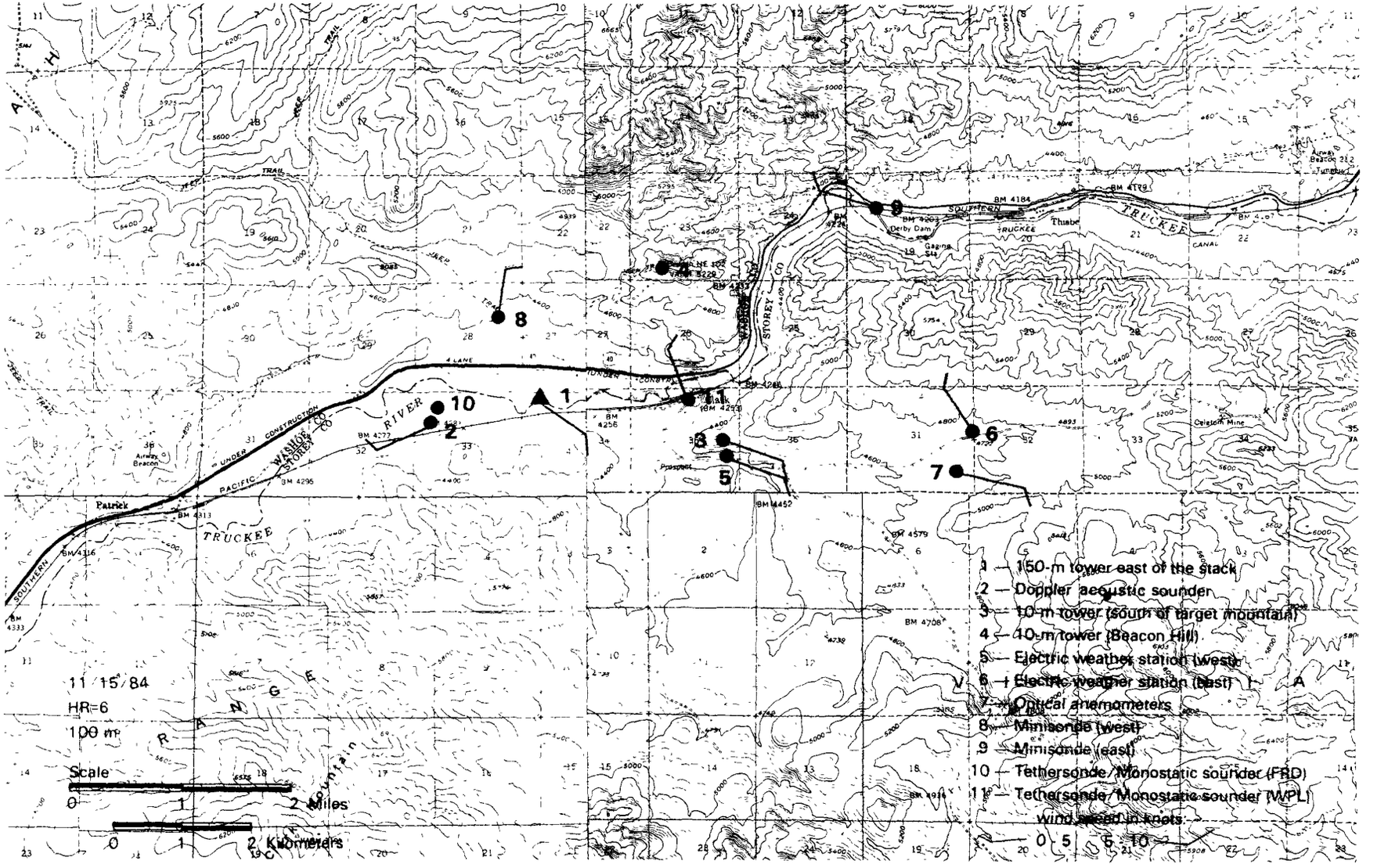

Figure 83 (Continued). Geographic distribution of 100-m winds, November 15, 1983.

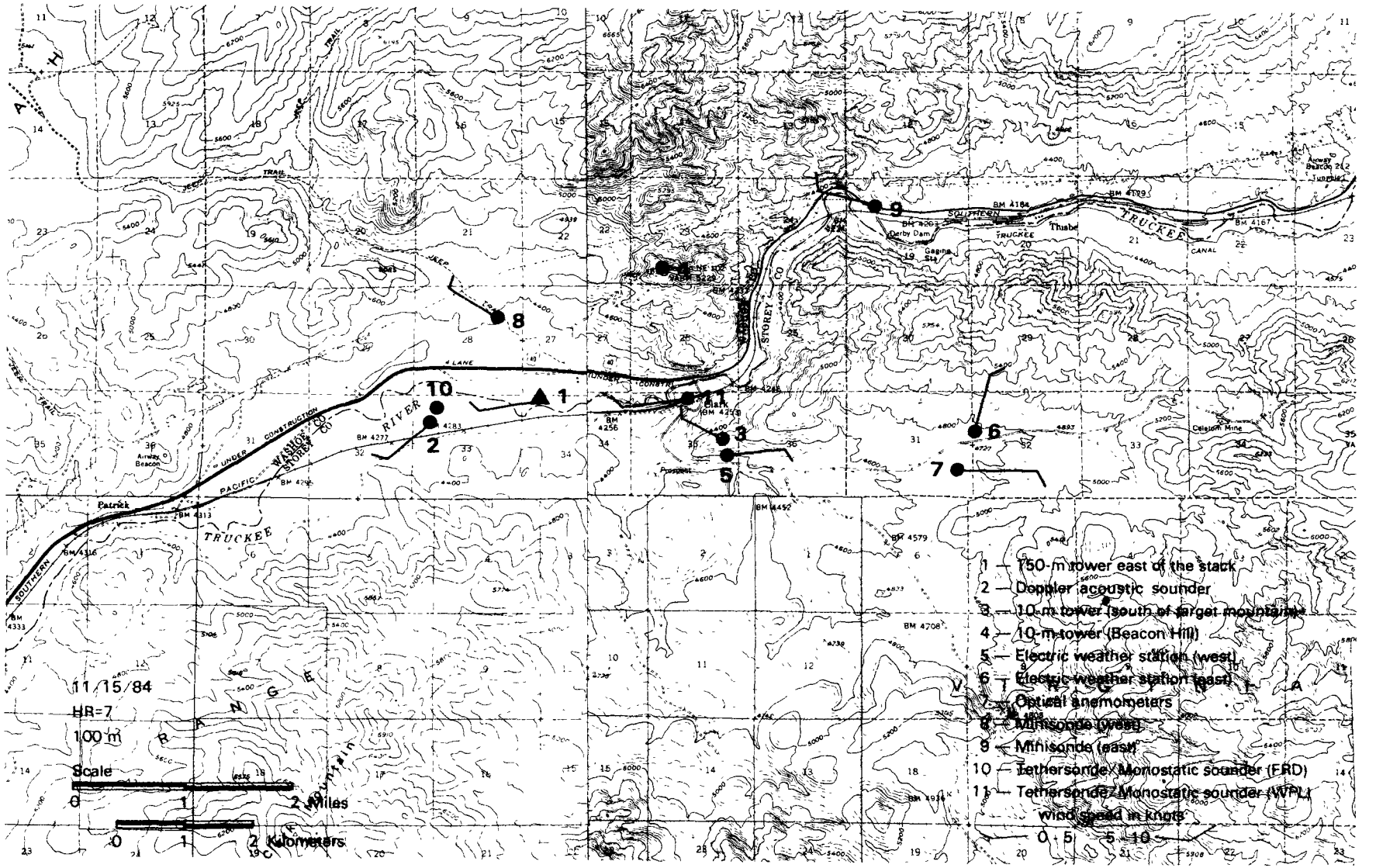

Figure 83 (Continued). Geographic distribution of 100-m winds, November 15, 1983.

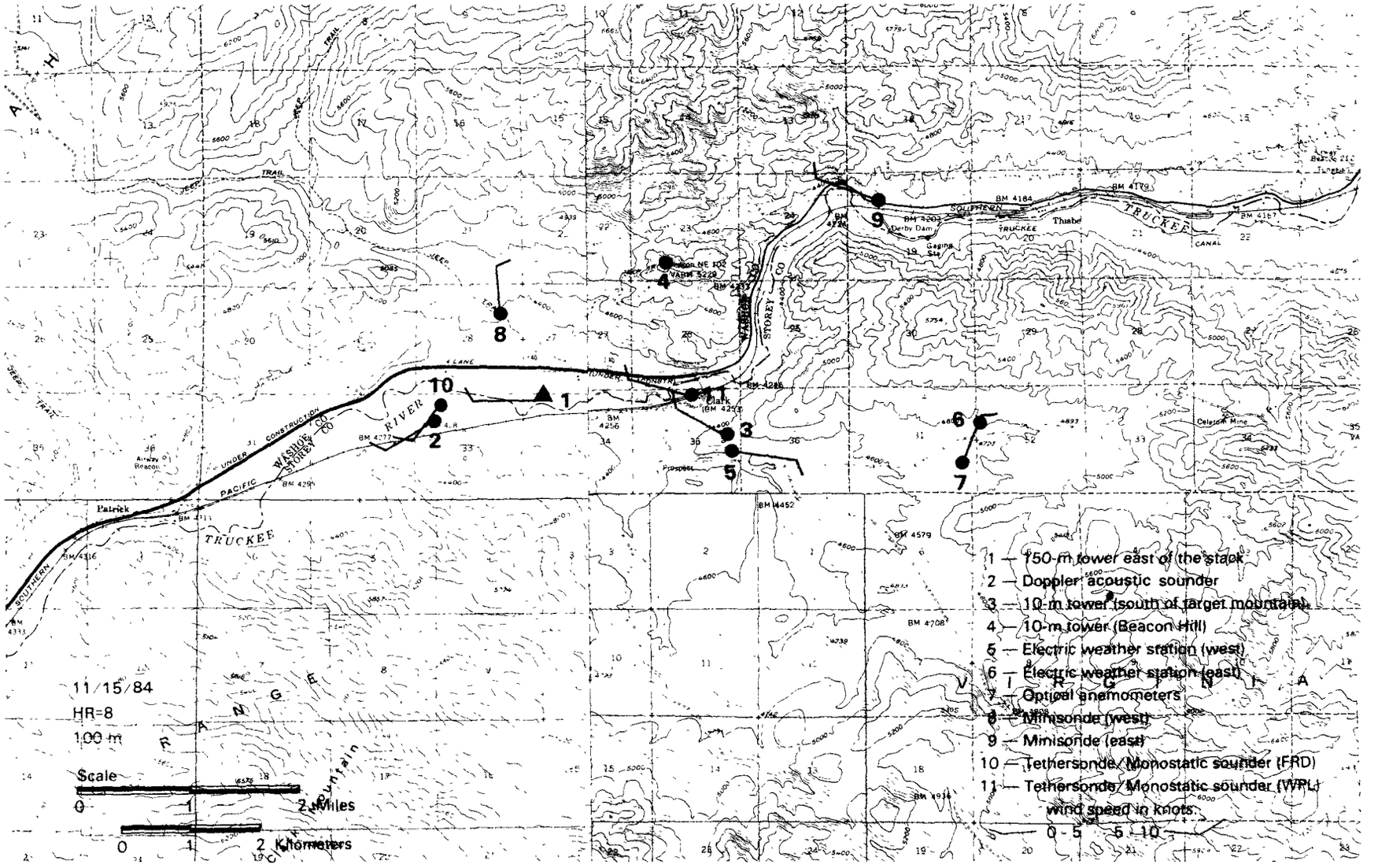

Figure 83 (Continued). Geographic distribution of 100-m winds, November 15, 1983.

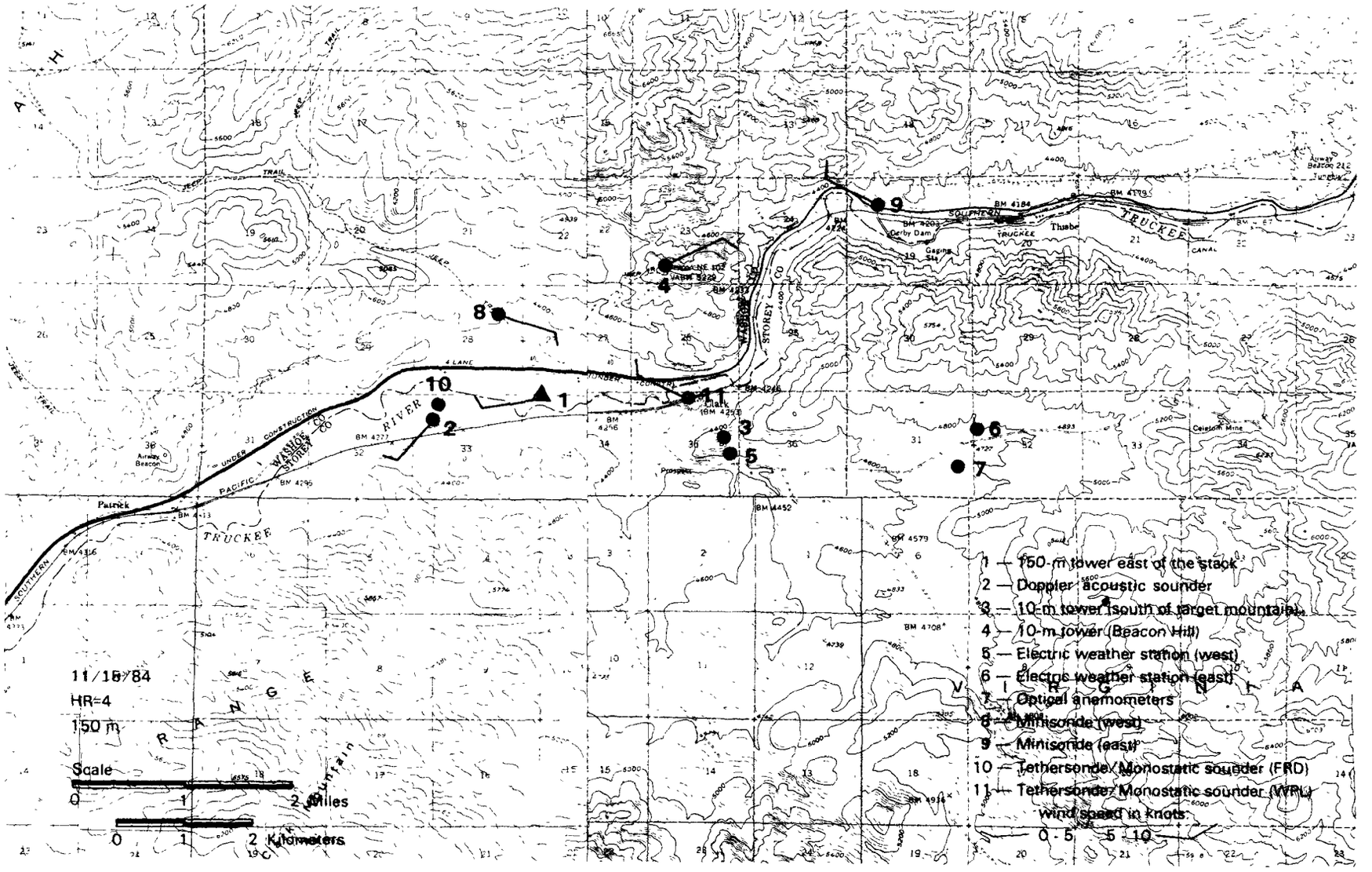

Figure 84. Geographic distribution of 150-m winds, November 15, 1985, 0300-0800.

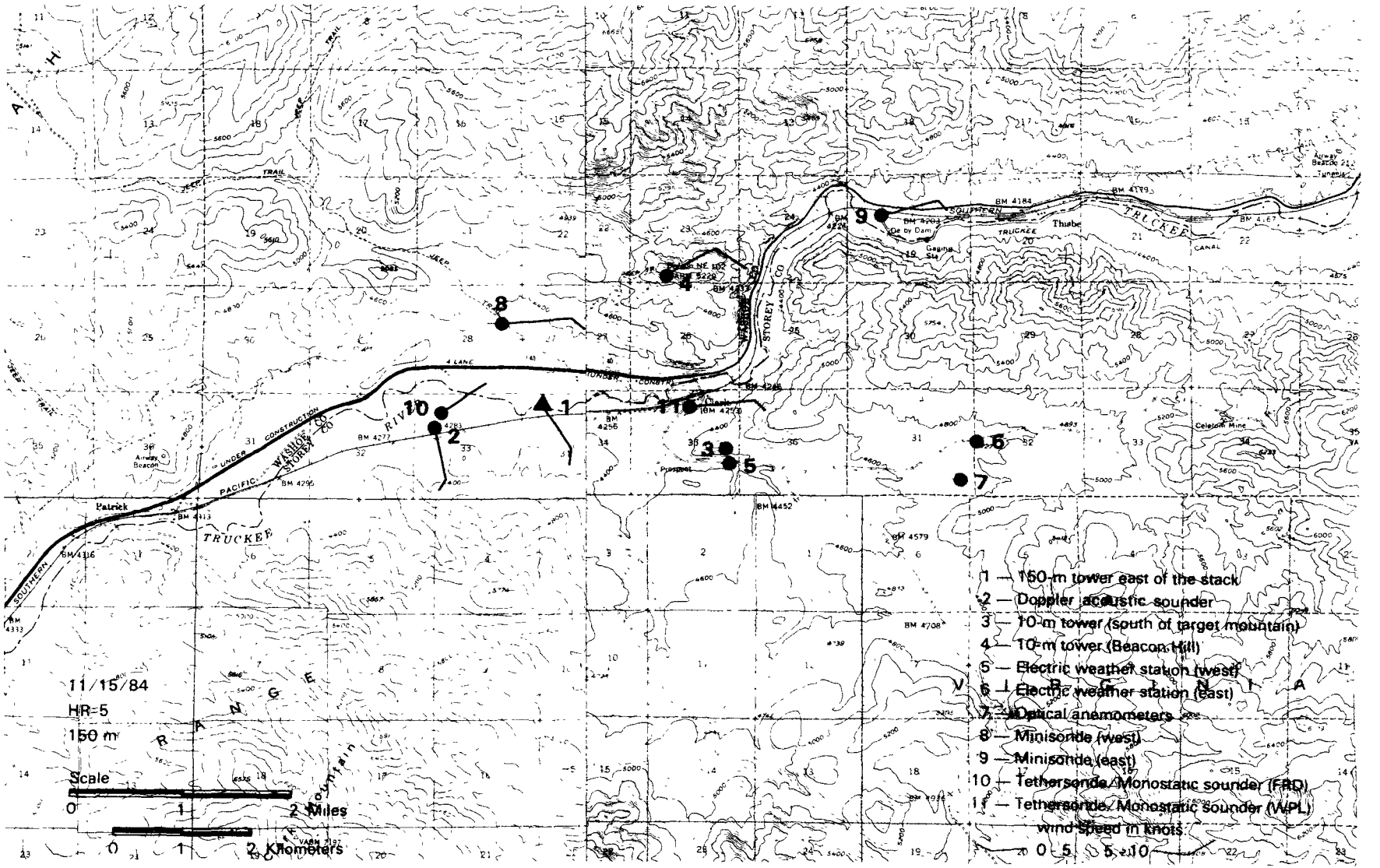

Figure 84 (Continued). Geographic distribution of 150-m winds, November 15, 1985, 0300-0800.

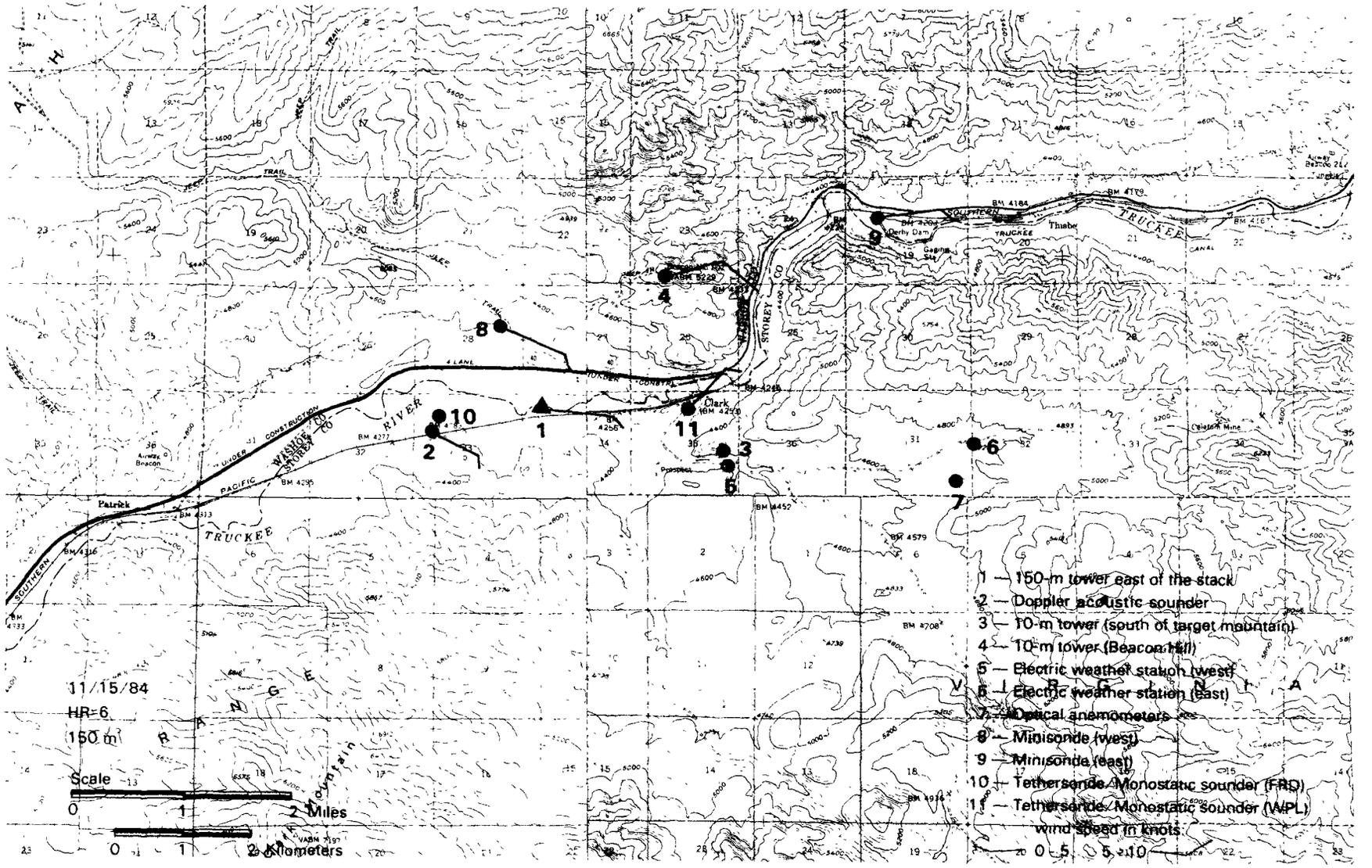

Figure 84 (Continued). Geographic distribution of 150-m winds, November 15, 1985, 0300-0800.

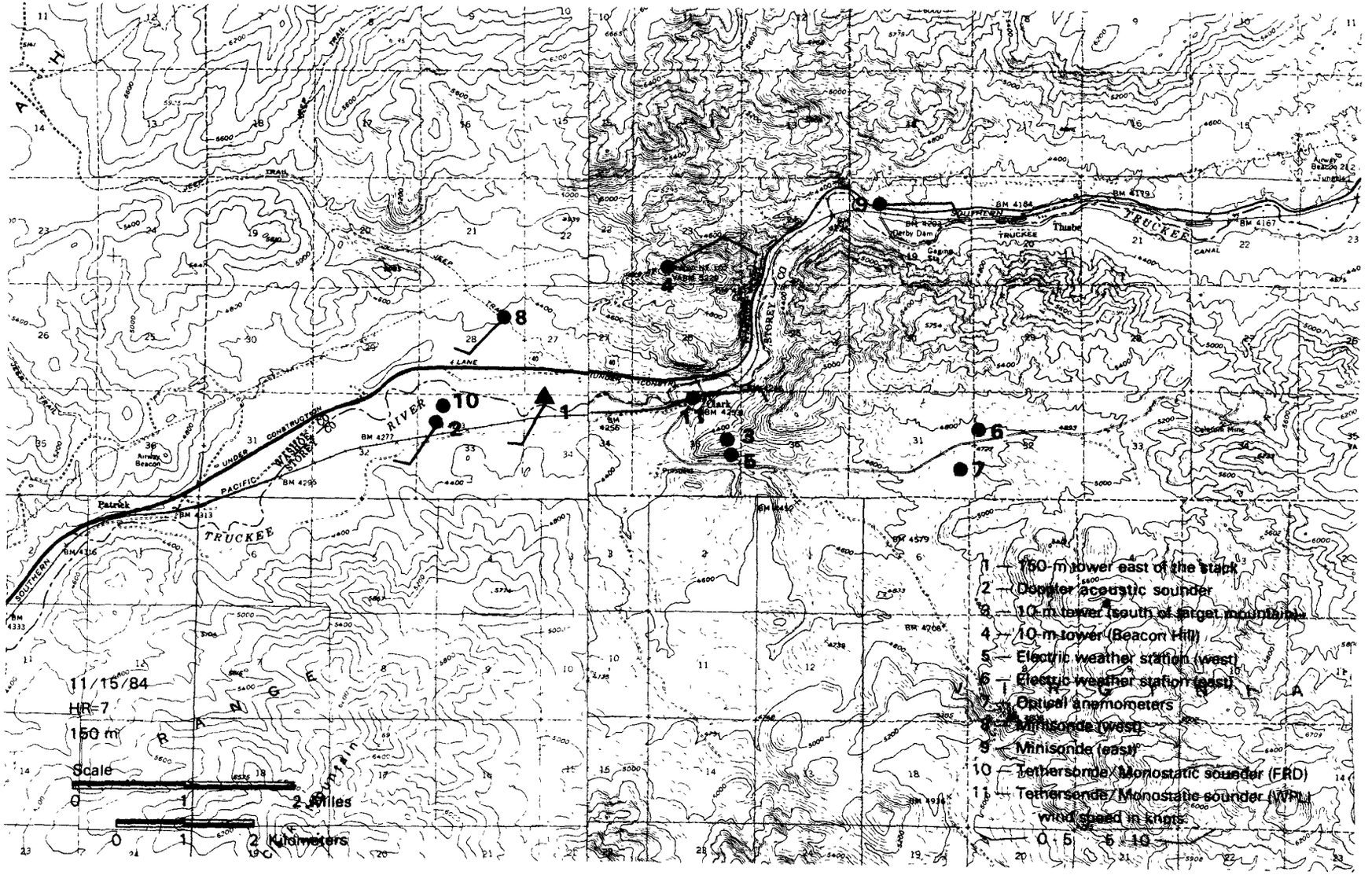

Figure 84 (Continued). Geographic distribution of 150-m winds, November 15, 1985, 0300-0800.

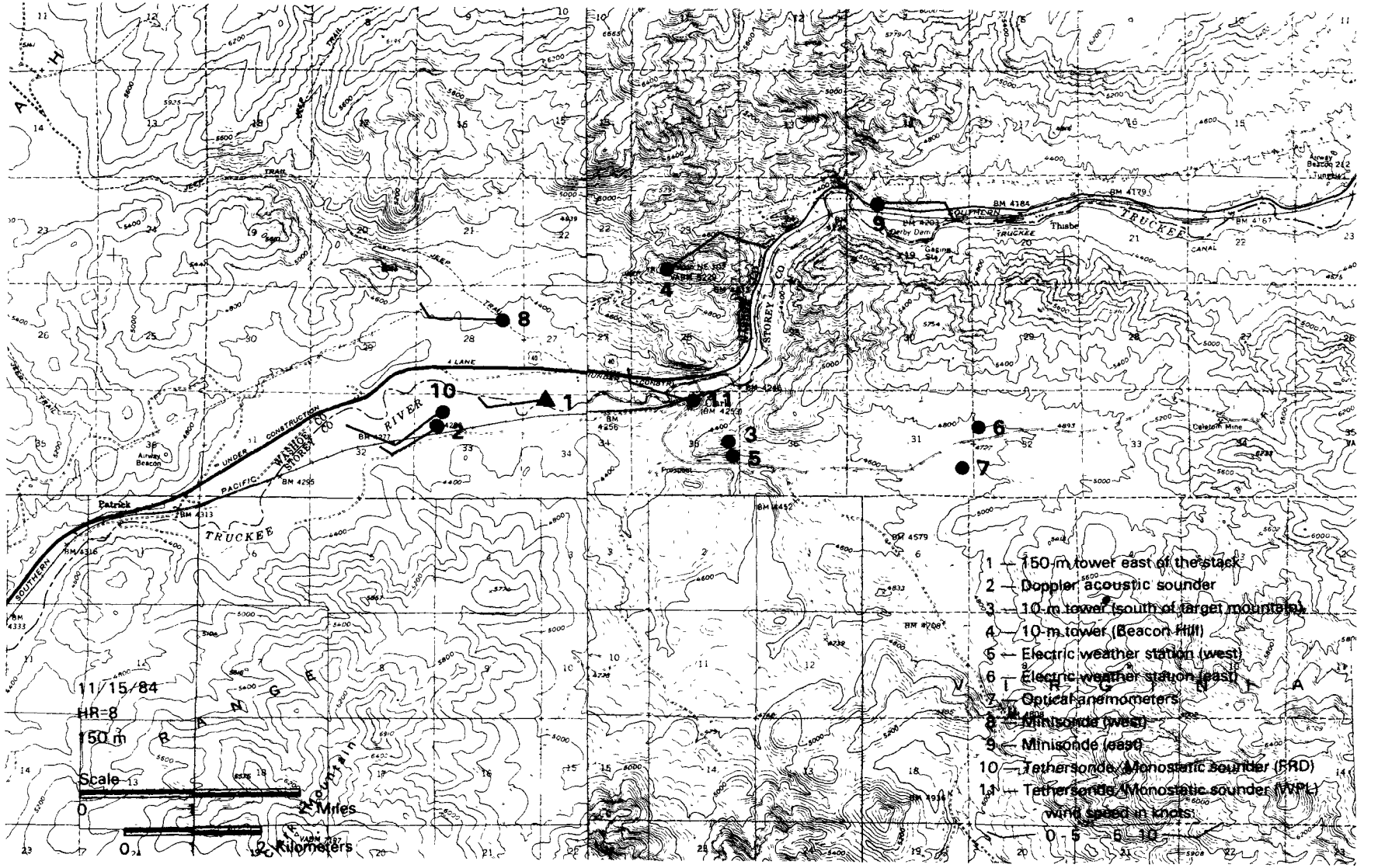

Figure 84 (Continued). Geographic distribution of 150-m winds, November 15, 1985, 0300-0800.

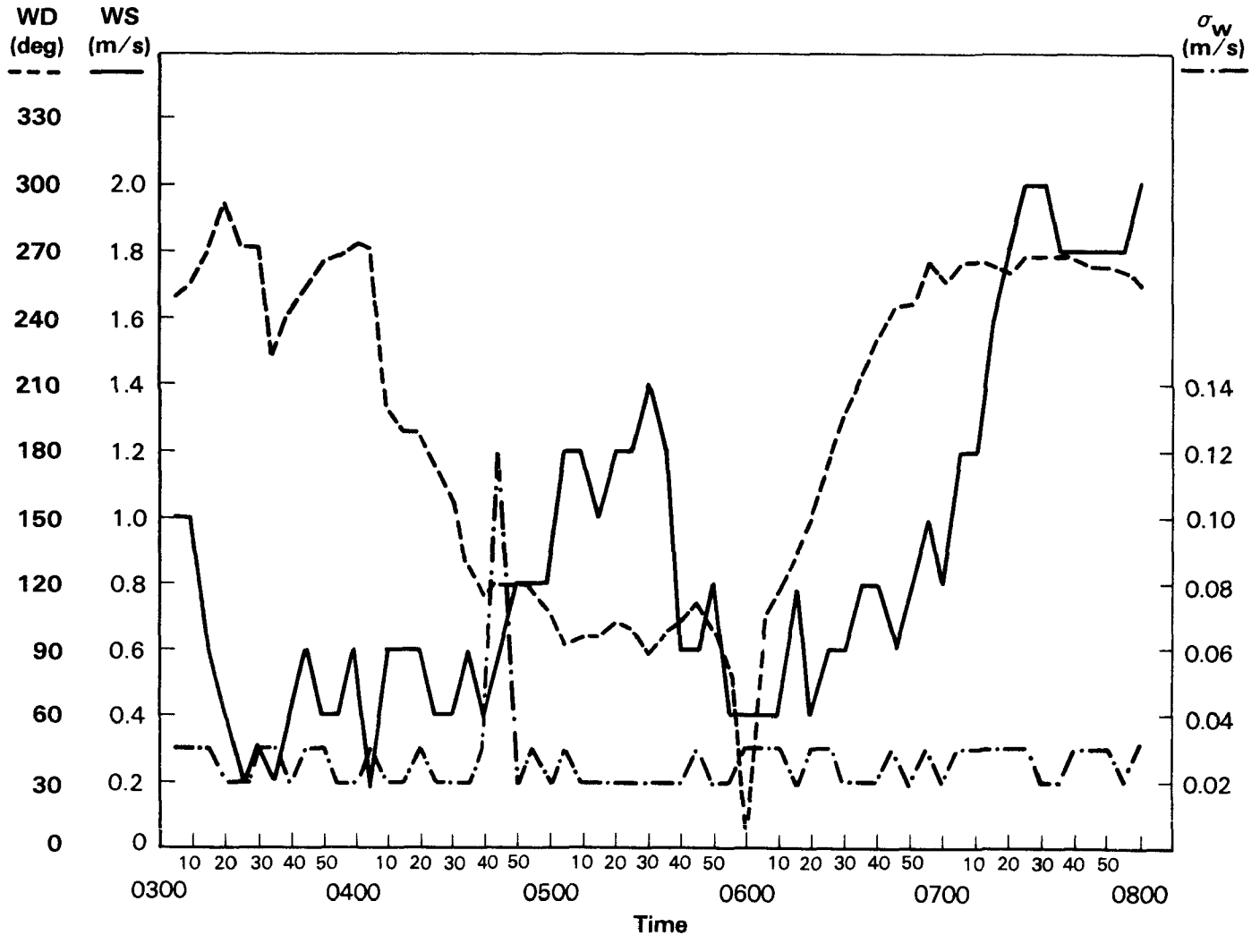

Figure 85. Meteorological data 150-m level November 15, 1983.

Time (Ending Hour)	Sampler Site	Conc. ppt	R km	θ deg	ΔZ m*
0400	10	648	5.3	89	241
	3	216	5.4	84	154
	2	180	5.0	90	170
0500	2	417	5.0	90	170
	3	313	5.4	84	165
	10	269	5.3	89	241
0600	28	92	4.5	71	113
	1	83	4.6	95	158
	31	67	3.2	62	170
	25	65	5.1	73	20
0700	56	126	5.3	231	254
	28	96	4.5	71	113
	1	77	4.6	95	158
	22	76	4.1	103	56
	53	76	5.8	246	224
0800	58	462	4.8	265	208
	56	211	5.3	231	254
	60	139	8.7	225	370

*ΔZ measured from the base of stack. Stack height is about 91 m.

During the hour 0300-0400 the plume was transported directly (but slowly) from the stack to the southwest corner of target mountain. Figures 86 and 87 show photographs of the oil-fog plume taken from Prospect hill at 0315 and 0330. The first five-minute exposure shows a very stable plume being transported from the stack toward the east at an altitude near the top of the 150-m tower. The second exposure shows plume material in the valley south of beacon hill being advected into target mountain. Figure 88 gives a photograph of the plume

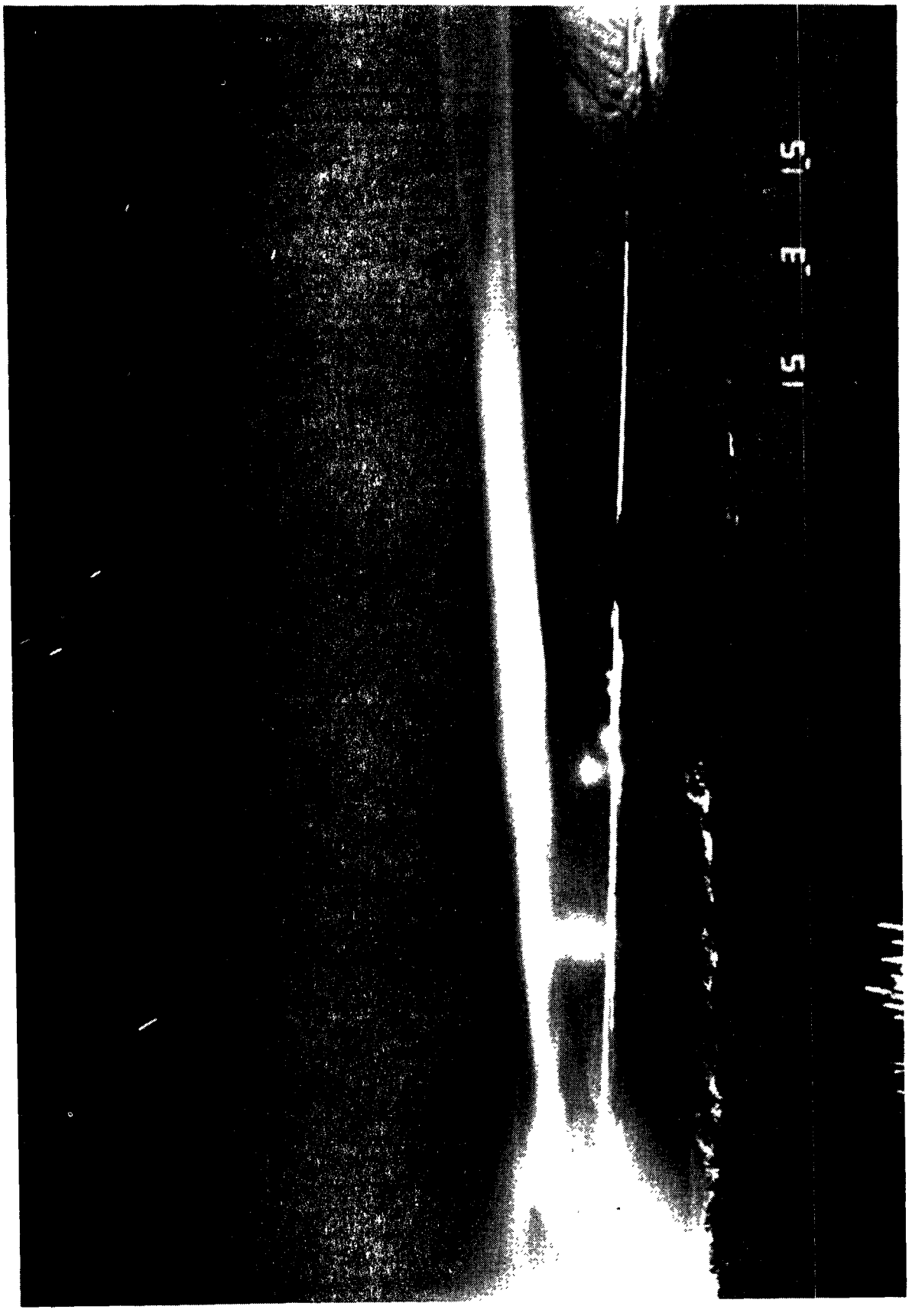

Figure 86. Five-minute exposure (Camera 1) November 15, 1983 at 0315.

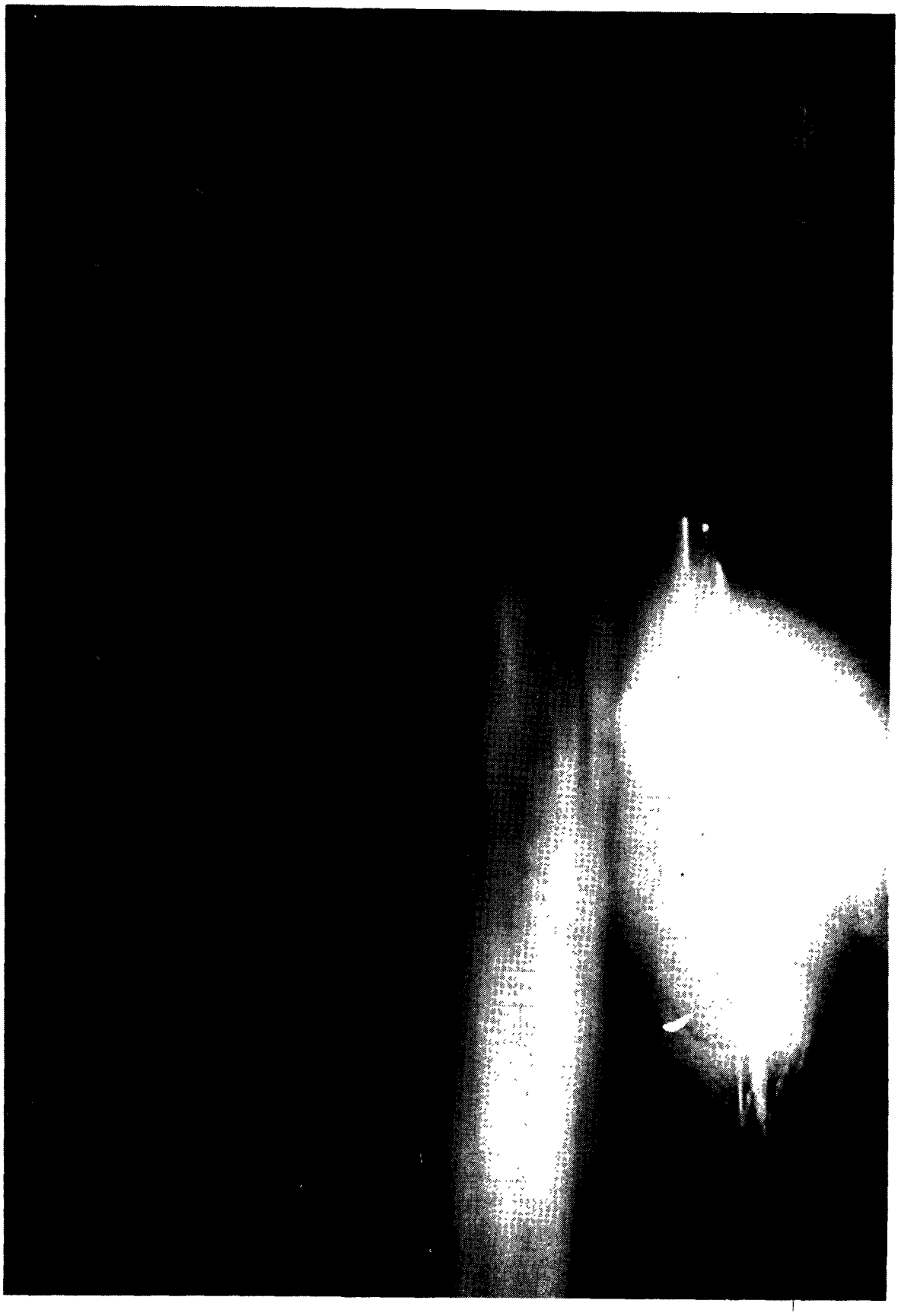

Figure 87. Five-minute exposure (Camera 1) November 15, 1983 at 0330.

Figure 88. Five-minute exposure (Camera 3) November 15, 1983 at 0330.

taken from position #3 at the west end of the valley at 0300. The exposure shows a plume with extensive crosswind diffusion being transported toward the east.

Sampler 10, at an elevation of 241 m above the stack base, measured a concentration of 648 ppt, the highest concentration observed during the entire 10-day experiment. This peak concentration, normalized by the SF_6 emission rate, is 3.1 $\mu sec/m^3$. The calculated value of H_c is 245 m.

SF_6 tracer gas remained on target mountain during the hour ending at 0500 despite the fact that winds gradually shifted to generally easterly. A photograph (Figure 89) taken at 0430 from Prospect Hill shows plume material overhead. A photograph (Figure 90) taken at 0615 from the west end of the valley shows plume material approaching from the east, eventually producing concentrations above 100 ppt at samplers west of the plant. By 0900 concentrations above 200 ppt were again observed in the target area.

Experiment 9 (November 19, 1983) 0000-0100

Figure 91 shows hourly tracer gas concentrations observed during a windy neutral period. The photograph in Figure 92 illustrates a persistent, coherent plume from the Tracy stack to the haul road south of target mountain. The winds in the valley (Figure 93) were all west-northwesterly at about 8 m/sec.

5.5 Summary of the Preliminary Experiment

The analysis of the three case study experiments and a preliminary analysis of the other data show the occurrence of stable plume impingement conditions. SF_6 concentrations were observed during stable conditions on target mountain and beacon hill. Although the sampler coverage was relatively sparse, concentrations were also observed during stable conditions in the hill 5610 complex northwest of the plant.

The highest SF_6 concentrations were observed on the southwest corner (samplers 10, 3, 2) of target mountain during Experiment 7. The elevations of the samplers that captured plume material were a few meters below the calculated hourly values of H_c. During other hours of stable plume impingement conditions, plume material was observed to stay below H_c. In short, it appears that the concept of a dividing-streamline height will be useful to distinguish flow regimes and to help simulate observed tracer gas concentration patterns in the Tracy area.

Drainage winds and katabatic effects were seen to produce ground-level concentrations on the valley floor in the gorge where the Truckee River bends to the north. Observer comments, photographs and acoustic sounder records all suggest the turbulent transport of "old" plume material from aloft to the valley floor. The fumigation of oil-fog by drainage winds was also observed on the south side of target mountain. These katabatic effects were not observed at CCB and HBR and must be accounted for in the final design of the FSPS.

Figure 89. Five-minute exposure (Camera 1) November 15, 1983 at 0430.

Figure 90. Five-minute exposure (Camera 3) November 15, 1983 at 0615.

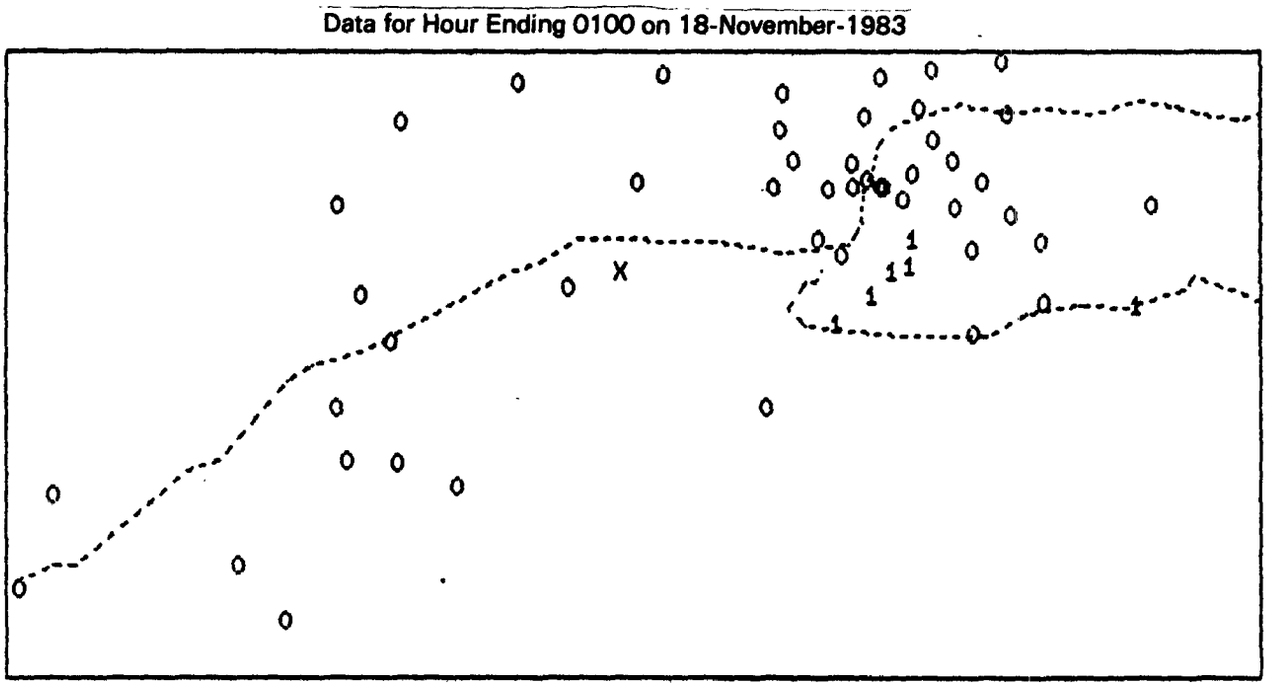

Figure 91. Hourly SF_6 concentrations November 18, 1983.

Figure 92. Five-minute exposure (Camera 3) November 18, 1983 at 0030.

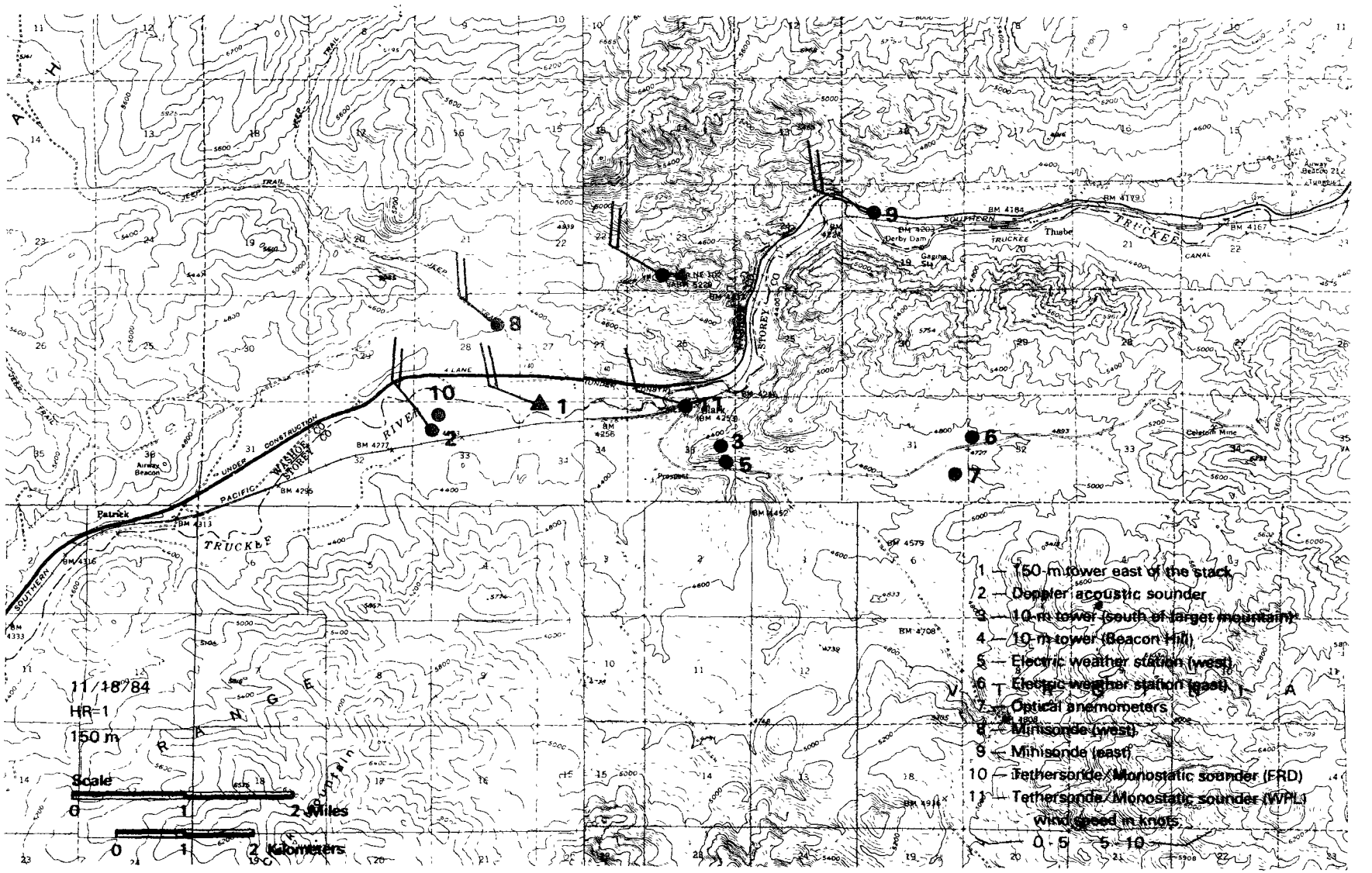

Figure 93. Geographic distribution of 150-m winds, November 18, 1983, 0000-0100.

The meteorological measurements depicted very complicated wind flows during the November experiment. Horizontal and vertical wind shears were common. These were probably caused by the combined effects of the complex terrain and migratory anticyclones and cyclones moving over the area in November. In summer and early fall we expect the flows in the valley to be more dominated by drainage flows, principally drainage down the Truckee River. In any event, during the FSPS there must be a sufficient number of meteorological measurement systems to provide information on the three-dimensional structure of winds in the valley.

Finally, the November experiment produced a data base with a wide variety of dispersion conditions--from windy, neutral cases to stable plume impingement. About 34 hours were judged good for modeling. The CTDM concepts will be tested using this data base.

5.6 Plans for the Full Scale Plume Study

The FSPS* will be conducted at the Tracy plant during the period August 6, 1984 through approximately August 27, 1984. The participants will include ERT, NOAA WPL, NOAA ARLFRD, and SRI International. Table 20 provides a schedule of the daily experiments.

The FSPS will commence with two 4-hour shakedown experiments on the 6th and 7th. These will start around 0300 PST and end around 0700 PST and will be conducted to test the equipment and the experiment protocol. The shakedown experiments will be followed by 12 10-hour tracer and simultaneous flow visualization experiments. These will run primarily during the nighttime hours to capture stable conditions and are scheduled to take photographic advantage of the full moon on the 11th.

The experimental methods of the FSPS are based on the preliminary experiment conducted in November and to a large extent are similar to the methods used and tested at CCB and HBR. The FSPS at the Tracy station will include:

- Releases of SF_6 and oil-fog from the 300-ft stack and CF_3Br from various heights on the 150-m tower;
- Operation of 110 tracer gas samplers at 107 locations (four will be on the 150-m tower);

---

*The detailed plans are described in the Work Plan for the Full Scale Plume Study, ERT document P-B876-625, May, 1984.

TABLE 20. FSPS SCHEDULE*

M	6 Aug	0300 - 0700**
T	7 Aug	0300 - 0700
T	9 Aug	2000 - 0600
F	10 Aug	2000 - 0600
S	11 Aug	2000 - 0600
W	15 Aug	2200 - 0800
T	16 Aug	2200 - 0800
F	17 Aug	2200 - 0800
M	20 Aug	2200 - 0800
T	21 Aug	2200 - 0800
W	22 Aug	2200 - 0800
S	25 Aug	0000 - 1000***
S	26 Aug	0000 - 1000
M	27 Aug	0000 - 1000

*Schedule subject to change depending on weather conditions.
**Only the fan for the 300-ft stack will be operating during the first 11 experiments.
***The 120-MW unit will be operated during the last three experiments.

- Fixed meteorological measurements:
  - a 150-m tower instrumented at six levels (instruments will include sonic, propeller and cup-and-vane anemometers and temperature and radiation sensors),
  - three 10-m towers instrumented at one level,
  - one 10-m tower instrumented at two levels,
  - three monostatic acoustic sounders,
  - two doppler acoustic sounders, and
  - two solar-powered electronic weather stations;
- Two tethersondes:
  - one operated at plume elevation to document meteorological conditions representative of the effective source height, and
  - one operated to measure vertical profiles of meteorological parameters upwind of the source;
- Two radar balloon tracking systems:
  - one located near the west end of the valley to measure the approach flow, and
  - one located north of the plant to document the winds near potential impact areas;
- Ground-level tracer gas concentrations;
- Airborne and ground-based lidar measurements;
- Photographs (from five locations) and movies; and
- A command post near the 150-m tower that includes:
  - real-time display of data from the 150-m and 10-m towers,
  - radio base station, and
  - facsimile output of weather maps.

The meteorological data will be archived and displayed in real-time by a system of onsite minicomputers. Real-time information on ambient meteorological conditions will aid in understanding the dispersion phenomena and will help the field managers maintain real-time experimental control. The real-time operations management will be supplemented by near real-time lidar data, a 48-hour turnaround on the tracer gas concentrations, and a 48-hour turnaround on the photographs. Provisions will be made for data analysis in the field to help guide the experiment. Figure 94 illustrates the layout of the FSPS.

Oil-fog and SF_6 will be released from the 91.4-m stack. CF_3Br will be released from one of the three levels (100, 120 or 140 m) on the 150-m tower. The tracer gases will be sampled at about 107 locations in the valley and on the mountains.

ARLFRD will operate 110 samplers during each approximately 10-hour experiment. All samplers will be used to get one-hour averages. Four samplers will be operated at the 150-m tower. Each 10-hour experiment could produce 1,100 bags and 2,200 concentrations. The samples will be analyzed and concentration maps produced within about 48 hours after collection of the bags.

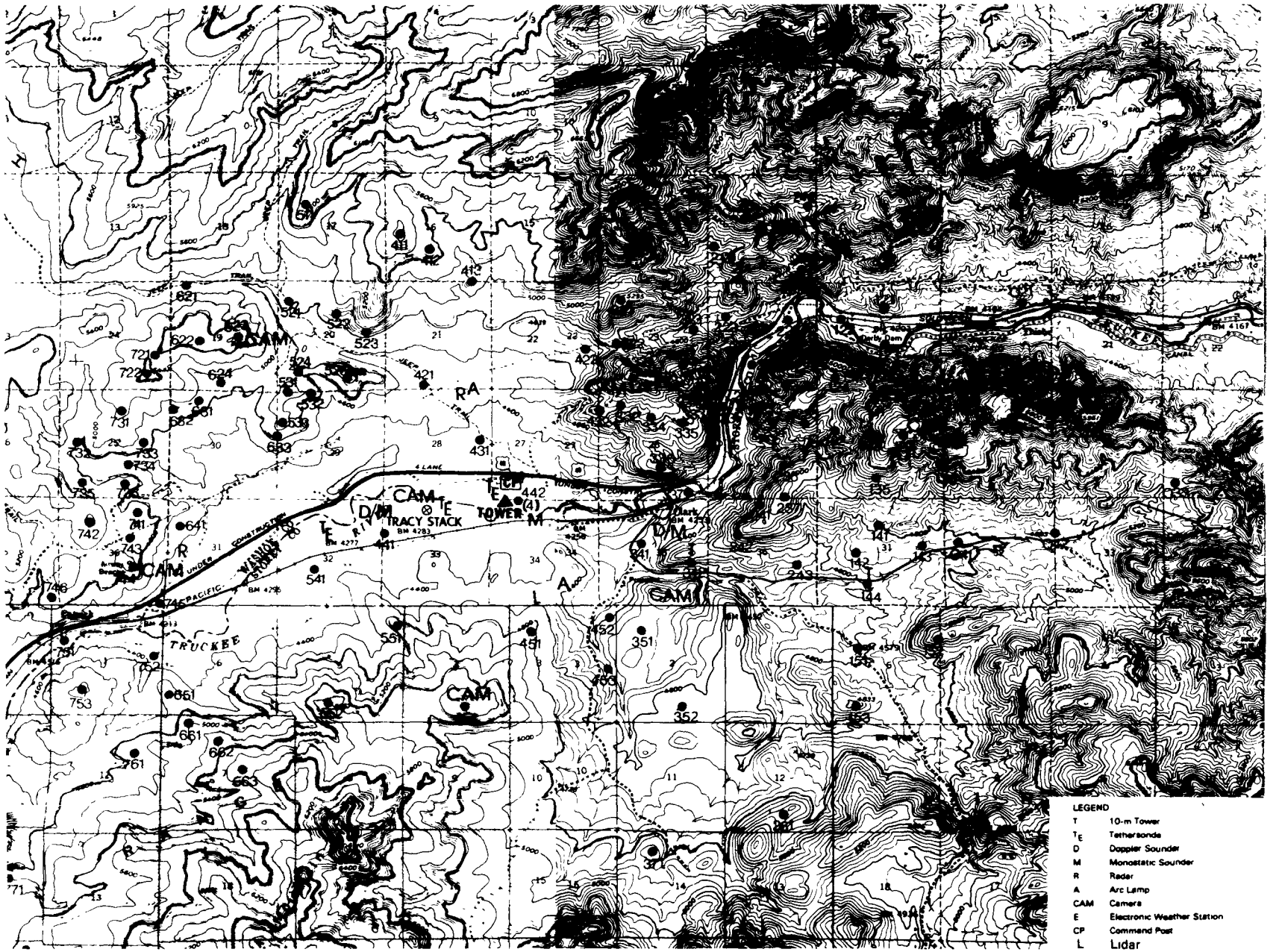

Figure 94. FSTPS site layout.

The sampler network (see Figure 94) was designed principally from the results of the preliminary experiment that was held in November 1983. It will measure ground-level tracer concentrations during several plume dispersion conditions:

1) transport along known (observed) plume paths,
2) stable plume impaction,
3) channeling by major terrain features,
4) lee side phenomena,
5) katabatic fumigation,
6) recirculation in the valley, and
7) flat terrain versus hill effects.

Samplers on target mountain and beacon hill and the string of samplers west of the plant are located to measure concentrations during events similar to those observed in November and during previous field experiments. The samplers on target mountain, beacon hill and on the hill 5085 - hill 5610 complex are located to measure concentrations during stable plume impaction conditions.

The meteorological towers, the acoustic sounder systems, the radar wind systems and the tethersondes will provide information to characterize the three-dimensional structure of the wind and temperature fields in the valley. The 150-m tower, which will be instrumented with sonic, propeller and cup-and-vane anemometers, will provide data on the winds and turbulence near the elevation of the Tracy plume and data to define the meteorological conditions near the height of the Freon emissions.

The lidar systems and photographs will document the path and growth of the oil-fog (and coincidental SF_6) plume upwind of the major terrain elements. They will provide information to calculate σ_y and σ_z as a function of downwind distance and ambient meteorological conditions.

It is currently planned that the bulk of the FSPS data base will be complete by March 15, 1985. The modeling will begin at that time.

SECTION 6

SUMMARY, CONCLUSIONS, AND RECOMMENDATIONS FOR FURTHER STUDY

This Fourth Milestone Report documents the further evolution of CTDM and presents a detailed mathematical description of the model components, including those that explicitly account for the effects that terrain has on plume dispersion. The latest version of CTDM has been evaluated using an 80-hour subset of the SHIS #1 data base. The report also describes an empirical modeling approach to the Hogback Ridge data base. It provides an overview of the preliminary dispersion experiment that was conducted at the Tracy Power Plant in November, 1983 and presents plans for the Full Scale Plume Study.

6.1 Principal Accomplishments and Conclusions

The Complex Terrain Dispersion Model (CTDM)

Substantial progress has been made in the development of CTDM as a method for simulating tracer gas concentrations observed at CCB and as a practical regulatory model. The central feature of the model still is its use of the concept of a dividing streamline to separate the flow into two discrete layers. The upper weakly stratified layer is handled by the LIFT component and the lower stable layer by the WRAP component. Both model components include explicit mathematical expressions that account for the important phenomena that control dispersion in mountainous terrain:

- streamline contraction in the vertical,
- streamline distortion in the horizontal,
- acceleration of the flow, and
- changes in lateral and vertical diffusivities.

CTDM also includes a method to simulate the transition between the upper and lower flows and subsequent ground-level concentrations and to simulate the temporal variability of the H_c interface. The model also includes new formulations for σ_z and σ_y and now accounts for the density of the tracer gases and the vertical wind speed shear.

The SHIS #1 Modelers' Data Archive (MDA)

The SHIS #1 MDA has continued to evolve over the last 12 months. Recall (see Third Milestone Report) that the MDA consists of Tower A meteorological data that were objectively interpolated to the heights of the SF_6 and CF_3Br releases, as well as concentration and emission data. The MDA was compiled to be used by modelers in simulating concentrations collected at CCB and is available from the

EPA Project Officer. The MDA was evaluated by comparing interpolated winds and turbulent intensities to those estimated from lidar data and plume photos. The analysis indicates that the MDA values are generally appropriate for modeling, although photo and lidar estimates were substituted in some cases when warranted. A subset of 80 hours of SF_6 and coincidental meteorological data was selected to evaluate CTDM.

Investigations of Plume Growth

An analysis of SHIS #1 Tower A turbulence intensity measurements with values of σ_z estimated from plume photographs and lidar data suggests the following model of vertical dispersion of elevated releases in the stable boundary layer:

$$\sigma_z = \frac{\sigma_w t}{(1 + t/2T_L)^{0.5}}$$

The dispersion time scale T_L is given by

$$T_L = \ell/\sigma_w$$

where the mixing length ℓ is

$$\frac{1}{\ell} = \frac{1}{\ell_n} + \frac{1}{\ell_s}$$

and the neutral length scale ℓ_n and the stable length scale ℓ_s are given by

$$\ell_n = \Gamma z_r \; ; \; \ell_s = \gamma^2 \sigma_w/N$$

The variance of the vertical velocity fluctuations σ_w^2 and the Brunt-Vaisala frequency N are evaluated at the release height z_r. The constants γ^2 and Γ were derived from surface layer flux-gradient relationships and were found to have values of 0.27 and 0.32.

Evaluation of CTDM

The current version of CTDM was evaluated by comparing model calculations to (1) observed SF_6 concentrations, (2) concentration estimates based on a flat terrain model, and (3) concentration estimates based on the COMPLEX I/II plume path assumptions. The 80-hour subset of the MDA was divided into four classes: neutral, weakly stratified, impingement, and very stable. Performance statistics were generated for each class as well as the entire subset. The results show that CTDM simulates the observations better than the other two approaches. CTDM has a weak overall bias toward

overestimating the larger concentrations (m_g = 0.84), the COMPLEX modeling approach generally overestimates by more than a factor of two (m_g = 0.42), and the flat terrain model generally underestimates by more than a factor of two (m_g = 2.2). The noise in the CTDM calculations is lower for the time- and space-paired statistics, which indicates that CTDM is better able to simulate the observed distribution of concentrations. These comparisons illustrate the importance of including H_c and the stagnation streamline in a modeling framework such as CTDM.

The performance of CTDM in each of the four classes indicates that the model tends to overestimate the larger observed concentrations for H_c greater than 1.25 times the release height (the two "more stable" classes). These classes include the hours in which the largest concentrations (scaled by the emission rate) were observed at CCB. CTDM tends to underestimate in the other two "less stable" classes, producing estimates that are 70% to 80% of the larger observed concentrations. These results indicate that more work is needed to further improve CTDM performance within each of the classes.

Model Performance for Various Quantities of Onsite Meteorological Data

The ability of CTDM to simulate the CCB observations with various quantities of onsite meteorological data was evaluated by constructing three alternate model input data sets: (1) 5-minute meteorological data contained in the MDA; (2) an hourly data set constructed from one-hour wind and temperature data measured at 10-m and 150-m; and (3) an hourly data set constructed from wind and temperature data measured at 10-m only. The results suggest that the 5-minute simulations improve some individual hours but do not substantially change the overall performance statistics. The results from the simulations using the simplified meteorological input are inferior to those based on the full MDA even though MDA wind directions were used for each. The conclusion of this analysis is that onsite measurements of turbulence intensity near release height and detailed vertical profiles of wind and temperature are essential for accurately simulating concentrations at a complex terrain site such as CCB.

Modeling the Hogback Ridge Data Base

To help understand the phenomena that control dispersion at the ridge site a simple empirical modeling approach was taken. A model was constructed by modifying the effective plume height as a function of H_c. Model simulations were performed using a subset of the SHIS #2 CF_3Br data base. These empirical model calculations were compared to observed CF_3Br concentrations and to calculations made with a flat terrain model and a model based on the half-height plume path assumption. The empirical model performed better than the other two models. Furthermore, for both CCB and HBR the flat terrain model underestimated concentrations while the COMPLEX (or half-height) model overestimated concentrations by roughly a factor of two.

Fluid Modeling Facility Simulations

A series of tows was conducted in the EPA FMF salt-water-stratified towing tank using, as the basic hill shape, the fourth-order polynomial hill as used by Hunt and Snyder (1980). Linear density gradients were established in the tank and the hill was towed at a speed such that the Froude number Fr was 0.5. Since the density gradient was linear and Fr = 0.5, the dividing-streamline height was 0.5h. After that series was completed, a second series of tows was conducted wherein the entire model was raised out of the water to the point where the water surface was precisely at the dividing-streamline height, i.e., the water surface was at half the hill height. The model was towed at the same speed as in the full-immersion tows, so that the Froude number with this now half-height hill was unity, and all streamlines passed over the hill top. The flat water surface thus forced a flat dividing-streamline surface. The resulting surface concentration patterns were then compared with the corresponding full-immersion tows. These simulations, which are described in Appendix A, were performed to answer the question: how good is the assumption of a flat dividing-streamline surface?

The results suggest that this assumption is a reasonable approximation to make, at least with regard to predicting the locations and values of maximum concentrations and areas of coverage on the windward side of the hill. When the stack heights are relatively close to the dividing-streamline height, the lee-side concentrations are also predicted reasonably well. These results were used directly in the formulation of CTDM.

The FMF staff also conducted wind-tunnel studies (Appendix B) to investigate the influence of an idealized three-dimensional hill on ground-level concentrations from upwind sources in a neutral atmospheric boundary layer and to locate the source locations where this influence is the greatest.

The presence of the hill was found to influence the dispersion of the plume to increase the maximum concentration in three ways. For low sources, at moderate distances from the hill, the reduction in mean wind speed allows the plume to reach the ground surface closer to the source, producing higher concentrations than in the absence of the hill. Plumes from higher sources can be thought of as being intercepted by the hill. That is, the hill penetrates the plume where the concentrations are greater than those that would occur at ground level farther downstream over flat terrain. For yet higher sources, the streamline convergence over the hilltop and the corresponding downward flow in the lee of the hill brings the plume to the ground more rapidly than over flat terrain. The maximum concentration for these three regimes occurs upwind of the hilltop, near or on the hilltop, or downwind of the hilltop, respectively. Terrain amplification factors ranged from near 1.0 to 3.63. The region of source locations that produced an amplification factor of 1.4 or more extended to an upwind distance of 14 hill heights.

6.2 Recommendations for Further Study

6.2.1 The SHIS #2 Data Base

Further refinements are recommended in screening and adjusting the meteorological data obtained at the three primary towers at HBR. Once this is completed, the Quality Assurance Report for SHIS #2 can be completed, and the modelers will have better guidance in interpreting the data.

In addition to the sonic anemometer data used in the preliminary modeling reported in this Milestone Report and the acoustic profile data, the meteorological measurements from the 150-m and 30-m towers (towers A and B) are essential to investigating the flow properties below H_c. The temperature patterns and changes in the turbulence properties will be investigated. A comparison of profiles of these data within 30 m of the surface at these two towers should essentially provide a description of the flow field within the "blocked" region below H_c for nearly all releases below H_c.

For releases above H_c, comparison and integration of tethersonde data, acoustic profile data, and measurements from towers A and C are particularly important. Also, because of the oil-fog plume rise so characteristic of many of the experiment-hours, analysis of the photographs and the lidar scans of the visible plume will be pursued to document and model the plume rise, and to model the initial growth of the visible plume. Analysis of lidar scans and photographs will also document patterns of streamline deflections in the flow over the crest of HBR, and possibly the distribution of plume material near the surface.

6.2.2 CTDM

Application of CTDM to the SHIS #1 data base has reached a stage where the modeling framework is largely complete. Some effort will be devoted to investigating the LIFT/WRAP transition zone, and fluid modeling studies at the EPA FMF will help refine the formulation of the flow in this region. In addition, it appears that the performance of the model will be improved by including directional wind shear, which so far has been ignored. Also ignored has been the variation of the turbulence with height (away from the plume centerline).

Aside from these enhancements to CTDM, most of the work remaining in applying CTDM to the SHIS #1 data base will focus on the terrain-effects factors T_h, T_ℓ, T_u, and T_i. The present formulation will be compared with computations performed using thin aerofoil theory as well as results from fluid modeling simulations. Also, particular model parameters will be selected for optimization in order to infer the terrain effect description which best matches the observed concentrations and meteorological data. Presumably, alternate choices of the terrain-effect parameters will be needed to improve the model performance. The specification of T_i (either T_{iz} or T_{iy}) is a good example. Our present calculations are made with $T_i = 1$. Rapid distortion theory will be used to infer non-zero values for T_i. Optimized values of T_i will be compared with those computed from the rapid distortion theory.

Application of CTDM to other sites will require some generalization of the code. A good test-case for such a generalization is HBR. The model will be altered so that the present CTDM "assumptions" can be tested at HBR. The experiments at the Tracy Power Plant (FSPS preliminary and FSPS) also need to be considered in structuring the general CTDM. New algorithms will surely be needed in some circumstances, but we also need to know when the detail in the present CTDM is most needed. A sensitivity analysis will help define the conditions in which the terrain effects contained in CTDM have the greatest and least impact on the magnitude of the concentration estimates compared to estimates made by means of a simple "flat-terrain" model. Key input parameters could then be designed to signal a "CTDM" calculation or a "FLAT" calculation when the model is applied in a regulatory permitting mode.

The development of a theoretical rather than an empirical model for HBR will receive much attention in the next year. We first need to identify the circumstances in which CTDM does as well as the empirical model, and circumstances in which CTDM does much worse. The cases in which CTDM fails must be analyzed in detail to develop a rationale (theory) for modifying CTDM. In this way CTDM will increase its range of applicability, and the need for empiricism will be reduced. This process will begin by applying CTDM to the subset of 35 hours modeled in this Milestone Report. Although the meteorological data are incomplete, we expect to learn something from this preliminary modeling. We expect to develop a framework to simulate the effects of an unsteady, "blocked" flow upwind of a ridge.

6.2.3 The FSPS Data Base

The FSPS at Tracy Power Plant has been designed to provide a data base that will augment our understanding of how a plume in large-scale stable flow interacts with topography and local slope flows to reach the surface. The phenomena observed at this site will be described and documented, and the relationship between these phenomena and observed ground-level concentrations will be investigated. This investigation will include comparisons with both the SHIS #1 and #2 results. We expect that the similarities among the FSPS and the SHIS observations will identify those aspects of the FSPS data base that can be modeled with CTDM directly. The dissimilarities will focus attention on aspects that will require modification to CTDM.

REFERENCES

Briggs, G.A. 1973. Diffusion Estimation for Small Emissions, ATDL Contribution File No. 79, Atmospheric Turbulence and Diffusion Laboratory.

Briggs, G.A. 1975. Plume Rise Predictions. Lectures on Air Pollution and Environmental Impact Analyses. AMS, Boston.

Brighton, P.W.M. 1978. Strongly Stratified Flow Past Three-Dimensional Obstacles. Quarterly Journal of the Royal Meteorological Society, 104: 289-307.

Businger, J.A. 1973. Turbulent Transfer in the Atmospheric Surface Layer. In Workshop on Micrometeorology, AMS, Boston, 67-100.

Csanady, G.T. 1973. Turbulent Diffusion in the Environment. D. Reidel Publishing Co., Dordrecht, Holland.

Deardorff, J.W. and G.E. Willis 1975. A Parameterization of Diffusion into the Mixed Layer. J. Appl. Met., 14: 1451-1458.

Drazin, P.G. 1961. On The Steady Flow of a Fluid of Variable Density Past an Obstacle. Tellus, 13: 239-251.

Gifford, F.A. 1980. Smoke as a Quantitative Atmospheric Diffusion Tracer. Atmospheric Environment, 14: 1119-1121.

Holzworth, G.C. 1980. The EPA Program for Dispersion Model Development for Sources in Complex Terrain. Second Joint Conference on Applications of Air Pollution Meteorology, New Orleans, LA. AMS, Boston.

Hunt, J.C.R., and R.J. Mulhearn 1973. Turbulent Dispersion from Sources Near Two-Dimensional Obstacles. J. Fluid Mech., 61: 245-274.

Hunt, J.C.R. and W.H. Snyder 1980. Experiments on Stably and Neutrally Stratified Flow Over a Model Three-Dimensional Hill. J. Fluid Mech., 96: 671-704.

Hunt, J.C.R. 1981. Diffusion in the Stable Boundary Layer. Atmospheric Turbulence and the Pollution Modelling, F.T.M. Nieustadt and H. Van Dop (Ed.). D. Reidel, Holland.

Hunt, J.C.R. 1982. Diffusion in the Stable Boundary Layer. In Atmospheric Turbulence and Air Pollution Modeling, D. Reidel Publishing Company, Dordrecht, Holland, 231-274.

Hunt, J.C.R., J.C. Kaimal, J.E. Gaynor and A. Korrell 1983. Observations of Turbulence Structure in Stable Layers at the Boulder Atmospheric Laboratory. In Studies of Nocturnal Stable Layers at BAO, Report Number Four, Jan. 1983. Available from NOAA/ERL, Boulder, CO 80303, U.S.A., 1-52.

Kapsha, T.P., et al. 1976. Behavior of SO_2 Plumes from Tracy and Fort Churchill Generating Stations Under Stable Atmospheric Conditions in the Vicinity of Complex Terrain, Westinghouse Electric Corporation, Pittsburgh.

Lavery, T.F., A. Bass, D.G. Strimaitis, A. Venkatram, B.R. Greene, P.J. Drivas, and B.A. Egan 1982. EPA Complex Terrain Model Development: First Milestone Report - 1981. EPA-600/3-82-036, Research Triangle Park, NC. 304 p.

Lauwerier, H.A. 1954. Diffusion from a Source in a Skew Velocity Field. Appl. Sci. Res., 4, p153.

Overcamp, T.J. 1983. A Surface-Corrected Gaussian Model for Elevated Sources. J. of Climate and Applied Met., 22: 1111-1115.

Pasquill, F., and F.B. Smith 1983. Atmospheric Diffusion, 3rd Edition. Ellis Horwood Ltd, England.

Pearson, H.J., J.S. Puttock and J.C.R. Hunt 1983. A Statistical Model of Fluid Element Motions and Vertical Diffusion in a Homogeneous Stratified Turbulent Flow. J. Fluid Mech., 129: 219-249.

Riley, J.J., Liu, H.T. and Geller, E.W. 1976. A Numerical and Experimental Study of Stably Stratified Flow Around Complex Terrain, EPA Report No. EPA-600/4-76-021, Res. Tri. Pk., NC, 41p.

Sheppard, P.A. 1956. Airflow Over Mountains. Quart. J. R. Meteor. Soc., 82: 528-529.

Snyder, W.H., R.E. Britter and J.C.R. Hunt 1980. A Fluid Modeling Study of the Flow Structure and Plume Impingement on a Three-Dimensional Hill in Stably Stratified Flow. Proc. Fifth Int. Conf. on Wind Engr. (J.E. Cermak, ed.), 1: 319-329, Pergamon Press, NY, NY.

Snyder, W.H. and J.C.R. Hunt 1984. Turbulent Diffusion from a Point Source in Stratified and Neutral Flows Around a Three-Dimensional Hill; Part II - Laboratory Measurement of Surface Concentrations. Submitted to Atmospheric Environment.

Uthe, E.E. and B.M. Morley 1984. Alpha-1 Observations of Plume Behavior for PMV&D Tracy Site, Electric Power Research Institute, Palo Alto, California.

Venkatram, A. and R. Paine 1984. Development of a Model to Estimate Dispersion of Elevated Releases in the Shear-Dominated Boundary Layer. ERT Report No. P-B846-500. Prepared for the Maryland Power Plant Siting Program.

Venkatram, A., D. Strimaitis, D. DiCristofaro 1984. A Semiempirical Model to Estimate Vertical Dispersion of Elevated Releases in the Stable Boundary Layer. Atmospheric Environment, 18: 923-928.

APPENDIX A

STABLE PLUME DISPERSION OVER AN ISOLATED HILL

RELEASES ABOVE THE DIVIDING-STREAMLINE HEIGHT

STABLE PLUME DISPERSION OVER AN ISOLATED HILL
Releases above the Dividing-Streamline Height

by

William H. Snyder *

and

Robert E. Lawson, Jr. *

Meteorology and Assessment Division
Atmospheric Sciences Research Laboratory
U.S. Environmental Protection Agency
Research Triangle Park, NC 27711

December 1983

*On Assignment from the National Oceanic and Atmospheric Administration, U.S. Department of Commerce.

ABSTRACT

A series of tows was conducted in a stably stratified salt-water towing tank wherein the density gradient was linear and the dividing-streamline height was half the hill height. Effluent was released at three elevations above the dividing-streamline height. Pairs of tows were made such that, in one tow, the hill (upside-down) was fully-immersed in the water and the towing speed was adjusted to provide a "natural" dividing-streamline surface. In the second tow of the pair, the hill was raised out of the water to the point where only the top half of the hill was immersed, thus, forcing a flat dividing-streamline surface, while all other conditions were maintained identical. Concentration distributions were measured on the hill surface and in the absence of the hill. Concentration distributions from each pair of tows were compared to ascertain effects of an assumed flat dividing-streamline surface as is used in some mathematical models. The results suggest that the assumption of a flat dividing-streamline surface is a reasonable approximation to make, at least with regard to predicting the locations and values of maximum concentrations and areas of coverage on the windward side of the hill. When the stack heights are relatively close to the dividing-streamline height, the lee-side concentrations are also predicted reasonably well. The apparent cause of the relatively poor agreement between lee-side concentration patterns in the higher stack cases is the presence of a hydraulic jump at the downwind base of the hill in the full-immersion case which was absent in the half-immersion case.

1. INTRODUCTION

The structure of strongly stratified flows over a three-dimensional hill has been envisioned as composed of two layers: a lower layer of essentially horizontal flow wherein plumes from upwind sources impinge directly on the hill surface, and an upper layer wherein plumes from upwind sources may pass over the hill top. This basic concept was suggested by theoretical arguments of Drazin (1961) and Sheppard (1956) and was demonstrated through laboratory experiments by Riley et al. (1976), Brighton (1978), Hunt and Snyder (1980), Snyder et al. (1980) and Snyder and Hunt (1983). Complex terrain diffusion models utilizing this concept have been developed by Hunt, Puttock and Snyder (1979) and, more extensively, by Lavery et al. (1982), Strimaitis et al. (1982), and Lavery et al. (1983). The basic parameter characterizing the flow structure is the Froude number, F (see Snyder and Hunt, 1984).

We are concerned in this report with the upper-layer flow. The basic assumption in this approach is that, in strongly stratified flows ($0<F<1$), a dividing-streamline height H_c exists wherein streamlines below H_c have insufficient kinetic energy to surmount the hill top and hence must pass around the sides of the hill; streamlines above H_c may pass over the hill top. The simplest and easiest assumption to make in constructing a mathematical model (and the only one made to date) is that the dividing-streamline surface is perfectly flat, i.e., that the upper- and lower-layer flow regimes are separated by a horizontal plane. As discussed by Snyder and Hunt (1984), a plume released in the upper-layer flow (at H_s) upstream of a hill of height h may be treated like a release from a stack of height $H_s - H_c$ upstream of a hill of height $h - H_c = Fh$, i.e., as if a ground plane were inserted at height H_c. The stratification above H_c, of course, has important influences on the diffusion as well as the vertical convergence and horizontal divergence of the streamlines, so that the flow structure over the hill of height Fh must be treated like that with $F = 1.0$, i.e., the Froude number of the flow over this smaller hill is unity (Bass et al., 1981; Hunt et al., 1984).

The crucial question upon which we attempt to shed light in this report is: how good is the assumption of a flat dividing-streamline surface? We know from laboratory studies that, even well within the lower layer, streamline trajectories are not contained within horizontal planes. Indeed, Riley et al. (1976), Brighton (1978) and Hunt and Snyder (1980) used an extension of Drazin's (1961) theory to predict vertical displacements of streamlines in the lower layer. Furthermore, the streamline originating at the dividing-streamline height far upstream on the flow centerline, by Sheppard's (1956)

hypothesis (balance of kinetic and potential energy), terminates on the surface at the top of the hill, again suggesting that the dividing-streamline surface cannot be flat. On the other hand, concentration measurements on hill surfaces (Snyder and Hunt, 1984) suggested that a flat surface approximation may yield reasonable estimates. From a practical viewpoint, the mathematical models are vastly simplified if such an assumption yields reasonable estimates of surface concentration. Hence, we attempt to answer the question not from a detailed analysis of the shape of such a dividing streamline surface, but from the more practical comparison of surface concentration patterns.

A series of tows was conducted in the salt-water-stratified towing tank using, as the basic hill shape, the fourth-order polynomial hill as used by Hunt and Snyder (1980). Linear density gradients were established in the tank and the hill was towed at a speed U such that the Froude number F (= U/Nh, where N is the Brunt-Vaisala frequency) was 0.5. Effluent was released at heights of H_S = 0.6h, 0.7h and 0.8h, and the resulting hill-surface concentration patterns were measured. Since the density gradient was linear and F=0.5, the dividing-streamline height was also 0.5h (H_c/h = 1 - F); since the effluent was released above H_c, the plumes did not impinge directly on the hill, but instead pollutants reached the hill surface by the combination of streamline displacement and diffusion. After that series was completed, a second series of tows was conducted wherein the entire model (hill, baseplate and stack, as a unit) was raised out of the water* to the point where the water surface was precisely at the dividing-streamline height, i.e., the water surface was at half the hill height. The model was towed at the same speed as in the full-immersion tows, so that the Froude number with this now half-height hill was unity, and all streamlines passed over the hill top. The flat water surface thus forced a flat dividing-streamline surface. The resulting surface concentration patterns were then compared with the corresponding full-immersion tows to ascertain the effects of a flat dividing-streamline surface.

*The model is routinely mounted upside-down such that the baseplate is submerged a few millimeters below the water surface. In discussion of flow structure and plume behavior, however, we discuss the results as if the model were right-side up.

2. EXPERIMENTAL APPARATUS AND TECHNIQUES

Most of the details of the experimental apparatus and techniques were given by Hunt and Snyder (1980) and in a laboratory report by Hunt, Snyder and Lawson (1978). The basic method of making concentration measurements was described by Snyder and Hunt (1984). Only a brief overview is given here, but changes in the techniques and apparatus as well as special features of these experiments are described in detail.

A fourth-order polynomial hill ($z(r) = h/(1+(r/L)^4)$) of height 24.3 cm was used in a stratified towing tank. The tank, 1.2 m in depth, 2.4 m in width and 25 m in length, was stably stratified with layered mixtures of salt water. This dye mixture was emitted at four times the isokinetic rate from a bent-over "stack" of 0.635 cm o.d. The stack exit was located 84.8 cm (3.5 h) upstream of the hill center. The non-isokinetic effluent release rate was used to obtain a realistic plume size and shape, i.e., in the isokinetic releases used previously by Snyder and Hunt (1984), because of the nonexistent approach-flow turbulence, the plumes tended to be exceptionally thin and narrow. With the four-times-isokinetic rate, a weak but turbulent jet was formed at the stack exit. This jet grew in size with downstream distance to provide a plume with dimensions not insignificant in comparison with, say, the hill height and hence, a more realistic simulation of a typical atmospheric situation. The maximum jet velocity at the hill center was estimated to be about 2 cm/s relative to the hill (Townsend, 1956), i.e., small compared with the towing speed. Characteristics of the plume in the absence of the hill were measured with horizontal and vertical rakes of sampling tubes, and are also presented herein.

One hundred sampling ports were fixed on the hill surface, distributed as shown in Figure A-1. In some preliminary tows, the sampling ports (2.4 mm o.d.) protruded 2.5 mm above the smooth hill surface, but as the plumes were spread broadly to cover most of the hill surface (but very thinly in the direction normal to the surface), narrow, clear wakes were observed down-stream of the protuberant sampling tubes. This disturbance caused strong reductions in concentrations measured at ports directly downstream from others, e.g., ports along the 0° line (Figure A-1). The sampling ports were then cut to be flushed with the hill surface, but some amount of interference was still observed in the concentration distributions, apparently due to the withdrawal of sample fluid through the ports. After considerable experimentation, a final configuration was found that displayed no interference: the ports were raised to the original 2.5 mm above the smooth hill surface and the hill was covered with

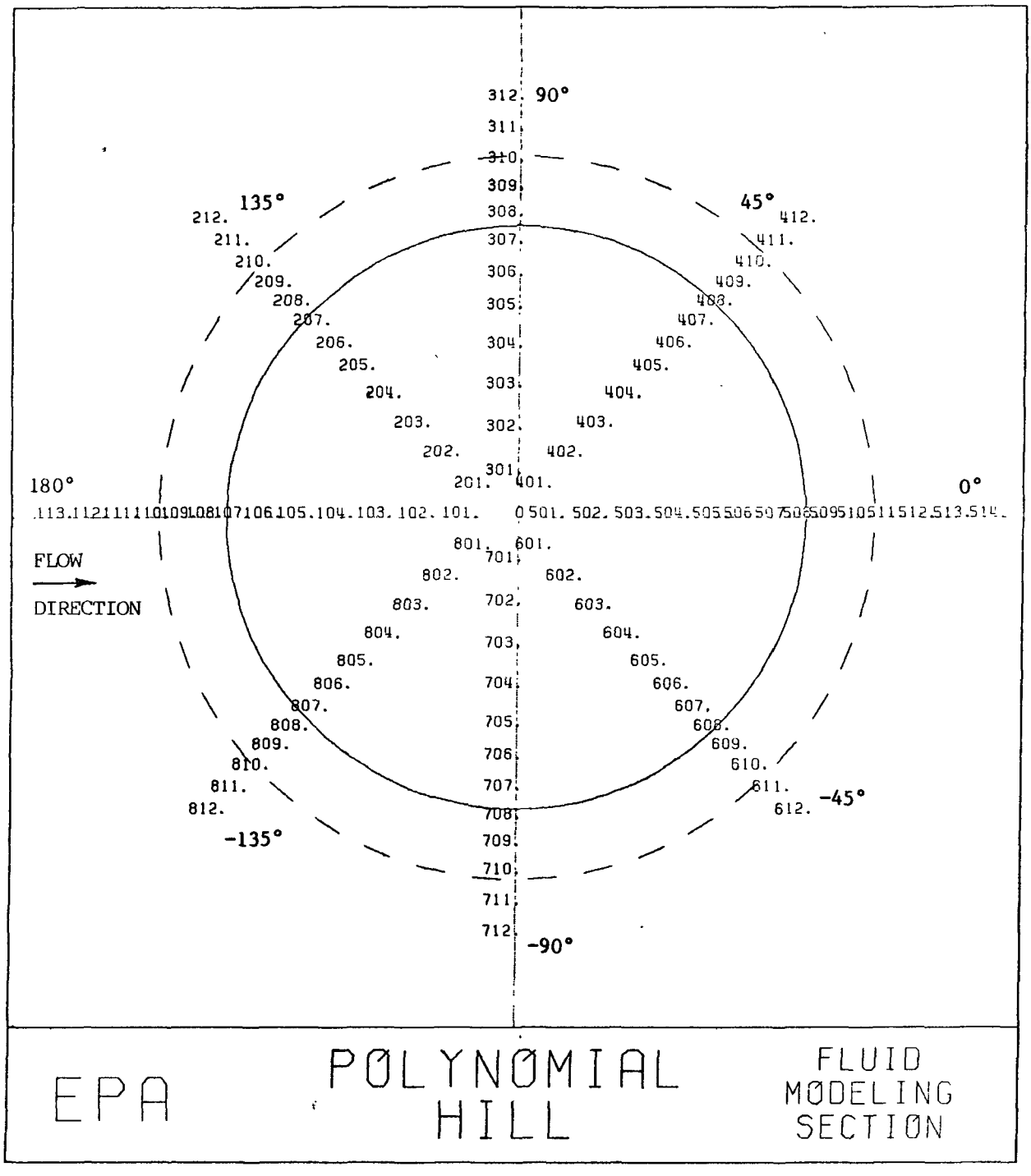

Figure A-1. **Port locations and numbering system for lift study. (Precise location is at decimal point. Dashed circle marks half the hill height.)**

sharp-edged gravel of grain size (longest dimension) 2 to 4 mm. Also, the sample withdrawal rate was reduced by a factor of about 4, to 13 cm^3/min. This corresponds to a sampling "stream tube" diameter of 1.3 mm at the typical tow speed. The rough surface provided the additional benefit of eliminating a viscous sublayer on the hill surface, hence, avoided problems of molecular diffusion through this viscous sublayer.

The concentration of dye in the collected samples were analyzed on a Brinkman Model PC-600 probe colorimeter. The fiber-optics probe was immersed sequentially into the sample test tubes. The wavelength used was 570 nm. The output of the colorimeter, a voltage related to the opacity of the solution being tested, was fed to a PDP 11/44 minicomputer, where it was converted to a concentration in percent dye. The conversion utilized a calibration curve formed by recording the output voltage versus concentration for at least 12 "standards" which consisted of accurately known dilutions of the same dye used for the effluent source. A "Beer's Law" type of curve was best-fit to the standards for use in converting the voltage from the unknown sample into a dye concentration. Although the instrument required care in use (by frequently checking the "zero transmittance" and "zero absorbance" controls), frequent checks of the calibration showed excellent repeatability. A typical calibration curve is shown in Figure A-2. The concentration of dye in the effluent was occasionally adjusted such that the majority of samples would be within the most reliable range of the calibration curve, i.e., the vast majority of samples analyzed were in the range of 0.005 to 0.25%.

The sample lines leading from the ports on the hill surface (or rake) to the sample test tubes had to be filled prior to the beginning of a tow in order for the vacuum-sampling system to work properly. Because of the reduced sample flow rate, the volume of dye-free water stored in the lines (and which was thereafter drawn into the test tubes along with the dye samples) was approximately 25% of the total sample collected. A first-order correction to the measured concentrations was made to account for this dilution of the samples. However, the precise volume of sample collected in each test tube varied slightly from one tube to the next, so that the accuracy of the concentration-measurement system is estimated to be in the range of $\pm$10 to 15%.

Figure A-2. Typical calibration curve for colorimeter.

3. PRESENTATION AND DISCUSSION OF RESULTS

3.1 Plumes in the Absence of the Hill

Vertical and horizontal concentration profiles measured at the downstream position of the center of the hill (but in its absence) are presented in Figures A-3 and A-4, respectively. Profiles were measured for each of three stack heights, 0.1 h, 0.2 h and 0.6 h. For the two lowest stack heights, the baseplate was raised out of the water; for the highest stack height, it was submerged as it was for the full-immersion tows with the hill (approximately 6 mm). Concentrations have been nondimensionalized as $\chi = CU_\infty h^2/Q$, where C is the dimensional dye concentration, U_∞ is the towing speed, h is the hill height, and Q is the volume flow rate of dye in the effluent. The calculated plume parameters are listed in Table A-1. The two higher-level plumes are essentially identical and are very nearly Gaussian in shape. (Best-fit Gaussian curves are shown for comparison in the figures. The parameter χ_{mxg} shown in Table A-1 is the maximum concentration in the best-fit Gaussian distribution with the same standard deviation as the measured data.) The lower-level plume, however, has clearly diffused to the water surface (Figure A-3); a reflected-Gaussian profile assuming an effective stack height of 0.09 h appears to fit the data quite well. The standard deviation of the vertical distribution σ_z (calculated assuming perfect reflection at the water surface), however, is 40% larger than those of the higher level plumes. The standard deviation of the lateral distribution σ_y of the lower level plume is also somewhat larger (10%) than that of the upper level plumes. The probable cause of this increased diffusion is the reduced stability near the water surface, as shown in Figure A-5. Ideally, the density gradient would have been perfectly constant all the way to the water surface, so that the plume released at the lowest level (0.1 h) in the half-immersion case would have been essentially identical in shape to that released at the upper level (0.6 h) in the full-immersion case. However, as will be shown later, these differences in approaching plume shapes appeared to have little effect on the concentration distributions measured on the hill surface.

3.2 Distributions on the Hill Surface

Figure A-6 shows side and top views of the plume surmounting the hill, in this case with the hill fully immersed and the effluent emitted at 0.6 h. These photographs show the plume to be deformed to cover essentially the entire surface of the hill above half the hill

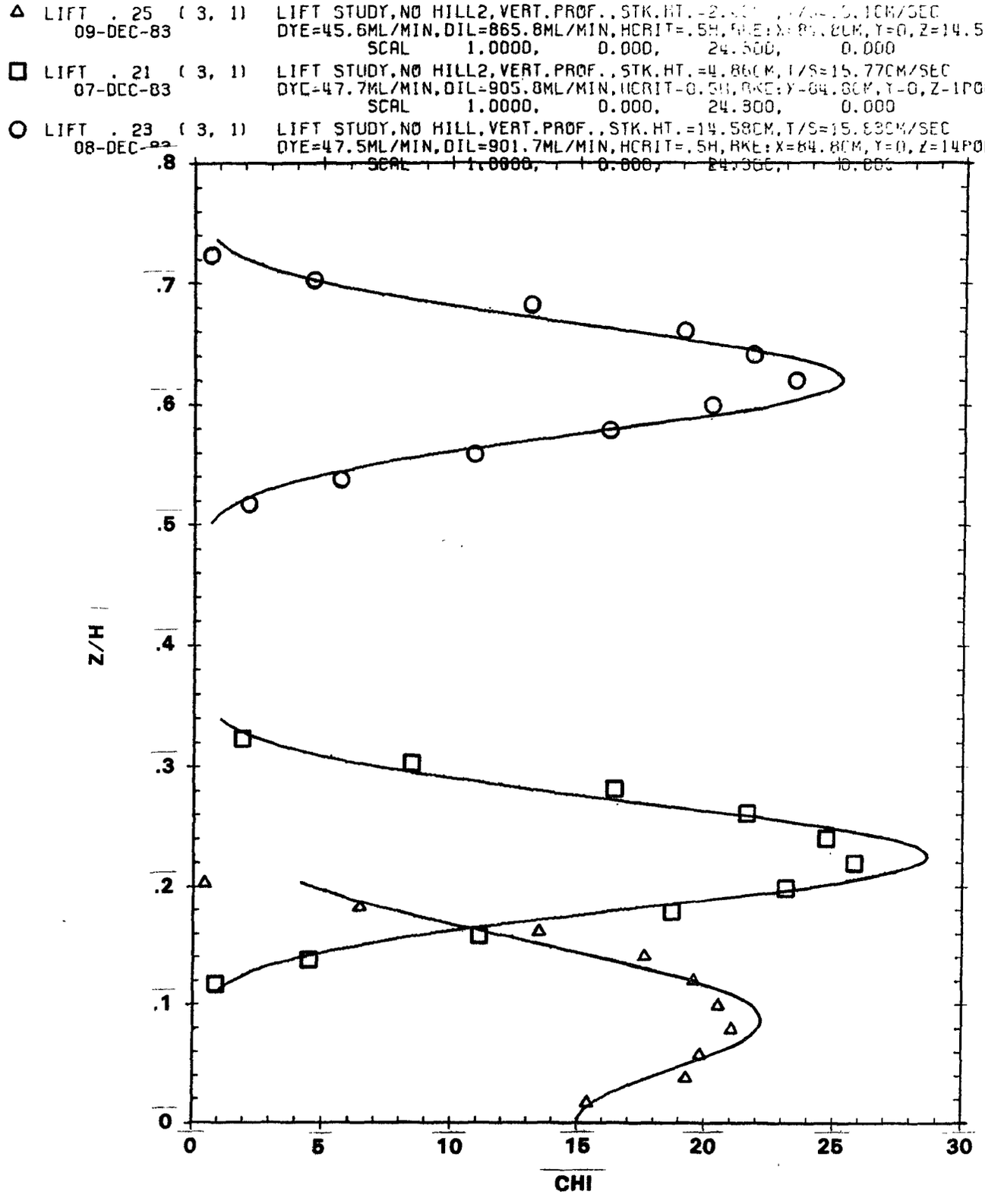

Figure A-3. **Vertical concentration profiles measured at the downstream position of the center of the hill, but in its absence.**

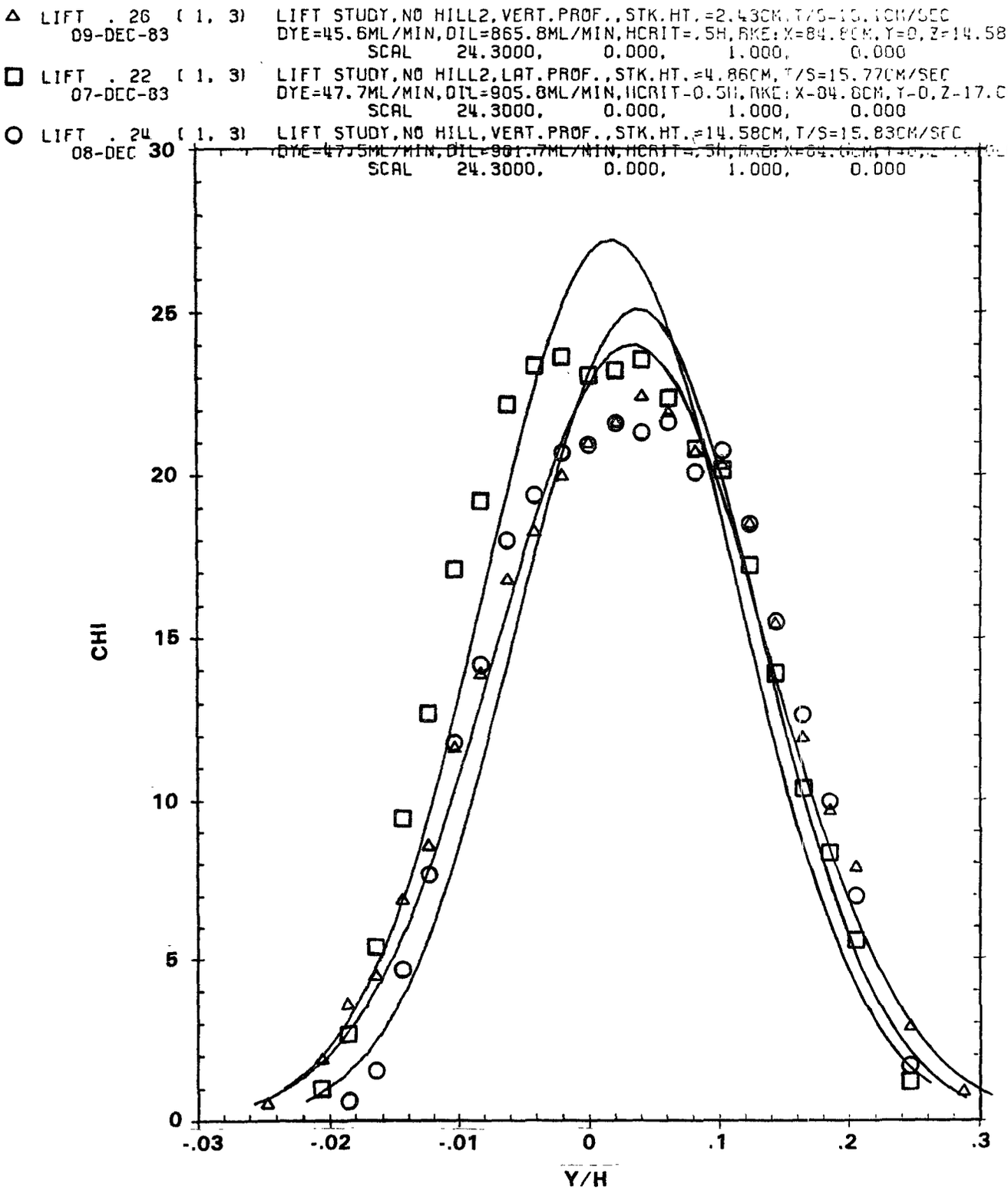

Figure A-4. Horizontal concentration profiles measured at the downstream position of the center of the hill, but in its absence.

File No.	Horizontal/ Vertical	H_s/h	χ_{mx}	σ (cm)	χ_{mxg}
21	V	0.2	25.8	1.07	28.7
22	H	0.2	23.6	2.36	27.2
23	V	0.6	23.4	1.07	25.3
24	V	0.6	21.6	2.28	25.1
25	V	0.1	21.1	1.50[a]	22.2
26	H	0.1	22.4	2.55	24.0

(a) Calculated assuming perfect reflection at the water surface and an effective stack height of 2.2 cm (0.09 h).

△ PLSRS . 36 (3, 1) POLYHILL LIFT STUDY,WATER HT.=100.8CM,METTLER(PL200)
09-DEC-83 TIME: 0810
SCAL 1.0000, 0.000, 24.500, 0.000

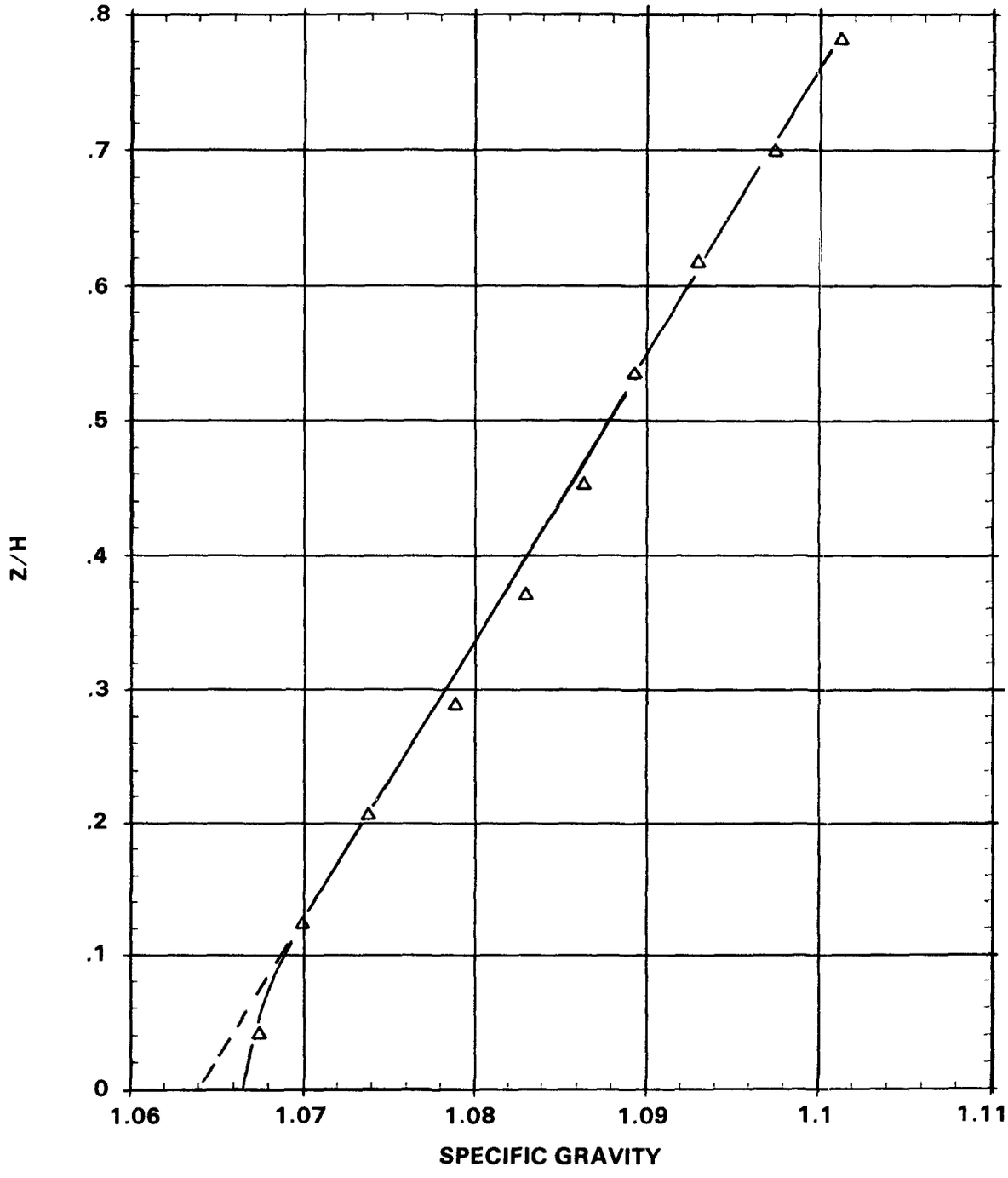

Figure A-5. Density profile measured prior to Tow #25. (Concentration distributions shown as lower plume in Figures A-3 and A-4.)

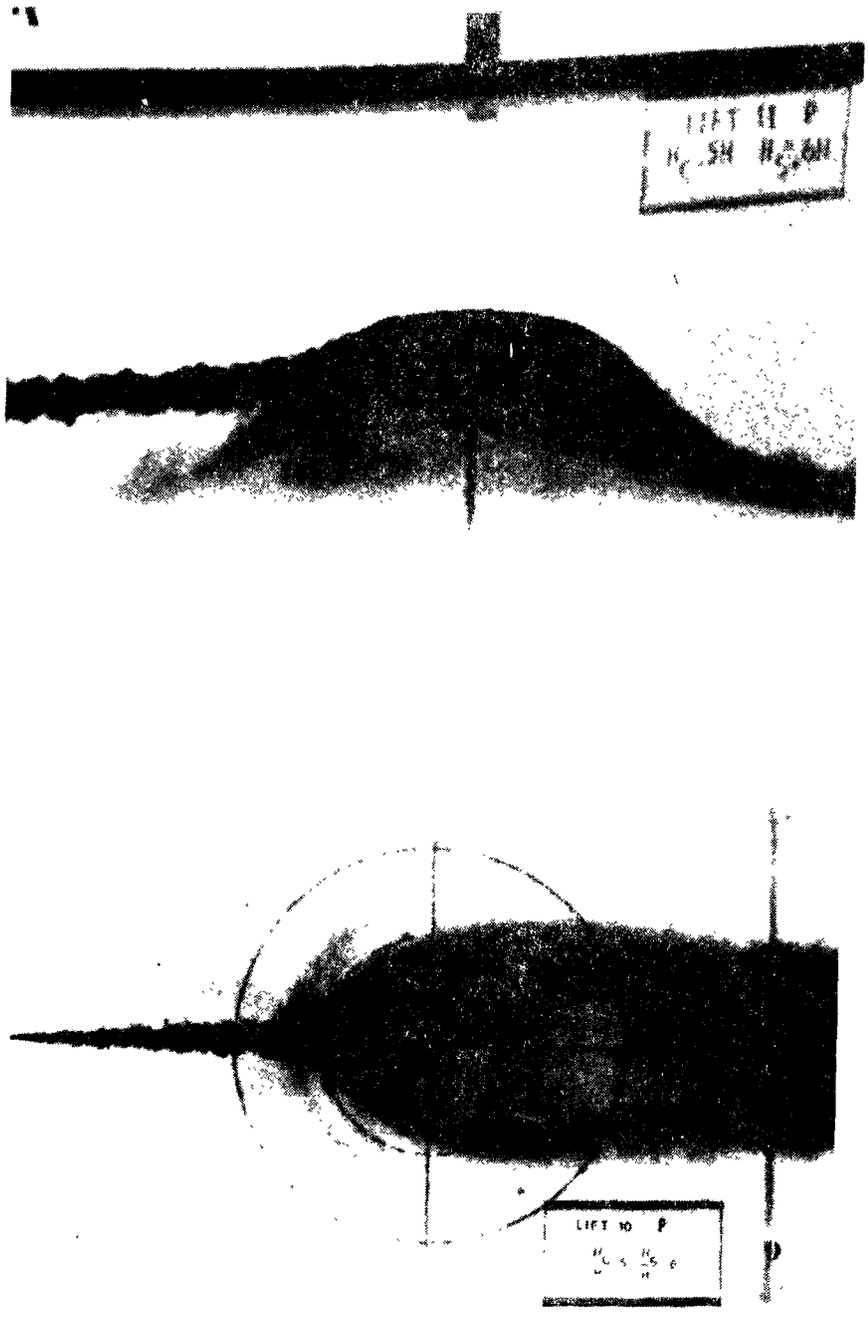

Figure A-6. Side and top-views of plume released at 0.6 H. F = 0.5, fully submerged.

height and yet to be quite thin in the direction normal to the hill surface (the dotted line on the photographs marks half the hill height). Notice that, on the lee side, the plume sweeps to much lower elevations, so that we may expect to see substantial surface concentrations on the lee side below half the hill height.

Figure A-7 presents a scatter diagram showing the repeatability of surface concentration measurements from one tow to the next. In this case, both tows (numbers 10 and 11) were made with the hill fully-immersed and the stack height fixed at 0.6 h. From the diagram, it may be seen that, for any port, repeatability is well-within a factor of two. At large values of concentration, repeatability is generally within 10%. The repeatability is less good at the lower concentrations. A few points with the largest percentage differences between the tows are marked with the port number (see Figure A-1); these show that the largest differences occurred below half the hill height, i.e., on the lower edges of the plume.

Figures A-8 and A-9 show the concentration distributions measured on the hill surface in the full-immersed and half-immersed cases, respectively. The most obvious difference between the two cases is the absence of lee-side concentrations below half the hill height in the half-immersed case. Of course, in the half-immersed case, concentrations at positions below half the hill height are zero, because that portion of the hill is outside the water. In the fully-immersed case, the plume diffused to some extent below half the hill height around the upwind side, but also, as mentioned earlier, this plume "hugged" the hill surface as it was swept down the lee side to much lower elevation than the release height. Just beyond the downwind base of the hill (not shown on the photographs), the flow appeared to separate from the surface and rise abruptly in a hydraulic jump (see Hunt and Snyder, 1980).

Side and top views of this plume in the half-immersed case are shown in Figure A-10. These are to be compared with the full-immersion case of Figure A-6. The comparison shows similar behavior as discussed in the above paragraph.

Figure A-11 presents a scatter diagram comparing, on a port-to-port basis, the surface concentrations measured in the half- and fully-immersed cases. Measurements at points below half the hill height are not included here because, of course, in the half-immersion case, these ports were out of the water. Within the region of large concentrations, the two cases compare quite favorably, the half-immersed case yielding concentrations approximately 10 to 20% larger than the fully-immersed case. In the region of low concentration, quite large differences occur (worst case, a factor of 10). However, a close examination shows that in all cases where concentrations differed by more than a factor of 2, the port locations were very close to half the hill height i.e., either at 0.505 h or 0.59 h (port numbers are marked on Figure A-11 for those cases where concentrations differed by more than a factor of 2).

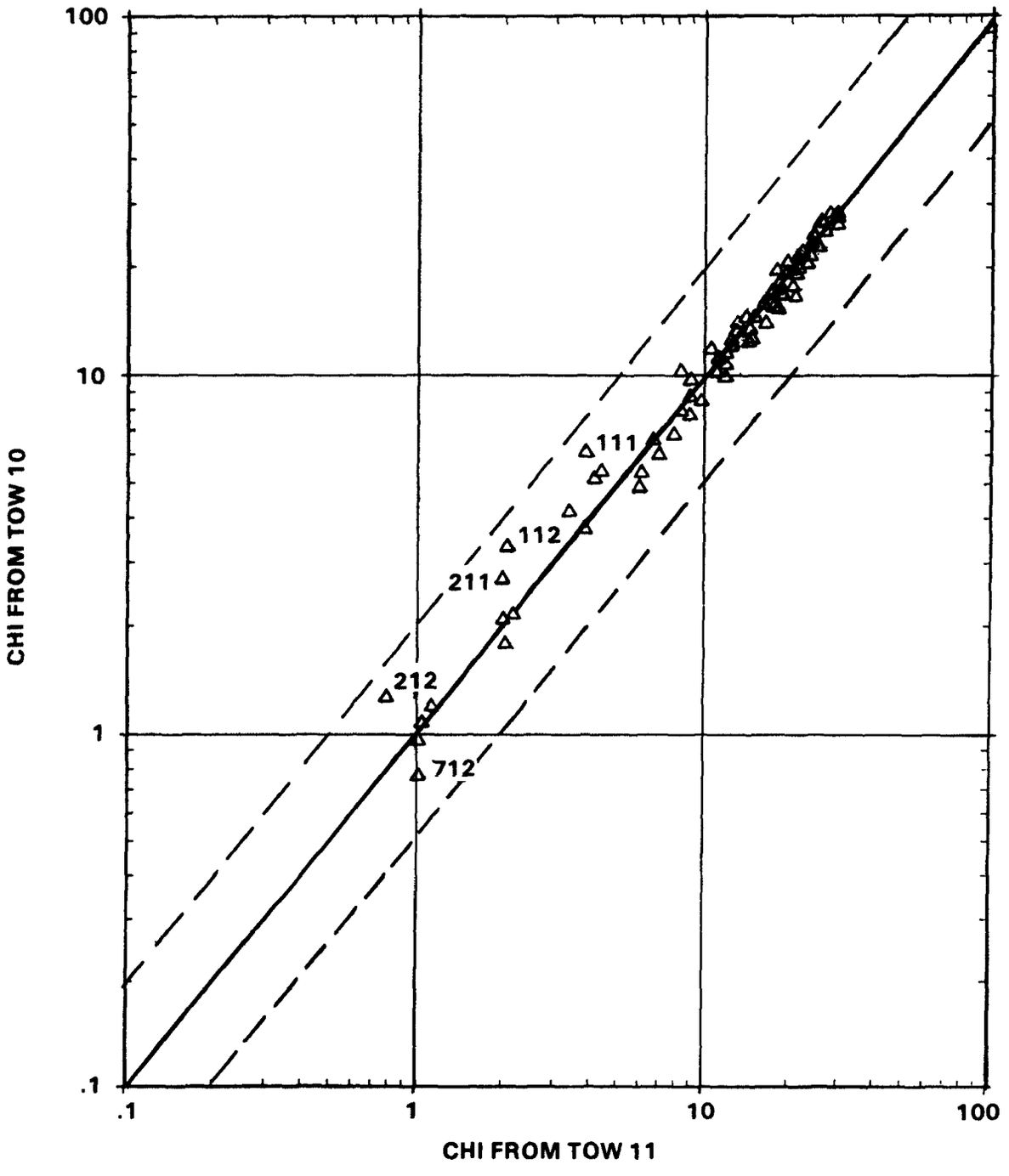

Figure A-7. Repeatability of surface concentration measurements. F = 0.5. HS/H = 0.6, fully submerged.

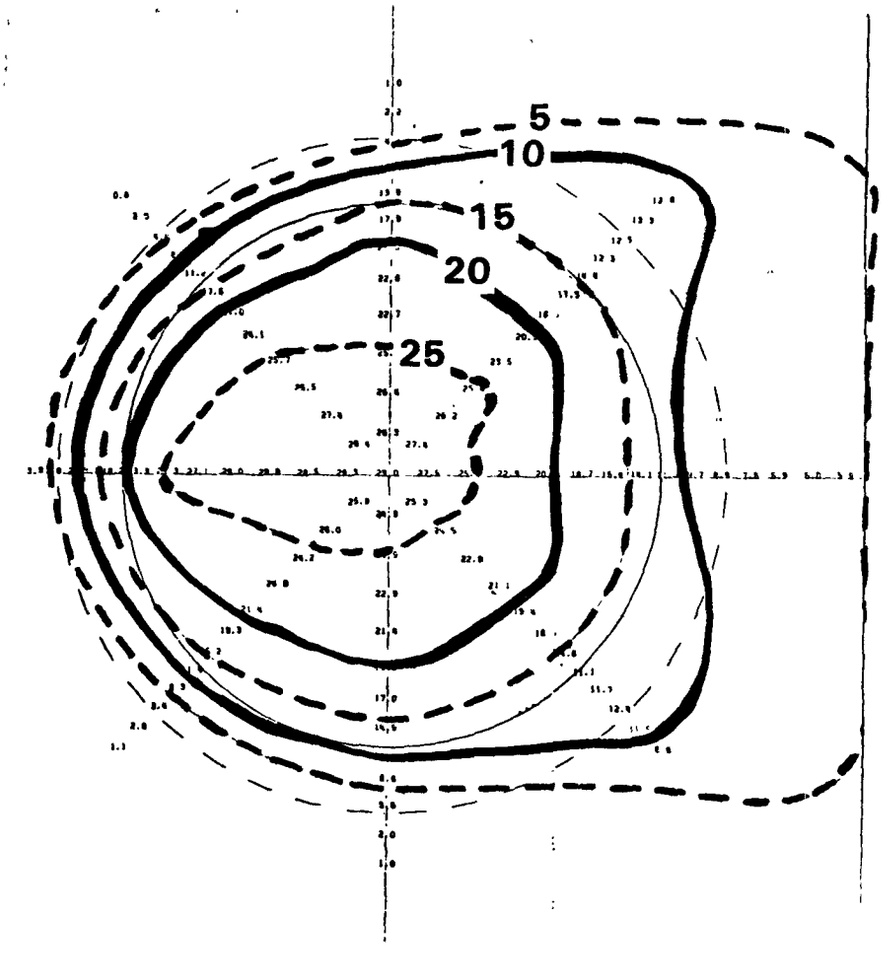

Figure A-8. Concentration distributions measured on the hill surface. F = 0.5. HS/H = 0.6, fully submerged.

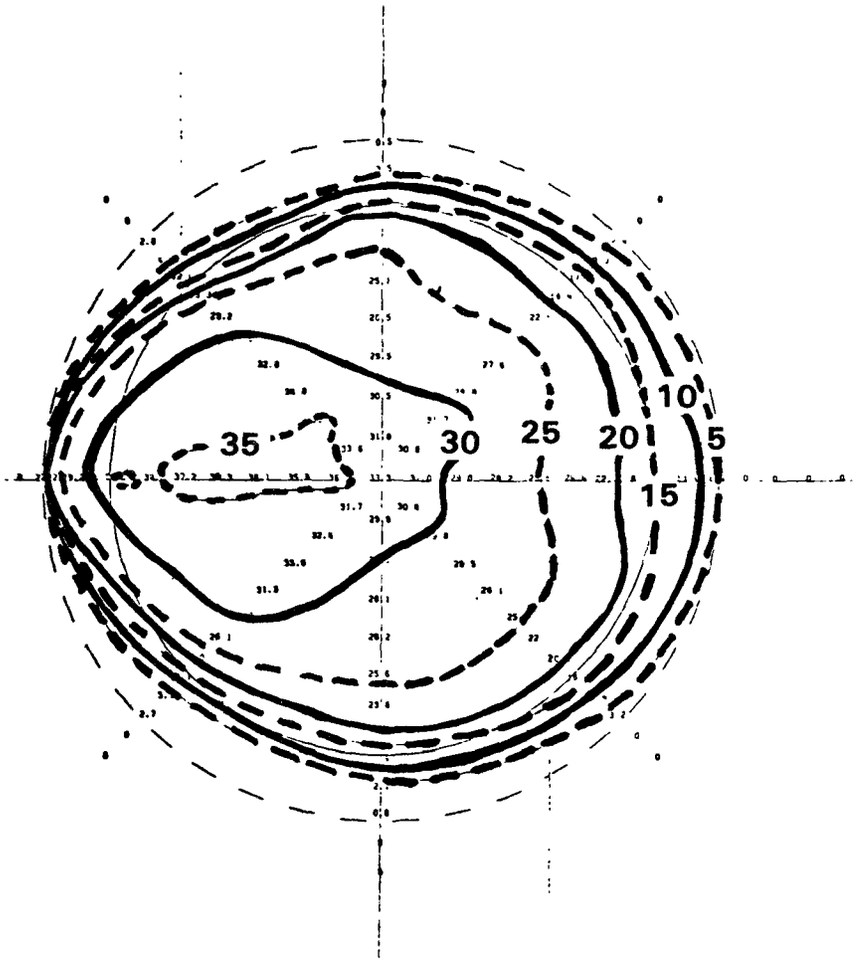

Figure A-9. Concentration distributions measured on the hill surface. F = 0.5, HS/H = 0.6, half submerged.

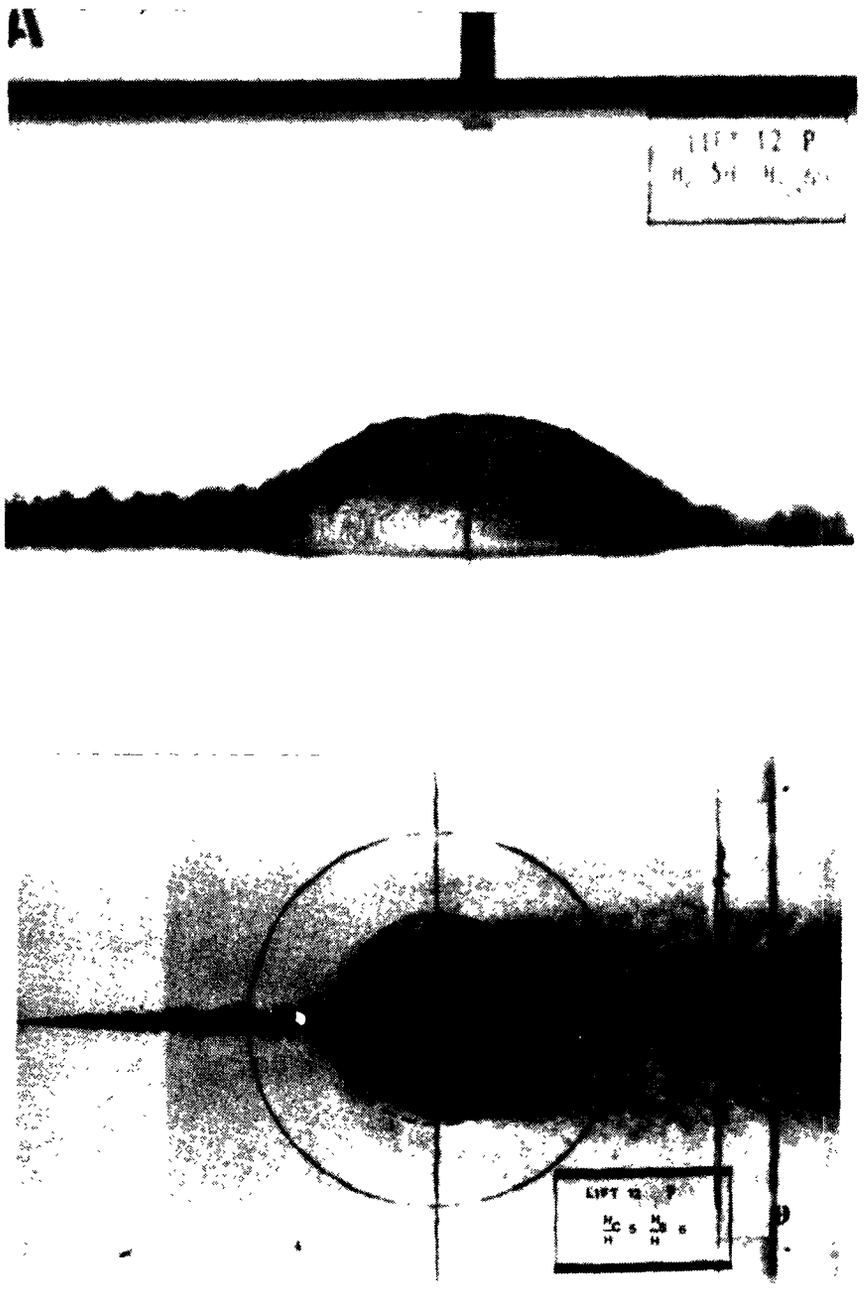

Figure A-10. Side and top views of plume released at 0.6 H. F = 0.5, half submerged.

△ LIFDIF. 7 (4, 3) POLYHIL LIFT STUDY. COL 1, PORT NO.: COL.2 TO 4, CONC. FROM LIFT.010
22-NOV-83 TO .012

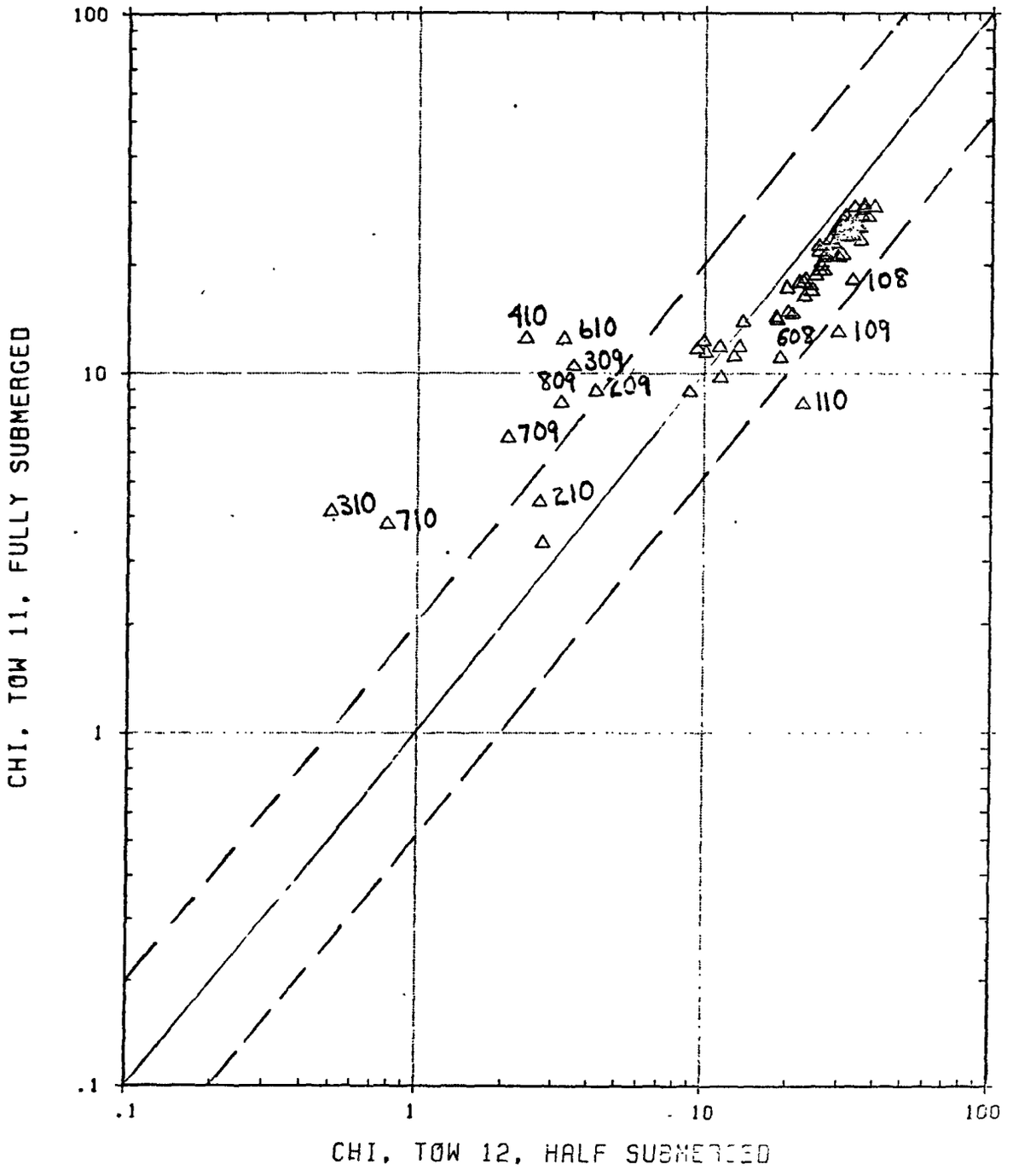

Figure A-11. **Comparison of concentrations, half submerged versus fully submerged. F = 0.5, HS/H = 0.6.**

Note that the maximum hill-surface concentration is in the range of 25 to 30, whereas the maximum in the plume in the absence of the hill was in the range of 20 to 25. This suggests that even though the plume shape was highly contorted through the streamline deformation process, the basic diffusion process was limited by the presence of the surface; this "reflection" at the hill surface resulted in a maximum surface concentration that was 20 to 25% larger than that observed at the center of the plume in the absence of the hill. However, as mentioned earlier, the accuracy of the concentration-measurement system was estimated to be in the range of $\pm$10 to 15%, so that the above estimates of increased concentration should be taken with caution.

Figures A-12 and A-13 show the concentration distributions resulting from sources elevated at 0.7 h. As was the case with a source height of 0.6 h, the contours on the windward side of the hill are roughly circular, but, in this case, somewhat more elongated in the streamwise direction. Again, of course, no concentrations were observed below half the hill height in the half-immersion case; in the full-immersion case, the plume "hugged" the lee side of the hill, but was spread less broadly in the crosswind direction and lifted off the surface into the hydraulic jump somewhat sooner.

Also, as was the case at a source height of 0.6 h, the maximum concentration is about 10% larger in the half- than in the full-immersion case. The location of the maximum, however, has moved from the windward side to the lee side of the hill.

A scatter diagram comparing concentrations on a port-by-port basis for the half- and fully-sumberged hills with a source height of 0.7 h is shown in Figure A-14. The correspondence between the full and half-depth immersions is not as good as was the case with a source height of 0.6 h. For the large concentrations, the agreement is excellent, but for small concentrations, the scatter is quite large. Port numbers where the concentrations differed by more than a factor of two are marked on the figure. These show that the comparisons were poor only in the elevation range of 0.5 h to 0.67 h, i.e., near the water surface in the half-immersion case. In the half-depth case, concentrations were larger on the windward line of ports, apparently related to the wider vertical diffusion of the plume to the water surface, whereas concentrations elsewhere round the sides of the hill were considerably smaller than in the full-depth case.

Figures A-15 and A-16 show the concentration distributions resulting from sources elevated at 0.8 h. In this case, the correspondence between the two distributions is not nearly as good as was the case at the lower stack heights. Whereas the locations of the maximum concentrations are approximately the same, the values in the full-immersion case are 55% larger and the area of plume contact on the hill surface is nearly quadrupled over the half-immersion case. Note that the location of the maximum concentration is well to the lee side of the hill and that the area of plume contact is much smaller than for the lower stack heights.

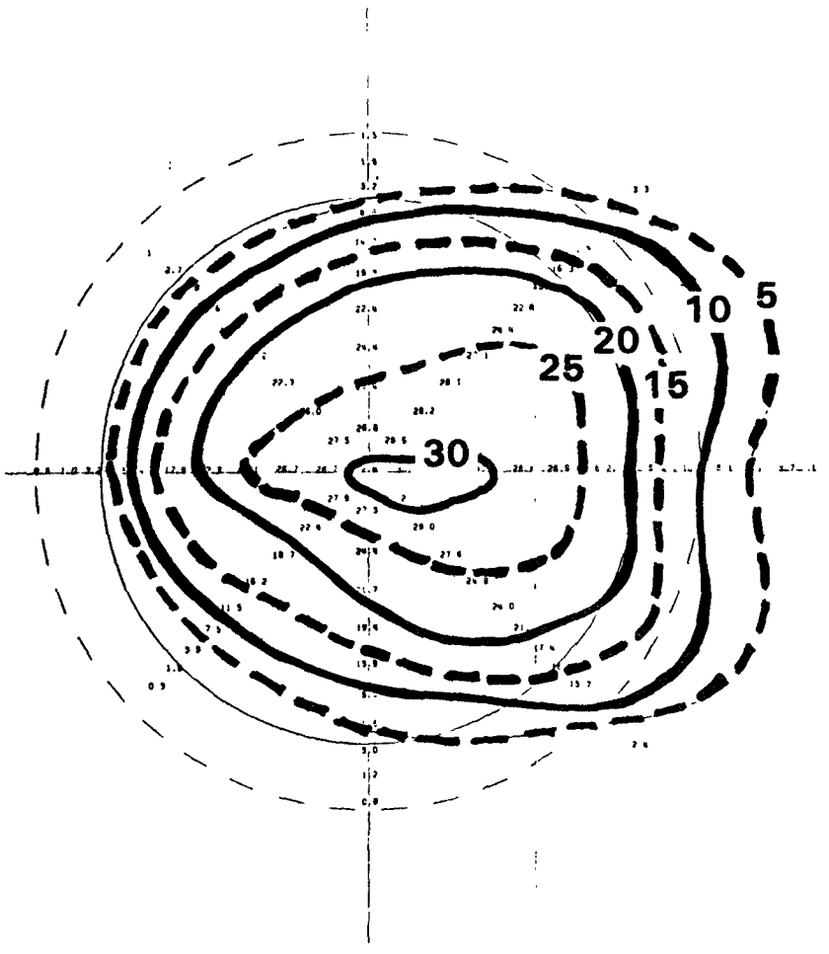

Figure A-12. Concentration distribution measured on the hill surface. F = 0.5, HS/H = 0.7, fully submerged.

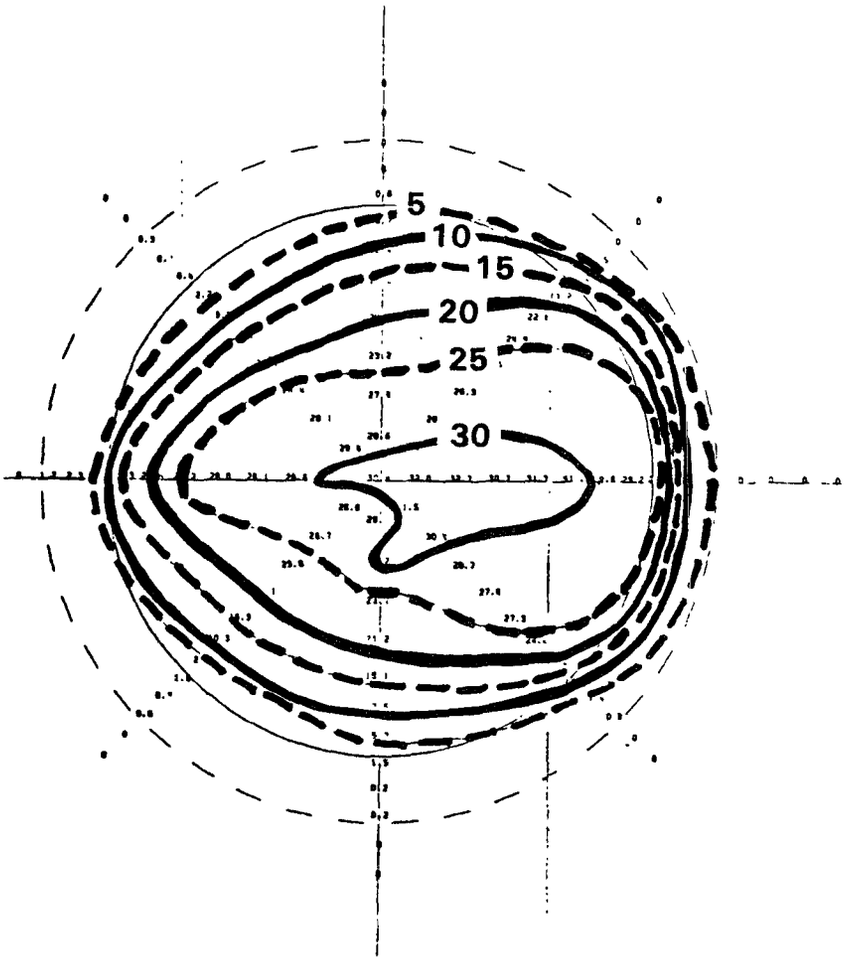

Figure A-13. Concentration distribution measured on the hill surface. F = 0.5, HS/H = 0.7, half submerged.

△ LIFDIF. 8 (2, 3) POLYHIL LIFT STUDY. COL 1, PORT NO.;COL 2 TO 7, CONC. FROM LIFT.013,
01-DEC-83 .017, .014, .015, .016, AND .018, RESPECTIVELY.

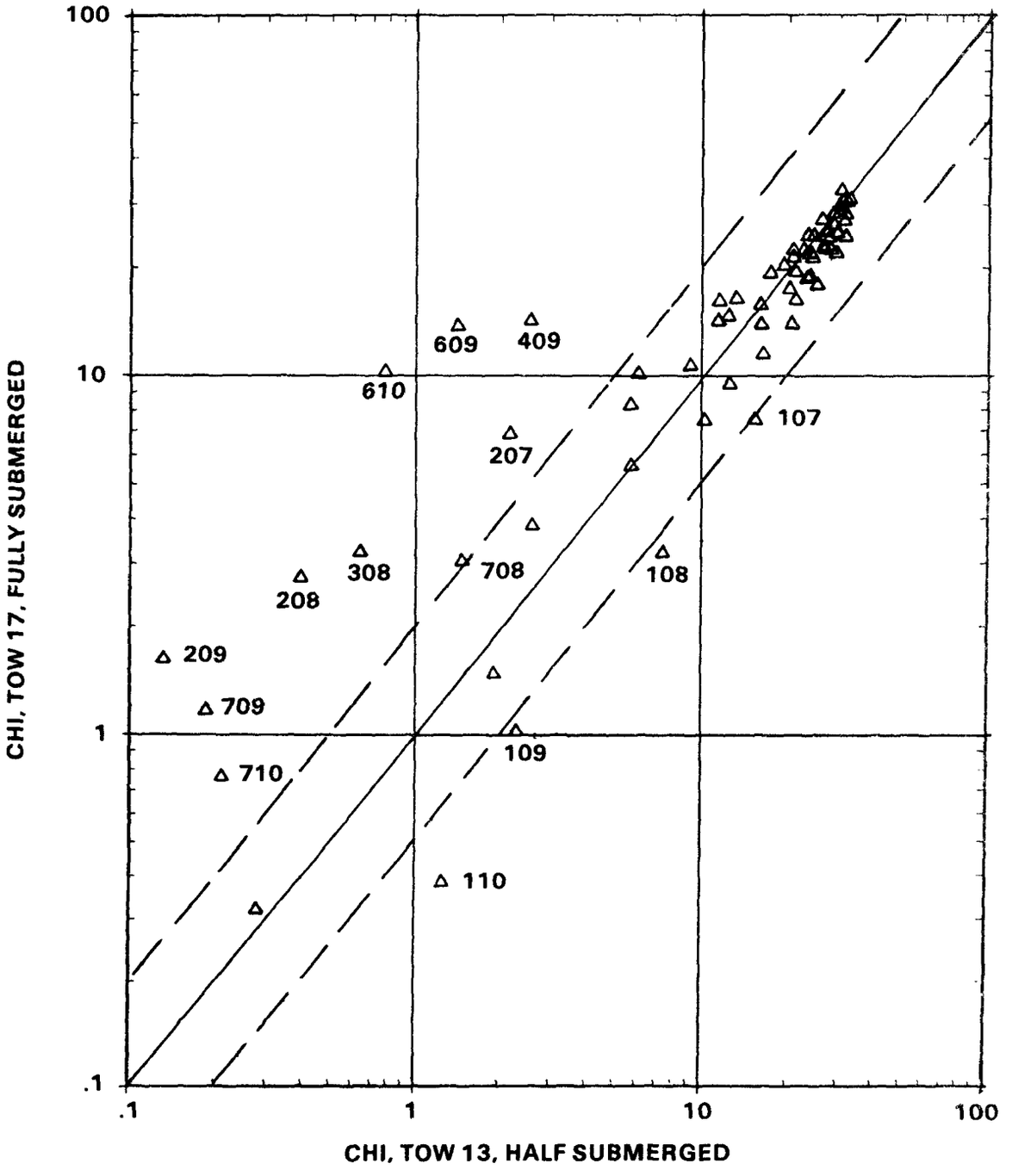

Figure A-14. Comparison of concentrations. Half submerged versus fully submerged. F = 0.5, HS/H = 0.7.

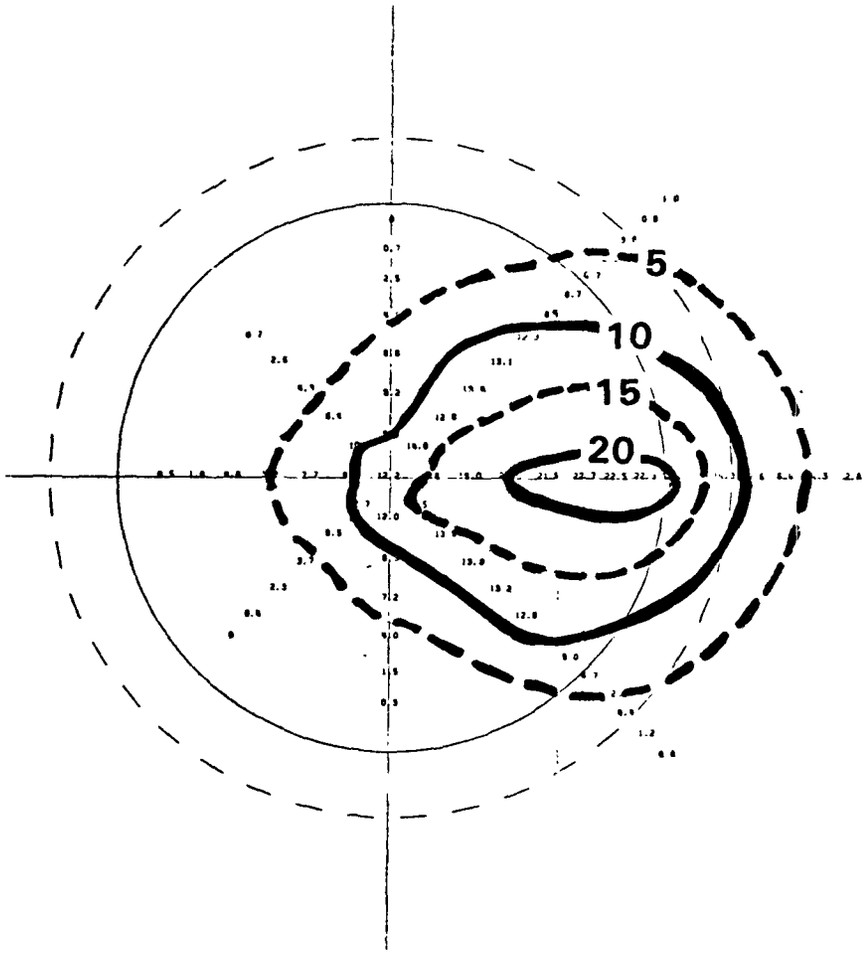

Figure A-15. Concentration distributions measured on the hill surface. F = 0.5, HS/H = 0.8, fully submerged.

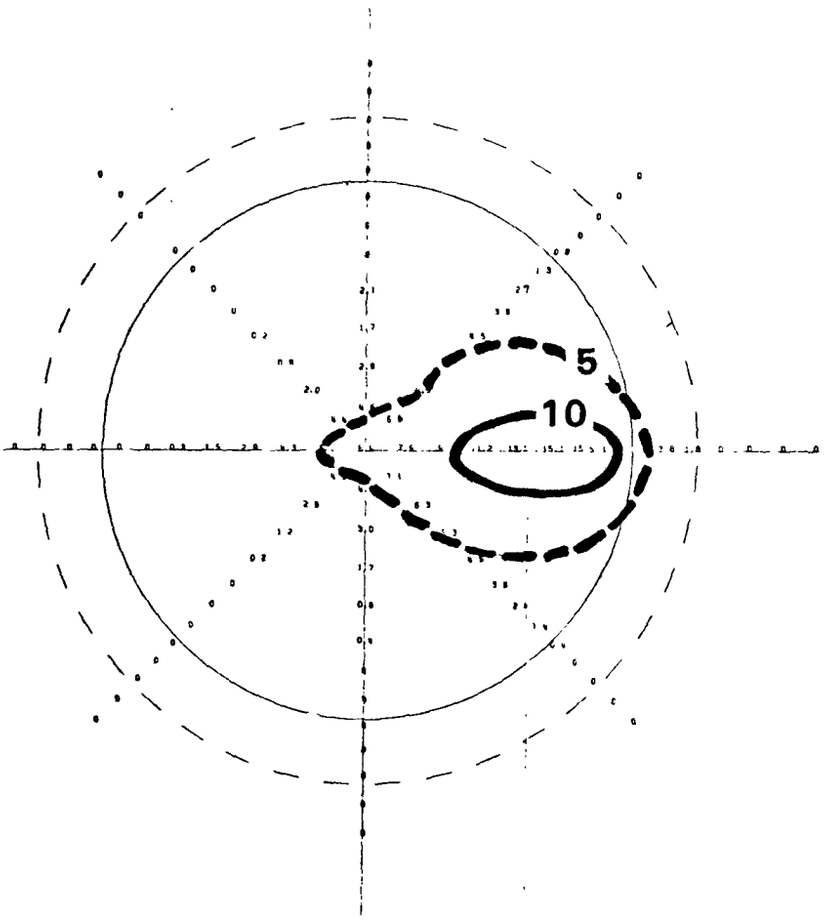

Figure A-16. Concentration distributions measured on the hill surface. F = 0.5, HS/H = 0.8, half submerged.

A scatter diagram comparing these two cases is presented in Figure A-17. The correspondence between the full- and half-depth immersion cases is clearly poor, with the half-depth immersion tow exhibiting surface concentrations that are generally less than half those from the full-depth tow. Both of these tows were repeated and the repeatability was found to be excellent, i.e., similar to that shown in Figure A-7 for the lower stack height of 0.6 h.

The poor correspondence in this case may be partially understood by examining the side- and top-view photographs of the plume as shown in Figures A-18 and A-19. The top-views show that, in the half-depth tow, the plume was much narrower on the lee side of the hill. The side views show that, in the full-depth tow, the plume "hugged" the hill surface on the lee side to elevations considerably lower than half the hill height, then lifted off the surface and rose somewhat in elevation with the hydraulic jump at the downwind base of the hill (not seen in the photograph). This hydraulic jump was not present in the half-depth tow, and the plume remained essentially at the water surface. The presence of the hydraulic jump evidently affects the flow structure on the lee side of the hill and, therefore, the concentration distributions on the lee side.

△ LIFDIF. B (4, 6) POLYNIL LIFT STUDY. COL 1, PORT NO.;COL 2 TO 7, CONC. FROM LIFT.015, .017, .014, .015, .016, AND .018, RESPECTIVELY.
01-DEC-83

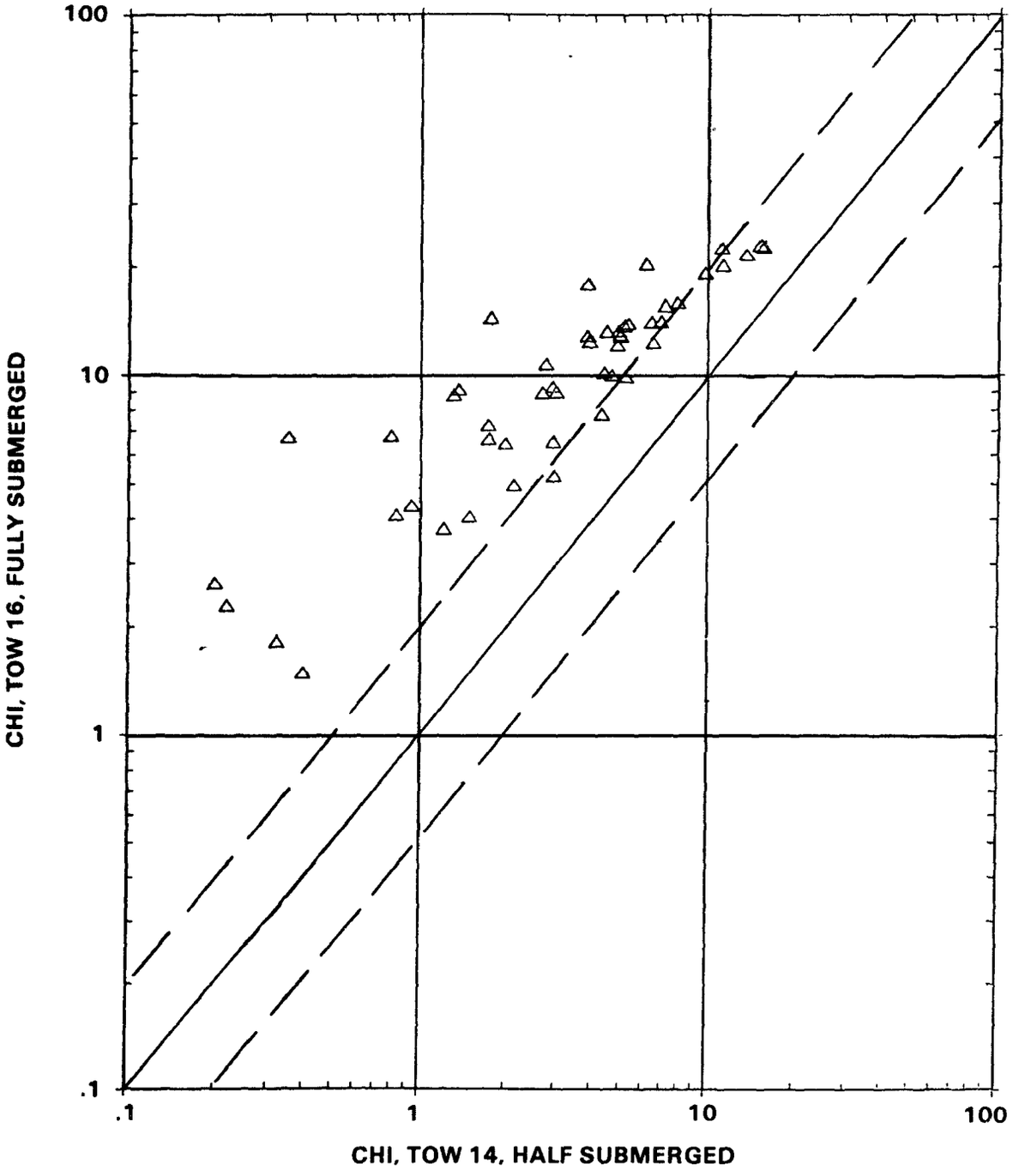

Figure A-17. Comparison of concentrations. Half submerged versus fully submerged. F = 0.5, HS/H = 0.8.

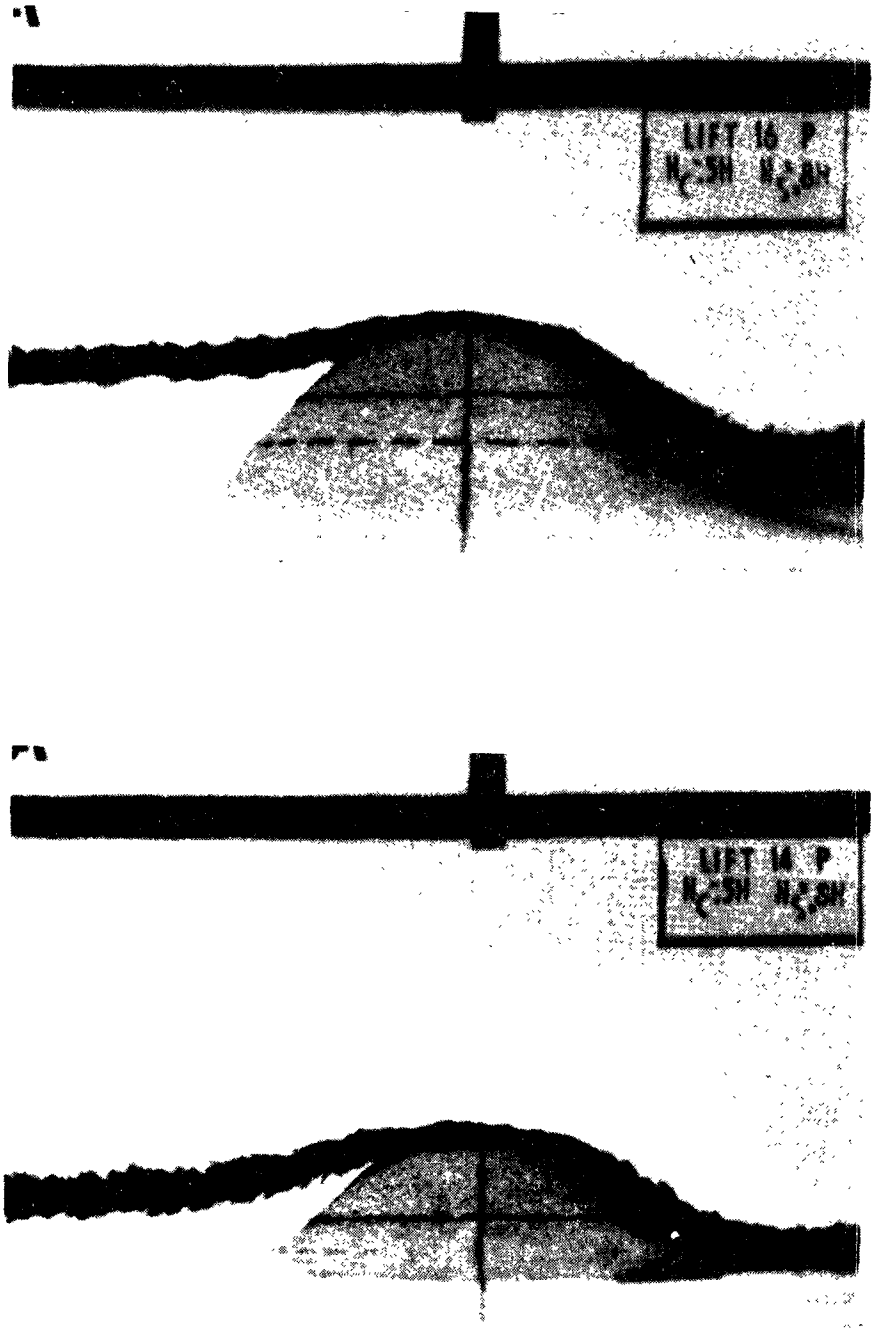

Figure A-18. Side views of plume released at 0.8 H. F = 0.5; upper, fully submerged; lower, half submerged.

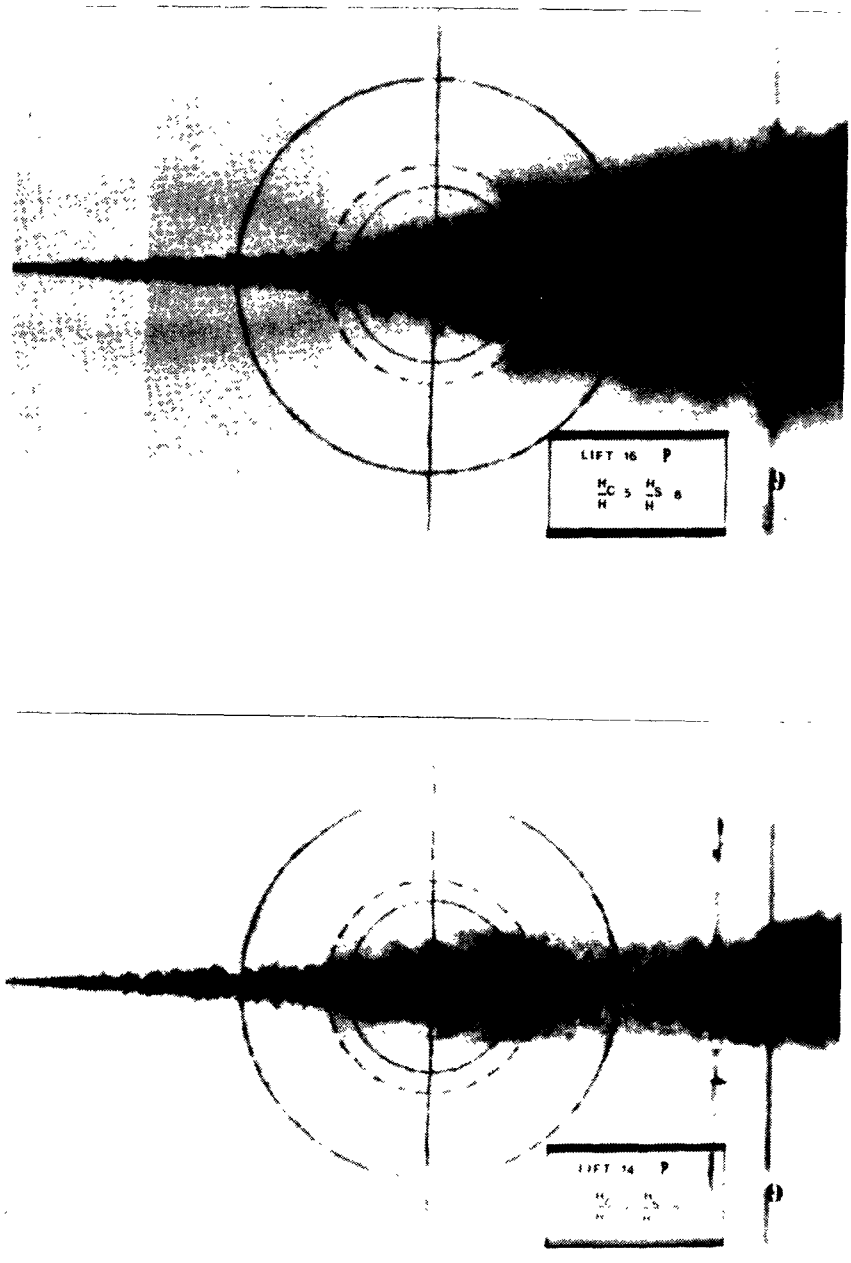

Figure A-19. Top views of plume released at 0.8 H. F = 0.5; upper, fully submerged; lower, half submerged.

4. CONCLUSIONS

A series of tows was conducted in a stably stratified, salt-water towing tank wherein the density gradient was linear and the dividing-streamline height was half the hill height. Effluent was released at 0.1 h, 0.2 h and 0.3 h above the dividing-streamline height, i.e., at elevations above the base of the hill of 0.6 h, 0.7 h and 0.8 h. Pairs of tows were made such that, in one tow, the hill was fully immersed in the water and the towing speed was adjusted to provide a "natural" dividing-streamline surface (i.e., not flat) of half the hill height (far upstream). In the second tow of the pair, the hill was raised out of the water to the point where only the top half of the hill was immersed; this, in effect, forced a flat dividing-streamline surface (the water surface itself). In both tows of each pair, all other conditions were maintained identical, e.g., towing speed, effluent release height and flow rate, and density gradient. Concentration distributions were measured on the hill surface and in the absence of the hill. The distributions from each pair of tows were compared to ascertain the effects of an assumed flat dividing-streamline surface.

Conclusions that may be drawn from this study are as follows:

1. Repeatability of concentration patterns from one tow to the next, under ostensibly identical conditions, is regarded as excellent, generally within $\pm$10%. The few points outside this range (but generally well within a factor of two) were found to be on the edges of the plume where the concentrations were quite small and the turbulent fluctuations naturally gave rise to this kind of variability.

2. At a stack height of 0.6 h (0.1 h above H_c), the maximum concentration occurred on the windward side of the hill; the plume was spread broadly to cover essentially the entire top half of the hill, but its thickness in the direction normal to the hill surface was small. Isoconcentration contours on the windward side were roughly circular. Comparison of the concentration patterns from the half- and full-immersion tows showed remarkable similarities over the top half of the hill. The locations of the maxima were essentially the same, although the value of the maxima was 10 to 20% larger for the half-immersion case. Regions of poor agreement included a thin band just above the half-hill height (where concentrations differed, in the worst case, by a factor of about four) and, of course, everywhere below the half-hill height.

3. At a stack height of 0.7 h (0.2 h above H_c), the maximum surface concentration occurred just downwind of the hill center, with a value nearly the same as with the stack height of 0.6 h. The plume was again spread broadly to cover most of the top half of the hill. Isoconcentration contours were again roughly circular on the windward side, but somewhat elongated in the flow direction. Comparison of the concentration patterns from the full- and half-depth tows again showed remarkable similarities and quite good agreement in the areas of higher concentration. Regions of poor agreement covered a broader band just above the half-hill height and, in that region, concentration values differed by as much as a factor of 8.

4 At a stack height of 0.8 h (0.3 h above H_c), the maximum concentration occurred well to the lee side of the hill and its value was substantially smaller than the maxima observed in the lower stack cases. Also in comparison with the lower stack cases, this plume was quite narrow, and the area of coverage on the hill surface was quite small. Comparison of the concentration patterns from the full- and half-depth tows showed that, in areas of large concentration, values of concentration differed by roughly factors of two. In areas of low concentration, values of concentration differed by up to a factor of 10.

5. Observations of the flow structure revealed that a hydraulic jump occurred near the downwind base of the fully immersed hill, but was absent in the case of the half-immersed hill. This hydraulic jump appeared to have a rather minor effect on the streamline pattern near the surface on the lee side of the hill, but, as pointed out by Snyder and Hunt (1984), surface concentrations are extremely sensitive to the ratio of the plume width to the normal distance of the plume centerline from the hill surface when this ratio is near unity. Hence, even a seemingly minor change in the streamline patterns can have a major effect on the concentration patterns.

6. Maximum concentrations on the surface under the "worst" conditions were equal to or somewhat greater than those observed at the plume centerline in the absence of the hill.

7. These results suggest that the assumption of a flat dividing-streamline surface in a mathematical model is a reasonable approximation to make, at least with regard to predicting the locations and values of maximum concentrations (and areas of coverage) on the windward side of the hill. When the stack heights are relatively close to the dividing-streamline height, the lee-side concentrations would also be predicted reasonably well.

8. Future work should include an improved concentration-measurement technique to resolve the question of whether or not hill-surface concentrations can exceed those at the plume centerline in the absence of the hill (and by how much).

REFERENCES

Bass, A., Strimaitis, D.G. and Egan, B.A., 1981: Potential Flow Model for Gaussian Plume Interaction with Simple Terrain Features, Rpt. to Envir. Prot. Agcy. under Contract No. 68-02-2759, Res. Tri. Pk., NC, p. 201.

Brighton, P.W.M., 1978: Strongly Stratified Flow Past Three-Dimensional Obstacles, Quart. J. Roy. Meteorol. Soc., v. 104, p. 289-307.

Drazin, P.G., 1961: On the Steady Flow of a Fluid of Variable Density Past an Obstacle, Tellus, v. 13, no. 2, p. 239-51.

Hunt, J.C.R., Puttock, J.S. and Snyder, W.H., 1979: Turbulent Diffusion from a Point Source in Stratified and Neutral Flows around a Three-Dimensional Hill: Part I: Diffusion Equation Analysis, Atmos. Envir., v. 13, p. 1227-39.

Hunt, J.C.R., Richards, K.J. and Brighton, P.W.M., 1984: Stratified Shear Flow over Low Hills: II. Stratification Effects in the Outer Flow Region, To be submitted to Quart. J. Roy. Meteorol. Soc.

Hunt, J.C.R. and Snyder, W.H., 1980: Experiments on Stably and Neutrally Stratified Flow over a Model Three-Dimensional Hill, J. Fluid Mech., v. 96, pt. 4, p. 671-704.

Hunt, J.C.R., Snyder, W.H., and Lawson, R.E. Jr., 1978: Flow Structure and Turbulent Diffusion around a Three-Dimensional Hill: Fluid Modeling Study on Effects of Stratification; Part I: Flow Structure, Rpt. No. EPA-600/4-78-041, Envir. Prot. Agcy., Res. Tri. Pk., NC.

Lavery, T.F., Bass, A., Strimaitis, D.G., Venkatram, A., Greene, B.R., Drivas, P.J. and Egan, B.A., 1982: EPA Complex Terrain Modeling Program: First Milestone Report - 1981, Rpt. No. EPA-600/3-82-036, Envir. Prot. Agcy., Res. Tri. Pk., NC, p. 304.

Lavery, T.F., Strimaitis, D.G., Venkatram, A., Greene, B.R., DiCristofaro, D.C. and Egan, B.A., 1983: EPA Complex Terrain Model Development: Third Milestone Report-1983, Rpt. No. EPA-600/3-83-101, Envir. Prot. Agcy. Rpt., Res. Tri. Pk., NC, p. 271.

Riley, J.J., Liu, H.T. and Geller, E.W., 1976: A Numerical and Experimental Study of Stably Stratified Flow Around Complex Terrain, Rpt. No. EPA-600/4-76-021, Envir. Prot. Agcy., Res. Tri. Pk., NC, p. 41.

Sheppard, P.A., 1956: Airflow over Mountains, Quart. J. Roy. Meteorol. Soc., v. 82, p. 528-9.

Snyder, W.H., Britter, R.E. and Hunt, J.C.R., 1980: A Fluid Modeling Study of the Flow Structure and Plume Impingement on a Three-Dimensional Hill in Stably Stratified Flow, Proc. Fifth Int. Conf. on Wind Engr. (J.E. Cermak, ed.), v. 1, p. 319-29, Pergamon Press, NY, NY.

Snyder, W.H. and Hunt, J.C.R., 1984: Turbulent Diffusion from a Point Source in Stratified and Neutral Flows around a Three-Dimensional Hill; Part II: Laboratory Measurements of Surface Concentration, Atmos. Envir. (to appear).

Strimaitis, D.G., Venkatram, A., Greene, B.R., Hanna, S., Heisler, S., Lavery, T.F., Bass, A., and Egan, B.A., 1982: EPA Complex Terrain Model Development: Second Milestone Report - 1982, Rpt. No. EPA-600/3-83-015, U.S. Envir. Prot. Agcy. Rpt., Res. Tri. Pk., NC.

Townsend, A.A., 1956: The Structure of Turbulent Shear Flow, Cambridge Univ. Press, Cambridge, England, p. 315.

APPENDIX B

DISPERSION FROM A SOURCE UPWIND OF A THREE-DIMENSIONAL HILL OF MODERATE SLOPE

DISPERSION FROM A SOURCE UPWIND OF A THREE-DIMENSIONAL HILL OF MODERATE SLOPE

Roger S. Thompson
and
William H. Snyder*

Meteorology and Assessment Division
Atmospheric Sciences Research Laboratory
Environmental Protection Agency
Research Triangle Park, NC 27711

May 1984

*On assignment from the National Oceanic and Atmospheric Administration, U.S. Department of Commerce.

1. INTRODUCTION

The series of experiments performed in 1980 at Cinder Cone Butte (CCB), Idaho, by Environmental Research and Technology, Inc. (Strimaitis et al., 1983 and Lavery et al., 1983) provide a data base for development and evaluation of dispersion models for complex terrain situations. As a follow-up and companion effort, fluid modeling studies have been performed at the EPA Fluid Modeling Facility using both a stratified towing tank and a meteorological wind tunnel. The work described in this report was inspired by an earlier case study of a one-hour period of the field study for which the atmosphere was neutral. That wind-tunnel study (see Appendix A of Lavery et al., 1983) provided good agreement between laboratory and field measurements of concentrations. However, the maximum observed concentration on the hill surface was found to be only about 10% greater than that observed from the same source over flat terrain; that is, the influence of CCB in increasing the maximum observed ground-level concentration (glc) was not dramatic. Thus, a set of experiments to determine the influence of the hill on the maximum glc and to locate the source positions where this influence is the greatest was a natural continuation of the fluid modeling effort. The data base for mathematical modeling evaluation is extended by these measurements. All measurements were made under simulated atmospheric conditions.

The nearly-axisymmetric CCB shape was replaced with a truly axisymmetric hill having a simple mathematical formula. The average silhouette of CCB was best fit by the formula to maintain a close relationship with the previous efforts: the maximum slope of CCB was matched in the model.

Since, for upwind sources, the maximum ground-level concentration can be expected to occur from sources on the centerline, this study was restricted to only those source positions. The maximum concentrations from these sources are expected to occur along the centerline through the source and hill center; thus, measurements were limited to centerline sampling port locations.

The measure of the influence of the hill on the maximum glc was computed as a "terrain amplification factor" A. This factor is defined as the ratio of the maximum glc observed with the hill present to the maximum observed in the absence of the hill. The location of the maxima are not considered in this evaluation.

2. EXPERIMENTAL DETAILS

The model selected for this study is an idealization of Cinder Cone Butte (CCB), an isolated three-dimensional hill about 100 meters high. As described in the First Milestone Report (Lavery et al., 1982), CCB has a double peak but is roughly axisymmetric. Typical maximum slopes are about 25 degrees.

Profiles of the shape of CCB along radial lines for azimuths of 0, 10, 20, ..., and 350 degrees were graphed. Several functional forms were considered as approximations to the average silhouette of CCB. The function that was found to best fit the hill shape is

$$h(r) = \begin{cases} (H+\delta)/(1+(r/L)^4) - \delta & 0 \leq r \leq R \\ 0 & r > R \end{cases}$$

where: r is the radius,
h is the local height,
H is the height at the center,
δ is a vertical offset for a finite model,
L is the radius for which $h = H/2$ if $\delta = 0$,
and R is the radius of the modeled area.

The vertical offset was included in the formula to avoid a discontinuity at the edge of the model. For CCB, H = 100 m, L = 250 m, R = 500 m, and δ = 6.25 m were chosen. This gives a maximum slope angle of 24.4 degrees. Comparison of this function with CCB silhouettes at intervals of 90 degrees in the azimuth are shown in Figure B-1.

Another appealing reason to use this hill shape is that Hunt et al. (1978) previously used the same functional form (however, with H/L = 1 which gives a maximum slope angle of 45 degrees) in experiments that established a large data base, which is available for comparison. Also, the Fourier transform of this function should be obtainable for use in mathematical models.

A scale model of the idealized CCB was vacuum molded of acrylic plastic over a wood form. The height of the model was 15.5 cm which corresponds to a scale of 1:640 based on the 100 m height assumed for CCB. The radius of the model was 0.78 m. The vertical offset in the shape function prevented a discontinuity in the surface at the edge of the model. If the model had followed the formula exactly there would have been a discontinuity in the slope at the model edge of 2.7 degrees. But the edge was faired during construction.

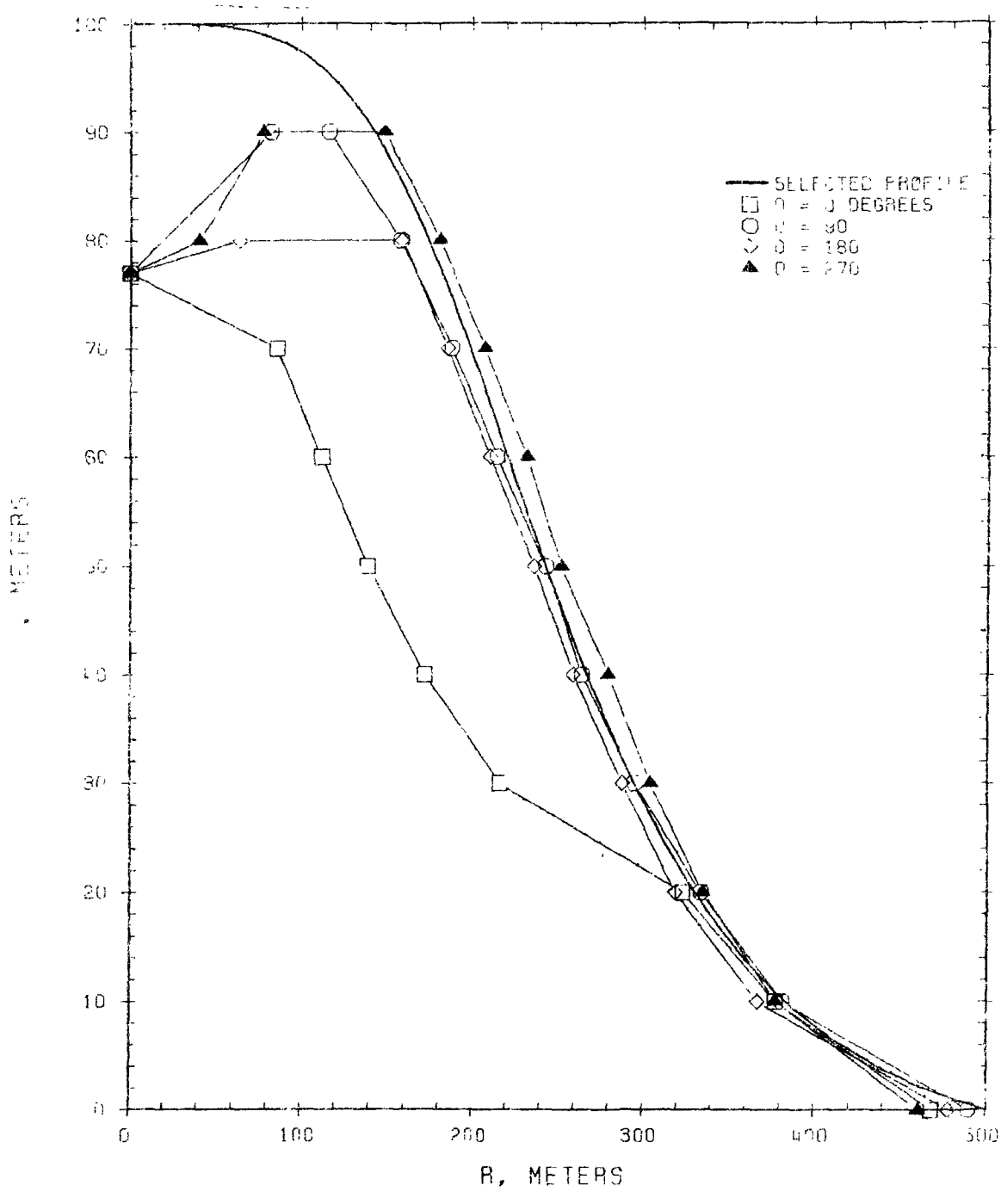

Figure B-1. Silhouettes of Cinder Cone Butte and the profile selected for this axisymmetric hill study.

The model was covered with gravel of the same size used in roughening the test section floor for boundary layer generation. The same boundary layer generating devices used in the study described in the Third Milestone Report (Lavery et al., 1983) were again used for this study. The model was located with its center at a distance of 13.8 m downstream of the entrance to the test section.

Mean velocity and turbulence intensity measurements were made with hot-film anemometers (TSI model 1241 probes and model 1053B anemometers). A bent-over brass tube (o.d. = 0.32 cm) was used to emit a non-buoyant tracer gas (methane, 99% pure). The emission rate was 2950 cm^3/min which gave an exit velocity of about two times the local speed. Samples were drawn through ports located on the hill surface or through sampling rakes, positioned with the instrument carriage, for locations upwind or downwind of the hill or in the absence of the hill. Flame ionization detectors (Beckman model 400 Hydrocarbon Analyzers) were used to measure the sampled concentration. Two-minute averages were obtained of values sampled at rates of one sample per second for the flame ionization detectors and 500 samples per second for the anemometers with the laboratory's minicomputer.

When necessary to consider actual concentrations rather than terrain amplification factors or other ratios of concentrations, a non-dimensional concentration χ was calculated according to

$$\chi = CU(H)H^2/Q$$

Where C = the measured concentration,
$U(H)$ = the approach wind speed at $z = H$,
H = the hill height, and
Q = the emission rate of tracer.

For visualization, plumes were generated with cotton tipped glass tubes of liquid titanium tetrachloride (marketed as "smoke sticks" by E. Vernon Hill, Inc.). Photographs of these plumes were taken with a Graphlex 4X5 camera fitted with a Polaroid back and type 55 P/N film. Two 500 w photolamps were directed at the hill from elevated positions downwind of the hill on either side of the test section. A "time-averaged" photograph was obtained by making eight one-second exposures with an interval of a few seconds between the exposures.

3. MEASUREMENTS AND RESULTS

Vertical and lateral profiles of mean velocity and turbulence intensity were obtained in the wind tunnel test section before installing the model. The vertical profiles were measured at distances of 10 and 14 m from the beginning of the floor roughness (11.6 hill heights upstream and 14.2 hill heights downstream of the position selected for the hill center). These profiles define the approach wind field and demonstrate the uniformity of the wind tunnel flow over the portion of the test section used for this study (Figures B-2 and B-3). Lateral traverses were made at the 10 m distance at heights of one-half and one times the hill height. Along these traverses, the mean velocity and turbulence intensities varied by less than 4%.

Fitting a power-law profile to the approach flow mean velocity gives an exponent of 0.166, that is, $u(z) \propto z^{0.166}$. A logarithmic fit gives z_o = 0.2 mm or 0.0013 times the hill height and u_*/k = 0.51 m/s.

As required for computation of A, ground-level concentrations were measured for sources in the absence of the hill. Stack heights of 0, 40, 80, 120, 160, and 200 mm were selected to be integer multiples of 1/4 of the anticipated hill height of 160 mm; however, the true height of the model came out to be 155 mm. These same stack heights were used with the model in place and are referred to as stack heights of 1/4, 1/2, 3/4, 1, and 1 1/4 hill heights. The distances from the hill center to the source were also scaled by the hill height.

The reference (no hill) data base consists of longitudinal profiles of glc for the various stack heights (Figure B-4) normalized (Berlyand, 1975) using the maximum glc (χ_{max}) and the distance to that maximum (x_{max}) as similarity parameters (Figure B-5). The dependence of these parameters on the source height H_s was determined to be

$$\chi_{max} \propto H_s^{-2.08}, \text{ and}$$

$$x_{max} \propto H_s^{1.15}.$$

The maximum concentrations from these profiles were used to calculate the terrain amplification factors.

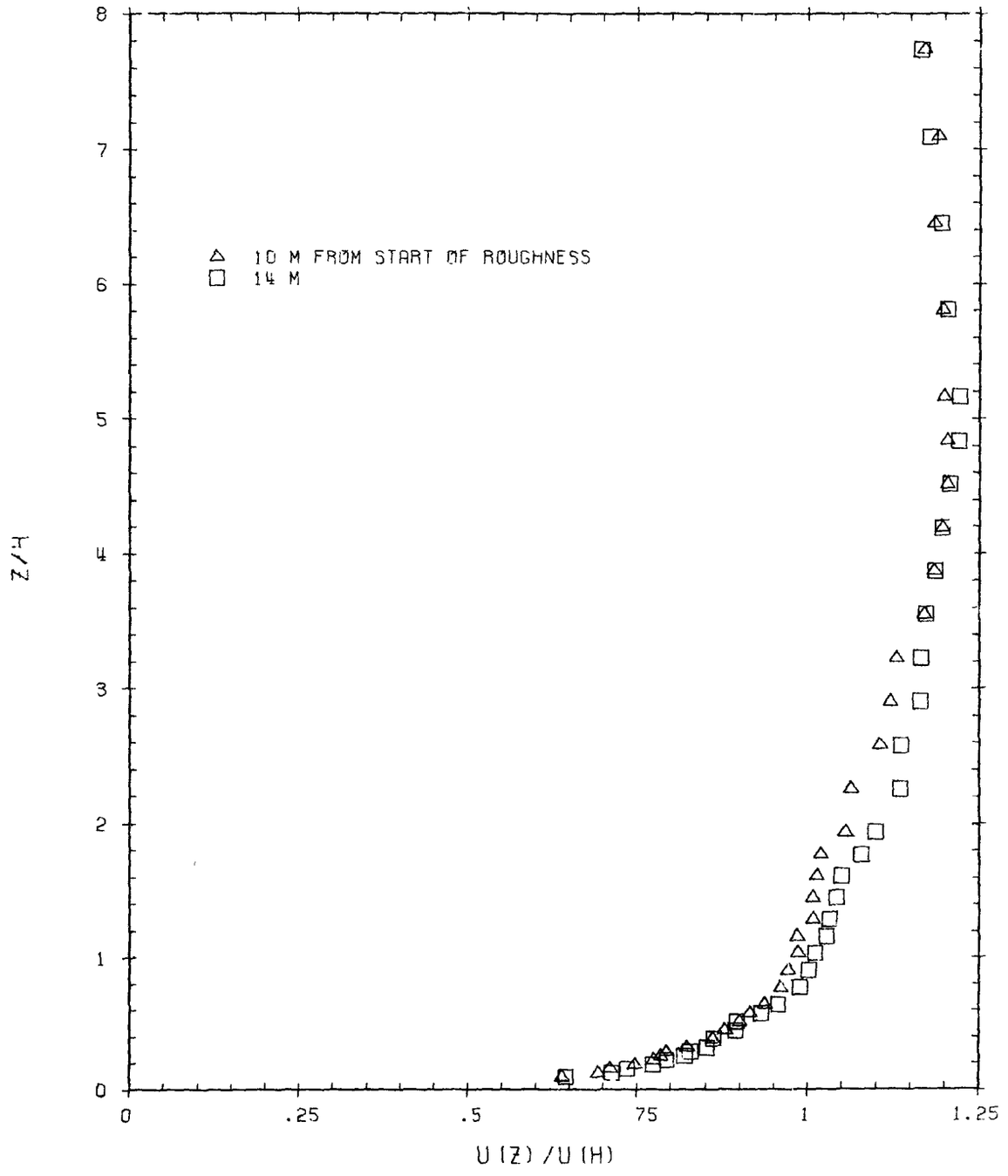

Figure B-2. Vertical profiles of the mean air speed in the test section of the wind tunnel. H = Hill height.

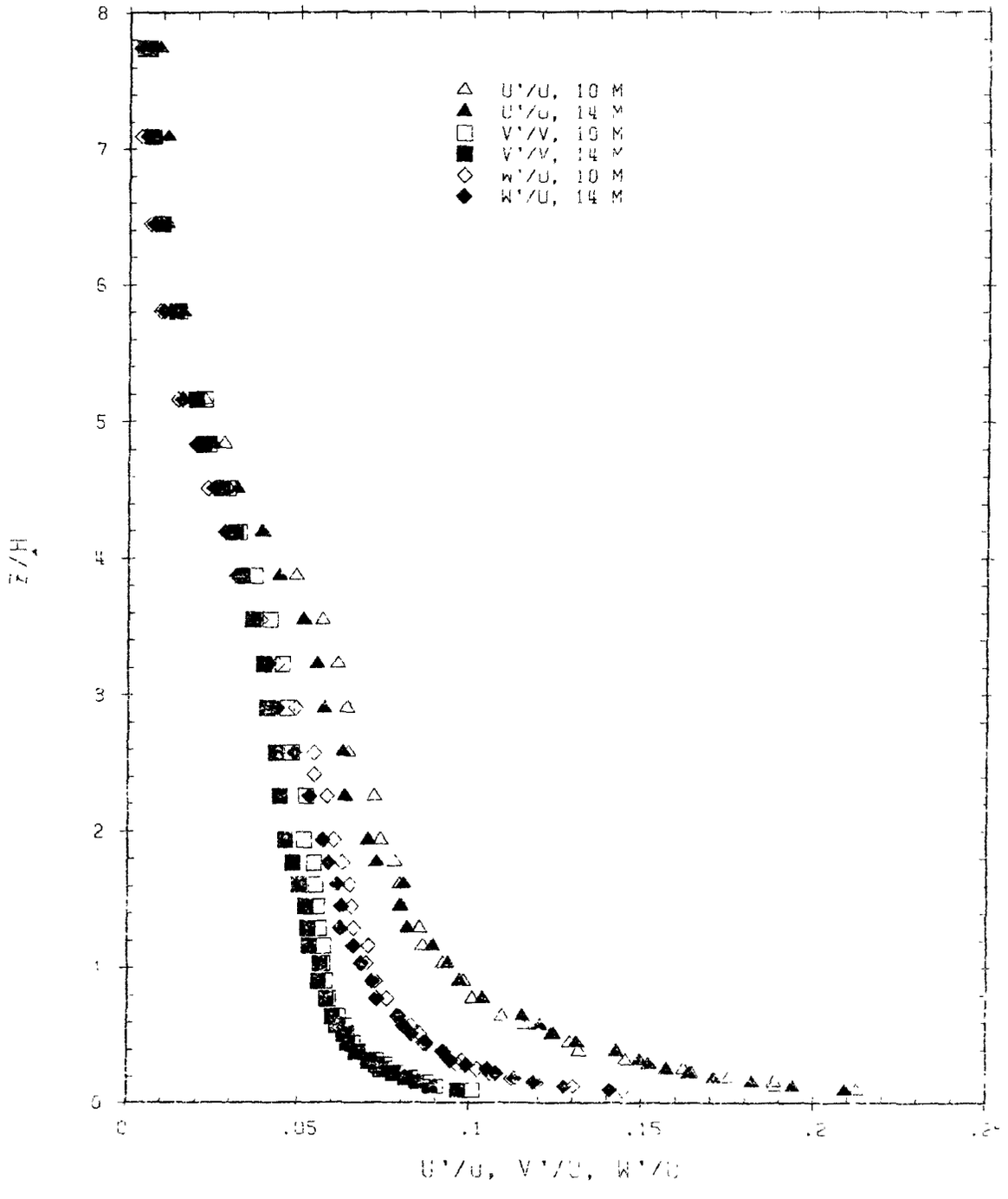

Figure B-3. Vertical profiles of local turbulence intensities in the test section of the wind tunnel.

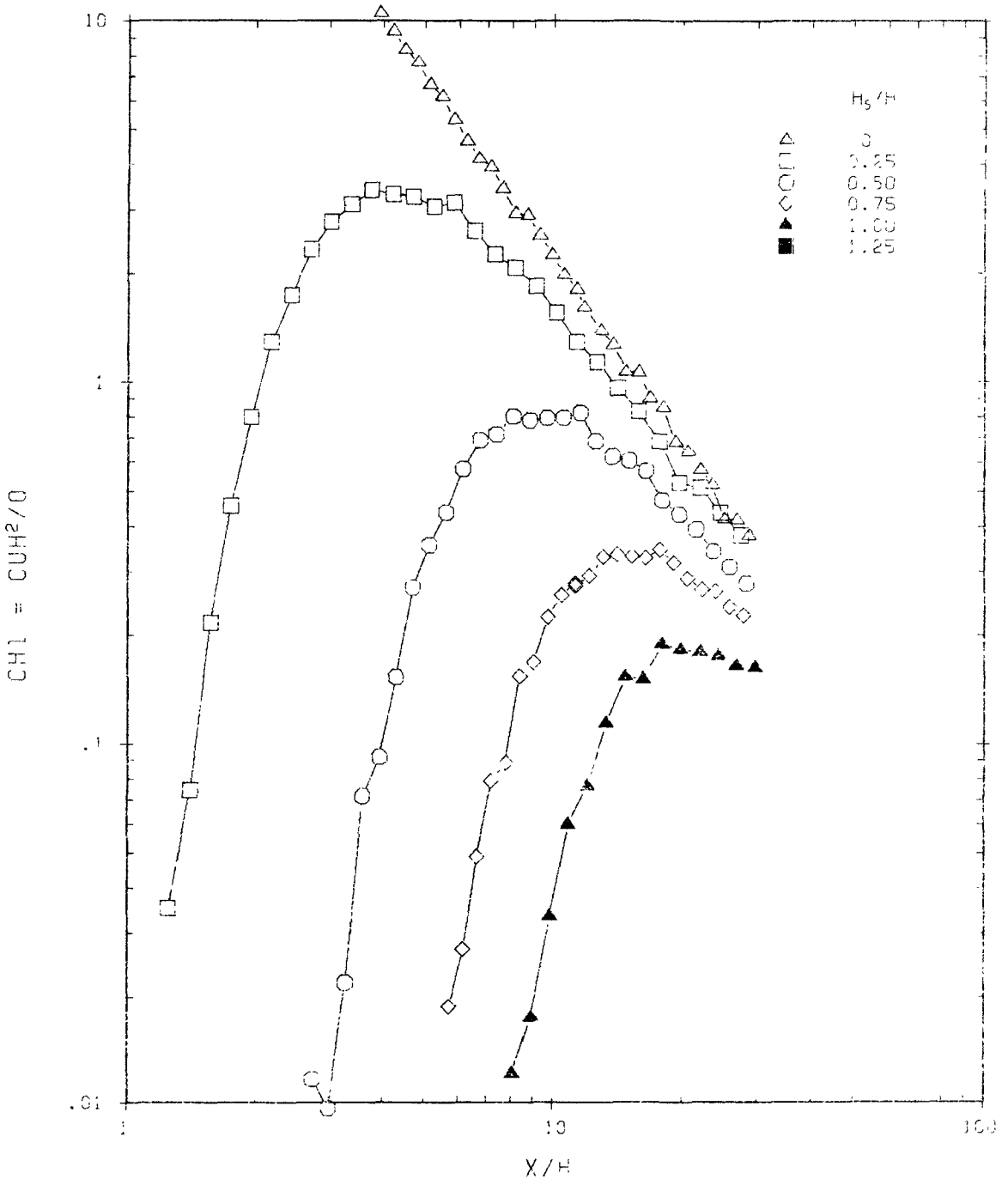

Figure B-4. Longitudinal profiles of ground-level concentration from point sources in the absence of the model.

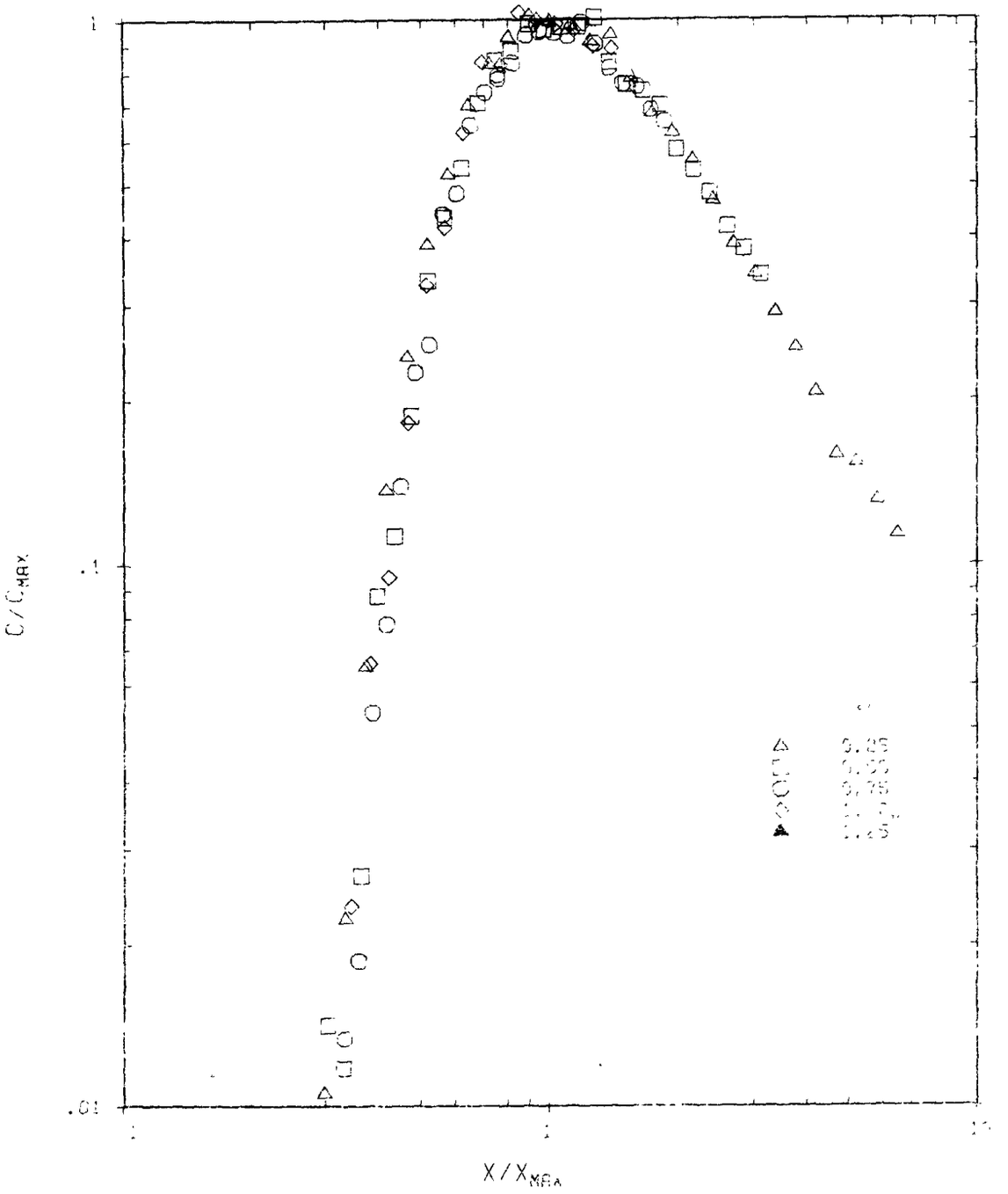

Figure B-5. **Longitudinal profiles of ground-level concentration from point sources in the absence of the model plotted in similarity coordinates.**

With the hill in place, glc's were measured on the hill via surface ports on the hill and both upwind and downwind of the hill with sampling rakes. Sources were located at distances of 4 to 16 hill heights upwind of the center of the model and at heights of 1/4 to 1 1/4 times the hill height. Complete longitudinal profiles of the glc were obtained for selected source positions; but for most positions, only sufficient measurements were made to find the maximum glc.

The presence of the hill may be considered to influence the transport and dispersion of the plume to increase the maximum glc in three ways. For low sources, at moderate distances from the hill, the reduction in mean wind speed allows the plume to reach the ground surface closer to the source, producing higher concentrations than in the absence of the hill. Plumes from higher sources can be thought of as being intercepted by the hill. That is, the hill penetrates the plume where the concentrations are greater than those that would occur at ground level farther downstream over flat terrain. For yet higher sources, the streamline convergence over the hilltop and the corresponding downward flow in the lee of the hill brings the plume to the ground more rapidly than over flat terrain. The maximum concentration for these three regimes occurs upwind of the hilltop, near or on the hilltop, or downwind of the hilltop, respectively. The distance from the source to the maximum glc was always observed to be less in the presence of the hill. No amplification factors less than 1.0 were observed in this study; that is, the hill's presence never influenced the dispersion from these upwind sources to produce a maximum glc that was less than would occur over flat terrain.

Hunt et al. (1979) presented a theoretical argument for the presence of a "window" of upwind source locations that produce a terrain amplification factor of 2 or greater for three-dimensional terrain objects. They show that for sources within this window, the maximum concentrations occur on or near the hill.

A series of longitudinal profiles of glc for all source heights at a distance of six hill heights upwind of the hill center exhibit these types of influence (Figure B-6). The H_s = 0.25 H source has its maximum glc occur near the upwind base of the hill; a low plume being slowed by the presence of the hill. The maximum glc for the H_s = 0.75 H stack occurs on the hill top; the hill intersecting the plume. The H_s = 0.5 H stack produces a large region of nearly constant concentration over the upwind face and crest of the hill; a combination of the first two types of influence. Two nearly equal maxima occur for the H_s = 1.0 H stack, one on the hill top and one downwind of the hill. The maximum glc for the H_s = 1.25 H stack clearly occurs downwind of the hill. Figure B-7 gives photographs of the H_s = 0.5 H and H_s = 1.25 H plumes to illustrate their behavior.

All of the above concentration profiles exhibit a rapid reduction in concentration at approximately 1 1/2 to 2 hill heights downwind of the hill center. The flow separated from the hill surface at this point and concentrations just downstream were determined by the concentrations in the recirculating flow.

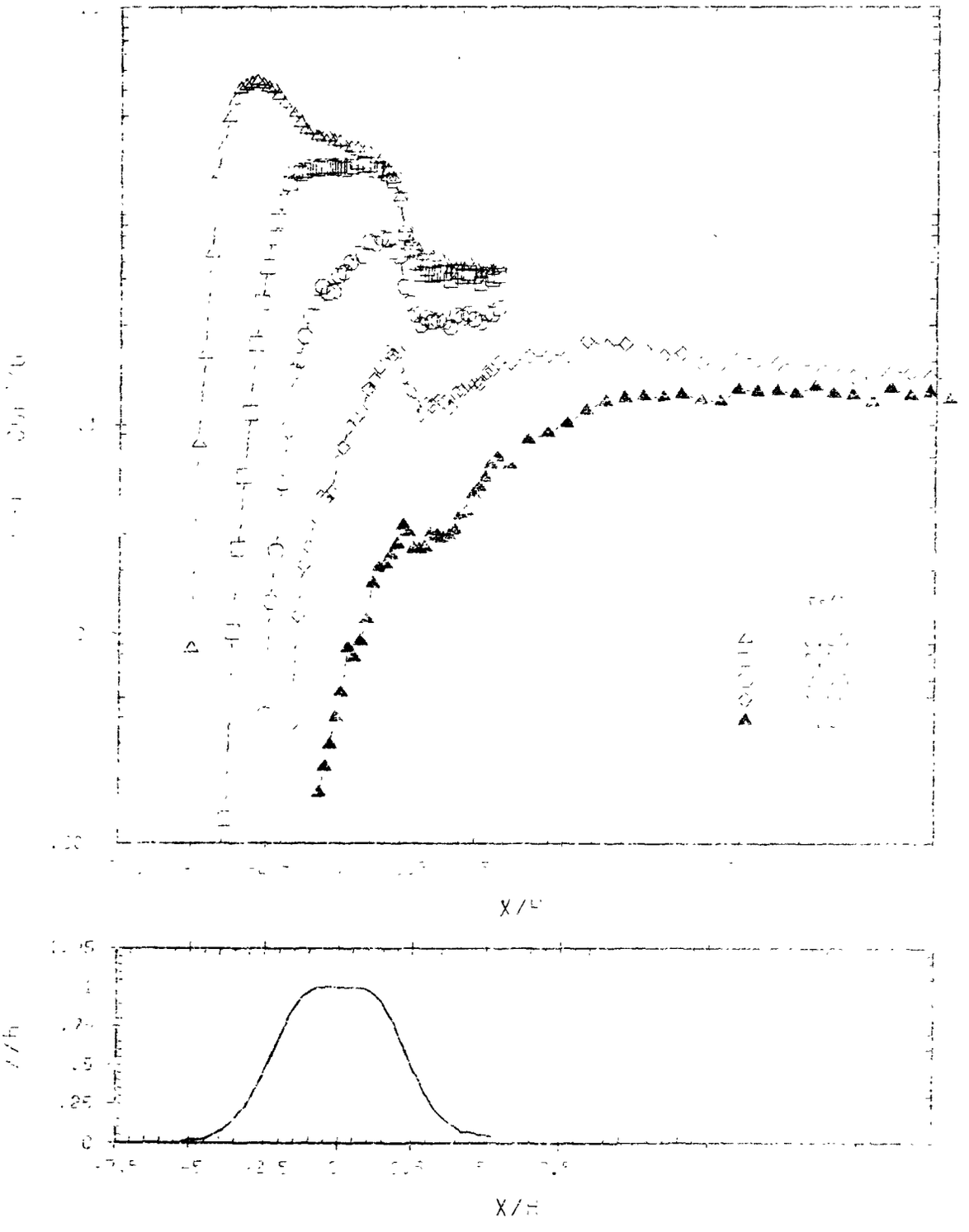

Figure B-6. Longitudinal profiles of glc for sources located six hill heights upwind of the hill center. Hill profile shown below; note exaggerated scale.

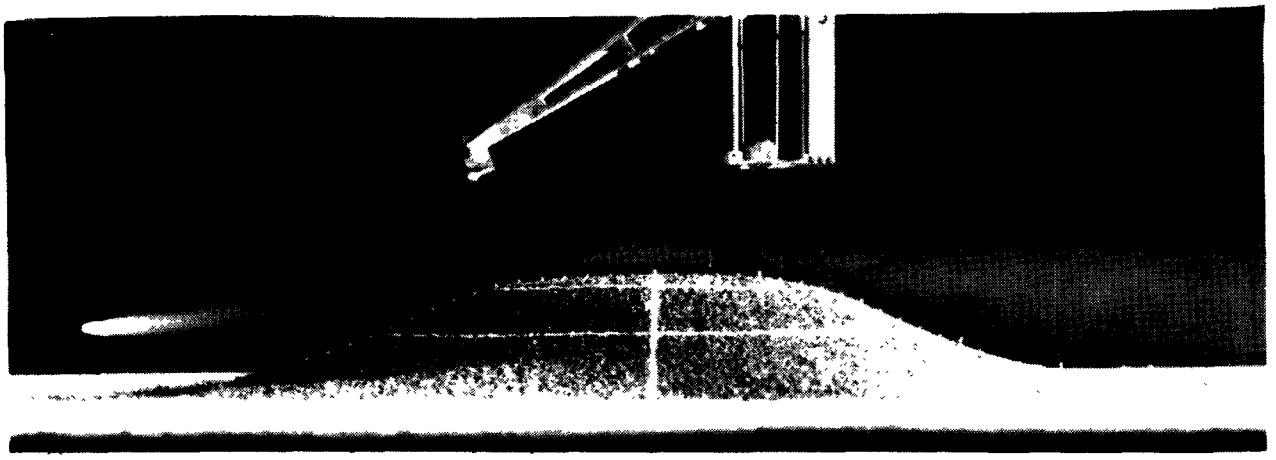

a) $H_s/H = 0.50$

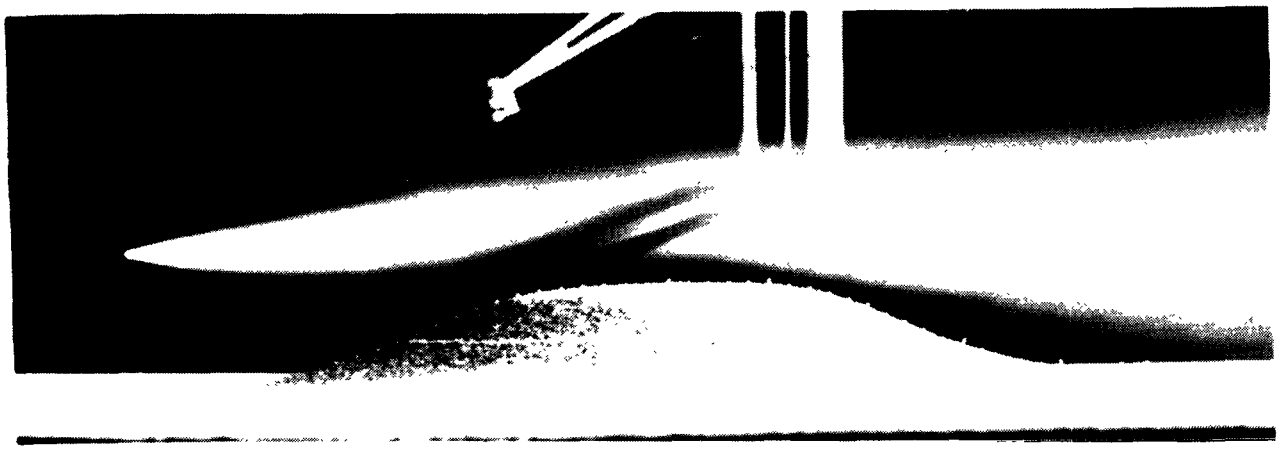

b) $H_s/H = 1.25$

Figure B-7. Visualization of plumes from sources at x/H = -5.

Terrain amplification factors for all source positions are presented in Figure B-8. Lines of constant A (= 1.4 and 2.0) are shown as dashed lines. The solid lines divide the area into three regions, where the source produces its maximum glc upwind of the hilltop, on the hilltop (between the peak and the separation point), and downwind of the hill.

Terrain amplification factors were computed for a hill of similar functional form but much greater slope (45°) using data from Snyder and Britter (1979) who report on a continuation of the work by Hunt et al. (1978). That study used a boundary layer of approximately the same depth but it was generated with a rougher surface (larger size of gravel coating) and a smooth hill that was one and a half times the height of the hill used in the present effort. The rougher surface produced turbulence intensities a factor of two larger than in the present study. Surface concentration profiles were obtained for two source positions: release heights of one-half and one times the hill height at a distance of 3.62 hill heights upwind of the hill center.

The terrain amplification factors for these source locations were computed to be A = 4.00 and 1.27 for the stacks one-half and one times the hill height, respectively. Values for the present study were calculated from releases at a slightly greater upwind distance (4 hill heights). They were 3.63 and 1.27 for the same stack heights, respectively.

The earlier work with the scale model of Cinder Cone Butte (see Appendix A, Lavery et al., 1983) also provides a point for comparison. The source was located 10 hill heights upwind, if we consider the hill height to be 100 m. However, it was not directly upwind of the hill center but on a line 3° from the mean wind direction. The source height was 0.42 H. The maximum concentration occurred at a position toward the side of the hill about halfway up. The terrain amplification factor was computed to be 1.08. This falls between the values for the present study of 1.0 and 1.55 for stacks at the same upwind distance but heights of 0.25 H and 0.50 H, respectively.

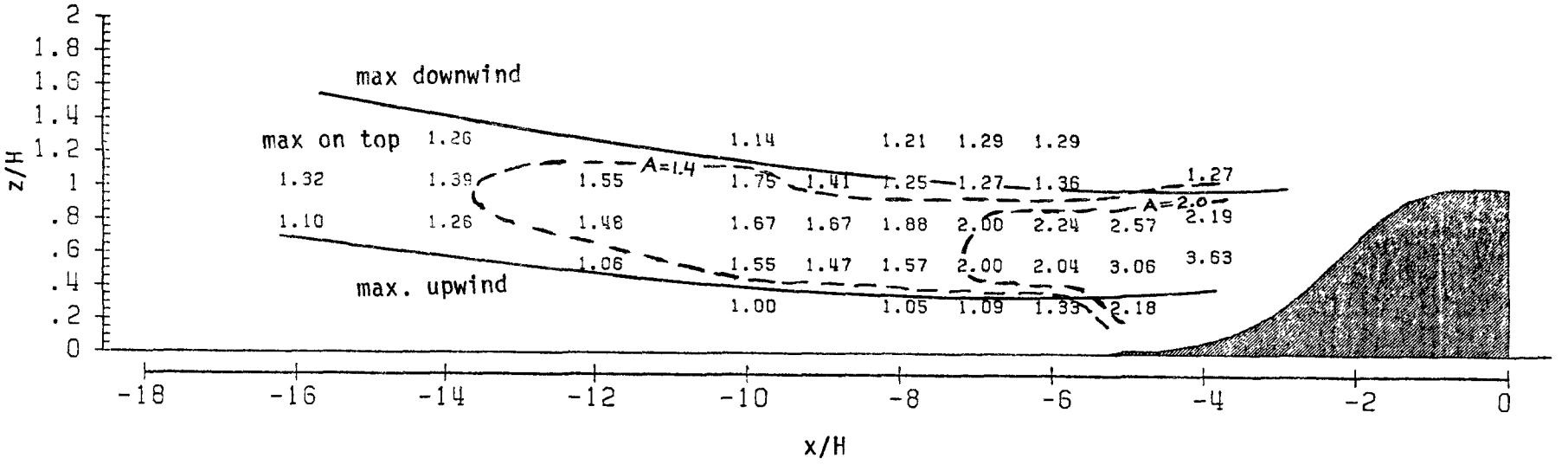

Figure B-8. Terrain amplification factors for sources upwind of the axisymmetric hill. Solid lines divide the region into areas where the source produced the maximum glc upwind of the hilltop, between the hilltop and the separation point, and downwind of the hill.

4. SUMMARY AND CONCLUSIONS

A wind-tunnel study was performed to investigate the influence of an idealized three-dimensional hill on ground-level concentrations from upwind sources in a neutral atmospheric boundary layer and to locate the source locations where this influence is the greatest.

The presence of the hill was found to influence the transport and dispersion of the plume to increase the maximum glc in three ways. For low sources, at moderate distances from the hill, the reduction in mean wind speed allows the plume to reach the ground surface closer to the source, producing higher concentrations than in the absence of the hill. Plumes from higher sources can be thought of as being intercepted by the hill. That is, the hill penetrates the plume where the concentrations are greater than those that would occur at ground level farther downstream over flat terrain. For yet higher sources, the streamline convergence over the hilltop and the corresponding downward flow in the lee of the hill brings the plume to the ground more rapidly than over flat terrain. The maximum concentration for these three regimes occurs upwind of the hilltop, near or on the hilltop, or downwind of the hilltop, respectively. Terrain amplification factors ranged from near 1.0 to 3.63. The region of source locations that produced an amplification factor of 1.4 or more extended to an upwind distance of 14 hill heights.

REFERENCES

Berlyand, M.G., 1975: Contemporary Problems of Atmospheric Diffusion and Air Pollution, Hydromet. Press, Leningrad, USSR, 448p.

Hunt, J.C.R., Puttock, J.S. and Snyder, W.H., 1979: Turbulent Diffusion from a Point Source in Stratified and Neutral Flows Around a Three Dimensional Hill: Part I: Diffusion Equation Analysis, Atmos. Envir., v. 13, p. 1227-39.

Hunt, J.C.R., Snyder, W.H. and Lawson, R.E., 1978: Flow Structure and Turbulent Diffusion around a Three-Dimensional Hill: Fluid Modeling Study on Effects of Stratification: Part I: Flow Structure, Rpt. No. EPA 600/4-78-041, Envir. Prot. Agcy., Res. Tri. Pk., NC, 96p.

Lavery, T.F., Bass, A., Strimaitis, D.G., Venkatram, A., Greene, B.R., Drivas, P.J. and Egan, B.A., 1982: EPA Complex Terrain Model Development: First Milestone Report - 1981, Rpt. No. EPA 600/3-82-036, Envir. Prot. Agcy., Res. Tri. Pk., NC, 304p.

Lavery, T.F., Strimaitis, D.G., Venkatram, A., Greene, B.R., DiCristofaro, D.C. and Egan, B.A., 1983: EPA Complex Terrain Model Development: Third Milestone Report - 1983, Rpt. No. EPA 600/3-83-101, Envir. Prot. Agcy., Res. Tri. Pk., NC, 271p.

Snyder, W.H. and Britter, R.E., 1979: Aspect Ratio Study: Unpublished In-house Data Report, Envir. Prot. Agcy., Res. Tri. Pk., NC.

Strimaitis, D.G., Venkatram, A., Greene, B.R., Hanna, S.R., Heisler, S., Lavery, T.F., Bass, A. and Egan, B.A., 1983: EPA Complex Terrain Model Development: Second Milestone Report - 1982, EPA 600/3-85-015. Envir. Prot. Agcy., Res. Tri. Pk., NC 375p.

APPENDIX C

ALPHA-1 OBSERVATIONS OF THE TRACY OIL-FOG PLUME*

*This appendix is a condensation of a report by Uthe and Morley (1984).

C.1 Introduction

During the November experiment the ALPHA-1 airborne lidar mapped aerosol plume behavior in the vicinity of the Tracy Generating Station. The ALPHA-1 was based at the Reno airport and was operated by SRI International under the sponsorship of the Electric Power Research Institute.

An oil-fog tracer aerosol was generated and emitted from the Tracy Station with a plume sufficiently dense for photographic purposes. The ALPHA-1 mapped the plume behavior by making cross-plume traverses above the plume at various downwind distances from the Tracy Station. Typically, the plume traverses were made at downwind increments of 0.5 nmi from the Tracy Station to 6 nmi downwind. The aircraft typically operated at an altitude of 10,000 ft MSL, although lower altitudes were flown during cloudy conditions. The mountainous terrain and nighttime conditions prevented data collection during times when cloud bases were below 7500 ft. The experimental data collection typically began at about midnight and extended to 0900 PST. The ALPHA-1 normally made two flights, each between three and four hours in duration.

The ALPHA-1 operation consisted of transmitting 1.06 μm wavelength laser pulses at a repetition rate of 5/second (horizontal resolution of about 12 m depending on aircraft ground speed). See Uthe et al. (1980a and 1980b) for a description of the ALPHA-1 system. Received energy was detected, logarithmically amplified, and digitized at 20 ns (3 meter) intervals. Lidar signatures were stored on nine-track 1600 bpi magnetic tape and were also used to generate real-time facsimile pictorial displays of plume, atmosphere and terrain structure. Aircraft location was determined both by a LORAN-C and RNAV system. The RNAV was programmed to provide distance and bearing to the Tracy Station. Aircraft location and time information were recorded on magnetic tape for each laser firing. The RNAV data also were plotted on the facsimile recorder to provide the information needed to direct the lidar data collection. The ALPHA-1 logarithmic amplifier saturates for signals greater than about four orders of magnitude (40 dB). The ground returns are normally saturated. Because of the dense aerosol plume, plume returns near the source were near saturation of the receiver amplifiers. Therefore, near-surface plume returns were difficult to separate from ground returns. To solve this problem, the transmitted energy was decreased by a factor of 2 (3 dB), providing more dynamic range between plume and ground returns. However, the reduced transmitted energy also decreased sensitivity to low-density atmospheric aerosol features. A log of data collection times is presented in Table C-1.

The ALPHA-1 data records are stored on nine-track 1600 bpi magnetic tape in binary forms. The data consists of 1000 8-bit lidar backscatter values for each laser firing. Also recorded in each block of data are the time and location. The magnetic tape records are maintained at SRI for future analysis.

TABLE C-1

LOG OF ALPHA-1 DATA COLLECTION
TRACY GENERATING STATION, NOVEMBER 1983

Date (Nov 83)	Time (PST)	Flight Time (hr)	Remarks
5	---	1.2	ferry
6	1125-1140	1.0	test flight
7	0155-0420	3.5	
8	0015-0325	3.7	
9	0240-0530	3.4	
12	0035-0340	3.6	
12	0500-0720	2.8	2nd flight
14	0040-0335	3.4	
14	0435-0800	3.8	2nd flight
15	0025-0340	3.7	
15	0435-0735	3.4	2nd flight
15	2135-2330	2.5	
16	0235-0240	0.5	clouds and turbulence
17/18	2225-0130	3.5	
18	0320-0345	0.8	2nd flight/clouds
19	0025-0130	1.5	rain and snow
19	---	1.8	ferry
	Total	44.1	

The ALPHA-1 magnetic tapes were used to generate facsimile displays that depict plume, atmosphere, and terrain structure. The displays also provide time and aircraft location. Tables presenting information needed to interpret the lidar pictures are given in Section C.2 and the lidar pictures are reproduced in Section C.3. The reproduced pictorial records are reduced in size and the originals provide a better indication of plume behavior. These original facsimile records are available on a loan basis from SRI.

C.2 Date, Time, Altitude, and Location Data

This section provides a listing (Table C-2) of date and time information needed to interpret the ALPHA-1 facsimile data plots presented in Section C.3.

The listing provides the page number of Appendix B of the original report by Uthe and Morley (1984) that presents facsimile plots for each of the 87 data tapes collected during the Tracy program. Tape number is identified on the lower left hand side of the facsimile plots. Picture number refers to the data presented within vertical solid lines and each picture presents an individual ALPHA-1 cross section. The ALPHA-1 was turned off during times between the individual cross sections. Time (PST) is given for the first time mark of each picture. Time marks are identified in the key to reading the lidar cross sections presented in Figure C-1. In Section C.3 only the facsimile plots representative of the three case studies described in Section 6 of this Milestone Report are given.

Aircraft location is determined by an area navigation (RNAV) system that provides information on bearing and distance to a selected waypoint position. The waypoint was established at the Tracy Station, and distance and bearing to the station are plotted on the facsimile data displays. Figure C-2 presents a map of the Tracy area with ALPHA-1 coordinates of distance (nmi) and bearing to the Tracy Station superimposed. LORAN-C data on longitude and latitude were also recorded but not plotted on the displays. Figure C-1 is an example of ALPHA-1 backscatter signatures processed as a facsimile record for Tape 45 (page B-23). Terrain, plume, and atmospheric features are identified. Location of time marks, altitude scale, and aircraft location plots are given as a key for interpreting the cross sections presented in Section C.3. The altitude scale is 600 m/division for all data.

TABLE C-2

DATE AND TIME DATA FOR ALPHA-1 DATA COLLECTION
AT THE TRACY GENERATING STATION, NOVEMBER 1983

Gray Scale Depiction			Date/
Page *	Tape	Picture	Time (PST)
B-2			6 Nov 1983(1)
	1	1	1125
			7 Nov 1983(2)
B-2	2	1	0156
		2	0159
		3	0202
		4	0204
		5	0207
		6	0212
		7	0216
		8	0219
B-3	3	1	0223
		2	0225
		3	0227
		4	0230
		5	0233
		6	0236
		7	0242
		8	0245
B-3	4	1	0253
		2	0256
		3	0259
		4	0303
		5	0307
		6	0310
		7	0314
B-4	5	1	0317
		2	0321
		3	0325
		4	0329
		5	0332
		6	0338
		7	0342

Gray Scale Depiction			Date/
Page	Tape	Picture	Time (PST)
B-4	6	1	0346
		2	0349
		3	0354
		4	0356
		5	0359
		6	0401
		7	0404
		8	0406
B-5	7	1	0409
		2	0411
		3	0414
		4	0416
		5	0419
			8 Nov 1983
B-5	8	1	0014
		2	0017
		3	0020
		4	0023
		5	0026
		6	0029
		7	0031
		8	0034
		9	0037
B-6	9	1	0042
		2	0045
		3	0048
		4	0054
		5	0059
		6	0102
		7	0105
B-6	10	1	0109
		2	0113
		3	0116

(1) Location from Reno Vortac (test flight).

(2) All following locations from Tracy Power Plant.

*** Page number of the original report by Uthe and Morley (1984).**

TABLE C-2 (Continued)

Gray Scale Depiction			Date/ Time (PST)
Page	Tape	Picture	
			8 Nov 1983
B-6	10	4	0119
		5	0123
		6	0128
		7	0131
B-7	11	1	0138
		2	0141
		3	0144
		4	0149
		5	0154
B-7	12	1	0200
		2	0203
		3	0206
		4	0216
		5	0219
		6	0222
B-8	13	1	0227
		2	0331
		3	0235
		4	0243
		5	0246
		6	0251
		7	0253
B-8	14	1	0257
		2	0300
		3	0303
		4	0306
		5	0310
		6	0312
		7	0316
B-9	15	1	0326
			9 Nov 1983
B-9	16	1	0244
		2	0246
		3	0250
		4	0252
		5	0255
		6	0258

Gray Scale Depiction			Date/ Time (PST)
Page	Tape	Picture	
			9 Nov 1983
B-9	16	7	0302
		8	0304
		9	0307
		10	0309
B-9	17	1	0312
		2	0314
		3	0317
		4	0319
		5	0322
		6	0325
		7	0328
		8	0330
B-10	18	1	0336
		2	0342
		3	0345
		4	0348
		5	0352
		6	0354
		7	0358
		8	0401
B-10	19	1	0406
		2	0409
		3	0412
		4	0414
		5	0417
		6	0420
		7	0422
		8	0425
B-11	20	1	0434
		2	0438
		3	0442
		4	0446
		5	0449
		6	0453
B-11	21	1	0459
		2	0506
		3	0509
		4	0513

TABLE C-2 (Continued)

Gray Scale Depiction			Date/ Time (PST)
Page	Tape	Picture	
			9 Nov 1983
B-11	21	5	0516
B-12	22	1	0522
		2	0528
			12 Nov 1983
B-12	23	1	0035
		2	0038
		3	0042
		4	0046
		5	0049
B-13	24	1	0057
		2	0102
		3	0106
		4	0110
		5	0113
		6	0116
B-13	25	1	0120
		2	0124
		3	0128
		4	0131
		5	0135
		6	0138
B-14	26	1	0143
		2	0146
		3	0150
		4	0153
		5	0157
		6	0203
B-14	27	1	0207
		2	0213
		3	0216
		4	0220
		5	0223
B-15	28	1	0228
		2	0231
		3	0235
		4	0242

Gray Scale Depiction			Date/ Time (PST)
Page	Tape	Picture	
			12 Nov 1983
B-15	28	5	0247
B-15	29	1	0253
		2	0258
		3	0302
		4	0307
		5	0311
B-16	30	1	0317
		2	0322
		3	0329
		4	0334
		5	0338
B-16	31	1	0503
		2	0506
		3	0512
		4	0519
B-17	32	1	0525
		2	0532
		3	0536
		4	0539
		5	0543
B-17	33	1	0549
		2	0554
		3	0558
		4	0602
		5	0605
		6	0609
B-18	34	1	0613
		2	0617
		3	0621
		4	0625
		5	0630
B-18	35	1	0636
		2	0641
		3	0644
		4	0647
		5	0650

TABLE C-2 (Continued)

Gray Scale Depiction			Date/
Page	Tape	Picture	Time (PST)
			12 Nov 1983
B-18	35	6	0655
B-19	36	1	0702
		2	0709
		3	0712
		4	0718
			14 Nov 1983
B-19	37	1	0043
		2	0046
		3	0049
		4	0052
		5	0055
		6	0100
		7	0105
B-20	38	1	0110
		2	0114
		3	0119
		4	0125
		5	0130
B-20	39	1	0134
		2	0139
		3	0142
		4	0147
		5	0151
B-21	40	1	0200
		2	0204
		3	0208
		4	0213
		5	0216
B-21	41	1	0222
		2	0226
		3	0231
		4	0234
		5	0240
B-22	42	1	0246
		2	0250
		3	0252

Gray Scale Depiction			Date/
Page	Tape	Picture	Time (PST)
			14 Nov 1983
B-22	42	4	0256
		5	0259
		6	0303
B-22	43	1	0313
		2	0317
		3	0320
		4	0323
		5	0326
		6	0330
		7	0334
		8	0336
B-23	44	1	0439
		2	0441
		3	0444
		4	0467
		5	0451
		6	0454
B-23	45	1	0459
		2	0502
		3	0506
		4	0509
		5	0513
		6	0516
B-24	46	1	0521
		2	0524
		3	0528
		4	0539
		5	0547
B-24	47	1	0551
		2	0555
		3	0558
		4	0602
		5	0605
		6	0608
B-25	48	1	0624
		2	0626
		3	0629

TABLE C-2 (Continued)

Gray Scale Depiction			Date/ Time (PST)
Page	Tape	Picture	
			14 Nov 1983
B-25	48	4	0632
		5	0634
		6	0637
		7	0640
		8	0642
B-25	49	1	0647
		2	0650
		3	0652
		4	0655
		5	0658
		6	0701
		7	0704
		8	0707
B-26	50	1	0712
		2	0715
		3	0717
		4	0720
		5	0722
		6	0724
		7	0726
		8	0728
		9	0730
B-26	51	1	0734
		2	0738
		3	0741
		4	0743
		5	0746
		6	0750
		7	0753
B-27	52	1	0757
		2	0800
			15 Nov 1983
B-27	53	1	0026
		2	0028
		3	0031
		4	0033
		5	0036

Gray Scale Depiction			Date/ Time (PST)
Page	Tape	Picture	
			15 Nov 1983
B-27	53	6	0039
		7	0042
		8	0044
		9	0047
B-28	54	1	0051
		2	0055
		3	0057
		4	0100
		5	0105
		6	0108
		7	0111
B-28	55	1	0115
		2	0119
		3	0122
		4	0124
		5	0127
		6	0130
		7	0136
B-29	56	1	0139
		2	0143
		3	0146
		4	0149
		5	0152
		6	0155
		7	0158
B-29	57	1	0202
		2	0205
		3	0209
		4	0212
		5	0215
		6	0219
B-30	58	1	0226
		2	0229
		3	0233
		4	0237
		5	0241
		6	0245

TABLE C-2 (Continued)

Gray Scale Depiction			Date/
Page	Tape	Picture	Time (PST)
			15 Nov 1983
B-30	59	1	0249
		2	0253
		3	0256
		4	0301
		5	0305
		6	0309
B-31	60	1	0313
		2	0317
		3	0320
		4	0323
		5	0326
		6	0328
		7	0332
		8	0334
B-31	61	1	0339
B-32	62	1	0437
		2	0440
		3	0444
		4	0448
		5	0452
		6	0455
B-32	63	1	0459
		2	0505
		3	0510
		4	0515
B-33	64	1	0521
		2	0525
		3	0530
		4	0534
		5	0538
B-33	65	1	0542
		2	0546
		3	0552
		4	0557
		5	0600
		6	0603

Gray Scale Depiction			Date/
Page	Tape	Picture	Time (PST)
			15 Nov 1983
B-34	66	1	0606
		2	0609
		3	0612
		4	0615
		5	0618
		6	0621
		7	0624
B-34	67	1	0633
		2	0636
		3	0638
		4	0641
		5	0644
		6	0649
		7	0651
B-35	68	1	0656
		2	0701
		3	0704
		4	0707
		5	0710
		6	0713
		7	0716
B-35	69	1	0719
		2	0722
		3	0725
		4	0729
		5	0732
B-36	70	1	2137
		2	2139
		3	2142
		4	2146
		5	2151
		6	2154
		7	2157
		8	2201
B-36	71	1	2206
		2	2209
		3	2213

TABLE C-2 (Continued)

Gray Scale Depiction			Date/
Page	Tape	Picture	Time (PST)
			15 Nov 1983
B-36	71	4	2219
		5	2222
		6	2229
B-37	72	1	2233
		2	2238
		3	2240
		4	2243
		5	2245
		6	2249
		7	2252
B-37	73	1	2259
		2	2302
		3	2306
		4	2309
		5	2313
		6	2317
		7	2320
B-38	74	1	2325
		2	2328
			16 Nov 1983
B-38	75	1	0235
		2	0237
			17 Nov 1983
B-38	76	1	2228
		2	2232
		3	2236
		4	2239
		5	2243
		6	2247
		7	2250
B-39	77	1	2254
		2	2257
		3	2300
		4	2304
		5	2307
		6	2311
		7	2315

Gray Scale Depiction			Date/
Page	Tape	Picture	Time (PST)
			17 Nov 1983
B-39	78	1	2319
		2	2324
		3	2331
		4	2335
		5	2340
B-40	79	1	2345
		2	2349
		3	2353
		4	2357
			18 Nov 1983
B-40	79	5	0001
		6	0004
B-40	80	1	0008
		2	0011
		3	0013
		4	0016
		5	0018
		6	0024
		7	0026
		8	0029
		9	0031
B-41	81	1	0034
		2	0038
		3	0040
		4	0043
		5	0046
		6	0049
		7	0054
		8	0057
		9	0059
B-41	82	1	0103
		2	0105
		3	0108
		4	0110
		5	0112
		6	0115
		7	0117
		8	0123

TABLE C-2 (Continued)

Gray Scale Depiction			Date/	Gray Scale Depiction			Date/
Page	Tape	Picture	Time (PST)	Page	Tape	Picture	Time (PST)
			18 Nov 1983				
B-41	82	9	0126*				
B-42	83	1	0131*				
B-42	84	1	0322*				
		2	0327*				
		3	0330*				
		4	0336*				
		5	0339*				
			19 Nov 1983				
B-42	85	1	0023				
		2	0025				
		3	0028				
		4	0030				
		5	0033				
		6	0036				
		7	0038				
		8	0042				
B-43	86	1	0054				
		2	0059				
		3	0101				
		4	0105				
		5	0107				
		6	0110				
		7	0112				
		8	0114				
B-43	87	1	0118				
		2	0122				
		3	0125*				
		4	--				
		5	0130				

*Cross section along axis of the plume.

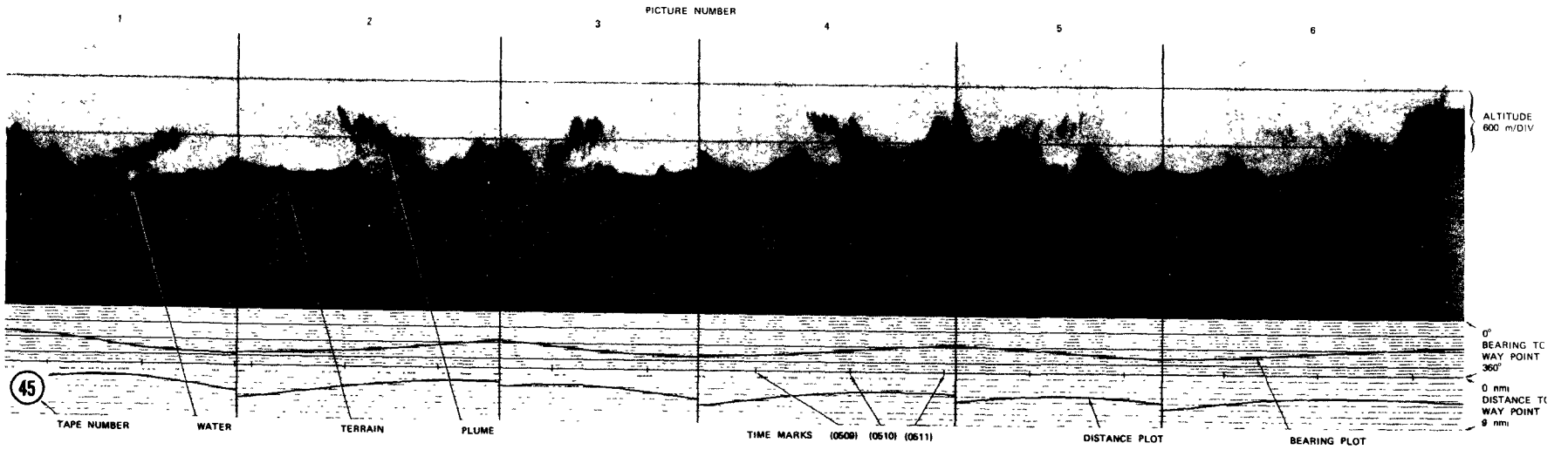

Figure C-1 Key to reading ALPHA-1 cross sections

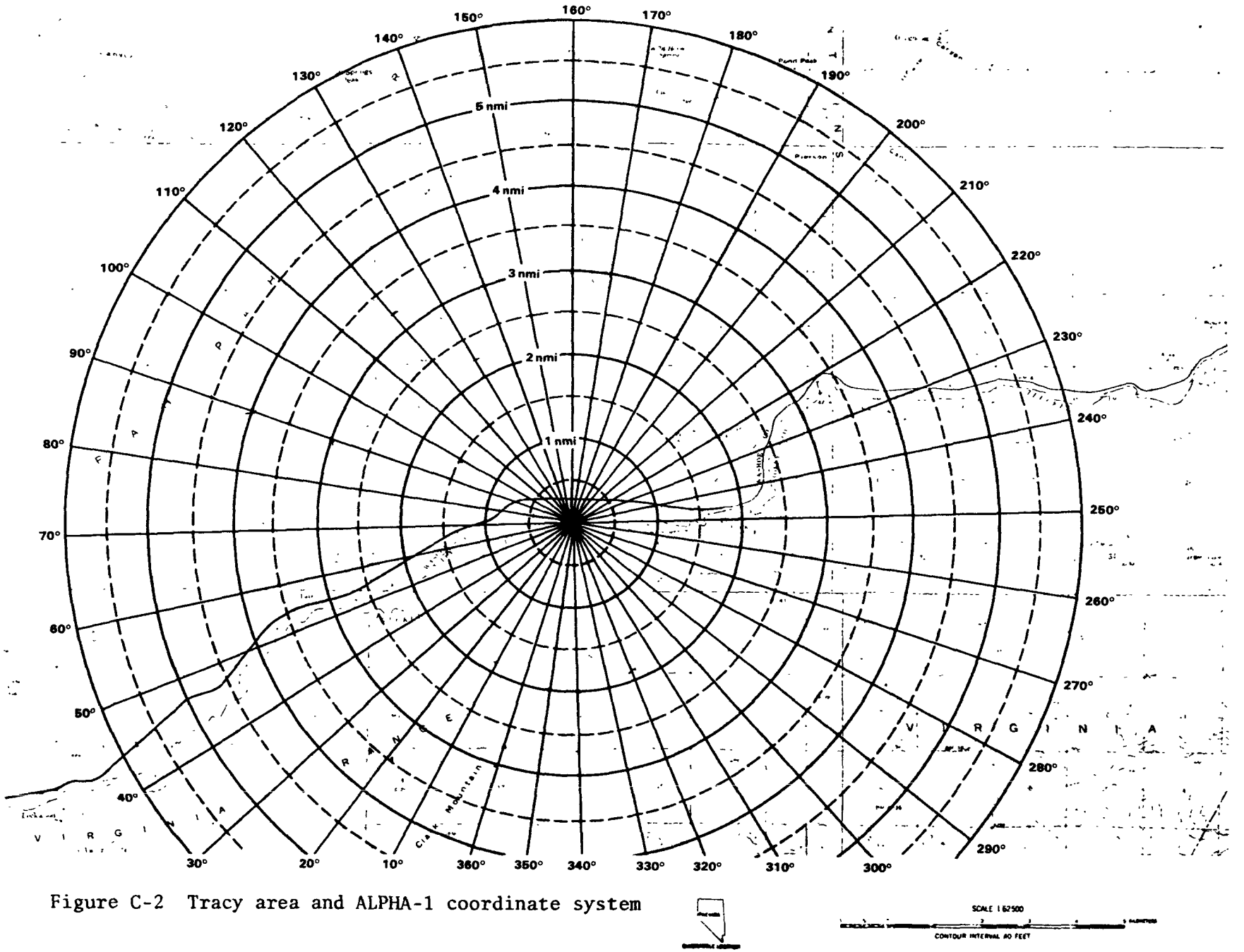

Figure C-2 Tracy area and ALPHA-1 coordinate system

C.3 ALPHA-1 Facsimile Records for the Case Study Experiments Discussed in Section 5

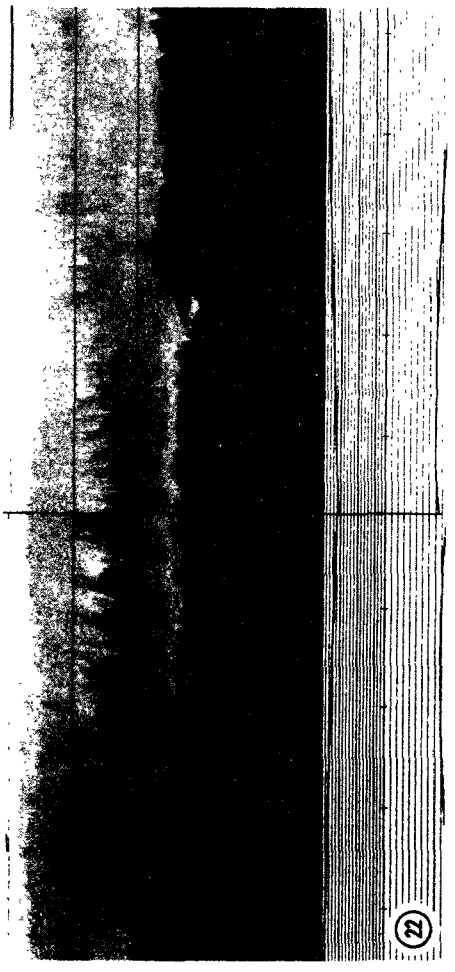

(22)

(23)

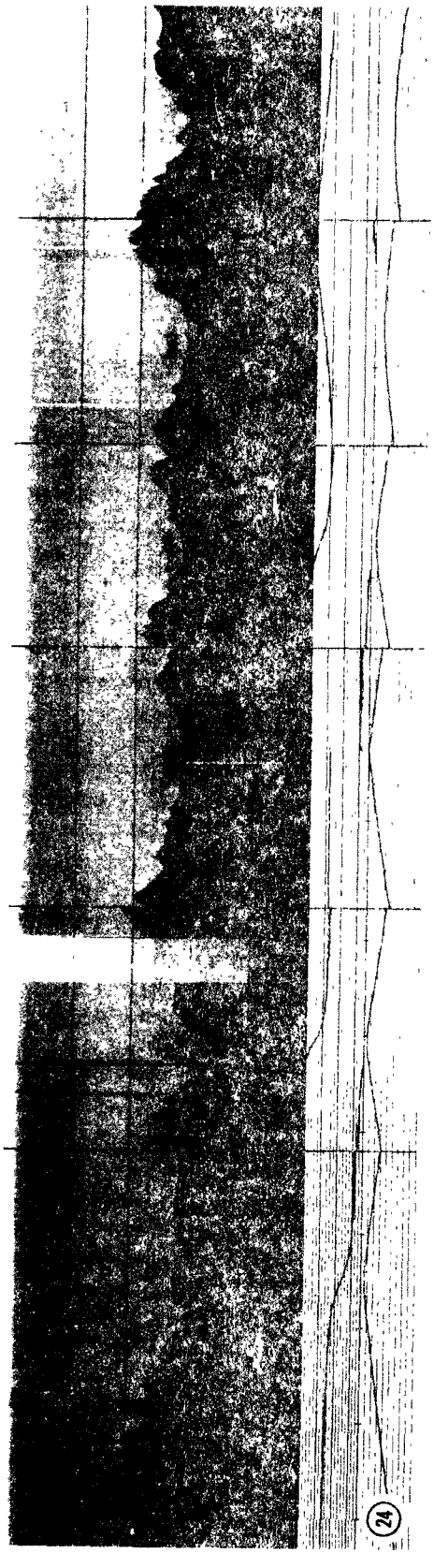

(24)

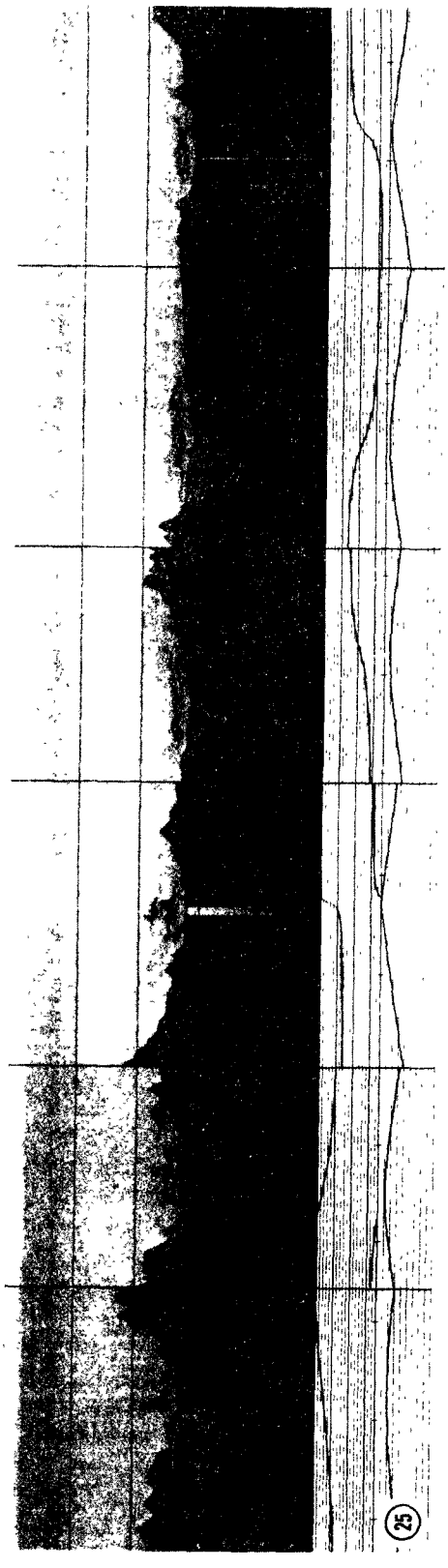

(25)

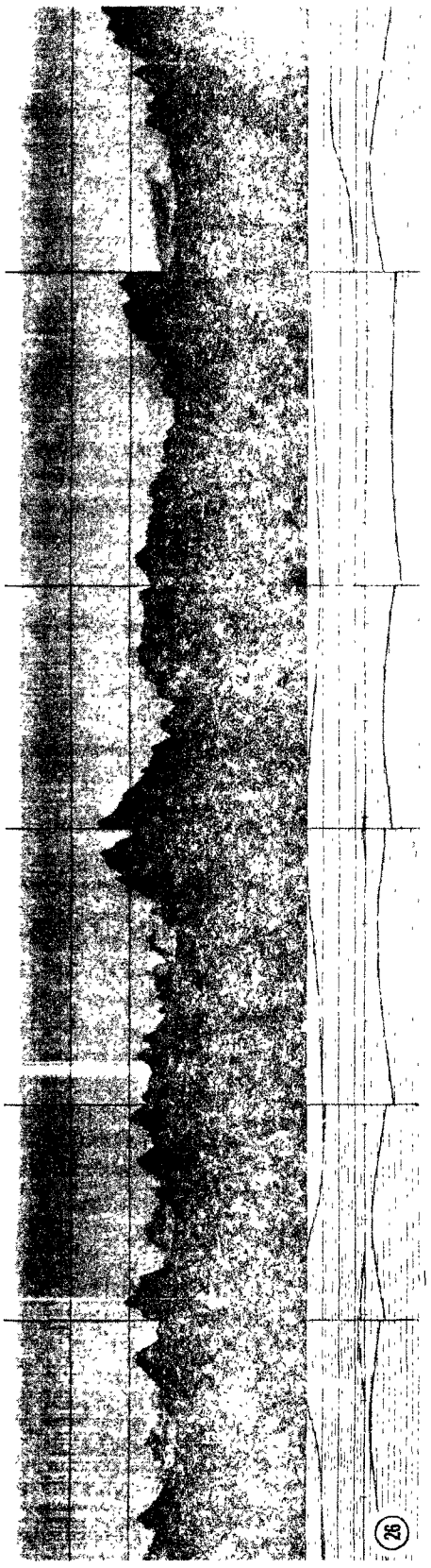

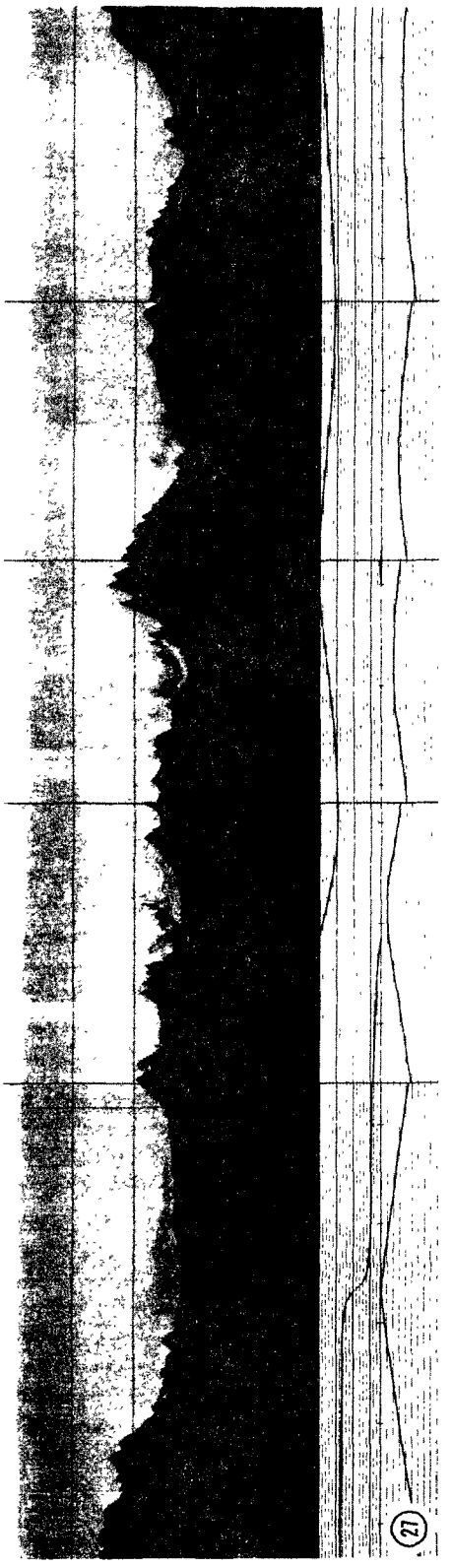

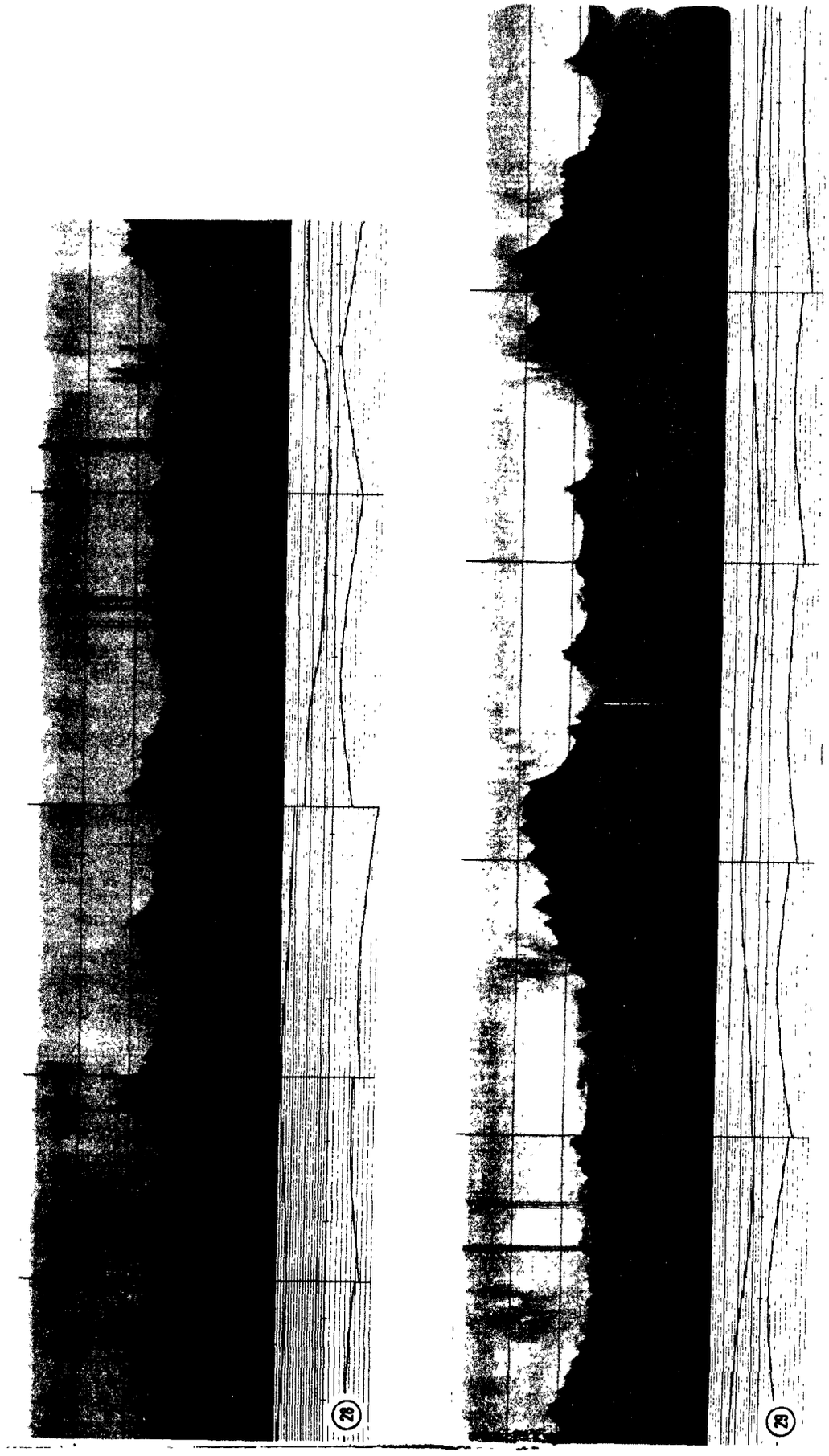


30


31

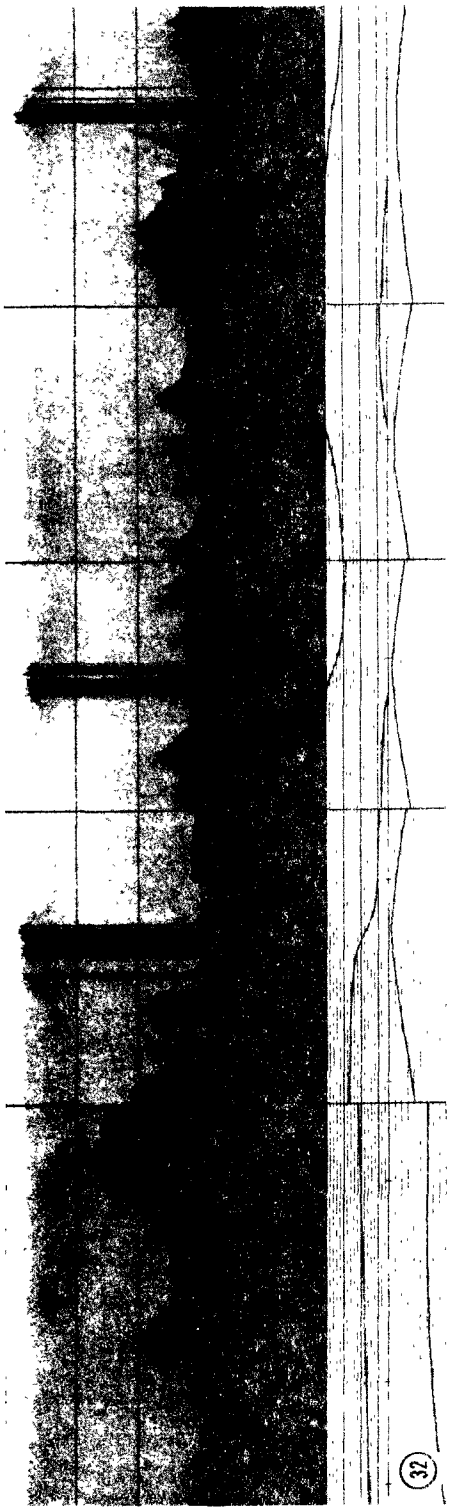
32

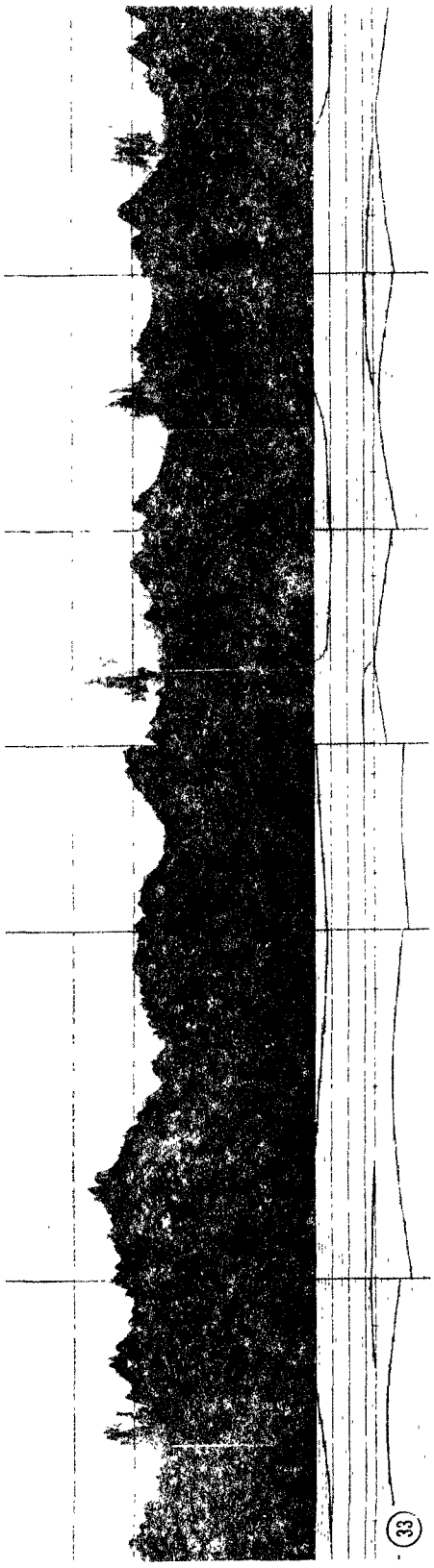
33


34

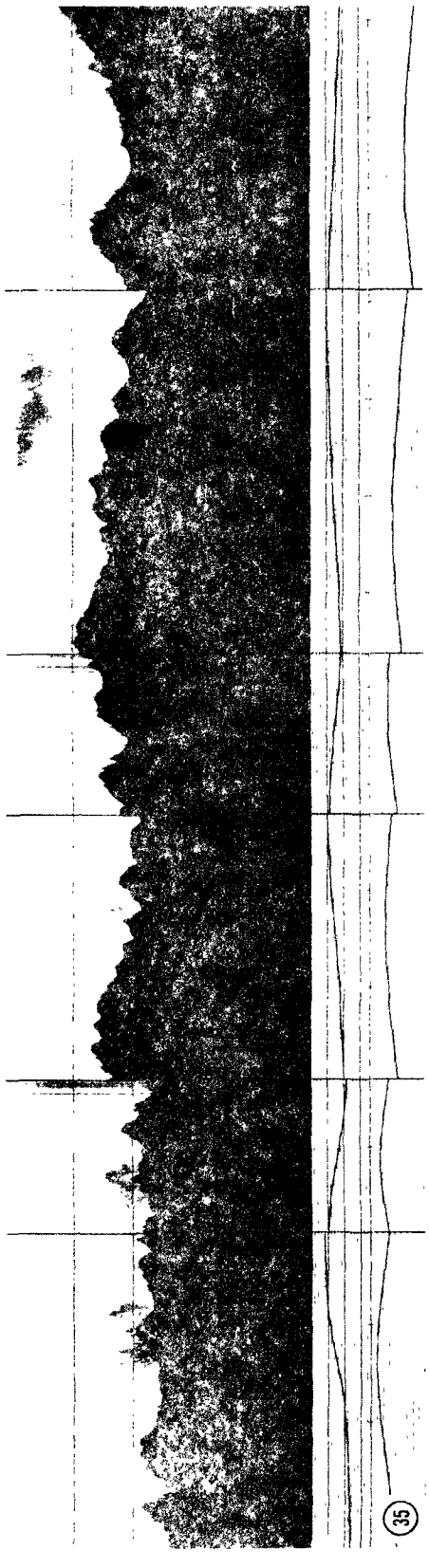
35

(36)

(37)


38


39

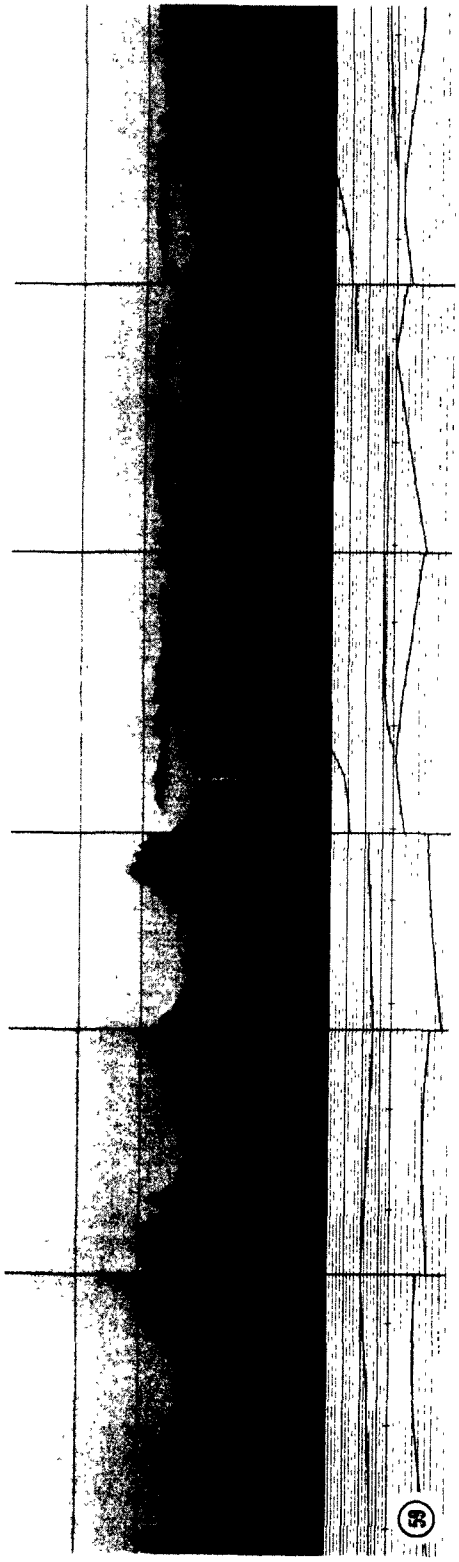

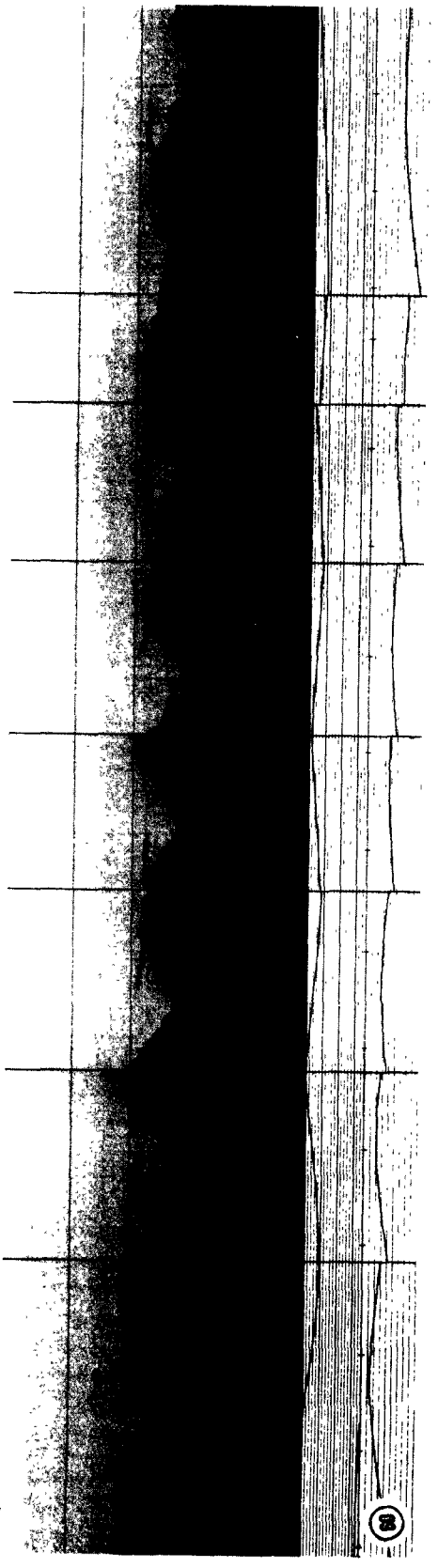
60

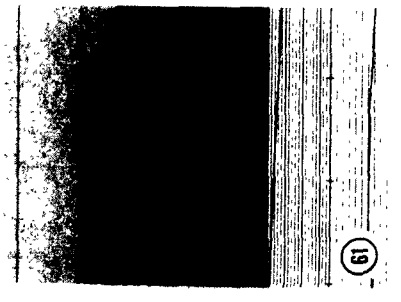
61

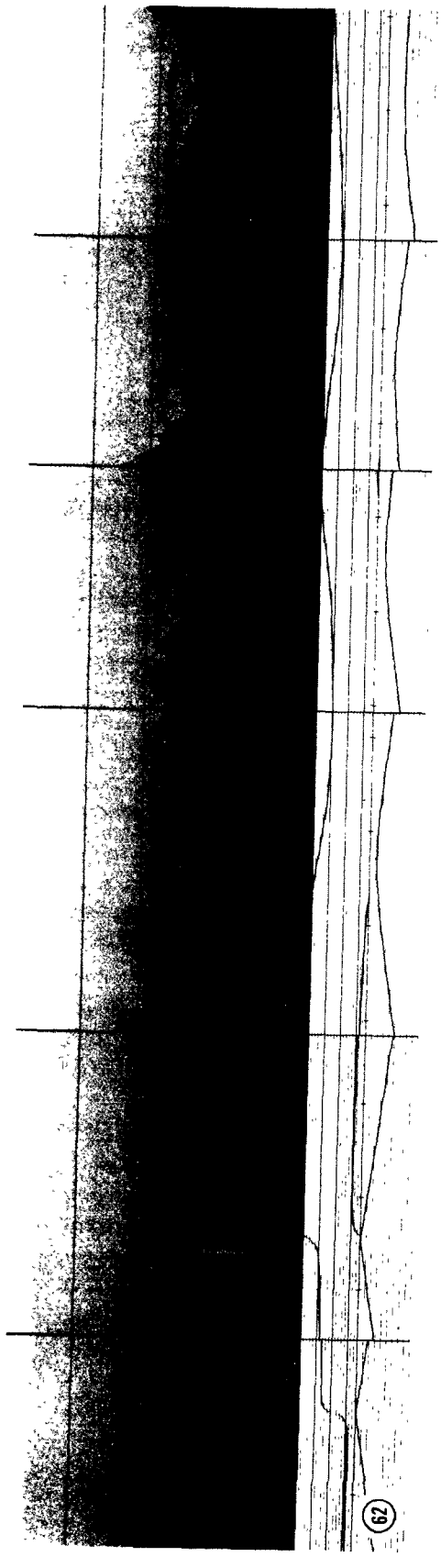
62

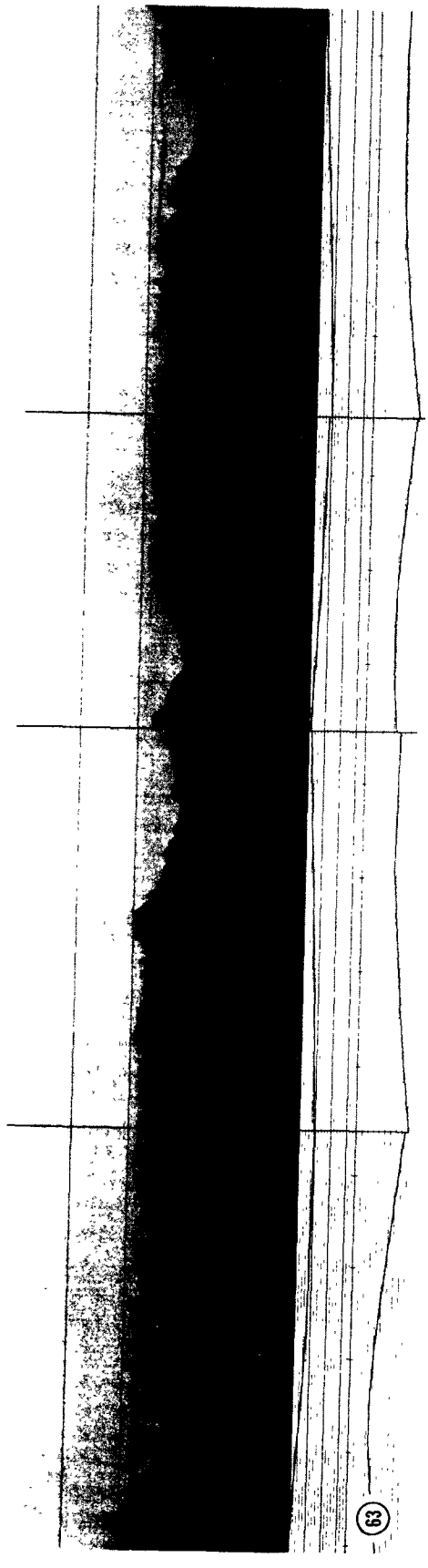
63

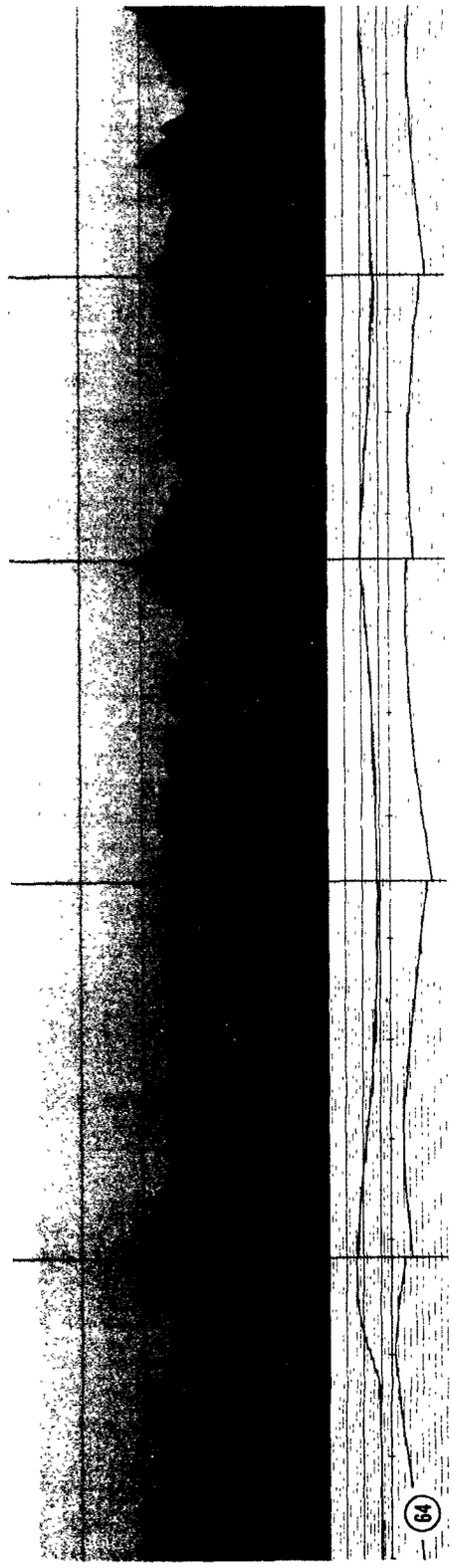
64

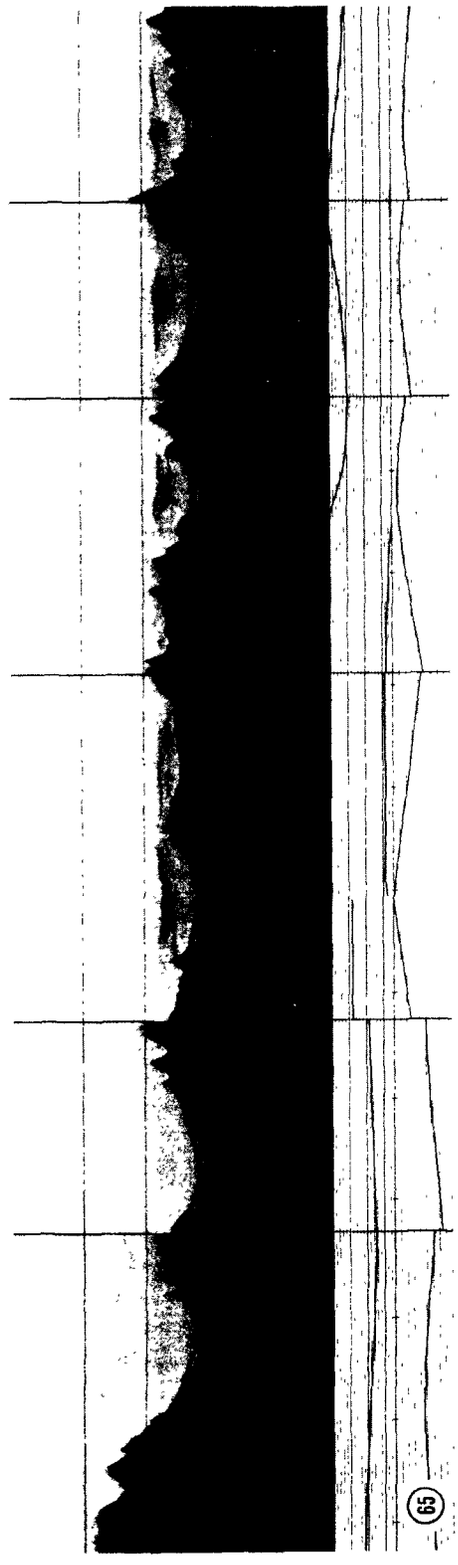
65

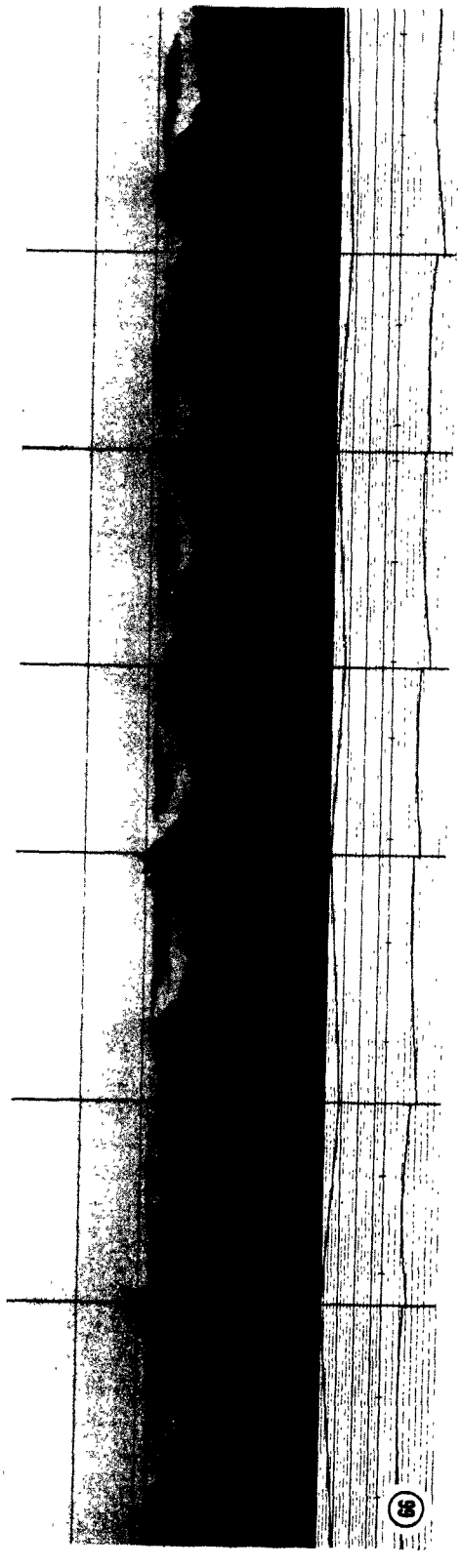
66

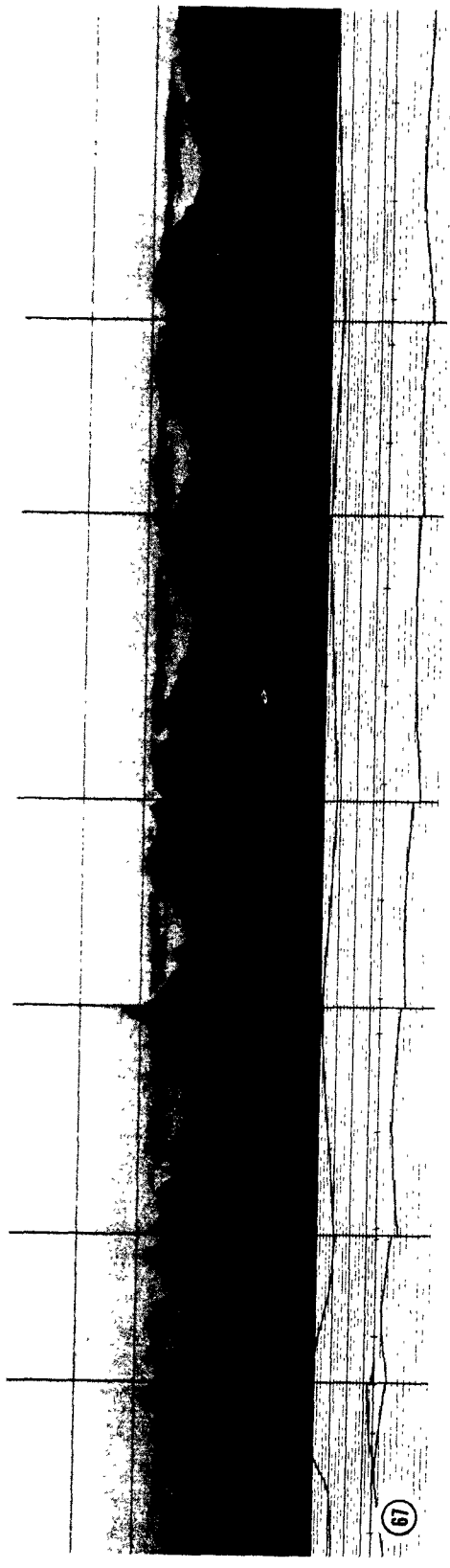
67


68

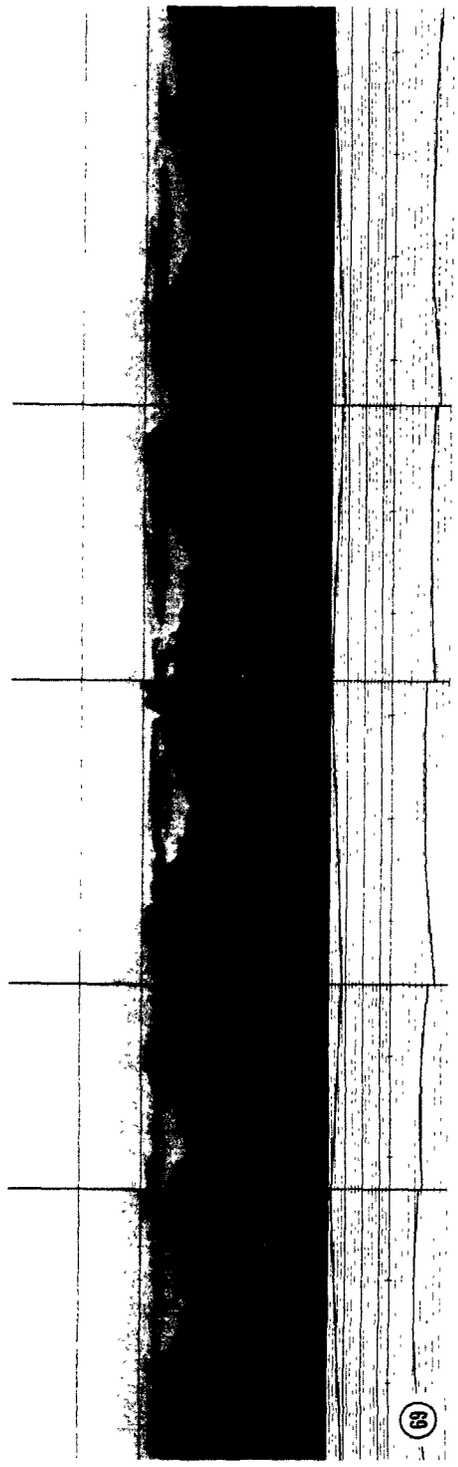
69

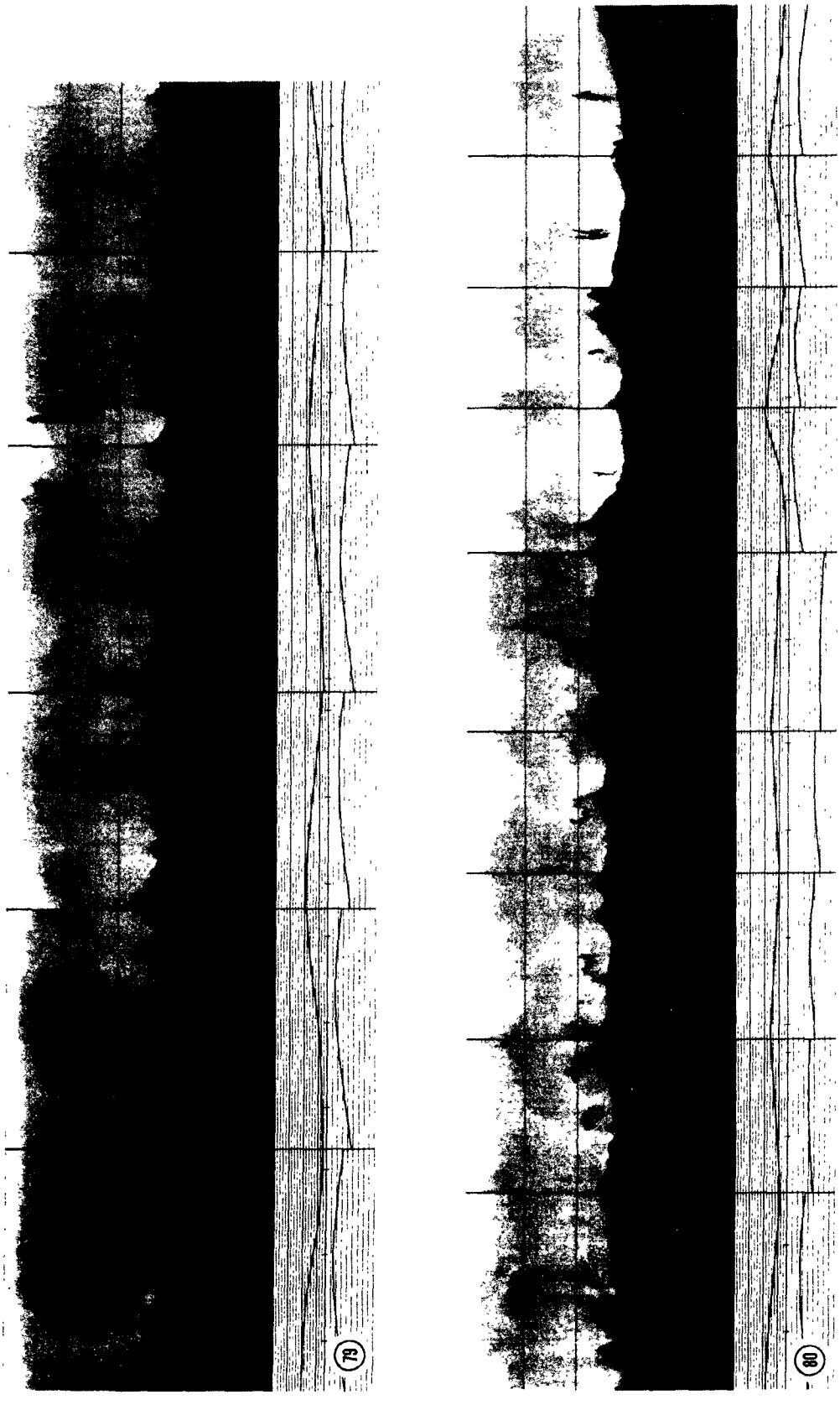
84
80

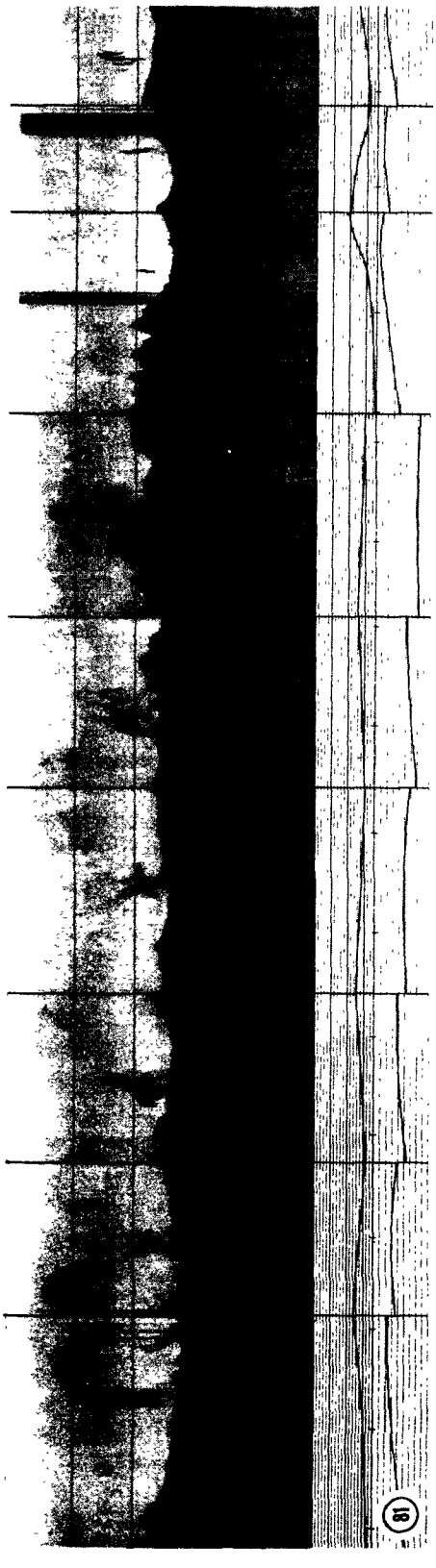
81


82

REFERENCES FOR APPENDIX C

Uthe, E.E., N.B. Nielsen, and W.L. Jimison 1980a: "Airborne Lidar Plume and Haze Analyzer (ALPHA-1)," Bull. Amer. Meteorol. Soc., 61, 1035-1043.

Uthe, E.E., W.L. Jimison, and N.B. Nielsen 1980b: "Development of an Airborne Lidar for Characterizing Particle Distribution in the Atmosphere," Final Report, EPRI No. EA-1538, SRI International, Menlo Park, CA.

Uthe, E.E. and B.M. Morley 1984. Alpha-1 Observations of Plume Behavior for PMV&D Tracy Site, prepared for Electric Power Research Institute, Palo Alto, California.

U S GOVERNMENT PRINTING OFFICE—559-013/20008